Winter 2023

Role of Peripheral Contacts in Structure and Function of c-Type Cytochromes

Dong Woo Shin
dong.woo.shin.gr@dartmouth.edu

Role of Peripheral Contacts in Structure and Function of *c*-Type Cytochromes

A Thesis

Submitted to the Faculty
in partial fulfillment of the requirements for the
degree of

Doctor of Philosophy

In

Chemistry

by

Dong Woo Shin

Guarini School of Graduate and Advanced Studies
Dartmouth College
Hanover, New Hampshire

November 2022

Examining Committee:

_____
Ekaterina V. Pletneva, Ph.D. (advisor)

_____
David S. Glueck, Ph.D.

_____
Dean E. Wilcox, Ph.D.

_____
Ann M. English, Ph.D.

_____

F. Jon Kull, Ph.D.
Dean of the Guarini School of Graduate and Advanced Studies

Abstract

Structural perturbations influence many properties of proteins, but sequence variations are frequently observed in nature without perturbing the overall stability, fold, and function. In this thesis work, heme proteins cytochrome *c* and c_2 have been used to provide insight into the relationship between peripheral contacts and its function.

Recent studies with pathogenic cytochrome *c* mutations G41S and Y48H, and growth-inhibiting mutation K72A, have highlighted the importance of contacts between loops C and D in function of the protein. Characterization of these variants shows that loop D local stability and dynamics are altered upon loop C perturbation, influencing electron transfer, alkaline transition, and peroxidase activity. Effects of these structural perturbations are different for human and horse heart proteins. Computational models suggest these differences may depend on whether the native peripheral contacts involving loops C and D are preserved. These contacts are also important for the cooperative acid unfolding transition.

Loop D packs closely to the 60's helix, forming additional intermolecular contacts for the protein to fold into a compact state with a Met80-ligated 6-coordinate heme iron. Y67R mutation perturbs these inner peripheral contacts and triggers a conformational rearrangement to induce Lys-ligation. Conformational rearrangements are important in cytochrome *c*. Interaction between cardiolipin and cytochrome *c* breaks up native peripheral contacts, which triggers a conformational rearrangement that enhances peroxidase activity so the protein functions as a peroxidase instead of an electron carrier. The heme ligation state of the species responsible for the increased peroxidase activity has been under debate. Characterization of Y67H, a variant that readily forms bisHis-ligation

upon structural perturbation, suggests that bisHis-ligated species is not the species responsible for the enhanced peroxidase activity.

Peripheral contacts are key participants in the proton-coupled electron transfer mechanism of cytochrome c_2, an electron carrier in the bacterial photosynthetic electron transfer pathway. A calorimetric characterization of *Rhodospirillum rubrum* cytochrome c_2 suggests that His42, a residue hydrogen-bonded to heme propionate 7, participates in proton transfer and is responsible for the pH-dependent reduction potential.

Preliminary studies designed to probe the relationship between peripheral contacts and the heterogeneity of unfolded states are also discussed.

Acknowledgements

This thesis work would not have been completed without help and support from many individuals. First and foremost, I am grateful to my advisor, Professor Kate Pletneva for her guidance throughout my journey. She never ceased to amaze me with her insight and suggestions when there were roadblocks—something that occurred frequently. I learned a lot and am truly thankful to her for providing me the opportunity to grow as a scientist.

I would also like to express gratitude to my committee members (past and present), Professors David Glueck, Dean Wilcox, and Jane Lipson. They were available for help outside of scheduled meetings, for which I am extremely grateful. I vividly remember how Professor Glueck patiently took his time to show me how to search compounds on SciFinder, Professor Wilcox showed me the art of re-sealing EPR tubes, and Professor Lipson helped me to get into the habit of re-deriving equations. I also want to thank Professor Ann English for agreeing to take time out of her schedule to serve as an external examiner.

I also thank Dr. Alexandre Pletnev for synthesizing photosensitizers, Professor Robert Ditchfield for taking his time out to answer questions about weighing errors, and Professor Michael Ragusa for helping me troubleshoot vesicle preparation methods. Without their help, research would have been much more arduous.

Most of my time at Dartmouth was spent with fellow members in the Pletneva lab, Dr. Fangfang Zhong, Dr. Xiaolei Chen, Dr. Jie Gu, Dr. Yunling Deng, and Jessica Carpenter. They were wonderful colleagues to discuss science, collaborate, and troubleshoot problems with. I also thank members in the Wilcox lab, Dr. Michael Cukan, Kaitlyn Connelly, and Dr. Matthew Mehlenbacher, who also provided invaluable insight and help.

The departmental staff kept everything in order and functional; Phyllis Ford, Jean Carlan, and Charlie Ciambra have been especially helpful.

I could not be more thankful for the love and encouragement from my parents. Without their help and support, I would not have made it this far.

Table of Contents

List of Tables

List of Figures

List of Commonly Used Abbreviations

AcMP	*N*-acetyl Microperoxidase
ABTS	2,2'-azino-bis(3-ethylbenzothiazoline-6-sulfonic acid)
ACES	*N*-2(2-Acetamido)-2-aminoethanesulfonic acid
bisTris	2-[Bis-(2-hydroxyethyl)-amino]-2-hydroxymethyl-propane-1.3-diol
CcO	Cytochrome *c* Oxidase
CD	Circular Dichroism
CL	Cardiolipin
CT	Charge-transfer
Cyt	Cytochrome
DTPA	2-[Bis[2-bis(carboxymethyl) amino]ethyl]amino]acetic acid
DLS	Dynamic Light Scattering
EPR	Electronic Paramagnetic Resonance
ESE	Electron Self-exchange
ET	Electron Transfer
GCE	Gel Calomel Electrode
GuHCl	Guanidine Hydrochloride
HB	Hydrogen-bonding
HEPES	4-(2-hydroxyethyl)-1-piperazineethansesulfonic acid
HP	Heme Propionate
MD	Molecular Dynamics
MES	2-(*N*-morpholino)ethanesulfonic acid
MOPS	3-(*N*-morpholino)propanesulfonic acid
MP	Microperoxidase
NMR	Nuclear Magnetic Resonance
PCET	Proton-coupled Electron Transfer
PT	Proton Transfer
PDB	Protein Data Bank
R. rubrum	Rhodospirillum rubrum
RMSD	Root Mean Square Deviation

RMSF	Root Mean Square Fluctuation
ROS	Reactive Oxygen Species
SHE	Standard Hydrogen Electrode
SVD	Singular Value Decomposition
TES	2-(Tris(hydroxymethyl)methylamino)ethane-1-sulfonic acid
Tm	Trimethylated
Tris	2-amino-1-(hydroxymethyl)-1,3-propanediol
UV	Ultraviolet
vdW	van der Waal
WT	Wild-type

Chapter 1

Introduction

Metalloproteins have diverse functions and are essential participants in biological processes.[1] Twenty amino acids and select transition metals form metalloproteins, and diversity in function is provided, in part, by structural variations of the polypeptide chain.[1] The residues in the polypeptide chain provide coordinating ligands to the metal, and polypeptide fold alters the geometry of the metal complex, which tunes the chemical properties of the metal center.[2] For example, in heme proteins that participate in electron transfer (ET) pathways, the reduction potential of the metal center can change dramatically depending on whether one of the axial ligand is methionine or cysteine.[1, 2] More modest changes can also influence the properties of the metal site.

Besides alterations in the first coordination sphere, changes in the secondary coordination sphere can dramatically alter the chemical properties of the metal and influence protein function. Changes within the polypeptide chain can tune the solvent exposure, environment, and electronic properties of the metal site. Such tuning is commonly observed in heme proteins. For example, myoglobin with a 5-coordinate heme iron behaves as small molecule transporters.[3] On the other hand, peroxidases also with a 5-coordinate heme iron efficiently bind and utilize H_2O_2 to oxidize biological substrates due to the presence of catalytic amino acids in the secondary coordination sphere that are absent in myoglobin.[3] Modifications in the secondary coordination sphere do not have to be directly adjacent to the metal center. Changes in distal contacts of the polypeptide chain have been shown to tune the enzymatic activity in peroxidases.[1, 4, 5] Furthermore, comparisons between structurally similar and related proteins from thermophilic, mesophilic, and psychrophilic organisms have suggested that changes in peripheral contacts between residues on the surface of the protein modify thermodynamic and kinetic

properties of the folded polypeptide chain, which ultimately influence the enzymatic properties of the protein.[6-8]

The relationship between function and modification in intraprotein peripheral contacts is of particular interest. Although changes in the secondary coordination sphere and peripheral contacts can have dramatic effects on protein function, these changes are generally well tolerated. Sequence variations are frequently observed in nature without radically changing the metal coordination geometry or the global structural and functional properties of the protein.[1, 2] Yet, comparisons of proteins containing sequence variations show that, although *similar*, thermodynamic and kinetic properties are *varied* in proteins from different species. Such variations suggest that sequence variations introduce local variations that alters properties in the protein. Further, it is unclear why some changes in peripheral contacts are tolerated while others are not, and how these sequence variations translate to altering thermodynamic and kinetic properties of the polypeptide.

Thesis Objectives and Outline.

c-type cytochromes, mitochondrial cytochrome *c* (cyt *c*) from horse, human, and yeast, and *Rhodospirillum rubrum* (*R. rubrum*) cytochrome c_2 (cyt c_2), are used as models to explore how peripheral contacts tune protein function. A brief overview of cyt *c*, a multifunctional protein whose structure and function have been well-documented in a variety of species, is introduced in Chapter 2. The bulk of the experimental work presented in this thesis focuses on horse heart cyt *c*. Studies with cyt *c* probe the structure-function relationship commonly observed in metalloproteins and show that preservation of the overall structure (polypeptide fold as well as metal ligation and geometry) do not necessarily indicate that the function is unaffected. Mutational studies are conducted to

explore how variations in peripheral contacts are reflected in the local (and at times, global) thermodynamic and kinetic properties of the protein, and how these changes affect function. Cyt c_2 is studied to illustrate how perturbations in peripheral contacts modify proton-coupled electron transfer (PCET) properties.

Cyt *c* has loosely structured loops C and D near the heme that also contain varied sequences when compared across species. Chapter 3 explores how peripheral contacts in loop C of cyt *c* tune the local polypeptide stability, dynamics, and peroxidase activity of the protein. Wild-type (WT) cyt *c* proteins from human, horse heart, and yeast are compared through molecular dynamics (MD) simulations and previous literature results. These comparisons are then used to explain the differential responses of human and horse heart cyt *c* to structural perturbations introduced by hereditary thrombocytopenia mutations. Chapter 4 describes how perturbations in the loop regions affect the ET properties of cyt *c*. This chapter highlights that even with a similar heme ligation, peripheral changes at or near loop D and the heme can affect the ET properties of the protein.

Previous mutational studies with yeast cyt *c* have shown that peripheral contacts to the heme propionate (HP) "staples" loops C and D, promoting the native fold with a Met-ligated heme iron.[9] Depending on the pH, cyt *c* undergoes multiple conformational rearrangements, and these peripheral contacts near HP have been suggested to play a role. Chapter 5 presents the characterizations of cyt *c* variants during acid-induced unfolding.

In cyt *c*, the identity of the 6th axial heme iron ligand is critical in tuning the reduction potential of the iron center and in switching the protein function from an electron carrier to a peroxidase. Many residues in loop D can act as heme iron ligands, and its fold

is essential in determining the residue that coordinates to the heme iron. Chapter 6 discusses how tertiary contacts modulate native packing and heme iron ligation.

Although many sequence variations are present in the vicinity of the heme in cyt *c* across many species,[10] only a selected set of amino acids is observed at residue locations where sequences do vary. Chapter 7 illustrates how certain residues alter the function of the protein even if it does not alter the heme iron ligation or the native polypeptide fold. Discrepancies in Lys- and His-ligated heme iron species reported in the literature are also explored in Chapters 6 and 7, respectively.

Importance of peripheral contacts and roles of residues near the HP groups of other cytochrome proteins is highlighted in Chapter 8 with *R. rubrum* cyt c_2, a bacterial cytochrome that has been suggested to have a PCET mechanism due to its pH-dependent reduction potential.[11, 12] Previous studies with *R. rubrum* cyt c_2 have suggested that the peripheral interaction between one of the HP group and a histidine residue (His42) plays a role in the PCET mechanism, with either His42 and/or the HP acting as the ionizable group. However, it has been difficult to characterize this mechanism by NMR spectroscopy, as shifts in signals can stem from changes in ionization and conformational changes in the polypeptide packing unrelated to PCET mechanism. To avoid these complications, a calorimetric characterization of PCET mechanism in cyt c_2 has been attempted.

Many proteins interact with lipids, and cyt *c* is of no exception. In cells, the interaction of cyt *c* with the mitochondrial membrane promotes the functional switch in cyt *c* from an electron carrier to a peroxidase. Appendix I describes attempts at probing whether structural perturbations near the heme alter the conformational ensemble in the lipid-bound state. Preliminary spectral measurements have shown discrepancies between

different spectroscopic measurements, requiring further optimization in sample preparation. The effects of different lipid preparations on spectroscopic features are also presented in this Appendix.

The polypeptide of cyt *c* accesses multiple conformations in the unfolded state, some of which are stabilized when histidine residues in the polypeptide coordinate to the heme iron.[13] This tendency for His residues to coordinate to the heme iron can have potential effects in many mutational studies with cyt *c* where His residues are introduced in the polypeptide chain. Additional spectroscopic measurements of variants with non-native histidine residues at positions 48 or 67 are presented in Appendix II. Variation is observed in the folded state for one of the variants., most likely due to the local structural perturbation in the folded state when the non-native His residue is introduced. In contrast, differences between variants are more pronounced in the unfolded state, highlighting the conformational heterogeneity of the unfolded state. It is most likely that the introduction of non-native His residue in the polypeptide stabilizes different polypeptide conformations depending on the location in the polypeptide chain, suggesting that some unfolded conformations are favored over others.

References

1. Bertini, I., Gray, H.B., Stiefel, E.I. & Valentine, J.S. *Biological inorganic chemistry : structure and reactivity*. (University Science Books, Sausalito, Calif.; 2007).

2. Liu, J. *et al.* Metalloproteins containing cytochrome, iron-sulfur, or copper redox centers. *Chem Rev* **114**, 4366-4469 (2014).

3. Poulos, T.L. Heme Enzyme Structure and Function. *Chem Rev* **114**, 3919-3962 (2014).

4. Nagano, S., Tanaka, M., Ishimori, K., Watanabe, Y. & Morishima, I. Catalytic roles of the distal site asparagine-histidine couple in peroxidases. *Biochemistry* **35**, 14251-14258 (1996).

5. Rodriguez-Lopez, J.N., Smith, A.T. & Thorneley, R.N.F. Recombinant horseradish peroxidase isoenzyme C: the effect of distal haem cavity mutations (His42→Leu and Arg38→Leu) on compound I formation and substrate binding. *JBIC Journal of Biological Inorganic Chemistry* **1**, 136-142 (1996).

6. Smalas, A.O., Heimstad, E.S., Hordvik, A., Willassen, N.P. & Male, R. Cold adaption of enzymes: structural comparison between salmon and bovine trypsins. *Proteins* **20**, 149-166 (1994).

7. Gerday, C. *et al.* Psychrophilic enzymes: a thermodynamic challenge. *Biochim Biophys Acta* **1342**, 119-131 (1997).

8. Lonhienne, T., Gerday, C. & Feller, G. Psychrophilic enzymes: revisiting the thermodynamic parameters of activation may explain local flexibility. *Biochim Biophys Acta* **1543**, 1-10 (2000).

9. Deng, Y., Weaver, M.L., Hoke, K.R. & Pletneva, E.V. A Heme Propionate Staples the Structure of Cytochrome c for Methionine Ligation to the Heme Iron. *Inorg Chem* **58**, 14085-14106 (2019).

10. Moore, G.R. & Pettigrew, G.W. *Cytochromes c : evolutionary, structural, and physicochemical aspects*. (Springer-Verlag, Berlin ; New York; 1990).

11. Pettigrew, G.W., Bartsch, R.G., Meyer, T.E. & Kamen, M.D. Redox potentials of the photosynthetic bacterial cytochromes c2 and the structural bases for variability. *Biochim Biophys Acta* **503**, 509-523 (1978).

12. Carpenter, J.M. in Chemistry, Vol. Bachelor of Science (Dartmouth College, Hanover, NH; 2018).

13. Colon, W., Wakem, L.P., Sherman, F. & Roder, H. Identification of the predominant non-native histidine ligand in unfolded cytochrome c. *Biochemistry* **36**, 12535-12541 (1997).

Chapter 2

Cytochrome *c*

_c_-type Cytochromes.

_c_-type cytochromes are Fe-containing heme proteins that have a covalently bound _c_-type porphyrin with an Fe center, usually with one or two amino acid ligands provided by the polypeptide chain to serve as axial ligands to the metal ion (Figure 2.1). Depending on the axial ligand, the reduction potentials of Fe-containing hemes can vary widely, and cytochromes are commonly found as participants in ET reactions. In particular, mitochondrial cyt _c_ in the cytochrome family of proteins is a well-studied protein where much is known about its function, folding, and structure.[1, 2]

Cyt _c_ is a multi-functional protein that can switch its function from an electron carrier in the biological electron transfer chain (ETC) to a peroxidase to initiate apoptosis (programmed cell death) in many organisms (Figure 2.2).[3] These functions are regulated by structural properties that differ in ligation and fold of the protein. Cyt _c_ is present in the intermembrane space of the mitochondria and transfers electrons between the Fe heme in cytochrome bc_1 (cyt bc_1) and the Cu_A center in cytochrome _c_ oxidase (CcO).[1, 4] In the presence of cardiolipin (CL) and reactive oxygen species (ROS), such as H_2O_2, structural change occurs within cyt _c_, activating the secondary function of the protein as a peroxidase that oxidizes the mitochondrial membrane to allow the release of cyt _c_ into the cytosol (Figure 2.2).[5] Depending on the oxidation state of the protein, cyt _c_ in the cytosol interacts with Apaf-1 and forms the apoptosome complex that initiates apoptosis.[6-10] In some organisms such as yeast, apoptosis can be triggered independent of cyt _c_.[9, 11] These different functions in cyt _c_ make it a good model to correlate how intermolecular contacts alter the global and local properties of the protein, and how these structural changes are relayed to affect protein functions.

Figure 2.1. (Left) A molecular depiction of a *c*-type heme (heme *c*), in the *x*, *y*-plane. In class I *c*-type cytochromes, His and Met serves as axial ligands to the heme iron (through the *z*-axis according to the depiction, with His on the bottom and Met on the top of the *x*, *y*-plane). In hemoproteins containing *c*-type hemes, the heme moiety is covalently linked to Cys residues in the polypeptide chain. In cyt *c* and cyt c_2, solvent-exposed heme edge is located on the side of the heme porphyrin with heme propionate 6 (HP6). (Right) Range of reduction potentials in proteins and model compounds with *c*-type hemes. Type of axial ligands can tune the reduction potential of the heme iron, as observed in microperoxide-11 (MP11, contains heme with a 11-residue peptide chain containing His18 and Cys-linkers).[12] In class I *c*-type cytochromes with His/Met coordination, reduction potential can range from 450 mV to -80 mV.[13] Depending on the polypeptide fold and heme iron ligation, an even wider range of potentials can be observed as exemplified by Met-ligated (native) cyt *c*,[12, 14] Lys-ligated (alkaline) cyt *c*,[12] bisHis-ligated (imidazole bound) cyt *c*,[12] and H_2O-ligated cyt *c* in the molten globular (MG) state.[15] Other relevant reduction potentials of CcO,[16] cyt bc_1,[17] and cyt c_2,[18] are also shown.

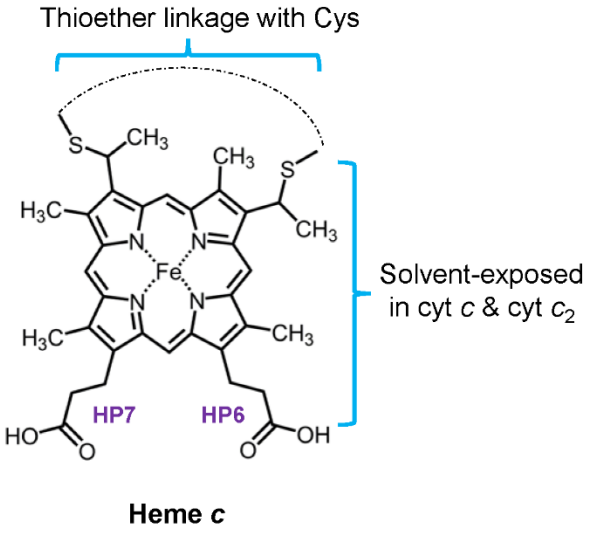
Thioether linkage with Cys
Solvent-exposed
in cyt c & cyt c2
HP7
HP6
Heme c

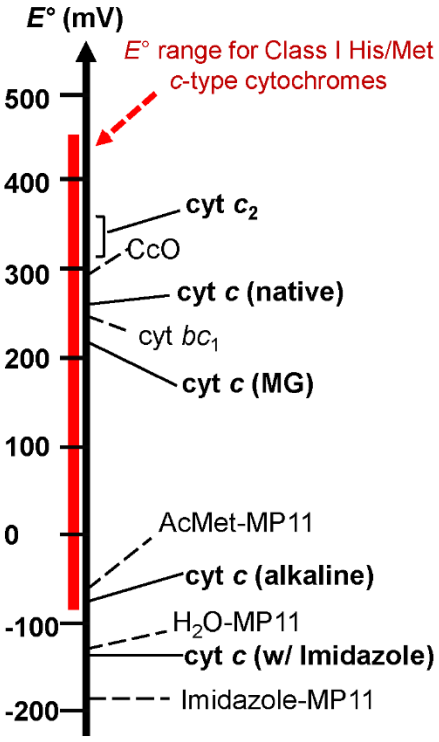
E° (mV)
E° range for Class I His/Met
c-type cytochromes
500
400
300
200
100
0
-100
-200
cyt c2
CcO
cyt c (native)
cyt bc1
cyt c (MG)
AcMet-MP11
cyt c (alkaline)
H2O-MP11
cyt c (w/ Imidazole)
Imidazole-MP11

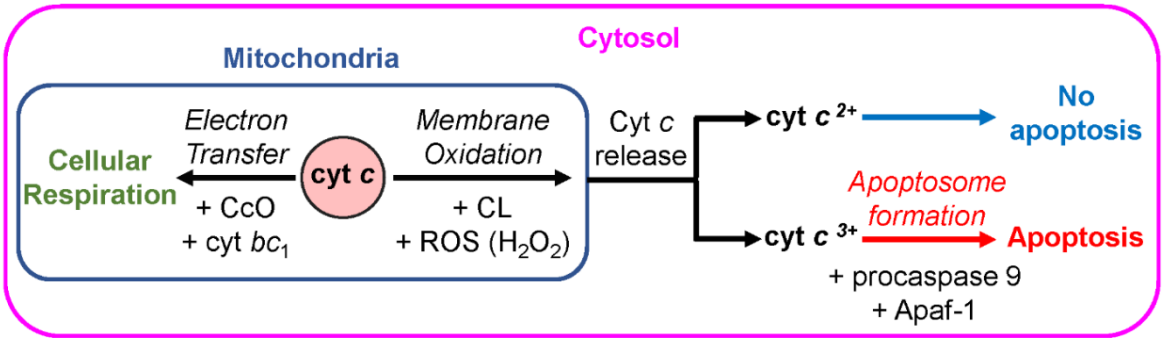

Figure 2.2. A schematic depicting the biological function of cyt *c* in cellular respiration and apoptosis in many organisms, including mammals, based on refs. [4, 8, 13]. Cyt *c* primarily shuttles electrons between complex III (cyt bc_1) and complex IV (CcO) of the oxidative phosphorylation pathway in the mitochondria.[13] Cyt *c* is also involved in the initial steps leading to programmed cell-death (apoptosis).[5] In the presence of CL and ROS, cyt *c* oxidizes the mitochondrial membrane to promote cyt *c* release into the cytosol.[19] Ferric cyt *c* (cyt c^{3+}) binds with Apaf-1, forming the apoptosome complex that activates procaspase 9, required to initiate the caspase cascade that leads to apoptosis.[7, 8] On the other hand, ferrous cyt *c* (cyt c^{2+}) cannot initiate the caspase cascade and does not induce apoptosis.[8]

Furthermore, cyt *c* has been widely studied in multiple organisms, including horse, yeast, and human. Comparing cyt *c* from various organisms provides an insight as to how natural sequence variations influence the structural and functional properties.

Cyt *c* Structure.

Mitochondrial cyt *c* is a small, globular ~12 kDa protein that contains a *c*-type heme covalently linked to the polypeptide chain.[1, 2] In the pH range from 3.5 to 8, Met and His from the polypeptide chain act as axial ligands to the heme iron (native state).[20] Like cyt *c* from other organisms, horse heart cyt *c* is composed of five α-helical segments, a short β-sheet segment, and three loosely structured loop regions. Folding regions (foldons) have been identified from extensive hydrogen-exchange (HX) experiments with horse heart cyt *c*: blue foldon comprised of *N*- and *C*-terminal helices, green foldon comprised of 20's loop and 60's helix, yellow foldon comprised of anti-parallel β-sheet, red foldon comprised of loop D, and infrared foldon comprised of loop C (Figure 2.3).[21-24] These foldons differ in stability, and have been shown to fold in a cooperative manner at near neutral pH conditions.[21-23, 25, 26] Intermolecular contacts between these foldons have been shown to promote cooperativity in folding of cyt *c*.[26] Perturbation in these contacts leads to subsequent loss in cooperativity, as observed at lower pH conditions where protonation of residues severed key hydrogen-bonding contacts.[27] The least stable foldons, loops C and D (Figure 2.3 left, with loops colored white and red, respectively), have been observed to fold independently of one another.[26] These two loops are of particular interest as their thermodynamic and kinetic properties are involved in pH-dependent conformational rearrangements.[28, 29]

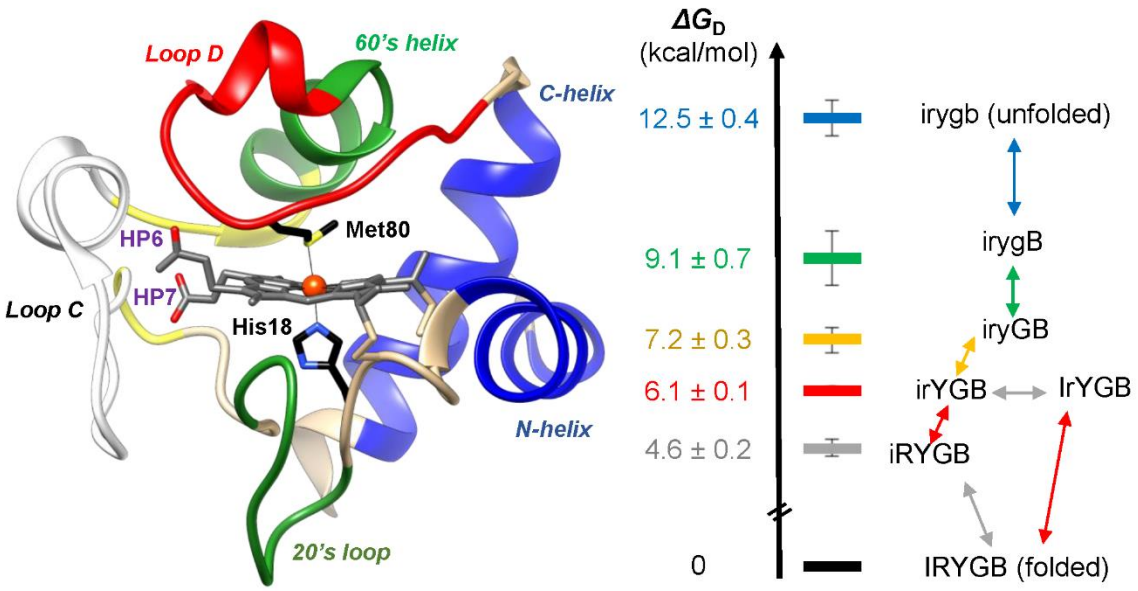

Figure 2.3. (Left) X-ray crystal structure of horse heart cyt *c* (PDB ID: 1HRC).[30] Highlighted are residues according to the color assignments used in classifying the foldons of cyt *c*, based on HX experiments:[21] in *N*- and *C*-terminal helices, residues 3 to 13 and 88 to 101, respectively (blue), in 20's loop and 60's helix, residues 20 to 30 and 62 to 70, respectively (green), in anti-parallel β-sheet region, residues 37 to 39 and 58 to 61 (yellow), in loop C, residues 40 to 57, also referenced as infrared (iR) foldon (white), and in loop D, residues 71 to 85 (red). In this thesis, residue 70 is included as a residue that makes up loop D, as the secondary structure prediction includes residue 70 in the α-helical segment in loop D, and HX experiments did not assign residue 70 as a marker residue in determining the foldon units.[22-24, 31] (Right) Gibbs free energy for unfolding (ΔG_D in kcal/mol) as determined from HX experiments at pD 7.4 for WT horse heart cyt *c* from refs. [22-24]. A schematic depicting the sequential folding pathway for WT horse heart cyt *c* from refs. [21-23, 25, 26]. Loops C and D have been suggested to unfold separately,[26] and at lower pH conditions, unfolding of the 60's helix and the 20's loop is no longer cooperative.[27]

Such rearrangements in the polypeptide are ultimately related to the functional control of the protein, as conformational rearrangements can change heme iron ligation and alter heme potential.

Proper protein folding is important for native conformation and Met-ligation to the heme iron, which are essential properties for cyt *c* to act as an electron carrier in the ETC. Furthermore, local and global unfolding of the polypeptide can readily result in dissociation and replacement of Met-ligation to the heme iron. A soft Met is a poor ligand for the hard ferric heme iron and can be readily replaced by exogenous ligands such as imidazole and cyanide, or other endogenous ligands such as His or Lys upon structural perturbations.[32-34] Spectroscopic titrations with *N*-terminal acetylated microperoxidase 8 (AcMP8, heme with a 8-residue peptide chain that contains His18 and Cys-linkers) and *N*-acetylmethionine (AcMet) have shown that the dissociation constant for AcMet adduct of AcMP8 is two orders of magnitude lower in the ferrous heme (Fe^{II}) than in the ferric heme (Fe^{III}),[35] a difference not observed in other ligands such as imidazole or lysine.[35, 36] This does not, however, indicate that the Fe-Met bond is stronger in the ferrous Fe over the ferric Fe, and the strength of the Fe-Met bond alone does not promote native Met-to-heme iron ligation in cyt *c*. Resonance inelastic X-ray scattering measurements with horse heart cyt *c* have shown that the bond strength of Met-Fe(II) bond is weaker than that of Met-Fe(III) bond by ~2 kcal/mol, with a bond enthalpy difference of ~3 kcal/mol between the ferric and the ferrous Met-ligated species.[37] What, then, promotes Met-ligation to the heme iron in cyt *c*?

In cyt *c*, the polypeptide fold plays a role in maintaining a Met-ligated heme iron. Ultrafast X-ray spectroscopy and DFT measurements with ferrous horse heart cyt *c* have shown that structural constraints from the polypeptide stabilize the ferrous Met-Fe(II) bond

by ~4 kcal/mol in bond enthalpy.[38] Besides global polypeptide constraints, peripheral contacts also play a role in Met-ligated heme iron. Analyses of recent X-ray crystal structures of yeast cyt *c* have shown that the elimination of trimethylated Lys72 in loop D facilitates the dissociation of Met80 from the heme, suggesting that steric hinderance promotes native ligation in cyt *c*.[39] Furthermore, ligand substitution reactions of Met-ligated horse heart cyt *c* have shown that the rate-limiting step of Met-ligand dissociation is the opening of the heme crevice,[40] further suggesting that the kinetics of Met-ligand dissociation is sensitive to the local dynamic properties of loop D. Recent DFT calculations and MD simulations have shown that, depending on the identity of the endogenous ligand (such as Met, His, or Lys) and the oxidation state of the heme iron, interloop contacts between loops C and D are different.[33] Furthermore, resulting changes in solvation due to variations in these structural contacts have also been suggested to play a role in altering the stability of these ligated species.[33] Yet, variations in peripheral contacts at and around loop D are frequently observed across species in the form of sequence variation, suggesting that some variations in these contacts are tolerated.

Cyt *c* Sequence and Structure Conservation.

Alignment of horse heart cyt *c* sequence to those from > 250 species shows that the sequences of cyt *c* are highly conserved across species, with its overall sequence identity ranging from 40 to 99 %.[41] Besides the polypeptide sequence, the structure of cyt *c* is also highly conserved. Comparisons of X-ray crystal structures from mammals, fish, and bacteria show that all of these cyt *c* proteins have a highly conserved globular fold.[1]

Despite the high structural and sequence conservation, there are variations in peripheral contacts near the heme. For example, Tyr67 and Met80 are highly conserved

across species, and these residues are prominent residues in making up the heme cavity of cyt *c* (Figure 2.4). Comparisons of various X-ray crystal structures show a conserved structural water forming a hydrogen-bonding (HB) network involving residues Tyr67 and Met80 (Figure 2.4).[30, 42-44] Although observed in X-ray crystal structures of many organisms, the placement of this internal water molecule varies, and is susceptible to structural perturbations in the polypeptide. Examinations of X-ray crystal structures of cyt *c* proteins containing N52I, N52I/Y67F, and Y67F point mutations show different or lost internal water-mediated network,[45, 46] highlighting that peripheral structural perturbations may affect intramolecular contacts of the protein at or near the heme.

Mutational studies with cyt *c* have implicated peripheral contacts near the HPs and loop regions to influence protein fold.[47, 48] Much of the polypeptide fold near the heme is conserved, and cyt *c* has similar heme ligation and functional properties across species. Furthermore, many of the global properties, such as polypeptide fold and stability, are similar across species. However, although many properties are *similar*, they are not *identical*, raising the possibility that sequence variations contribute to these minor differences between cyt *c* from various species. In cyt *c*, the heme is encapsulated largely by the loosely packed 20's loop, and loops C and D (Figure 2.3). Loop D contains most of the endogenous heme iron ligands, while loop C and the 20's loop pack near the heme edge, with loop C packing tightly near HP6 and HP7. Based on the analysis of sequences from 96 species,[2] loop D is highly conserved and sequence identity ranges from 63% to 100%. In contrast, residues in both loop C and the 20's loop are more frequently varied than in loop D. In a similar sample of 96 species, sequence identity of loop C ranges from 33 to 100%, with an average sequence identity of 70%.

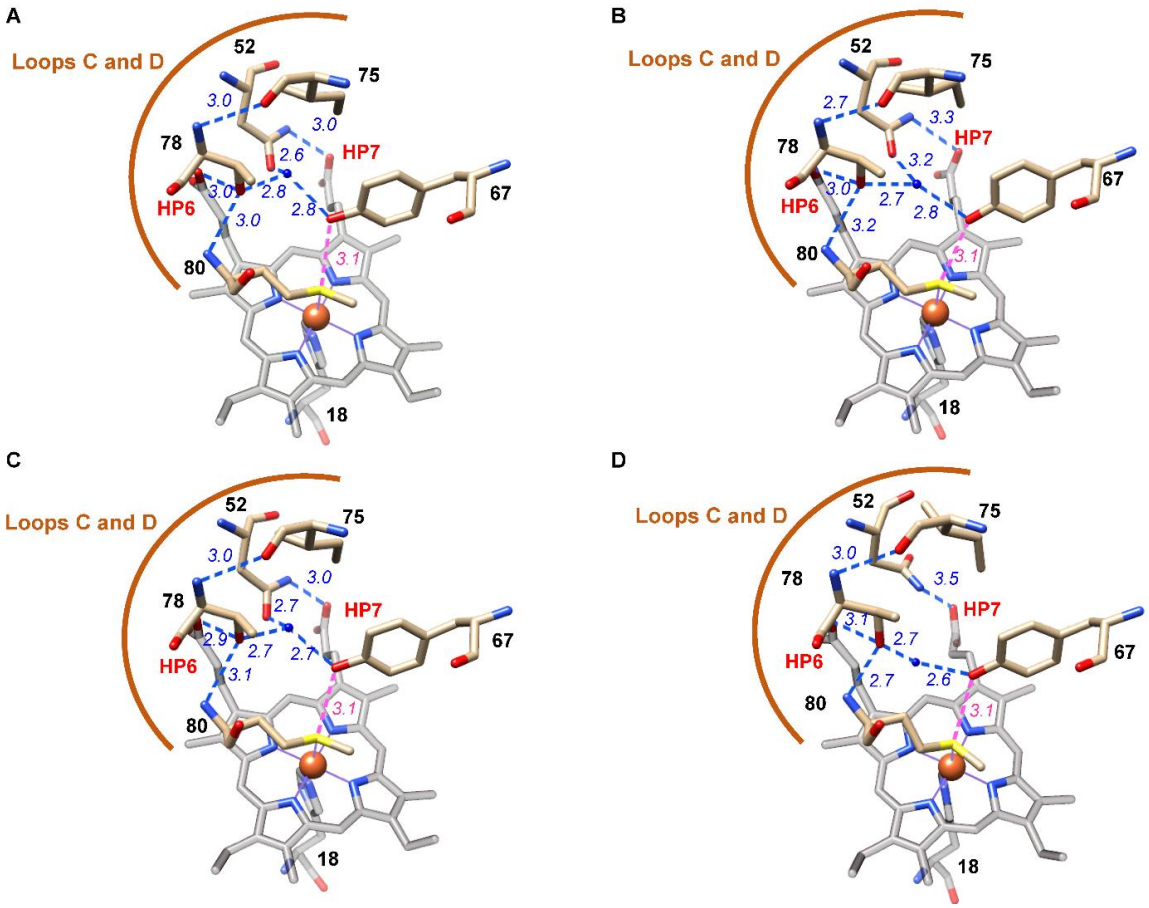

Figure 2.4. Figure showing the inner HB network in X-ray crystal structures of select WT cyt *c* from (A) human (PDB ID 3ZCF),[42] (B) horse (1HRC),[30] (C) rat (5C0Z),[43] and (D) *iso-1* yeast (2YCC).[49] Shown are the residues 67, 52, 75, 78, and 80, with HP6 and HP7. HB (blue, dotted lines) are depicted with the distances (blue, italics). Distance between oxygen of Tyr67 and sulfur of Met80 are also shown (pink, dotted line).

Like loop C, 20's loop is frequently varied across species and sequence identity ranges from 27 to 100%. Furthermore, regions where sequence variations are present may also be involved in functional tuning. In loop D, sequence variations, if present, are more commonly observed in regions containing residues 81 to 85.[41] In loop C, sequence variations are more common in regions close to HP6.[2, 41] This variation is observed even amongst mammals that usually have global (and local) higher sequence identities. For example, residues 45 to 49 in cyt *c* from human and higher apes are comparable with yeast than with other mammals, such as horse. Sequence variations in these regions adjacent to HP6 have previously been implicated in altering the various functional and dynamic properties of cyt *c*,[50] but how these variations affect the local properties of the protein requires more exploration.

pH-Dependent Conformational Changes.

Cyt *c* undergoes many structural rearrangements depending on the pH conditions, which alter the polypeptide fold, heme iron ligation, and functional properties—more so for ferric cyt *c* than in ferrous cyt *c* (Figure 2.5). There are three conformational states of ferrous cyt *c*, with pK_a values < 4 and > 12 for the acid and alkaline denatured states from the native Met-ligated state in horse heart cyt *c*.[2, 20] In contrast, there are five conformational states of ferric cyt *c*, with two distinct states at acidic and alkaline conditions that have not been observed in ferrous cyt *c*.[51] Previous HX experiments with horse heart cyt *c* have suggested that loops C and D are involved in these pH-dependent conformational rearrangements.[28, 29]

Figure 2.5. A plot showing the pH ranges potentially experienced by cyt *c* in the cell, along with pH-dependent changes in heme iron ligation experienced by WT horse heart cyt *c* (bottom).

[a]From refs. [52-54]. In U937 (human histiocytic lymphoma) cells using flow cytometry using fluorescent pH probes, pH = 7.2 ± 0.1.[52] In kidney cells using pH-sensitive fluorophore (SNARF-1), pH = 7.4.[53] In ECV304 (human urinary bladder carcinoma T24)[55] cells using fluorescent proteins, pH = 7.59 ± 0.01.[54]

[b]From ref. [53]. In kidney cells with pH-sensitive fluorophore, pH decreased from 7.4 to 7.1 ± 0.1 after 40 minutes upon introduction of a solution containing 10 mM 2-deoxy-*d*-glucose at pH 7.4 to induce metabolic inhibition.

[c]From refs. [56, 57]. In single cell hepatocytes with single cell fluorescence imagining, chemical hypoxia decreased intracellular pH from 7.4 to pH 6.1-6.5.[56] Similar acidic hypoxia observed in rat hepatocytes, intracellular pH decreased to 6.3.[57]

[d]From ref. [52]. In human lymphoma cells, exposure to TNF-α (tumor necrosis factor) for 4 hours decreased the cytosolic pH from 7.2 ± 0.1 to 5.8 ± 0.1.[52]

[e]From refs. [53, 54, 58]. In kidney cells, pH = 7.7.[53] In ECV304 cells, pH = 7.78 ± 0.17.[54] In HeLa and cardiomyocytes, pH = 7.98 ± 0.07 and 7.91 ± 0.16, respectively.[58]

[f]From ref. [54], for the IMS in the mitochondria in ECV304 cells. pH = 6.88 ± 0.09, compared to pH = 7.59 ± 0.01 in the cytosol,[54] consistent with previous observation that suggested the pH in the IMS is lower than bulk pH of the cell by 0.4 to 0.5 pH units.[59]

[g]From ref. [60], measured in human T lymphocyte cells.

Figure 2.5 caption, continued.

[h]From refs. [2, 20, 51], for horse heart WT cyt *c*. His18 can be dissociated or ligated to the ferric heme iron, depending on ionic concentrations.[61-66] At acidic conditions, pK_a of His18 is observed to range from having pK_a of 2.5 at 0.01 M Cl^- to having pK_a of 1.4 at 0.1 M Cl^-.[67]

[i]From ref. [34], determined from pH titrations monitoring the Soret absorption band of the electronic absorption spectra in a 50 mM phosphate and 4.5 M GuHCl buffer, for WT, H26Q, and H33N variants of horse heart cyt *c*.

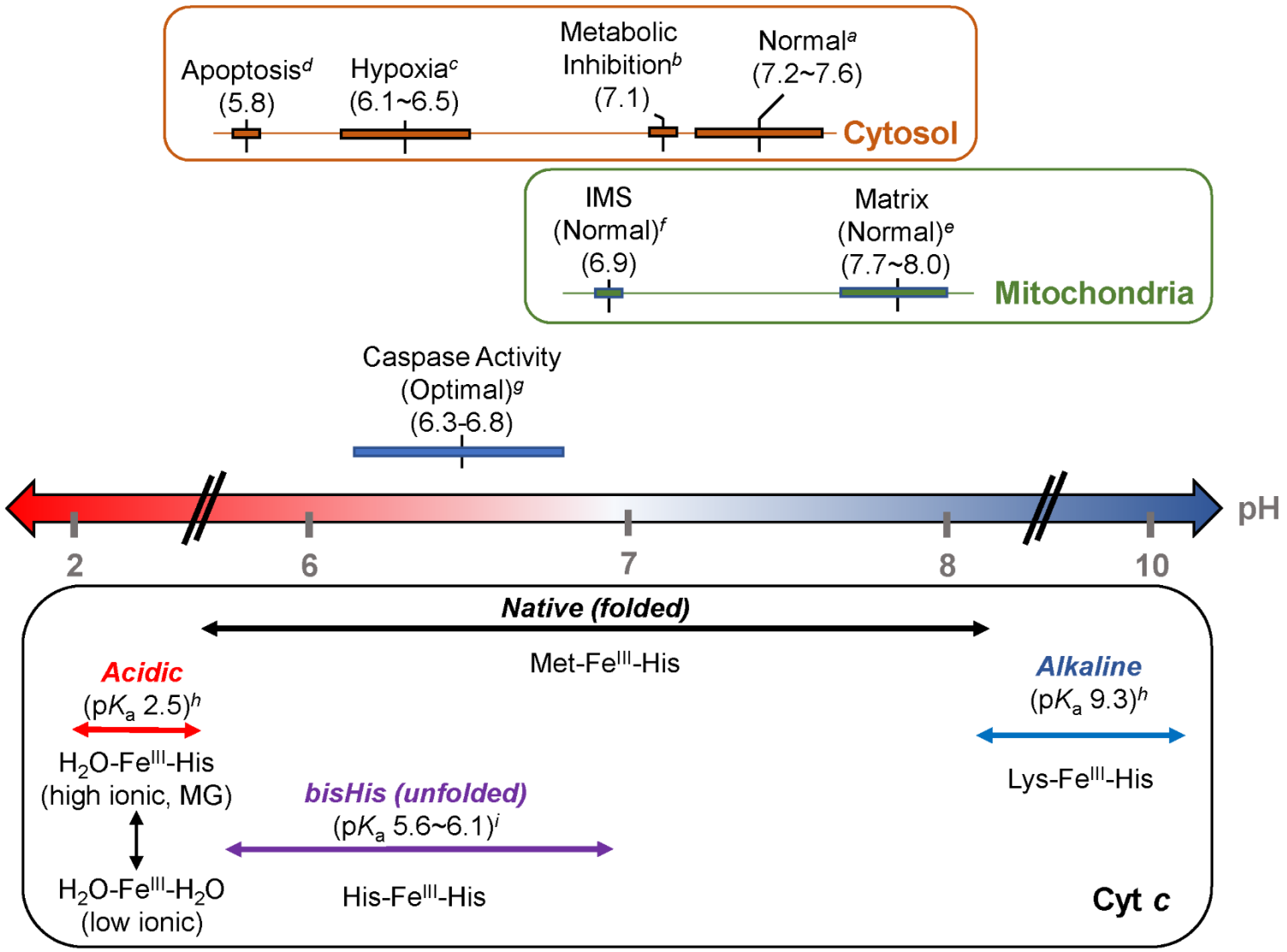
Apoptosis[d]
(5.8)
Hypoxia[c]
(6.1~6.5)
Metabolic
Inhibition[b]
(7.1)
Normal[a]
(7.2~7.6)
Cytosol
IMS
(Normal)[f]
(6.9)
Matrix
(Normal)[e]
(7.7~8.0)
Mitochondria
Caspase Activity
(Optimal)[g]
(6.3-6.8)
pH
2
6
7
8
10
Native (folded)
Met-Fe[III]-His
Acidic
(pKa 2.5)[h]
H2O-Fe[III]-His
(high ionic, MG)
H2O-Fe[III]-H2O
(low ionic)
bisHis (unfolded)
(pKa 5.6~6.1)[i]
His-Fe[III]-His
Alkaline
(pKa 9.3)[h]
Lys-Fe[III]-His
Cyt c

Acidic Transition.

Under acidic conditions, Met is no longer coordinated to the heme iron in the ferric protein. Depending on the ionic conditions, His18 can dissociate or remain ligated to the ferric heme iron,[61-66] as its pK_a can range from 2.5 at low ionic conditions to 1.4 at higher ionic conditions.[67] At high ionic conditions, molten globular (MG) state can also be observed, which lacks the Met80-ligation to the heme iron but has a native-like polypeptide packing.[2, 66-71] Polypeptide segments in loop C and the 20's loop near the HP have been implicated in triggering the acid unfolding transition in cyt *c*.[72-74]

Alkaline Transition.

At alkaline conditions, Met80 acting as a heme iron ligand in cyt *c* is replaced by a Lys residue, Lys73 or 79 in horse heart cyt *c*,[29] to form the alkaline species (Figure 2.5).[75] Replacing Met with Lys as an axial ligand to the heme iron requires partial unfolding and refolding of loop D.[29] Yet, the extent of loop D arrangement is different depending on which Lys residue coordinates to the heme iron. Comparison of simulated structures of Lys 73- and 79-ligated yeast cyt *c* suggests that replacing Met with Lys73 requires a substantial structural rearrangement in loop D, compared to replacing with Lys79.[76] Analysis of the ^{1}H NMR structure of Lys73-ligated K72A/K79A/C102T yeast cyt *c* have shown that large structural changes in loop D are required to accommodate Lys73 ligation to the heme iron.[77] Examination of the X-ray crystal structure of Lys73-ligated T78C/K79G yeast cyt *c* variant shows that loop D refolds into a β-hairpin structure.[78] Difference in loop rearrangements with heme iron ligation is reflected in the thermodynamic properties of the alkaline transition. Studies with variable-temperature ^{1}H NMR have shown that thermodynamic parameters in forming Lys73 and Lys79-ligated heme iron species in the

alkaline transition are distinct from one another, and both the entropic and enthalpic changes associated with Met80 to Lys73 conversion are close to twice of those for Met80 to Lys79 conversion.[79, 80] This contrast in both the thermodynamic parameters and the extent of loop D rearrangement in forming the Lys73- versus the Lys79-ligated species strongly suggests that the cyt *c* alkaline transition could also be sensitive to the changes in peripheral contacts involving loop D in the Met-ligated state.

Besides loop D, structural features and stability of loop C have also been implicated in influencing the kinetic properties of the alkaline transition.[28, 50] Mutational perturbations in loop C have been shown to decrease the pK_a of the alkaline transition and alter the kinetic parameters of loop D rearrangement in human cyt *c*. This change in the alkaline transition pK_a have been observed without perturbing its global fold,[81-84] suggesting that minor peripheral perturbations can influence not only the coordination environment but also alter the local biophysical properties of the protein.

Local structural differences affect the kinetic properties of the alkaline transition. Kinetic properties of the alkaline transition have been described by a generalized two-step mechanistic model (Figure 2.6, eq 2.1).[75]

$$k_{obs}=k_b+k_f \frac{K_H}{K_H+[H^+]} \quad (2.1)$$

In this model, the observed rate constant (k_{obs}) for the alkaline transition is described by the rapid deprotonation of a "trigger" group (K_H) followed by the conformational equilibrium (K_C) consisting of forward (k_f) and reverse (k_b) rates for the replacement of the Met ligand with an unspecified Lys ligand to the ferric heme iron.[75]

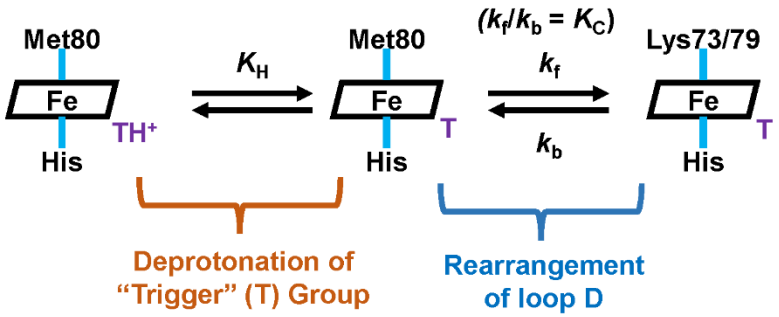

Figure 2.6. A schematic describing the alkaline transition mechanism, based on ref. [75].

The sum of the equilibrium parameters in this model yields the apparent pK_a of the alkaline transition (eq 2.2).[75]

$$pK_a = pK_H + pK_C \quad (2.2)$$

Although Lys residues are not differentiated in this model, the extrapolated parameters provide insight into how local structural properties may alter the alkaline transition.

pK_C parameter provides insight into dynamic properties of loop D, and describes the rates associated with rearranging loop D to form the Lys-ligated or the Met-ligated state. Further, this parameter is sensitive to structural changes in loop D. For example, studies with K79H yeast cyt *c* variant have shown that when trimethylated Lys72 (TmK72) is present, value of k_f associated with the alkaline transition decreases, compared to variants that contained the K72A mutation.[85] Comparison of X-ray crystal structures of yeast cyt *c* variants with either TmK72 or K72A have shown that TmK72 forms peripheral interactions with other residues in the loop, suggesting that such interactions may hinder displacement of Met80.[39] Although presence of TmK72 does not alter global stability or the global fold of the protein,[86] local structural differences affect the properties of the loop and the pK_C parameter of the alkaline transition.

On the other hand, pK_H parameter presents insights into the local structure near the "trigger" group, as this parameter is sensitive to changes in solvent-accessibility and environment. The identity of the "trigger" group has been speculated, and HP groups,[87, 88] Tyr67,[89] inner water molecule,[89, 90] His18,[91] or surface Lys residues[92] have been proposed to be the "trigger" group. More recently a "trigger" unit has been proposed, composed of peripheral contacts formed between residues in loops C and D.[82] Regardless of the identity,

the “trigger” group is particularly sensitive to changes in loops C and D. For example, K79G mutation in yeast cyt *c* has been shown to decrease the pK_H by ~1 pK_a unit,[93] and this change has been suggested to be due to increased solvent accessibility and modified inner water network near the “trigger” group.[93] Alterations in the pK_H have also been observed with perturbations in loop C. Studies with A51V human cyt *c* and T49V/K79G yeast cyt *c* have shown that pK_H values decreased by ~2 pK_a units compared to WT and K79G variants, respectively.[47, 83] Alkaline transition has been extensively studied, and many mutational studies in yeast, human, and horse heart cyt *c* have suggested that the formation of these various pH-dependent conformers are sensitive to structural perturbations. Yet, thermodynamic and kinetic properties of the alkaline transition are similar between many organisms despite sequence variations in loops C and D.[2] This discrepancy observed between WT proteins and some variants highlights the need for further clarification in the roles of loops C and D in tuning the properties of the alkaline transition.

Biological Relevance.

Understanding how structural perturbations influence the pH-dependent conformational transitions is important to understand how these structural changes affect biological function. Depending on cellular conditions, external stimuli, and location of the protein, cyt *c* is exposed to a wide range of pH conditions (Figure 2.5). In the intermembrane space (IMS) of the mitochondria where cyt *c* is usually present, the pH is slightly acidic compared to the more alkaline mitochondrial matrix.[53, 54, 58] Upon CL oxidation, cyt *c* is released into the cytosol, which also experiences a wider range of pH fluctuations depending on external stimuli. At normal conditions, cytosol is at near-neutral pH,[52-54] but is slightly alkaline

compared to the IMS. In response to stimuli such as metabolic inhibition and hypoxia, cytosolic pH is decreased substantially compared to normal conditions.[53, 56, 57] During apoptosis, pH measurements in apoptotic cells and measurements of caspase activity at various pH conditions suggest that cyt *c* is exposed to acidic conditions during apoptosis.[52, 60] Thus, exploration of how structural perturbations affect both the acidic and alkaline transitions will provide a good insight into protein function at physiological conditions.

Role of Structure in Functional Regulation.

Biological ET.

Thermodynamic description of ET illustrates the reaction to occur in the overlap between the potential energy curves of the reactant and the product surfaces.[2] In long-distance ET commonly observed in biological systems, the increased distance between the electron donor (D) and the acceptor (A) decreases electronic coupling.[94] Thus, biological ET is widely described using semi-classical theory which rationalizes k_{ET} in terms of 1) the thermodynamic driving force of the reaction ($-\Delta G°$), 2) electronic coupling between the donor and the acceptor (H_{AB}), and 3) reorganization energy (λ) (eq 2.3).[94-96]

$$k_{ET} = \sqrt{\frac{4\pi^3}{h^2 \lambda k_B T}} H_{AB}^2 \exp\left\{-\frac{(\Delta G° + \lambda)^2}{4\lambda k_B T}\right\} \quad (2.3)$$

$-\Delta G°$ of the ET reaction is dependent on the reduction potential of the D-A pair.[2, 96] λ is the sum of the reorganization energy, and is described to be composed of the inner- (λ_{in}) and outer-sphere (λ_o) components. λ_{in} is determined by free energy change associated with redox-induced structural changes in the primary coordination sphere.[94, 97] λ_o describes the

rest of the nuclear rearrangement and is dependent on the dielectric constant of the medium, which is readily altered by the extent of metal cofactor encapsulation in metalloproteins.[94] In proteins, H_{AB} is described as a product of individual couplings from covalent bonds, HB, and through-space van der Waals (vdW) contact .[95] In metalloproteins, the polypeptide plays a large role in balancing -$\Delta G°$ and λ parameters and tuning the electronic coupling between the D-A pairs.[98]

In cases where the D and A groups are in separate complexes, bimolecular ET rate constant between complex 1 and 2 (k_{12}) is described as eq 2.4:[96]

$$k_{12}=\sqrt{(k_{11}\times k_{22}\times K_{12})} \tag{2.4}$$

where k_{11} and k_{22} is the self-exchange rate constants for complex 1 and 2, respectively (Figure 2.7A). K_{12} is the equilibrium constant for the cross-reaction, and is dependent on the difference in the reduction potentials (ΔE) between 1 and 2 (eq 2.5):[99]

$$K_{12}=\exp\left(\frac{nF\Delta E}{RT}\right) \tag{2.5}$$

As an electron carrier, cyt *c* exists in two oxidation states, channeling electrons between Complexes III and IV in the respiratory chain. For cyt *c* to behave as both an electron acceptor and a donor in cellular respiration, the reduction potential of cyt *c* must be within the reduction potential gap between the two cyt *c* partners, which is around 20 mV[16, 17] (Figure 2.1). The reduction potential of native, Met-ligated cyt *c* is within the narrow reduction potential window of these two biological partners, highlighting the importance of correct ligation and fold in cyt *c* for the protein to act as an electron carrier.

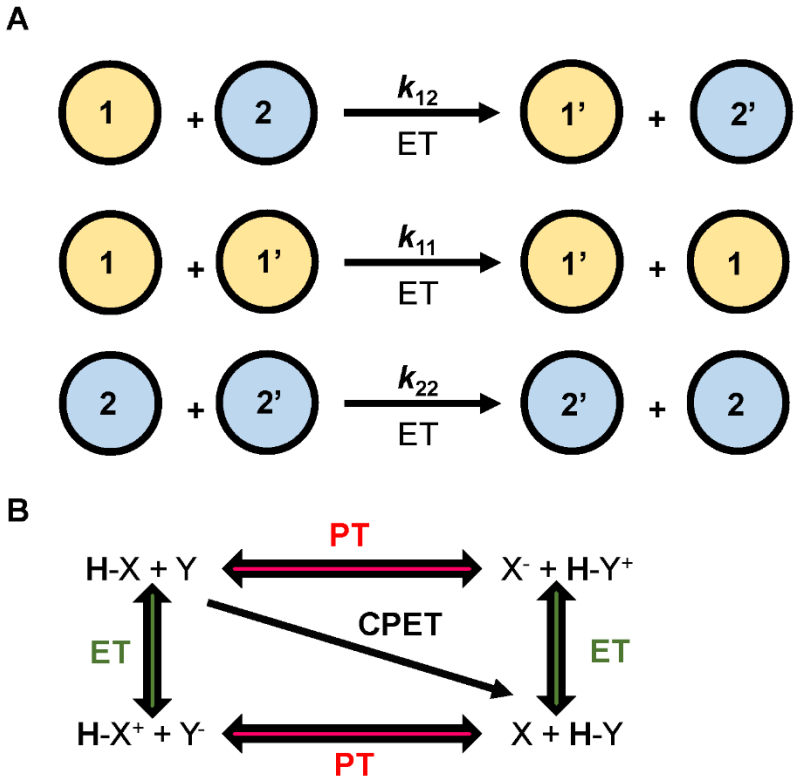

Figure 2.7. (A) A schematic showing the bimolecular ET reaction between two complexes 1 and 2 that undergoes changes in oxidation states to 1' and 2', respectively. In bimolecular ET, electrons can be transferred between complexes 1 and 2, 1 and 1', or 2 and 2' at a rate k_{12}, k_{11}, and k_{22}, respectively. (B) A scheme of the PCET mechanism, based on ref. [100]. In PCET, PT and ET can occur in a stepwise (along the edges of the scheme), or in a concerted (CPET, across the diagonal) mechanism.

Studies with microperoxidase (MP) systems (proteolytically digested horse heart cyt *c* that possesses His18-coordinated hemes with residues 14 to 21 in MP8 or 11 to 21 in MP11) have shown that changing the axial ligand of the heme iron alone alters the reduction potential (Figure 2.1).[12] Folding the polypeptide chain around the metal cofactor increases the reduction potential by a couple hundred mV: compared to Met-ligated MP11 with the reduction potential of near -70 mV, the reduction potential of Met-ligated native cyt *c* is well over +250 mV.[12] As such, native fold and ligation in cyt *c* are instrumental in ensuring that the reduction potential of cyt *c* is tuned to be within desired reduction potential range.

Peripheral changes in the polypeptide chain and the identity of the amino acid surrounding the heme moiety influence the reduction potential. In *c*-type cytochromes, the reduction potential can vary between 450 mV to -80 mV, despite having similar 6-coordinate Met- and His-ligated heme iron species.[13] Even within cyt *c*, reduction potential of acid-denatured cyt *c* in the molten globular (MG) state containing the H_2O-ligated heme iron has been shown to be near that of Met-ligated cyt *c* than the H_2O-ligated MP11 at near-neutral pH.[12, 15, 101] Yet, the replacement of Met80 with Ala forms the hydroxide-ligated heme iron species,[102] and reduces the reduction potential by ~70 mV compared to that of WT at pH 7.0.[103] Mutational studies comparing K79G and K79A cyt *c* variants have shown that the reduction potential for K79G have been decreased by nearly 20 mV at pH 6.0 when compared to that of WT,[80, 93] while such changes have not been observed with K79A.[104] These differences have been argued to stem from differences in solvation in the heme crevice,[93] highlighting the possibility that the identities of residues near the heme may be important in tuning the electrochemical properties of the protein.

Besides tuning the reduction potential, peripheral contacts tune k_{ET} through structural rearrangements that alter peripheral contacts and solvent exposure (eq 2.3). In bimolecular ET, the interface between cyt *c* and CcO or cyt bc_1 involves portions of the polypeptide (Figure 2.8). Again, polypeptide fold, particularly in regions involving loop D and near the solvent-exposed heme edge, is important for ET. Analysis of X-ray crystal structures of yeast cyt bc_1 and cyt *c* have shown that cyt *c* interacts with cyt bc_1 along the heme edge, and forms contacts with cyt bc_1 through residues in loop D and the 20's loop (Figure 2.8A).[105] Examination of the X-ray crystal structure with bovine CcO and horse heart cyt *c* have shown that direct electrostatic interactions are limited to few residues in the α-helices,[106] and ^{1}H-^{15}N HSQC NMR spectra of bovine CcO and human cyt *c* have shown significant shifts in the signals pertaining to residues in the 20's loop and loop D (Figure 2.8B).[107] The interactions between cyt *c* and cyt bc_1 or CcO do not involve residues in loop C (Figure 2.8). However, loop C is in constant contact with both loop D and the 20's loop in the folded Met-ligated state. Thus, it is likely that perturbations in loop C that also affect either of the loops will influence the biological ET between cyt *c* with its partners.

PCET.

In many biological ET systems, proton transfer (PT) is coupled with ET,[108] where PT occurs with ET in either a sequential or concerted manner (Figure 2.7B). D-A pairs involved in PT can be same as the D-A pairs involved in ET, or different.[100, 108] Although PCET is frequently observed in biological systems, there are difficulties in understanding PCET mechanisms in proteins. In many cases, D-A pairs for PT and ET may be unknown.[109]

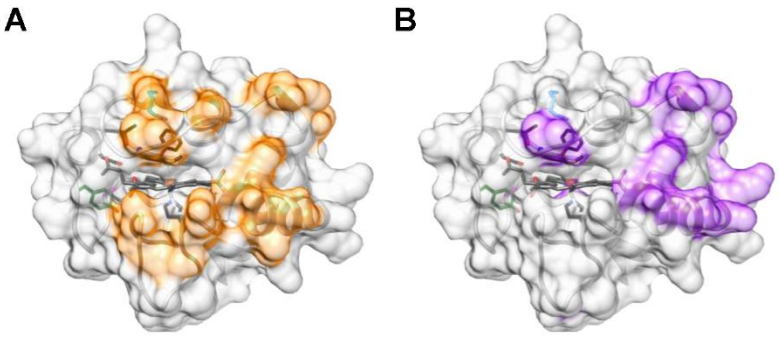

Figure 2.8. Representation of possible interaction sites between horse heart cyt *c* and (A) cyt bc_1 (orange) or (B) CcO (purple). Highlighted are surface regions where protein-protein surface interactions are thought to occur, based on refs. [105-107]. X-ray crystal structure of horse heart cyt *c* (PDB: 1HRC) is used.[30]

Although proton D-A pairs are limited to HB distances,[108] multiple ionizable groups may be present within the protein.[110] Understanding how properties of the polypeptide fold affect PCET in large proteins can be difficult. In proteins such as photosystem II or CcO, multiple protons and electrons are transferred simultaneously, complicating the efforts to better understand the PCET process in biological systems.[108-110] Thus, there are advantages in studying the PCET mechanism with smaller proteins. PCET mechanism is observed in many cytochromes including *Pseudomonas* cytochrome c_{551} (cyt c_{551}), and *Rhodopseudomonas (Rps.) palustris* or *R. rubrum* cyt c_2.[18, 111, 112] Compared to larger proteins such as PSII and CcO, these smaller single-heme cytochromes contain a known ET site and a relatively smaller pool of PT candidates, serving as good models to study how the polypeptide tunes PCET.

Intrinsic Peroxidase Activity.

Peroxidase proteins contain 5-coordinated heme iron species, with His serving as the sole amino acid axial ligand coordinated to the heme iron (Figure 2.9A). Residues near the heme tune the reactivity of the heme moiety to ensure that the O-O bond in H_2O_2 is heterolytically cleaved (Figure 2.9B).[94, 113] Peroxidases oxidize a wide variety of substrates including lignin, lipids, halides, and organic aromatic molecules.[114-117] In peroxidases, the axial His residue is in a HB contact with a nearby Asp residue, which introduces anionic character to the axial His ligand and stabilize the Fe^{III} species (Figure 2.9B, right).[94, 115] In cyt *c* and globin proteins, axial His ligand does not have an anionic character as it is HB to an oxygen atom in the carbonyl backbone of the polypeptide chain.[94] Mutational studies have shown that the anionic character of the axial ligand influences the peroxidase activity and have been suggested to play a role in stabilizing the intermediate species.[118]

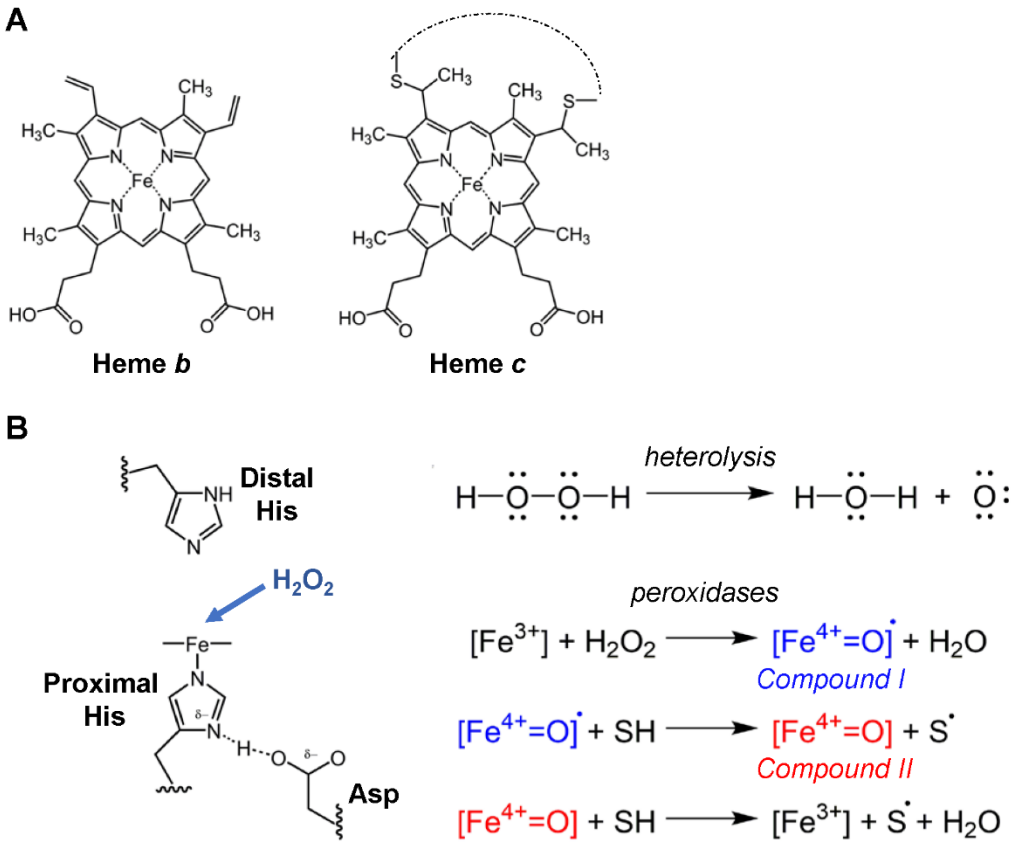

Figure 2.9. (A) A molecular depiction of a *b*-type heme (also known as protoporphyrin IX) found in many peroxidases.[94] Heme *c* is shown for comparison. (B) Active-site structure of peroxidases, based on refs. [94, 113] is shown (left). General mechanisms showing the heterolytic cleavage of H_2O_2 and peroxidases with a substrate (SH) are shown (right).

A distal His behaves as an acid-base catalyst and assists the initial deprotonation of the coordinated H_2O_2 and the following protonation of the cleaved oxygen atom (Figure 2.9B, left).[113, 119] During the heterolytic cleavage, bound H_2O_2 removes an electron from the heme iron and either the porphyrin or a nearby amino acid residue, and a Fe^{IV}-oxo radical species (compound I) is formed.[113] Oxidation of a substrate by compound I removes the radical species in the protein and a Fe^{IV}-oxo species (compound II) is formed.[113] Subsequent oxidation of a second substrate by compound II regenerates the 5-coordinate Fe^{III} heme species.[113]

Cyt *c* also functions as a peroxidase, and this switch-in-function has been of great interest.[1, 120] Studies with MP8 and MP11 have shown that the heme moiety has peroxidase activity in the presence of H_2O_2.[101, 121, 122] Although the activities of these MP systems are lower than that of true peroxidases, spectroscopic studies have shown that the heme forms both the compound I and compound II species observed in peroxidases.[101, 122-124] It is likely that in cyt *c*, peroxidase activity proceeds through a similar mechanism as proposed in MP systems (Figure 2.10). Spectroscopic studies of the dimeric cyt *c* detected spectroscopic signatures of compound I species, as well as compound III (Fe^{III}-superoxo) species with high excess of H_2O_2,[125] a species observed in HRP that have been suggested to form after the compound II species in the presence of excess H_2O_2 or O_2.[126-128] In the formation of compound I, previous studies have detected spectroscopic signatures of porphyrin radicals in acetylated (Ac)-MP8 systems.[123] While this may also be the case in cyt *c*, formation of Tyr radicals have also been proposed to be present in H_2O_2-activated cyt *c*.[129]

Figure 2.10. A schematic representation of the pseudo-peroxidase activity of cyt *c* based on the proposed mechanism for MP systems.[101, 124, 130, 131] Many chemical compounds, including ABTS, have been shown to be oxidized in the peroxidase activity of MP systems[124, 132] and in true peroxidases.[133] CL is a structurally diverse lipid group that has many structural variations in the lipid tail, and is also the selectively oxidized biological substrate in the cyt *c* peroxidase mechanism. Of the many CL species found in the cell,[134] those containing the linoleoyl acyl chains (highlighted), such as tetralinoleyl cardiolipin (TLCL, 18:2-cardiolipin), are selectively oxygenated.[5, 19, 129, 134, 135] In the absence of linoelic acid groups, the lipid is no longer oxidized, such as with tetraoleoyl cardiolipin (TOCL, 18:1-cardiolipin),[5] despite similarities in cyt *c*-to-liposome binding and liposome-bound cyt *c* peroxidase activity to TLCL.[136] Although tetramyristoleoyl cardiolipin (TMCL, 14:1-cardiolipin) also do not contain linoleoyl acyl chains, TOCL is used rather than TMCL in many studies and this thesis work since the peroxidase activity of liposome-bound cyt *c* is much more effective with TOCL than with TMCL.[137, 138] Free radical oxidation of linoleoyl acyl chains by cyt *c* has been shown to produce various products as determined from mass spectrometry (MS) studies,[139] including, but not limited to, hydroxy, epoxy, and hydroperoxy products.[19, 129, 134, 140-142] Formation of peroxy-type products leads to other fragmentation reactions.[139, 143] Structure of yet another common lipid, dioleoyl phosphatidylcholine (DOPC) found in high abundance that do not undergo oxidation is also shown.[5, 134]

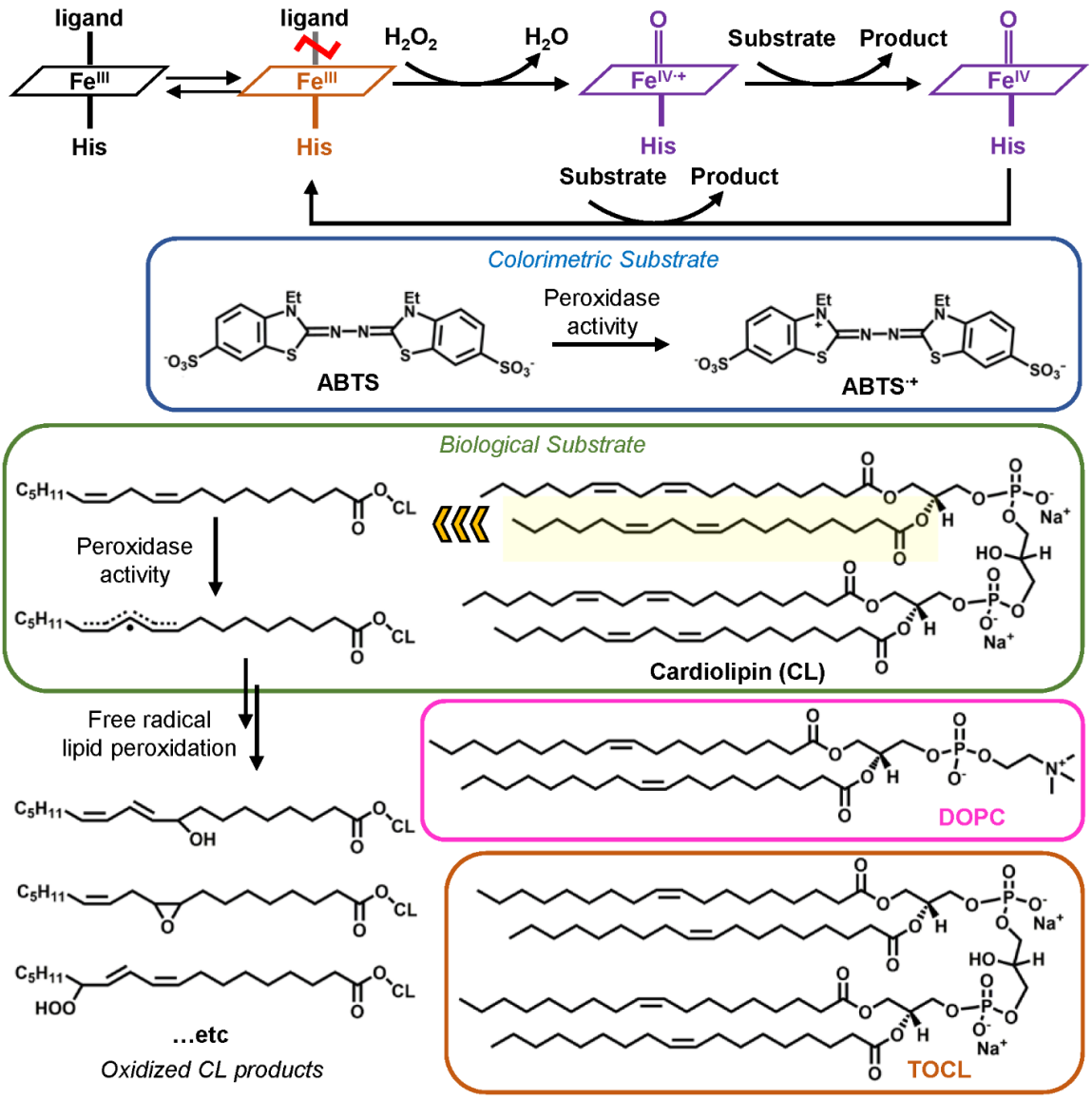
ligand
Fe^III
His
ligand
Fe^III
His
H2O2
H2O
O
Fe^IV·+
His
Substrate
Product
O
Fe^IV
His
Substrate
Product
Colorimetric Substrate
Peroxidase activity
ABTS
ABTS·+
Biological Substrate
Peroxidase activity
Cardiolipin (CL)
Free radical lipid peroxidation
DOPC
TOCL
...etc
Oxidized CL products

The steady-state peroxidase reaction has been described as a two-substrate enzyme system (ping-pong mechanism), where the peroxidase reaction is dependent on both H_2O_2 and the substrate oxidized by compounds I and II.[133, 144] Assays that probe protein peroxidase activity uses colorimetric substrates, such as ABTS, instead of biological substrates to spectroscopically track the reaction and obtain the initial rates.[133] At steady-state conditions where the concentration of one of the substrates are kept constant while other is varied, the enzymatic reaction can be explained by Michaelis-Menten type parameters. [133, 144] A more generalized Michaelis-Menten treatment has been used to characterize the peroxidase activity of the protein in cytochrome proteins, such as in cyt *c* and cyt c_{550}.[145, 146] Difference in mechanistic models describing activities between cyt *c* and true peroxidases (such as horseradish peroxidases and cytochrome *c* peroxidases) pose difficulties in directly comparing peroxidase activities. However, activity assays help rationalize how changes in polypeptide affect the peroxidase activity of cyt *c* proteins.

Polypeptide fold helps suppress this innate peroxidase activity of the heme moiety in cyt *c*. Intrinsic peroxidase activity is still observed even in folded cyt *c* because Met80 can rapidly dissociate and allow H_2O_2 to coordinate to the heme iron (Figure 2.11). Yet, the compact, native fold provides a tightly regulated heme crevice that limits solvent access to the heme iron. As a result, the peroxidase activity of cyt *c* in the folded state is low compared to peroxidase activities of unfolded cyt *c*, MP8, or MP11 that do not possess this layer of protection offered by the native packing of the polypeptide chain.[121, 122, 147-149]

Figure 2.11. A diagram depicting the various pathways observed to enhance the peroxidase activity of cyt *c*.

[a]In ferric native cyt *c*, Met80 readily dissociates from the heme iron and is readily replaced by small molecule ligands,[40] such as H_2O_2. Studies with MP8 and MP11 obtained from proteolytic digestion of horse heart cyt *c* that contains heme with residues 14-21 (MP8) or 11-21 (MP11), show that *c*-type heme moiety is capable of having peroxidase activity in the presence of H_2O_2.[101, 113, 122] Peroxidase activity of native cyt *c* is lower than that of MP8 or MP11, but higher than that of bisHis ligated cyt *c* observed at near-neutral pH conditions in the unfolded state.[32] Studies with closely related cyt c_{550} showed that peroxidase activity in the Lys-ligated state at alkaline conditions is lower than that of Met-ligated state,[147] suggesting that alkaline cyt *c* also has lower activity than that of native cyt *c*.

[b]Based on ref. [137]

[c]Based on ref. [120, 150]

[d]Based on ref.[151]

[e]Various modes of heme iron ligations in the CL-bound state have been reported. Changes in heme iron ligation upon CL binding have been proposed to play a role in enhancing the peroxidase activity of cyt *c*.

[f]Peroxidase activity of CL-bound cyt *c* is enhanced compared to intrinsic peroxidase activity. This enhancement in activity is argued to oxidize and permeabilize the CL-containing mitochondrial membrane, allowing cyt *c* to be released into the cytosol and initiate apoptosis.

Figure 2.11 caption, continued.

[g]In both CL-bound and unbound cyt *c*, signs of oxidation and radical formation in the polypeptide chain have been observed in the presence of ROS. These chemical modifications to the residues in the polypeptide chain have been shown to enhance peroxidase activity.

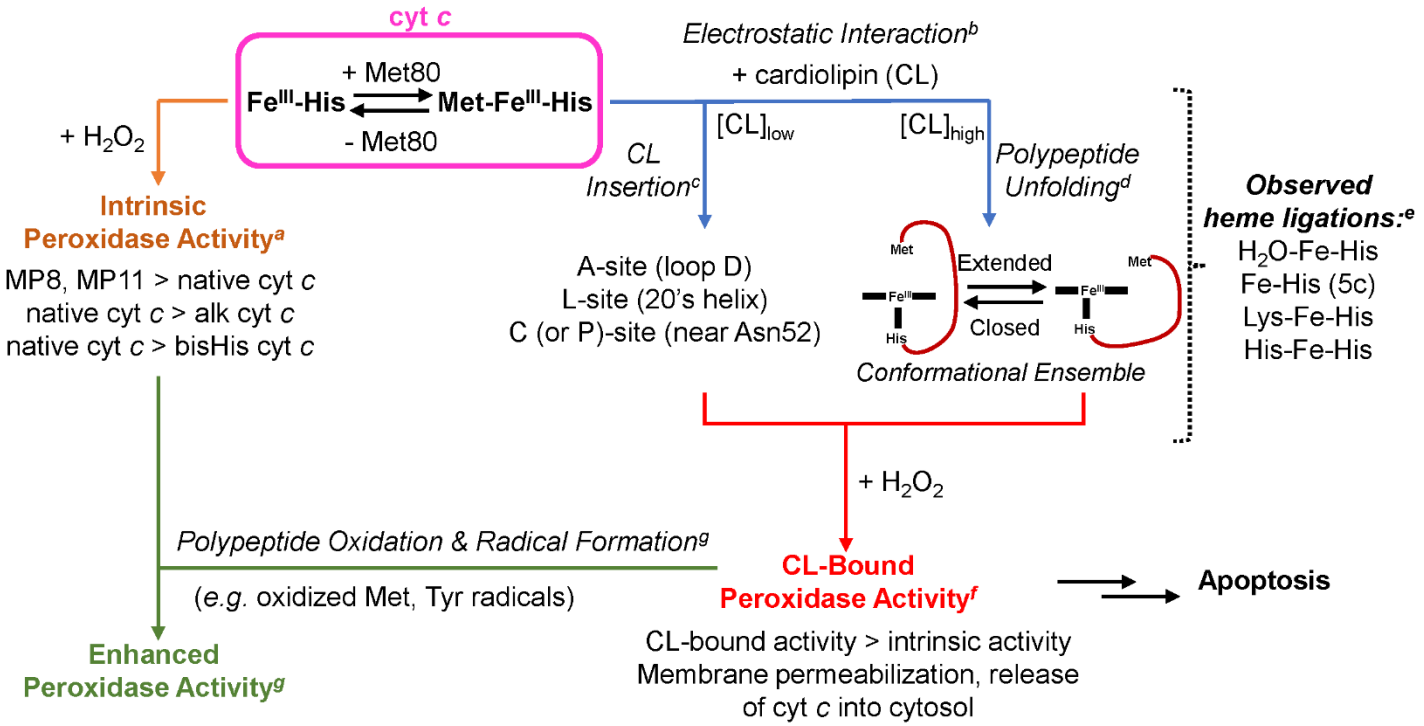
cyt c
+ Met80
Fe^III-His ⇌ Met-Fe^III-His
- Met80
+ H2O2
Intrinsic Peroxidase Activity[a]
MP8, MP11 > native cyt c
native cyt c > alk cyt c
native cyt c > bisHis cyt c
Electrostatic Interaction[b]
+ cardiolipin (CL)
[CL]low
[CL]high
CL Insertion[c]
Polypeptide Unfolding[d]
A-site (loop D)
L-site (20's helix)
C (or P)-site (near Asn52)
Met
Fe^III
His
Extended
Closed
Conformational Ensemble
Observed heme ligations:[e]
H2O-Fe-His
Fe-His (5c)
Lys-Fe-His
His-Fe-His
+ H2O2
Polypeptide Oxidation & Radical Formation[g]
(e.g. oxidized Met, Tyr radicals)
CL-Bound Peroxidase Activity[f]
CL-bound activity > intrinsic activity
Membrane permeabilization, release of cyt c into cytosol
Apoptosis
Enhanced Peroxidase Activity[g]

The nature of heme iron axial ligand is also important in regulating the innate peroxidase function. Peroxidase activity of Lys-bound cyt c_{550} is lower than that of Met-ligated cyt c_{550} at neutral pH conditions,[152] suggesting that the peroxidase activity of Lys-ligated alkaline cyt *c* at alkaline conditions is also low compared to the Met-ligated cyt *c*. Unfolded cyt *c* that contains bisHis-ligated species also has lower peroxidase activity compared to that of the Met-ligated cyt *c*.[32] A possible explanation for the difference in the intrinsic peroxidase activity between hemes with different heme iron ligations can be explained by the hard-soft acid base theory, where a hard lysine or a borderline base imidazole are both better ligands for a hard ferric iron than a soft base Met.[94] Recent DFT calculations agrees with this pattern, as dissociation of His and Lys ligands from the ferric heme iron was more unfavored compared to dissociation of Met from the ferric heme iron.[33] Since peroxidase activity requires H_2O_2 to coordinate to the heme iron, it may be that the difference in peroxidase activity between the Met-, His-, and Lys-ligated heme species depend on how readily these ligands dissociate from the heme iron. To test this hypothesis, one possible method would be to compare the peroxidase activity of variants that have Lys- or His-ligated heme iron instead of the usual Met-ligated heme iron in the folded state at similar pH conditions.

CL-Bound Peroxidase Activity.

In the presence of CL, a diverse lipid group abundantly found in the mitochondria,[134] peroxidase activity of cyt *c* increases dramatically.[137] Although CL is structurally diverse, CL species containing the linoelic group (for example 18:20 CL) is selectively oxidized, [5, 19, 129, 134, 135] which then triggers radical lipid peroxidation mechanisms that lead to lipid oxidation and fragmentation reactions (Figure 2.10). [19, 129, 134, 139-143] Although CL is

consumed as a substrate in cyt *c* peroxidase activity, it is also a conformational trigger that perturbs the polypeptide fold and increase the peroxidase activity in cyt *c*.[120]

Positively-charged cyt *c* electrostatically binds to the negatively-charged membrane surface, and much has been studied regarding this interaction (Figure 2.11).[120] Depending on the CL content, *in vitro* experiments have shown various types of interaction between the lipid and cyt *c*, which also differ in the extent of structural perturbation experienced by the protein. While some studies note significant conformational rearrangements, depending on CL content and/or lipid to protein ratio, others did not.[151, 153, 154] Furthermore, how cyt *c* binds to CL-containing liposomes varies depending on the ionic concentrations, pH conditions, and CL content. Various CL binding sites and interactions have been proposed: 1) electrostatic binding in the A-site involving residues Lys72 and Lys73, 2) HB in the C-site and between Asn52 and phosphate lipid head group at low pH (binding interaction at this site occurs at higher pH levels with increasing CL), and 3) L-site binding at pH conditions below 7 that involves Lys 22, 25, and 27 (and potentially His26 and 33), which have recently been shown to involve electrostatically driven conformational change at relative higher CL content up to 1:50 protein to CL ratio.[150] Other studies have suggested that lipid tails insert into the hydrophobic cavity of the protein near Asn52,[155] or into the channel formed by residues 67-71 and 82-85.[156] A more extensive conformational rearrangement have been observed at conditions with relative higher CL concentrations (near 1:66 protein to CL ratio), where the protein is in an equilibrium between the unfolded (extended, E) and native-like (compact, C) species.[151] The relative population of the conformational ensemble at high CL conditions have been

shown to also depend on the ionic conditions, CL concentration, and available membrane surface area.[151 157]

Binding of cyt *c* to CL is highly variable depending on the experimental conditions, and conformational heterogeneity of the CL-bound species complicates efforts to understand the source of increased peroxidase activity in the CL-bound state. Various ligands have been observed to occupy the axial coordination site of the heme iron where H_2O_2 needs to coordinate. Various spectroscopic studies have suggested a presence of 5-coordinate and/or 6-coordinate heme iron species (where the 6th axial heme iron ligand is H_2O, Lys, or His) in the CL-bound state.[153, 158-161] And yet, Lys, and His-ligated 6-coordinate heme iron species have been shown to suppresses peroxidase activity in studies with chemically unfolded cyt *c*. Previously, many mutational studies in cyt *c* have probed the role of structure-function relationship in regulating the peroxidase activity, and the presence of catalytic radicals near the heme have been accredited to increase the peroxidase activity of cyt *c*.[5, 129] Although oxidative damage to the polypeptide from extended exposure to H_2O_2 has been shown to increase peroxidase activity,[162, 163] peroxidase activity can also increase by increasing the accessibility of ROS to the heme iron.[164]

Understanding how structural perturbations alter apoptotic peroxidase activity is crucial, as alterations in the polypeptide can result in disease. In humans, genetically inherited single-point mutations in loop C (G41S, Y48H, or A51V) or deletions in *C*-terminal helix (K100del) of cyt *c* has been associated with thrombocytopenia, a disorder characterized by low platelet counts.[165-168] Of many components involved in platelet formation,[169] components that make up the apoptosome are found in human platelets, including cyt *c*.[170] Furthermore, caspase-activation is argued to be implicated in the

formation and release of platelets into the bloodstream,[171] and abnormalities in this mechanism have been suggested to cause disease in humans with pathogenic G41S and Y48H cyt *c* mutations.[165, 167] These pathogenic cyt *c* variants show that structural perturbations outside of loop D, such as loop C and the *C*-terminal helix, can alter functional properties of the protein.

References

1. Alvarez-Paggi, D. *et al.* Multifunctional Cytochrome c: Learning New Tricks from an Old Dog. *Chem Rev* **117**, 13382-13460 (2017).

2. Moore, G.R. & Pettigrew, G.W. *Cytochromes c : evolutionary, structural, and physicochemical aspects*. (Springer-Verlag, Berlin ; New York; 1990).

3. Cai, J., Yang, J. & Jones, D.P. Mitochondrial control of apoptosis: the role of cytochrome c. *Biochim Biophys Acta* **1366**, 139-149 (1998).

4. Alberts, B., Wilson, J.H. & Hunt, T. *Molecular biology of the cell*, Edn. 5th. (Garland Science, New York; 2008).

5. Kagan, V.E. *et al.* Cytochrome c acts as a cardiolipin oxygenase required for release of proapoptotic factors. *Nat Chem Biol* **1**, 223-232 (2005).

6. Iverson, S.L. & Orrenius, S. The cardiolipin-cytochrome c interaction and the mitochondrial regulation of apoptosis. *Arch Biochem Biophys* **423**, 37-46 (2004).

7. Kim, H.-E., Du, F., Fang, M. & Wang, X. Formation of apoptosome is initiated by cytochrome c-induced dATP hydrolysis and subsequent nucleotide exchange on Apaf-1. *Proceedings of the National Academy of Sciences* **102**, 17545-17550 (2005).

8. Brown, G.C. & Borutaite, V. Regulation of apoptosis by the redox state of cytochrome c. *Biochim Biophys Acta* **1777**, 877-881 (2008).

9. Yuan, S. & Akey, Christopher W. Apoptosome Structure, Assembly, and Procaspase Activation. *Structure* **21**, 501-515 (2013).

10. Yuan, S.J. *et al.* Structure of an Apoptosome-Procaspase-9 CARD Complex. *Structure* **18**, 571-583 (2010).

11. Carmona-Gutierrez, D. *et al.* Apoptosis in yeast: triggers, pathways, subroutines. *Cell Death Differ* **17**, 763-773 (2010).

12. Battistuzzi, G., Borsari, M., Cowan, J.A., Ranieri, A. & Sola, M. Control of cytochrome c redox potential: Axial ligation and protein environment effects. *J Am Chem Soc* **124**, 5315-5324 (2002).

13. Liu, J. *et al.* Metalloproteins containing cytochrome, iron-sulfur, or copper redox centers. *Chem Rev* **114**, 4366-4469 (2014).

14. Eddowes, M.J. & Hill, H.A.O. Electrochemistry of Horse Heart Cytochrome-C. *J Am Chem Soc* **101**, 4461-4464 (1979).

15. Santucci, R. *et al.* Anion size modulates the structure of the A state of cytochrome c. *Biochemistry* **39**, 12632-12638 (2000).

16. Wang, H., Blair, D.F., Ellis, W.R., Gray, H.B. & Chan, S.I. Temperature-Dependence of the Reduction Potential of Cua in Carbon-Monoxide Inhibited Cytochrome-C-Oxidase. *Biochemistry* **25**, 167-171 (1986).

17. Meinhardt, S.W. & Crofts, A.R. Kinetic and Thermodynamic Resolution of Cytochrome-C1 and Cytochrome-C2 from Rhodopseudomonas-Sphaeroides. *Febs Lett* **149**, 223-227 (1982).

18. Pettigrew, G.W., Bartsch, R.G., Meyer, T.E. & Kamen, M.D. Redox potentials of the photosynthetic bacterial cytochromes c2 and the structural bases for variability. *Biochim Biophys Acta* **503**, 509-523 (1978).

19. Maguire, J.J. *et al.* Known unknowns of cardiolipin signaling: The best is yet to come. *Bba-Mol Cell Biol L* **1862**, 8-24 (2017).

20. Theorell, H. & Akesson, A. Studies on cytochrome c. III. Titration curves. *J Am Chem Soc* **63**, 1818-1820 (1941).

21. Krishna, M.M.G., Lin, Y., Mayne, L. & Englander, S.W. Intimate view of a kinetic protein folding intermediate: Residue-resolved structure, interactions, stability, folding and unfolding rates, homogeneity. *J Mol Biol* **334**, 501-513 (2003).

22. Maity, H., Maity, M. & Englander, S.W. How cytochrome c folds, and why: Submolecular foldon units and their stepwise sequential stabilization. *J Mol Biol* **343**, 223-233 (2004).

23. Hu, W.B., Kan, Z.Y., Mayne, L. & Englander, S.W. Cytochrome c folds through foldon-dependent native-like intermediates in an ordered pathway. *P Natl Acad Sci USA* **113**, 3809-3814 (2016).

24. Milne, J.S., Mayne, L., Roder, H., Wand, A.J. & Englander, S.W. Determinants of protein hydrogen exchange studied in equine cytochrome c. *Protein Sci* **7**, 739-745 (1998).

25. Hoang, L., Bedard, S., Krishna, M.M.G., Lin, Y. & Englander, S.W. Cytochrome c folding pathway: Kinetic native-state hydrogen exchange. *P Natl Acad Sci USA* **99**, 12173-12178 (2002).

26. Krishna, M.M.G., Maity, H., Rumbley, J.N., Lin, Y. & Englander, S.W. Order of steps in the cytochrome c folding pathway: Evidence for a sequential stabilization mechanism. *J Mol Biol* **359**, 1410-1419 (2006).

27. Krishna, M.M.G., Maity, H., Rumbley, J.N. & Englander, S.W. Branching in the sequential folding pathway of cytochrome c. *Protein Sci* **16**, 1946-1956 (2007).

28. Hoang, L., Maity, H., Krishna, M.M., Lin, Y. & Englander, S.W. Folding units govern the cytochrome c alkaline transition. *J Mol Biol* **331**, 37-43 (2003).

29. Maity, H., Rumbley, J.N. & Englander, S.W. Functional role of a protein foldon - An Omega-Loop foldon controls the alkaline transition in ferricytochrome c. *Proteins* **63**, 349-355 (2006).

30. Bushnell, G.W., Louie, G.V. & Brayer, G.D. High-resolution three-dimensional structure of horse heart cytochrome c. *J Mol Biol* **214**, 585-595 (1990).

31. Xu, Y., Mayne, L. & Englander, S.W. Evidence for an unfolding and refolding pathway in cytochrome c. *Nat Struct Biol* **5**, 774-778 (1998).

32. Diederix, R.E.M., Ubbink, M. & Canters, G.W. Peroxidase activity as a tool for studying the folding of c-type cytochromes. *Biochemistry* **41**, 13067-13077 (2002).

33. Zhong, F., Alden, S.L., Hughes, R.P. & Pletneva, E.V. Comparing Properties of Common Bioinorganic Ligands with Switchable Variants of Cytochrome c. *Inorg Chem* (2021).

34. Colon, W., Wakem, L.P., Sherman, F. & Roder, H. Identification of the predominant non-native histidine ligand in unfolded cytochrome c. *Biochemistry* **36**, 12535-12541 (1997).

35. Tezcan, F.A., Winkler, J.R. & Gray, H.B. Effects of ligation and folding on reduction potentials of heme proteins. *J Am Chem Soc* **120**, 13383-13388 (1998).

36. Zhong, F. & Pletneva, E.V. Ligation and Reactivity of Methionine-Oxidized Cytochrome c. *Inorg Chem* **57**, 5754-5766 (2018).

37. Kroll, T. *et al.* Resonant Inelastic X-ray Scattering on Ferrous and Ferric Bis-imidazole Porphyrin and Cytochrome c: Nature and Role of the Axial Methionine–Fe Bond. *J Am Chem Soc* **136**, 18087-18099 (2014).

38. Mara, M.W. *et al.* Metalloprotein entatic control of ligand-metal bonds quantified by ultrafast x-ray spectroscopy. *Science* **356**, 1276-1280 (2017).

39. McClelland, L.J., Mou, T.C., Jeakins-Cooley, M.E., Sprang, S.R. & Bowler, B.E. Structure of a mitochondrial cytochrome c conformer competent for peroxidase activity. *P Natl Acad Sci USA* **111**, 6648-6653 (2014).

40. Sutin, N. & Yandell, J.K. Mechanisms of the reactions of cytochrome c. Rate and equilibrium constants for ligand binding to horse heart ferricytochrome c. *The Journal of biological chemistry* **247**, 6932-6936 (1972).

41. Zaidi, S., Hassan, M.I., Islam, A. & Ahmad, F. The role of key residues in structure, function, and stability of cytochrome-c. *Cell Mol Life Sci* **71**, 229-255 (2014).

42. Rajagopal, Badri S. *et al.* The hydrogen-peroxide-induced radical behaviour in human cytochrome c–phospholipid complexes: implications for the enhanced pro-apoptotic activity of the G41S mutant. *Biochem J* **456**, 441-452 (2013).

43. Kalpage, H.A. *et al.* Serine-47 phosphorylation of cytochrome c in the mammalian brain regulates cytochrome c oxidase and caspase-3 activity. *The FASEB Journal* **33**, 13503-13514 (2019).

44. Berghuis, A.M. & Brayer, G.D. Oxidation state-dependent conformational changes in cytochrome c. *J Mol Biol* **223**, 959-976 (1992).

45. Berghuis, A.M. *et al.* The role of a conserved internal water molecule and its associated hydrogen bond network in cytochrome c. *J Mol Biol* **236**, 786-799 (1994).

46. Berghuis, A.M., Guillemette, J.G., Smith, M. & Brayer, G.D. Mutation of tyrosine-67 to phenylalanine in cytochrome c significantly alters the local heme environment. *J Mol Biol* **235**, 1326-1341 (1994).

47. Deng, Y., Weaver, M.L., Hoke, K.R. & Pletneva, E.V. A Heme Propionate Staples the Structure of Cytochrome c for Methionine Ligation to the Heme Iron. *Inorg Chem* **58**, 14085-14106 (2019).

48. Krishna, M.M.G., Lin, Y., Rumbley, J.N. & Englander, S.W. Cooperative omega loops in cytochrome c: Role in folding and function. *J Mol Biol* **331**, 29-36 (2003).

49. Berghuis, A.M. & Brayer, G.D. Oxidation State-Dependent Conformational-Changes in Cytochrome-C. *J Mol Biol* **223**, 959-976 (1992).

50. Saigo, S. Kinetic and equilibrium studies of alkaline isomerization of vertebrate cytochromes c. *Biochim Biophys Acta* **669**, 13-20 (1981).

51. Theorell, H. & Akesson, A. Studies on cytochrome c. II. The optical properties of pure cytochrome c and some of its derivatives. *J Am Chem Soc* **63**, 1812-1818 (1941).

52. Nilsson, C., Kagedal, K., Johansson, U. & Ollinger, K. Analysis of cytosolic and lysosomal pH in apoptotic cells by flow cytometry. *Methods in cell science : an official journal of the Society for In Vitro Biology* **25**, 185-194 (2003).

53. Balut, C. *et al.* Measurement of cytosolic and mitochondrial pH in living cells during reversible metabolic inhibition. *Kidney International* **73**, 226-232 (2008).

54. Porcelli, A.M. *et al.* pH difference across the outer mitochondrial membrane measured with a green fluorescent protein mutant. *Biochemical and biophysical research communications* **326**, 799-804 (2005).

55. Xiong, W.-C. & Simon, S. ECV304 Cells: An Endothelial or Epithelial Model? *Journal of Biological Chemistry* **286**, le21 (2011).

56. Gores, G.J., Nieminen, A.L., Wray, B.E., Herman, B. & Lemasters, J.J. Intracellular pH during "chemical hypoxia" in cultured rat hepatocytes. Protection by intracellular acidosis against the onset of cell death. *The Journal of clinical investigation* **83**, 386-396 (1989).

57. Qian, T., Nieminen, A.L., Herman, B. & Lemasters, J.J. Mitochondrial permeability transition in pH-dependent reperfusion injury to rat hepatocytes. *The American journal of physiology* **273**, C1783-1792 (1997).

58. Llopis, J., McCaffery, J.M., Miyawaki, A., Farquhar, M.G. & Tsien, R.Y. Measurement of cytosolic, mitochondrial, and Golgi pH in single living cells with green fluorescent proteins. *Proceedings of the National Academy of Sciences* **95**, 6803-6808 (1998).

59. Cortese, J.D., Voglino, A.L. & Hackenbrock, C.R. The ionic strength of the intermembrane space of intact mitochondria is not affected by the pH or volume of the intermembrane space. *Biochim Biophys Acta* **1100**, 189-197 (1992).

60. Matsuyama, S., Llopis, J., Deveraux, Q.L., Tsien, R.Y. & Reed, J.C. Changes in intramitochondrial and cytosolic pH: early events that modulate caspase activation during apoptosis. *Nature Cell Biology* **2**, 318-325 (2000).

61. Stupák, M., Bágelová, J., Fedunová, D. & Antalík, M. CONFORMATIONAL TRANSITIONS OF FERRICYTOCHROME c IN STRONG INORGANIC ACIDS. *ChemPlusChem* **71**, 1627 (2006).

62. Stellwagen, E. & Babul, J. Stabilization of the globular structure of ferricytochrome c by chloride in acidic solvents. *Biochemistry* **14**, 5135-5140 (1975).

63. Oellerich, S., Wackerbarth, H. & Hildebrandt, P. Spectroscopic Characterization of Nonnative Conformational States of Cytochrome c. *The Journal of Physical Chemistry B* **106**, 6566-6580 (2002).

64. Cohen, J.S. & Hayes, M.B. Nuclear magnetic resonance titration curves of histidine ring protons. V. Comparative study of cytochrome c from three species and the assignment of individual proton resonances. *The Journal of biological chemistry* **249**, 5472-5477 (1974).

65. Goto, Y., Hagihara, Y., Hamada, D., Hoshino, M. & Nishii, I. Acid-induced unfolding and refolding transitions of cytochrome c: a three-state mechanism in H2O and D2O. *Biochemistry* **32**, 11878-11885 (1993).

66. Hamada, D. *et al.* Role of heme axial ligands in the conformational stability of the native and molten globule states of horse cytochrome c. *J Mol Biol* **256**, 172-186 (1996).

67. Dyson, H.J. & Beattie, J.K. Spin state and unfolding equilibria of ferricytochrome c in acidic solutions. *Journal of Biological Chemistry* **257**, 2267-2273 (1982).

68. Goto, Y., Calciano, L.J. & Fink, A.L. Acid-Induced Folding of Proteins. *P Natl Acad Sci USA* **87**, 573-577 (1990).

69. Goto, Y., Takahashi, N. & Fink, A.L. Mechanism of Acid-Induced Folding of Proteins. *Biochemistry* **29**, 3480-3488 (1990).

70. Indiani, C. *et al.* Effect of pH on axial ligand coordination of cytochrome c" from Methylophilus methylotrophus and horse heart cytochrome c. *Biochemistry* **39**, 8234-8242 (2000).

71. Jeng, M.F., Englander, S.W., Elove, G.A., Wand, A.J. & Roder, H. Structural description of acid-denatured cytochrome c by hydrogen exchange and 2D NMR. *Biochemistry* **29**, 10433-10437 (1990).

72. Balakrishnan, G. *et al.* A conformational switch to beta-sheet structure in cytochrome c leads to heme exposure. Implications for cardiolipin peroxidation and apoptosis. *J Am Chem Soc* **129**, 504-505 (2007).

73. Wandschneider, E., Hammack, B.N. & Bowler, B.E. Evaluation of cooperative interactions between substructures of iso-1-cytochrome c using double mutant cycles. *Biochemistry* **42**, 10659-10666 (2003).

74. Redzic, J.S. & Bowler, B.E. Role of hydrogen bond networks and dynamics in positive and negative cooperative stabilization of a protein. *Biochemistry* **44**, 2900-2908 (2005).

75. Davis, L.A., Schejter, A. & Hess, G.P. Alkaline isomerization of oxidized cytochrome c. Equilibrium and kinetic measurements. *The Journal of biological chemistry* **249**, 2624-2632 (1974).

76. Ness, S.R., Lo, T.P. & Mauk, A.G. Structural models for the alkaline conformers of yeast iso-1-ferricytochrome c. *Israel J Chem* **40**, 21-25 (2000).

77. Assfalg, M. *et al.* Structural model for an alkaline form of ferricytochrome c. *J Am Chem Soc* **125**, 2913-2922 (2003).

78. Amacher, J.F. *et al.* A Compact Structure of Cytochrome c Trapped in a Lysine-Ligated State: Loop Refolding and Functional Implications of a Conformational Switch. *J Am Chem Soc* **137**, 8435-8449 (2015).

79. Rosell, F.I. in Biochemistry and Molecular Biology, Vol. PhD 218 (University of British Columbia, 1999).

80. Rosell, F.I., Ferrer, J.C. & Mauk, A.G. Proton-linked protein conformational switching: Definition of the alkaline conformational transition of yeast iso-1-ferricytochrome c. *J Am Chem Soc* **120**, 11234-11245 (1998).

81. Deacon, O.M. *et al.* Heightened Dynamics of the Oxidized Y48H Variant of Human Cytochrome c Increases Its Peroxidatic Activity. *Biochemistry* **56**, 6111-6124 (2017).

82. Deacon, O.M., Svistunenko, D.A., Moore, G.R., Wilson, M.T. & Worrall, J.A.R. Naturally Occurring Disease-Related Mutations in the 40-57 Omega-Loop of Human Cytochrome c Control Triggering of the Alkaline Isomerization. *Biochemistry* **57**, 4276-4288 (2018).

83. Deacon, O.M., White, R.W., Moore, G.R., Wilson, M.T. & Worrall, J.A.R. Comparison of the structural dynamic and mitochondrial electron-transfer properties of the proapoptotic human cytochrome c variants, G41S, Y48H and A51V. *Journal of inorganic biochemistry* **203**, 110924 (2020).

84. Karsisiotis, A.I. *et al.* Increased dynamics in the 40-57 Omega-loop of the G41S variant of human cytochrome c promote its pro-apoptotic conformation. *Scientific reports* **6**, 30447 (2016).

85. Cherney, M.M., Junior, C.C. & Bowler, B.E. Mutation of Trimethyllysine 72 to Alanine Enhances His79-Heme-Mediated Dynamics of Iso-1-cytochrome c. *Biochemistry* **52**, 837-846 (2013).

86. Pollock, W.B.R., Rosell, F.I., Twitchett, M.B., Dumont, M.E. & Mauk, A.G. Bacterial expression of a mitochondrial cytochrome c. Trimethylation of Lys72 in yeast iso-1-cytochrome c and the alkaline conformational transition. *Biochemistry* **37**, 6124-6131 (1998).

87. Tonge, P., Moore, G.R. & Wharton, C.W. Fourier-transform infra-red studies of the alkaline isomerization of mitochondrial cytochrome c and the ionization of carboxylic acids. *The Biochemical journal* **258**, 599-605 (1989).

88. Cherney, M.M. & Bowler, B.E. Protein dynamics and function: Making new strides with an old warhorse, the alkaline conformational transition of cytochrome c. *Coordin Chem Rev* **255**, 664-677 (2011).

89. Rosell, F.I. *et al.* Characterization of an alkaline transition intermediate stabilized in the Phe82Trp variant of yeast iso-1-cytochrome c. *Biochemistry* **39**, 9047-9054 (2000).

90. Silkstone, G.G., Cooper, C.E., Svistunenko, D. & Wilson, M.T. EPR and optical spectroscopic studies of Met80X mutants of yeast ferricytochrome c. Models for intermediates in the alkaline transition. *J Am Chem Soc* **127**, 92-99 (2005).

91. Gadsby, P.M., Peterson, J., Foote, N., Greenwood, C. & Thomson, A.J. Identification of the ligand-exchange process in the alkaline transition of horse heart cytochrome c. *Biochem J* **246**, 43-54 (1987).

92. Battistuzzi, G. *et al.* Free energy of transition for the individual alkaline conformers of yeast iso-1-cytochrome c. *Biochemistry* **46**, 1694-1702 (2007).

93. Deng, Y.L., Zhong, F.F., Alden, S.L., Hoke, K.R. & Pletneva, E.V. The K79G Mutation Reshapes the Heme Crevice and Alters Redox Properties of Cytochrome c. *Biochemistry* **57**, 5827-5840 (2018).

94. Bertini, I., Gray, H.B., Stiefel, E.I. & Valentine, J.S. *Biological inorganic chemistry : structure and reactivity*. (University Science Books, Sausalito, Calif.; 2007).

95. Beratan, D.N., Betts, J.N. & Onuchic, J.N. Protein electron transfer rates set by the bridging secondary and tertiary structure. *Science* **252**, 1285-1288 (1991).

96. Marcus, R.A. & Sutin, N. Electron transfers in chemistry and biology. *Biochimica et Biophysica Acta (BBA) - Reviews on Bioenergetics* **811**, 265-322 (1985).

97. Alvarez-Paggi, D. *et al.* Electrostatically Driven Second-Sphere Ligand Switch between High and Low Reorganization Energy Forms of Native Cytochrome c. *J Am Chem Soc* **135**, 4389-4397 (2013).

98. Gray, H.B. & Winkler, J.R. Electron tunneling through proteins. *Quarterly reviews of biophysics* **36**, 341-372 (2004).

99. Mcardle, J.V., Gray, H.B., Creutz, C. & Sutin, N. Kinetic Studies of Oxidation of Ferrocytochrome-C from Horse Heart and Candida-Krusei by Tris(1, 10-Phenanthroline)Cobalt(Iii). *J Am Chem Soc* **96**, 5737-5741 (1974).

100. Warren, J.J., Tronic, T.A. & Mayer, J.M. Thermochemistry of Proton-Coupled Electron Transfer Reagents and its Implications. *Chem Rev* **110**, 6961-7001 (2010).

101. Marques, H.M. Insights into porphyrin chemistry provided by the microperoxidases, the haempeptides derived from cytochrome c. *Dalton T*, 4371-4385 (2007).

102. Bren, K.L. & Gray, H.B. Structurally Engineered Cytochromes with Novel Ligand-Binding Sites - Oxy and Carbonmonoxy Derivatives of Semisynthetic Horse Heart Ala80 Cytochrome-C. *J Am Chem Soc* **115**, 10382-10383 (1993).

103. Wallace, C.J. & Clark-Lewis, I. Functional role of heme ligation in cytochrome c. Effects of replacement of methionine 80 with natural and non-natural residues by semisynthesis. *The Journal of biological chemistry* **267**, 3852-3861 (1992).

104. Ferrer, J.C. *et al.* Identification of Lys79 as an Iron Ligand in One Form of Alkaline Yeast Iso-1-Ferricytochrome-C. *J Am Chem Soc* **115**, 7507-7508 (1993).

105. Solmaz, S.R.N. & Hunte, C. Structure of complex III with bound cytochrome c in reduced state and definition of a minimal core interface for electron transfer. *Journal of Biological Chemistry* **283**, 17542-17549 (2008).

106. Shimada, S. *et al.* Complex structure of cytochrome c-cytochrome c oxidase reveals a novel protein-protein interaction mode. *Embo J* **36**, 291-300 (2017).

107. Sakamoto, K. *et al.* NMR basis for interprotein electron transfer gating between cytochrome c and cytochrome c oxidase. *Proc Natl Acad Sci U S A* **108**, 12271-12276 (2011).

108. Dempsey, J.L., Winkler, J.R. & Gray, H.B. Proton-coupled electron flow in protein redox machines. *Chem Rev* **110**, 7024-7039 (2010).

109. Hammes-Schiffer, S. Proton-Coupled Electron Transfer: Moving Together and Charging Forward. *J Am Chem Soc* **137**, 8860-8871 (2015).

110. Kaila, V.R.I., Verkhovsky, M.I. & Wikström, M. Proton-Coupled Electron Transfer in Cytochrome Oxidase. *Chem Rev* **110**, 7062-7081 (2010).

111. Leitch, F.A., Moore, G.R. & Pettigrew, G.W. Structural basis for the variation of pH-dependent redox potentials of Pseudomonas cytochromes c-551. *Biochemistry* **23**, 1831-1838 (1984).

112. Battistuzzi, G., Borsari, M., Dallari, D., Ferretti, S. & Sola, M. Cyclic Voltammetry and 1H-NMR of Rhodopseudomonas palustris Cytochrome c2. *Eur J Biochem* **233**, 335-339 (1995).

113. Poulos, T.L. Heme Enzyme Structure and Function. *Chem Rev* **114**, 3919-3962 (2014).

114. Ruiz-Dueñas, F.J. *et al.* Substrate oxidation sites in versatile peroxidase and other basidiomycete peroxidases. *Journal of experimental botany* **60**, 441-452 (2009).

115. Veitch, N.C. Horseradish peroxidase: a modern view of a classic enzyme. *Phytochemistry* **65**, 249-259 (2004).

116. Sharma, S. *et al.* Lactoperoxidase: structural insights into the function,ligand binding and inhibition. *International journal of biochemistry and molecular biology* **4**, 108-128 (2013).

117. Singh, A.K. *et al.* Binding modes of aromatic ligands to mammalian heme peroxidases with associated functional implications: crystal structures of lactoperoxidase complexes with acetylsalicylic acid, salicylhydroxamic acid, and benzylhydroxamic acid. *The Journal of biological chemistry* **284**, 20311-20318 (2009).

118. Choudhury, K. *et al.* Role of the proximal ligand in peroxidase catalysis. Crystallographic, kinetic, and spectral studies of cytochrome c peroxidase proximal ligand mutants. *The Journal of biological chemistry* **269**, 20239-20249 (1994).

119. Chreifi, G. *et al.* Crystal structure of the pristine peroxidase ferryl center and its relevance to proton-coupled electron transfer. *Proc Natl Acad Sci U S A* **113**, 1226-1231 (2016).

120. Muenzner, J. & Pletneva, E.V. Structural transformations of cytochrome c upon interaction with cardiolipin. *Chem Phys Lipids* **179**, 57-63 (2014).

121. Baldwin, D.A., Marques, H.M. & Pratt, J.M. Hemes and Hemoproteins .5. Kinetics of the Peroxidatic Activity of Microperoxidase-8 - Model for the Peroxidase Enzymes. *Journal of inorganic biochemistry* **30**, 203-217 (1987).

122. Marques, H.M. Peroxidase activity of the hemeoctapeptide N-acetylmicroperoxidase-8. *Inorg Chem* **44**, 6146-6148 (2005).

123. Wang, J.-S., Baek, H.K. & Van Wart, H.E. High-valent intermediates in the reaction of Nα-acetyl microperoxidase-8 with hydrogen peroxide: Models for compounds 0,I and II of horseradish peroxidase. *Biochemical and biophysical research communications* **179**, 1320-1324 (1991).

124. Yeh, H.C., Wang, J.S., Su, Y.O. & Lin, W.Y. Stopped-flow kinetic study of the H2O2 oxidation of substrates catalyzed by microperoxidase-8. *J Biol Inorg Chem* **6**, 770-777 (2001).

125. Wang, Z.H., Matsuo, T., Nagao, S. & Hirota, S. Peroxidase activity enhancement of horse cytochrome c by dimerization. *Org Biomol Chem* **9**, 4766-4769 (2011).

126. Nakajima, R. & Yamazaki, I. The mechanism of oxyperoxidase formation from ferryl peroxidase and hydrogen peroxide. *The Journal of biological chemistry* **262**, 2576-2581 (1987).

127. Berglund, G.I. *et al.* The catalytic pathway of horseradish peroxidase at high resolution. *Nature* **417**, 463-468 (2002).

128. Van Wart, H.E. & Zimmer, J. Resonance Raman evidence for the activation of dioxygen in horseradish oxyperoxidase. *The Journal of biological chemistry* **260**, 8372-8377 (1985).

129. Kapralov, A.A. *et al.* Topography of tyrosine residues and their involvement in peroxidation of polyunsaturated cardiolipin in cytochrome c/cardiolipin peroxidase complexes. *Bba-Biomembranes* **1808**, 2147-2155 (2011).

130. Marquez, L.A., Huang, J.T. & Dunford, H.B. Spectral and Kinetic-Studies on the Formation of Myeloperoxidase Compound-I and Compound-Ii - Roles of Hydrogen-Peroxide and Superoxide. *Biochemistry* **33**, 1447-1454 (1994).

131. Adams, P.A. & Goold, R.D. Hypervalent Iron-Oxo Porphyrin Cation Radical Formation on Reaction of H2o2 with the Cytochrome-C-Derived Heme Octapeptide Microperoxidase-8 (Mp-8) in Aqueous-Solution. *J Chem Soc Chem Comm*, 97-98 (1990).

132. Adams, P.A. The Peroxidasic Activity of the Heme Octapeptide Microperoxidase-8 (Mp-8) - the Kinetic Mechanism of the Catalytic Reduction of H2o2 by Mp-8 Using 2,2'-Azinobis-(3-Ethylbenzothiazoline-6-Sulfonate) (Abts) as Reducing Substrate. *J Chem Soc Perk T 2*, 1407-1414 (1990).

133. Perez Galende, P. *et al.* Kinetics of Spanish broom peroxidase obeys a Ping-Pong Bi-Bi mechanism with competitive inhibition by substrates. *International journal of biological macromolecules* **81**, 1005-1011 (2015).

134. Mao, G. *et al.* Mitochondrial Redox Opto-Lipidomics Reveals Mono-Oxygenated Cardiolipins as Pro-Apoptotic Death Signals. *ACS Chemical Biology* **11**, 530-540 (2016).

135. Kagan, V.E. *et al.* Redox phospholipidomics of enzymatically generated oxygenated phospholipids as specific signals of programmed cell death. *Free Radical Biology and Medicine* **147**, 231-241 (2020).

136. Tyurina, Y.Y. *et al.* Mechanisms of cardiolipin oxidation by cytochrome c: relevance to pro- and antiapoptotic functions of etoposide. *Molecular pharmacology* **70**, 706-717 (2006).

137. Belikova, N.A. *et al.* Peroxidase activity and structural transitions of cytochrome c bound to cardiolipin-containing membranes. *Biochemistry* **45**, 4998-5009 (2006).

138. Steele, H.B.B., Elmer-Dixon, M.M., Rogan, J.T., Ross, J.B.A. & Bowler, B.E. The Human Cytochrome c Domain-Swapped Dimer Facilitates Tight Regulation of Intrinsic Apoptosis. *Biochemistry* **59**, 2055-2068 (2020).

139. Yin, H. & Zhu, M. Free radical oxidation of cardiolipin: chemical mechanisms, detection and implication in apoptosis, mitochondrial dysfunction and human diseases. *Free radical research* **46**, 959-974 (2012).

140. Tyurina, Y.Y. *et al.* "Only a Life Lived for Others Is Worth Living": Redox Signaling by Oxygenated Phospholipids in Cell Fate Decisions. *Antioxid Redox Signal* **29**, 1333-1358 (2018).

141. Miyamoto, S. *et al.* Cytochrome c-promoted cardiolipin oxidation generates singlet molecular oxygen. *Photochemical & photobiological sciences : Official journal of the European Photochemistry Association and the European Society for Photobiology* **11**, 1536-1546 (2012).

142. Kagan, V.E. *et al.* Redox Epiphospholipidome in Programmed Cell Death Signaling: Catalytic Mechanisms and Regulation. *Frontiers in Endocrinology* **11** (2021).

143. Liu, W., Porter, N.A., Schneider, C., Brash, A.R. & Yin, H. Formation of 4-hydroxynonenal from cardiolipin oxidation: Intramolecular peroxyl radical addition and decomposition. *Free radical biology & medicine* **50**, 166-178 (2011).

144. Dunford, H.B. *Heme peroxidases*. (John Wiley, New York; 1999).

145. Diederix, R.E.M., Ubbink, M. & Canters, G.W. The peroxidase activity of cytochrome c-550 from Paracoccus versutus. *Eur J Biochem* **268**, 4207-4216 (2001).

146. Wang, Z.H. *et al.* Converting cytochrome c into a peroxidase-like metalloenzyme by molecular design. *Chembiochem* **8**, 607-609 (2007).

147. Diederix, R.E.M., Ubbink, M. & Canters, G.W. Effect of the protein matrix of cytochrome c in suppressing the inherent peroxidase activity of its heme prosthetic group. *Chembiochem* **3**, 110-112 (2002).

148. Patriarca, A. *et al.* Conversion of cytochrome c into a peroxidase: inhibitory mechanisms and implication for neurodegenerative diseases. *Arch Biochem Biophys* **522**, 62-69 (2012).

149. Clore, G.M., Hollaway, M.R., Orengo, C., Peterson, J. & Wilson, M.T. The Kinetics of the Reactions of Low-Spin Ferric Heme Undecapeptide with Hydrogen-Peroxide. *Inorg Chim a-Bioinor* **56**, 143-148 (1981).

150. Milorey, B., Schweitzer-Stenner, R., Kurbaj, R. & Malyshka, D. pH-Induced Switch between Different Modes of Cytochrome c Binding to Cardiolipin-Containing Liposomes. *ACS omega* **4**, 1386-1400 (2019).

151. Hanske, J. *et al.* Conformational properties of cardiolipin-bound cytochrome c. *P Natl Acad Sci USA* **109**, 125-130 (2012).

152. Worrall, J.A. *et al.* The effects of ligand exchange and mobility on the peroxidase activity of a bacterial cytochrome c upon unfolding. *Chembiochem* **6**, 747-758 (2005).

153. Spooner, P.J.R. & Watts, A. Cytochrome c interactions with cardiolipin in bilayers: a multinuclear magic-angle spinning NMR study. *Biochemistry* **31**, 10129-10138 (1992).

154. Mandal, A. *et al.* Structural Changes and Proapoptotic Peroxidase Activity of Cardiolipin-Bound Mitochondrial Cytochrome c. *Biophysical journal* **109**, 1873-1884 (2015).

155. Rytomaa, M. & Kinnunen, P.K. Reversibility of the binding of cytochrome c to liposomes. Implications for lipid-protein interactions. *The Journal of biological chemistry* **270**, 3197-3202 (1995).

156. Rajagopal, B.S., Silkstone, G.G., Nicholls, P., Wilson, M.T. & Worrall, J.A.R. An investigation into a cardiolipin acyl chain insertion site in cytochrome c. *Bba-Bioenergetics* **1817**, 780-791 (2012).

157. Hong, Y.N., Muenzner, J., Grimm, S.K. & Pletneva, E.V. Origin of the Conformational Heterogeneity of Cardiolipin-Bound Cytochrome c. *J Am Chem Soc* **134**, 18713-18723 (2012).

158. Oellerich, S., Lecomte, S., Paternostre, M., Heimburg, T. & Hildebrandt, P. Peripheral and Integral Binding of Cytochrome c to Phospholipids Vesicles. *The Journal of Physical Chemistry B* **108**, 3871-3878 (2004).

159. Capdevila, D.A. *et al.* Active Site Structure and Peroxidase Activity of Oxidatively Modified Cytochrome c Species in Complexes with Cardiolipin. *Biochemistry* **54**, 7491-7504 (2015).

160. Sinibaldi, F. *et al.* Role of lysines in cytochrome c-cardiolipin interaction. *Biochemistry* **52**, 4578-4588 (2013).

161. Bradley, J.M., Silkstone, G., Wilson, M.T., Cheesman, M.R. & Butt, J.N. Probing a complex of cytochrome c and cardiolipin by magnetic circular dichroism spectroscopy: implications for the initial events in apoptosis. *J Am Chem Soc* **133**, 19676-19679 (2011).

162. Yin, V., Shaw, G.S. & Konermann, L. Cytochrome c as a Peroxidase: Activation of the Precatalytic Native State by H2O2-Induced Covalent Modifications. *J Am Chem Soc* **139**, 15701-15709 (2017).

163. Tomášková, N. *et al.* Early modification of cytochrome c by hydrogen peroxide triggers its fast degradation. *International journal of biological macromolecules* **174**, 413-423 (2021).

164. Tomášková, N., Varhač, R., Lysáková, V., Musatov, A. & Sedlák, E. Peroxidase activity of cytochrome c in its compact state depends on dynamics of the heme region. *Biochimica et Biophysica Acta (BBA) - Proteins and Proteomics* **1866**, 1073-1083 (2018).

165. De Rocco, D. *et al.* Mutations of cytochrome c identified in patients with thrombocytopenia THC4 affect both apoptosis and cellular bioenergetics. *Bba-Mol Basis Dis* **1842**, 269-274 (2014).

166. Johnson, B. *et al.* Whole exome sequencing identifies genetic variants in inherited thrombocytopenia with secondary qualitative function defects. *Haematologica* **101**, 1170-1179 (2016).

167. Morison, I.M. *et al.* A mutation of human cytochrome c enhances the intrinsic apoptotic pathway but causes only thrombocytopenia. *Nat Genet* **40**, 387-389 (2008).

168. Uchiyama, Y. *et al.* A novel CYCS mutation in the alpha-helix of the CYCS C-terminal domain causes non-syndromic thrombocytopenia. *Clin Genet* **94**, 548-553 (2018).

169. Patel, S.R., Hartwig, J.H. & Italiano, J.E., Jr. The biogenesis of platelets from megakaryocyte proplatelets. *The Journal of clinical investigation* **115**, 3348-3354 (2005).

170. Wolf, B.B. *et al.* Calpain functions in a caspase-independent manner to promote apoptosis-like events during platelet activation. *Blood* **94**, 1683-1692 (1999).

171. De Botton, S. *et al.* Platelet formation is the consequence of caspase activation within megakaryocytes. *Blood* **100**, 1310-1317 (2002).

Chapter 3

Differences in Functional Cross-Talk Between Low-Energy Foldons in Two Closely-Related Cytochrome *c* Proteins

pH jump experiments were performed by Dr. Fangfang Zhong.

Preparation of the plasmid containing a G41S mutation in horse heart cyt *c* and GuHCl global stability measurements for the expressed and purified protein were performed by Nicholas Shallow.

The plasmid for WT horse heart cyt *c* was provided by Dr. Kara L. Bren.

Introduction

Protein sequence is considered to dictate the structure of the protein, which in turn defines its function.[1] Recently, the dogma has been challenged as various proteins challenge this assumption. For example, many proteins found in mesophiles, have structurally homologous counterparts in extremophiles, but varied global stability and conformational dynamics essential for enzymatic activity.[2-4] Sequence variations between species fine-tune the strength and the number of intramolecular interactions; more stabilizing interactions decrease the flexibility of the protein in thermophiles, and less stabilizing interactions increase the flexibility of the protein in psychrophiles.[2-5] Relationship between protein stability and polypeptide dynamics has been described in terms of the folding energy funnel with mutational studies with yeast cyt *c*; decrease in the global stability of the protein lowered energy barriers between conformations, increasing the kinetic rates of interconversion between different conformational states.[6]

However, this direct global stability-flexibility relationship is not universal. For example, cyt c_{552} proteins from mesophilic and thermophilic organisms are structurally and sequentially similar,[7] and seem to follow the global stability-flexibility relationship.[7-9] However, recent studies with cyt c_{552} from a psychrophilic organism have shown comparable T_m and lower ΔH when compared to other mesophilic *c*-type cytochromes,[10] contrary to what is generally expected from psychrophilic proteins that are usually more flexible and less sterically hindered.[5, 11] The relationship between steric hinderance and local biophysical properties of the protein has been implicated in mutational studies that introduced cavities in SNase, whose changes in local stability and dynamics depended on the relative rigidity of the region.[12] A similar disconnect between global stability and local

dynamics has been shown with yeast cyt *c* with a L85A mutation, where a globally destabilizing mutation does not increase protein dynamics.[13] Further, comparison between salmon and bovine trypsin has suggested that weakened interdomain interactions might be enough to reduce local flexibility, highlighting the subtle roles of innate residue variations between species that do not perturb the global properties of the protein.[14] Studies with other psychrophilic enzymes have also suggested that local flexibility can be decoupled from global stability.[5] Although these findings suggest that innate sequence variations may have dramatic local effects on both stability and dynamics without perturbing the global properties, the exact role of sequence variation and local changes between species remains elusive. Lack of data makes it difficult to relate global and local thermodynamic data to kinetic loop dynamics and enzymatic activity in terms of sequence variation. Not only a good understanding of the folding pathway of the protein is required, but also a good method to quantitatively measure the local dynamics and stability is essential to explain the relationship between sequence variation, local and global stability, and conformational dynamics.

A good model protein to explore this issue is cyt *c*. Cyt *c* is a small mitochondrial protein with high structure and sequence conservation across multiple species. Cyt *c* has been a model for studying protein folding, as it contains clearly defined folding regions (foldons) that differ in thermodynamic stability.[15, 16] Of the five foldons in cyt *c*, loops C (nested-yellow foldon, residues 40 to 55) and D (red foldon, residues 70 to 85) are the least stable and unstructured, but relatively well-conserved foldons in cyt *c*.[15] In human, horse heart, and yeast WT proteins (Figure 3.1 and Table 3.1), sequences of these two loops are highly varied.

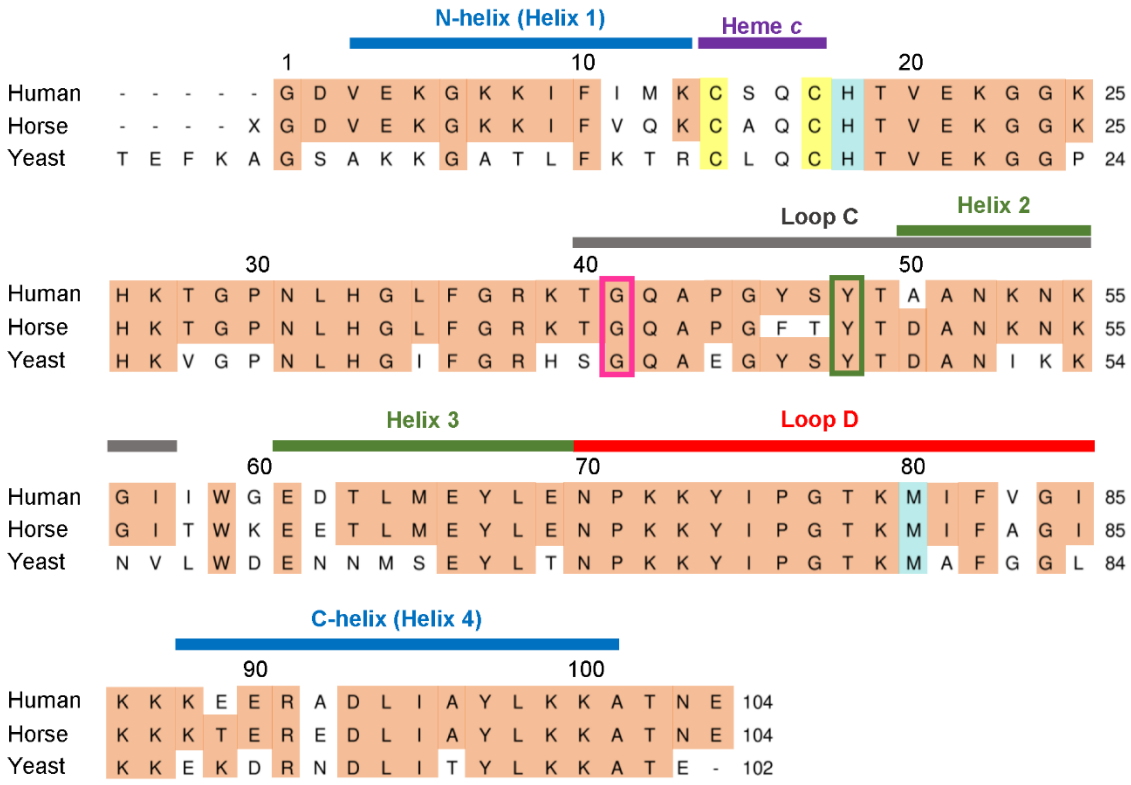

Figure 3.1. Sequence alignment of human (Protein Data Bank (PDB) ID 3ZCF),[17] horse heart (1HRC),[18] and yeast (2YCC)[17] WT cyt *c* using Clustal Omega.[19] Highlighted are conserved sequences across species (orange), cysteines conjugated to the heme (yellow), and native axial ligands (teal). Regions of the sequences conjugated to the heme (purple), loops C and D (grey and red, respectively), and the *N*-terminal, 50's, 60's, and *C*-terminal α-helices (blue) are indicated. Sites of mutations discussed in this study, Glys41 (pink), and Tyr48 (green), are boxed.

Table 3.1. Sequence and Structure Conservation in Cyt *c*

	Sequence Conservation[a]		Structure Conservation	
	Human	Yeast	Human	Yeast
Human	--	63.46 %	--	75.73 %
Horse Heart	88.46 %	61.90 %	93.27 %	73.79 %
Yeast	63.46 %	--	75.73 %	--

[a]Sequence alignment of human, horse heart, and yeast WT cyt *c* using Clustal Omega.[19] Structure alignment was performed using the structure alignment tool on the PDB website, using the jFATCAT-flexible algorithm.[20, 21]

The sequence identity of the least stable loop C and slightly more stable loop D ranges from 31% to 94 % and 63% to 94%, respectively, when compared between cyt *c* from 96 species to human cyt *c*.[22] Cyt *c* functions as both a peroxidase and a participant in the caspase cascade, as well as an electron carrier in the ET pathway for cellular respiration; in both functions, properties of loops C and D play a major role. At alkaline pH conditions, the axial ligand switch between Met and Lys is dependent upon stability and dynamics of loop D.[23, 24] Switch in axial heme iron ligation not only alters the local fold, but also directly dictates the capacity of the protein as an peroxidase, an instrumental function to initiate apoptosis.[25, 26] The peroxidase activity is regulated and tuned, in part, by loop dynamics that alter the heme ligation and environment. In recent years, role of sequence variation in proteins have heightened due to the discovery of mutations resulting in human diseases[27, 28] or abnormal embryonic development[29] in loops C and D.

It is yet unclear how the innate sequence variations in loops C and D influence the various functions of cyt *c*, particularly when comparing results across species. For example, a lethal K72A mutation in loop D slightly enhanced intrinsic peroxidase activity in cellular studies compared to WT, despite similar levels of cyt *c* release and oxygen consumption.[29] Further, the magnitude of increase in peroxidase activity with the K72A mutation observed in human cyt *c* differs from that observed in yeast cyt *c*, despite many similar global characteristics.[30, 31] Replacement of side chains in loop C of human cyt *c* sequence to those present in spider monkey cyt *c* sequence altered the pK_a of the alkaline transition, while the global chemical stability remained consistent.[32] Similarly, genetic mutations in loop C, G41S and Y48H, did not exhibit any growth defects in humans.[27, 28] However, G41S and Y48H human cyt *c* were also shown to enhance intrinsic peroxidase activity *in vitro*, but

the data are conflicting as to whether the mutation enhances peroxidase activity compared to WT *in vivo*.[33-35] Although these mutations are hypothesized to influence the apoptotic pathway based on their intrinsic activity,[28] this alone would not fully explain the conflicts in apoptotic peroxidase activity from cyt *c* from different species. These data suggest that inherent minor sequence differences in loop C affect the properties of loop D. This may also be an important factor in tailoring protein function for the organism, especially when accommodating unnatural mutations that may disrupt the delicate balance to ensure proper function. Further, understanding the role of sequence variation in local dynamics and stability is critical in resolving these functional conflicts, which require a detailed characterization of intrinsic and dynamic properties for the series of the mutants.

Many biophysical and biochemical properties of cyt *c*, such as heme iron ligation, global stability, and enzymatic activity remain similar among human, horse heart, and yeast cyt *c*. Yet, subtle differences do exist between species, posing a barrier in addressing conflicts in data obtained from different organisms. For example, despite the high sequence conservation in loop D between yeast and human WT proteins, local loop D stability is not conserved.[32, 36] Despite maintaining many similar biophysical characteristics such as heme iron ligation and secondary fold,[17, 34] other biochemical properties, such as the pK_a of the alkaline transition, are different between yeast and human cyt *c*.[32, 37] While these differences hint that innate sequence variations in the two loop regions may be contributing to functional differences, it is difficult to relate such differences to sequence variations, as global stabilities of yeast and human WT cyt *c* are very different,[31, 36] and many of the biophysical studies have been conducted with either yeast or horse heart cyt *c*.

We thus wondered whether we could better define the local biophysical and biochemical contributions from sequence variations. For this purpose, we have chosen horse heart cyt *c*, a well-studied model system that, unlike yeast cyt *c*, has similar global stability to human cyt *c* to address these questions.[38] Furthermore, we have also sought to clarify the conflicting data in the effects of the disease mutations, G41S and Y48H, particularly when comparing functional results across different species.

Herein, we have studied a series of horse heart cyt *c* variants containing G41S or Y48H mutations, which have also been characterized with human cyt *c*. Horse heart cyt *c*, because of its well-characterized folding and other conformational transitions, is a good system for examining the relationship between global and local effects on the biophysical properties of the protein in respect to local sequence variation. Horse heart cyt *c* has a higher sequence similarity and is more structurally homologous to human cyt *c* than yeast cyt *c*, making it a better model system to apply the biophysical data in understanding the biological pathways in humans (Table 3.1). By comparing variants with mutations in both loops C and D (Figure 3.2), we highlight the feedback (cross-talk) between these two foldons in tuning the local thermodynamic and kinetic properties of the protein.

In this chapter, we compare the effects of several mutations in perturbing both the global and local stability of the protein and relate these stabilities to changes in local dynamics of loop D and Met ligand dissociation from the heme iron. We obtain parameters associated with alkaline transition and peroxidase activity to better understand how the mutations and surrounding residues affect the kinetic and thermodynamic landscape associated with loop rearrangement, heme iron ligand dissociation and exchange.

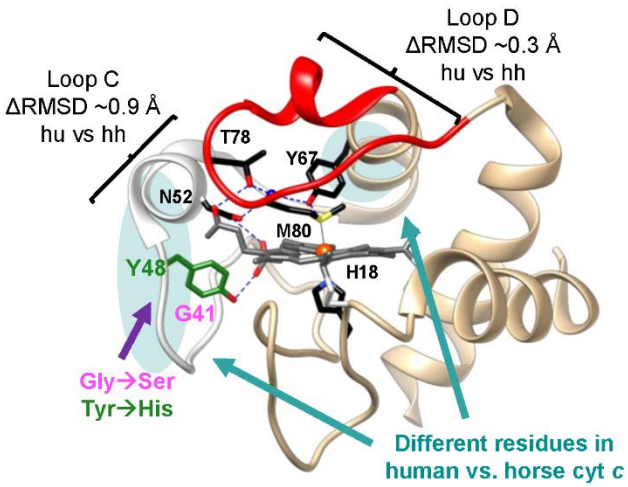

Figure 3.2. Structure of WT horse heart cyt *c* (PDB 1HRC);[18] highlighted are the residues discussed in this chapter. Mutation of Gly41 (pink) and Tyr48 (green) to Ser and His, respectively, was shown to yield mild thrombocytopenia in humans. Regions in loops C and D that are different between human (hu) and horse heart (hh) WT cyt *c* are indicated (teal), with the calculated RMSD values (ΔRMSD) in loop regions, obtained from the structural overlay of the horse heart and human WT cyt *c* X-ray crystal structures, are labeled. Loops D (residues 70 to 85, red) and C (residues 40 to 58, white) carrying the examined mutations are highlighted.

The local sequences and packing of loop D in horse heart and human cyt *c* are nearly identical, except for the region near HP6 (Figures 3.1 and 3.2). Mutations near these regions previously have been shown to alter polypeptide dynamics and stability, but their effects on altering function are different depending on the species. We explore the how sequence variations in cyt *c* proteins may alter function by altering loop contacts in cyt *c* proteins. Since structural data on G41S and Y48H variants in horse heart cyt c are lacking, MD simulations have been conducted on both human and horse heart cyt *c* proteins to compare how G41S and Y48H mutations alter packing in loops C and D. These changes have potential to decrease the thermodynamic barrier associated with accessing different ligated states of the heme iron and/or increase the kinetic rate associated with loop D rearrangement, without major perturbations in the global properties of the protein. With this work and prior series, we comment on the biological implications and role of sequence variations, but also provide further mechanistic information on the origin of k_f and the nature of the trigger group in alkaline transition of cyt *c*.

Materials and Methods

General. All aqueous solutions were prepared using water from Barnstead E-Pure Ultrapure Water Purification System, purified to a resistivity of 18 MΩ·cm. Reagents and columns were purchased from Millipore Sigma and GE Healthcare, unless noted otherwise. Gas-tight Hamilton syringes were used for all titrations and quantitative dilutions. pH was adjusted using sodium hydroxide or hydrochloric acid and monitored with an AB15 pH meter (Fisher Scientific) or a UB10 pH meter (Denver Instrument).

Sequence Alignments and Molecular Dynamics Simulations. Sequence alignments for figures and structural analyses were performed using Clustal Omega[19] and Chimera,[39]

respectively. Energy-minimized models of protein variants were obtained with Visual Molecular Dynamics (VMD)[40] and Not Just a Molecular Dynamics (NAMD)[41] as previously described,[42] starting from crystal structures of human (PDB ID: 3ZCF, ferric)[34] and horse heart cyt *c* (PDB ID: 1HRC, ferric)[18]. Previously published force field parameters for the Met-ligated ferric *c*-type heme[43] and backbone peptides[44] were employed and protein structures were solvated by building a 3-Å water box from the protein surface.

To compare the structural differences in the ferric variants between horse heart and human cyt *c*, a total of 2-fs snapshots spaced 1 ps apart were acquired during 0.01 ns simulations for geometry optimization. These short timescale simulations were then equilibrated for 15,000,000 steps (at 2 fs per step, total of 30 ns) at 300 K, and trajectory data saved every 10,000 steps (20 ps), as previously described.[45]

To test whether longer timescale simulations were required, snapshots obtained for a total simulation length of 120 ns were also obtained. Plots of per residue root mean square fluctuation (RMSF) values of protein backbone α-carbons (αC) atoms in WT for all the structures in the trajectory compared to the initial structure were obtained for MD simulations obtained from either 30 ns or 120 ns total simulation times. Comparison of the per residue RMSF showed that after the initial 10 ns, there were no differences in the per residue RMSF value between two simulation time scales (Figure 3.3). Thus, longer timescales beyond 30 ns were not explored for the variants, as large differences were not picked up at 30 ns versus 120 ns simulation times in WT. For each variant, independent 30 ns timescale simulations were repeated from the initial 0.01 ns simulations in triplicates.

Figure 3.3. Plots showing the per residue RMSF of αC positions in the polypeptide backbone from various MD-simulated structures horse heart WT cyt *c* at 300 K. (A) Comparison of RMSF plots of Cα from single MD-simulated structures for horse heart WT cyt *c*, at timescales of 0.12 ns (grey), 30 ns (green), 50 ns (pink), and 120 ns (black). (B) Plots comparing the per residue RMSF of αC positions in the polypeptide backbone from MD-simulated structures at 30 ns time scale for first (blue), second (purple), and third (pink) independent simulations. Plot of per residue RMSF of αC positions in the polypeptide backbone obtained from three combined simulations are also shown (black, dotted line). (C) RMSF plots of Cα from MD simulated structures at 120 ns time scale (black) and averaged RMSF plot obtained from the average of 3 simulations (red) compared to RMSF plot of Cα from MD-simulated structure reported in literature for 50 ns simulation (green), from ref. [46].

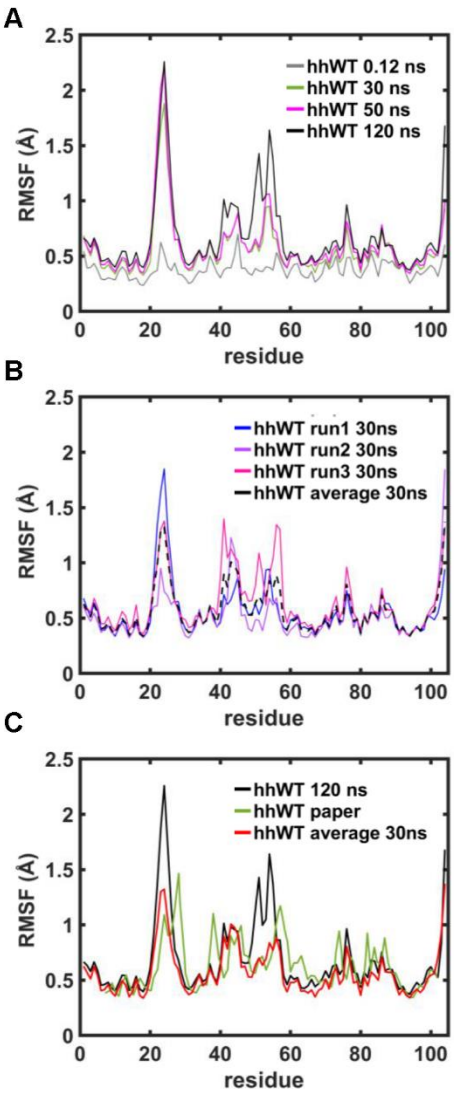
A
RMSF (Å)
residue
hhWT 0.12 ns
hhWT 30 ns
hhWT 50 ns
hhWT 120 ns
B
RMSF (Å)
residue
hhWT run1 30ns
hhWT run2 30ns
hhWT run3 30ns
hhWT average 30ns
C
RMSF (Å)
residue
hhWT 120 ns
hhWT paper
hhWT average 30ns

To determine timescale regions where the structures reached an equilibrium, root-mean-square deviation (RMSD) values of protein backbone atoms of the structures in the trajectory relative to the protein backbone atoms in the initial structure of the protein were plotted using VMD.[40] Analyses of RMSD values of the protein backbone atoms of the simulated structures relative to initial structure of the protein showed no large fluctuations in the RMSD value after 10 to 15 ns, suggesting that the MD simulation reached equilibrium after 20 ns. Therefore, only the structures from trajectories obtained in the 20 to 30 ns simulation time range were used to calculate the pairwise RMSD distributions of αC for loops C and D (where each structure in the trajectory was compared to every other structure in the trajectory) and per residue RMSF distributions of αC using GROMACS.[47-53]

Crystal structures of variants of human cyt *c* (G41S, PDB: 3NWV, ferrous;[54] Y48H, PDB: 5O10, ferric[35]) were employed in comparisons to both the crystal structure of WT human cyt *c* and the MD simulations of the variants. To compare the hydrophobic packing of the proteins from different species, total solvent-excluded molecular surface volume (V_{MS}), void volume (V_{void}), and the Van der Waals (VdW) volume (V_{VdW}) for the structures of human (PDB ID: 3ZCF),[34] horse heart (PDB ID: 1HRC),[18] and *iso-1* yeast (PDB ID: 2YCC)[17] WT cyt *c* were calculated using ProteinVolume,[55] using energy minimization with 0.08 Å starting probe size, 0.02 Å ending probe size, and 0.1 Å surface probe minimum distance. Contributions from *N*- and *C*-helices were also considered using the PDB data for the residues 3 to 13 and 88 to 101; for this analysis, only the PDB data from residues in the *N*- and *C*-helices, the heme porphyrin coordinates, and the solvent data were used. In cases where multiple protein structures were present in the same unit cell, total

computed volumes were divided by the number of protein structures in the unit cell to obtain the average value.

Contact Maps. Contact maps from crystal structures of WT cyt *c* from human (PDB ID: 3ZCF, chain A),[34] spider monkey (PDB ID: 5DFS, chain A),[32] horse heart (PDB ID: 1HRC),[18] bovine (PDB ID: 2B4Z and 6FF5),[56, 57] bonito tuna (PDB ID: 1CYC),[58] albacore tuna (PDB ID: 5CYT),[59] yeast *iso-1* (PDB ID: 2YCC),[17] and yeast *iso-2* (PDB ID: 1YEA)[60] were obtained by using calculated pairwise interatomic distances with a 5 Å cut-off. In the analyses of MD structures for every variant, structures in trajectories from 20 to 30 ns from three separate repeats were combined into a single trajectory, and this combined trajectory was used to calculate pairwise interatomic distances, with either a 3 Å or a 5 Å cut-off. Using calculated distances, contact maps of contact frequencies were generated, and heat maps of contact frequencies plotted using Python 3. Python 3 script used for generating heat maps of contact frequencies was provided by Dr. Fangfang Zhong.

For loops C and D, contact maps illustrating HB and vdW interactions were also prepared for human (PDB ID: 3ZCF),[34] horse heart (PDB ID: 1HRC),[18] and yeast (PDB ID: 2YCC)[17] WT cyt *c*. In the presence of multiple structures within the unit cell, each structure was examined individually, and the results were subsequently averaged. HB interactions were identified using the prediction constraints relaxed by 0.4 Å and 20 degrees to the nearest residue, for up to two water molecules between the residues using Chimera,[39, 61] and the strength of the interaction scaled using the $1/(r)^3$ potential energy distance relationship for a dipole-to-dipole interaction.[62] In the presence of bridging waters, the distance between the residues of interest was estimated to be the total sum of the HB distances between the residues for simplicity. vdW interactions were identified according

to recommended ranges for detecting contacts for all atoms of interest,[39, 63, 64] and the strength of the interactions scaled using the $1/r^6$ estimate based on the attractive term in Lennard-Jones potential energy distance relationship,[62] and grouped the individual atom contributions to be representative of the entire residue.

Site-Directed Mutagenesis, Protein Expression, and Purification. WT horse heart cyt *c* was purchased from Sigma-Aldrich (C2506). Desired point mutations were introduced in the pBTR plasmid encoding horse heart cyt *c* using a QuikChange kit (Agilent).[65] PCR products were transformed into XL1-Blue competent cells (Agilent), and cells grown using 14 mL polypropylene Falcon Tubes (Ref 352059) and grown on LB agar plates containing 100 mg/mL carbenicillin at 37 °C. Humidity was adjusted by placing 500 mL of water inside the incubator to prevent agar plates from drying out. Plasmid DNA was extracted using a QIAprep Spin Miniprep Kit (Qiagen) and the purity was determined by obtaining the absorbance ratio of 1.7-1.8 at 260/280 nm. To improve the purity ratio, plasmid DNA was washed twice in the miniprep step. Desired mutations were confirmed by sequencing at the Molecular Biology & Proteomics Core Facility (Dartmouth College). At times, DNA sequencing chromatogram was visualized by using FinchTV v.1.4.0 (Geospiza) and sequences were reconfirmed.

Large-scale protein expression was performed as previously described,[38] except for using 2 L of TB media in a 2.8-L flask to prevent heme degradation and increase protein yield. Protein extraction was performed at 4 °C using French Press to prevent thermal denaturation. Mutations and purity of the expressed proteins were confirmed by Matrix-Assisted Laser Desorption Ionization (MALDI) at the Molecular Biology & Proteomics Core Facility (Dartmouth College). Extinction coefficients of protein variants were

determined at pH 7.4 in a 25 mM HEPES or a 100 mM sodium phosphate buffer using hemochrome assays.[65]

Spectroscopic Measurements. All spectroscopic measurements were obtained at room temperature (22 ± 2 ºC) unless noted otherwise. Ferric proteins were prepared by treating protein samples with excess potassium ferricyanide and then purified by size exclusion (PD-10 desalting column) or ion-exchange (Sepharose HP SP) chromatography. Ferrous proteins were prepared by treating protein samples with excess sodium dithionite, and the excess of the reductant was removed with a PD-10 column in the N_2-filled glove box (COY Laboratory Products).

Electronic absorption spectra were recorded using an Agilent 8453 diode-array spectrophotometer. Circular dichroism (CD) spectra were measured on a JASCO-J815 CD spectropolarimeter equipped with a variable temperature Peltier cell device (JASCO, Inc.). Quartz cuvettes and tubes were purchased from Starna Scientific and Wilmad Lab Glass, respectively.

^{1}H NMR spectra were recorded on a 500 MHz Bruker NMR spectrometer (Bruker Biosciences) at 25 ºC. For ^{1}H NMR measurements of ferric proteins, samples of freshly oxidized cyt *c* variants at protein concentration ranging from 0.5 to 3 mM were prepared in a 50 mM borate buffer at pD 10.5, a 50 mM sodium phosphate buffer at pD 7.4, or a 50 mM acetic acid d_4 buffer at pD 4.5 in 100% D_2O. For ^{1}H NMR measurements of ferrous proteins, samples of freshly reduced cyt *c* variants at 0.5 mM protein concentration were prepared in a 50 mM sodium phosphate buffer containing 10% D_2O (*v*/*v*) at pH 7.4, with 5 mM excess dithionite. The standard 2,2-dimethyl-2-silapentane-5-sulfonic acid (DSS) was employed as a reference.

Low-temperature EPR spectra were obtained at 10 K on a Bruker EMX 300 X-band spectrometer (Bruker Biosciences). Spectra were acquired using the following parameters: microwave frequency of 9.49 GHz, microwave power of 3.21 mW, modulation frequency of 100 kHz, modulation amplitude of 3.21 mW, modulation amplitude of 1.00 G, and time constant of 20.48 ms. All samples contained 20% (*v*/*v*) glycerol and were prepared in a 50 mM sodium phosphate at pH 7.4 or a 50 mM sodium acetate buffer at pH 4.5. Buffers were treated with a Chelex resin (Millipore Sigma), a copolymer containing chelating groups, to remove traces of excess metal ions.

Denaturation Experiments. Ultrapure GuHCl (Alfa Aesar) was dissolved in a 100 mM sodium phosphate buffer at pH 7.4, and solutions at varying concentrations of the denaturant were prepared and pH adjusted as needed. Ferric protein samples were aliquoted using a Hamilton syringe and final protein concentrations ranged from 8 to 10 μM for measurements monitoring α-helical signals at 222 nm and 180 to 230 μM for measurements monitoring the CT absorption band at 695 nm. CD ellipticity at 222 nm was observed using a 1-mm pathlength CD cuvette for global stability measurements, and electronic absorption at 695 nm was observed using a 1-cm pathlength quartz cuvette. The signals were fitted to eq 3.1:[66]

$$f(x) = \frac{[m_f[\text{GuHCl}]+b_f+(m_u[\text{GuHCl}]+b_u)\exp(\frac{m_D([\text{GuHCl}]-[\text{GuHCl}]_{1/2})}{RT})]}{[1+\exp(\frac{m_D([\text{GuHCl}]-[\text{GuHCl}]_{1/2})}{RT})]} \quad (3.1)$$

where m_f and b_f, m_u and b_u are the slope and *y*-intercept of the ellipticity signal of the folded and unfolded regions, respectively, in terms of the concentration of the denaturant, [GuHCl]; R is the gas constant and T is the experimental temperature. With the midpoint

of the transition, $[GuHCl]_{1/2}$, and slope of the transition, m_D, Gibbs free energy of unfolding (ΔG_D) was calculated using eq 3.2:

$$\Delta G_D = m_D[GuHCl]_{1/2} \tag{3.2}$$

Eqs 3.1 and 3.2 were obtained by assuming a 2-state mechanism where native folded species is in equilibrium with the denatured species have been derived previously.[67, 68]

In comparison studies, one often interprets smaller experimental values of *m* (shallow steps of unfolding curves) as indicators of fewer changes in solvent exposure of the residue groups i.e., more compact denatured or more open native state, since $m_D = \bar{\alpha} \sum \eta_i \delta g_{tr,i}$ (where α_i is the average fractional change in exposure, η_i is the total number of groups present in the protein, and $\delta g_{tr,i}$ is the free energy of transfer). [68-70]

Changes in CD ellipticity at 222 nm were recorded in the temperature range 20 to 90 ºC (rate of 1 ºC/min). Protein concentrations were around 10 μM. Thermal denaturation of all variants were 99% reversible, as calculated by the CD ellipticity signal of the protein sample at 222 nm taken before and after the temperature melt. Dependencies of CD ellipticity signals (θ) on temperature (*T*) were fitted to eq 3.3:[66, 71]

$$\theta = \left[\frac{m_f T + b_f + (m_u T + b_u) \exp\left(\frac{-\Delta H_{vH}}{R} \left(\frac{1}{T} - \frac{1}{T_m} \right) \right)}{1 + \exp\left(\frac{-\Delta H_{vH}}{R} \left(\frac{1}{T} - \frac{1}{T_m} \right) \right)} \right] \tag{3.3}$$

where m_f and b_f, m_u and b_u are the slope and *y*-intercept of the ellipticity signal of the folded and unfolded regions, respectively, and *R* is the gas constant. Fit of the ellipticity signals

versus temperature to eq 3.3 yielded T_m and ΔH_{vH}, the midpoint of the unfolding transition and the van't Hoff enthalpy of denaturation, respectively.

pH Titrations and Analyses. Solutions containing proteins at concentrations of 8 to 10 μM or 200 to 300 μM in a 100 mM sodium phosphate buffer at pH 7.4 were used to monitor changes in the Soret (350 to 500 nm) and CT (580 to 750 nm) spectral regions, respectively.

pH titration profiles were analyzed using singular value decomposition (SVD) as described previously.[72-74] The obtained pH titration profile **A** (λ_m, pH_n) was deconvoluted into wavelength dependence vectors **U** (λ, x-value), square roots of the eigenvalues **S** (*k*, significance), and pH dependence **V** (pH, populations for the corresponding **S** vector) using the MATLAB SVD function ($\mathbf{A}=\mathbf{U}\cdot\mathbf{S}\cdot\mathbf{V}^T$). Number of significant components, *i*, was determined from log of $S_{j,j}$ values, $S_{j,j}$ percentages ($\frac{S_{j,j}^2}{\sum_{j=1}^{k} S_{j,j}^2}$)×100%, error levels ($\sqrt{\frac{\sum_{j=i}^{k} S_{j,j}^2}{\sum_{j=1}^{k} S_{j,j}^2}}$), autocorrelation of U(λ) and V(pH) matrices, as previously described.[72, 73 74]

pH-dependent significant vectors, **V**, from both Soret and CT bands were globally fitted to eq 3.4 using SigmaPlot 10.0:

$$\mathbf{V} = \sum \frac{B_i + A_i \times 10^{n(pK_{app,i} - pH)}}{1 + 10^{n(pK_{app,i} - pH)}} + C \qquad (3.4)$$

where A_i and B_i are the slope and y-intercept of the *i*th transition, pK_{app} is the apparent pK_a for the *i*th transition, *n* is the number or protons involved in the *i*th transition, and C is a constant. Spectra of the respective components were deconvoluted using eq 3.5:

$$D = AF^{-1} \tag{3.5}$$

where D is the spectra of the component, A is the absorption of the spectra at a given pH, and F is the fractional population change of the major component as a function of pH.

pH-Jump Kinetics. Data for pH jump experiments were obtained by Dr. Fangfang Zhong. For pH-jump measurements, stock solutions of ferric proteins were prepared in an aqueous solution containing 100 mM sodium chloride at pH 6.2. The jump buffers used in the measurements contained 10 mM sodium phosphate for final pH 7.0 to 8.0; sodium borate for final pH 8.5 to 10.0; CAPS for final pH 10.5 to 12.5, containing 100 mM NaCl. The final protein concentration was 8 to 10 μM and the final pH was achieved by mixing the stock protein sample with jump buffers in a 1:5 (*v*/*v*) ratio using a Bio-Logic SFM-300 stopped-flow instrument. The k_{obs} values were obtained by fitting the time course of the absorbance at 405 nm to a monoexponential equation at all pH ranges. The goodness of each fit was evaluated with analyses of the residuals of the fit. The kinetic parameters, k_f, k_b, and K_H, were determined from fitting dependencies of k_{obs} on $[H^+]$, the concentration of protons, to eq 3.6 as described previously:[75]

$$k_{obs} = k_b + k_f \frac{K_H}{K_H + [H^+]} \tag{3.6}$$

where k_{obs} is the observed rate constant, k_b and k_f are the Lys coordination rate constants for the dissociation and association reactions, respectively, and K_H is the protonation equilibrium constant. The conformational equilibrium constant (K_C) was related to pK_H and the apparent pK_a through the relationship pK_a = pK_C+pK_H, and was calculated from the rate

constants k_b and k_f through the relationship $K_C = k_f/k_b$. The pK_a values obtained from equilibrium pH titrations (eq 3.4) were used as constraints in these fittings.

Preparation of Lipid Vesicles. All lipids were obtained from Avanti Polar Lipids, Inc., and lipid vesicles prepared using the extruder apparatus equipped with an enclosed warmer (Eastern Scientific LLC) and membranes (Eastern Scientific LLC) with pore radius of 0.1 μm. Lipids 1,1'2,2'-tetraoleoylcardiolipin (TOCL) and 1,2-dioleoyl-*sn*-glycero-3-phosphocholine (DOPC) were mixed in a 1:1 molar ratio and lipid vesicles were prepared as previously described.[76] Lipids were in a freshly prepared 25 mM HEPES buffer at pH 7.4 containing 0.1 mM 2-[Bis[2-bis(carboxymethyl) amino]ethyl]amino]acetic acid (DTPA). Buffers were treated with a Chelex resin (Sigma) to remove excess metal ions in solution prior to use. Lipid vesicle solutions were used within the day. Lipid vesicle sizes and distributions were determined using dynamic light scattering (DLS) instrument (Wyatt Technologies).

Liposome-Binding Assays. Liposome solutions having concentrations of total lipid in the range from 40 to 500 μM were mixed with 10 μM ferric protein in a 1:1 (*v*/*v*) ratio. Samples were incubated at room temperature, under foil, for at least 30 minutes and centrifuged for 1 to 1.5 hours using a Beckman Airfuge tabletop ultracentrifuge with a Beckman A-11 motor at 120 000 × *g*. Measurements of the Soret absorption band taken immediately after centrifugation were used to determine the amount of protein left in solution.

Peroxidase Assays. Assays were performed in a freshly prepared and Chelex resin treated 25 mM HEPES buffer at pH 7.4 containing 0.1 mM DTPA. All substrates were kept on ice and in the dark prior use, and all protein solutions and buffer were kept at room temperature and in the dark to avoid heme bleaching. A colorimetric reducing substrate, ABTS (2,2'-

Azino-bis(3-ethylbenzthiazoline-6-sulphonic acid)diammonium salt; ultrapure, AMRESCO), was used to monitor the peroxidase activity at 735 nm assuming ε_{735} = 14 $mM^{-1}cm^{-1}$.[77] Each assay contained maximum concentrations of 0.2 to 1.0 mM H_2O_2, depending on the variant, and 200 μM ABTS with 1 to 2 μM freshly prepared ferric protein. At these substrate concentrations, it was assumed that maximum velocity was reached for both substrates. Higher substrate concentrations were avoided for some of the variants to avoid heme degradation and substrate inhibition. Activity assays for CL-bound cyt *c* were performed by mixing solutions of the protein and the liposomes (at 250-molar excess of total lipid) in a 1:1 (*v*/*v*) ratio to avoid aggregation. Samples were incubated for at least 30 minutes at room temperature prior to adding other components of the assay. For each assay, the absorbance signal at 735 nm was recorded every second for a total of 120 seconds. Linear phase of the reaction was then fitted to a single polynomial function to obtain the slope of the phase, which corresponded to the initial velocity of the reaction. The dependencies of concentration-corrected rates ($v_{cor} = v/([E]\cdot\varepsilon_{735})$) versus concentration of H_2O_2 were fitted to a Michaelis-Menten equation to yield k_{cat} and K_M values in respect to H_2O_2 (eq 3.7).[78]

$$v_{cor} = \frac{k_{cat}[H_2O_2]}{K_M + [H_2O_2]} \tag{3.7}$$

where k_{cat} is the catalytic rate constant and K_M is the inverse of the affinity of H_2O_2 for the protein.

Results

Molecular Dynamics Simulations. When the X-ray crystal structures of human and horse heart cyt *c* are compared, the calculated RMSD value of horse heart cyt *c* relative to the

structure of human cyt *c* is ~ 0.3 Å. Additionally, ~88% of total sequences are conserved between human and horse heart cyt *c* (Table 3.1). High sequence and structural similarity between the two species highlight the suitability of horse heart cyt *c* as good model to compare to structural characteristics of human cyt *c*. Furthermore, comparing these two similar proteins provides clues as to whether sequence differences alter protein structure and backbone dynamics important for function.

Although the protein structures of the two species are similar, they are not identical (Table 3.1 and Figure 3.2). Thus, simple homology modeling is insufficient to explore variations in analogous mutants of human and horse heart cyt *c*. While there are X-ray crystal structures of the G41S and Y48H variants in human cyt *c*, only the X-ray crystal structure of WT is available for horse heart cyt *c*, creating a need for structural data of G41S and Y48H variants in horse heart cyt *c*. To allow structural analysis and to account for the dynamic fluctuations that exist in structures, we elected to do MD simulations. Structural information from MD simulations allowed us to obtain the needed structural data to compare between human and horse heart cyt *c* variants under similar conditions and understand how the mutations alter the structural properties of cyt *c*.

MD Simulations of WT Cyt c. Suitable calibration of the method would reveal significant differences between the protein backbone dynamics of human and horse heart WT cyt *c*. Comparisons of per residue RMSF values for the backbone αC have shown that, on average, residue fluctuations in the simulated structures are low and comparable between the two species (Figure 3.4). There are regions of the protein containing residues with higher RMSF values, particularly with the residues in the 20's loop region.

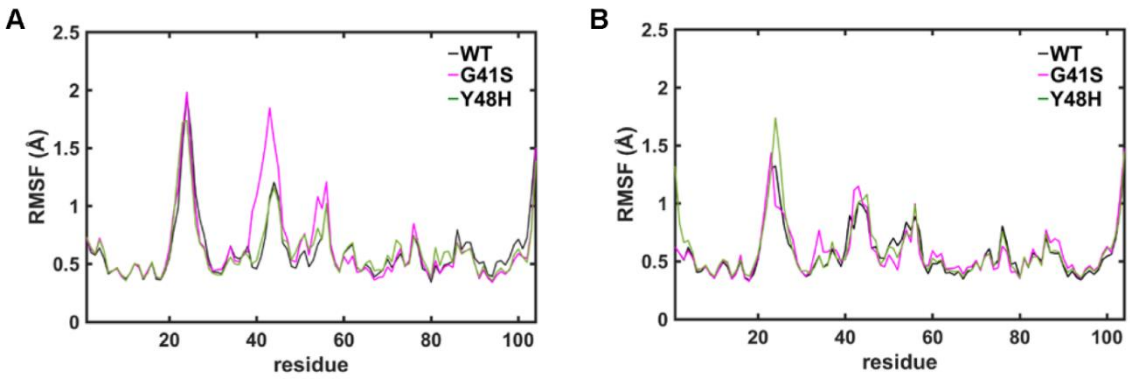

Figure 3.4. Plots of averaged per residue RMSF values for αC atoms in the protein backbone obtained from MD simulations, relative to the reference structure of the protein for (A) human and (B) horse heart WT (black), G41S (pink), and Y48H (green) cyt *c* variants. For each simulation, RMSF values were separately calculated and then averaged to obtain the average per residue RMSF value. Only the frames from 20 to 30 ns simulation times were used for these calculations, and the X-ray crystal structure of WT cyt *c* (horse heart,[18] PDB: 1HRC; human,[34]) was used as the reference structure.

Calculation of pairwise RMSD values for the protein backbone atoms in each frame of the trajectory to all other frames in the trajectory can provide insight into the conformational diversity of the simulated structures.[79, 80] Comparison of the distribution of pairwise RMSD values of the 20's loop shows that the 20's loop in human WT cyt *c* more frequently samples conformations that are different from one another, than does the 20's loop in horse heart WT cyt *c* (Figure 3.5 top). In comparison, distribution of calculated pairwise RMSD values for loops C and D are narrower than in the 20's loop for both human and horse heart WT cyt *c* (Figures 3.6 and 3.7, top). Furthermore, loops C and D regions of the simulated structures in both human and horse heart WT cyt *c* have lower RMSD values, suggesting that these loop regions tend to converge to similar conformations during the simulation.

We aimed to confirm if key inter-foldon contacts observed in the X-ray crystal structures are still present in the MD simulations, and whether simulations could pick up differences between the two species. Previous MD simulations and mutational studies in proteins and peptides, have suggested HB and vdW contacts to play a role in tuning protein stability ,[81-83] but its role has been unclear. Obtaining structural analyses comparing the weak native contacts in cyt *c*, along with experimental data, would provide further insight into how these contacts may tune stability and function in proteins. Heat maps obtained from pairwise interatomic distance calculations showed that key inter-residue HB contacts between the residues in loop C ,60's helix, and loop D observed in the X-ray crystal structures of human and horse heart WT cyt *c* are also detected in our MD simulations (Figure 3.8A and B, top).

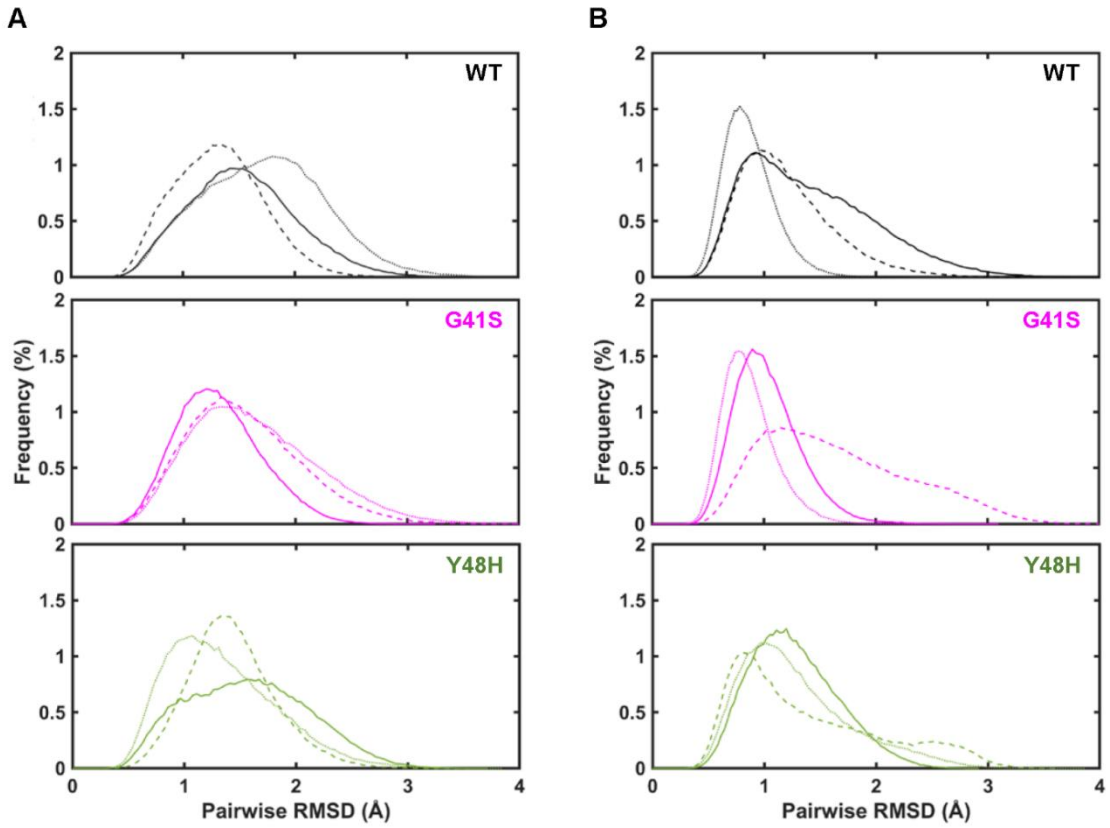

Figure 3.5. Plots showing the distribution of pairwise RMSD values calculated for αC atoms in 20's loop (residues 20 to 30) versus frequency, for structures obtained from MD simulations. Shown are the RMSD value distributions for (A) human and (B) horse heart WT (black), G41S (pink), and Y48H (green) cyt *c*. Distributions of RMSD values between each structure to all other structures from individual MD simulations are shown (first run, solid line; second run, dotted line; third run, solid line). All frames in the trajectory from 20 ns up to 35 ns simulation times were used to calculate the RMSD values.

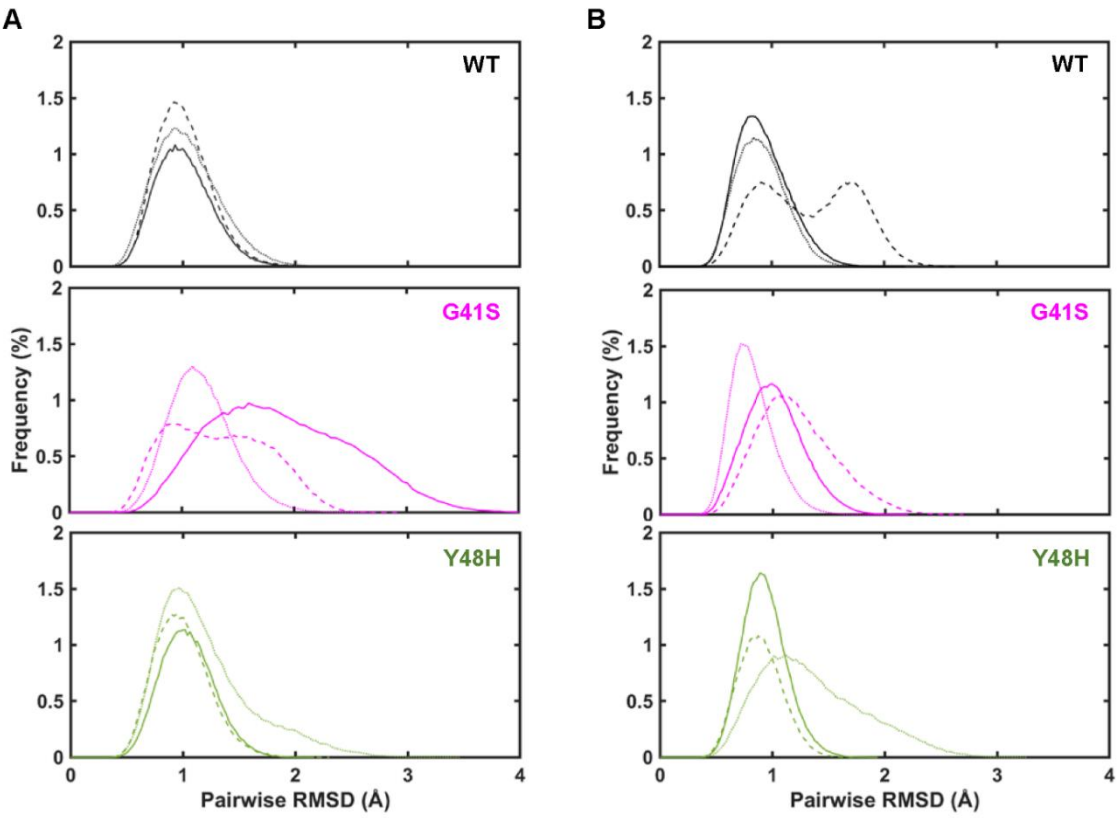

Figure 3.6. Plots showing the distribution of pairwise RMSD values for αC atoms in loop C (residues 40 to 57) versus frequency, for structures obtained from MD simulations. Shown are the RMSD value distributions for (A) human and (B) horse heart WT (black), G41S (pink), and Y48H (green) cyt *c*. Distributions of RMSD values between each structure to all other structures from individual MD simulations are shown (first run, solid line; second run, dotted line; third run, solid line). All frames in the trajectory from 20 ns up to 35 ns simulation times were used to calculate the RMSD values.

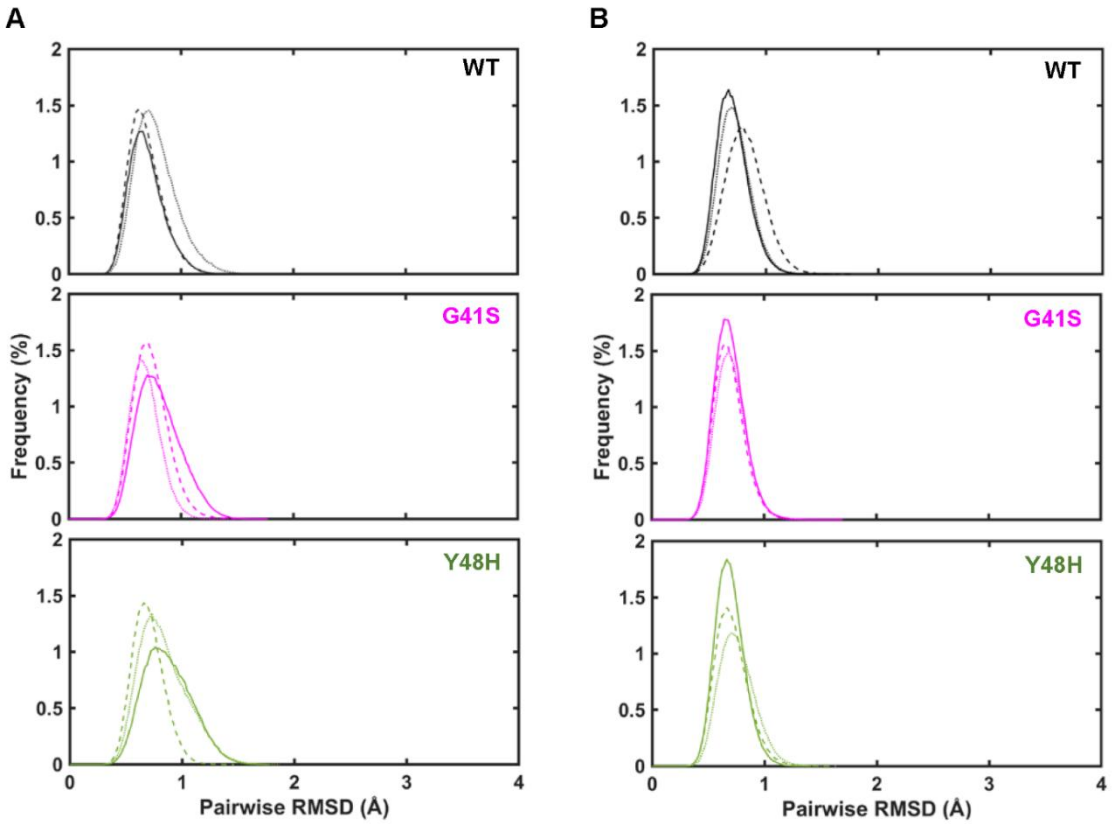

Figure 3.7. Plots showing the distribution of pairwise RMSD values for αC atoms in loop D (residues 70 to 85) versus frequency, for structures obtained from MD simulations. Shown are the RMSD value distributions for (A) human and (B) horse heart WT (black), G41S (pink), and Y48H (green) cyt *c*. Distributions of RMSD values between each structure to all other structures from individual MD simulations are shown (first run, solid line; second run, dotted line; third run, solid line). All frames in the trajectory from 20 ns up to 35 ns simulation times were used to calculate the RMSD values.

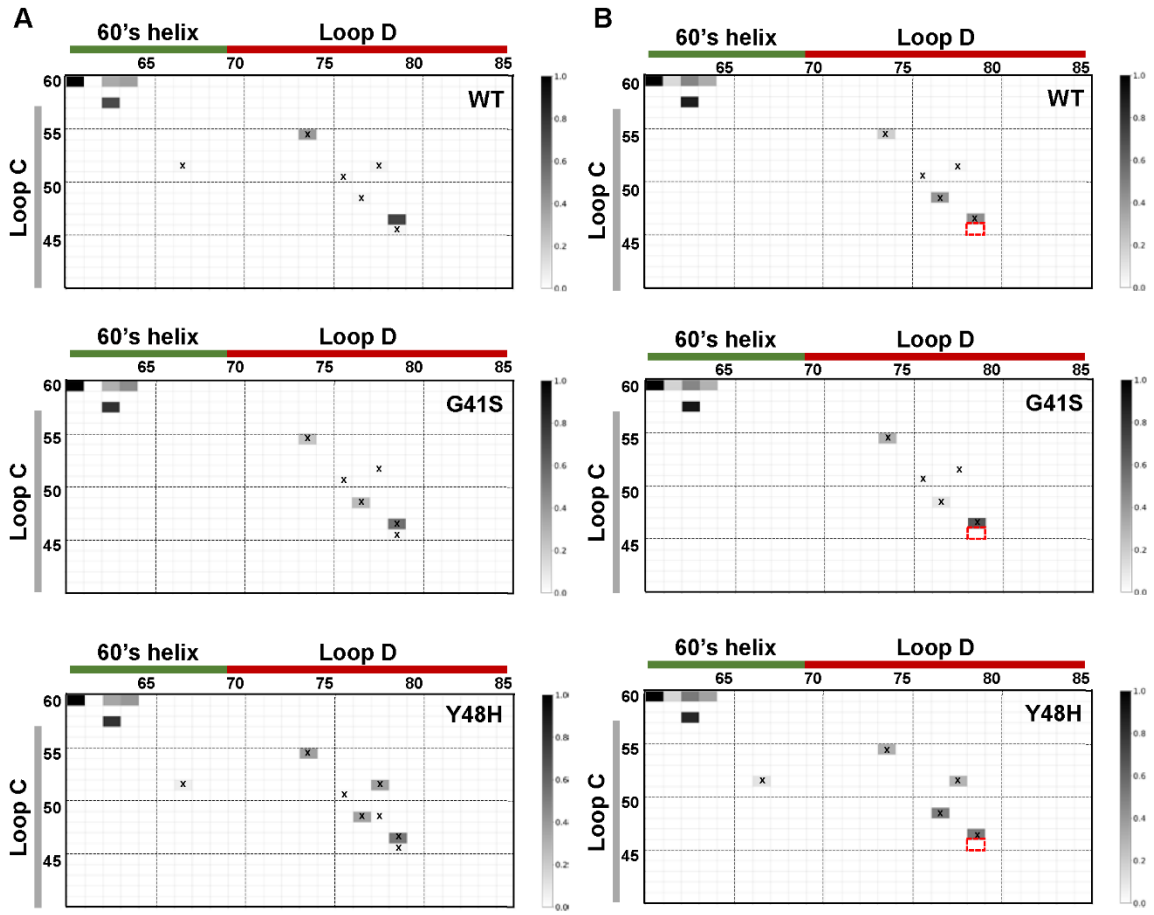

Figure 3.8. Heat map plots of contact frequencies between residues in loop C, 60's helix, and loop D based on the MD simulated structures of WT (top), G41S (middle), Y48H (bottom) variants of (A) human and (B) horse heart cyt *c*. Plotted are the frequency of contacts between residues within the contact distance of 3 Å from all three simulations. All frames in the trajectory from 20 ns up to 30 ns simulation times were used to generate the heat maps. Site of consistently observed key difference between human and horse heart cyt *c* are highlighted (red box).

As expected for proteins with a similar fold, heat maps plotting the frequencies of inter-residue contacts within the vdW distance are comparable between human and horse heart WT cyt *c* (Figure 3.9A and B, top). Although water-mediated HB contacts, such as the water-mediated inner HB networks involving Tyr67, Asn52, and Thr78 were not considered in our distance calculations, subtle differences in the loops C and D interface between human and horse heart WT cyt *c* are observed. For example, the residue-contacts between residue 79 and residues in loop C are more numerous in human WT cyt *c* than in horse heart WT cyt *c* (Figure 3.8), as suggested by comparison of the X-ray crystal structures (Figure 3.10). Furthermore, heat maps plotting the frequency of both HB and vdW contacts show small variations between species (Figure 3.9A versus B, top).

MD Simulations of G41S and Y48H Cyt c. Since we confirmed MD simulations can predict contacts observed in X-ray crystal structures and pick up differences in human and horse heart WT cyt *c*, we needed to determine how structurally similar the biologically relevant variants (G41S, and Y48H) would be between human and horse heart cyt *c*. MD structures show that with the same G41S and Y48H mutations, their consequences are different in horse heart cyt *c* and human cyt *c*. Plots of the per residue RMSF values of the ferric G41S and Y48H horse heart cyt *c* variants show that although much of the residues experience similar amount of structural fluctuations as was observed in WT, small regional variations are present (Figure 3.4B). In human cyt *c*, per residue RMSF values are also similar between Y48H and WT. However, differences are observed with G41S, where an increase in the RMSF values for residues in loop C are observed. Previously, 200-ns simulations in the human cyt *c* variants detected rearrangements in loop C with RMSF values > 2Å at longer time scales, which occurred earlier for the G41S variant (~30 ns)

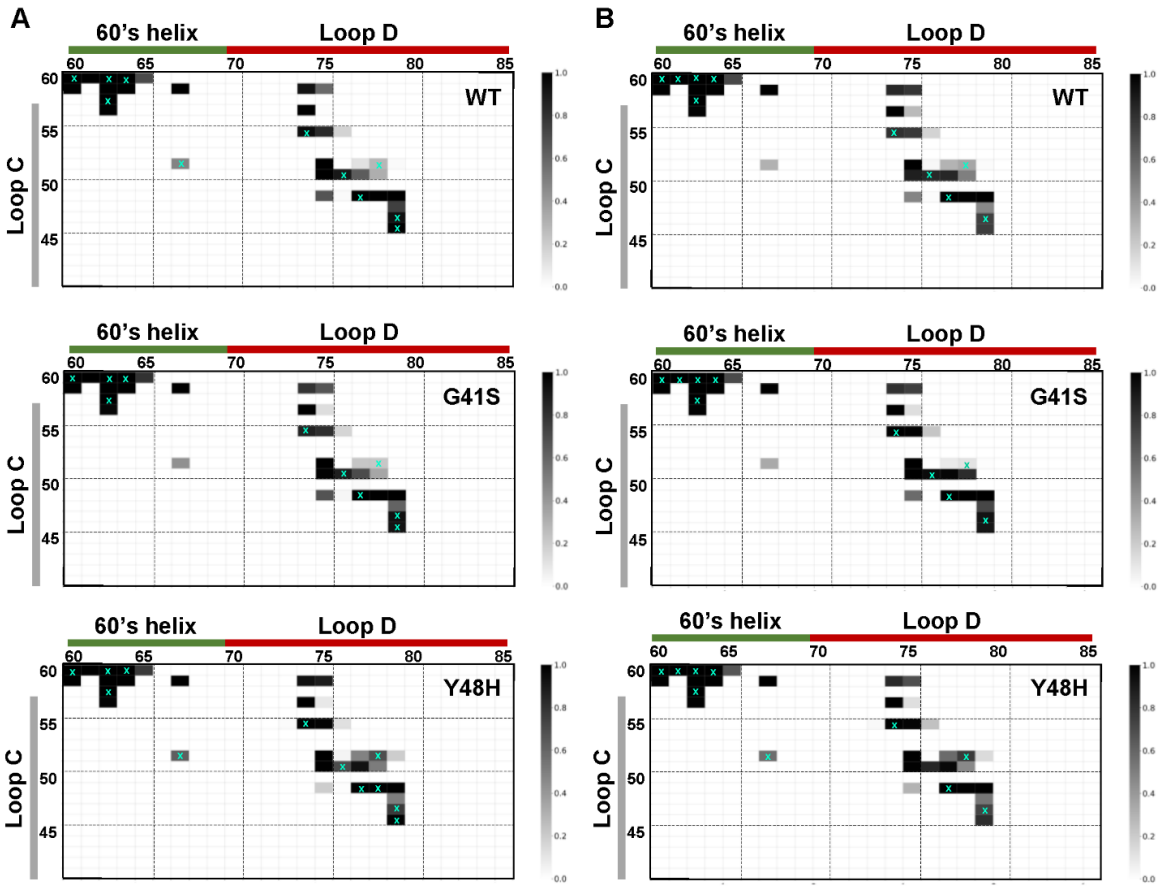

Figure 3.9 Heat map plots of contact frequencies between residues in loop C, 60's helix, and loop D based on the MD simulated structures of WT (top), G41S (middle), Y48H (bottom) variants of (A) human and (B) horse heart cyt *c*. Plotted are the frequency of contacts between residues within the contact distance of 5 Å from all three simulations. All frames in the trajectory from 20 ns up to 30 ns simulation times were used to generate the heat maps. Inter-residue contacts that were within 3 Å are marked with a 'x'.

compared to WT (~100 ns).[84] It is possible that higher RMSF values in loop C are observed in our simulations with the human G41S cyt *c* variant if we were also starting to detect similar large conformational rearrangements at later time scales near 30 ns.

In horse heart G41S and Y48H cyt *c*, distributions of pairwise RMSD values for αC in the 20's loop are like that for WT (Figure 3.5B). Compared to WT, however, the frequency at which structures have higher RMSD values from one another are lower in the horse heart G41S and Y48H variants (Figure 3.5B), suggesting that while some conformations requiring larger rearrangements are observed, most of the sampled conformations tend to be alike one another. In human cyt *c*, effects of G41S and Y48H mutations are less prominent. Both the range of the calculated pairwise RMSD values and the frequency at which similar RMSD values were observed in G41S and Y48H are comparable to that of WT (Figure 3.5A).

For horse heart cyt *c*, local variations are more prominently observed in loop C. In horse heart G41S cyt *c*, range of pairwise RMSD values are comparable to that of WT; however, larger pairwise RMSD values are more frequently observed in G41S than in WT (Figure 3.6B). In Y48H horse heart cyt *c*, pairwise RMSD values > 2 Å are observed at a higher frequency than in G41S or WT (Figure 3.6B). For both G41S and Y48H, larger pairwise RMSD values are observed at a higher frequency than in WT. This difference suggests that with G41S and Y48H mutations, loop C samples conformations that require extensive rearrangements to the protein backbone more frequently than in WT, and that G41S and Y48H have different mutational effects on loop C.

There are differential effects between the two species with the same loop C perturbations. Unlike in horse heart Y48H cyt *c*, pairwise RMSD values in loop C of human

Y48H cyt *c* is comparable to that of WT (Figure 3.6B). In contrast, a more diverse set of conformations is sampled in the loop C for human G41S cyt *c* than for horse heart G41S cyt *c*, as larger pairwise RMSD values are observed at a higher frequency in human G41S cyt *c* (Figure 3.6, middle).

Large variations in pairwise RMSD values observed with G41S and Y48H mutations in 20's loop and loop C are not observed in loop D for human or horse heart cyt *c* (Figure 3.7B).

Contact Maps. These differences in conformational ensemble also affect the distances between interloop residue that are within distance of forming HB and vdW contacts. In G41S and Y48H human cyt *c* variants, residues in loops C and D that are within HB distances vary in both location and frequencies at which they are formed compared to WT (Figure 3.8A). In human G41S cyt *c*, some residue pairs within distances of forming HB contacts observed in WT are either no longer observed or are predicted to form at different frequencies (Figure 3.8A, middle), perhaps due to sampling conformations that require larger loop rearrangements in loop C (Figure 3.6A). In human Y48H cyt *c*, more residue pairs are within HB distances, and some residues are within contact-forming distances at a higher frequency compared to WT (Figure 3.8A, bottom).

In the horse heart G41S cyt *c*, variations in the frequency at which residues are in HB distances are observed, but formation of potential new contacts are not observed compared to WT (Figure 3.8B, middle). With the Y48H mutation, there are variations in the residue pairs that are within HB distance between loops C and D (Figure 3.8B, bottom). Additionally, a new residue pair between the residue 52 in loop C and residue 67 in the 60's helix, is within HB distance is observed in horse Y48H cyt *c* (Figure 3.8B, bottom).

In our MD simulations, this contact is present in WT human cyt *c*, but not in WT horse cyt *c* (Figure 3.8, top), and in the X-ray crystal structure of both human and horse heart WT cyt *c* is present as a water-mediated HB network.[18, 34]

In general, residue pairs that are within vdW distance present in either human and horse heart WT cyt *c* are also present in G41S and Y48H variants, but with different frequencies at which the residues come into vdW distances (Figure 3.9). However, new potential contacts are formed in some variants. For example, residues 79 and 52 are within distance of forming a vdW contact in Y48H, but not in WT or G41S (Figure 3.9). For both species, there are variations in the frequency at which residue pairs come within distances of forming vdW contacts with the mutations compared to those for WT (Figure 3.9). However, more variations in frequencies of residue pairs coming within vdW distances are observed in horse heart cyt *c* than in human cyt *c*, suggesting that the mutations influence the weak residue pair interactions differently between species.

Horse heart cyt *c* variants G41S and Y48H maintain many structural properties found in WT, highlighting the adaptability of the overall peptide backbone to accommodate minor perturbations in the polypeptide. Further, despite the natural sequential differences between human and horse heart cyt *c*, X-ray crystal structures and MD simulations suggest similar HB and vdW interactions (Figures 3.5A and 3.6A). However, subtle differences are observed in the regional RMSD values of the MD structures of human and horse heart WT cyt *c*. Differences are magnified in the presence of mutation-induced loop perturbations, suggesting the existence of subtle variations in tertiary packing and loop dynamics, as well as the adaptability of the peptide backbone. This difference in how the polypeptide accommodates mutational perturbations could arise from the natural sequence variations

present in the loops C and D (Figures 3.5 and 3.6). For example, residues 46 and 47 are two of the three varied loop C residues in human and horse heart cyt *c*. The residues at positions occupied by Tyr and Ser in human cyt *c* are occupied by Phe and Thr in horse heart cyt *c*, eliminating the additional hydrogen bonding interactions involving HP6 and Lys79 (Figures 3.10A and B). In human cyt *c*, more of the native contacts are maintained even with the G41S or Y48H mutations, as observed in the X-ray crystal structures.[35, 54] Along loop D, the only sequence difference between human and horse cyt *c* is on residue 83, where residue 83 is Val in human cyt *c* or Ala in horse cyt *c*. Replacement of Val with a smaller residue Ala could provide additional flexibility to the loop. Although this variation may increase the overall dynamics of loop D, it is unlikely that this residue variation alters the HB and vdW contacts between loops C and D, as loop D residues involved in this inter-foldon contact is mainly limited to residues 74 to 79 (Figures 3.9 and 3.10).

Heme Coordination and Protein Fold.

Electronic Absorption Spectra. At pH 7.4, the electronic absorption spectra of ferric G41S and Y48H are different from that of WT, and the λ_{max} of the Soret band slightly blue shifts from 409 nm in WT to 408 and 407 nm, respectively (Figure 3.11A). For G41S, λ_{max} of the Soret band shifts by 1 nm depending on the buffer used (Table 3.2), and no such buffer dependence is observed with the other variants. In variants of horse heart cyt *c*, the extinction coefficients differ slightly from those in WT. The electronic absorption spectra for G41S and Y48H all exhibit a CT band at 695 nm as was observed in WT, and the extinction coefficient of this band decreases for G41S compared to that of WT (Figure 3.11A, inset and Table 3.2).

Figure 3.10. Distance-based contour contact maps and figures depicting HB interactions near or at HPs 6 and 7 based on X-ray crystal structures for (A) human WT cyt *c* (PDB ID 3ZCF),[34] (B) horse heart WT cyt *c* (1HRC)[18] and (C) *iso-1* yeast WT cyt *c* (2YCC).[17] In the contact maps, additional interactions that are present/changed in human or horse heart WT cyt *c* but absent in yeast WT cyt *c* are highlighted (red dotted line). Depictions of the HB interactions show the HB distances (blue), with the HP groups (green) and Lys79 (orange) highlighted. In human WT cyt *c*, HB between residues 46 and 79 are not predicted, and instead, the distance between the residues is shown (pink). Left depictions show the Lys79-HP6 interactions involving the residues in loop C and 20's loop, center depictions show the HP6 interactions involving the residues in loops C and D, and right depictions show the HP7 interactions involving the residues in the loop C and the anti-parallel β strands.

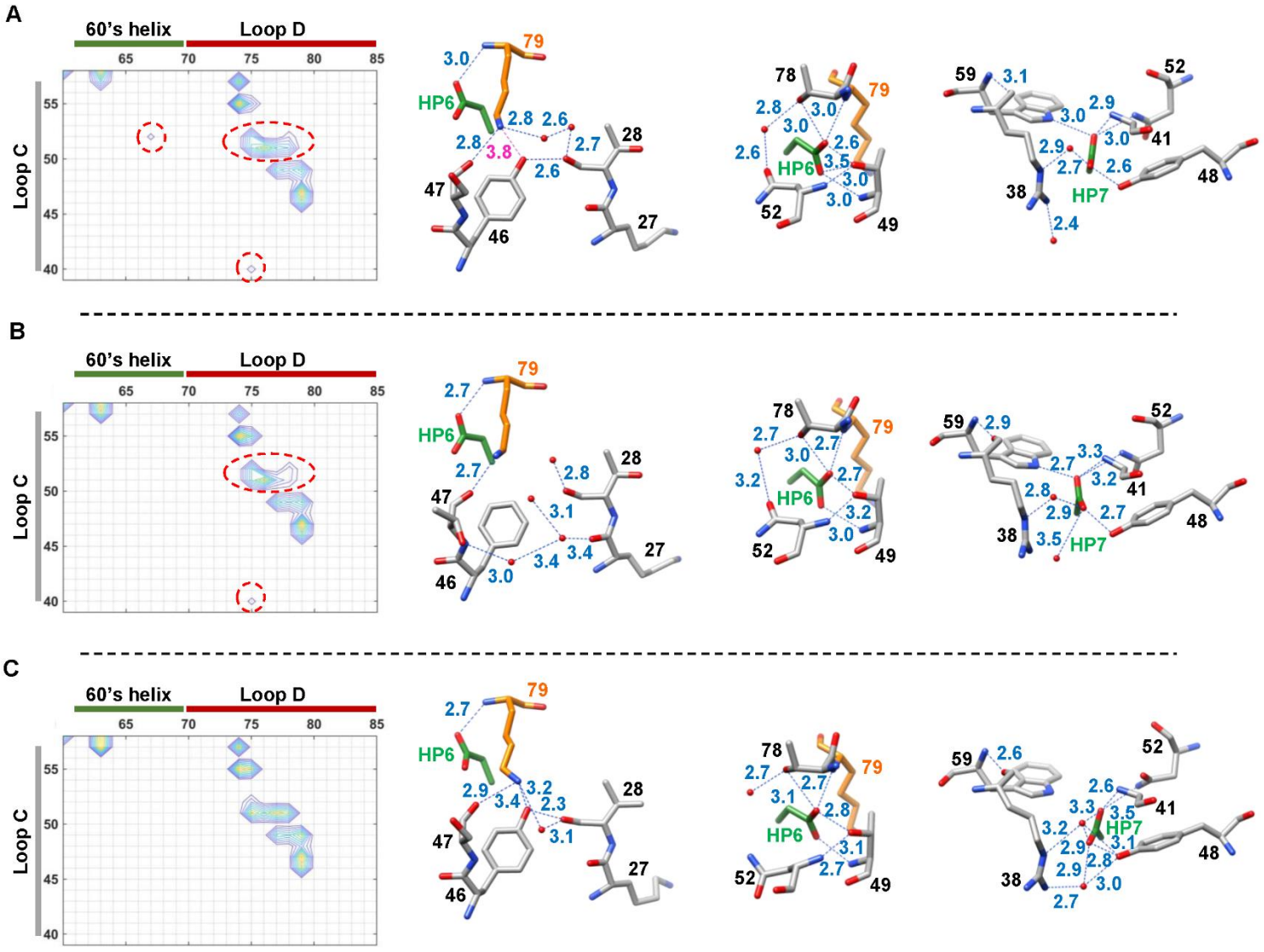
A
60's helix
Loop D
65
70
75
80
85
Loop C
55
50
45
40
79
HP6
47
46
28
27
78
52
49
59
41
48
38
HP7
B
C

Figure 3.11. Electronic absorption spectra of (A) ferric and (B) ferrous WT (black), G41S(pink), and Y48H (green) cyt *c* variants in a 100 mM sodium phosphate buffer at pH 7.4, with the near-IR CT band shown for the ferric species (inset, A). (D) Numberings for heme and Met protons for labeling peaks in the ^{1}H NMR of (C) ferric and (E) ferrous WT (black), G41S (pink), and Y48H (green) cyt *c* variants in a 50 mM sodium phosphate buffer at pD 7.4 and 100% D_2O or pH 7.4 with 10% D_2O (*v*/*v*), respectively. Peaks are labeled according to refs. [37, 85]. (F) EPR spectra at 10 K for WT (black), G41S (pink), and Y48H (green) cyt *c* variants in a 50 mM sodium phosphate buffer at pH 7.4 with 20% (*v*/*v*) glycerol at 10 K.

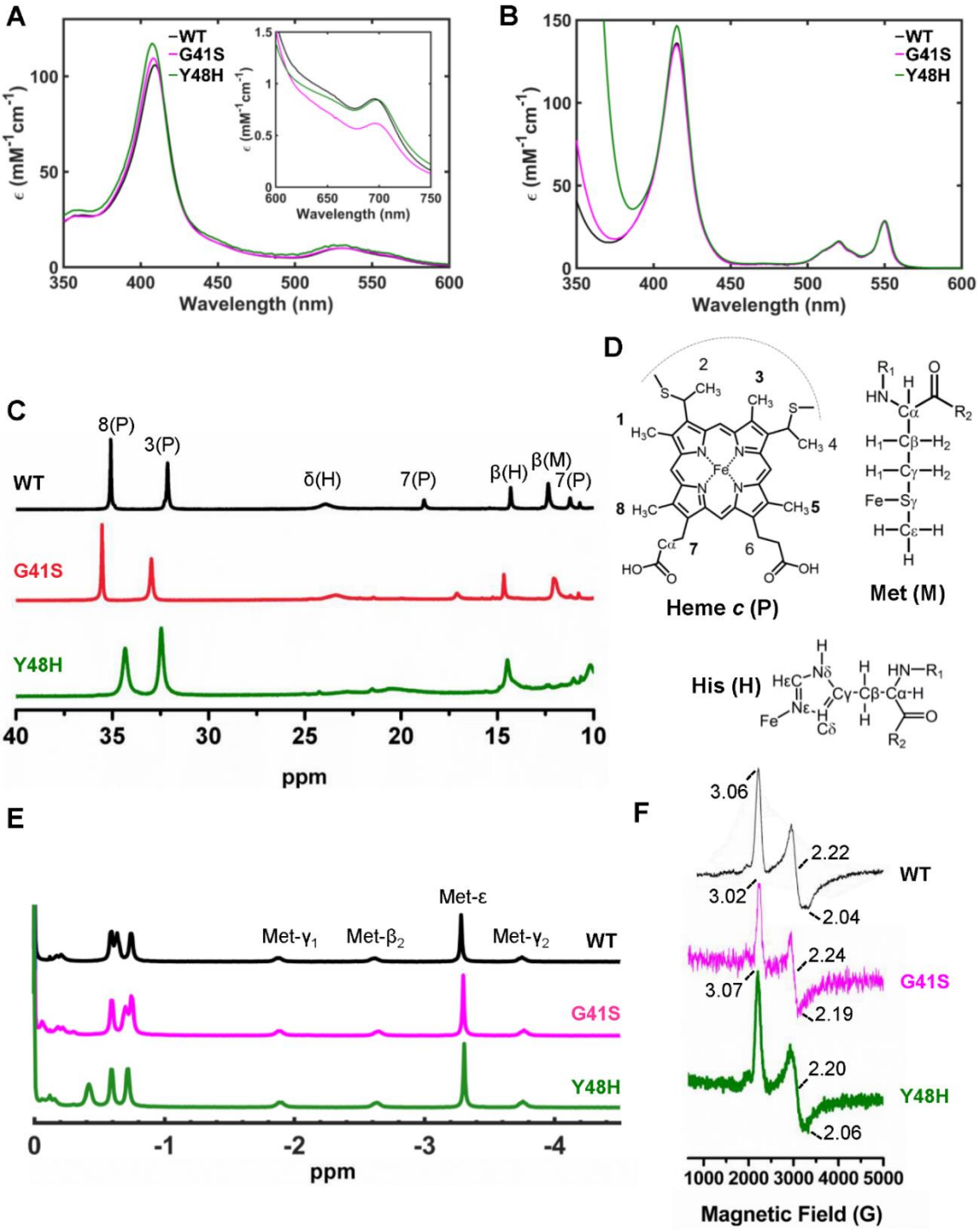
A
WT
G41S
Y48H
ϵ (mM-1cm-1)
Wavelength (nm)
B
C
8(P)
3(P)
δ(H)
7(P)
β(H)
β(M)
7(P)
ppm
D
Heme c (P)
Met (M)
His (H)
E
Met-ε
Met-γ1
Met-β2
Met-γ2
F
3.06
2.22
3.02
2.04
2.24
3.07
2.19
2.20
2.06
Magnetic Field (G)

Table 3.2. Extinction Coefficients for Variants

	Ferric	
Variant	λ (nm)	ε ($mM^{-1}cm^{-1}$)
G41S	408[a]	109.5[a]
	407[b]	100.7[b]
	695[a]	0.53[a]
Y48H[c]	407[b]	117.1[b]
	695[a]	0.71[a]

[a]In a 100 mM sodium phosphate buffer at pH 7.4.

[b]In a 25 mM HEPES buffer at pH 7.4.

[c]Positions of λ_{max} of the Soret band did not change in different buffers.

Differences in the extinction coefficient for the Soret and the CT band in the absence of large differences in the λ_{max} of both the Soret and CT band suggest a distinct heme environment for ferric G41S and Y48H cyt *c* variants, but similar heme iron ligation, compared to that of WT (Table 3.2). The electronic absorption spectra of the ferric species provide evidence that these variants most likely have a Met-ligated heme at pH 7.4, as the shift in λ_{max} for Soret is not large and the CT band observed in Met-ligated WT cyt c are observed. Yet, minor variations in the Soret and CT-band characteristics are observed depending on the mutation, suggesting differences in the variants compared to WT at pH 7.4. The electronic absorption spectra of the ferrous variants have shown no observable differences in the position of the Soret band, except for the slight changed extinction coefficient for the variants (Figure 3.11B), suggestive of the 6-coordinated heme iron.

^{1}H NMR. ^{1}H NMR spectra obtained for the ferric protein also support the presence of a primarily Met-ligated heme iron species at pH 7.4 (Figure 3.11C). However, the positions and intensities of 8-methyl and 3-methyl signals of the heme porphyrin are not identical to those of Met-ligated WT, suggesting difference between the heme environments in the variants, as supported by the differences observed in the electronic absorption spectra (Figures 3.11A and C). The signals observed in the ^{1}H NMR spectra for G41S and Y48H are broader and/or shifted, suggesting faster exchange on the NMR timescale.[22] This have been previously observed in human Y48H, and have been argued to be due to increased heterogeneity in the region.[35, 86] However, small satellite signals are observed for Y48H at pD 7.4, suggesting the presence of a small population of differently-ligated heme iron species, and its signal intensities increase by pD 10.5 (Figure 3.12).

Figure 3.12. (A) ^{1}H NMR spectra at 25 ºC for ferric horse heart cyt *c* variants. Shown are the spectra of WT at pD 7.4 (black, see Figure 3.11D for labeling) and pD 10.5 (gray, from ref. [74]), Y48H at pD 10.5 (blue), pD 7.4 (green), and pD 4.5 (red), and M80A at pD 4.5 (orange, from ref [74]). Samples were prepared in 100 % D_2O buffers containing 50 mM borate, sodium phosphate, or acetic acid d_4 at pD 10.5, 7.4, or 4.5, respectively. (B) Electronic absorption spectra of the CT region of ferric Y48H shown at pD 4.5 (red), 7.4 (green), and 10.5 (blue), with WT at pH 7.4 for reference (pink).

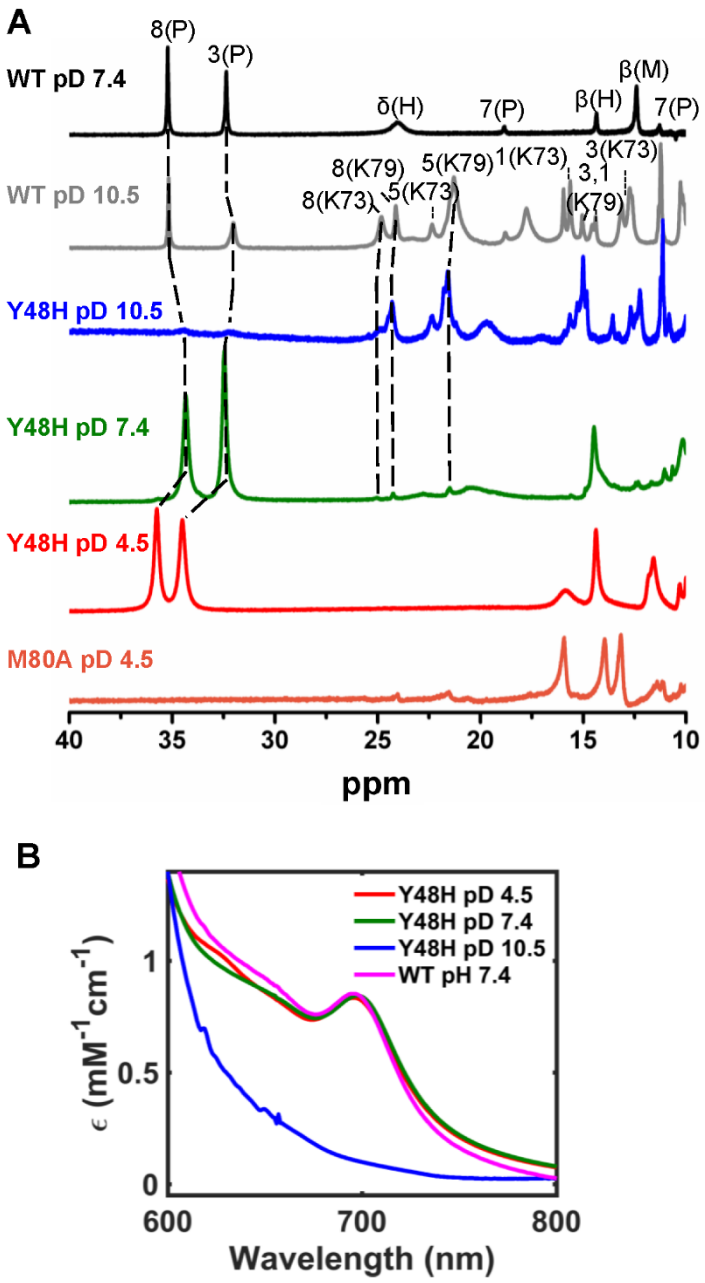
A
8(P)
3(P)
WT pD 7.4
δ(H)
7(P)
β(H)
β(M)
7(P)
WT pD 10.5
8(K79)
8(K73)
5(K79)
5(K73)
1(K73)
3(K73)
3,1
(K79)
Y48H pD 10.5
Y48H pD 7.4
Y48H pD 4.5
M80A pD 4.5
40
35
30
25
20
15
10
ppm

B
Y48H pD 4.5
Y48H pD 7.4
Y48H pD 10.5
WT pH 7.4
ϵ (mM-1cm-1)
1
0.5
0
600
700
800
Wavelength (nm)

At pD 10.5, porphyrin methyl signals of the Lys-ligated heme iron species in WT cyt *c*[37, 87, 88] are predominantly observed, and porphyrin methyl signals of the Met-ligated heme iron species [37] are diminished.

In the ^{1}H NMR spectra for ferric Y48H, while satellite signals likely corresponding to porphyrin methyl groups of a Lys-ligated heme iron are observed at pD 7.4, prominent signals are from porphyrin methyl groups of the Met-ligated heme iron species, which is the only species observed at pD 4.5. Although the Y48H ^{1}H NMR spectrum at pD 4.5 is distinct from the spectrum of M80A variant containing the high-spin H_2O-ligated heme iron species at pD 4.5 (Figure 3.12A),[74] it is difficult to conclude as to whether there are also high-spin species in Y48H at pD 4.5, as the high-spin signal of the H_2O-ligated heme iron species in ^{1}H NMR appears further downfield. However, the 695 nm CT band of the electronic absorption spectra is unchanged at either pH 4.5 or 7.4 and is comparable to that of WT at pH 7.4, where the heme iron is Met-ligated (Figure 3.12B). Similarities in CT band suggests that Y48H likely does not contain high-spin H_2O-ligated heme iron species at pH 4.5, and that most of the population is Met-ligated at pD 7.4 for ferric horse heart Y48H cyt *c* as observed in the human Y48H cyt *c*.[35]

The ^{1}H NMR spectra of the ferrous protein show the presence of predominantly Met-ligated species in all the variants (Figure 3.11E).

EPR Spectra at 10K. EPR spectra for the ferric G41S or Y48H are similar to that of WT at pH 7.4, showing characteristic EPR spectral features of a low-spin Met-ligated heme iron in cyt *c* (g_z = 3.06, g_y = 2.22, and g_x = 2.04) for all the variants (Figure 3.11F).[89] Signals observed in the EPR spectra of Lys-ligated alkaline cyt *c* or hydroxide-ligated M80A yeast cyt *c*,[22, 89] whose prominent signals are observed at g_z = 3.3 or g_z = 2.6, respectively, were

not distinguishable in the low-temperature EPR spectra of G41S and Y48H horse heart cyt *c* at this pH (Figure 3.11F).[89] It is possible that Lys-ligated heme iron species are present in the ferric Y48H variant based on the ^{1}H NMR spectra (Figure 3.11C). Even if that is the case, the population of Lys-ligated heme iron species is likely low and EPR signals of the Lys-ligated heme iron species are indistinguishable with the Met-ligated heme iron species due to the proximity of the g_z values.

The electronic absorption, ^{1}H NMR, and EPR spectral data all show that G41S and Y48H variants of horse heart cyt *c* contain mostly Met-ligated heme iron species in both ferric and ferrous states at pH 7.4. However, minor shifts in the λ_{max} of the Soret band in G41S and Y48H, decrease in the extinction coefficient of the CT band observed in G41S, and the presence of satellite peaks corresponding to Lys-ligated heme iron in the ^{1}H NMR spectra for Y48H, suggests that a minor population of Lys-ligated heme iron species may be present in G41S and Y48H variants at pH 7.4.

Secondary Structure. At pH 7.4, the far-UV CD spectra for all ferric variants show similar intensities and ratios at 220 and 210 nm, characteristic of a primarily α-helical protein secondary structure (Figure 3.13). Although the variants G41S and Y48H contain perturbations in loop C, the mutations do not seem to affect the overall secondary fold of the protein. The secondary CD spectra of G41S and Y48H strongly suggest that most of the native secondary structure is preserved, as predicted in the MD simulations and as suggested by the X-ray crystal structures of human cyt *c* variants.[31, 35, 54]

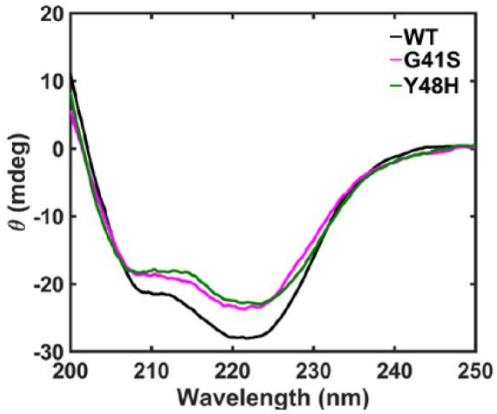

Figure 3.13. Far-UV CD spectra of WT (black), G41S (pink), and Y48H (green) variants of horse heart cyt *c* in a 100 mM sodium phosphate buffer at pH 7.4 at 20 ºC and *l* = 1 mm. Spectra were normalized to [cyt *c*] = 20 μM

Global and Local Stability.

Thermal Stability. Global stabilities with respect to thermal denaturation for the variants are unchanged to that of WT, as the melting transition temperatures (T_m) and enthalpies of denaturation (ΔH_{vH}) are comparable for WT and variants (Table 3.3).[90] However, spectral measurements at higher temperatures (above 90 °C) were not obtained to avoid possible protein aggregation from boiling the aqueous protein solution (Figure 3.14). Since the T_m values of the variants were near this limit, we opted to rely on a more trackable GuHCl denaturation to determine the stability changes with the mutations.[91]

Chemical Denaturation with GuHCl. Unfolding parameters, m_D and $[GuHCl]_{1/2}$, reveal the thermodynamic details of the unfolded protein.[67, 68] The parameter m_D reflects the difference in solvation of the polypeptide in the folded and unfolded state, and reflects the compactness of the denatured state; the midpoint of the transition, $[GuHCl]_{1/2}$, is the concentration of GuHCl at which half of the protein is unfolded.[69, 92] These two parameters are used to obtain the free energy of denaturation(ΔG_D) to compare the overall stability of proteins, and minor variations in the m_D and $[GuHCl]_{1/2}$ parameters show differences in the folding properties.[66] In horse heart G41S and Y48H cyt *c*, slight variations in the m_D and/or $[GuHCl]_{1/2}$ parameters are observed, but ΔG_D values are all within error to that of WT (Figure 3.15A and Table 3.4). In G41S, $[GuHCl]_{1/2}$ remains unchanged and m_D decreases; in Y48H, the $[GuHCl]_{1/2}$ value decreases, while m_D value is within error of WT. In horse heart G41S and Y48H cyt *c*, any changes in the stability parameters $[GuHCl]_{1/2}$ and m_D are balanced out and the overall global stability remains unchanged.

Table 3.3. Parameters from Global Thermal Denaturation of Ferric Cyt *c* Variants at pH 7.4[a]

Variant	T_m (K)	ΔH_{vH} (kJ mol^{-1})
WT	357.1[b]	360 ±30[b]
G41S	358 ±5	332 ±49
Y48H	357 ±4	340 ±46

[a]Monitored is ellipticity at 222 nm.

[b]From ref. [90], in a 10 mM sodium phosphate buffer at pH 7.0.

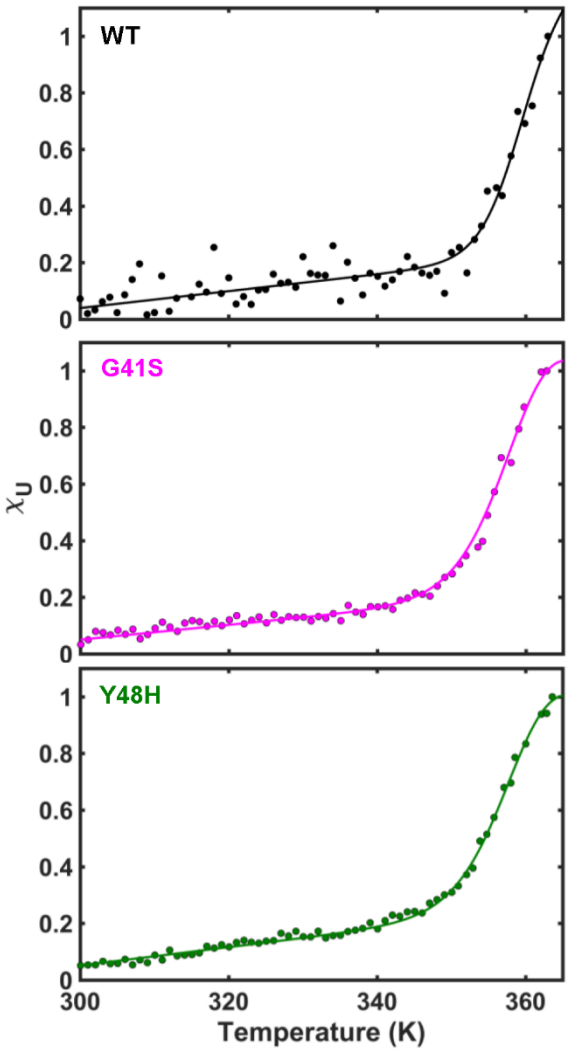

Figure 3.14. Representative temperature unfolding curves and fits in fraction unfolded (χ_U) versus temperature for horse heart cyt *c* variants WT (black, from ref [38]), G41S (pink), and Y48H (green), in a 100 mM sodium phosphate buffer at pH 7.4. Monitored is the ellipticity at 222 nm.

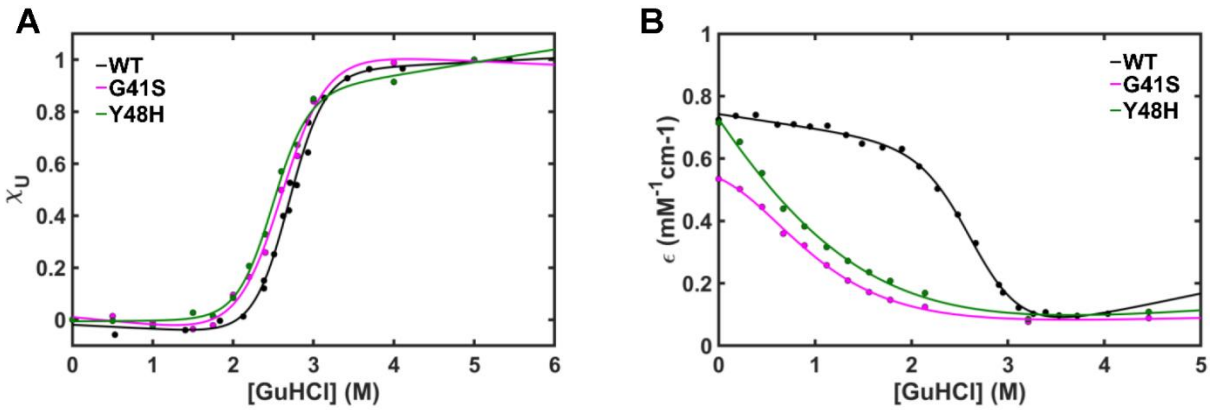

Figure 3.15. Chemical denaturation curves monitoring (A) α-helicity at 222 nm (fraction unfolded, χ_U) and (B) CT (extinction coefficient, ε_{695}) plotted versus [GuHCl] and with corresponding fits for WT (black, from ref. [38] for global, and ref. [93] for CT), G41S (pink), and Y48H (green) in a 100 mM sodium phosphate buffer at pH 7.4. Measurements were performed at 20 °C for monitoring α-helicity and at 22 ±2 °C for monitoring the CT band of the electronic absorption spectra.

Table 3.4. Parameters from GuHCl Unfolding for Cyt *c* Variants at pH 7.4[a]

Variant	$[GuHCl]_{1/2}$ (M)	m_D (kJ mol^{-1} M^{-1})	ΔG_D (kJ mol^{-1})
		Horse Heart	
WT[b]	2.7 ±0.1	11.5 ±2.6	31.1 ±7.1
G41S	2.7 ±0.1	9.9 ±1.4	26.1 ±3.7
Y48H	2.5 ±0.1	11.0 ±4.0	27.5 ±10.1
		Human	
WT[c]	2.55 ±0.01	15.5 ±0.2	39.6 ±0.5
G41S[d]	2.25 ±0.05	12.5 ±0.4	28.2 ±0.4
Y48H[d]	1.98 ±0.05	10.7 ±0.4	21.3 ±0.7
		Yeast	
WT[e]	1.15 ±0.01	20.6 ±1.7	23.7 ±2.0

[a]Monitored is ellipticity at 222 nm, performed at 20 ºC.

[b]From ref. [38], at pH 7.4 and room temperature.

[c]From ref. [31], at pH 7.5.

[d]From ref. [94], at pH 6.5 and 15 ºC.

[e]From ref. [36], at pH 7.5 and 25 °C. Contains C102S mutation and expressed in yeast.

Both the chemical and thermal denaturation data show that, at pH 7.4, the mutations G41S and Y48H in horse heart cyt *c* have minimal effect on the global stability of the protein.

Loop D Stability. To further quantify whether the mutations affect local stability, loop D stability was probed by observing changes in the CT absorption band with increasing concentration of GuHCl at pH 7.4. CT band at 695 nm argued to be the metal-to-ligand CT of heme iron to Met80 and observed in cyt *c* proteins with a Met-ligated heme iron.[22] The electronic absorption of this band decreases with the loss of Met-ligation to the heme iron, either due to ligand switch or from unfolding of the polypeptide.[93, 95] Because Met80 is located in loop D, CT band serves as a probe to detect changes to the native packing of loop D that promotes Met80-ligation to the heme iron. Unfolding experiments monitoring this CT band has been previously performed in horse heart WT cyt *c*, but fitted stability parameters were not reported.[93] Refit of the previously reported WT data[93] suggests $[GuHCl]_{1/2}$ value at 2.7 ±0.1 M, m_D value at 9.1 ±1.7 kJ·mol^{-1}·M^{-1}, and ΔG_D as 24.6 ±4.7 kJ·mol^{-1}, within error of the parameters from global unfolding measurements.[38] In comparison, stability parameters for G41S and Y48H show that loop C perturbations alter loop D stability. The CT absorption band for G41S and Y48H decreases at much lower [GuHCl] concentrations than for WT (Figure 3.15B). Although both $[GuHCl]_{1/2}$ and m_D parameters were difficult to fit accurately (eq 3.1), the values of the parameters can be estimated to be less than 1 M and 6 kJ·mol^{-1}·M^{-1}, respectively. Although global stabilities of G41S and Y48H variants are similar to that of WT, the local stability of loop D appears to be greatly perturbed compared to that of WT. These results suggest that loop C perturbations can alter the local stability of loop D without changing the global stability.

Alkaline Transition.

At mildly alkaline pH conditions, a still unknown "trigger group" becomes deprotonated, and the Fe-bound Met80 dissociates to allow a Lys residue to coordinate to the heme iron to form the Lys-ligated alkaline species. This transition is controlled by both thermodynamic and kinetic factors associated with forming the Lys-ligated state and can be described as a combination of the equilibrium constant of the trigger group (pK_H) and conformational rearrangement equilibrium of loop D (pK_C) determined from the rate constants of forming the Lys-ligated heme.[75] Loop D contains Lys72, 73, and 79 in both human and horse heart WT cyt *c*, and Lys73 and Lys79 act as primary Lys ligands that replace Met80.[22, 31, 96, 97] MD simulations of Lys73-ligated WT, and ^{1}H NMR solution structure of Lys73-ligated K79A yeast cyt *c* all suggest that coordination of Lys73 requires a substantial rearrangement in loop D.[98-100] Studies with Lys73-ligated yeast T78C/K79G cyt *c* illustrate the extent of the loop D rearrangement; in the X-ray crystal structure, loop D is folded into a tight β-hairpin structure.[25] Although MD simulations of yeast and horse heart WT cyt *c* suggest that ligation of Lys79 requires very little movement in loop D compared to ligation of Lys73,[97, 98, 100] loop D rearrangement is still required. Because alkaline transition is dependent on properties of loop D, it is a good probe to obtain information regarding loop D dynamics and gain insight into how structural perturbations alter the properties of loop D rearrangement.

Changes to the Alkaline Transition pKa. First, we sought to determine whether the mutations alter the alkaline transition properties of the protein. SVD analyses have suggested that a single transition is sufficient to describe pH-dependent changes in the Soret band (pH 6.02 to 11.08 for WT; pH 6.57 to 10.39 for G41S; pH 6.43 to 9.26 for

Y48H) and the CT band (pH 6.29 to 10.6 for WT; pH 6.52 to 9.94 for G41S; pH 6.49 to 10.22 for Y48H) in the electronic absorption spectra. In horse heart cyt *c*, G41S and Y48H mutations lower the pK_a for the alkaline transition compared to WT, as determined from global fittings of the changes in the Soret and 695 nm CT band of the electronic absorption spectra from pH titrations (Table 3.5 and Figures 3.16 to 3.18). Although the number of protons involved in the transition (*n*) is lower than the expected value of 1, fixing *n* as 1 during global fittings did not alter the pK_a values.

Based upon the pK_a values, G41S and Y48H in horse heart cyt *c* have higher percentage of the Lys-ligated heme present at pH 7.4 compared to that of WT (Table 3.5). Generally, Lys-ligation at near-neutral pH is unfavorable as Lys prefers to be protonated at this pH and Lys deprotonation is required prior to heme iron ligation.[22] Furthermore, Lys-ligated species at near-neutral pH conditions have lower global stability and increased random coil characteristics compared to WT.[74, 101] Despite the presence of a minor population of Lys-ligated heme iron species in G41S and Y48H, global thermal and chemical stabilities are comparable to those of WT (Tables 3.3 and 3.4) and random coil characteristics are not observed in the CD measurements (Figure 3.13). Perhaps, concentration of Lys-ligated species is low enough in G41S and Y48H, and error bars in the global stability measurements for WT large enough that contributions from the Lys-ligated species that have lower stability than the Met-ligated species at pH 7.4 could not be distinguished from that of WT.

Kinetic Parameters for Alkaline Transition. Since the increase in pK_a stem from changes in parameters pK_H and pK_C, pH-jump kinetic measurements were performed to obtain rates of ligand exchange from the native Met-ligated heme iron to the alkaline Lys-ligated heme

Table 3.5. Parameters for the pH-Dependent Alkaline Transition in Cyt *c* Variants[a]

Variant	pK_a	*n*	ΔΔG (kJ mol^{-1})[b]	% Lys at pH 7.4
	Horse Heart		*vs. WT*[c]	
WT	9.27 ±0.01	0.87 ±0.02	0	1.3
G41S	7.81 ±0.01	0.94 ±0.02	-8.26 ±0.08	28
Y48H	8.04 ±0.02	0.93 ±0.04	-6.95 ±0.13	19
	Human			
WT[d]	9.54 ±0.03	1.03 ±0.02	0	0.7
G41S[e]	8.5 ±0.2	--	-5.87 ±1.14	7.3
Y48H[e]	8.4 ±0.1	--	-6.43 ±0.59	9.1
	Yeast			
WT[f]	8.7 ±0.02	--	--	4.8

[a]In a 100 mM sodium phosphate buffer at pH 7.4 and 22 ± 2 °C. Significant vectors identified from SVD analysis of pH titrations monitoring both the Soret and CT were globally fitted to obtain the pK_a and *n* (number of protons) values. Fixing $n = 1$ for global fittings yielded similar pK_a values to fitted pK_a values when *n* was not fixed.

[b]Calculated from ΔpK_a assuming conditions T = 22 °C.

[c]ΔΔG values were calculated by comparing the pK_a values for horse heart WT cyt *c* for the horse heart cyt c variants and human WT cyt *c* for the human cyt *c* variants.

[d]From ref. [32].

[e]From ref. [35], monitoring CT band in the electronic absorption spectra.

[f]From ref. [37].

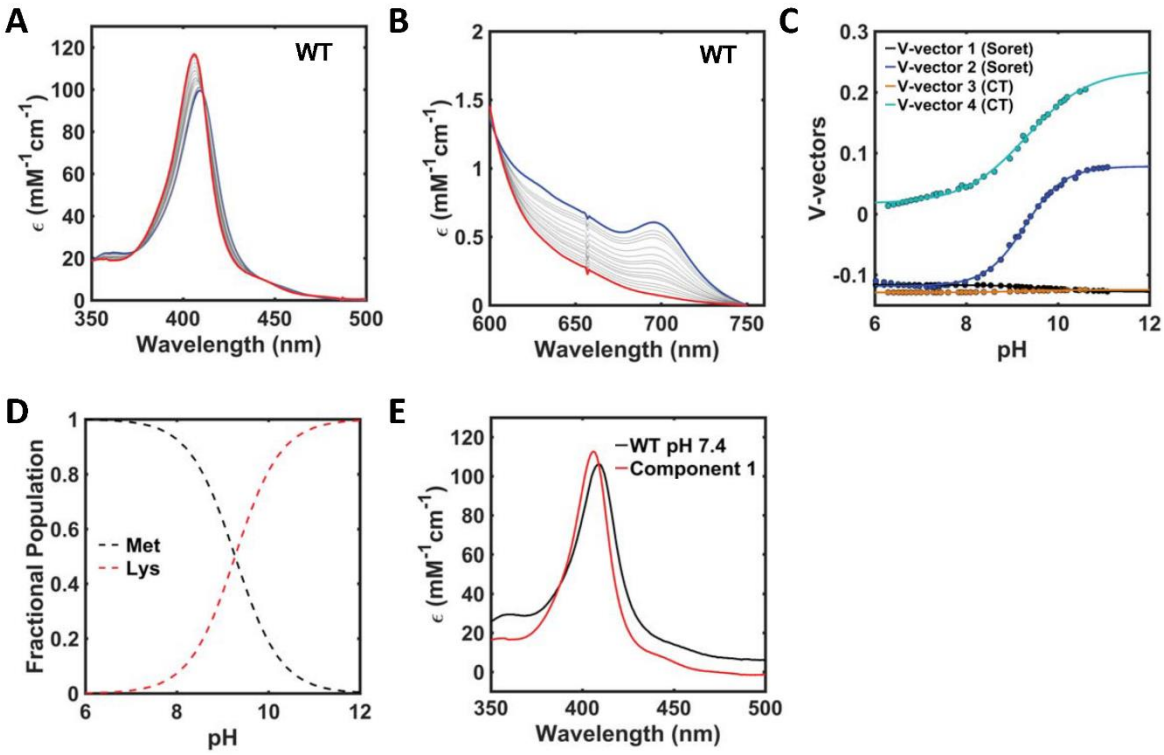

Figure 3.16. pH titrations of horse heart WT cyt *c* in μ = 0.1 M conditions at room temperature and SVD analysis for the Soret and CT bands in the electronic absorption spectra. Shown are the electronic absorption spectra of the (A) Soret band from neutral (blue) to alkaline (red) conditions in pH ranges 6.02 to 11.08, and (B) the CT band from neutral (blue) to alkaline (red) conditions in pH ranges 6.29 to 10.6, and (C) significant vectors and fits obtained from the combined SVD analysis of pH titrations in both the Soret and CT bands. The pK_a value of the alkaline transition obtained from global fits of the data was used to obtain the (D) fractional populations. Using the spectrum of WT at pH 7.4 as a reference, (D) the deconvoluted spectrum of the second component was obtained.

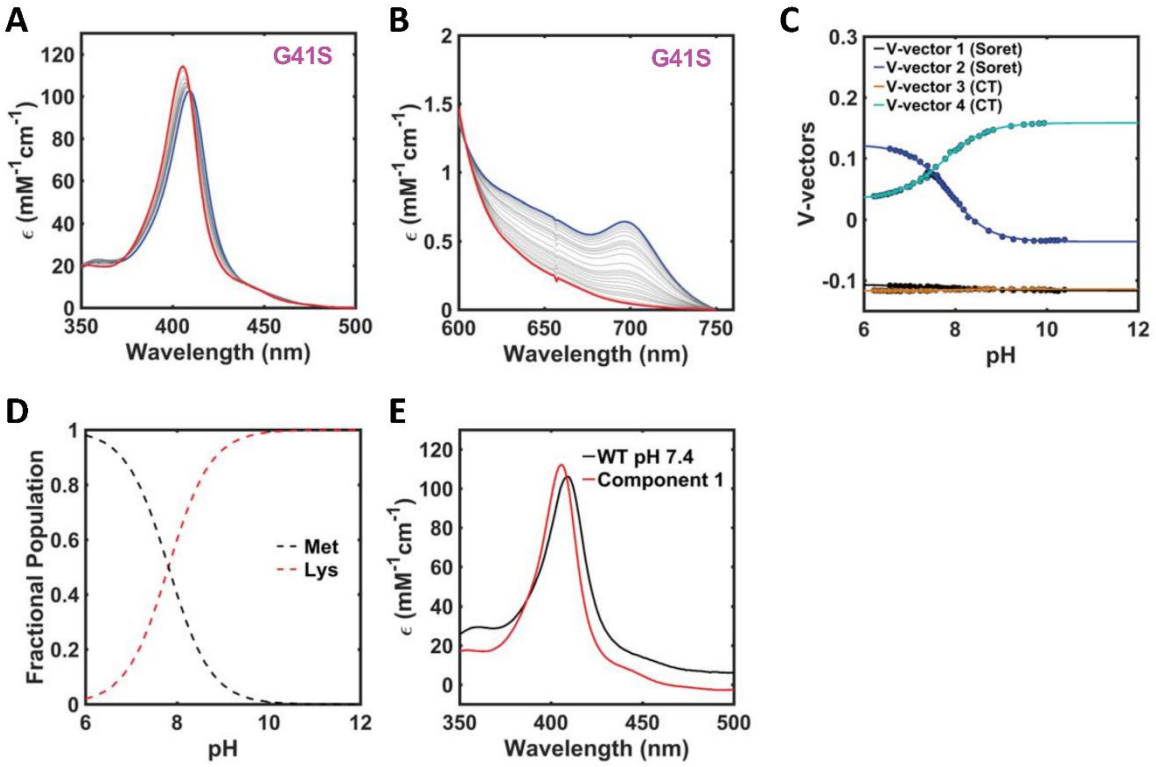

Figure 3.17. pH titrations of horse heart G41S cyt *c* in μ = 0.1 M conditions at room temperature and SVD analysis for the Soret and CT bands in the electronic absorption spectra. Shown are the electronic absorption spectra of the (A) Soret band from neutral (blue) to alkaline (red) conditions in pH ranges 6.57 to 10.39, and (B) the CT band from neutral (blue) to alkaline (red) conditions in pH ranges 6.52 to 9.94, and (C) significant vectors and fits obtained from the combined SVD analysis of pH titrations in both the Soret and CT bands. The pK_a value of the alkaline transition obtained from global fits of the data was used to obtain the (D) fractional populations. Using the spectrum of WT at pH 7.4 as a reference, (D) the deconvoluted spectrum of the second component was obtained.

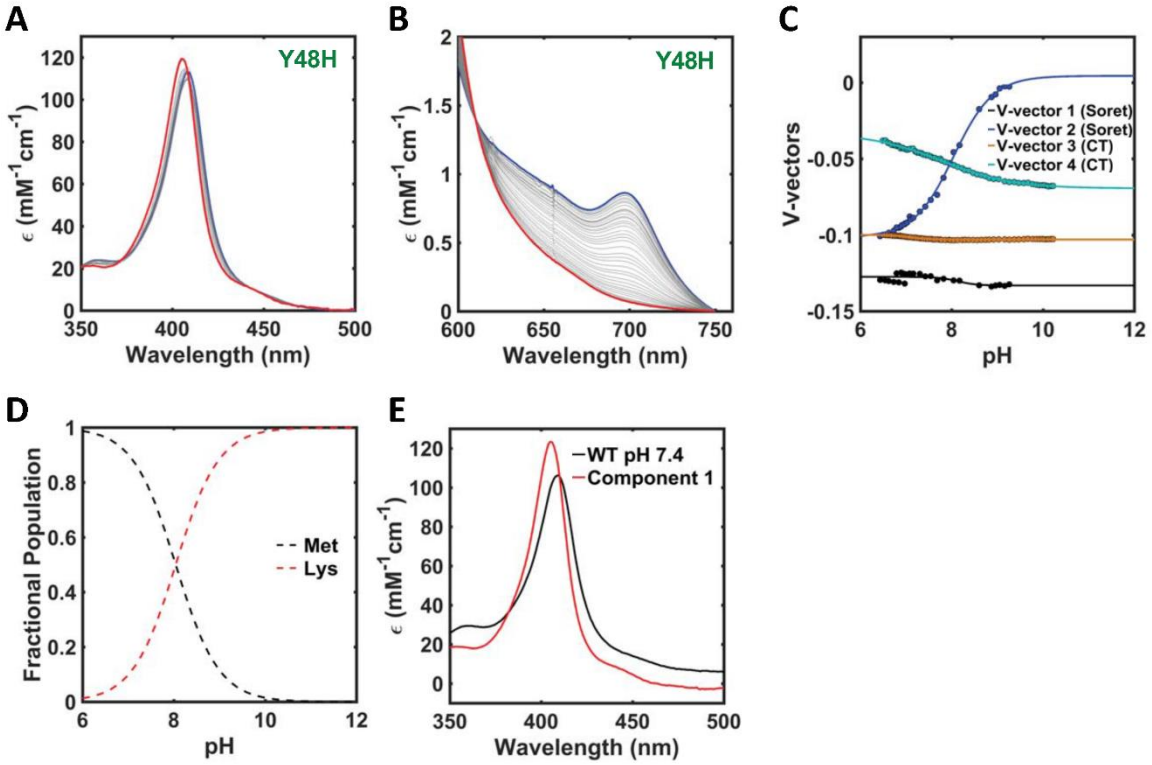

Figure 3.18. pH titrations of horse heart Y48H cyt *c* in μ = 0.1 M conditions at room temperature and SVD analysis for the Soret and CT bands in the electronic absorption spectra. Shown are the electronic absorption spectra of the (A) Soret band from neutral (blue) to alkaline (red) conditions in pH ranges 6.43 to 9.26, and (B) the CT band from neutral (blue) to alkaline (red) conditions in pH ranges 6.49 to 10.22, and (C) significant vectors and fits obtained from the combined SVD analysis of pH titrations in both the Soret and CT bands. The pK_a value of the alkaline transition obtained from global fits of the data was used to obtain the (D) fractional populations. Using the spectrum of WT at pH 7.4 as a reference, (D) the deconvoluted spectrum of the second component was obtained.

iron (Figure 3.19 and Table 3.6). From pH-dependent kinetic measurements, pK_H, k_b, and k_f were determine and the pK_C parameter was obtained.

Both the G41S and Y48H mutations in horse heart cyt *c* the pK_H value decreases in both horse heart G41S and Y48H cyt *c* compared to WT (Table 3.6). With the G41S mutation, both pK_C and k_b are comparable to corresponding values of WT, but k_f is greater. Differences in k_b and k_f hint that the rate of formation for the Lys-ligated state from the native Met-ligated state is affected by the mutation (Table 3.6). Although G41S mutation destabilizes loop D in the Met-ligated state (Figure 3.15B), it does not seem to influence the conformational dynamics of loop D for the alkaline transition. The decrease in the pK_a of the alkaline transition in this variant is mostly driven by the decrease in the pK_H of the trigger group rather than the changes in the conformational loop dynamics.

In contrast, Y48H mutation in cyt *c* increases the pK_C value compared to that of WT and both k_f and k_b increase (Table 3.6). Although both G41S and Y48H mutations cause destabilization of loop D, only the Y48H mutation noticeably affects the pK_C parameter in the alkaline transition. This difference in alkaline transition parameters between the variants suggests that the region of the loop C containing residue 48 is more sensitive in tuning the loop D dynamics required for the formation of the alkaline species than the region containing residue 41. If locations of the mutations play a role in influencing the kinetic-thermodynamic relationship of the loop in alkaline transition, location of sequence variations may also alter the alkaline transition parameters in WT proteins.

Interactions with a Biologically Relevant Denaturant. A biological denaturant for cyt *c* is CL, which is known to induce extensive unfolding upon binding to CL.[38]

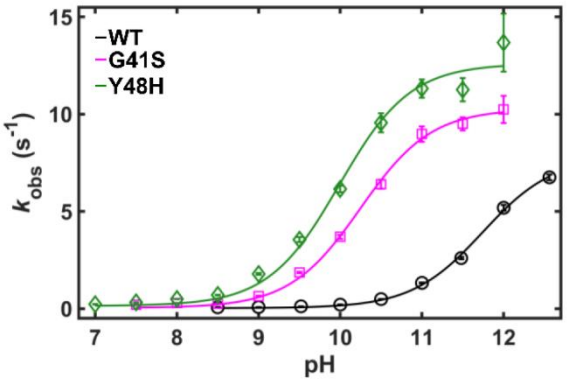

Figure 3.19. pH dependence of k_{obs} for the alkaline transition of G41S (pink) and Y48H (green) variants of horse heart cyt *c* determined from upward pH-jump experiments. Each point is an average of results from at least three measurements and error bars indicate the standard deviations from these measurements.

Table 3.6. Parameters for the Alkaline Transition of Ferricytochrome *c* Variants

	pK_{app}[a]	pK_H	k_f (s^{-1})	k_b (s^{-1})	pK_C
			Horse Heart		
WT	9.27 ±0.01	11.7 ±0.1	7.8 ±0.4	0.026 ±0.004	-2.48 ±0.07
G41S	7.81 ±0.01	10.3 ±0.1	10.2 ±0.3	0.033 ±0.008	-2.49 ±0.09
Y48H	8.04 ±0.02	10.0 ±0.1	12.5 ±0.9	0.14 ±0.03	-1.96 ±0.10
			Human[b]		
WT	9.3 ±0.9	12.0 ±0.4[c]	17 ±13[c]	0.034 ±0.060[d]	-2.70 ±0.78
G41S	8.5 ±0.2	10.5 ±0.1[c]	8.4 ±1.3[c]	0.084 ±0.055[d]	-2.00 ±0.27
Y48H	8.4 ±0.1	10.4 ±0.2[c]	7.4 ±1.4[c]	0.074 ±0.051[d]	-2.00 ±0.29
			Yeast		
WT[e]	8.7 ±2	11.7 ±2	48 ±2	0.035 ±0.010	-3.14 ±0.57

[a] pK_H + pK_C was fixed as the pK_{app} value (Table 3.5) determined from equilibrium pH titration for the fitting of k_{obs} vs pH.

[b] pK_c values and pK_{app} for WT were calculated based upon the reported values from refs. [94] and [102].

[c] From ref. [94].

[d] From ref. [102].

[e] From ref. [37], contains tmK72 and a background C102T mutation.

If the CL interaction sites are unperturbed by mutations, the nature of the CL-induced unfolded state should be thermodynamically like one another, as observed in the GuHCl titrations. In the presence of CL-containing lipid vesicles (50% CL), the binding affinity is largely unchanged with the mutations (Figure 3.20A). The G41S and Y48H variants are fully bound to CL-containing lipid vesicles by 20 to 1 (lipid to protein) ratio as observed with WT, confirming that neither of the loop C mutations alter the CL binding affinity of the protein. In the fully bound form, the electronic absorption of the Soret band increases slightly, suggesting an altered heme environment (Figure 3.20B). Although there are small differences in the intensity of the Soret band, its position is largely unchanged across the variants, suggesting a similar heme environment in the CL-bound unfolded state in all the variants. These results are in good agreement with the comparable ΔG_D values obtained from the GuHCl denaturation data, where we have seen that the variants behave similarly in the unfolded state (Table 3.4).

Peroxidase Activity. Intrinsic peroxidase activity of cyt *c* is sensitive to loop D dynamics involved in Met-dissociation and heme exposure in the absence of major conformational rearrangements.[30, 103] Thus, we argued that if the mutations in loop C affect the local dynamics of D around the heme and/or alter heme exposure at pH 7.4, changes should be observed in intrinsic peroxidase activity of G41S and Y48H variants compared to that of WT.

At pH 7.4, intrinsic peroxidase activity is greater for G41S and Y48H variants of horse heart cyt *c* compared to that for WT (Table 3.7). Increase in k_{cat} for G41S and Y48H is around an order of magnitude compared to that of WT at pH 7.4.

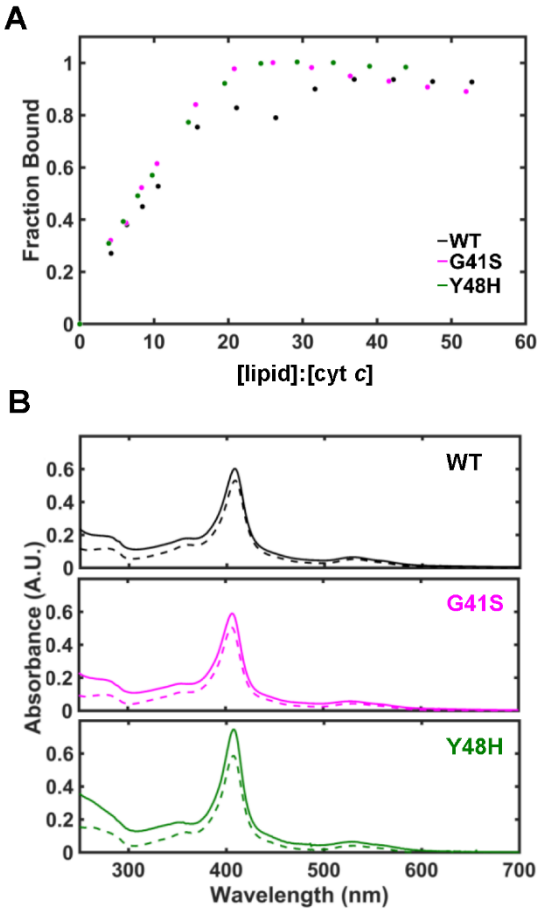

Figure 3.20. (A) A representative plot showing the fraction of the bound protein in respect to ratio of CL-containing lipid vesicle to protein concentration for ferric WT (black), G41S (pink), and Y48H (green). Horse heart cyt *c* variants ([cyt *c*] = 5 μM) with were mixed with CL-containing lipid vesicles (50% CL, 50% PC), in a 25 mM HEPES + 0.1 mM DTPA buffer at pH 7.4 and 22 ± 2 ºC. (B) Electronic absorption spectra of ferric variants in native (dotted line) and lipid vesicle bound (solid line) forms for WT (black), G41S (pink), and Y48H (green). All samples were in a 25 mM HEPES + 0.1 mM DTPA buffer at pH 7.4. Lipid bound cyt *c* contained 196 to 200 times the molar excess of lipids to the final protein concentration (5 μM).

Table 3.7. Peroxidase Activity of Cyt *c* Variants[a]

Variant	k_{cat} (s^{-1})	K_M (mM)	k_{cat}/K_M
	Intrinsic		
WT	0.0034 ±0.0004	0.45 ±0.05	0.0075 ±0.001
G41S	0.018 ±0.0006	0.49 ±0.02	0.037 ±0.002
Y48H	0.024 ±0.004	0.52 ±0.1	0.046 ±0.01
	Low CL[b]		
WT	0.019 ±0.001	0.40 ±0.06	0.047 ±0.007
G41S	0.020 ±0.001	0.42 ±0.05	0.048 ±0.006
Y48H	0.023 ±0.002	0.48 ±0.07	0.048 ±0.008
	High CL[c]		
WT	0.075 ±0.007	0.94 ±0.09	0.080 ±0.01
G41S	0.10 ±0.02	0.71 ±0.1	0.14 ±0.03
Y48H	0.095 ±0.003	0.78 ±0.1	0.12 ±0.02

[a]Measured at pH 7.4 and 22 ± 2 °C, with 0.2 mM ABTS.

[b][CL]/[protein] = 2.5

[c][CL]/[protein] = 125

Differences in peroxidase activity for G41S and Y48H are not observed (Table 3.7 and Figure 3.21A). At pH 7.4, both G41S and Y48H have some Lys-ligated species. Although Lys-ligated heme iron species at lower pH can increase the intrinsic peroxidase activity,[101] enhancements in peroxidase activity are observed with human G41S and Y48H cyt *c* compared to human WT cyt *c* at pH 6.5,[33, 35] where only Met-ligated species exist. Since enhancements in peroxidase activity are observed even in the absence of Lys-ligated species in human cyt *c* variants, it is likely that increased activity in horse heart cyt *c* variants at pH 7.4 do not stem from the minor Lys-ligated species. Structural simulations show that loop C in both horse heart G41S and Y48H cyt *c* variants more frequently sample distinct conformations compared to that of WT (Figure 3.6B). Furthermore, in G41S and Y48H, loop D stability is decreased compared to WT (Figure 3.15B) and backbone rearrangement kinetics increases (Table 3.4). These changes in loop D stability and dynamic properties will readily dissociate Met80, accounting for higher intrinsic peroxidase activities of G41S and Y48H compared to that of WT (Figure 3.21, top).

To understand whether the differences in global and local stabilities influence the peroxidase activity in CL-bound state, peroxidase activities at both low and high CL-to-protein ratios were obtained. CL-binding affinity of the protein are unaffected by mutations in loop C (Figure 3.20A), probing whether the peroxidase activity changes in the CL-bound state is a good measure of assessing whether CL alters the local kinetic properties in this partially unfolded state.

At low CL conditions where the CL lipid content to protein ratio is at 2.5 to 1, only a minor population of cyt *c* is bound to the CL-containing lipids (Figure 3.20A). Although some rate enhancement is observed with WT compared to the intrinsic peroxidase activity,

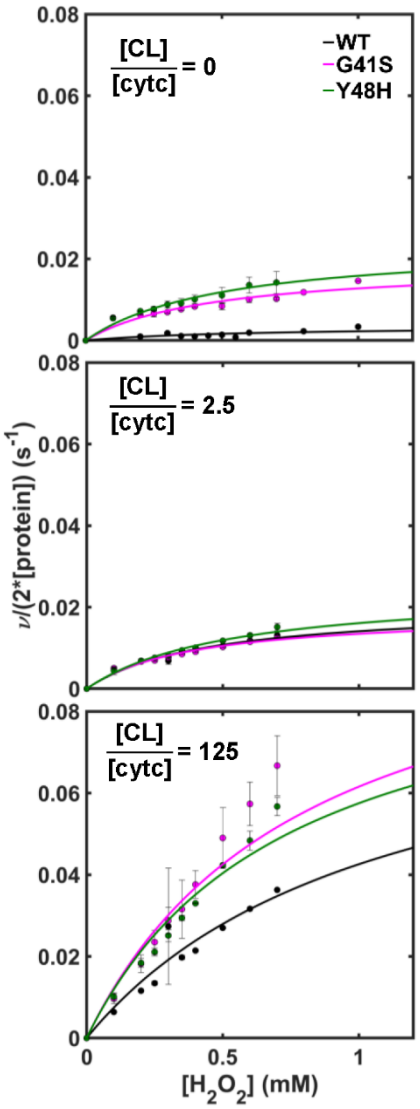

Figure 3.21. Michaelis-Menten plots of peroxidase activity for intrinsic (top), low CL-to-protein ratio (middle) and high CL-to-protein ratio (bottom) in a 25 mM HEPES + 0.1 mM DTPA buffer at pH 7.4 and 22 ± 2 ºC for WT (black), G41S (pink), and Y48H (green). Each sample contained 0.2 to 1 mM H_2O_2, 1 to 2 μM protein, 250 μM ABTS, and 250-fold molar excess of lipids for high-ratio samples and 5-fold molar excess of lipids for low-ratio samples, in which the lipid vesicles were composed of 50% CL and 50% PC. Assays were performed in triplicates and error bars were obtained from calculating the standard deviation of the measurements.

such enhancement is not observed for G41S and Y48H (Figure 3.21 and Table 3.7). At conditions where CL to protein ratio is below 15, observed peroxidase activity should be a combination of activities from both the CL-bound and -unbound (intrinsic) species. Then, it is of no surprise that WT would show a rate enhancement with a small population of CL-unfolded species, as a small population of CL-bound (yet faster and more catalytically efficient) species should contribute to an overall increase in peroxidase activity. With G41S and Y48H, since the intrinsic activity is already high, contribution by a small population of CL-bound species should not be as noticeable when compared to WT. At low CL-to-protein ratios of 2.5, ~30 to 40 % of the cyt *c* population could be estimated to be bound to CL under these conditions (Figure 3.20 A). It is likely that the rates are sensitive to both the intrinsic activity and the relative population of CL-bound and native species at low CL ratio conditions.

At high CL ratio conditions where the CL to protein ratio is at 125 to 1, peroxidase activity parameters are higher for WT, G41S, and Y48H variants (Figure 3.21, bottom, and Table 3.7). The value for k_{cat} is increased for all three proteins by an order of magnitude compared to the k_{cat} value obtained in the absence of CL (Table 3.7). Although the CL-induced unfolding event involves loop D and C-terminal helix movement,[38] destabilized loop D does not seem to contribute to forming more unfolded CL-bound species under high CL ratio conditions. Had this been the case, the k_{cat} values for G41S and Y48H should have been higher than those of WT, and the electronic absorption spectra of the CL-bound species should have been different for both variants compared to that of WT (Figure 3.20B). Instead, the rates are similar, consistent with global stability measurements which suggested that, overall, the variants behave similarly in the presence of a denaturant at pH

7.4. These results imply that the local loop D stability is not the only factor in determining the extent of protein unfolding in the presence of CL.

Discussion

Sequences and Stability. While horse heart cyt *c* is a commonly used model system to study protein folding, cyt *c* is a protein that is present in many species. Despite the wide range of sequence variations that exist between species,[22, 104] much of the tertiary structure and chemical properties are highly conserved. However, upon further comparison, possible influences of the sequence variations on tuning the biochemical and biophysical properties of the protein emerge.

Both hydrophobic core packing and peripheral intermolecular interactions are important for global stability and protein folding.[105-107] The more shielded hydrophobic residues are from the solvent and the more stabilizing contacts a protein backbone makes, the more thermodynamically costly it would be to break those contacts to unfold the protein and expose the residues to the solvent.[67-69, 106] Furthermore, depending on the identity and location of the varied residue in proteins from different species, efficiency of the packing and weak intermolecular interactions would change. For example, mutational studies with tryptophan synthase showed that global stability of the protein increases with increasing hydrophobicity of the residue, as long as the residue volume did not exceed a certain limit.[108] Elimination of a HB contact in yeast T49V/K79G and T78V.K79G cyt *c* has also been suggested to reduce global stability compared to the WT.[101] Hydrophobic effects and HB play a critical role in tuning protein folding and stability,[107] and one would expect to see minor variations in stability when comparing between proteins with different sequences in the polypeptide chain.

We can readily observe the effects of sequence variations in global stability. Global stabilities[31, 36, 38, 106, 109, 110] of many highly conserved mammalian WT cyt *c* share comparable midpoints and m_D values (Table 3.8), but differ from those of non-mammalian WT cyt *c* proteins having a lower degree of sequence conservation (Tables 3.8 and 3.9). But these global stabilities are not identical, even between species with high sequence identity (Table 3.9). Stability parameters are *comparable*, but not *identical* across species, suggesting that sequence variations help tune the global stability of the protein.

Sequence and stability comparisons among WT human, horse heart, and yeast cyt *c* offer insights for testing this hypothesis. In cyt *c*, the most stable blue foldon (*N*- and *C*-helices) accounts for roughly quarter of the protein core (V_{VdW}), loosely packed by the least stable red and nested-yellow foldons (loops C and D) (Table 3.10). Most of the sequences in the *N*- and *C*- helices are highly conserved in human and horse heart WT cyt *c*, with less variations in loop D compared to that in loop C (Figure 3.1 and Table 3.8). Subsequentially, global stabilities of human and horse heart WT cyt *c* are very similar to one another, with comparable m_D and $[GuHCl]_{1/2}$ parameters that are dependent on the α-helical signals of *N*- and *C*-terminal helices (Table 3.4). In the presence of sequence variations, differences in stability are observed. For example, fewer residues in *N*- and *C*-terminal helices in yeast WT cyt *c* are conserved compared to human WT cyt *c* (Table 3.8). m_D parameters are reflective of the changes in the solvent exposure in the unfolded state,[66, 92] and this parameter is very similar between yeast and human WT cyt *c* (Table 3.9). However, $[GuHCl]_{1/2}$ and global stability are much lower between these two species (Table 3.9).

Table 3.8. Sequence Similarities of WT Cyt *c* from from Different Species Compared to the Sequence of Human WT Cyt *c*[a]

Species	Total Identity	*N*- helix	*C*- helix	Loop C	Loop D
Spider Monkey	95.2%	90.9%	100%	77.8% (44S ,46F, 47T, 50E)	100%
Mouse	91.3%	81.8%	92.9%	83.3% (44A, 46F, 50D)	93.7% (83A)
Bovine	90.4%	81.8%	85.7%	88.9% (46F, 50D)	93.7% (83A)
Horse Heart	88.5%	81.8%	85.7%	83.3% (46F, 47T, 50D)	93.7% (83A)
Donkey	89.4%	81.8%	85.7%	88.9% (46F, 50D)	93.7% (83A)
Dog	89.4%	81.8%	85.7%	88.9 % (46F, 50D)	93.7% (83A)
Rabbit	91.3%	81.8%	92.9%	83.3% (44V, 46F, 50D)	93.7% (83A)
Chicken	87.5%	72.7%	78.6%	83.3% (44E, 46F, 50D)	93.7% (83A)
Tuna (bonito)	80.6%	63.6%	71.4%	83.3% (44E, 50D, 54S)	93.7% (83A)
Tuna (albacore)	80.6%	63.6%	71.4%	83.3% (44E, 50D, 54S)	93.7% (83A)
iso-1 yeast	62.5%	27.3%	64.3%	61.1% (40S, 44E, 50D, 53I, 54K, 56N, 57V)	81.3% (81A, 83G, 85L)
iso-2 yeast	58.7%	27.3%	50%	61.1% (40S, 43V, 44K, 50D, 53I, 56N, 57V)	81.3% (81A, 83A, 85L)
C. krusei	57.7%	27.3%	35.7%	66.7% (40S, 44E, 50D, 54R, 55A, 57V)	81.3% (81A, 83G, 85L)
C. elegans 2.1	56.7%	45.5%	50%	55.6% (40S, 42T, 43V, 44S, 46F,47D, 49S, 57V)	81.3% (81V, 83A, 85L)
C. elegans 2.2	55.8%	63.6%	42.9%	61.1% (40S, 43V, 44A, 46F, 47D, 49S, 57V)	75% (70D, 81V, 83A, 85L)

Table 3.8. Footnotes

[a] Sequences were obtained from the UniProt database[111] for human (UniProt ID P99999), spider monkey (P00003), mouse (P62897), bovine (P62894), horse heart (P00004), *C. krusei* (P00041), donkey (P68097), dog (P00011), rabbit (P00008), chicken (P67881), tuna (bonito, P00025; albacore P81459; sequence identity between two species is 98.1% with differences in residues 61 and 62), *iso*-1 yeast (P00044), *iso*-2 yeast (P00045), *C. elegans* 2.1 (P19974), and *C. elegans* 2.2 (Q23240). Helical segments and residue numberings were determined based upon secondary structure assignment for horse heart WT cyt *c* in UniProt database.[111] In addition to total identities, regional identities for the *N*-terminal helix (*N*-helix, residues 3 to 13), *C*-terminal helix (*C*-helix, residues 88 to 101), loop C (residues 40 to 57), and loop D (residues 70 to 85) were obtained in comparison to the WT human cyt *c* sequence.

Table 3.9. Global Unfolding Parameters of WT Cyt *c* from Previously Studied Species

Species	$[GuHCl]_{1/2}$ (M)	m_D (kJ mol^{-1} M^{-1})	ΔG_D (kJ mol^{-1})
Human[a]	2.55 ±0.01	15.5 ±0.2	39.6 ±0.5
Spider Monkey[b]	2.48 ±0.02	14.6 ±0.79	36.4 ±1.7
Bovine[c]	2.63	13.3	35.0
Horse Heart[d]	2.7 ±0.1 (2.42)	11.5 ±2.6 (12.6)	31.1 ±7.1 (30.5)
Donkey[e]	2.58	13.0	34.3
Dog[e]	2.45	15.0	36.7
Rabbit[e]	2.51	12.5	31.4
Chicken[e]	2.59	9.6	24.9
Tuna[e]	2.65	11.7	31.0
iso-1 yeast[f]	1.15 ± 0.01	20.6 ± 1.7	23.7 ± 2.0
iso-2 yeast[g]	1.5 ±0.2	12.5 ±0.8	19.2 ±0.3
C. krusei[c]	1.89	16.0	30.2
C. elegans 2.1[h]	1.72 ±0.03	16 ±3	28 ±4
C. elegans 2.2[h]	1.16 ±0.04	16 ±2	18 ±3

[a]From ref [31], GuHCl denaturation at pH 7.5 and 25 °C.

[b]From ref [32], GuHCl denaturation at pH 7.0 and 25 °C.

[c]From ref. [106], GuHCl denaturation at pH 6.5 and 25 °C for ferricytochrome c. ΔG_D values were calculated from the reported $[GuHCl]_{1/2}$ and m_D values.

[d]From ref. [38], GuHCl denaturation at pH 7.4 and room temperature. Values in parenthesis from GuHCl denaturation at pH 6.5 and 25 °C reported in ref. [106] listed for comparison.

[e]From ref. [109], GuHCl denaturation at pH 7, at 25 °C for ferricytochrome *c*. ΔG_D values were calculated from the reported $[GuHCl]_{1/2}$ and m_D values.

[f]From ref. [36], refitted from data reported in ref. [95] GuHCl denaturation at pH 7.5 and 25 °C.

[g]From ref. [112], GuHCl denaturation at pH 6.0 and 20 °C.

[h]From ref. [113], GuHCl denaturation at pH 7.4 and room temperature.

Table 3.10. Volumes and Packing Densities of WT Cyt *c* from X-ray Structures[a]

Species	V_{MS} (Å^3)	V_{void} (Å^3)	V_{VdW} (Å^3)	ρ
		Full structure		
Human[b]	13812	3252	10560	0.765
Horse Heart	13858	3248	10610	0.766
iso-1 yeast	13917	3207	10710	0.770
		N- and C- helices only[c]		
Human[b]	--	--	2779	--
Horse Heart	--	--	2791	--
iso-1 yeast	--	--	2703	--

[a]X-ray crystal structures of human (PDB ID 3ZCF),[34] horse heart (1HRC),[18] and yeast (2YCC)[17] WT cyt *c* were used to calculate the packing density of the protein (ρ), and the total solvent-excluded molecular surface volume (V_{MS}), a geometric volume contribution of a protein; V_{MS} is a sum of the void volume (V_{void}) and the VdW volume (V_{VdW}), using ProteinVolume.[55]

[b]Since the X-ray crystal structure of human WT cyt *c* (PDB ID 3ZCF)[34] contains 4 structures in the unit cell, computed values were divided by 4 to show the average volume values for the individual protein chain.

[c]For calculations of only *N*- and *C*- helices, PDB data for the residues 3 to 13 and 88 to 101 were included with the solvent data and heme coordinates; only the V_{VdW} value is shown.

Similar sequence-stability relationships are also observed between *iso*-2 yeast, *C. krusei*, and *C. elegans* (Tables 3.8 and 3.9). Could sequence variations affect the global packing of the protein, exposing more residues to denaturants and hence lowering the stability parameters in these species? While this may be a possibility, the *N*- and *C*-terminal helices contributions to packing density and the molecular surface volume (V_{MS}) for yeast WT cyt *c* are comparable to both human and horse heart WT cyt *c* (Tables 3.8 and 3.9). These results suggest that minor stability variations observed across different WT cyt *c* proteins may not necessarily arise from differences in hydrophobic core packing.

If the overall packing is unaffected by natural residue variations, does it mean that the contacts that form the interfoldon network is unaffected as well? Many of the same residues and secondary elements (such as α-helices) are found within HB and vdW distances as observed in X-ray crystal structures of spider monkey, horse heart, bovine, tuna (bonito and albacore), and yeast (both *iso*-1 and *iso*-2) WT cyt *c* compared to human WT cyt *c* (Figures 3.22 and 3.23). However, some correlations between residue variations and changes in connectivity between structural elements are observed. For example, contacts between the 60's helix and the *C*-terminal helix are different between human and horse heart or bovine WT cyt *c* (Figure 3.22). More variations in contacts are observed between the helical structures in human WT cyt *c* and less conserved WT cyt *c* proteins from bonito and albacore tuna (Figures 3.23A and B), or from *iso*-1 and *iso*-2 yeast (Figures 3.23C and D).

However, not all sequence variations modify inter-residue contacts, and similarities of inter-residue contacts are not solely dependent on the total number of sequence variations.

Figure 3.22. Distance contact maps with a 5 Å cutoff based on the X-ray crystal structures of WT cyt *c* proteins that share high total sequence identity with the human WT cyt *c* (95.2% to 88.5%), shown for WT cyt *c* from (A) spider monkey (teal, PDB ID 5DFS, chain A),[32] (B) horse heart (teal, 1HRC),[18] and bovine at different ionic strengths (C) low (teal, 2B4Z)[56] and (D) high (teal, 6FF5).[57] All structures are compared to the WT human cyt *c* (red, 3ZCF, chain A).[34] Boxed are the contacts between helices (helix 1 (*N*-helix), residues 3 to 13; helix 2, residues 50 to 54; helix 3, residues 61 to 67; helix 4 (*C*-helix), residues 88 to 101) for all variants, with the locations of the helices determined based on the UniProt database and ref. [22]. Red arrows indicate the interhelical contact regions that differ from interhelical contacts in human WT cyt *c*.

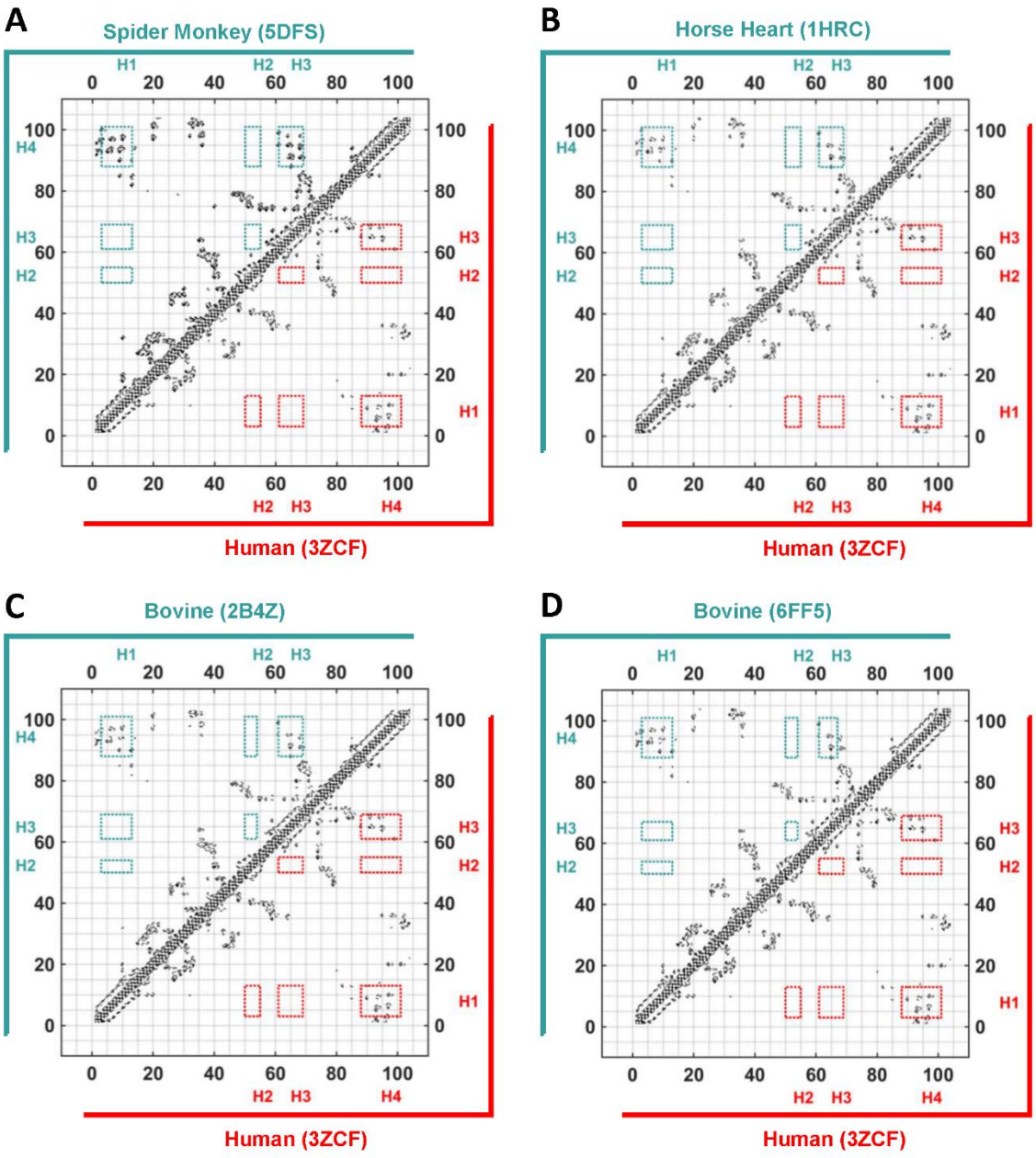
A
Spider Monkey (5DFS)
B
Horse Heart (1HRC)
C
Bovine (2B4Z)
D
Bovine (6FF5)
H1
H2
H3
H4
0
20
40
60
80
100
Human (3ZCF)

Figure 3.23. Distance contact maps with a 5 Å cutoff based on the X-ray crystal structures of WT cyt *c* that share lower total sequence identity with the WT human cyt *c* (80.6% to 58.7%), shown for WT cyt *c* from (A) bonito tuna (teal, PDB ID 1CYC),[58] B) albacore tuna (teal, 5CYT), C) yeast *iso*-1 (teal, 2YCC), and D) yeast *iso*-2 (teal, PDB ID: 1YEA). All structures are compared to the WT human cyt *c* (red, 3ZCF chain A). Boxed are the contacts between helices (helix 1 (*N*-helix), residues 3 to 13 for yeast *iso*-1 and albacore tuna, residues 3 to 14 for bonito tuna, and residues 2 to 14 for yeast *iso*-2; helix 2, residues 50 to 55 for yeast *iso*-1 and bonito tuna (predicted to be β-hairpin, but assigned as a helix for simplicity), residues 50 to 54 for albacore tuna, and residues 49 to 56 for yeast *iso*-2; helix 3, residues 61 to 69 for yeast *iso*-1, albacore and bonito tuna, residues 60 to 70 for yeast *iso*-2; helix 4 (*C*-helix), residues 88 to 101 for yeast *iso*-1, albacore and bonito tuna, and residues 87 to 103 for yeast *iso*-2) for all variants, with the locations of the helices determined based on the UniProt database. Red arrows indicate the interhelical contact regions that differ from interhelical contacts in human WT cyt *c* and/or their close relative (bonito versus albacore, yeast *iso*-1 versus yeast *iso*-2).

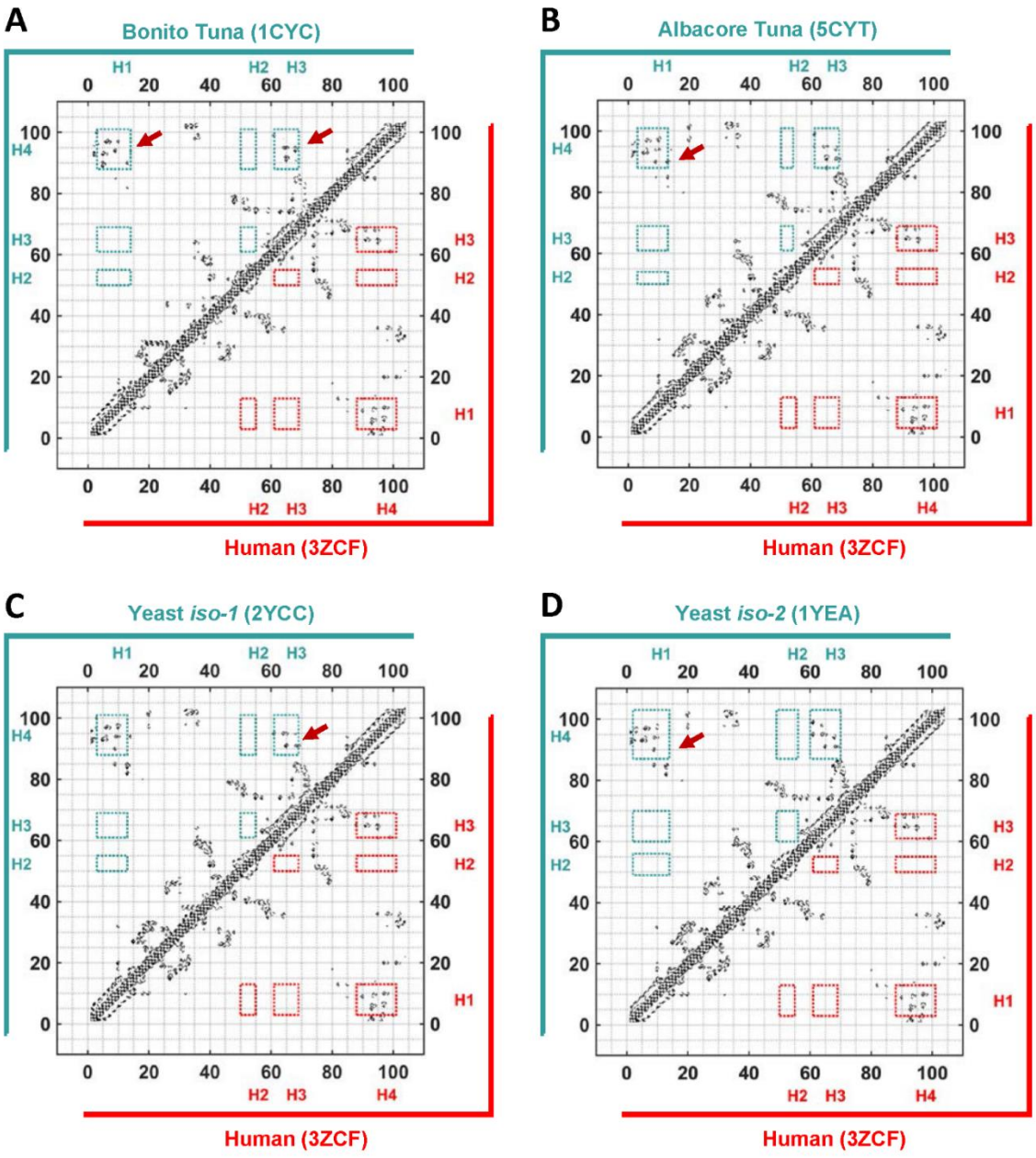
A
Bonito Tuna (1CYC)
B
Albacore Tuna (5CYT)
C
Yeast iso-1 (2YCC)
D
Yeast iso-2 (1YEA)
H1
H2
H3
H4
0
20
40
60
80
100
Human (3ZCF)

Despite the lower sequence conservation in *N*- and *C*-terminal helices in *iso*-1 yeast, contact regions between the α-helices are comparable to those in human WT cyt *c* (Figure 3.23C), while clear differences are observed between more sequentially conserved bonito tuna and human WT cyt *c* (Figure 3.23A). Despite high sequence identities between the two species of tuna (over 90%) and yeast (over 80%), differences even in the α-helical contacts are observed (Figures 3.23A and B, Figures 3.23C and D). This observation suggests that sheer number of residue variations do not necessarily alter the inter-residue contacts. Had these contacts been dictated by the sheer number of residue variations, inter-helical contacts should have been more conserved in bonito tuna cyt *c* rather than in *iso*-1 yeast cyt *c* compared to the human cyt *c*. Further, some changes are observed even between WT cyt *c* from closely related species, such as between bonito and albacore tuna, or *iso*-1 and *iso*-2 yeast. It is thus likely that some residue variations based on their identity *and* location modify these contacts, while others do not.

Do these changes in contacts affect the stability of the protein? A potential relationship emerges when comparing between *iso*-1 and *iso*-2 yeast WT cyt *c*. WT cyt *c* protein from *iso*-2 yeast is more stable toward chemical[112] and thermal[114, 115] denaturation compared to protein from *iso*-1 yeast, where even slight modifications in C102 in *iso*-1 yeast cyt *c* have been shown to yield differences in global stability.[115] It has been speculated that these minor differences in global stability arise from local rearrangements at or near residue 102. Mutational studies have suggested that the presence of a more bulky Met at residue position 98 in *iso*-2 cyt *c* fills in a buried cavity, slightly increasing the thermostability of the iso-2 protein compared to *iso*-1 cyt *c* where position 98 is Leu.[60] Furthermore, interactions between His26 and amino acid side chain at 102 in *iso*-1 cyt *c*

has been suggested to modulate the HB interactions between His26 and residues 44 and 31, resulting in a decreased stability at lower pH, compared to *iso-2* cyt *c* where residue 26 is Asn instead of His and such decrease in stability with pH is not observed.[115] Although it is difficult to pinpoint how these local changes may have propagated to differences in global contacts as observed in the α-helical regions, differences in packing and peripheral contacts and resulting changes in stability trends observed between *iso*-1 and *iso*-2 yeast strongly suggest that sequence variations play a role in tuning both the structure and global stability of the protein.

The relationship between inter-foldon contacts and stability has also been observed with many variants of horse heart cyt *c*. Detailed studies by Englander *et al*. show how residue contacts are involved in inter-foldon communication and tune the stability of the protein.[116] For example, G66A mutation that was designed to disrupt a stabilizing contact between the two foldons, 60's helix and loop D, equally destabilizes loop D and all subsequent higher energy foldons without altering the native fold of the protein.[116, 117] This result highlights the extensive feedback network that exists between the foldons, as well as the influence weak contacts that are formed between foldons have in tuning the global stability of the protein. Further, contacts have different roles and influences on the protein. E62G variant eliminated a salt bridge between Glu62 and Lys60 (both located in the yellow foldon between loop C and the 60's helix), and this specific alteration of an inter-residue contact destabilizes all foldons except for the least stable loops C and D. The different mutational effects of G66A and E62G variants on loops C and D show that perturbations in the cross-talk network have varying effects depending on whether the inter-foldon contacts in loops C and D are involved.

From these comparisons we could then argue that: 1) variations in global stability stem from stabilizing interactions that would not perturb the overall core packing but differ depending on the identity of the residues in the protein chain, and that, 2) similarities in core packing or high sequence do not mean that the local contacts are conserved.

Testing these hypotheses is difficult when comparing human and yeast WT cyt *c*. Local and global stability of these proteins are very different.[118, 119] Further, approximating HB and vdW contacts in yeast WT cyt *c* show that these contacts are fewer in number compared to those in human WT cyt *c* (Figure 3.24), even in regions where sequences are conserved between human and yeast WT cyt *c* (Figure 3.1). Comparing human with horse heart WT cyt *c*, however, is ideal in probing this relationship because global stabilities are similar between these two proteins and relationship between local stability to structure is well-documented for horse heart cyt *c*. Further, while *N*- and *C*-helical inter-helical contacts are conserved between human and horse heart WT cyt *c* (Figure 3.22B), differences in location or the relative strength of HB and vdW contacts still exist in loops C and D (Figures 3.8 and 3.9). Variations are observed between these two species, showing that the horse heart WT cyt *c* has its own cross-talk network depending on the residues in loops C and D. Thus, comparing human with horse heart cyt *c* allows us to better relate how natural sequence variations in the loops affect the interloop contacts, and how the adaptability of local contacts affect the chemical properties of the protein.

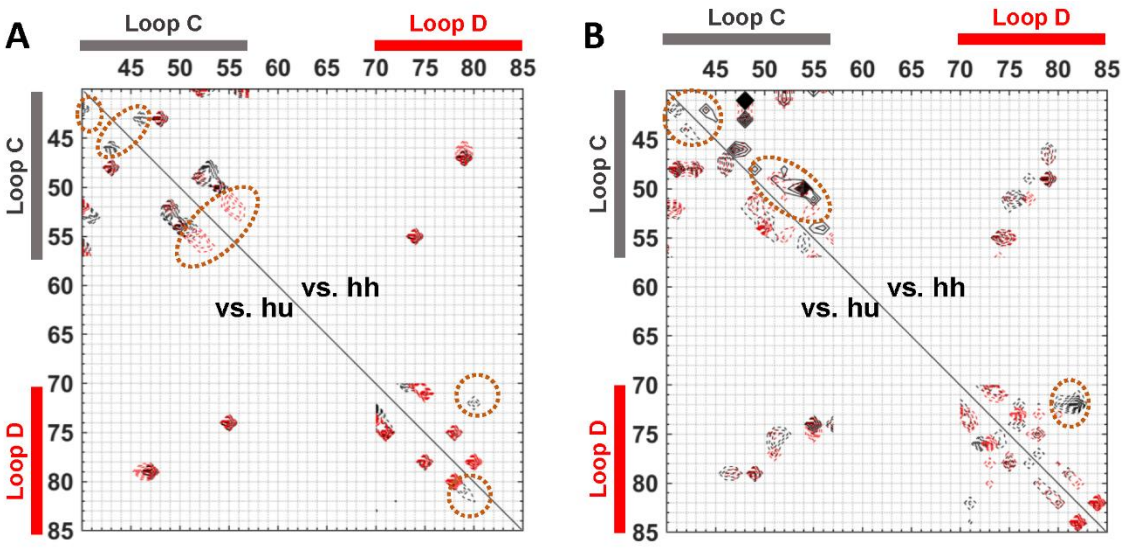

Figure 3.24. Contour plots of inter-residue (A) HB and (B) vdW contacts in yeast (y,red) human (hu, black), and horse heart (hh, black) WT cyt *c* based upon the X-ray crystal structures (PDB ID 2YCC for yeast,[17] 1HRC for horse heart,[18] and 3ZCF for human[34] WT cyt *c*). In each plot, (A) HB or (B) vdW contacts are compared between yeast (red) versus human (black) WT cyt *c* (bottom) or yeast (red) versus horse heart (black) WT cyt *c* (top). Highlighted are the notable differences in contacts observed when compared across species.

Interloop Contacts and Loop C Properties. Analyses of structural and functional properties associated with loops C and D of human and horse heart cyt *c* provide insight into the roles of local contacts in proteins. Based on simple sequence comparisons, most of the sequence variations in WT human and horse heart cyt *c* are in loops C and D (Figure 3.1). Further, of the least stable foldons in horse heart cyt *c*, the stability and kinetic properties of the red foldon (loop D) can be readily monitored, making it a good candidate to relate the cross-talk between loops C and D to protein function such as alkaline transition and peroxidase activity.

The cross-talk network in the variable loop regions are similar in human and horse heart WT cyt *c* (Figure 3.9). Despite the similarity, the adaptability of the polypeptide fold to residue variations is different between the two species, as observed by G41S or Y48H mutations in loop C. These mutations decrease the global stability in human cyt *c* variants, but similar decrease is not readily observed in horse heart cyt *c* variants. Trends in the m_D parameter offer clues to the origin of the different trends in global stability observed between human and horse heart cyt *c*. Since the m_D parameter is proportional to the changes in solvent exposed surface area upon denaturation,[69] this parameter is reflective of the changes in packing and native solvent exposure of the overall protein backbone. With loop C mutations, the m_D values remain comparable for all horse heart cyt *c* variants at pH 7.4. Yet, the m_D values in these horse heart cyt *c* variants are still lower than the human cyt *c* variants, suggesting surface area exposure is different upon unfolding. Foldon stabilities have been reported in the literature from various HX experiments in human and horse heart WT cyt *c*. [31, 32, 38, 93, 106, 119-122] However, incorrect units have been used in the calculations for the reported foldon energy levels in human WT cyt *c*,[119] requiring recalculations based

on the reported k_{ex} values. Foldon stability recalculations based on the previously reported k_{ex} values (also performed with horse heart WT cyt *c* as an internal check) from various HX experiments show that the protein global stability (and foldon stability) decreases with pH (Figure 3.25).[31, 32, 38, 93, 106, 119-122] If the sequence variations had identical effect on the global stability of the protein in both human and horse heart cyt *c*, we should have observed similar lower stability parameters of for both WT cyt *c* proteins at pH 6.5. However, this is not the case (Figure 3.25, see captions *a* and *g*),[106, 119] suggesting other factors at play. In terms of solvent exposure, folded state is different from the unfolded state in that many of the hydrophobic residues are shielded away from the solvent through the polypeptide packing. In the unfolded state, the secondary structure is perturbed, and the previously shielded residues are exposed to the solvent. If we assume that fully unfolded polypeptide for human and horse heart cyt *c* are comparable and the residues have similar degrees of solvent exposure, difference in m_D values between WT proteins would be due to differences in the solvent exposure of the polypeptide in the folded state. The more solvent-exposed the polypeptide is in the folded state, the lower the m_D value would be, as fewer residues would become solvent exposed to reach the unfolded state.

Pairwise RMSD value calculations show that loop C mutations in human cyt *c* increase the diversity of the sampled conformational ensemble in the loop regions (Figure 3.6A), more so in the G41S variant than in the Y48H variant. This difference is in good agreement with the NMR H/D exchange experiments, which have shown that the Y48H and G41S mutations increase the loop C dynamics of the folded state in human cyt *c*.[35, 119] Similar trends in MD simulations observed in human cyt *c* variants (Figure 3.6A) are also observed in the horse heart cyt *c* variants (Figure 3.6B).

Figure 3.25. Plots of the five foldon stabilities (ΔG_D in kcal/mol) for human (left), horse heart (center), and *iso*-1 yeast (right) WT cyt *c*. Foldon energies determined from HX experiments are colored in dark blue, green, yellow, red, and gray for the blue, green, yellow, red, and infra-red (iR) foldons, respectively. (Left) HX energies for human WT cyt *c* recalculated from k_{ex} values from HX experiments in ref. [119] at pD 6.9 and 288 K, using k_{ch} values calculated from CIntX.[120] Marker residues used in horse heart WT cyt *c* were used for the calculations;[121] Leu64 was used in the yellow foldon, and residues 40, 42, 43, 53, and 54 were used to calculate the energies for the infra-red (iR) foldon. Stability parameters obtained from monitoring 222 nm in CD (light blue) or from monitoring the 695 nm CT absorption band (light pink) are shown, with the ΔG_D values (in kcal/mol) inside the parentheses. (Center) HX energies and error bars for horse heart WT cyt *c* foldons are from ref. [15] at pD 7.4 and 293 K, excluding the iR foldon. Energies for residue 32 for the green foldon and residues 40, 42, 43, 53, and 54 for the iR foldon were recalculated from the reported k_{ex} values in ref. [122] and k_{ch} values calculated from CIntX.[120] Stability parameters obtained from monitoring 222 nm in CD (light blue) or from monitoring the 695 nm CT absorption band (light pink) are also shown. (Right) Stability parameters for *iso*-1 WT cyt *c* for the iR foldon from limited proteolysis are shown (light gray), along with parameters obtained from monitoring 222 nm in CD (light blue) or from monitoring the 695 nm CT absorption.

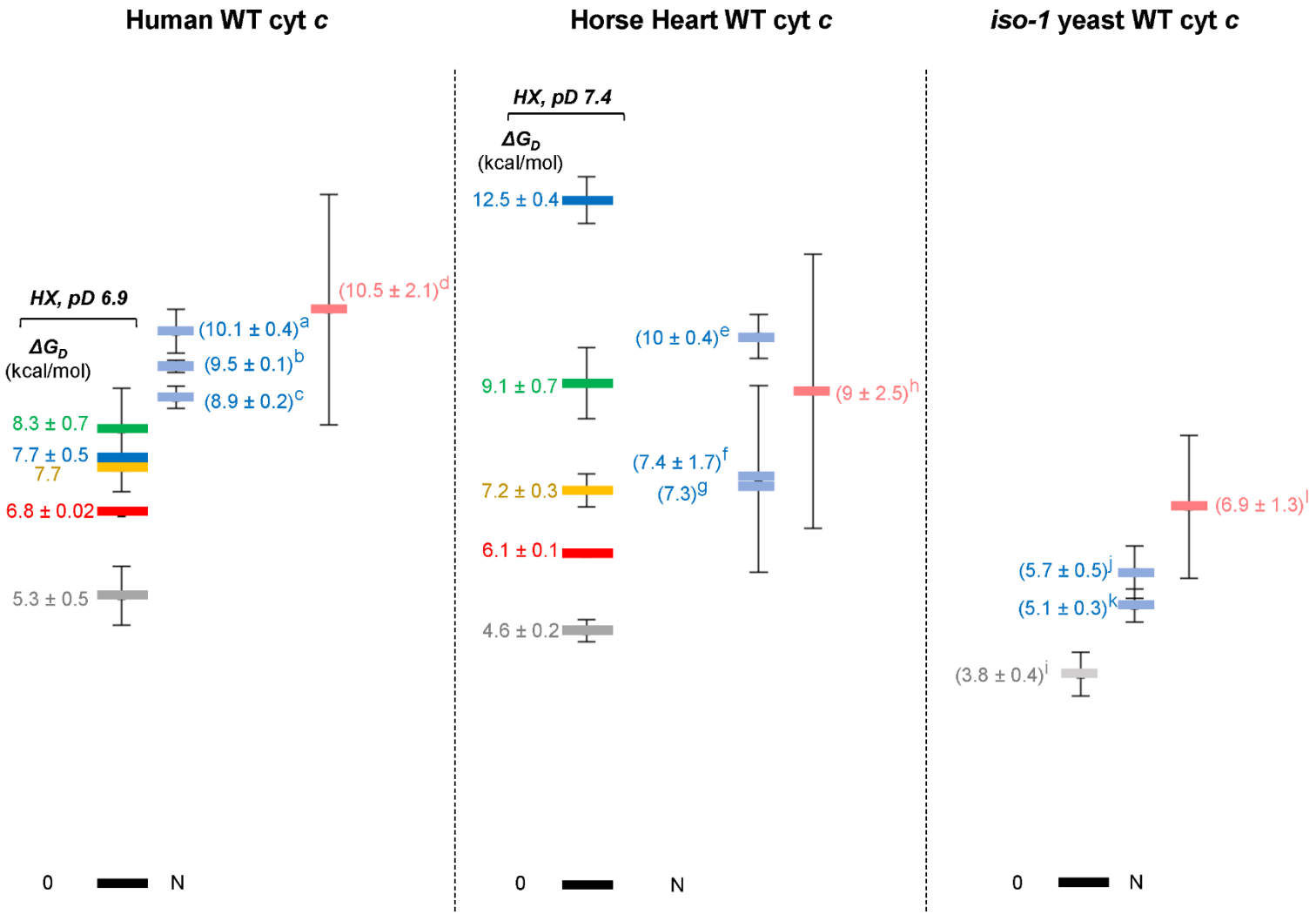
Human WT cyt c
HX, pD 6.9
ΔG_D
(kcal/mol)
8.3 ± 0.7
7.7 ± 0.5
7.7
6.8 ± 0.02
5.3 ± 0.5
(10.1 ± 0.4)a
(9.5 ± 0.1)b
(8.9 ± 0.2)c
(10.5 ± 2.1)d
0
N
Horse Heart WT cyt c
HX, pD 7.4
ΔG_D
(kcal/mol)
12.5 ± 0.4
9.1 ± 0.7
7.2 ± 0.3
6.1 ± 0.1
4.6 ± 0.2
(10 ± 0.4)e
(7.4 ± 1.7)f
(7.3)g
(9 ± 2.5)h
0
N
iso-1 yeast WT cyt c
(3.8 ± 0.4)i
(5.7 ± 0.5)j
(5.1 ± 0.3)k
(6.9 ± 1.3)l
0
N

Figure 3.25 Footnotes

[a]From ref. [119], denaturation monitoring ellipticity at 222 nm, at pH 6.5 and 15 °C.

[b]From ref. [31], GuHCl denaturation monitoring ellipticity at 222 nm, at pH 7.4 and 25 °C.

[c]From ref. [32], GuHCl denaturation monitoring ellipticity at 222 nm, at pH 7.0 and 25 °C.

[d]GuHCl denaturation monitoring the 695 nm CT band at pH 7.4, data provided by Dr. Fangfang Zhong.

[e]From ref. [123], GuHCl denaturation monitoring ellipticity at 222 nm, at pD 7.4 and 30 °C.

[f]From ref. [38], GuHCl denaturation monitoring ellipticity at 222 nm, at pH 7.4 and 24 °C.

[g]From ref. [106], GuHCl denaturation monitoring ellipticity at 222 nm, at pH 6.5 and 25 °C.

[h]Refitted from data in ref. [93], GuHCl denaturation monitoring the 695 nm CT band at pH 7.4.

[i]From ref. [118], limited proteolysis at pH 7.0 and 22 °C. Protein contains C102S mutation and is expressed in *E. coli*.

[j]From ref. [36], GuHCl denaturation monitoring ellipticity at 222 nm, at pH 7.5 and 25 °C. Protein contains C102S mutation and is expressed in yeast (TmK72).

[k]From ref. [118], GuHCl denaturation monitoring ellipticity at 222 nm, at pH 7.5 and 22 °C.

[l]Refitted from ref. [95], GuHCl denaturation monitoring the 695 nm CT band at pH 7.5 and 25 °C. Protein contains C102S mutation and TmK72.

However, comparison of pairwise RMSD values from horse heart WT cyt *c* to human WT cyt *c* suggests a possibility that loop C in horse heart cyt *c* sample conformations that require larger rearrangements in the polypeptide at a higher frequency than in human cyt *c* (Figure 3.6B). A more dynamic loop C in horse heart WT cyt *c* would decrease the frequency of loops C and D coming into contact with one another, and would make loop C in horse heart cyt *c* more prone to solvent exposure than loop C in human cyt *c*. Heat maps of contact frequencies illustrate this possibility, as fewer residues in loops C and D come within HB distances in horse heart WT cyt *c* compared to human WT cyt *c* (Figure 3.8). In the presence of mutations in loop C that increase dynamics of this loop, mutational effects as observed in pairwise RMSD values are not as dramatic in horse heart cyt *c*. Perhaps then, pairwise RMSD calculations for variants of human cyt *c* suggest a more conformational rearrangements than for horse heart cyt c variants because it can make contacts that cannot be made in horse heart cyt *c*, and stabilizes compact conformations. Further, previous MD simulations have revealed that long-scale loop C dynamics are readily observed in WT human cyt *c* by 100 ns.[84] Yet, no noticeable changes in the RMSD are observed in WT horse heart cyt *c* even beyond 100 ns, suggesting that the loop dynamics, in both shorter and longer time scales, may be different for human and horse heart cyt *c*.

Loop C mutations G41S and Y48H in horse heart cyt *c* do not seem to influence the global stability and solvent exposure of the protein as was observed in human cyt *c*. What about loop D? Per residue RMSF values for the residues in the loop D regions are comparable between human and horse heart WT cyt *c* even with the G41S and Y48H mutations (Figure 3.4). In horse heart G41S and Y48H cyt *c* variants, random coil features

that may arise from unfolded loop D are not observed in the far-UV CD spectra (Figure 3.13), suggesting similar loop D structural features to that in horse heart WT cyt *c*. Yet, loss of cooperativity in unfolding the polypeptide is observed, suggestive of an altered inter-foldon communication network. As a consequence of cooperative folding,[95, 123, 124] stability parameters obtained from monitoring changes in the 695 nm CT band are comparable to the stability parameters obtained from monitoring changes in the α-helical signals in WT cyt *c* from human, horse heart, and even yeast.[31, 32, 36, 38, 93, 95, 118, 119, 123] In horse heart cyt *c* variants, the stability parameters obtained from monitoring 695 nm CT band are different from those obtained from monitoring signals from the α-helices, suggesting a disruption in the inter-foldon network of loop D with other parts of the protein. Compared to the loop D stability from HX experiments of ΔG_D of ~6 kcal/mol for horse heart WT cyt *c*,[121] stability of loop D obtained from monitoring the 695 nm CT band is much lower in our G41S and Y48H variants with ΔG_D of ~1.4 kcal/mol (Figure 3.15B). It is most likely that the intraloop D connections are still maintained in the absence of denaturants as random coil characteristics are not observed in the CD spectra of horse heart G41S and Y48H variants (Figure 3.13), and MD simulations suggest that the loop D does not sample large and varied conformational rearrangements one would expect from an unfolded polypeptide (Figures 3.4B and 3.7B). However, the interloop D connections may have been disrupted, as suggested by the difference in stability parameters obtained from observing either the 695 nm CT band or the α-helical signals.

Preservation of native fold and maintaining similar global stability does not necessarily indicate the local stability is preserved, as the loop D stability is diminished by nearly 4 kcal/mol in our horse heart G41S and Y48H cyt *c* variants. This decrease may be

due to the presence of a more structurally dynamic loop C and varied loops C and D interactions in horse heart G41S and Y48H cyt *c* variants, which would increase the likelihood of increasing the solvent-exposure of loop D. Analyses of loops C and D inter-foldon contacts show that the cross-talk network is altered in horse heart cyt *c* variants (Figure 3.9), which could help explain the decrease in loop D stability. EXAFS measurements of horse heart WT cyt *c* have suggested that the strength of the Met80-Fe bond is dependent on the contacts from polypeptide, including the residues in loop D.[125] This suggests that there are preferred contacts that must be preserved to favor native packing of loop D. Perhaps, altering loops C and D contacts creates a domino effect and alters other inter-residue contacts loop D that form to pack the loop.

Although it is unclear if loop D stability is similarly altered in human cyt *c* with G41S and Y48H mutations as in horse heart cyt *c*, it is likely that structural effects of G41S or Y48H mutations are different in human and horse heart cyt *c*. Comparison of X-ray crystal structures suggests that human WT cyt *c* has residues that can form additional interloop contacts between loops C and D than in horse heart WT cyt *c* (Figure 3.10). Introduction of G41S and Y48H mutations also influence loop C properties in human cyt *c*; previous HX experiments[35, 119] and our MD simulations suggest that G41S and Y48H mutations make loop C more dynamic, allowing the loop to samples a wider range of conformations. Yet, analyses of MD simulations suggest that many residue pairs are within HB distance at similar frequencies in G41S, Y48H, and WT for human cyt *c* than for horse heart cyt *c* (Figure 3.8). Some of these contacts are persistently observed only in the human cyt *c* proteins, such as the contact between residues 46 and 79 (Figure 3.8). Perhaps these readily formed additional contact pairs observed in human cyt *c* but not in horse heart cyt

c limit the conformational sampling in dynamic loop C, and we observe fewer variations in interloop contacts for human cyt *c* variants than for horse heart cyt *c* variants.

Alkaline Transition. Can differences in loops C and D contacts influence other protein properties besides stability? Dynamics and stability of loops C and D are linked to alkaline transition. Loop D contains the heme iron ligands involved in the transition, and in the native state, residues in loop D make HB contacts with loop C. Unfolding of the loop C has been argued to expose the trigger group for deprotonation, triggering the conformational switch to rearrange the loop D to allow replacement of Met80 with Lys73/79 as an axial ligand to the heme iron.[23] Usually, this event occurs at mildly alkaline pH, dictated by the pK_a of the yet unknown trigger group (pK_H). Alkaline transition is dependent on the dynamics of loop D in forming the Lys ligated species (k_f and k_b), relative stability of Met- and Lys-ligated forms (pK_C), and the environment of the trigger group that tunes the chemical properties (pK_H)—which are all dependent on how well the loops C and D can rearrange.

Comparisons of the k_b Parameter. The back reaction of the alkaline transition involves the dissociation of a Lys-ligand from the heme iron and loop D rearrangement. The fold of loop D in the Lys-ligated state is different from the fold in the Met-ligated state. Analysis of X-ray crystal structure of the Lys73-ligated yeast cyt *c* shows that loop D is a relatively compact β-sheet with a loop turn involving residues 76 to 79.[25] MD simulations suggest that although the extent of loop D rearrangement in the Lys79-ligated state is thought to be smaller than in the Lys73-ligated state, loop D rearrangement is still required.[98] Because the sequences in these loops do vary among WT cyt *c* proteins, one might expect that sequence variations may alter the k_b values. Yet, the k_b values for human and horse heart

cyt *c* variants are within error (Table 3.6). This trend is consistent with trends observed in other mutational studies in yeast, human, and horse heart cyt *c* that perturb regions in loops C and D, or with other WT cyt *c* proteins (Table 3.11)..[37, 74, 101-103, 126, 127] Studies comparing imidazole binding kinetics and redox-linked ligand substitution kinetics with yeast M80K and Met80SO cyt *c* variants have shown that Lys dissociation is the rate limiting step for Lys-ligand substitution reactions.[128] Recent ligand substitution kinetics with Lys80-ligated yeast K72A/K73A/K79G/M80K cyt *c* variant also suggests that Lys dissociation is the rate-limiting step in the back reaction for alkaline transition; even in the absence of large polypeptide rearrangements in the M80K variant, the rate for Lys dissociation is slow (k_{off} = 0.013 ± 0.001),[45] and is in the similar time scale of the k_b values observed in various cyt *c* variants (Table 3.11) . Furthermore, k_b has also been argued to be dependent on the thermodynamic stability of the Fe-N bond strength, as k_b increased by one to two orders of magnitude in the ferrous state than in the ferric state.[101] It is possible that differences in k_b are not observed between WT yeast, human, and horse heart cyt *c*, or between G41S or Y48H human and horse heart cyt *c* variants, because the sequences involved in forming the Lys-ligated loop structure are conserved between these species. Further, if loop rearrangements occur at a much faster time scale than the rate-limiting step, it may be difficult to alter the k_b of the transition.

Variations in the k_f Parameter and Loops C and D Contacts. Differences, however, are observed in k_f, with rate enhancements observed with the mutations in horse heart cyt *c* variants and not in human cyt *c* variants (Table 3.11). This difference in k_f trends could be explained by differences in loops C and D connectivity that exist in horse heart and human cyt *c* variants.

Table 3.11. Parameters for the Alkaline Transition of Ferricytochrome *c* Variants from Previously Studied Variants[a]

	pK_{app}	pK_H	k_f (s^{-1})	k_b (s^{-1})	pK_C	Ref
			Horse Heart			
T49V	7.0 ±0.1	9.1 ±0.1	13.7 ±0.9	0.11 ±0.02	-2.3 ±0.2[a]	74
			Human			
K8R	9.63 ±0.07	--	--	--	--	32
K8R/P44S	9.51 ±0.05	--	--	--	--	32
Y46F[b]	9.15 ±0.02	--	--	--	--	32
Y46F/S47T[b]	9.05 ±0.01	--	--	--	--	32
Y46F/S47T/A50E[b]	9.32 ±0.03	--	--	--	--	32
S47D	9.2 ±0.01	--	--	--	--	129
S47A	9.1 ±0.0	--	--	--	--	129
A51V	8.3 ±0.1	10.8 ±0.1	8.3 ±1.1	0.027 ±0.012	-2.5 ±0.5[a]	102
I81A	9.4 ±0.2	11.6 ±0.1	6.5 ±1.6	--	-2.2 ±0.2[c]	94, 130
V83G	10.1 ±0.1	11.7 ±0.2	8.9 ±3.4	--	-1.6 ±0.2[c]	94, 130
I81A/V83G	9.7 ±0.1	11.8 ±0.2	7.3 ±2.5	--	--	94
			iso-1 Yeast			
K73A[d]	8.82 ±0.02	10.8 ±0.2	1.51 ±0.05	0.016 ±0.001	-2.0 ±0.1[a]	37
T49V/K79G[e]	6.7 ±0.1	8.2 ±0.2	2.0 ±0.1	0.061 ±0.01	-1.5 ±0.1	101
T78V/K79G[e]	6.7 ±0.1	8.4 ±0.2	4.1 ±0.4	0.060 ±0.016	-1.8 ±0.02	101
K79G[e]	8.6 ±0.1	10.5 ±0.1	8.4 ±1.9	0.106 ±0.034	-1.9 ±0.2	25, 103
K79A[d]	8.44 ±0.01	12.0 ±0.3	160 ±5	0.040 ±0.007	-3.6 ±0.2[a]	37
C102S[f]	8.00 ±0.05	10.59 ±0.07	20.5 ±2.4	0.11 ±0.03	-2.3 ±0.3[a]	118, 126

Table continued onto next page

Table 3.11 continued

	pK_{app}	pK_H	k_f (s^{-1})	k_b (s^{-1})	pK_C	Ref
A81I[f]	8.29 ±0.13	10.23 ±0.03	13.6 ±0.5	0.17 ±0.03	-1.9 ±0.2[a]	126
G83V[f]	8.21 ±0.03	10.46 ±0.06	15.4 ±0.8	0.07 ±0.12	-2.3 ±1.7[a]	126
C102T[d]	8.5	10.9 ±0.1	13.4 ±0.7	0.029 ±0.004	-2.7 ±0.1[a]	127
F82G[d]	7.7	9.1 ±0.3	1.1 ±0.2	0.049 ±0.004	-1.3 ±0.2[a]	127
F82S[d]	7.7	9.2 ±0.7	0.9 ±0.2	0.055 ±0.005	-1.2 ±0.2[a]	127

[a]pK_C values were calculated based upon the reported k_f and k_b values.

[b]Contains K8R/P44S mutation.

[c]From ref. [130].

[d]Contains C102T mutation and was expressed in yeast. pK_C values were calculated using reported k_f and k_b values.

[e]Contains C102T and K72A mutation.

[f]Contains C102S mutation and was expressed in *E. coli* to prevent trimethylation of Lys72. pK_H in the table are obtained from fits of the from $k_{obs,2}$ dependence on pH.

Analyses of MD simulations and X-ray crystal structure suggest that loop D is restructured to accommodate Lys79- or Lys73-ligation to the heme.[25, 97, 99] Further, rearrangement of loop D is argued to be dependent on contacts with loop C,[23, 131] and loss of a compact native packing may also facilitate loop D rearrangement. Study of the X-ray crystal structure of calixarene-bound WT horse heart cyt *c* has demonstrated that loop D rearrangement led to a disordered loop C,[132] suggesting that loop C packing is related to loop D rearrangement. Yet not all structural perturbations in loops C or D affect the kinetics of loop D rearrangement, and the number of interloop contacts cannot explain the different trends in k_f when comparing across different species. Studies with yeast cyt *c* have shown that perturbations in loops C and D can result in a slower k_f than human or horse heart WT cyt *c* (Table 3.11), and WT yeast cyt *c* inherently has fewer contacts between loops C and D than either human or horse heart cyt *c* (Figure 3.9). If the total number of contacts between loops C and D does not alter the k_f value, another possibility is that the location of these contacts may influence the kinetic and thermodynamic parameters for the alkaline transition.

In human cyt *c*, G41S and Y48H mutations decrease k_f, despite having similar interloop contacts to the WT, suggesting that the loops C and D are behaving differently with the loop C mutations than in horse heart cyt *c*. In human and horse heart cyt *c*, the stretch of loop D (residues 70 to 80) that contains all the ligands associated with the alkaline transition and the contact surface with loop C is highly conserved. However, sequence variations are present in loop C of human and horse heart cyt *c* only along the stretch of residues that are in contact with loop D. If there are residues in loop C that exist in human cyt *c*, but not in horse heart cyt *c*, that can form transient contacts to either prevent local

unfolding or rearrangement of the loop in the native state, it may well explain the difference in the k_f trends.

Sequences of loop C in human and horse heart cyt *c* vary in residues 46, 47, and 50. The identity of residue 46 has been implicated in tuning the structural properties of the protein, and presence of Tyr46 has been suggested to reduce the conformational heterogeneity near the heme crevice.[86] Further, the identity of residue 46, which is either Phe or Tyr in many organisms, was previously suggested to play a role in tuning the alkaline transition properties of cyt *c* for various organisms.[86, 131] Previous kinetic studies suggest that residue 46 influences the conformational rearrangements prior to the deprotonation of the trigger group,[23, 86, 131]

The importance of this region in tuning the alkaline transition is also observed in human and spider monkey cyt *c*.[32] In human and spider monkey WT cyt *c*, most of the natural sequence variations exist within loop C (Table 3.8). Interestingly, the spider monkey sequence contains Phe instead of Tyr at residue 46, and additional interactions provided by Tyr46 observed in human WT cyt *c* are not observed in the X-ray crystal structures of spider monkey WT cyt *c*.[32] Mutational studies with human cyt *c* to mimic the spider monkey sequence have shown that each corresponding mutations at residues 46, 47, and 50, located near HP6 slightly alter the pK_a of the alkaline transition (Table 3.11), while the mutation at residue 44 does not.[32] This difference in pK_a with site of the mutation again strongly suggests that the identities of the residues in positions 46, 47, and 50 are influential in altering the alkaline transition properties of cyt *c*. The most destabilizing mutation is on residue 46 to Phe that altered electrostatic interactions of Lys79 with Thr28 and Tyr46 through the water-mediated network.[32] Further, S47D and S47A variants of human cyt *c*

have shown decrease in pK_a values and increased random-coil character in the near-UV CD spectra,[129] further supporting the hypothesis that residues in this region may be influential in altering the properties of loop D. Although it is unclear how pK_H and pK_C have been affected in these variants, identity of residues and whether it can form the HB network or perturb loop packing, in 46 and 47 may be important in tuning the alkaline transition parameters.

If the alkaline transition is sensitive to the contacts near residue 46, it is possible that the k_f could be altered if the mutations affect this area. For example, T49V mutation reduces the pK_a of the alkaline transition for both horse heart and yeast cyt *c*. Yet, the k_f value increases for the horse heart T49V cyt *c*,[74] while the k_f value for the yeast T49V cyt *c*, which also contains Tyr46, decreases compared to that for WT (Table 3.11).[101] Similar trends in k_f and structural differences are observed in G41S and Y48H variants for human and horse heart cyt *c*. In G41S and Y48H human cyt *c* variants, X-ray crystal structures show that residues 46 and 47 are still involved in HB interactions between residues 28 and 79 as in WT,[35, 54] and most of the inter-residue loops C and D contacts in observed in WT are preserved (Figure 3.9). Even with the Y48H mutation that modifies the HB network with HP6, the water-mediated HB network involving residue 46 is still present in human cyt *c*. In contrast, G41S and Y48H horse heart cyt *c* variants have Phe and Thr, instead of Tyr and Ser, as residues 46 and 47, and similar inter-residue contacts observed in human cyt *c* will not be formed. Analysis of X-ray crystal structure of WT horse heart cyt *c* shows that having Phe46 instead of Tyr46 in horse heart cyt *c* results in a different HB network that connects the three loop-regions compared to human cyt *c* (Figure 3.10).[18, 32] Perhaps, this contact is instrumental in providing a structural linker between the most dynamic loops

C and D, as well as provide additional structural support to Lys79, one of the participating ligands in the alkaline transition. One way to test this hypothesis would be to introduce additional Tyr46 and Ser47 mutations in horse heart G41S and Y48H cyt *c* variants and see if similar trends in k_f are observed as was in human G41S and Y48H cyt *c* variants.

pK$_H$ Values. The pK_a values, which are the sums of pK_C and pK_H values, of the alkaline transition vary widely for WT cyt *c* proteins from different species.[22, 32, 37, 42, 94, 110, 127, 131, 133-137] Interestingly, pK_H values do not vary to the same extent (Tables 3.6). This suggests that, regardless of the sequence identity that can range from 100 to 75 % in loop D and 83 to 55% in loop C for studied WT cyt *c* proteins (Table 3.8), chemical properties of the trigger group are most likely conserved across WT cyt *c* from different species. However, some perturbations can readily decrease the pK_H value (Table 3.11). Comparison of loop C variants in human and horse heart cyt *c* shows that despite the differences in k_f, values or contacts between the loops, similar decrease in pK_H value is observed. Since pK_H reports on the deprotonation of the trigger group, similarity in pK_H value in G41S and Y48H variants from both human and horse heart cyt *c* suggests that the loop C mutations are in the vicinity of the trigger group.

The identity of the trigger group has been highly speculated, with HP6 being one of the contenders.[138] Recently, Deacon *et.al* have also proposed a possible trigger unit, comprised of internal HB network involving Met80, Tyr67/internal water, Asn52, Thr78, and the HP groups, in which a deprotonation in this unit disrupts the linkage between loops C and D.[94] Compared to human WT cyt *c*, horse heart WT cyt *c* has different contacts between loops C and D (Figure 3.10). Furthermore, contacts between loops C and D are more frequently made in human cyt *c* variants than in horse heart cyt *c* variants (Figure

3.8). Yet, comparable changes in the pK_H value are observed in both the human and horse heart cyt *c* variants (Table 3.6). Had pK_H value been solely dependent on the inner HB network and how well loops C and D are linked together (regardless of where the contacts are between the loops), the pK_H value should be different between human and horse heart cyt *c* variants. However, this is not the case, suggesting that other groups may also be involved in this trigger unit.

In the alkaline transition, endogenous Lys residues (73, or 79) must be deprotonated prior to coordinating to the heme. It is unlikely that these Lys residues are the sole trigger group, as the pK_a of these residues is high and vary based on the location and species.[37, 97, 139, 140] However, these factors are all a prerequisite to forming the alkaline species, and thus should contribute to the pK_H of the alkaline transition. Although Lys73 is solvent-exposed as observed in the X-ray crystal structures of Met-ligated human and horse heart WT cyt *c*, Lys79 is tucked away near the heme edge and forms contacts with the residues in the polypeptide, depending on the sequences of nearby residues.[18, 34] For example, Lys79 forms a HB contact with residue 47 in horse heart cyt *c* (Figure 3.10B), but additional interactions with residues 46 and 28 are observed in human and yeast cyt *c* (Figure 3.10A and C). Despite variations in HB contacts, MD simulations show that vdW contacts between Lys79 and loop C are similar between human and horse heart cyt *c* variants (Figure 3.9). If Lys deprotonation is part of alkaline transition mechanism, how well Lys79 is packed next to the polypeptide may be important in tuning the pK_H values. Differences in pK_H values between human and horse heart G41S and Y48H cyt *c* may not have been observed because vdW contacts near Lys79 are comparable in addition to similarities in the inner HB network.

Perhaps, pK_H is a composite value that includes all fractional contributions from inner HB network and Lys residues, in which a structural perturbation that perturbs either of these groups contributes to lowering or increasing the pK_H of the alkaline transition. It is possible that similar decrease in the pK_H value was observed in G41S and Y48H variants if there is a limit to how much pK_H can be lowered without perturbing the tertiary fold of the protein. Furthermore, slight differences in the loops C and D contacts near the vicinity of the trigger unit in horse heart and human cyt *c* may not be sufficient to alter the pK_H because the loop D is highly conserved between the two species.

Regardless of the identity of the trigger group, our comparison of human and horse heart cyt *c* variants suggests the trigger group/unit is largely unaffected in the presence of sequence variations in horse heart and human cyt *c*. Similarities of pK_H values for different WT cyt *c* proteins strongly suggest that, while the contended trigger group is highly conserved, it is also adaptable to the sequence variations near this trigger group.

Peroxidase Activity. Properties of loop C determine accessibility of the heme edge to small molecules, crucial for peroxidase activity in cyt *c*. Studies using guaiacol and ABTS as substrates suggest that the substrates access the heme edge rather than the iron center of peroxidases,[141, 142] making intrinsic peroxidase activity a good functional probe of local dynamics of loop D. Since peroxidase activity requires an open coordination site, Met80 ligand must first dissociate from the heme. Thus, increases in intrinsic peroxidase activity will reflect the lability of the Met80 ligand and decreased packing of the loops.

With the mutations in horse heart cyt *c*, the k_{cat} values increase for all the variants, with the greatest being that of Y48H. This observed trend in intrinsic peroxidase activity is in good agreement with the trend observed in human cyt *c*, where Y48H has higher

peroxidase activity than G41S at pH 6.5, although the reverse is observed at pH 5.4.[35, 84, 143] Pairwise RMSD calculations suggest that loop C in G41S variant generally experiences a more diverse set of conformations compared to that for the Y48H variant, in both human and horse heart cyt *c*. And yet, in horse heart cyt *c*, peroxidase activity of G41S is lower than that for Y48H at pH 7.4, suggesting that the increased loop C dynamics in G41S variant do not necessarily increase the heme exposure as opposed to the Y48H variant. This difference in activity between horse G41S and Y48H cyt *c* is consistent with the observation in ferric ^{1}H NMR (Figure 3.11C), where line broadening is observed in Y48H, possibly due to a greater heterogeneity of the protein conformational ensemble in regions next to the heme.[35, 86] These results suggest that although the G41S and Y48H are not located in loop D, the changes experienced in loop C are also communicated to loop D, modifying the inter-loop contacts and influence loop D dynamics and Met80 ligation to the heme, increasing the intrinsic peroxidase activity of the protein.

Cyt *c* is a key player in apoptosis, and its interactions with biological partners CL and Apaf-1 are important in early stages of apoptosis. In the presence of high CL concentrations, cyt *c* undergoes large-scale unfolding to expose the heme, priming the protein for enhanced peroxidase activity. Residues Lys72, 73, 79, 86, and 87 in loop D are implicated to be one of multiple CL interaction sites, whose binding initiates the unfolding of the polypeptide backbone to expose the heme.[26, 144, 145] The CL-bound protein is in equilibrium between the compact and extended states with different distances between the *N*- and *C*-terminal helices,[38, 145] where loop dynamics and protein stability play a role. Although the mutations of G41S and Y48H are not at the known sites for interactions with CL, symptoms of apoptotic malfunction have been observed in humans. However, recent

CL-bound peroxidase studies with G41S and Y48H mutations in human cyt *c* have been contentious,[33-35] where the rates have been reported to be either greater or comparable to the CL-unfolded WT data, depending on the CL to protein ratio used. This discrepancy in peroxidase activity rates for CL-bound cyt *c* raises the question as to whether the mutations alter the CL-induced unfolding of cyt *c*, and whether the non-interacting residues play a role in the CL-induced unfolding of the protein.

Our studies show that at both low and high CL conditions, the overall enzyme kinetics are comparable in all three variants of horse heart cyt *c*. It is not surprising that there are no observable differences between the variants and WT at either low or high CL conditions, since the global stability parameters are comparable at pH 7.4. Inconsistencies observed in previous studies exploring the peroxidase activity of human G41S in the presence of CL may be due to the different CL-to-protein ratios used.[33-35] Further, as CL-cyt *c* interaction is driven by electrostatic interactions at near-neutral pH conditions,[146] there could be variations in percentage of the bound and unbound species at low CL conditions, introducing additional heterogeneity.

Importance of Varied Sequences. Comparison of cyt *c* variants from different species suggests residue 46 may influence the structural properties of loop C and tune the dynamic properties of loop D. Sequence variation of residue 46 is limited, most often being either Tyr or Phe.[22] In species with Tyr at position 46, alkaline transition parameters and intrinsic peroxidase activities are somewhat inhibited even with mutations designed to disrupt loop C.[33, 94, 129] X-ray crystal structures of *iso*-1 yeast and human WT cyt *c* show that Tyr46 is positioned to form interloop contacts involving residues in the 20's loop and loop D.

Perhaps such transient contacts form in solution, helping to prevent uncontrolled rearrangement even in the presence of G41S and Y48H mutations.

Tyr46 is commonly found in bacteria and plants, but is uncommon in mammals; most mammals have Phe instead of Tyr at residue 46, with great apes being an uncommon exception amongst mammals.[22] The presence of Tyr46 alone does not stabilize the protein—non-mammalian species that have Tyr46 exhibit lower stability parameters compared to mammalian species that do contain Phe46 (Tables 3.8 and 3.9).[32, 36, 38, 106, 109, 112] In the context of sequence variations in mammals, having Tyr46 instead of Phe46 seems to provide an additional safety net in the case that unnatural mutations occur in loop C, as observed in differences with G41S and Y48H mutation in human versus horse heart cyt *c*. There may be functional implications as well. Post-translation nitration of Tyr residues in human cyt *c* has been linked to signaling of proteases for cyt *c* degradation[147-149] and tyrosine nitration is also utilized for signal transduction in yeast.[150] The difference between having Tyr and Phe at position 46 highlights that certain residue variations can alter protein function only in the context of other residues and available signaling mechanisms in the organism. However, there are difficulties in expanding the analysis of the relationship between residue 46 sequence conservation and protein function due to the limited data set in the literature that details the characterization of various WT proteins.

Conclusion

Characterization of horse heart G41S and Y48H cyt *c* variants have shown that global properties of the protein, such as heme iron ligation, secondary fold, and global stability are comparable to that of WT at near-neutral pH conditions. Yet, local changes are observed with the mutations in loop C. Analyses of MD simulations suggest that HB and

vdW contacts between loops C and D are perturbed in the variants compared to that of WT. With G41S and Y48H mutations, folding is no longer cooperative, and the stability parameter obtained from monitoring the CT band is different from that of monitoring the α-helices. Furthermore, functional properties dependent on loop D dynamics and packing, such as alkaline transition and intrinsic peroxidase activity, are altered. These results suggest that loop C contact with loop D may be important in maintaining communication between loop D and the rest of the protein, as well as in tuning the dynamic properties of loop D important for protein function.

Comparison of the data obtained for horse heart G41S and Y48H cyt *c* variants to data in the literature for human G41S and Y48H cyt *c* has shown that mutational effects on protein stability and function are different in horse heart and human cyt *c*. Differences in human and horse heart cyt *c* G41S and Y48H variants suggest that unique contacts that support the native loop D packing are important; disruption to this network modifies the kinetic and thermodynamic parameters associated with the alkaline transition, particularly in the presence of destabilizing perturbations. These findings provide insight into how cyt *c* proteins with highly conserved sequence and global properties could have variations in stability and function.

References

1. Lehninger, A.L., Nelson, D.L. & Cox, M.M. *Lehninger principles of biochemistry*, Edn. 5th. (W.H. Freeman, New York; 2008).

2. Razvi, A. & Scholtz, J.M. Lessons in stability from thermophilic proteins. *Protein Sci* **15**, 1569-1578 (2006).

3. Lonhienne, T., Gerday, C. & Feller, G. Psychrophilic enzymes: revisiting the thermodynamic parameters of activation may explain local flexibility. *Biochim Biophys Acta* **1543**, 1-10 (2000).

4. D'Amico, S., Marx, J.C., Gerday, C. & Feller, G. Activity-stability relationships in extremophilic enzymes. *The Journal of biological chemistry* **278**, 7891-7896 (2003).

5. Feller, G. Psychrophilic enzymes: from folding to function and biotechnology. *Scientifica* **2013**, 512840 (2013).

6. Bandi, S. & Bowler, B.E. Probing the Bottom of a Folding Funnel Using Conformationally Gated Electron Transfer Reactions. *J Am Chem Soc* **130**, 7540-7541 (2008).

7. Nakamura, S. *et al.* Structure of cytochrome c552 from a moderate thermophilic bacterium, Hydrogenophilus thermoluteolus: comparative study on the thermostability of cytochrome c. *Biochemistry* **45**, 6115-6123 (2006).

8. Oikawa, K. *et al.* Five amino acid residues responsible for the high stability of Hydrogenobacter thermophilus cytochrome c552: reciprocal mutation analysis. *The Journal of biological chemistry* **280**, 5527-5532 (2005).

9. Hasegawa, J. *et al.* Selected mutations in a mesophilic cytochrome c confer the stability of a thermophilic counterpart. *The Journal of biological chemistry* **275**, 37824-37828 (2000).

10. Oswald, V.F., Chen, W., Harvilla, P.B. & Magyar, J.S. Overexpression, purification, and enthalpy of unfolding of ferricytochrome c552 from a psychrophilic microorganism. *Journal of inorganic biochemistry* **131**, 76-78 (2014).

11. Feller, G. Life at low temperatures: is disorder the driving force? *Extremophiles* **11**, 211-216 (2007).

12. Roche, J. *et al.* Structural, energetic, and dynamic responses of the native state ensemble of staphylococcal nuclease to cavity-creating mutations. *Proteins* **81**, 1069-1080 (2013).

13. McClelland, L.J. & Bowler, B.E. Lower Protein Stability Does Not Necessarily Increase Local Dynamics. *Biochemistry* **55**, 2681-2693 (2016).

14. Smalas, A.O., Heimstad, E.S., Hordvik, A., Willassen, N.P. & Male, R. Cold adaption of enzymes: structural comparison between salmon and bovine trypsins. *Proteins* **20**, 149-166 (1994).

15. Maity, H., Maity, M. & Englander, S.W. How cytochrome c folds, and why: Submolecular foldon units and their stepwise sequential stabilization. *J Mol Biol* **343**, 223-233 (2004).

16. Krishna, M.M.G., Maity, H., Rumbley, J.N., Lin, Y. & Englander, S.W. Order of steps in the cytochrome c folding pathway: Evidence for a sequential stabilization mechanism. *J Mol Biol* **359**, 1410-1419 (2006).

17. Berghuis, A.M. & Brayer, G.D. Oxidation State-Dependent Conformational-Changes in Cytochrome-C. *J Mol Biol* **223**, 959-976 (1992).

18. Bushnell, G.W., Louie, G.V. & Brayer, G.D. High-resolution three-dimensional structure of horse heart cytochrome c. *J Mol Biol* **214**, 585-595 (1990).

19. Sievers, F. *et al.* Fast, scalable generation of high-quality protein multiple sequence alignments using Clustal Omega. *Molecular systems biology* **7**, 539 (2011).

20. Prlic, A. *et al.* Pre-calculated protein structure alignments at the RCSB PDB website. *Bioinformatics* **26**, 2983-2985 (2010).

21. Ye, Y.Z. & Godzik, A. Flexible structure alignment by chaining aligned fragment pairs allowing twists. *Bioinformatics* **19**, Ii246-Ii255 (2003).

22. Moore, G.R. & Pettigrew, G.W. *Cytochromes c : evolutionary, structural, and physicochemical aspects*. (Springer-Verlag, Berlin ; New York; 1990).

23. Hoang, L., Maity, H., Krishna, M.M., Lin, Y. & Englander, S.W. Folding units govern the cytochrome c alkaline transition. *J Mol Biol* **331**, 37-43 (2003).

24. Maity, H., Rumbley, J.N. & Englander, S.W. Functional role of a protein foldon - An Omega-Loop foldon controls the alkaline transition in ferricytochrome c. *Proteins* **63**, 349-355 (2006).

25. Amacher, J.F. *et al.* A Compact Structure of Cytochrome c Trapped in a Lysine-Ligated State: Loop Refolding and Functional Implications of a Conformational Switch. *J Am Chem Soc* **137**, 8435-8449 (2015).

26. Sinibaldi, F. *et al.* Role of lysines in cytochrome c-cardiolipin interaction. *Biochemistry* **52**, 4578-4588 (2013).

27. Morison, I.M. *et al.* A mutation of human cytochrome c enhances the intrinsic apoptotic pathway but causes only thrombocytopenia. *Nat Genet* **40**, 387-389 (2008).

28. De Rocco, D. *et al.* Mutations of cytochrome c identified in patients with thrombocytopenia THC4 affect both apoptosis and cellular bioenergetics. *Bba-Mol Basis Dis* **1842**, 269-274 (2014).

29. Hao, Z.Y. *et al.* Specific ablation of the apoptotic functions of cytochrome c reveals a differential requirement for cytochrome c and apaf-1 in apoptosis. *Cell* **121**, 579-591 (2005).

30. McClelland, L.J., Mou, T.C., Jeakins-Cooley, M.E., Sprang, S.R. & Bowler, B.E. Structure of a mitochondrial cytochrome c conformer competent for peroxidase activity. *P Natl Acad Sci USA* **111**, 6648-6653 (2014).

31. Nold, S.M., Lei, H.T., Mou, T.C. & Bowler, B.E. Effect of a K72A Mutation on the Structure, Stability, Dynamics, and Peroxidase Activity of Human Cytochrome c. *Biochemistry* **56**, 3358-3368 (2017).

32. Goldes, M.E., Jeakins-Cooley, M.E., McClelland, L.J., Mou, T.C. & Bowler, B.E. Disruption of a hydrogen bond network in human versus spider monkey cytochrome c affects heme crevice stability. *Journal of inorganic biochemistry* **158**, 62-69 (2016).

33. Josephs, T.M., Morison, I.M., Day, C.L., Wilbanks, S.M. & Ledgerwood, E.C. Enhancing the peroxidase activity of cytochrome c by mutation of residue 41: implications for the peroxidase mechanism and cytochrome c release. *Biochem J* **458**, 259-265 (2014).

34. Rajagopal, Badri S. *et al.* The hydrogen-peroxide-induced radical behaviour in human cytochrome c–phospholipid complexes: implications for the enhanced pro-apoptotic activity of the G41S mutant. *Biochem J* **456**, 441-452 (2013).

35. Deacon, O.M. *et al.* Heightened Dynamics of the Oxidized Y48H Variant of Human Cytochrome c Increases Its Peroxidatic Activity. *Biochemistry* **56**, 6111-6124 (2017).

36. Godbole, S. & Bowler, B.E. Effect of pH on formation of a nativelike intermediate on the unfolding pathway of a Lys 73 --> His variant of yeast iso-1-cytochrome c. *Biochemistry* **38**, 487-495 (1999).

37. Rosell, F.I., Ferrer, J.C. & Mauk, A.G. Proton-linked protein conformational switching: Definition of the alkaline conformational transition of yeast iso-1-ferricytochrome c. *J Am Chem Soc* **120**, 11234-11245 (1998).

38. Hanske, J. *et al.* Conformational properties of cardiolipin-bound cytochrome c. *P Natl Acad Sci USA* **109**, 125-130 (2012).

39. Pettersen, E.F. *et al.* UCSF Chimera--a visualization system for exploratory research and analysis. *Journal of computational chemistry* **25**, 1605-1612 (2004).

40. Humphrey, W., Dalke, A. & Schulten, K. VMD: visual molecular dynamics. *Journal of molecular graphics* **14**, 33-38, 27-38 (1996).

41. Phillips, J.C. *et al.* Scalable molecular dynamics with NAMD. *Journal of computational chemistry* **26**, 1781-1802 (2005).

42. Ying, T. *et al.* Evolutionary alkaline transition in human cytochrome c. *J Bioenerg Biomembr* **41**, 251-257 (2009).

43. Autenrieth, F., Tajkhorshid, E., Baudry, J. & Luthey-Schulten, Z. Classical force field parameters for the heme prosthetic group of cytochrome c. *Journal of computational chemistry* **25**, 1613-1622 (2004).

44. Mackerell, A.D., Jr., Feig, M. & Brooks, C.L., 3rd Extending the treatment of backbone energetics in protein force fields: limitations of gas-phase quantum mechanics in reproducing protein conformational distributions in molecular dynamics simulations. *Journal of computational chemistry* **25**, 1400-1415 (2004).

45. Zhong, F., Alden, S.L., Hughes, R.P. & Pletneva, E.V. Comparing Properties of Common Bioinorganic Ligands with Switchable Variants of Cytochrome c. *Inorg Chem* (2021).

46. Oviedo-Rouco, S. *et al.* Electron transfer and conformational transitions of cytochrome c are modulated by the same dynamical features. *Arch Biochem Biophys* **680**, 108243 (2020).

47. Abraham, M.J. *et al.* GROMACS: High performance molecular simulations through multi-level parallelism from laptops to supercomputers. *SoftwareX* **1-2**, 19-25 (2015).

48. Hess, B., Kutzner, C., van der Spoel, D. & Lindahl, E. GROMACS 4: Algorithms for Highly Efficient, Load-Balanced, and Scalable Molecular Simulation. *Journal of chemical theory and computation* **4**, 435-447 (2008).

49. Lindahl, E., Hess, B. & van der Spoel, D. GROMACS 3.0: a package for molecular simulation and trajectory analysis. *J Mol Model* **7**, 306-317 (2001).

50. Páll, S., Abraham, M.J., Kutzner, C., Hess, B. & Lindahl, E. 3-27 (Springer International Publishing, Cham; 2015).

51. Pronk, S. *et al.* GROMACS 4.5: a high-throughput and highly parallel open source molecular simulation toolkit. *Bioinformatics* **29**, 845-854 (2013).

52. Van Der Spoel, D. *et al.* GROMACS: fast, flexible, and free. *Journal of computational chemistry* **26**, 1701-1718 (2005).

53. Berendsen, H.J.C., van der Spoel, D. & van Drunen, R. GROMACS: A message-passing parallel molecular dynamics implementation. *Computer Physics Communications* **91**, 43-56 (1995).

54. Liptak, M.D., Fagerlund, R.D., Ledgerwood, E.C., Wilbanks, S.M. & Bren, K.L. The Proapoptotic G41S Mutation to Human Cytochrome c Alters the Heme Electronic Structure and Increases the Electron Self-Exchange Rate. *J Am Chem Soc* **133**, 1153-1155 (2011).

55. Chen, C.R. & Makhatadze, G.I. ProteinVolume: calculating molecular van der Waals and void volumes in proteins. *BMC Bioinformatics* **16**, 101 (2015).

56. Mirkin, N., Jaconcic, J., Stojanoff, V. & Moreno, A. High resolution X-ray crystallographic structure of bovine heart cytochrome c and its application to the design of an electron transfer biosensor. *Proteins* **70**, 83-92 (2008).

57. Merlino, A. X-ray structure of bovine heart cytochrome c at high ionic strength. *Biometals* **31**, 277-284 (2018).

58. Tanaka, N., Yamane, T., Tsukihara, T., Ashida, T. & Kakudo, M. The crystal structure of bonito (katsuo) ferrocytochrome c at 2.3 A resolution. II. Structure and function. *Journal of biochemistry* **77**, 147-162 (1975).

59. Takano, T. *et al.* Tuna cytochrome c at 2.0 A resolution. II. Ferrocytochrome structure analysis. *The Journal of biological chemistry* **252**, 776-785 (1977).

60. Murphy, M.E.P., Nall, B.T. & Brayer, G.D. Structure Determination and Analysis of Yeast Iso-2-Cytochrome-C and a Composite Mutant Protein. *J Mol Biol* **227**, 160-176 (1992).

61. Mills, J.E. & Dean, P.M. Three-dimensional hydrogen-bond geometry and probability information from a crystal survey. *Journal of computer-aided molecular design* **10**, 607-622 (1996).

62. Anslyn, E.V. & Dougherty, D.A. *Modern physical organic chemistry*. (University Science, Sausalito, CA; 2006).

63. Tsai, J., Taylor, R., Chothia, C. & Gerstein, M. The packing density in proteins: Standard radii and volumes. *J Mol Biol* **290**, 253-266 (1999).

64. Meng, E.C. & Lewis, R.A. Determination of molecular topology and atomic hybridization states from heavy atom coordinates. *Journal of computational chemistry* **12**, 891-898 (1991).

65. Patel, C.N., Lind, M.C. & Pielak, G.J. Characterization of horse cytochrome c expressed in Escherichia coli. *Protein expression and purification* **22**, 220-224 (2001).

66. Pace, C.N. Measuring and increasing protein stability. *Trends in biotechnology* **8**, 93-98 (1990).

67. Pace, C.N. The stability of globular proteins. *CRC critical reviews in biochemistry* **3**, 1-43 (1975).

68. Pace, C.N. Determination and analysis of urea and guanidine hydrochloride denaturation curves. *Methods in enzymology* **131**, 266-280 (1986).

69. Bowler, B.E. Thermodynamics of protein denatured states. *Mol Biosyst* **3**, 88-99 (2007).

70. Hammack, B.N., Smith, C.R. & Bowler, B.E. Denatured state thermodynamics: residual structure, chain stiffness and scaling factors. *J Mol Biol* **311**, 1091-1104 (2001).

71. Pielak, G.J. *et al.* Protein thermal denaturation, side-chain models, and evolution: amino acid substitutions at a conserved helix-helix interface. *Biochemistry* **34**, 3268-3276 (1995).

72. Galo, A.L. & Colombo, M.F. Singular Value Decomposition and Ligand Binding Analysis. *J Spectrosc* (2013).

73. Hendler, R.W. & Shrager, R.I. Deconvolutions Based on Singular-Value Decomposition and the Pseudoinverse - a Guide for Beginners. *J Biochem Bioph Meth* **28**, 1-33 (1994).

74. Gu, J., Shin, D.W. & Pletneva, E.V. Remote Perturbations in Tertiary Contacts Trigger Ligation of Lysine to the Heme Iron in Cytochrome c. *Biochemistry* **56**, 2950-2966 (2017).

75. Davis, L.A., Schejter, A. & Hess, G.P. Alkaline isomerization of oxidized cytochrome c. Equilibrium and kinetic measurements. *The Journal of biological chemistry* **249**, 2624-2632 (1974).

76. Muenzner, J., Toffey, J.R., Hong, Y.N. & Pletneva, E.V. Becoming a Peroxidase: Cardiolipin-Induced Unfolding of Cytochrome c. *J Phys Chem B* **117**, 12878-12886 (2013).

77. Re, R. *et al.* Antioxidant activity applying an improved ABTS radical cation decolorization assay. *Free radical biology & medicine* **26**, 1231-1237 (1999).

78. Dunford, H.B. *Heme peroxidases*. (John Wiley, New York; 1999).

79. Palopoli, N., Monzon, A.M., Parisi, G. & Fornasari, M.S. Addressing the Role of Conformational Diversity in Protein Structure Prediction. *Plos One* **11**, e0154923-e0154923 (2016).

80. Srivastava, A. *et al.* Conformational ensemble of an intrinsically flexible loop in mitochondrial import protein Tim21 studied by modeling and molecular dynamics simulations. *Biochimica et Biophysica Acta (BBA) - General Subjects* **1864**, 129417 (2020).

81. Pantoliano, M.W. *et al.* Large increases in general stability for subtilisin BPN' through incremental changes in the free energy of unfolding. *Biochemistry* **28**, 7205-7213 (1989).

82. Alber, T. Mutational effects on protein stability. *Annu Rev Biochem* **58**, 765-798 (1989).

83. Tiana, G., Simona, F., De Mori, G.M., Broglia, R.A. & Colombo, G. Understanding the determinants of stability and folding of small globular proteins from their energetics. *Protein Sci* **13**, 113-124 (2004).

84. Fellner, M. *et al.* Altered structure and dynamics of pathogenic cytochrome c variants correlate with increased apoptotic activity. *Biochem J* **478**, 669-684 (2021).

85. Feng, Y.Q., Roder, H. & Englander, S.W. Assignment of paramagnetically shifted resonances in the 1H NMR spectrum of horse ferricytochrome c. *Biophysical journal* **57**, 15-22 (1990).

86. Burns, P.D. & La Mar, G.N. Characterization of conformational heterogeneity in the heme pocket of ferricytochrome c using high field proton nuclear magnetic resonance spectroscopy. *The Journal of biological chemistry* **256**, 4934-4939 (1981).

87. Hong, X.L. & Dixon, D.W. NMR study of the alkaline isomerization of ferricytochrome c. *Febs Lett* **246**, 105-108 (1989).

88. Ferrer, J.C. *et al.* Identification of Lys79 as an Iron Ligand in One Form of Alkaline Yeast Iso-1-Ferricytochrome-C. *J Am Chem Soc* **115**, 7507-7508 (1993).

89. Silkstone, G.G., Cooper, C.E., Svistunenko, D. & Wilson, M.T. EPR and optical spectroscopic studies of Met80X mutants of yeast ferricytochrome c. Models for intermediates in the alkaline transition. *J Am Chem Soc* **127**, 92-99 (2005).

90. Sedlak, E. Characterization of the polyanion-induced molten globule-like state of cytochrome c. *Biopolymers* **86**, 119-126 (2007).

91. Freire, E., Schon, A., Hutchins, B.M. & Brown, R.K. Chemical denaturation as a tool in the formulation optimization of biologics. *Drug discovery today* **18**, 1007-1013 (2013).

92. Myers, J.K., Nick Pace, C. & Martin Scholtz, J. Denaturant m values and heat capacity changes: Relation to changes in accessible surface areas of protein unfolding. *Protein Sci* **4**, 2138-2148 (1995).

93. Zhong, F.F., Lisi, G.P., Collins, D.P., Dawson, J.H. & Pletneva, E.V. Redox-dependent stability, protonation, and reactivity of cysteine-bound heme proteins. *P Natl Acad Sci USA* **111**, E306-E315 (2014).

94. Deacon, O.M., Svistunenko, D.A., Moore, G.R., Wilson, M.T. & Worrall, J.A.R. Naturally Occurring Disease-Related Mutations in the 40-57 Omega-Loop of Human Cytochrome c Control Triggering of the Alkaline Isomerization. *Biochemistry* **57**, 4276-4288 (2018).

95. Godbole, S., Dong, A., Garbin, K. & Bowler, B.E. A lysine 73-->histidine variant of yeast iso-1-cytochrome c: evidence for a native-like intermediate in the unfolding pathway and implications for m value effects. *Biochemistry* **36**, 119-126 (1997).

96. Weinkam, P., Romesberg, F.E. & Wolynes, P.G. Chemical Frustration in the Protein Folding Landscape: Grand Canonical Ensemble Simulations of Cytochrome c. *Biochemistry* **48**, 2394-2402 (2009).

97. Weinkam, P. *et al.* Characterization of alkaline transitions in ferricytochrome c using carbon-deuterium infrared probes. *Biochemistry* **47**, 13470-13480 (2008).

98. Ness, S.R., Lo, T.P. & Mauk, A.G. Structural models for the alkaline conformers of yeast iso-1-ferricytochrome c. *Israel J Chem* **40**, 21-25 (2000).

99. Assfalg, M. *et al.* Structural model for an alkaline form of ferricytochrome c. *J Am Chem Soc* **125**, 2913-2922 (2003).

100. Sedlák, E., Kožár, T., Varhač, R., Musatov, A. & Tomášková, N. Anion-Specific Effects on the Alkaline State of Cytochrome c. *Biochemistry (Moscow)* **86**, 59-73 (2021).

101. Deng, Y., Weaver, M.L., Hoke, K.R. & Pletneva, E.V. A Heme Propionate Staples the Structure of Cytochrome c for Methionine Ligation to the Heme Iron. *Inorg Chem* **58**, 14085-14106 (2019).

102. Deacon, O.M., White, R.W., Moore, G.R., Wilson, M.T. & Worrall, J.A.R. Comparison of the structural dynamic and mitochondrial electron-transfer properties of the proapoptotic human cytochrome c variants, G41S, Y48H and A51V. *Journal of inorganic biochemistry* **203**, 110924 (2020).

103. Deng, Y.L., Zhong, F.F., Alden, S.L., Hoke, K.R. & Pletneva, E.V. The K79G Mutation Reshapes the Heme Crevice and Alters Redox Properties of Cytochrome c. *Biochemistry* **57**, 5827-5840 (2018).

104. Zaidi, S., Hassan, M.I., Islam, A. & Ahmad, F. The role of key residues in structure, function, and stability of cytochrome-c. *Cell Mol Life Sci* **71**, 229-255 (2014).

105. Pletneva, E.V., Gray, H.B. & Winkler, J.R. Many faces of the unfolded state: Conformational heterogeneity in denatured yeast cytochrome c. *J Mol Biol* **345**, 855-867 (2005).

106. Knapp, J.A. & Pace, C.N. Guanidine-Hydrochloride and Acid Denaturation of Horse, Cow, and Candida-Krusei Cytochromes-C. *Biochemistry* **13**, 1289-1294 (1974).

107. G D Rose, a. & Wolfenden, R. Hydrogen Bonding, Hydrophobicity, Packing, and Protein Folding. *Annual Review of Biophysics and Biomolecular Structure* **22**, 381-415 (1993).

108. Yutani, K., Ogasahara, K., Tsujita, T. & Sugino, Y. Dependence of conformational stability on hydrophobicity of the amino acid residue in a series of variant proteins substituted at a unique position of tryptophan synthase alpha subunit. *Proc Natl Acad Sci U S A* **84**, 4441-4444 (1987).

109. McLendon, G. & Smith, M. Equilibrium and kinetic studies of unfolding of homologous cytochromes c. *The Journal of biological chemistry* **253**, 4004-4008 (1978).

110. Nall, B.T., Zuniga, E.H., White, T.B., Wood, L.C. & Ramdas, L. Replacement of a Conserved Proline and the Alkaline Conformational Change in Iso-2-Cytochrome-C. *Biochemistry* **28**, 9834-9839 (1989).

111. Bateman, A. *et al.* UniProt: a worldwide hub of protein knowledge. *Nucleic Acids Res* **47**, D506-D515 (2019).

112. McGee, W.A. & Nall, B.T. Refolding rate of stability-enhanced cytochrome c is independent of thermodynamic driving force. *Protein Sci* **7**, 1071-1082 (1998).

113. Vincelli, A.J. *et al.* Recombinant Expression, Biophysical Characterization, and Cardiolipin-Induced Changes of Two Caenorhabditis elegans Cytochrome c Proteins. *Biochemistry* **52**, 653-666 (2013).

114. Dumont, M.D. *et al.* Differential stability of two apo-isocytochromes c in the yeast Saccharomyces cerevisiae. *The Journal of biological chemistry* **265**, 2733-2739 (1990).

115. Liggins, J.R., Sherman, F., Mathews, A.J. & Nall, B.T. Differential Scanning Calorimetric Study of the Thermal Unfolding Transitions of Yeast Iso-1 and Iso-2 Cytochromes c and Three Composite Isoenzymes. *Biochemistry* **33**, 9209-9219 (1994).

116. Englander, S.W., Mayne, L. & Krishna, M.M. Protein folding and misfolding: mechanism and principles. *Quarterly reviews of biophysics* **40**, 287-326 (2007).

117. Maity, H., Maity, M., Krishna, M.M.G., Mayne, L. & Englander, S.W. Protein folding: The stepwise assembly of foldon units. *P Natl Acad Sci USA* **102**, 4741-4746 (2005).

118. Duncan, M.G., Williams, M.D. & Bowler, B.E. Compressing the free energy range of substructure stabilities in iso-1-cytochrome c. *Protein Sci* **18**, 1155-1164 (2009).

119. Karsisiotis, A.I. *et al.* Increased dynamics in the 40-57 Omega-loop of the G41S variant of human cytochrome c promote its pro-apoptotic conformation. *Scientific reports* **6**, 30447 (2016).

120. Richa, T. & Sivaraman, T. CIntX: A Software Tool for Calculating the Intrinsic Exchange Rates of Labile Protons in Proteins. *Journal of Pharmaceutical Sciences and Research* **4**, 1852-1858 (2012).

121. Krishna, M.M., Hoang, L., Lin, Y. & Englander, S.W. Hydrogen exchange methods to study protein folding. *Methods* **34**, 51-64 (2004).

122. Milne, J.S., Mayne, L., Roder, H., Wand, A.J. & Englander, S.W. Determinants of protein hydrogen exchange studied in equine cytochrome c. *Protein Sci* **7**, 739-745 (1998).

123. Mayne, L. & Englander, S.W. Two-state vs. multistate protein unfolding studied by optical melting and hydrogen exchange. *Protein Sci* **9**, 1873-1877 (2000).

124. Xu, Y., Mayne, L. & Englander, S.W. Evidence for an unfolding and refolding pathway in cytochrome c. *Nat Struct Biol* **5**, 774-778 (1998).

125. Mara, M.W. *et al.* Metalloprotein entatic control of ligand-metal bonds quantified by ultrafast x-ray spectroscopy. *Science* **356**, 1276-1280 (2017).

126. Lei, H.T. & Bowler, B.E. Humanlike substitutions to Omega-loop D of yeast iso-1-cytochrome c only modestly affect dynamics and peroxidase activity. *Journal of inorganic biochemistry* **183**, 146-156 (2018).

127. Pearce, L.L., Gartner, A.L., Smith, M. & Mauk, A.G. Mutation-Induced Perturbation of the Cytochrome-C Alkaline Transition. *Biochemistry* **28**, 3152-3156 (1989).

128. Zhong, F. & Pletneva, E.V. Ligation and Reactivity of Methionine-Oxidized Cytochrome c. *Inorg Chem* **57**, 5754-5766 (2018).

129. Guerra-Castellano, A., Diaz-Moreno, I., Velazquez-Campoy, A., De la Rosa, M.A. & Diaz-Quintana, A. Structural and functional characterization of phosphomimetic mutants of cytochrome c at threonine 28 and serine 47. *Biochim Biophys Acta* **1857**, 387-395 (2016).

130. Lei, H., Nold, S.M., Motta, L.J. & Bowler, B.E. Effect of V83G and I81A Substitutions to Human Cytochrome c on Acid Unfolding and Peroxidase Activity below a Neutral pH. *Biochemistry* **58**, 2921-2933 (2019).

131. Saigo, S. Kinetic and equilibrium studies of alkaline isomerization of vertebrate cytochromes c. *Biochim Biophys Acta* **669**, 13-20 (1981).

132. Engilberge, S., Rennie, M.L. & Crowley, P.B. Calixarene capture of partially unfolded cytochrome c. *Febs Lett* **593**, 2112-2117 (2019).

133. Josephs, T.M. *et al.* Conformational change and human cytochrome c function: mutation of residue 41 modulates caspase activation and destabilizes Met-80 coordination. *J Biol Inorg Chem* **18**, 289-297 (2013).

134. Caffrey, M.S. & Cusanovich, M.A. Site-Specific Mutagenesis Studies of Cytochromes-C. *Bba-Bioenergetics* **1187**, 277-288 (1994).

135. Koshy, T.I., Luntz, T.L., Schejter, A. & Margoliash, E. Changing the Invariant Proline-30 of Rat and Drosophila-Melanogaster Cytochromes-C to Alanine or Valine Destabilizes the Heme Crevice More Than the Overall Conformation. *P Natl Acad Sci USA* **87**, 8697-8701 (1990).

136. Feinberg, B.A., Petro, L., Hock, G., Qin, W.Y. & Margoliash, E. Using entropies of reaction to predict changes in protein stability: tyrosine-67-phenylalanine variants of rat cytochrome c and yeast Iso-1 cytochromes c. *J Pharmaceut Biomed* **19**, 115-125 (1999).

137. Luntz, T.L., Schejter, A., Garber, E.A.E. & Margoliash, E. Structural Significance of an Internal Water Molecule Studied by Site-Directed Mutagenesis of Tyrosine-67 in Rat Cytochrome-C. *P Natl Acad Sci USA* **86**, 3524-3528 (1989).

138. Cherney, M.M. & Bowler, B.E. Protein dynamics and function: Making new strides with an old warhorse, the alkaline conformational transition of cytochrome c. *Coordin Chem Rev* **255**, 664-677 (2011).

139. Battistuzzi, G. *et al.* Free energy of transition for the individual alkaline conformers of yeast iso-1-cytochrome c. *Biochemistry* **46**, 1694-1702 (2007).

140. Oviedo-Rouco, S. *et al.* The alkaline transition of cytochrome c revisited: Effects of electrostatic interactions and tyrosine nitration on the reaction dynamics. *Arch Biochem Biophys* **665**, 96-106 (2019).

141. Wang, Z.H., Matsuo, T., Nagao, S. & Hirota, S. Peroxidase activity enhancement of horse cytochrome c by dimerization. *Org Biomol Chem* **9**, 4766-4769 (2011).

142. Ator, M.A. & Demontellano, P.R.O. Protein Control of Prosthetic Heme Reactivity - Reaction of Substrates with the Heme Edge of Horseradish-Peroxidase. *Journal of Biological Chemistry* **262**, 1542-1551 (1987).

143. Parakra, R.D., Kleffmann, T., Jameson, G.N.L. & Ledgerwood, E.C. The proportion of Met80-sulfoxide dictates peroxidase activity of human cytochrome c. *Dalton transactions (Cambridge, England : 2003)* **47**, 9128-9135 (2018).

144. Rytomaa, M. & Kinnunen, P.K. Reversibility of the binding of cytochrome c to liposomes. Implications for lipid-protein interactions. *The Journal of biological chemistry* **270**, 3197-3202 (1995).

145. Hong, Y.N., Muenzner, J., Grimm, S.K. & Pletneva, E.V. Origin of the Conformational Heterogeneity of Cardiolipin-Bound Cytochrome c. *J Am Chem Soc* **134**, 18713-18723 (2012).

146. Rytomaa, M., Mustonen, P. & Kinnunen, P.K.J. Reversible, Nonionic, and Ph-Dependent Association of Cytochrome-C with Cardiolipin-Phosphatidylcholine Liposomes. *Journal of Biological Chemistry* **267**, 22243-22248 (1992).

147. Diaz-Moreno, I., Garcia-Heredia, J.M., Diaz-Quintana, A., Teixeira, M. & De la Rosa, M.A. Nitration of tyrosines 46 and 48 induces the specific degradation of cytochrome c upon change of the heme iron state to high-spin. *Bba-Bioenergetics* **1807**, 1616-1623 (2011).

148. Garcia-Heredia, J.M. *et al.* Nitration of tyrosine 74 prevents human cytochrome c to play a key role in apoptosis signaling by blocking caspase-9 activation. *Bba-Bioenergetics* **1797**, 981-993 (2010).

149. Rodríguez-Roldán, V., García-Heredia, J.M., Navarro, J.A., Rosa, M.A.D.l. & Hervás, M. Effect of Nitration on the Physicochemical and Kinetic Features of Wild-Type and Monotyrosine Mutants of Human Respiratory Cytochrome c. *Biochemistry* **47**, 12371-12379 (2008).

150. Kang, J.W. *et al.* Analysis of nitrated proteins in Saccharomyces cerevisiae involved in mating signal transduction. *Proteomics* **15**, 580-590 (2015).

Chapter 4

Dynamics and Packing Around Loop D Modulate Electron Transfer and Peroxidase Activity in Cytochrome *c*

pH jump experiments were performed by Dr. Fangfang Zhong.

The compound $Co(phen)_3Cl_3$ was synthesized by Dr. Alexandre Pletnev.

Primers for introducing the K72A mutation in horse heart cyt *c* were prepared by Andrey Maskaev.

The plasmid for WT horse heart cyt *c* was provided by Dr. Kara L. Bren.

Introduction

In metalloproteins, surface residues have been argued to be involved in tuning the redox properties of the metal center by altering the solvent entropic contributions that are dependent on the charged groups on the protein,[1] or by altering the polypeptide packing and backbone dynamics around the metal site. [2-6] In heme proteins, varying surface charges near the heme can mildly shift the reduction potential, suggesting a possible importance of residue identity in tuning the reduction potential.[2, 6]

Loop D contributes to the bulk of controlling heme edge solvent exposure to tune the reduction potential. This has been illustrated with yeast K79G cyt *c*, where removal of a bulky Lys increased heme solvent exposure and lowered the reduction potential of the heme iron compared to that of WT.[7] Flexibility of loop D is important for heme solvent accessibility and perturbations of contacts with loops C and D have been shown to alter the reduction potential in the Y67F and E66Q variants, and Tyr74-nitrated WT cyt *c*.[8] Although loop D alone does not encapsulate the heme moiety, the dynamic properties and contacts that this loop makes are clearly important for tuning the reduction potential of the heme iron.

It is interesting to note that there are sequence variations both in and around loop D.[9] Within loop D, sequence variations in residues 70 to 80 are low, but are more frequent in residues 81 to 85.[9, 10] Furthermore, loop D is in close contact with loop C, which is less conserved than loop D. Generally, the reduction potentials of different cyt *c* proteins are similar, but some variations do exist, depending on the sequence difference near the heme.[4, 11-15] Differences in reduction potential are subtle in WT proteins but are amplified in the presence of structural perturbations. For example, the Y67F mutation in yeast cyt *c*

decreased the reduction potential by nearly 60 mV, in contrast to the same Y67F mutation in rat cyt *c* where the reduction potential decreases by less than 30 mV,[11] despite similar heme iron ligation and protein fold of yeast and rat cyt *c*. ET studies with Y67F, N52I, and Y67F/N52I yeast cyt *c* variants have shown cooperativity between Tyr67 and Asn52 in influencing both the heme reduction kinetics[16] and protein stability.[17] It is possible then, that the natural sequence variations in different species may result in different contacts, ultimately affecting protein stability, dynamics, and function.

To explore the interplay of these factors and probe contributions of sequence variations in and around loop D, we decided to study the K72A variant of horse heart cyt *c*. This mutation was structurally non-invasive for yeast and human cyt *c*.[18, 19] Since the mutational effects on stability and dynamics of loop D are well-documented in both human and yeast cyt *c* systems, including horse heart cyt *c* in the series was thought to provide clarification in how the surface residue variations influence the second-sphere interactions around the heme. To correlate how surface mutations that affect loop D alter the ET properties of the protein, two other variants, G41S and Y48H, were also studied as they indirectly affect loop D. These mutations were selected since their effects have been documented *in vivo* models,[20-22] which would provide a way to understand how biophysical changes within the protein affect macromolecular function.

The K72A variant was previously studied in human and yeast cyt *c* and is one of a handful of cyt *c* variants that have *in vivo* models. K72A cyt *c* mutation in knock-in mice has been shown to impede neural development and impair lymphocyte homeostasis.[22] Although these growth defects suggest changes in apoptotic activity with K72A, the protein release to the cytosol and cellular oxygen consumption were similar to those with WT.[22]

However, comparison of biophysical and enzymatic properties of WT and K72A *in vitro* suggests that the K72A mutation alters the intrinsic peroxidase activity in yeast and human cyt *c* despite many similar global properties to that of WT.[18, 19] Further, the magnitudes of observed increase in peroxidase activity in human and yeast proteins are different, suggesting loop D dynamics may be affected differently.[18, 19]

Comparing human and yeast K72A to probe why such differences exist, however, poses additional challenges. Not only are the global stabilities vastly different between human and yeast cyt *c*, trimethylation of K72 (TmK72) in yeast expressed cyt *c* is not present in the human cyt *c*. Preventing Lys trimethylation by expressing the yeast cyt *c* protein in *E. coli* does not alter the reduction potential,[13] but does alter the inherent dynamics of loop D and the alkaline transition of yeast cyt *c*.[13, 18, 23] Additional information from horse heart K72A cyt *c* could clarify whether the sequence variations at and near loop D contribute to different effects on biophysical properties of human and yeast proteins. Further, since WT horse heart cyt *c* has similar global stability to WT cyt *c*, does not contain TmK72, and have fewer sequence variations in loops C and D than in yeast WT cyt *c*, having additional data on the horse heart protein could help to analyze *in vivo* data.

Herein, we introduce the K72A mutation in horse heart cyt *c* to understand how the loop D perturbation affects the stability and dynamic properties of the protein compared to those of WT. We compare the observed mutational effects of human, yeast, and horse heart cyt *c*. We also provide characterization of ET properties of this variant and relate how the polypeptide chain packing and sequence variations affect reduction potential of the heme iron. To better understand how sequence variations around loop D influence ET properties, we compare the ET properties of G41S and Y48H variants, whose loop C perturbations

also influence loop D dynamics, offering molecular insight on how disruptions in or around loop D alter ET properties of cyt *c*.

Materials and Methods

General. All aqueous solutions were prepared as described in Chapter 3. Site-directed mutagenesis, protein expression and purification for K72A variant of horse heart cyt *c* were performed as described in Chapter 3. Detailed procedure for obtaining the electronic absorption, ^{1}H NMR, and EPR spectra were discussed in Chapter 3.

Sequence Alignments and Molecular Dynamics Simulations. Sequence alignments for figures and structural analyses were performed as previously described in Chapter 3. Energy-minimized models of protein variants were performed and analyses of the trajectories performed as previously described in Chapter 3,[24] starting from the crystal structures of human (PDB ID: 3ZCF)[25] and horse heart cyt *c* (PDB ID: 1HRC).[26]

For comparison of structural fluctuations for the entire protein, 30 ns simulations were performed, and trajectories analyzed for horse heart and human K72A cyt *c* variants as previously described in Chapter 3. Hydrophobic packing of the polypeptide was compared by obtaining the total solvent-excluded molecular surface volume (V_{MS}), void volume (V_{void}), and the Van der Waals (VdW) volume (V_{VdW}) from the X-ray crystal structures of WT cyt *c* from human (PDB ID: 3ZCF),[25] horse heart (PDB ID: 1HRC),[26] and yeast (PDB ID: 2YCC),[27] and K72A cyt *c* from human (PDB ID: 5TY3)[19] and yeast (PDB ID: 4MU8),[18] using ProteinVolume with the following recommended parameters: energy minimization with 0.08 Å starting probe size, 0.02 Å ending probe size, and 0.1 Å surface probe minimum distance.[28]

Contact Maps. Heat maps showing the contact frequencies of the residue pairs within HB and vdW from MD simulations were calculated as previously described in Chapter 3. Contact maps showing the distances of the residue pairs within HB and vdW distances were obtained using X-ray crystal structures of WT cyt *c* from human (PDB ID: 3ZCF)[25] and yeast (PDB ID 2YCC),[27] and K72A cyt *c* from human (PDB ID 5TY3)[19] and yeast (PDB ID 4MU8).[18] Distances were obtained using pairwise interatomic distances with a 5 Å cut-off.

Thermal and Chemical Denaturation Experiments. Thermal denaturation and chemical denaturation of K72A variant of horse heart cyt *c* were performed, and data analyzed as previously described in Chapter 3. Thermal denaturation of K72A variant of horse heart cyt *c* was 99% reversible, as calculated by the CD ellipticity signal of the protein sample at 222 nm taken before and after the temperature melt.

pH Titrations and Analyses. Solutions containing proteins at concentrations of 8 to 10 μM or 200 to 300 μM in a 100 mM sodium phosphate buffer at pH 7.4 were used to monitor either the Soret or the charge-transfer (CT) absorption band, respectively. pH titrations profiles of the Soret region (350 to 600 nm) and CT region (580 to 750 nm) for K72A was analyzed using SVD, as previously described in Chapter 3. Analyses have suggested that a single transition is sufficient to describe pH-dependent changes in the Soret band (pH 6.27 to 10.69) and the CT band (pH 6.53 to 11.32) for K72A variant of horse heart cyt *c*.

pH-Jump Kinetics. Data from pH-jump measurements were obtained by Dr. Fangfang Zhong, as described in Chapter 3.

Measurements of Reduction Potentials. Reduction potentials were determined from titrations with varying concentrations of potassium ferricyaninde (ferriCN) and potassium

ferrocyanide (ferroCN) in presence of protein in a degassed 100 mM sodium phosphate buffer at pH 7.4. Solutions containing different ratios of ferriCN were prepared and absorption spectra at Q-band at 550 nm of the ferrous protein were measured, as described previously.[29] Ratios of ferrous and ferric protein versus total ferroCN and ferriCN in solution were plotted in a log-log plot and fitted to eq 4.1 to obtain the potential of the protein (*E*), where $E°$ = 430 mV.[29]

$$E = E^{\circ} - 2.303 \frac{RT}{nF} \log\left(\frac{[\text{ferroCN}]}{[\text{ferriCN}]}\right) \quad (4.1)$$

The final potential was obtained from an average of three to six separate measurements.

ET Measurements. Rates of oxidation of ferrous WT, K72A, G41S, and Y48H cyt *c* variants with $Co(phen)_3^{3+}$ were studied in a 50 mM sodium phosphate buffer at pH 7.4, either with or without added sodium chloride to yield solutions at ionic strengths of 0.1 M and 1.0 M, respectively. The $Co(phen)_3Cl_3$ compound were synthesized by Dr. Alexandre Pletnev, as described previously.[30]

Proteins were freshly purified using an ion-exchange column prior to use. Ferrous cyt *c* samples were prepared in an anaerobic glovebox (COY Laboratory Products) by adding an excess of sodium dithionite to the protein stock solution, followed by removal of the reductant and buffer exchange on a PD-10 desalting column. Columns were pre-treated with dithionite to avoid unwanted oxidation of the protein and equilibrated with the desired buffer prior to use. Stock protein solutions were quantified using the extinction coefficient of the Soret band for ferrous cyt *c* variants (for WT, ε_{415} = 125 $mM^{-1}cm^{-1}$, slightly lower than reported values at ε_{415} = 128 $mM^{-1}cm^{-1}$ at pH 6.8.[9, 31] For K72A ε_{415} =

142.5 $mM^{-1}cm^{-1}$; for G41S ε_{415} = 134.8 $mM^{-1}cm^{-1}$; for Y48H ε_{415} = 146.7 $mM^{-1}cm^{-1}$ in a 100 mM sodium phosphate buffer at pH 7.4) and diluted as necessary to final concentrations ranging from 40 to 60 μM. Stock solutions of $Co(phen)_3^{3+}$ were prepared immediately before use with concentrations ranging from 0.8 to 1.5 mM. Electronic absorption spectra (ε_{303} = 19.2 $mM^{-1}cm^{-1}$) were used for quantification of this small-molecule reductant.[32]

Kinetic traces monitoring the heme absorbance at 550 nm as a function of time were obtained on a Bio-Logic SFM-300 stopped-flow instrumentation inside an anaerobic glovebox. Before each experiment, the instrument lines were flushed with a sodium dithionite solution, rinsed thoroughly with degassed water, and pre-treated with the degassed buffer. Final concentrations of protein and $Co(phen)_3^{3+}$ ranged from 7 to 10 μM, and 0.15 to 1 mM, respectively. Traces were obtained using the BioKine program (BioLogic) and analyzed using SFit (BioLogic) and MATLAB (R2017a). At each concentration of $Co(phen)_3^{3+}$, four to six traces were recorded and were fitted to a monoexponential equation to obtain the rate constant k_{obs}.

Bimolecular reaction between $Co(phen)_3^{3+}$ and ferrous cyt *c* was studied under pseudo-first order conditions, where $[Co(phen)_3^{3+}] >> [cyt\ c^{II}]$. The dependence of k_{obs} on $[Co(phen)_3^{3+}]$ was fit to a linear function to determine the second-order rate constant, k_{12}. The electron-self-exchange (ESE) rate constant (k_{ESE}) for the cyt *c* variants (k_{22}) were calculated using the Marcus theory cross-relationship (eq 4.2): [33]

$$\log(k_{12}) = 0.5[\log(k_{11}) + \log(k_{22}) + 16.9\ \Delta E^{\circ}_{12}] \quad (4.2)$$

where k_{12} is the bimolecular rate constant for ET from ferrous cyt *c* to $Co(phen)_3^{3+}$, k_{11} is the ESE rate constant for $Co(phen)_3^{3+}$,corrected for ionic concentration, k_{22} (noted k_{ESE} here) is the ESE rate constant for cyt *c* and ΔE°_{12} is the difference between the reduction potentials of $Co(phen)_3^{2+/3+}$ (370 mV)[3, 34] and cyt$c^{2+/3+}$ couples (determined in this study for the variants). The equilibrium constant for ET, K_{12}, was obtained using eq 4.3:[33]

$$K_{12} = \exp\left(\frac{nF\Delta E^{\circ}_{12}}{RT}\right) \tag{4.3}$$

where *n* is the total number of electrons transferred in the reaction, *F* is the Faraday's constant, ΔE°_{12} is the difference between the reduction potentials of the electron acceptor($Co(phen)_3^{2+/3+}$) and the donor (cyt *c*), *R* is the gas constant, and *T* is the temperature.[33]

ESE rate constants k_{11} for $Co(phen)_3^{3+}$ were calculated considering the ionic strength of the solution (μ) using the Debye-Hückel treatment (eq 4.4):[34]

$$\ln k = \ln k_o + \frac{(2Z_1Z_2+Z_2^2)\alpha\sqrt{\mu}}{1+\kappa R_1} - \frac{Z_2^2\alpha\sqrt{\mu}}{1+\kappa R_2} \tag{4.4}$$

where $R_1 = R_2 = 7$ Å (radius of $Co(phen)_3^{3+}$), $Z_1 = +3$ and $Z_2 = +2$ (charge of the complex in the two oxidation states), $\alpha = 1.17$, $\kappa = 0.329\sqrt{\mu}$ ($Å^{-1}$).[34] Using the value of the ESE rate constant for $Co(phen)_3^{3+}$ of 4.5×10^1 $M^{-1}s^{-1}$ (μ = 0.1 M at 25 °C),[34] the rate constant at μ = 0 was obtained (k_o = 3.45 $M^{-1}s^{-1}$). Using this k_o value, the rate constant k_{11} for $Co(phen)_3^{3+}$ at μ = 1.0 M and 25 °C, was calculated to be 1.93×10^2 $M^{-1}s^{-1}$.

Biological ET Measurements. Rates of oxidation of bovine cytochrome CcO (Sigma) in the presence of cyt *c* were obtained by measuring oxygen consumption levels with an oxygen microsensor (Unisense). L-ascorbic acid was used as a sacrificial reductant. Assays were performed in a 50 mM Tris HCl buffer with 100 mM sodium chloride, 5 mM ethylenediaminetetraacetic acid (EDTA), and 0.02% (*v/v*) n-Dodecyl-β-D-maltoside (DDM) at pH 7.5. Ferric cyt *c* samples were freshly prepared by adding excess potassium ferricyanide and purified using the PD-10 column equilibrated with a 100 mM sodium phosphate buffer at pH 7.4.

Each reaction sample contained final concentrations of 2.5 mM L-ascorbic acid, cyt *c* varying from 5 to 50 μM, and 100-fold dilution of the original stock of CcO (5 mg/ml, containing at least 20 units of active CcO/mg protein). Samples were mixed and placed inside 400 μL chambers; oxygen consumption was measured for 15 to 30 minutes. Slopes obtained from linear fits of the data plotting oxygen consumption over time were calculated from μM O_2 consumed/sec to μM electrons consumed/sec by multiplying by 4 (CcO consumes 4 electrons for every O_2 reduced to H_2O). All kinetic traces were corrected for the baseline oxygen consumption rate for ascorbic acid in buffer, in the absence of both CcO and cyt *c*.

The electron consumption rate was then plotted versus the concentration of cyt *c* in a Lineweaver-Burke plot to obtain the slope and the intercept that was used to calculate the V_{max} and K_M for the biological electron transfer rate of cyt *c*, where slope = K_M/V_{max} and the y-intercept = $1/V_{max}$. Although V_{max} is proportional to k_{cat} from the expression $V_{max} = k_{cat}[E_T]$ and $[E_T] = [CcO]$ as cyt *c* was the limiting substrate (source of electrons), k_{cat} was

not calculated since the exact concentration of CcO was not known (estimates based upon dilutions yield a minimum of 1 nM (0.001 μM) CcO was present per reaction).

Preparation of Liposome Vesicles and Liposome Binding Assays. Preparation of CL-containing lipid vesicles and liposome binding assays with K72A were performed as previously described in Chapter 3.[35]

Peroxidase Assays. Peroxidase assays were performed, and data analyzed as previously described in Chapter 3.

Results

MD Simulations. Due to a lack of structural data for horse heart K72A cyt *c*, MD simulations were performed for both ferric human and horse heart K72A cyt *c*. For heart K72A cyt *c* from both human and horse heart, per residue RMSF values were comparable to those of WT, suggesting that much of the loop D dynamics were unperturbed (Figure 4.1). In horse heart cyt *c*, per residue RMSF values are unchanged with and without the K72A mutation (Figure 4.1B). The RMSF values in loop C for WT and K72A variants are slightly higher in human cyt *c* than in horse heart cyt *c*, and the fluctuation increases in loop C with the K72A mutation in human cyt *c* (Figure 4.1A). However, differences are small (within 0.5 Å), suggesting that there are little differences in the overall peptide dynamics. Since pairwise RMSD values compare the individual simulated structure to a reference structure, such analysis is a good way to assess the variations in the conformational ensemble. A closer look at pairwise RMSD plots suggests that the differences between WT and K72A in the 20's loop are small (Figure 4.2).

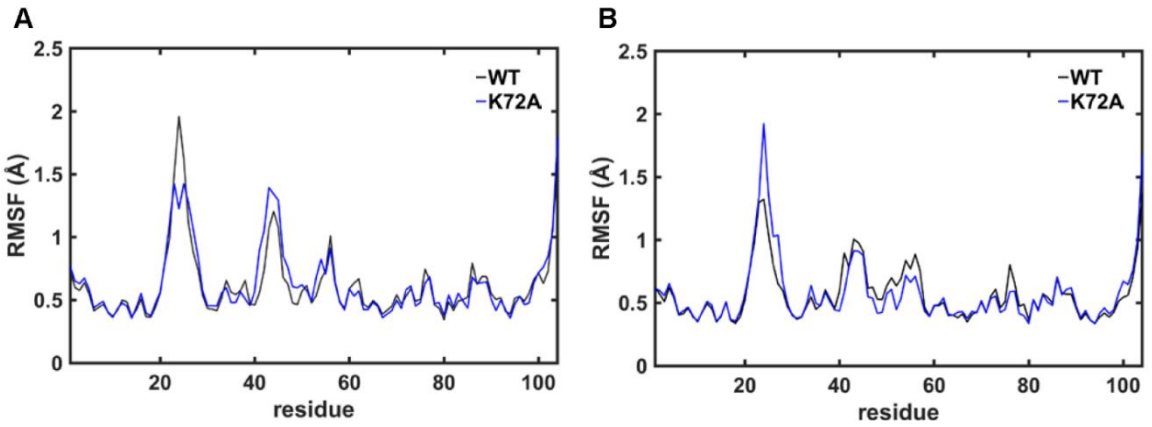

Figure 4.1. Plots of averaged per residue RMSF values for αC atoms in the protein backbone obtained from MD simulations, relative to the reference structure of the protein for WT (black) and K72A variant (blue) for (A) human and (B) horse heart cyt *c* variants. For each simulation, RMSF values were separately calculated, and then averaged to obtain the average per residue RMSF value for the variants of cyt *c*.

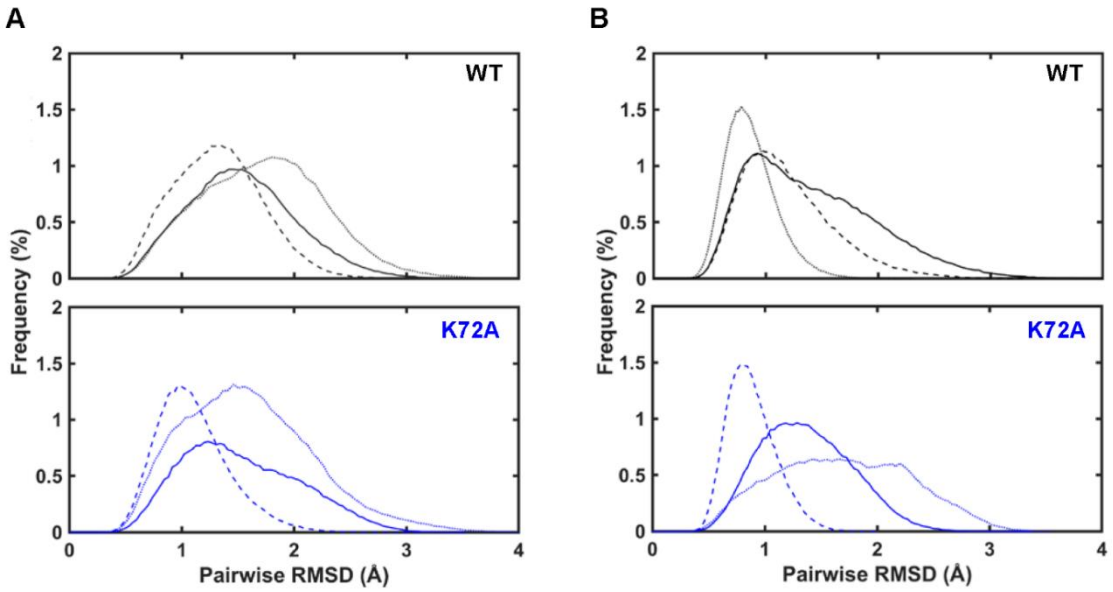

Figure 4.2. Plots showing the distribution of pairwise RMSD values for αC atoms in the 20's loop (residues 20 to 30) versus frequency, for structures obtained from MD simulations. Shown are the RMSD value distributions for WT (black) and K72A (blue) variants of (A) human and (B) horse heart cyt *c*. Distributions of RMSD values between each structure to all other structures from individual MD simulations are shown (first run, solid line; second run, dotted line; third run, solid line). All frames in the trajectory from 20 ns up to 35 ns simulation times were used to calculate the RMSD values.

In comparison, pairwise RMSD values in loop C are different for K72A variants in human and horse heart cyt *c* (Figure 4.3). Larger pairwise RMSD values are observed with the K72A mutation at higher frequency in human cyt *c*, suggesting that conformation of loop C in human cyt *c* do not converge in our simulations and the loop samples conformations that require larger rearrangements of the polypeptide backbone than in WT (Figure 4.3A). In contrast, pairwise RMSD values of loop C in horse heart K72A cyt *c* is narrow and the loop does not sample distinct loop conformations requiring larger rearrangements to the polypeptide backbone (Figure 4.3B). For both human and horse heart K72A cyt *c*, pairwise RMSD values for loop D are similar to those of WT, and differences are not observed between the two species (Figure 4.4).

Differences in pairwise RMSD distributions of loop C between human and horse heart cyt *c* with K72A mutation raised the possibility that loops C and D contacts may be different (Figure 4.3). To test this hypothesis, heat maps plotting the frequencies at which residues are in within HB (3 Å) and vdW (5 Å) distances were generated (Figure 4.5). Heat maps suggest that in both human and horse heart cyt *c*, K72A mutation forms additional residue pairs in loops C and D that come within HB distance, in addition to residue pairs that are observed in the WT protein (Figure 4.5A and B). Furthermore, there are additional residue pairs that come within vdW distance with the K72A mutation in human and horse heart cyt *c* (Figure 4.5C and D). Heat maps suggest that, in human and horse heart cyt *c*, K72A mutation increases the frequency and the number of residue pairs that come within forming weak contacts, suggesting that loops C and D generally forms more inter-loop contacts than in WT.

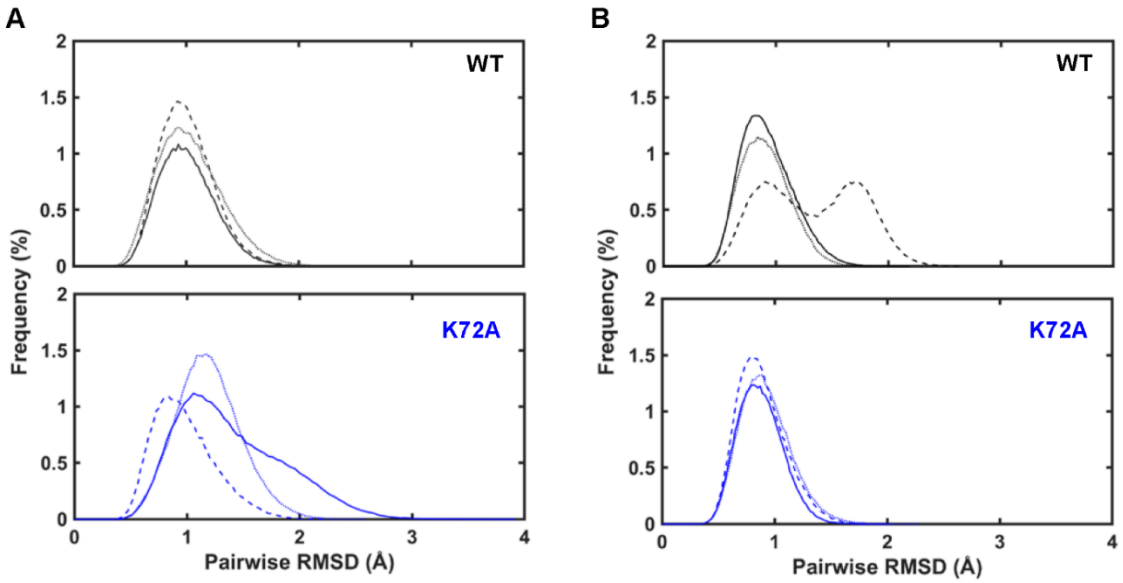

Figure 4.3. Plots showing the distribution of pairwise RMSD values for αC atoms in loop C (residues 40 to 57) versus frequency, for structures obtained from MD simulations. Shown are the RMSD value distributions for WT (black) and K72A (blue) variants of (A) human and (B) horse heart cyt *c*. Distributions of RMSD values between each structure to all other structures from individual MD simulations are shown (first run, solid line; second run, dotted line; third run, solid line). All frames in the trajectory from 20 ns up to 35 ns simulation times were used to calculate the RMSD values.

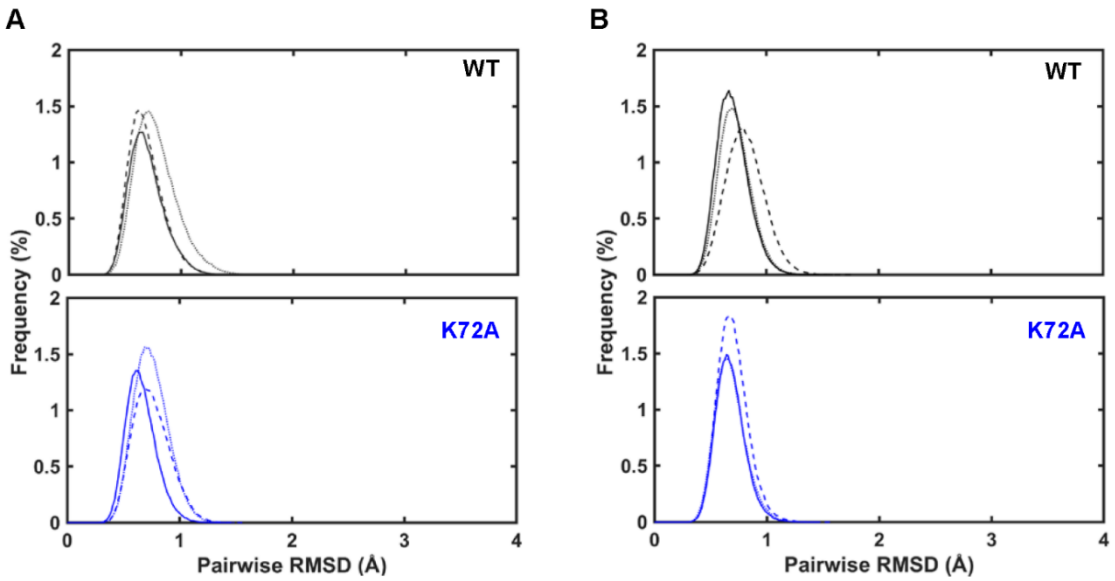

Figure 4.4. Plots showing the distribution of pairwise RMSD values for αC atoms in loop D (residues 70 to 85) versus frequency, for structures obtained from MD simulations. Shown are the RMSD value distributions for WT (black) and K72A (blue) variants of (A) human and (B) horse heart cyt *c*. Distributions of RMSD values between each structure to all other structures from individual MD simulations are shown (first run, solid line; second run, dotted line; third run, solid line). All frames in the trajectory from 20 ns up to 35 ns simulation times were used to calculate the RMSD values.

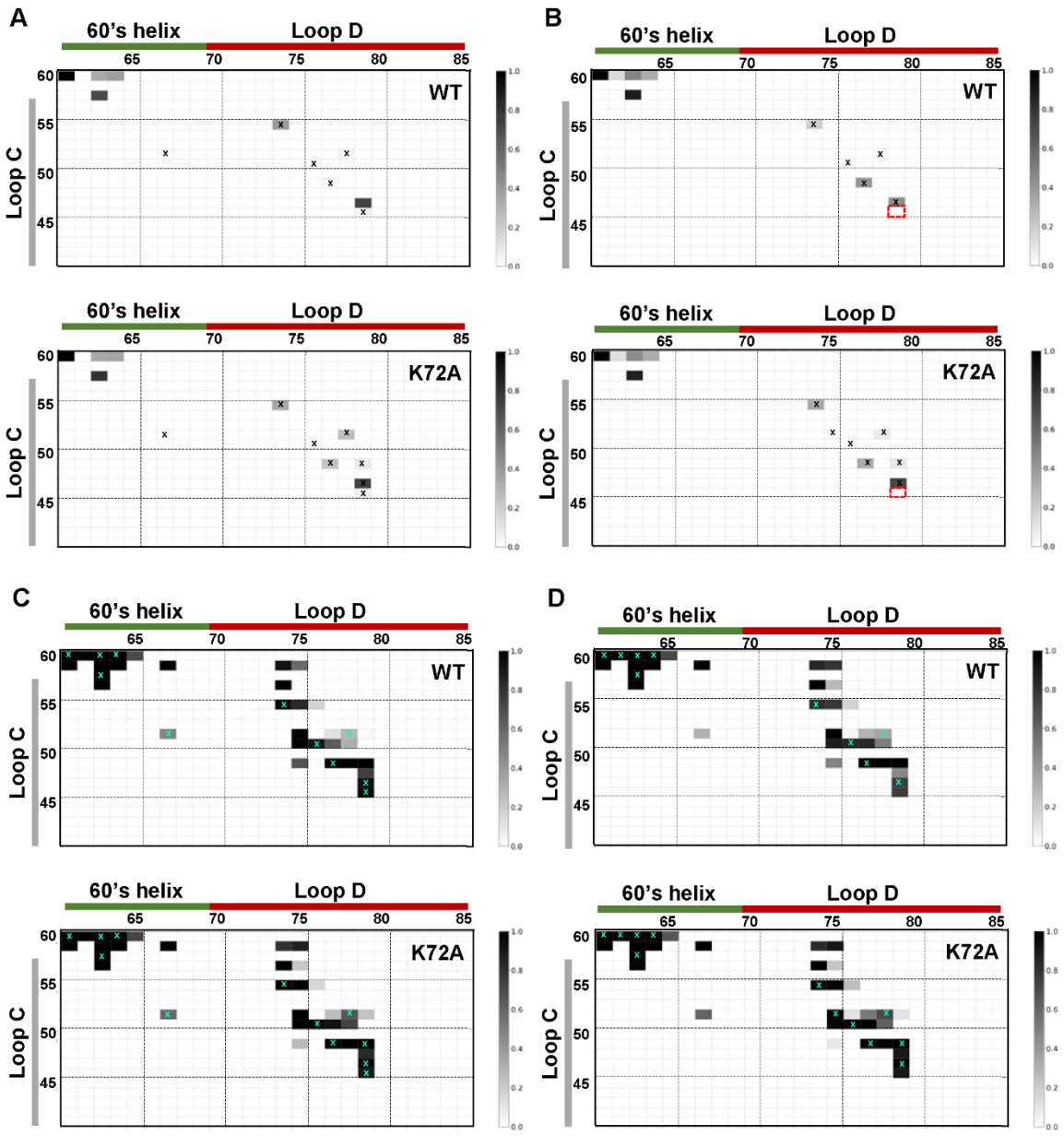

Figure 4.5. Heat map plots of contact frequencies between residues in loop C, 60's helix, and loop D based on the MD simulated structures of WT (top) and K72A (bottom) variants of (A,C) human and (B,D) horse heart cyt *c*. Plotted are the frequency of contacts between residues within the contact distance of 3 Å, for (A) and (B), or 5 Å, for (C) and (D), from all three simulations. All frames in the trajectory from 20 ns up to 30 ns simulation times were used to generate the heat maps.

Between human and horse heart K72A cyt *c*, many residue pairs that are within HB and vdW distances are similar between two species (Figure 4.5C and D). Yet, there are some variations with the mutations. New possible HB contacts are formed, particularly with residue 79 for both species (Figure 4.5, bottom), and a unique HB could form between residue 75 and 52 in horse heart K72A cyt *c* (Figure 4.5B, bottom). Overall, both human and horse heart K72A cyt *c* maintain a WT-like contact maps of loop C and D contacts. However, small differences in contacts exist, suggesting that perturbations to loop D are handled differently between the two different species.

Heme Coordination and Protein Fold. To better understand how the polypeptide perturbation affects the heme center, heme iron ligation and polypeptide fold were assessed at pH 7.4 with multiple spectroscopic techniques.

Electronic Absorption Spectra. At pH 7.4, the electronic absorption spectrum of ferric K72A shows that the Soret band and the CT band are similar to those of WT (Figure 4.6A). The electronic absorption spectrum of ferrous K72A at pH 7.4 is also comparable to that of WT (Figure 4.6B). For both ferric and ferrous species, the extinction coefficient of the Soret band for K72A (ε_{409} = 113.3 $mM^{-1}cm^{-1}$, ferric; ε_{415} = 142.5 $mM^{-1}cm^{-1}$, ferrous) is higher than that of WT, suggesting some alteration in the heme environment upon the mutation.

^{1}H NMR. The downfield region of the ^{1}H NMR spectrum of ferric K72A at pD 7.4 shows signals of the heme porphyrin methyl, at positions characteristic of the Met-ligated heme species (Figure 4.6C). However, the signals of the methyl protons for ferric K72A are shifted downfield compared to those for WT.

Figure 4.6. Electronic absorption spectra of (A) ferric and (B) ferrous WT (black), and K72A (blue) variants of horse heart cyt *c* in a 100 mM sodium phosphate buffer at pH 7.4, with the near-IR charge transfer band shown for the ferric species (inset, A). the ^{1}H NMR of WT (black) and K72A (blue) variants of horse heart cyt *c* in the (C) ferric state are shown, with (D) numberings for heme and Met protons for labeling peaks in WT. ^{1}H NMR of (E) ferrous proteins are also shown. ^{1}HNMR samples were prepared in a 50 mM sodium phosphate buffer at pD 7.4 in 100% D_2O or pH 7.4 with 10% D_2O (*v*/*v*), respectively. (F) EPR spectra at 10 K for ferric WT (black) and K72A (blue) variants of horse heart cyt *c* in a 50 mM sodium phosphate buffer at pH 7.4 with 20% (*v*/*v*) glycerol.

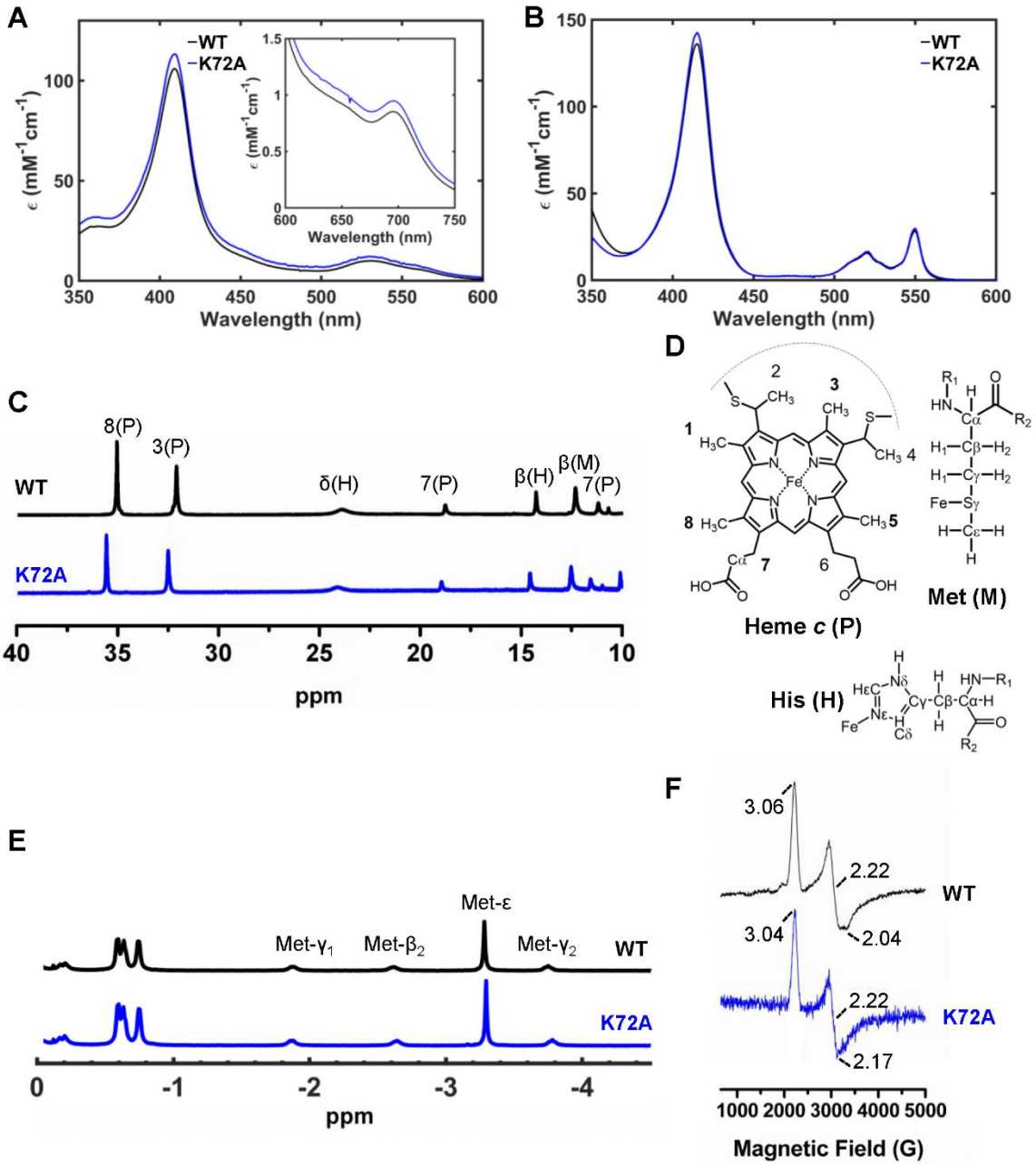
A
WT
K72A
ϵ (mM-1cm-1)
Wavelength (nm)
B
WT
K72A
ϵ (mM-1cm-1)
Wavelength (nm)
C
8(P)
3(P)
δ(H)
7(P)
β(H)
β(M)
7(P)
WT
K72A
ppm
D
Heme c (P)
Met (M)
His (H)
E
Met-ε
Met-γ1
Met-β2
Met-γ2
WT
K72A
ppm
F
3.06
2.22
WT
3.04
2.04
2.22
K72A
2.17
Magnetic Field (G)

The ^{1}H NMR spectrum of ferrous K72A at pD 7.4 shows signals corresponding to methyl protons of the Met-ligated heme iron and shifts in signals are not observed (Figures 4.6D and E). Additional signals in these regions, corresponding to species other than the Met-ligated hemes, are not observed in the ^{1}H NMR spectra for ferric and ferrous K72A.

EPR. The EPR spectrum for ferric K72A cyt *c* variant at pH 7.4 confirms the presence of the Met-ligated heme iron species, as the location of g_x, g_z, and g_y peaks corresponds to that of Met-ligated heme iron species observed in the WT spectrum (Figure 4.6F). No other species are detected, confirming the observations from the electronic absorption and ^{1}H NMR spectra.

Secondary Structure. At pH 7.4, the far-UV CD spectrum for ferric K72A shows negative signals at 220 and 210 nm peaks characteristic of a protein with primarily α-helical secondary structure at similar intensities and ratios as observed in the spectrum for WT (Figure 4.7).

Electronic absorption, ^{1}H NMR, EPR, and far-UV CD spectra all suggest that in the K72A horse heart cyt *c* variant, the mutation in loop D does not perturb the native Met-ligation or the fold of the protein at pH 7.4. Similarities in spectral features between WT and K72A variants of horse heart cyt *c* supports our findings from MD simulations that suggested that the bulk of the protein conformations and dynamics are comparable in WT and K72A variants of horse heart cyt *c*.

Global and Local Stability. We wanted to test whether K72A mutation in loop D altered the global and local stability of the protein, and whether stability trends upon this mutation are the same in different species.

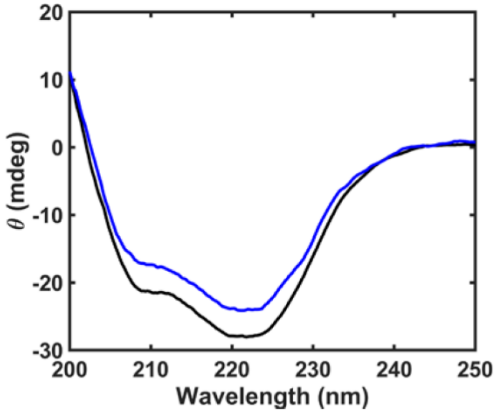

Figure 4.7. Far-UV CD spectra of WT (black) and K72A (blue) variants of horse heart cyt *c* in a 100 mM sodium phosphate buffer at pH 7.4 and 20 ºC, normalized to [cyt *c*] = 20 μM and *l* = 1 mm.

Global stability of the K72A variant was probed by monitoring the α-helical features of the protein and the local stability of loop D region was probed by monitoring the changes in the 695 nm CT band.

Thermal Denaturation. At pH 7.4, thermal denaturation of K72A cyt *c* shows T_m comparable to that of WT (Figure 4.8 and Table 4.1). However, thermal denaturation experiments were not carried out beyond 90 °C (363 K) as the proteins were in aqueous solutions. The T_m values are high for horse heart WT cyt *c* and more variations observed in the thermal denaturation curve for the WT (Figure 4.8, top) and larger error bar for the fitted ΔH_{vH} value in K72A variant of horse heart cyt *c* than that in WT (Table 4.1) make it difficult to reliably quantify the differences in global stability of the protein with respect to thermal denaturation.

Chemical Denaturation with GuHCl. For K72A at pH 7.4, a higher $[GuHCl]_{1/2}$ value is observed compared to that for WT, but the m_D parameter is within the error of that for WT. The overall ΔG_D values for the two variants are within error (Figure 4.9A and Table 4.2). Similar to what was observed for human cyt *c*,[19] the K72A mutation is a non-disruptive mutation in horse heart cyt *c* that does not disrupt the global stability of the protein. .

Loop D Stability. To probe whether the mutation affects the unfolding of loop D, changes in the 695 nm CT band was monitored with increasing concentration of GuHCl at pH 7.4. Since 695 nm CT band is argued to be the metal-to-ligand CT of the heme iron to Met80,[9] monitoring this absorption band acts as a direct probe to monitor the changes in Fe-Met80 ligation upon unfolding of the polypeptide.[36] In K72A horse heart cyt *c*, the values of $[GuHCl]_{1/2}$,m_D, and calculated ΔG_D parameters are within error to those of WT (Figure 4.9B and Table 4.2).[37]

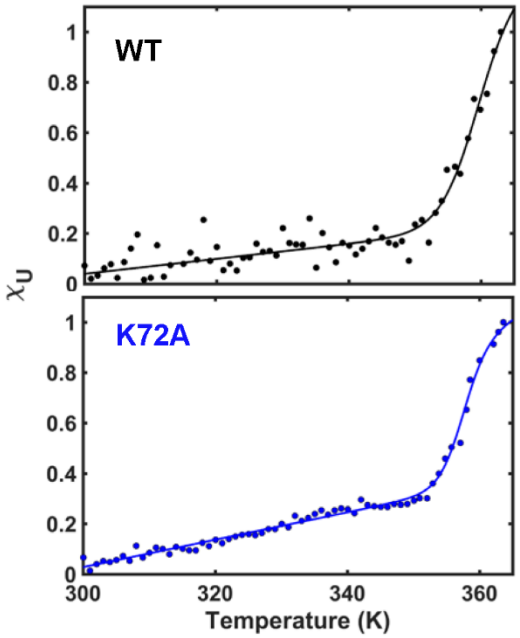

Figure 4.8. Representative temperature unfolding data and fits for fractions of the unfolded protein (χ_U) versus temperature for ferric WT (black) and K72A (blue) variants of horse heart cyt *c* in a 100 mM sodium phosphate buffer at pH 7.4. Monitored is the ellipticity at 222 nm.

Table 4.1. Thermal Denaturation Parameters for Global Unfolding of Variants of Horse Heart Cyt *c* at pH 7.4[a]

Variant	T_m (K)	ΔH_{vH} (kJ mol^{-1})
WT	357.1[b]	360 ± 30[b]
K72A	358 ±2	569 ± 128

[a]Monitored is ellipticity at 222 nm.

[b]From ref.[38].

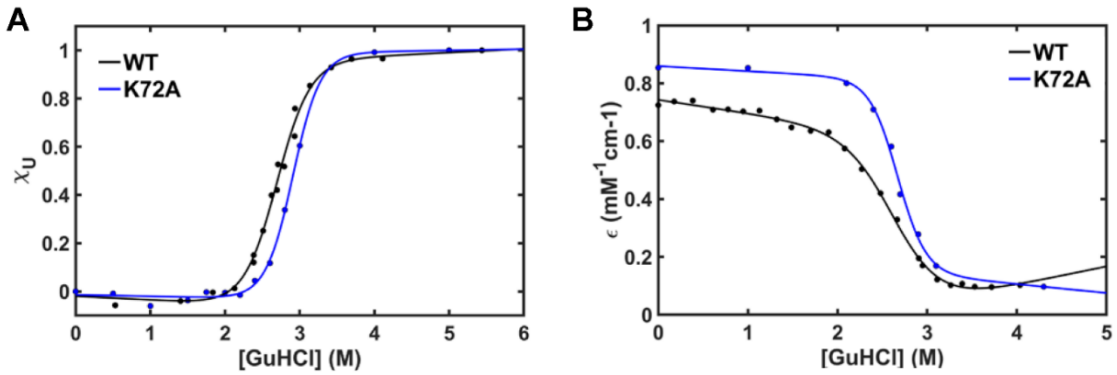

Figure 4.9. Chemical denaturation curves showing (A) α-helicity at 222 nm (fraction unfolded, χ_U) and (B) CT (extinction coefficient, ε_{695}) plotted versus [GuHCl] and with corresponding fits for ferric WT (black, from refs. [39] for global stability measurements and ref. [37] for CT) and K72A (blue) variants of horse heart cyt *c* in a 100 mM sodium α-helicity was monitored at 20 °C and the CT absorption band was monitored at 22 ± 2 °C.

Table 4.2. Thermodynamic Parameters of GuHCl Unfolding for Cyt *c* Variants[a]

Variant	Signal Monitored	$[GuHCl]_{1/2}$ (M)	m_D (kJ mol^{-1} M^{-1})	ΔG_D (kJ mol^{-1})
			Horse Heart	
WT	α-helices[b]	2.7 ± 0.1	11.5 ± 2.6	31.1 ± 7.1
	695 nm CT[c]	2.7 ± 0.1	9.1 ± 1.7	24.6 ± 4.7
K72A[d]	α-helices	2.9 ± 0.1	13.4 ± 2.9	38.9 ± 8.5
	695 nm CT	2.7 ± 0.1	13.9 ± 3.8	37.5 ± 10.3
			Human	
WT[e]	α-helices	2.55 ± 0.01	15.5 ± 0.2	39.6 ± 0.5
K72A[e]	α-helices	2.75 ± 0.03	15.2 ± 0.9	41.9 ± 1.3
			Yeast	
WT	α-helices[f]	0.96 ± 0.03	17.9 ± 1.1	17.2 ± 0.7
	695 nm CT[g]	0.88 ± 0.02	32.7 ± 6.7	28.8 ± 5.9
K72A[h]	α-helices	1.07 ± 0.07	12.9 ± 2.6	13.8 ± 2.9

[a]Changes in the ellipticity signals from the α-helices were monitored to obtain global stability parameters in respect to GuHCl titration. Changes in the absorption at 695 nm CT band was monitored to obtain loop D stability parameters in respect to GuHCl titration.

[b]From ref. [39].

[c]From ref. [37].

[d]From this work. Monitored is ellipticity at 222 nm, performed at 20 ºC and at pH 7.5.

[e]From ref. [19] at pH 7.5.

[f]From ref. [40].

[g]Refitted from ref. [41], as fitted values were not reported. Measured at pH 7.5 and 25 °C, protein contains C102S mutation and TmK72.

[g]From ref. [7] at pH 4.5, with a C102S background mutation.

From these results, the denaturation curve obtained by monitoring the 695 nm CT band may reflect the global unfolding of the protein, rather than reporting on the stability of loop D. ΔG_D is within error to that of WT (37.5 ± 10.4 kJ·mol^{-1} in K72A compared to 24.6 ± 4.7 kJ·mol^{-1} of WT), likely reflecting the global stability of the protein rather than the Loop D stability. From HX experiments, ΔG_D of loop D is much lower in WT horse cyt *c* than the ΔG_D value obtained from monitoring the 695 nm CT band by ~ 25 kJ/mol.[42] Assumption of a two-state unfolding may not describe well the unfolding of horse heart cyt *c*.[43] Yet, similarities in global stabilities from monitoring global and local denaturation does suggest that loop D is unfolds similarly in K72A as in WT.[41]

Both the chemical and thermal denaturation data show that at pH 7.4, the K72A mutation in horse heart cyt *c* has little to no effect on the global stability of the protein and does not seem to alter the local stability of loop D.

Alkaline Transition. To gain better understanding of changes in loop D dynamics with the K72A mutation, the alkaline transition in K72A was compared to that of WT. SVD analysis showed that a single transition is sufficient to describe the pH-dependent absorption profiles of the Soret band (350 to 500 nm, pH 6.27 to 10.69) and the CT band (580 to 750 nm, pH 6.53 to 11.32) in the K72A variant of horse heart cyt *c* (Figure 4.10). Global fit of the significant vectors obtained from the SVD analysis (Figure 4.10C) yielded a pK_a of 9.65 ± 0.05, ~0.5 pK_a unit higher than that of WT (Table 4.3) Using the spectrum of the Met-ligated WT cyt *c* at pH 7.4 as a reference, spectrum of the second component was obtained (Figure 4.10E).

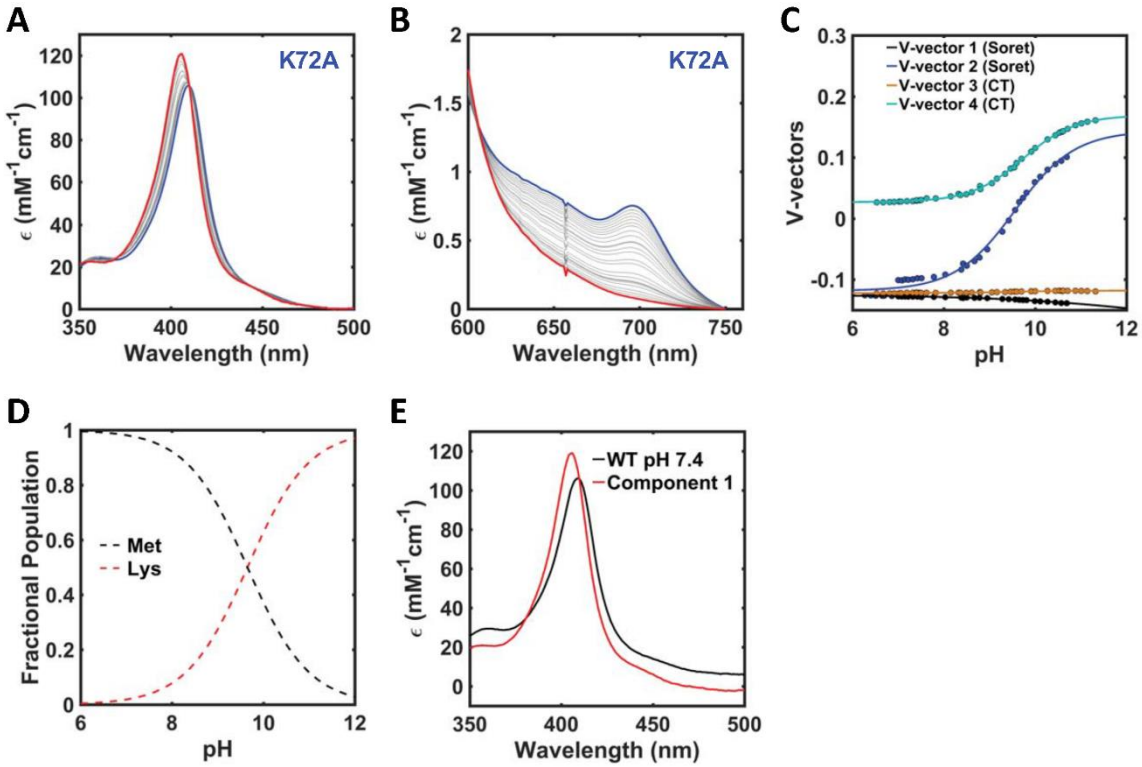

Figure 4.10. K72A pH titration and SVD analysis for the Soret and CT bands. pH titration traces for the Soret and CT regions for the K72A in μ = 0.1 M conditions at room temperature. Shown are the electronic absorption spectra of the (A) Soret band from neutral (blue) to alkaline (red) conditions in pH ranges 6.27 to 10.69, and (B) the CT band from neutral (blue) to alkaline (red) conditions in pH ranges 6.53 to 11.32, and (C) significant vectors and fits obtained from the combined SVD analysis of pH titrations in both the Soret and CT bands. The extrapolated pK_a value of the alkaline transition was used to obtain the (D) fractional populations. Using the WT spectrum at pH 7.4 as a reference, (E) the deconvoluted spectrum of the second component was obtained.

Table 4.3. Parameters for the pH-Dependent Alkaline Transition in Cyt*c* Variants[a]

Variant	pK_a	*n*	$\Delta\Delta G$ (kJ mol^{-1})[b]	% Lys at pH 7.4
	Horse Heart		*vs. WT*[c]	
WT	9.27 ± 0.01	0.87 ± 0.02	0	1.3
K72A	9.65 ± 0.05	0.65 ± 0.03	2.15 ± 0.29	0.6
	Human			
WT[d]	9.54 ± 0.03	1.03 ± 0.02	0	0.7
K72A[e]	10.0 ± 0.1	0.98 ± 0.06	2.60 ± 0.59	0.3
	Yeast			
WT[f]	8.7 ± 0.02	--	--	4.8
WT[g]	7.95 ± 0.02			
K72A[h]	8.8 ± 0.1	--	--	3.8

[a]In a 100 mM sodium phosphate buffer at pH 7.4 and 22 ± 2 °C. Significant vectors from both the Soret and charge-transfer pH titrations were globally fitted to obtain the pK_a and *n* (number of protons) values. Fixing $n = 1$ for global fittings yielded similar pK_a values to fittings when *n* was not fixed.

[b]Calculated from ΔpK_a assuming conditions $T = 22$ °C.

[c]$\Delta\Delta G$ values were calculated by comparing the pK_a values for horse heart WT cyt *c* for the horse heart cyt *c* variants and human WT cyt *c* for the human cyt *c* variants.

[d]From ref. [44].

[e]From ref. [19].

[f]From ref. [45], contains TmK72 and C102T mutation

[f]From ref. [13], contains K72 and a background C102T mutation, expressed in *E. coli*.

[h]From ref. [37], contains C102S mutation.

The deconvoluted spectra shows that the λ_{max} is blue shifted and the intensity increases, comparable to the species observed in the absorption profile of K72A at high pH conditions and Lys-ligated WT cyt *c* at alkaline conditions (compare to Figure 3.16).

To clarify why the pK_a value of the alkaline transition increased with the K72A mutation, pH-jump kinetic experiments were performed to obtain the rates of ligand exchange from Met-ligated heme iron to the Lys-ligated heme iron. With the K72A mutation, pK_H increases by ~0.5 pK_a units, while the pK_C parameter is within error to that of the WT (Table 4.4). These results suggest that the mutation affects the environment of the trigger group but does not greatly alter the conformational equilibrium of the loop D. Both kinetic parameters, k_f and k_b are comparable to those of WT, suggesting that the mutation does not alter the ligand exchange kinetics. On the other hand, the pK_H value is higher in K72A variant than in WT, suggesting that the mutation modifies the environment of the trigger group.

Reduction Potentials. Reduction potentials are a good probe of the mutational effects on heme environment. Since parameters for the alkaline transition suggest an altered heme environment in K72A, we wanted to explicitly examine the effects of the mutation on redox properties of the heme. To better understand the role of loop D dynamics and its with other regions in the protein, G41S and Y48H cyt *c* variants were also studied. Reduction potentials were obtained from ferricyanide titrations (Figure 4.11), as some mediators interfered with the monitored electronic absorption range (Figure 4.12). Furthermore, signs of interactions with other chemical mediators were observed in spectroelectrochemical titrations for some of the variants as the titration profiles deviated from a two-state model for the electrochemical titration of the ferric protein to ferrous protein (Figure 4.13).

Table 4.4. Alkaline Transition Parameters for the Variants of Cyt *c*

Variant	pK_{app}[a]	pK_H	k_f (s^{-1})	k_b (s^{-1})	pK_C
			Horse Heart		
WT	9.27 ± 0.01	11.7 ± 0.1	7.8 ± 0.4	0.026 ± 0.004	-2.48 ± 0.07
K72A	9.65 ± 0.05	12.2 ± 0.1	7.3 ± 0.9	0.021 ± 0.006	-2.55 ± 0.10
			Human		
WT[b]	9.3 ± 0.9 (9.54 ± 0.03)[e]	12.0 ± 0.4[c]	17 ± 13[c]	0.034 ± 0.060[d] (0.018 ± 0.002)[e]	-2.70 ± 0.78
K72A[e]	10.0 ± 0.1	>12	<WT	0.019 ± 0.001	>-2.70
			yeast		
WT[f]	8.70 ± 0.02	11.7 ± 0.2	48 ±2	0.035 ± 0.001	-3.14 ± 0.05
WT[g]	7.95 ± 0.02	--	--	--	--
WT[h]	8.6 ± 0.2	11.0 ± 0.1	8.5 ±0.3	0.035 ± 0.001	-2.34 ± 0.02
K72A[i]	8.8 ± 0.1	11.5 ± 0.1	41.0 ±4.4	0.080 ± 0.015	-2.71 ± 0.22

Table 4.4. Footnotes

[a]For the fitting of k_{obs} vs pH, pK_H+pK_C was fixed as the pK_{app} value (Table 4.3) determined from the equilibrium pH titration measurements.

[b]pK_c values and pK_{app} for WT were calculated based upon the reported values from refs. [46] and [47], unless noted otherwise.

[c]From ref. [46].

[d]From ref. [47].

[e]From ref. [19], the k_b value was set as the average value of k_{obs2} values from pH-jump experiments at low pH. k_f is k_{obs2} reported in the reference, tentatively attributed to the Lys73-ligated alkaline conformer. pK_H and k_f values were determined visually, as the data were not fit due to lack of data points and k_{obs} did not plateau at high pH conditions.

[f]From ref. [45], contains tmK72 and a background C102T mutation.

[g]From ref. [13], contains K72 and a background C102T mutation, expressed in *E. coli*.

[h]From refs. [48] and [45], contains C102T and TmK72

[i]From ref. [7], contains a background C102S mutation.

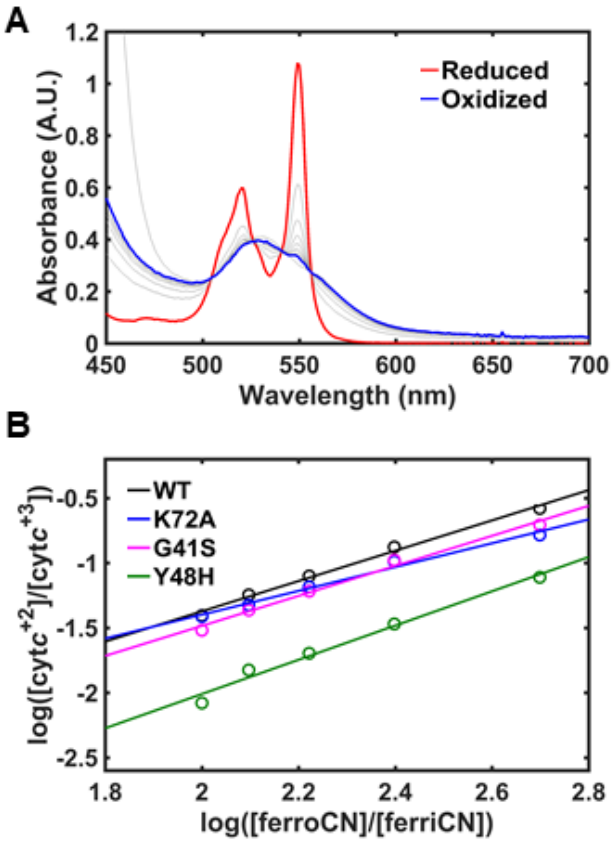

Figure 4.11. (A) Representative spectra from ferricyanide titrations; shown here are results for G41S. (B) Representative log-log plot of WT (black), K72A (blue), G41S (pink), and Y48H (green) variants of horse heart cyt *c* in a 100 mM sodium phosphate buffer at pH 7.4.

Figure 4.12. Electronic absorption spectra of mediators used in spectroelectrochemical experiments. Spectra of the mediators were obtained to check for possible contributions to the electronic absorption spectra in the 500 to 700 nm range Stock samples containing mediators were diluted using a 100 mM sodium phosphate buffer at pH 7.4 and absorption spectra measured at 22 ± 2 °C. Shown are the mediators with (A) positive reductive potentials: p-benzoquinone (M1, black line, 367 µM), TMPD (M2, red line, 185 µM), 1,2-naphthoquinone (M3, blue line, 19 µM), phenazine methosulfate (M4, green line, 127 µM), and gallocyanine (M5, purple line, 37 µM), and (B) with negative reduction potentials: indigo trisulfate (M6, red line, 64 µM), 2-OH-1,4-naphtoquinone (M7, blue line, 14x dilution of stock), anthraquinone 2-sulfonate (M8, green line, 714 µM), benzyl viologen (M9, black line, 1.43 mM), and methyl viologen (M9, purple line, 1.43 mM). Mediator stock solutions were prepared by Dr. Fangfang Zhong.

A

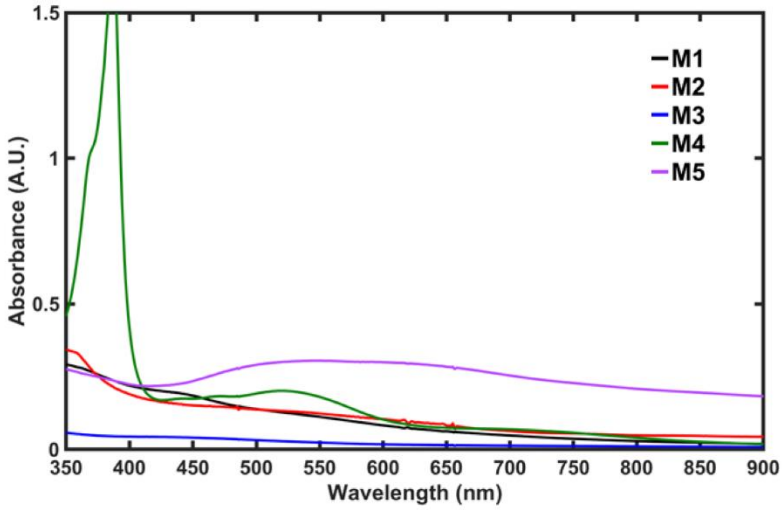
Absorbance (A.U.)
Wavelength (nm)
M1
M2
M3
M4
M5

B

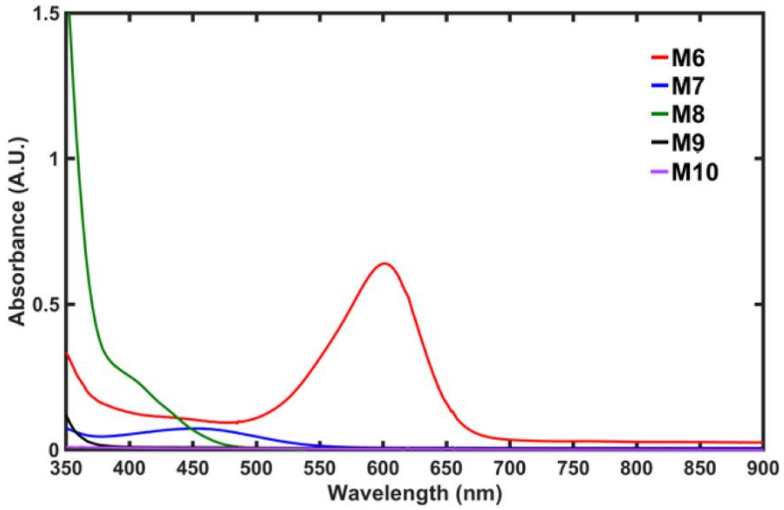
Absorbance (A.U.)
Wavelength (nm)
M6
M7
M8
M9
M10

Figure 4.13. Electronic absorption spectra for Y48H are shown at various potentials in (A) reductive and (B) oxidative titration directions in 100 mM sodium phosphate buffer at pH 7.4 and 22 ± 2 °C. Samples contained 75 μM protein with 75 μM of mediators (TMPD, 1,2-naphthoquinone, phenazine methosulfate, gallocyanine, indigo trisulfate, and 2-OH-1,4-naphtoquinone).[49, 50] Spectral measurements were taken from 350 mV to -350 mV applied potential (versus GCE) for the reductive titration, and -300 to 300 mV for the oxidative titration. For both electrochemical directions, a shift in the baseline and possible interferences from electrochemical mediators are observed (see Figure 4.12). (C) Plot showing the changes in percent reduced based on the absorbance at 550 nm versus potential (versus GCE) are plotted with the attempted fits for the reductive (blue) and oxidative (red) directions. Fits of the data yielded reductive potential of $E°$ = 240.3 ± 13.3 (versus SHE) and n = 0.60 ± 0.14, and oxidative potential of $E°$ = 310.6 ± 11.2 mV (versus SHE) and n = 0.39 ± 0.07, respectively. Since the data did not fit well to the two-species model, and substantial contributions from mediators to the electronic absorption spectra at 550 nm were observed, ferricyanide titrations were chosen to obtain the reduction potential of the Y48H as well as other cyt *c* variants.

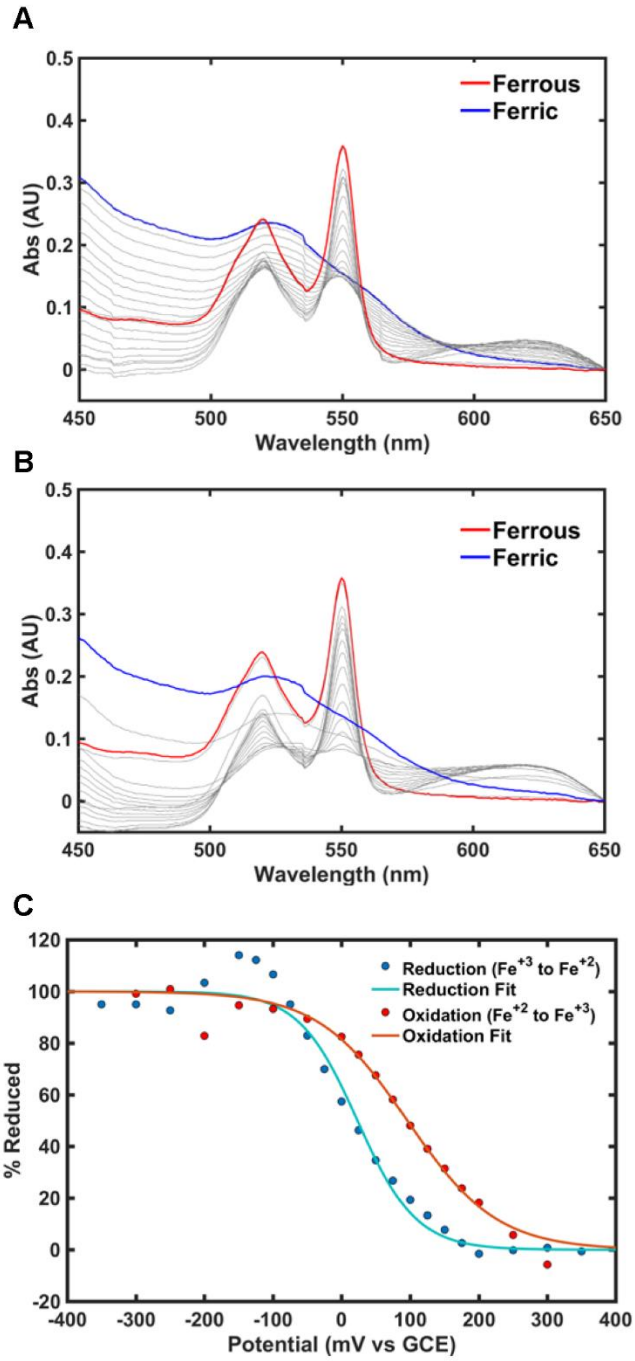
A
Ferrous
Ferric
Abs (AU)
Wavelength (nm)
B
Ferrous
Ferric
Abs (AU)
Wavelength (nm)
C
Reduction (Fe+3 to Fe+2)
Reduction Fit
Oxidation (Fe+2 to Fe+3)
Oxidation Fit
% Reduced
Potential (mV vs GCE)

At pH 7.4, the reduction potential for K72A is within error of that for WT and G41S (Table 4.5). In comparison, the reduction potential of Y48H is lower than those of the three other cyt *c* proteins (Table 4.5).

For both G41S and Y48H, there are sizeable populations of the Lys-ligated heme species at pH 7.4 (see Table 3.5). Since the reduction potential of the Lys-ligated *iso-1* yeast cyt *c* at alkaline pH is in the negative range (-230 mV vs SHE at pH 10.3),[51] the presence of such species would lower the overall observed reduction potential of the mixture.[52] However, the higher percentage of the Lys-ligated species does not appear to correlate with a greater decrease in reduction potentials. For G41S and Y48H at pH 7.4, the decrease in reduction potentials were minor compared to the population of the Lys-ligated species (Tables 4.3 and 4.5). Further, reduction potentials of K72A and G41S are within error of each other, despite clear differences in the population of the Lys-ligated species at pH 7.4 (Table 4.3 and 3.5). Thus, it is unlikely that the increased population of the Lys-ligated species is the only reason for the observed changes in potentials. Changes in the exposure of the heme upon mutations would alter the reduction potential of the heme iron. Stability of loop D is lower in G41S and Y48H (Figure 3.15B) compared to the stability of loop D in K72A and WT (Figure 4.9B). This difference suggests that for G41S and Y48H, loop D is clearly perturbed. Although loop D in K72A has the same stability as loop D in WT, differences in pK_H values for K72A and WT suggests the K72A mutation still modifies the properties of loop D. Yet, the reduction potentials of WT and K72A are similar. Since residue 72 is far away from the heme edge, it may be that the heme edge exposure is unaffected whether a bulky Lys is present in WT and K72A. In contrast, a more dynamic loop D in G41S and Y48H could increase exposure of the heme edge.

Table 4.5. Reduction Potentials of Variants of Cyt *c* and its Biological Redox Partners

Variants	*E*° (mV)
Horse Heart cyt c variants	
WT	242 ± 3[a], 255[b]
K72A	235 ± 7[a]
G41S	236 ± 3[a]
Y48H	207 ± 11[a]
Human cyt c variants	
WT	226 ± 3[c]
G41S	227 ± 4[c]
Cyt c partners	
CcO (Cu_A)	285 ± 3[d]
Cytbc_1 (c_1)	260 ± 1[e]
C*c*P (Trp^+)	650[f]
C*c*P (Cmpd I)	740[g]
C*c*P (Cmpd II)	1090[h]
Cyt c from other species	
WT (rat)	261[i], 259[j]
WT (yeast, TmK72)	280 ± 2[k], 290[l], 282 ± 2[m]
WT (yeast, K72)	283 ± 2[m]
WT (bovine)	263[n]
WT (spinach)	268[o]
WT (cucumber)	270[o]
WT (sweet potato)	274[o]

Table 4.5. Footnotes

[a]This work, ferricyanide titrations at pH 7.4.

[b]From ref. [15], vs NHE at pH 7.0 and 25 °C for horse heart cyt *c* with cyclic voltammetry.

[c]From ref. [53], from ascorbate reduction in a 50 mM citrate buffer at pH 6.5.

[d]From ref. [54], vs. NHE at pH 7.0 and 25 °C for beef heart CcO.

[e]From ref. [55], flash and dark redox titrations for *R. sphaeroides* at pH 7.0.

[f]From refs. [56] and [57].

[g]From ref. [56], vs. SHE at pH 6.1 and 4 °C for baker's yeast.

[h]From ref. [58], calculated from kinetic studies at pH 5.26 and 25 °C, μ = 0.1 M for baker's yeast.

[i]From ref. [11], Tm K72 vs SHE at pH 7.0.

[j]From ref. [12], titration with N,N,N',N'-tetramethylpheylenediamene, expressed in yeast, contains TmK72.

[k]From ref. [11].

[l]From ref. [45], vs. SHE in sodium phosphate buffer at μ = 0.1 M and pH 6.0 at 25 °C.

[m]From ref. [13], vs SHE from CV measurements at neutral pH.

[n]From ref. [4], vs SHE at pH 6.9.

[o]From ref. [14], vs SCE at 25 °C, pH 7.5 for WT spinach, pH 7.5 for WT cucumber, and pH 7.6 for WT sweet potato.

Differences in reduction potentials of the variants suggest that the location perturbation in loop D is important; unless the perturbation occurs near the heme edge, the reduction potential may not be as affected. Since the Y48H mutation modifies the region near the heme edge and G41S does not, reduction potential of Y48H is lower than that in the G41S variant and lower than those of WT and K72A.

ET Kinetics. Many biological ET reactions involving heme proteins occur at the heme edge, which is generally surrounded by the polypeptide in cyt *c* and its biological partners.[59-62] We decided to obtain ESE rate constants, k_{ESE}, from bimolecular rate constants, k_{12}, to evaluate whether the heme edge is affected by the mutations. Since the $Co(phen)_3^{3+}$ interaction site (Lys27) [63] is along the exposed heme edge and is not near the residue positions 41, 48, or 72(radius of $Co(phen)_3^{3+}$ is ~ 7 Å,[34, 64]and αC- αC distances between Lys27 and Gly41,Tyr48, or Lys72 is 15, 12, and 19Å, respectively, based on the X-ray crystal structure of horse heart WT cyt *c*[26]), any differences in ET kinetics would report on differences in heme edge exposure and not on alterations of $Co(phen)_3^{3+}$-protein interactions.

Kinetic traces of all the variants were fit to a monoexponential function. Bimolecular rate constants, k_{12} at both low (μ = 0.11 M) and high (μ = 1.0 M) ionic concentrations confirmed that high ionic conditions screened electrostatic effects (Table 4.6 and Figure 4.14). While K72A has the similar k_{12} rate constant at pH 7.4 at high ionic conditions compared to that of WT, both G41S and Y48H have larger values of k_{12} (Figure 4.14).

Table 4.6. Kinetic and Thermodynamic Parameters for ET of Variants of Cyt *c* to $Co(phen)_3^{3+}$

Variants	k_{12} (x10^3 $M^{-1}s^{-1}$)	k_{ESE} (x10^3 $M^{-1}s^{-1}$)[a]	K_{12}[b]
	(μ = 0.1 M)		
WT	2.50 ± 0.19	0.953 ± 0.18	154 ± 18
K72A	2.90 ± 0.15	0.979 ± 0.29	203 ± 56
G41S	11.7 ± 2.1	16.4 ± 6.3	195 ± 23
Y48H	63.0 ± 10	155 ± 79	609 ± 240
	(μ = 1.0 M)		
WT	6.79 ± 0.44	1.64 ± 0.29	--
K72A	6.87 ± 0.23	1.28 ± 0.36	--
G41S	12.8 ± 0.99	4.61 ± 0.89	--
Y48H	85.0 ± 8.2	65.9 ± 29	--

[a]Calculated using eq 4.2 and $k_{22} = 4.5 \times 10^1$ $M^{-1}s^{-1}$ for μ = 0.1 M at 25 °C or $k_{22} = 1.93 \times 10^2$ $M^{-1}s^{-1}$ for μ = 1.0 M at 25 °C, from the calculated k_o = 3.45 $M^{-1}s^{-1}$ at μ = 0 using eq 4.4.

[b]Calculated using eq 4.3, with $E°$ = 370 mV for $Co(phen)_3^{3+}$, with T = 22 °C.

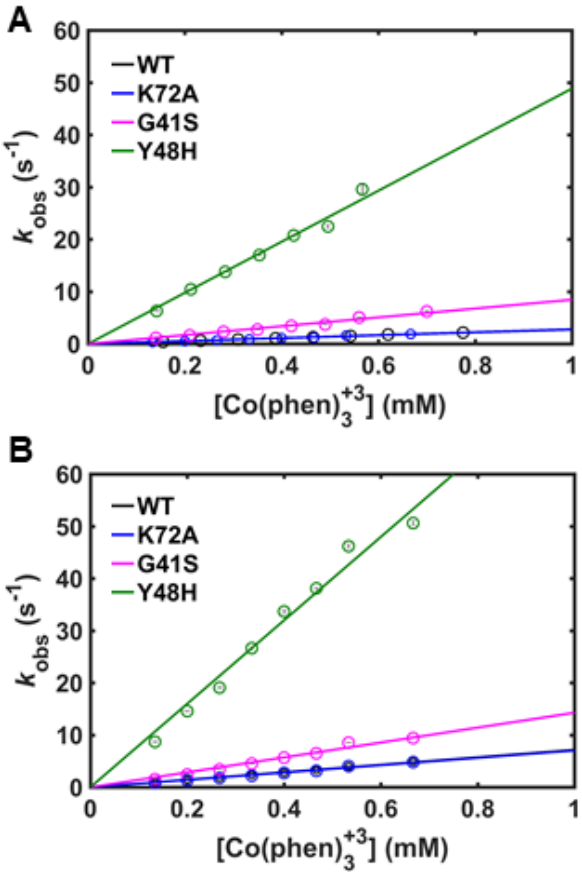

Figure 4.14. Representative plots of showing the dependence of k_{obs} values on $Co(phen)_3^{3+}$ concentration for WT (black), K72A (blue), G41S (pink), and Y48H (green) variants of horse heart cyt *c* at pH 7.4 and 22 ± 2°C. The final protein concentrations were between 40 and 55 μM, and in a 50 mM sodium phosphate buffer with total ionic concentrations of 0.11 M (A) or 1.0 M (B), adjusted with addition of NaCl as needed.

The k_{ESE} rate constant was calculated from eq 4.2 using the experimental k_{12} rate constant and ESE rate constant for $Co(phen)_3^{3+}$ calculated for desired ionic conditions. G41S and Y48H also have larger k_{ESE} rate constants than those of WT and K72A (Table 4.6). Of the series described in this chapter, the Y48H variant has the largest k_{ESE} value. Although both mutations G41S and Y48H affect loop C, if loop D is altered differently depending on the location of the perturbation in loop C, the degree of heme exposure maybe different, and distinct k_{ESE} values are observed. With a more exposed heme edge, Y48H may be primed for a faster ET process. Because loop D also perturbed in G41S and its heme edge is more exposed than that of WT or K72A, its ET kinetics are faster than those of the two counterparts.

Biological ET Properties with CcO. Previous RR experiments have suggested that conformational rearrangement in the cyt *c* heme crevice, which also alters the reduction potential, controls the ET between cyt *c* and CcO.[65] We thus hypothesized that our cyt *c* variants that contain local structural perturbations and altered ET properties would also affect the biological ET process between cyt *c* and CcO. To test this hypothesis, we measured the oxygen reduction activity of CcO. Measurements of ET to CcO at pH 7.4 show that V_{max} is largely unchanged for the variants (Figure 4.15 and Table 4.7). The fitted intercept from the Lineweaver-Burke plot have large error bars, propagates to similarly large errors for the derived K_M value. However, the error bars in the fitted slope are lower and differences are observed between the variants (Table 4.7). The slope decreases in Y48H, increases for K72A, and slope trends to decrease for G41S compared to that of WT (Table 4.7). Because the slope from the Lineweaver-Burke plot is proportional to the K_M value, we could more confidently conclude about differences in K_M values.

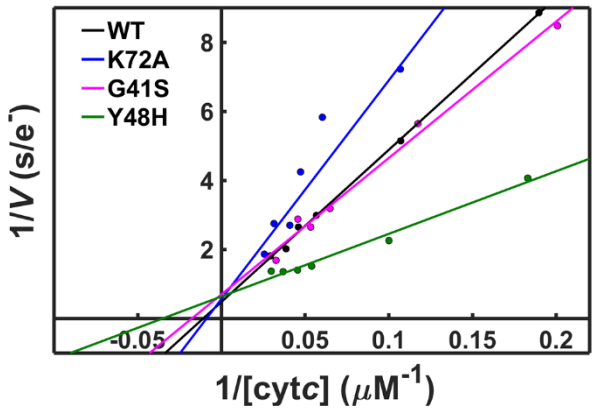

Figure 4.15. Representative Lineweaver-Burke plot of O_2 reduction activity assays of bovine CcO in the presence of WT (black), K72A (red), G41S (pink), or Y48H (green) variants of horse heart cyt *c*. Assays were performed in a 50 mM TrisHCl buffer at pH 7.5 containing 100 mM NaCl, 0.02% DDM (*v*/*v*), and 5 mM EDTA, at 20 ± 2 °C.

Table 4.7. Parameters Associated with CcO-catalyzed O_2 Reduction Measurements

Variant	Slope[a]	Intercept[a]	V_{max} (s^{-1})	K_M (μM)
WT	37.8 ± 4.1	0.6 ± 0.4	1.7 ± 1.2	64.3 ± 45.5
K72A	92.7 ± 19.6	0.9 ± 0.5	1.1 ± 0.7	105 ± 65.0
G41S	25.6 ± 9.3	0.8 ± 0.3	1.2 ± 0.4	31.5 ± 15.5
Y48H	16.6 ± 3.0	0.8 ± 0.3	1.2 ± 0.5	19.9 ± 8.6

[a]Slope = K_M/V_{max} and intercept = $1/V_{max}$ using Lineweaver-Burke Plot.

If we assume that the breakdown of the enzyme-substrate (ES) complex is much slower than binding of the substrate to the enzyme (in our case, CcO-cyt *c* breakdown is slower than CcO-cyt *c* formation), then K_M is a measure of the strength/affinity of the ES complex.[66] Our CcO activity data show that the K_M parameters are affected by the mutations. Y48H shows a clear decrease in the K_M value (Table 4.7). G41S may have decreased K_M values while K72A may have increased K_M value compared to that of WT (Table 4.7). Although our derived K_M value for WT is higher than that of the reported value of 18 μM at higher ionic conditions (200 mM NaCl),[67] it is still within the similar order of magnitude. However, large error bars for WT and K72A make it difficult to quantify these changes in the K_M values.

Interactions with CL. Since Lys72 is one of the residues suggested to be involved in interaction with CL at low CL concentrations,[68] we wanted to test whether the binding affinity of the K72A cyt *c* variant to CL changed. Binding affinity of K72A is unaltered in the presence of CL-containing vesicles (50% CL), and the protein was fully bound to the vesicles by 20 to 1 (total lipid to protein) ratio (Figure 4.16A). This is similar to the recent observations studies where K72A was bound to CL-containing liposomes, although the CL content was not specified in that work.[69] Further, electronic absorption spectrum for the CL-bound K72A is comparable to the spectrum of the CL-bound WT (Figure 4.16B), suggesting that CL-bound K72A is similar to the CL-bound WT at high CL conditions.

Peroxidase Activity. At pH 7.4, K72A shows a slightly enhanced intrinsic peroxidase activity than that of WT (Figure 4.17, top and Table 4.8), suggesting some increase in the intrinsic dynamics of loop D. However, the observed increase in the intrinsic peroxidase activity is minor (Table 4.8).

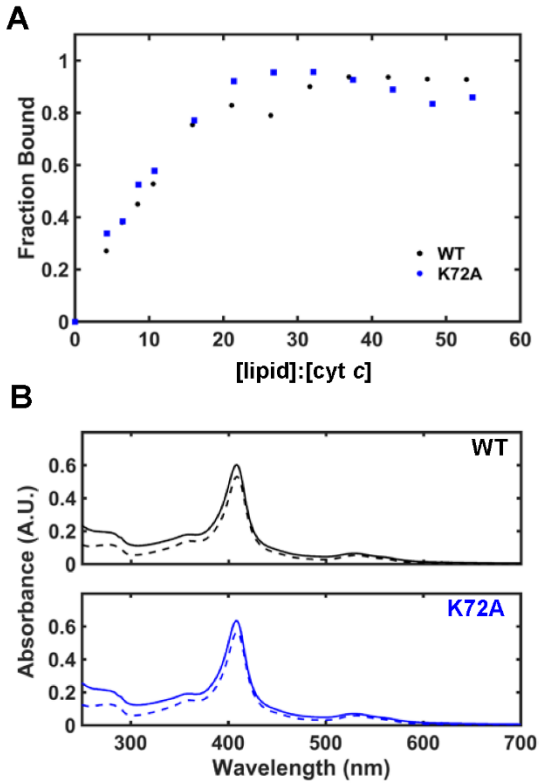

Figure 4.16. (A) A representative plot of vesicle binding assays for the WT and K72A variants of horse heart cyt *c* ([cyt *c*] = 5 μM) with lipid vesicles containing 50% CL and 50% PC, in a 25 mM HEPES + 0.1 mM DTPA buffer at pH 7.4 and 22 ± 2 ºC. Shown are the fractions of the bound protein versus the ratio of the total lipid concentration to protein concentration for WT (black) and K72A (blue). (B) Electronic absorption spectra of variants in the native (dashed line) and CL- bound (solid line) forms for WT (black) and K72A (blue). All samples were in a 25 mM HEPES + 0.1 mM DTPA buffer at pH 7.4. Lipid bound cyt *c* contained were in 196 to 200 times molar excess of lipids to the final protein concentration (5 μM).

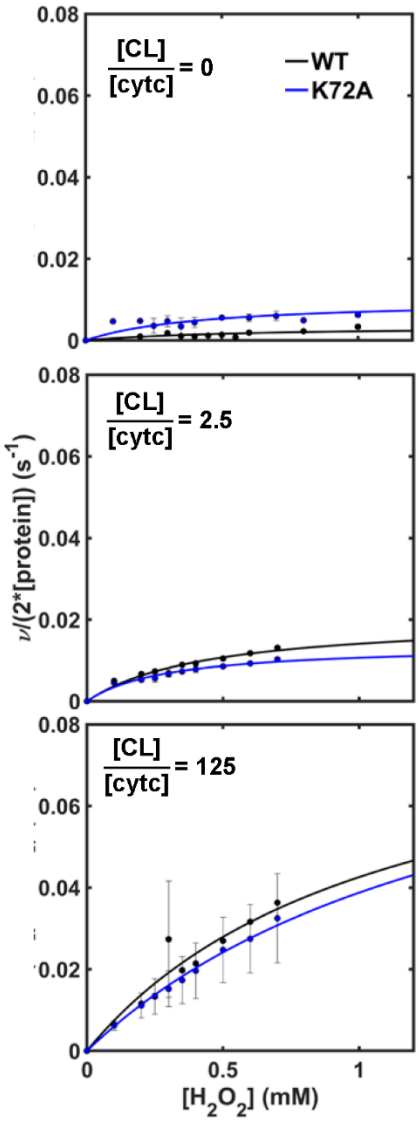

Figure 4.17. Representative Michaelis-Menten plots for intrinsic (top) and CL-bound proteins at low(middle) and high (bottom) CL to protein ratio for WT (black) and K72A (blue) variants of horse heart cyt *c* in a 25 mM HEPES + 0.1 mM DTPA buffer at pH 7.4 and 22 ± 2 ºC. Each sample contained 0.2 to 1 mM H_2O_2. 1 to 2 μM protein, 250 μM ABTS, and 250-fold molar excess of total lipid (125-fold molar excess CL) for high ratio samples and 5-fold molar excess of total lipid (2.5-fold molar excess CL) for low ratio samples.

Table 4.8. Peroxidase Activity of Variants of Horse Heart Cyt *c*[a]

Variant	k_{cat}^{H2O2} (s^{-1})	K_M^{H2O2} (mM)
	Intrinsic	
WT	0.0034 ± 0.0004	0.45 ± 0.05
K72A	0.010 ± 0.001	0.43 ± 0.2
	Low CL[b]	
WT	0.019 ± 0.001	0.40 ± 0.06
K72A	0.013 ± 0.0001	0.29 ± 0.03
	High CL[c]	
WT	0.075 ± 0.007	0.94 ± 0.09
K72A	0.080 ± 0.02	1.25 ± 0.5

[a]Measured at pH 7.4 and 22 ± 2 °C, with 0.2 mM ABTS.

[b][protein] to CL in 1:2.5 ratio.

[c][protein] to CL in 1:125 ratio.

At low CL concentrations where the CL to protein ratio is at 2.5 to 1, the protein is a mixture of the CL-bound and unbound species, and only ~30 to 40% of the protein is bound to CL-containing lipid vesicles (Figure 4.16A). Under these conditions, enhancement in the peroxidase activity would be from the enhancement of the activity in the CL-bound state, while the rest of the unbound protein (~60 to 70%) will have low peroxidase activity. True to this expectation, some enhancement in intrinsic peroxidase activity is observed with both WT and K72A (Figure 4.17, middle and Table 4.8).

Peroxidase activity parameters are comparable between WT and K72A cyt *c* at both low and high CL conditions (Figure 4.17, bottom, and Table 4.8). Previous studies suggest that CL-induced unfolding event involves changes in loop D and C-terminal helix movement.[35, 39] The presence of the K72A mutation does not seem to have a noticeable difference on activity. Consistent with unfolding measurements that revealed comparable global stabilities of WT and K72A, both variants behave similarly in the presence of denaturants at pH 7.4. These results, in combination of results observed for G41S and Y48H in Chapter 3, implies that other local factors besides stability of loop D determine the extent of protein unfolding in the presence of CL

Discussion

Differences in Loop D Connectivity Tunes the Stability of Cyt *c*. Even in highly conserved loop D, subtle differences are observed loop D-dependent functions (such as alkaline transition and ET).[37, 41] Comparison among WT cyt *c* from human, horse heart, and yeast shows that loop D stability of yeast WT cyt *c* is much lower than that of both human and horse heart cyt *c*.[37, 41, 42, 70] Simply mimicking the residues found in a species does not necessarily translate the properties of loop D from one organism to another.

Studies introducing human-like mutations, A81I and G83V, to yeast cyt *c* showed that mimicking sequences did not necessarily make the protein more stable than the yeast WT protein, despite stabilization of the Met-ligated state.[71] Studies with I81A, V83G, and I81A/V83G variants of human cyt *c* suggested that combination of sequence variation may be important in affecting protein stability and alkaline transition parameters that also are dependent on loop D.[46] This difference observed between human and yeast cyt *c* variants suggested that the identity of the residues in loop D alone does not determine the kinetic and thermodynamic properties of the loop. Differential response may stem from how loop D is packed, and the type of contacts made with other parts of the protein. It is difficult to predict how loop D differs between species just by comparing the WT proteins due to high conservation of loop D. We can, however, amplify the differences in loop D by introducing similar non-disruptive mutations and observe how same perturbations are tolerated across species.

K72A mutation in horse heart cyt *c* does not alter the global stability of the protein as was observed with the human K72A cyt *c* (Table 4.2). The same mutation in yeast cyt *c*, however, decreases the m_D value and the overall stability of the protein (Table 4.2). Differential effects in m_D parameter with the K72A mutation in yeast, human, and horse heart cyt *c* compared to respective WT proteins suggests that loop D responds differently in yeast cyt *c* than in human or horse cyt *c* with the K72A mutation. Since m_D can be used to approximate the solvent exposure in the denatured state,[72] this parameter provides clues to the solvent accessibility of the protein in the native state. WT yeast cyt *c* contains trimethylated K72 (TmK72) when expressed in yeast systems, and have been shown from thermal denaturation studies that the trimethylation of Lys72 has no effect on the stability

of the protein.[13] Studies comparing yeast K72A and TmK72 cyt *c* have suggested that TmK72 forms contacts with other residues and provide steric rigidity to loop D, and promote native packing and Met80-ligation.[13, 18] Perhaps then, sequence variations that are near loop D, such as in loop C, could also alter the properties of loop D.

In yeast WT cyt *c*, sequences are different to human WT cyt *c* in the region of loop C that forms the bulk of the loops C and D interface. Despite the location of the sequence variation, the fold is optimized, and residues in the loop C (residues 48 to 57) that are in contact with loop D, are within HB and vdW distances at similar distances like that of human cyt *c* (compare Figures 4.18A and B). Contact maps comparing yeast WT (TmK72) and K72A cyt *c* show overall decrease in the distance of contacts that are within vdW and HB distances (Figures 4.18B and D). Further, more variations in the location and number of contacts that form between loop C and D connectivity are observed with the K72A mutation in yeast cyt *c* (Figures 4.18B and D) than in human cyt *c* (Figures 4.18A and C). This rearrangement is most likely sub-optimal in yeast cyt *c*, as the K72A mutation increases the local dynamics of loop D in yeast cyt *c*,[13, 18] and alters the global stability of the protein.

In horse heart cyt *c*, fewer residues in loop C are varied compared to the human cyt *c*. MD simulations suggest that between human and horse heart cyt *c*, a large portion of the contacts are similar even with the K72A mutation (Figure 4.5). Perhaps, mutational effects of having K72A in loop D are muted in human and horse heart cyt *c*, because many of the contacts between loops C and D that are present in WT are preserved.

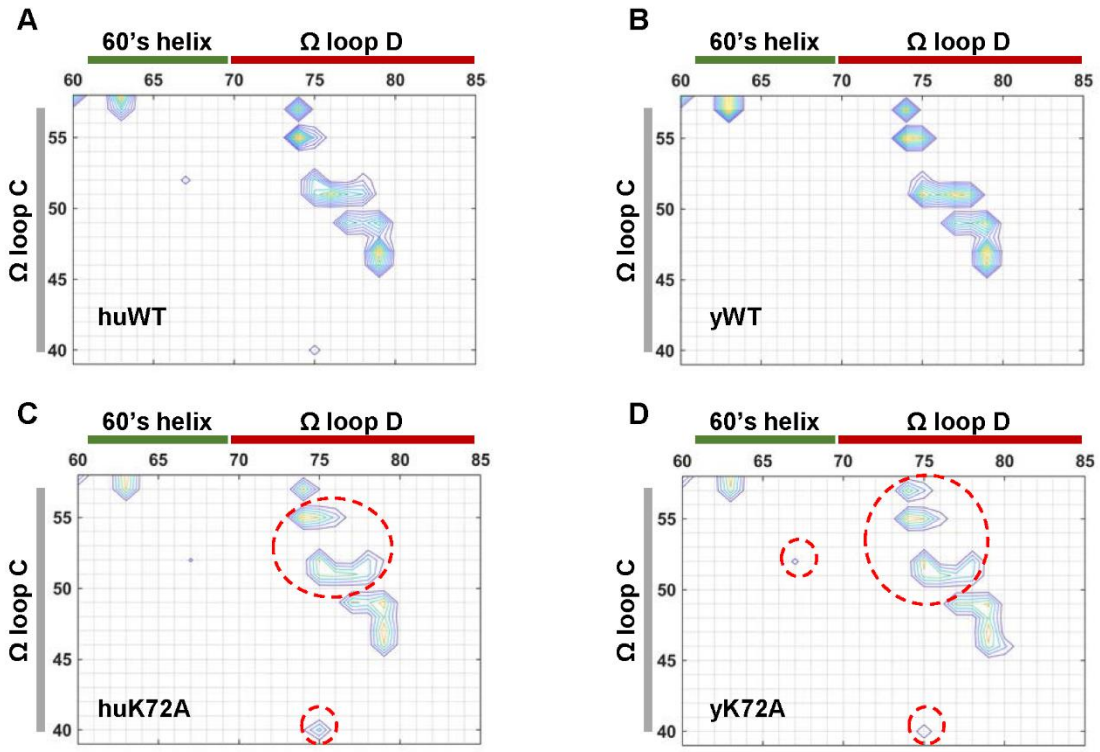

Figure 4.18. Distance contact maps for contacts within 5 Å from X-ray crystal structures of (A) human WT cyt *c* (PDB ID 3ZCF),[25] (B) yeast WT cyt *c* (PDB ID 2YCC),[27] (C) human K72A cyt *c* (PDB ID 5TY3),[19] and (D) yeast K72A cyt *c* (PDB ID 4MU8, contains C102S mutations, expressed in *E. coli*).[18] Regions that change with the mutation compared to WT of each respective species are circled (red, dotted line).

Variations in Loop D Contacts and Differential Response in Alkaline Transition. Do these differences in contacts have any influence on the conformational dynamics of the loop? Alkaline transition is one of the functions in cyt *c* that is dependent on both connectivity and dynamics of loop D, as switching between Met80 and innate Lys ligands (Lys79 and 73 in horse heart and human cyt *c*)[13,16] requires breaking contacts within and outside of loop D followed by a conformational loop D rearrangement.[73, 74] K72A mutation in yeast cyt *c* does not alter the apparent pK_a of the transition compared to that of WT that contains TmK72.[13] The apparent pK_H of the trigger group and the forward kinetic rate, k_f, are within reported ranges for TmK72-containing WT cyt *c* (Table 4.4).

This suggests that the variations observed in the interloop contacts in yeast cyt *c* do not affect the formation of the Lys-ligated species. The reverse kinetic rate, k_b, is increased in K72A relative to WT (Table 4.4), and this has been correlated to lowering the energetic barrier for opening and closing the heme crevice.[75] On the other hand, similar mutation in loop D affects horse heart cyt *c* differently. The apparent pK_a and pK_H values both increase in K72A relative to those in WT, while both k_f and k_b parameters for the Lys-coordinated species remain comparable to WT (Table 4.4). In human K72A cyt *c*, pK_H is within error of WT.[19] Even with the same loop D perturbations, differences in pK_a, as well as pK_H, are observed between human, horse heart, and yeast cyt *c*, but not in the kinetic rate parameters (particularly k_f). Trigger group is sensitive to subtle differences in contacts at and around loop D; otherwise, pK_H would have been similar for K72A variants of human, horse heart, and yeast cyt *c*.

Conserved Loop D but Different Local Dynamics and Packing. In the Met-ligated state, intrinsic peroxidase activity is rate-limited by the opening of the heme crevice,[76] which

also involves dissociation of Met80 from the ferric iron. K72A mutation enhanced the peroxidase activity of the horse heart cyt *c* protein, suggesting easier access to the heme by the exogenous ROS. Similar increase in intrinsic peroxidase activity was also observed with the human and yeast K72A cyt *c* variants, with the greater enhancement in intrinsic peroxidase activity being observed with a less sterically hindered yeast K72A cyt *c*.[77] Comparing the X-ray crystal structures of the human and yeast K72A cyt *c* provides clues for the differences in rate enhancements in yeast, human, and horse heart cyt *c* with the same K72A mutations. Calculations of the void volume and the vdW volume in the X-ray crystal structures show that, the K72A mutation in yeast cyt *c* increases the void volume in respect to the WT protein with the TmK72 (Table 4.9). In contrast, human K72A cyt *c* shows a decrease in void volume (Table 4.9). These differences suggest that the nature of the polypeptide chain packing and the heme pocket volume is different between the species, and the polypeptide packs more tightly in human cyt *c* than in yeast cyt *c* with similar mutations. Although the X-ray crystal structure of horse heart K72A cyt *c* is not available, it is likely that the changes to the heme pocket volume (and thus heme solvent exposure and accessibility) and polypeptide chain packing are more comparable with human K72A cyt *c* than with yeast K72A cyt *c*. However, differences are still observed between K72A variants of human and horse heart cyt *c* variants.

In horse heart cyt *c*, k_{cat} value for the intrinsic peroxidase activity is an order of magnitude higher with the K72A mutation, compared to the WT. In human cyt *c*, K72A mutation results in a 2-fold increase in k_{cat} compared to that of WT,[19] suggesting that small differences in and around loop D are still present between similar human and horse heart cyt *c*.

Table 4.9. Volume Calculations for the X-ray Crystal Structures of Cyt *c*[a].

Variant	Total Vol (Å^3)	Void Vol (Å^3)	vdW Vol (Å^3)	Packing Density
		Horse Heart		
WT[b]	13858.32	3249.43	10608.88	0.77
		Human		
WT[c]	13811.41	3253.99	10557.42	0.76
K72A[d]	13613.95	3133.15	10480.80	0.77
		Yeast		
WT[e]	13918.23	3206.52	10711.71	0.77
K72A[f]	13939.60	3267.76	10671.85	0.77

[a]Volume calculations were obtained based on ProteinVolume,[28] using energy minimization and standard parameters with starting probe of 0.08 Å, ending probe of 0.02 Å, and surface minimum distance of 0.1 Å.

[b]Based on X-ray crystal structure (PDB ID 1HRC), from ref. [26].

[c]Based on X-ray crystal structure (PDB ID 3ZCF), from ref. [25]. Values of the calculated volumes were averaged over 4 structures.

[d]Based on X-ray crystal structure (PDB ID 5TY3), from ref. [19]. Values of the calculated volumes were averaged over 2 structures.

[e]Based on X-ray crystal structure (PDB ID 2YCC), from ref. [27]. contains TmK72.

[f]Based on X-ray crystal structure (PDB ID 4MU8), from ref. [18]. Values of the calculated volumes were averaged over 2 structures.

Loops C, D, and ET properties. Can variations in loop D contacts affect the ET kinetics? Marcus Theory explains the thermodynamics of the ET process in terms of reorganization energy (λ), electronic coupling between the donor and the acceptor (H_{DA}), and the driving force (-ΔG°) which is dependent on the differences in reduction potential between the donor and the acceptor.[78, 79] In ESE, k_{ET} is dependent on λ and/or H_{DA}, which are sensitive to changes in solvation, electronic structure, first- and second-sphere covalent and non-covalent contacts.[80, 81]K72A mutation in horse heart cyt *c* does not change the heme iron ligation, global fold, and loop D dynamics compared to those in WT. Therefore, λ and H_{DA} parameters are unaffected, and are reflected in comparable k_{ESE} values in K72A and WT.

In contrast, k_{ESE} values for G41S and Y48H are higher than that of WT or K72A. Although G41S and Y48H variants have a similar global fold as with WT and K72A, loop D properties are different in G41S and Y48H. MD simulations suggest that loops C and D contacts are perturbed with the G41S and Y48H mutations. These mutations in loop C alter the dynamics of loop D, as observed by higher k_f values for alkaline transfer. Heme is more solvent exposed in G41S and Y48H compared to in WT and K72A, as suggested by increased intrinsic peroxidase activity is higher in G41S and Y48H. A more dynamic loop D (and possibly also loop C) can alter the λ and H_{DA} parameters to increase k_{ESE}. Recent study with E66Q and Y67F horse heart cyt *c* variants have suggested that increased flexibility in Loops D minimizes λ for the second-sphere interactions between the protein and the solvent and increase k_{ET}.[8] Furthermore, DFT calculations comparing the WT and G41S variants of human cyt c have shown that the G41S mutation modified the HB to HP7, affecting the electronic structure to increase the electron density on the exposed heme edge and alter the H_{DA} parameter.[82] Both loop D dynamics and heme exposure increases in G41S

and Y48H, which would alter λ and H_{DA} parameters to favor ET, increasing k_{ESE} compared to WT and K72A.

Difference in k_{ESE} values for Y48H and G41S suggest that variations in the polypeptide sequence may influence the ET properties. Although these variants are both in loop C, the mutations G41S and Y48H are on different locations of the loop. Regions at or near loop C, residues 45 to 47, 33 to 34, and 22 to 28, have been shown to undergo dynamic movement between the ferric and ferrous states in human cyt *c*.[83] These sites are in close contact with loop D and are near the heme edge, where ET is thought to occur based on structural studies of cyt *c* bound to its biological ET partners. [59 61, 62 84, 85] Removal of Lys79 in yeast has shown increase in heme edge exposure and lowered the reduction potential,[7] suggesting that burial and packing of the residue is important in controlling the ET properties of the protein. Perhaps, k_{ESE} is different between G41S and Y48H, because Y48H is located near the solvent-exposed heme edge.

G41S, Y48H, and K72A mutations provide clues as to how perturbations in loop D may alter the respiratory pathway. These sites are far away from the main site of the contact regions with the biological redox partners cyt bc_1,[59] CcO,[61, 62] CcP,[84, 85] that mainly involves the residues in *N*- and *C*- terminal helices and the 20's loop (Figure 4.19). Variants studied in this series alter properties of loop D but not the α-helical features of the helices as evidenced by the far-UV CD spectra. Thus, it is most likely that the bimolecular contact interface is not perturbed between the cyt *c* and the biological partners. Furthermore, the bimolecular ET is dependent on both k_{ESE} and difference in the reduction potential between the donor and the acceptor. This makes it possible to isolate the changes in the ET process solely due to the changes ET properties of cyt *c*.

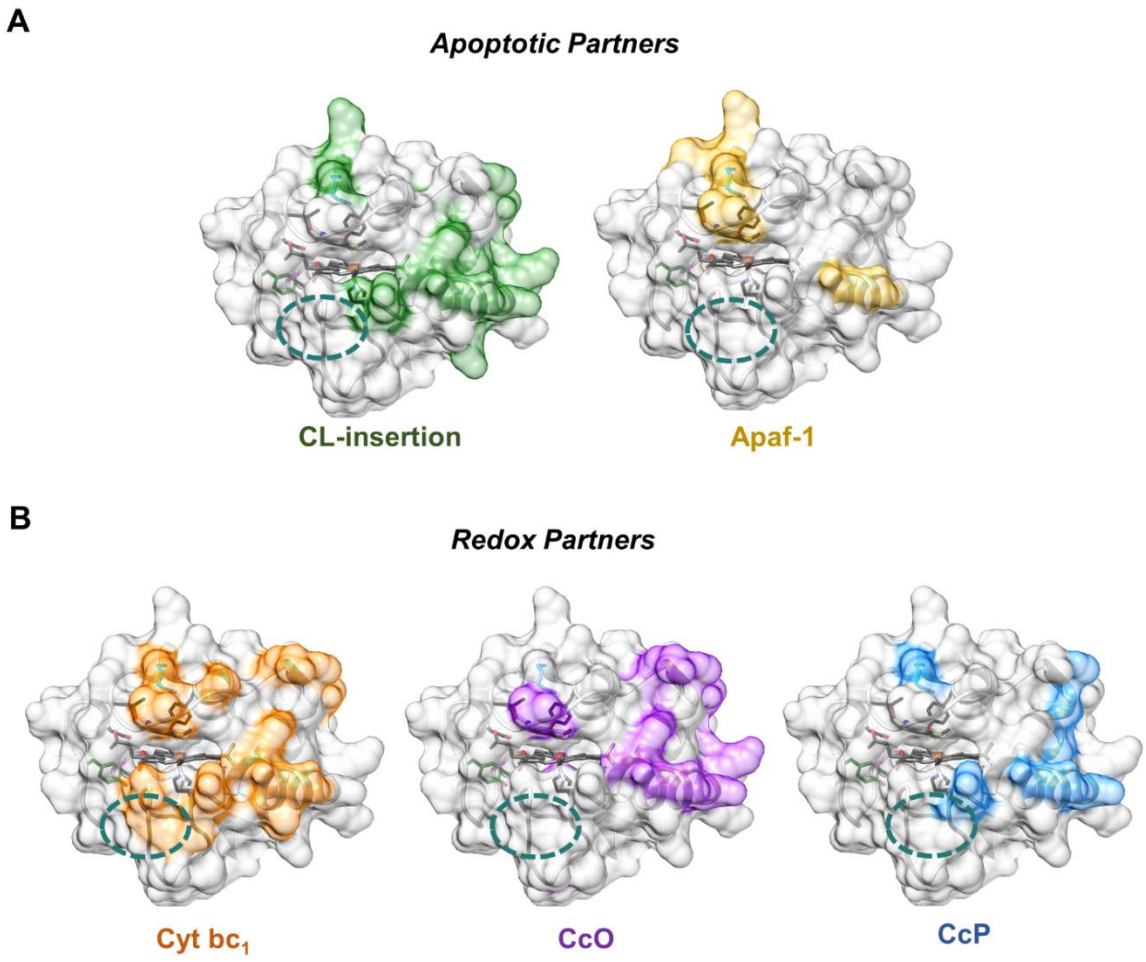

Figure 4.19. Interacting residues of cyt *c* with select biological partners are shown for (A) apoptotic partners CL (green) and Apaf-1 (specifically WD1 and 2, yellow) and (B) biological redox partners CcO (purple), Cyt bc_1(orange), and CcP(blue) are highlighted, with the $Co(phen)_3^{3+}$ sites circled (teal, dotted line).

Implications in Cellular Respiration. These changes in ET properties observed for G41S and Y48H variants would alter the respiratory pathway. In the context of the biological ET, changes in reduction potential in cyt *c* would alter the driving force (-ΔG) for ET. Decreasing the reduction potential of cyt *c* would thermodynamically disfavor the ET between Complex III and cyt *c*, while favoring the ET between cyt *c* and Complex IV (Figure 4.20). Examination of eq 4.2 suggests that a decrease in ΔE_{12} will decrease k_{ET}, while increase in ΔE_{12} will increase k_{ET}. Even if k_{ESE} of cyt *c* were not to change, decrease in reduction potential of cyt *c* will increase k_{ET} when cyt *c* donates an electron to CcO, and k_{ET} will decrease when it accepts an electron from cyt bc_1. Further, the rate of bimolecular electron transfer, k_{ET}, is dependent on k_{ESE} of both the donor and the acceptor; a fast k_{ESE} in cyt *c* would also contribute to increasing the k_{ET} of both processes. Increased k_{ESE} and a lowered reduction potential in cyt *c* could also alter the steady-state populations of ferric and ferrous proteins, introducing a possible bottleneck and reduce the efficiency of oxygen consumption. Recent steady-state CcO activity assays with the human G41S and Y48H variants show evidence of a potentially altered ETC.[47] Both variants favor the ferric state, but more so for Y48H compared to G41S, as the steady-state population of the ferric state is favored with the mutations compared to the WT,[47] depleting the steady state population of available electrons for the CcO. CcO activity with horse heart cyt *c* variants also show signs of altered CcO oxygen consumption with the variants (Table 4.7), supporting the observation made with the human cyt *c* variants. Although large error bars make it difficult to compute the catalytic efficiency, trends in the slopes obtained from the Lineweaver-Burke plot suggest that K_M may be affected with by the mutations, as V_{max} values are somewhat comparable.

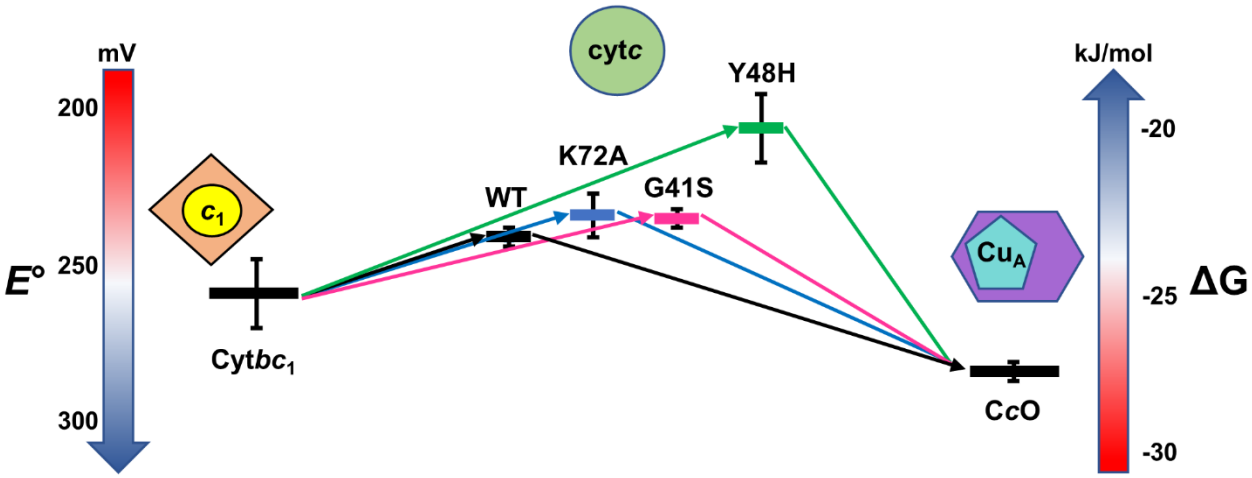

Figure 4.20. A representation of reduction potentials of cyt *c* variants and its biological redox partners, based upon Table 4.5.

Perhaps K_M values of O_2 affinity for CcO are affected, because of the decreased availability of ferrous cyt *c*. Interestingly, there are signs of an increase in K_M with the mutation of K72A, despite having WT-like reduction potential and k_{ESE}. It may be that upon complexation of cyt *c* and CcO, replacement of bulky and charged Lys to Ala eases any local conformational rearrangement upon protein-protein complexation.

Discrepancies observed with previous studies with G41S and Y48H cyt *c* among human, murine, and yeast models suggest biological ET processes may be sensitive to the innate differences in loop D.[20, 21] With the same G41S and Y48H mutations in human cyt *c*, humans do not exhibit any growth defects which would suggest problems with the respiratory pathway.[20, 21] On the other hand, signs of respiratory defects under heat stress and enhanced caspase-3 activation have been observed in yeast cellular studies.[20] Decrease in O_2 consumption have also been observed in murine cells, contrary to what was observed in humans.[20, 21] While the shift in the balance may not be drastic enough to have a detrimental effect on humans, differential effects in the reduction potential that may also affect self-exchange rates may explain the inconsistencies in respiratory defects observed in yeast,[21] murine,[21] and human[20] cellular studies with the G41S and Y48H cyt *c* mutations. Stability of cyt *c* is important for viability of the organism; G41S mutation is destabilizing in human and horse heart cyt *c*, so it may be more destabilizing in yeast cyt c. Discrepancies between murine and human cellular studies could be explained by the inherent sequence differences in mice versus human—in mice, residues 44 and 46 are Ala and Phe, respectively, compared to Pro and Tyr in human cyt *c*.[9] In particular, difference between Pro and Ala could potentially affect the loop dynamics of the region, which would also influence both the loop D and the heme edge. Our studies show that the Y48H and G41S

mutations do alter the ET thermodynamic and kinetic properties, but the magnitude of the effect depends on the organism as observed when comparing human to horse heart cyt *c* and may explain the differences between human and mice as well.

Loop D in Apoptosis. Cyt *c* is heavily involved in the steps leading up to apoptosis. Interaction with cardiolipin (CL) unfolds cyt *c*, which exposes the heme for enhanced peroxidase activity to oxidize the mitochondrial lipid membrane and allow release of cyt *c* into the cytosol to form the apoptosome with Apaf-1. In this process, loop D is directly interacting with its biological partners CL[86, 87] and Apaf-1.[88]

K72A horse heart cyt *c* showed comparable peroxidase activity to WT at both low and high CL conditions, as well as comparable CL binding affinity (Figure 4.17). This suggests that local dynamics of loop D does not influence cyt *c* interaction with CL. Although Lys72 is directly involved in the interaction with CL, no differences are observed compared to the WT.[89-91] Minor differences in loop D are not translated, perhaps because the CL-interaction at high CL content induces mass unfolding of the protein,[39, 68] and CL-cyt *c* interaction is driven by electrostatic interactions at near-neutral pH.[92] Thus, CL-cyt *c* could be insensitive to the small differences in loop D at certain experimental conditions. Sequence selection and variations may also be limited by how much the biological partners, such as CL, could tolerate the variations in surface charge of loop D, rather than the degree of loop D packing in the native state. Despite the elimination of Lys72, much of CL-induced peroxidase activity is unchanged and should not interfere with the CL-induced apoptotic peroxidase activity at high CL concentrations. This is in good agreement with calcein liposome leakage studies with K72A bound on CL-containing liposomes that have suggested Lys72 is not crucial for CL-bound cyt *c*-induced pore formation in the presence

of H_2O_2.[69] These data agrees with the hypothesis that K72A cyt *c* mutation in mice is lethal due to alterations in the WD2 domain of Apaf-1 contact rather than changes in apoptotic peroxidase activity,[88] as the contact with CL or the apoptotic peroxidase activity is comparable to that of the WT.

Conclusion

Despite the high sequence conservation of loop D in human, horse heart, and yeast cyt *c*, the responses to structural perturbations in the loop is not identical. Differences in pK_a and pK_H of the alkaline transition with the K72A variants from human, horse heart, and yeast cyt *c* suggest that the trigger group and the formation of Lys-ligated alkaline species, are sensitive to the species-specific differences around loop D. Local dynamics of loop D and heme exposure increases with K72A mutation in horse heart cyt *c* as suggested by slight increase in intrinsic peroxidase activity. Differences in how loop D adjusts to structural perturbations in human, horse heart, and yeast cyt *c* suggests that that loop D properties could also be influenced by residues outside of loop D. Comparison of K72A, G41S, and Y48H horse heart cyt *c* shows that ET properties of the protein can be modified by perturbing loops C and D. ET properties are altered in G41S and Y48H variants, and these changes may affect bimolecular ET reactions in the ETC.

References

1. Bertrand, P. *et al.* Control of the Redox Potential in C-Type Cytochromes - Importance of the Entropic Contribution. *Biochemistry* **34**, 11071-11079 (1995).
2. Battistuzzi, G., Borsari, M. & Sola, M. Redox properties of cytochrome c. *Antioxid Redox Sign* **3**, 279-291 (2001).
3. Taniguchi, V.T., Sailasuta-Scott, N., Anson, F.C. & Gray, H.B. in Pure and Applied Chemistry, Vol. 52 2275 (1980).

4. Battistuzzi, G., Borsari, M., Sola, M. & Francia, F. Redox thermodynamics of the native and alkaline forms of eukaryotic and bacterial class I cytochromes c. *Biochemistry* **36**, 16247-16258 (1997).

5. Banci, L. *et al.* Solution structure of oxidized Saccharomyces cerevisiae iso-1-cytochrome c. *Biochemistry* **36**, 8992-9001 (1997).

6. Liu, J. *et al.* Metalloproteins containing cytochrome, iron-sulfur, or copper redox centers. *Chem Rev* **114**, 4366-4469 (2014).

7. Deng, Y.L., Zhong, F.F., Alden, S.L., Hoke, K.R. & Pletneva, E.V. The K79G Mutation Reshapes the Heme Crevice and Alters Redox Properties of Cytochrome c. *Biochemistry* **57**, 5827-5840 (2018).

8. Oviedo-Rouco, S. *et al.* Electron transfer and conformational transitions of cytochrome c are modulated by the same dynamical features. *Arch Biochem Biophys* **680**, 108243 (2020).

9. Moore, G.R. & Pettigrew, G.W. *Cytochromes c : evolutionary, structural, and physicochemical aspects*. (Springer-Verlag, Berlin ; New York; 1990).

10. Zaidi, S., Hassan, M.I., Islam, A. & Ahmad, F. The role of key residues in structure, function, and stability of cytochrome-c. *Cell Mol Life Sci* **71**, 229-255 (2014).

11. Feinberg, B.A., Petro, L., Hock, G., Qin, W.Y. & Margoliash, E. Using entropies of reaction to predict changes in protein stability: tyrosine-67-phenylalanine variants of rat cytochrome c and yeast Iso-1 cytochromes c. *J Pharmaceut Biomed* **19**, 115-125 (1999).

12. Luntz, T.L., Schejter, A., Garber, E.A.E. & Margoliash, E. Structural Significance of an Internal Water Molecule Studied by Site-Directed Mutagenesis of Tyrosine-67 in Rat Cytochrome-C. *P Natl Acad Sci USA* **86**, 3524-3528 (1989).

13. Pollock, W.B.R., Rosell, F.I., Twitchett, M.B., Dumont, M.E. & Mauk, A.G. Bacterial expression of a mitochondrial cytochrome c. Trimethylation of Lys72 in yeast iso-1-cytochrome c and the alkaline conformational transition. *Biochemistry* **37**, 6124-6131 (1998).

14. Battistuzzi, G. *et al.* Redox chemistry and acid-base equilibria of mitochondrial plant cytochromes c. *Biochemistry* **38**, 5553-5562 (1999).

15. Eddowes, M.J. & Hill, H.A.O. Electrochemistry of Horse Heart Cytochrome-C. *J Am Chem Soc* **101**, 4461-4464 (1979).

16. Gu, J. *et al.* Control of cytochrome c redox reactivity through off-pathway modifications in the protein hydrogen-bonding network. *Chemical communications (Cambridge, England)* **50**, 5355-5357 (2014).

17. Redzic, J.S. & Bowler, B.E. Role of hydrogen bond networks and dynamics in positive and negative cooperative stabilization of a protein. *Biochemistry* **44**, 2900-2908 (2005).

18. McClelland, L.J., Mou, T.C., Jeakins-Cooley, M.E., Sprang, S.R. & Bowler, B.E. Structure of a mitochondrial cytochrome c conformer competent for peroxidase activity. *P Natl Acad Sci USA* **111**, 6648-6653 (2014).

19. Nold, S.M., Lei, H.T., Mou, T.C. & Bowler, B.E. Effect of a K72A Mutation on the Structure, Stability, Dynamics, and Peroxidase Activity of Human Cytochrome c. *Biochemistry* **56**, 3358-3368 (2017).

20. Morison, I.M. *et al.* A mutation of human cytochrome c enhances the intrinsic apoptotic pathway but causes only thrombocytopenia. *Nat Genet* **40**, 387-389 (2008).

21. De Rocco, D. *et al.* Mutations of cytochrome c identified in patients with thrombocytopenia THC4 affect both apoptosis and cellular bioenergetics. *Bba-Mol Basis Dis* **1842**, 269-274 (2014).

22. Hao, Z.Y. *et al.* Specific ablation of the apoptotic functions of cytochrome c reveals a differential requirement for cytochrome c and apaf-1 in apoptosis. *Cell* **121**, 579-591 (2005).

23. McClelland, L.J. *et al.* The response of Omega-loop D dynamics to truncation of trimethyllysine 72 of yeast iso-1-cytochrome c depends on the nature of loop deformation. *J Biol Inorg Chem* **20**, 805-819 (2015).

24. Ying, T. *et al.* Evolutionary alkaline transition in human cytochrome c. *J Bioenerg Biomembr* **41**, 251-257 (2009).

25. Rajagopal, Badri S. *et al.* The hydrogen-peroxide-induced radical behaviour in human cytochrome c–phospholipid complexes: implications for the enhanced pro-apoptotic activity of the G41S mutant. *Biochem J* **456**, 441-452 (2013).

26. Bushnell, G.W., Louie, G.V. & Brayer, G.D. High-resolution three-dimensional structure of horse heart cytochrome c. *J Mol Biol* **214**, 585-595 (1990).

27. Berghuis, A.M. & Brayer, G.D. Oxidation State-Dependent Conformational-Changes in Cytochrome-C. *J Mol Biol* **223**, 959-976 (1992).

28. Chen, C.R. & Makhatadze, G.I. ProteinVolume: calculating molecular van der Waals and void volumes in proteins. *BMC Bioinformatics* **16**, 101 (2015).

29. Craig, D.B. & Nichols, E.R. Spectroscopic Measurement of the Redox Potential of Cytochrome c for the Undergraduate Biochemistry Laboratory. *Journal of Chemical Education* **83**, 1325 (2006).

30. Maki, N. Methods of Preparing the 2,2′-Dipyridyl and 1,10-Phenanthroline Cobalt(III) Complexes of the [CoX2dip2]- and [CoX2phen2]-Type. *Bulletin of the Chemical Society of Japan* **42**, 2275-2281 (1969).

31. Margoliash, E. & Frohwirt, N. Spectrum of horse-heart cytochrome c. *Biochem J* **71**, 570-572 (1959).

32. Welch, T.W. & Thorp, H.H. Distribution of Metal Complexes Bound to DNA Determined by Normal Pulse Voltammetry. *The Journal of Physical Chemistry* **100**, 13829-13836 (1996).

33. Mcardle, J.V., Gray, H.B., Creutz, C. & Sutin, N. Kinetic Studies of Oxidation of Ferrocytochrome-C from Horse Heart and Candida-Krusei by Tris(1, 10-Phenanthroline)Cobalt(Iii). *J Am Chem Soc* **96**, 5737-5741 (1974).

34. Wherland, S. & Gray, H.B. Metalloprotein Electron-Transfer Reactions - Analysis of Reactivity of Horse Heart Cytochrome-C with Inorganic Complexes. *P Natl Acad Sci USA* **73**, 2950-2954 (1976).

35. Muenzner, J., Toffey, J.R., Hong, Y.N. & Pletneva, E.V. Becoming a Peroxidase: Cardiolipin-Induced Unfolding of Cytochrome c. *J Phys Chem B* **117**, 12878-12886 (2013).

36. Godbole, S. & Bowler, B.E. A histidine variant of yeast iso-1-cytochrome c that strongly affects the energetics of the denatured state. *J Mol Biol* **268**, 816-821 (1997).

37. Zhong, F.F., Lisi, G.P., Collins, D.P., Dawson, J.H. & Pletneva, E.V. Redox-dependent stability, protonation, and reactivity of cysteine-bound heme proteins. *P Natl Acad Sci USA* **111**, E306-E315 (2014).

38. Sedlak, E. Characterization of the polyanion-induced molten globule-like state of cytochrome c. *Biopolymers* **86**, 119-126 (2007).

39. Hanske, J. *et al.* Conformational properties of cardiolipin-bound cytochrome c. *P Natl Acad Sci USA* **109**, 125-130 (2012).

40. Godbole, S. & Bowler, B.E. Effect of pH on formation of a nativelike intermediate on the unfolding pathway of a Lys 73 --> His variant of yeast iso-1-cytochrome c. *Biochemistry* **38**, 487-495 (1999).

41. Godbole, S., Dong, A., Garbin, K. & Bowler, B.E. A lysine 73-->histidine variant of yeast iso-1-cytochrome c: evidence for a native-like intermediate in the unfolding pathway and implications for m value effects. *Biochemistry* **36**, 119-126 (1997).

42. Krishna, M.M., Hoang, L., Lin, Y. & Englander, S.W. Hydrogen exchange methods to study protein folding. *Methods* **34**, 51-64 (2004).

43. Mayne, L. & Englander, S.W. Two-state vs. multistate protein unfolding studied by optical melting and hydrogen exchange. *Protein Sci* **9**, 1873-1877 (2000).

44. Goldes, M.E., Jeakins-Cooley, M.E., McClelland, L.J., Mou, T.C. & Bowler, B.E. Disruption of a hydrogen bond network in human versus spider monkey cytochrome c affects heme crevice stability. *Journal of inorganic biochemistry* **158**, 62-69 (2016).

45. Rosell, F.I., Ferrer, J.C. & Mauk, A.G. Proton-linked protein conformational switching: Definition of the alkaline conformational transition of yeast iso-1-ferricytochrome c. *J Am Chem Soc* **120**, 11234-11245 (1998).

46. Deacon, O.M., Svistunenko, D.A., Moore, G.R., Wilson, M.T. & Worrall, J.A.R. Naturally Occurring Disease-Related Mutations in the 40-57 Omega-Loop of Human Cytochrome c Control Triggering of the Alkaline Isomerization. *Biochemistry* **57**, 4276-4288 (2018).

47. Deacon, O.M., White, R.W., Moore, G.R., Wilson, M.T. & Worrall, J.A.R. Comparison of the structural dynamic and mitochondrial electron-transfer properties of the proapoptotic human cytochrome c variants, G41S, Y48H and A51V. *Journal of inorganic biochemistry* **203**, 110924 (2020).

48. Pearce, L.L., Gartner, A.L., Smith, M. & Mauk, A.G. Mutation-Induced Perturbation of the Cytochrome-C Alkaline Transition. *Biochemistry* **28**, 3152-3156 (1989).

49. Verissimo, A.F., Sousa, F.L., Baptista, A.M., Teixeira, M. & Pereira, M.M. Thermodynamic redox behavior of the heme centers of cbb3 heme-copper oxygen reductase from Bradyrhizobium japonicum. *Biochemistry* **46**, 13245-13253 (2007).

50. Pintscher, S. *et al.* Tuning of Hemes b Equilibrium Redox Potential Is Not Required for Cross-Membrane Electron Transfer. *The Journal of biological chemistry* **291**, 6872-6881 (2016).

51. Barker, P.D. & Mauk, A.G. Ph-Linked Conformational Regulation of a Metalloprotein Oxidation Reduction Equilibrium - Electrochemical Analysis of the Alkaline Form of Cytochrome-C. *J Am Chem Soc* **114**, 3619-3624 (1992).

52. Gu, J., Shin, D.W. & Pletneva, E.V. Remote Perturbations in Tertiary Contacts Trigger Ligation of Lysine to the Heme Iron in Cytochrome c. *Biochemistry* **56**, 2950-2966 (2017).

53. Josephs, T.M. *et al.* Conformational change and human cytochrome c function: mutation of residue 41 modulates caspase activation and destabilizes Met-80 coordination. *J Biol Inorg Chem* **18**, 289-297 (2013).

54. Wang, H., Blair, D.F., Ellis, W.R., Gray, H.B. & Chan, S.I. Temperature-Dependence of the Reduction Potential of Cua in Carbon-Monoxide Inhibited Cytochrome-C-Oxidase. *Biochemistry* **25**, 167-171 (1986).

55. Meinhardt, S.W. & Crofts, A.R. Kinetic and Thermodynamic Resolution of Cytochrome-C1 and Cytochrome-C2 from Rhodopseudomonas-Sphaeroides. *Febs Lett* **149**, 223-227 (1982).

56. Mondal, M.S., Fuller, H.A. & Armstrong, F.A. Direct measurement of the reduction potential of catalytically active cytochrome c peroxidase compound I: Voltammetric detection of a reversible, cooperative two-electron transfer reaction. *J Am Chem Soc* **118**, 263-264 (1996).

57. Miller, M.A., Han, G.W. & Kraut, J. A cation binding motif stabilizes the compound I radical of cytochrome c peroxidase. *Proc Natl Acad Sci U S A* **91**, 11118-11122 (1994).

58. Purcell, W.L. & Erman, J.E. Cytochrome c peroxidase catalyzed oxidations of substitution inert iron(II) complexes. *J Am Chem Soc* **98**, 7033-7037 (1976).

59. Solmaz, S.R.N. & Hunte, C. Structure of complex III with bound cytochrome c in reduced state and definition of a minimal core interface for electron transfer. *Journal of Biological Chemistry* **283**, 17542-17549 (2008).

60. Lange, C. & Hunte, C. Crystal structure of the yeast cytochrome bc(1) complex with its bound substrate cytochrome c. *P Natl Acad Sci USA* **99**, 2800-2805 (2002).

61. Shimada, S. *et al.* Complex structure of cytochrome c-cytochrome c oxidase reveals a novel protein-protein interaction mode. *Embo J* **36**, 291-300 (2017).

62. Sakamoto, K. *et al.* NMR basis for interprotein electron transfer gating between cytochrome c and cytochrome c oxidase. *Proc Natl Acad Sci U S A* **108**, 12271-12276 (2011).

63. Butler, J. *et al.* Preferred Sites for Electron-Transfer between Cytochrome-C and Iron and Cobalt Complexes. *Journal of Biological Chemistry* **258**, 6400-6404 (1983).

64. Butler, J. *et al.* Preferred sites for electron transfer between cytochrome c and iron and cobalt complexes. *Journal of Biological Chemistry* **258**, 6400-6404 (1983).

65. Hildebrandt, P., Heimburg, T., Marsh, D. & Powell, G.L. Conformational changes in cytochrome c and cytochrome oxidase upon complex formation: a resonance Raman study. *Biochemistry* **29**, 1661-1668 (1990).

66. Marangoni, A.G. *Enzyme kinetics : a modern approach*. (Wiley-Interscience, Hoboken, N.J.; 2003).

67. Van Kuilenburg, A.B. *et al.* Presteady-state and steady-state kinetic properties of human cytochrome c oxidase. Identification of rate-limiting steps in mammalian cytochrome c oxidase. *Eur J Biochem* **205**, 1145-1154 (1992).

68. Muenzner, J. & Pletneva, E.V. Structural transformations of cytochrome c upon interaction with cardiolipin. *Chem Phys Lipids* **179**, 57-63 (2014).

69. Chertkova, R.V. *et al.* Lysine 72 substitutions differently affect lipid membrane permeabilizing and proapoptotic activities of horse heart cytochrome c. *Biochemical and biophysical research communications* **548**, 74-77 (2021).

70. Karsisiotis, A.I. *et al.* Increased dynamics in the 40-57 Omega-loop of the G41S variant of human cytochrome c promote its pro-apoptotic conformation. *Scientific reports* **6**, 30447 (2016).

71. Lei, H.T. & Bowler, B.E. Humanlike substitutions to Omega-loop D of yeast iso-1-cytochrome c only modestly affect dynamics and peroxidase activity. *Journal of inorganic biochemistry* **183**, 146-156 (2018).

72. Bowler, B.E. Thermodynamics of protein denatured states. *Mol Biosyst* **3**, 88-99 (2007).

73. Amacher, J.F. *et al.* A Compact Structure of Cytochrome c Trapped in a Lysine-Ligated State: Loop Refolding and Functional Implications of a Conformational Switch. *J Am Chem Soc* **137**, 8435-8449 (2015).

74. Assfalg, M. *et al.* Structural model for an alkaline form of ferricytochrome c. *J Am Chem Soc* **125**, 2913-2922 (2003).

75. Cherney, M.M., Junior, C.C. & Bowler, B.E. Mutation of Trimethyllysine 72 to Alanine Enhances His79-Heme-Mediated Dynamics of Iso-1-cytochrome c. *Biochemistry* **52**, 837-846 (2013).

76. Sutin, N. & Yandell, J.K. Mechanisms of the reactions of cytochrome c. Rate and equilibrium constants for ligand binding to horse heart ferricytochrome c. *The Journal of biological chemistry* **247**, 6932-6936 (1972).

77. McClelland, L.J. & Bowler, B.E. Lower Protein Stability Does Not Necessarily Increase Local Dynamics. *Biochemistry* **55**, 2681-2693 (2016).

78. Marcus, R.A. On Theory of Electron-Transfer Reactions .6. Unified Treatment for Homogeneous and Electrode Reactions. *J Chem Phys* **43**, 679-& (1965).

79. Marcus, R.A. & Sutin, N. Electron transfers in chemistry and biology. *Biochimica et Biophysica Acta (BBA) - Reviews on Bioenergetics* **811**, 265-322 (1985).

80. Beratan, D.N., Betts, J.N. & Onuchic, J.N. Protein electron transfer rates set by the bridging secondary and tertiary structure. *Science* **252**, 1285-1288 (1991).

81. Bertini, I., Gray, H.B., Stiefel, E.I. & Valentine, J.S. *Biological inorganic chemistry : structure and reactivity*. (University Science Books, Sausalito, Calif.; 2007).

82. Liptak, M.D., Fagerlund, R.D., Ledgerwood, E.C., Wilbanks, S.M. & Bren, K.L. The Proapoptotic G41S Mutation to Human Cytochrome c Alters the Heme Electronic Structure and Increases the Electron Self-Exchange Rate. *J Am Chem Soc* **133**, 1153-1155 (2011).

83. Imai, M. *et al.* Investigation of the redox-dependent modulation of structure and dynamics in human cytochrome c. *Biochemical and biophysical research communications* **469**, 978-984 (2016).

84. Pelletier, H. & Kraut, J. Crystal-Structure of a Complex between Electron-Transfer Partners, Cytochrome-C Peroxidase and Cytochrome-C. *Science* **258**, 1748-1755 (1992).

85. Guo, M.L., Bhaskar, B., Li, H.Y., Barrows, T.P. & Poulos, T.L. Crystal structure and characterization of a cytochrome c peroxidase-cytochrome c site-specific cross-link. *P Natl Acad Sci USA* **101**, 5940-5945 (2004).

86. Kobayashi, H., Nagao, S. & Hirota, S. Characterization of the Cytochrome c Membrane-Binding Site Using Cardiolipin-Containing Bicelles with NMR. *Angewandte Chemie* **55**, 14019-14022 (2016).

87. Rajagopal, B.S., Silkstone, G.G., Nicholls, P., Wilson, M.T. & Worrall, J.A.R. An investigation into a cardiolipin acyl chain insertion site in cytochrome c. *Bba-Bioenergetics* **1817**, 780-791 (2012).

88. Zhou, M.Y. *et al.* Atomic structure of the apoptosome: mechanism of cytochrome c- and dATP-mediated activation of Apaf-1. *Gene Dev* **29**, 2349-2361 (2015).

89. Sinibaldi, F. *et al.* Role of lysines in cytochrome c-cardiolipin interaction. *Biochemistry* **52**, 4578-4588 (2013).

90. Rytomaa, M. & Kinnunen, P.K. Reversibility of the binding of cytochrome c to liposomes. Implications for lipid-protein interactions. *The Journal of biological chemistry* **270**, 3197-3202 (1995).

91. Hong, Y.N., Muenzner, J., Grimm, S.K. & Pletneva, E.V. Origin of the Conformational Heterogeneity of Cardiolipin-Bound Cytochrome c. *J Am Chem Soc* **134**, 18713-18723 (2012).

92. Rytomaa, M., Mustonen, P. & Kinnunen, P.K.J. Reversible, Nonionic, and Ph-Dependent Association of Cytochrome-C with Cardiolipin-Phosphatidylcholine Liposomes. *Journal of Biological Chemistry* **267**, 22243-22248 (1992).

Chapter 5

Mutations in Loop C Influence the Protonation of Heme Propionates in Cytochrome *c*

Introduction

Many proteins have segments that differ in stability and dynamics.[1-5] These regions are in cross-talk with each other through weak intermolecular contacts and are important for the function and folding of the protein.[2, 6, 7] Such is the case of cyt *c*, a small mitochondrial protein that can act as an electron carrier in the respiratory pathway, a peroxidase, and an apoptotic signaling molecule depending on the structure, ligation, and fold of the protein.[8] In cyt *c*, thermodynamically distinct foldons are in cross-talk,[7, 9-13,] ensuring that the protein responds to biological redox partners and environmental signals. In particular, functions of cyt *c* are influenced by the dynamics and stability of the least stable foldons, loops C and D, which are the last to fold in the folding pathway.[14, 15]

One of the least stable loop D provides indigenous axial ligands and enables polypeptide packing around the heme to control the reduction potential and the innate peroxidase activity of the metal center.[16, 17] Much of the amino acids and HB that contains the native heme iron ligand Met80 is conserved among different species,[18-22] and perturbations in this network have shown to affect biophysical properties of the protein.[23-26] Loop D is in close contact with loop C, and many mutational studies in human, horse heart, and yeast cyt *c* have shown that perturbations in loop C also perturb the loop D-dependent enzymatic properties of the protein.[27-33]

Depending on the pH conditions, cyt *c* undergoes structural changes in loops C and D.[18] These changes affect the properties of the heme, and transitions from the native state are observed with a pK_a of 9.35 and 2.5 in WT horse heart cyt *c*.[34, 35] At alkaline conditions, loop D undergoes conformational rearrangements to form a Lys-ligated heme with either Lys79 or 73 in WT horse heart cyt *c*,[15] the transition requiring some disruption of some of

the loop C and D contacts.[15, 36-39] The protein unfolds in a cooperative manner as pH decreases,[40] and becomes fully unfolded at pH conditions below 2.[18, 35] Addition of anions allows the protein to form a loosely packed structure in a MG state from the largely unstructured acid-unfolded state, as anions decrease intramolecular charge repulsions in the unfolded state.[41, 42] Unfolding of loop C has been observed prior to loop D rearrangement at both alkaline[14, 43] and acidic conditions.[44] These structural changes influence the function of cyt *c*, as the heme environment and ligation heavily modulate the reduction potential and peroxidase activity of the heme.[16, 17, 45-47] At both low- and high-pH, the loops C and D unfold, and alter the heme environment. Although contributions of loops C and D at alkaline transitions is better understood,[30, 32, 33, 48-52] information regarding contributions of these loops during acid transition has been lacking.

In vivo, cyt *c* is exposed to different pH conditions, depending on its location and condition of the cell. At normal physiological conditions, the intermembrane surface has a pH of ~6.9 and is more acidic than the cytosol, where pH ranges from 7.4 to 7.6.[53, 54] The pH of the cytosol can decrease to 6.1 in response to cytoprotective acidosis and metabolic inhibition, [53, 55, 56] and further down to 5.8 during apoptosis.[57] Mitochondrial acidification is also observed in metabolic inhibition as a mechanism to control oxidative phosphorylation.[53, 58] Release of cyt *c* from the mitochondria during apoptosis requires initial binding of cyt *c* to CL to permeabilize the mitochondrial membrane.[59] pH is also important for initial steps of cyt *c*-mediated apoptosis, as binding of cyt *c* to CL and mitochondrial permeability is dependent on pH.[60, 61] To better relate biological role of cyt *c* and the changes in protein structure, understanding structural changes of cyt *c* under acidic conditions is crucial.

The acid unfolding of cyt *c* is a complex cooperative process that involves structural rearrangements of the polypeptide chain.[9] Protonation of multiple groups trigger changes in the polypeptide packing, resulting in dissociation of the Met-ligand from the heme iron, loss of the native secondary and tertiary structure, and different ligand and spin states of the heme iron.[18, 41, 42, 62-64] In horse heart WT cyt *c*, acid unfolding is observed with a composite pK_a value of near 2.5 for the loss of Met-ligation accompanied by the loss of tertiary and secondary structure.[18, 34, 63] Depending on ionic strength, either bis-aquo or His/H_2O ligated species form, owing to the different pK_a values of His18 at low (pK_a = 2.5 at 0.01 M Cl^-) or high (pK_a = 1.4 at 0.1 M Cl^-) concentrations of salt.[62] This gap in the His18 pK_a have been also observed in multiple spectroscopic titration measurements,[65-67] and plays a role in formation of the MG species.[68] Variations in the unfolding transition are also observed in the WT proteins from different species. Like in WT horse heart cyt *c*,[35] more than a single proton is involved in this process in human WT cyt *c* and has a similar pK_a.[49] Transition occurs earlier in WT yeast cyt *c*, by ~ 0.5 pK_a units.[18, 50, 69] Although differences in ionic conditions may complicate comparisons across different studies, mutational studies with yeast and human cyt *c* has shown that perturbations near the heme affect the pK_a of this transition.[49, 69] It is possible that differences in the acid unfolding transition are influenced by differences in sequences of yeast, human and horse heart WT cyt *c* proteins. In addition to sequence, global and local stability of yeast cyt *c* differ from those in human and horse heart cyt *c*.[18, 28, 38, 70-74]

The cooperativity of acid unfolding may readily break down with perturbations in the polypeptide, as observed with carboxymethylation of Met80 and Met63 in horse heart cyt *c*.[40] Studies of T49V/K79G and T78V/K79G yeast cyt *c* variants have shown that the

pK_a of the initial acid transition, from the native Met-ligated species to the H_2O-ligated HS species, is raised with peptide perturbations in loops C and D, highlighting the sensitivity of acid unfolding to properties of these two loops.[32] pH titrations monitoring Met80 dissociation in yeast G83V cyt *c* and human I81A and V83G cyt *c* variants showed the loss of cooperativity for acid unfolding.[49, 50] This loss of cooperativity have been argued to be due to sequence differences in loop C.[49] as Previously, a similar loss of cooperativity has been observed during acid unfolding of yeast K79A/N52G and K79A/K73H cyt *c* variants.[27, 75] Yeast K79A/N52G cyt *c* variant also has shown an intermediate transition at mildly acidic conditions between pH 4 to 6, although structural reasons for the loss of cooperativity are not clear.[27]

The protonation sites during the acid unfolding transition have been inferred to be His26 and either of the HP groups. [12, 27, 69, 75, 76] His26 shows a cooperative behavior with Asn52 in loop in folding of N52I and H26N yeast cyt *c* variants,[77, 78] suggesting that the loop C-His26 contacts may also be involved in the acid unfolding. Studies of H26Y yeast cyt *c* have suggested that disruption of the HB between His26-Glu44 triggers formation of the MG-like state at neutral pH,[79] highlighting the importance of His26 interactions in forming the compact native state of cyt *c*. Although WT horse heart cyt *c* has a Pro instead of Glu at position 44,[18] the X-ray crystal structure of horse heart cyt *c* shows the backbone of Pro44 is in HB contact with His26.[20] A rupture of this interaction, as well as of the one between Thr49 and HP6, was hypothesized to trigger the rearrangement of loop C into a β-sheet at pH 3.[44] HX experiments have also suggested that His26-residue 44 HB is the major source of pH-sensitivity of the 20's loop of the green foldon.[76] HX experiments with WT horse heart cyt *c* have shown that stability of loop C decreased with pH, but its pH

sensitivity at acidic conditions was hypothesized to stem from either HP6 or HP7, rather than His26.[12] The loss of cooperativity in the acid unfolding for the K79A/K73H yeast cyt *c* variant has been hypothesized to be a result of perturbation of the HB between Gly44 and His26,[27, 75] while MCD studies of yeast M80A, M80A/Y67H, and M80A/Y67A cyt *c* variants have related small spectral changes with pK_a ranging from 4.5 to 3.9 to the deprotonation of HP7.[69] Although multiple mutational studies suggest that loop C is critical for acid unfolding, much of the details of the mechanism of loop C unfolding, including the identity of the protonated groups, are unknown.

We explored the acid transitions of the G41S, Y48H, and K72A horse heart cyt *c* variants to examine this mechanism. These particular variants were studied in biological models related to apoptosis and inherited thrombocytopenia,[80-82] offering clues as to how these mutational effects may affect enzymatic activity under acidic conditions. Since G41S and Y48H contain perturbations in different parts of loop C, these variants are a good choice to test whether local differences within loop C affect the acid unfolding transition. With the G41S variant, we have identified a distinct structural change in mildly acidic, physiologically relevant pH range not observed with other variants. This acid-induced species in horse heart G41S cyt *c* were spectroscopically characterized to determine the heme iron ligation and polypeptide fold. Folding of horse heart cyt *c* has been extensively studied at both extremes of the pH spectrum,[10-12, 83-86] providing clues as to which structural perturbations in these variants affect the acidic unfolding transition. We suggest that loop C may protect the protonation site from forming an intermediate during acid unfolding and speculate on the identity of the possible protonation site.

Materials and Methods

General. All solutions and buffers were prepared using water from Barnstead E-Pure Ultrapure Water Purification System, purified to a resistivity of 18 MΩ·cm. Reagents and columns were purchased from Sigma-Aldrich and GE Healthcare, respectively, unless noted otherwise. Gas-tight Hamilton syringes were used to aliquot proteins for all titrations and quantitative dilutions. Quartz cuvettes and tubes were purchased from Starna Scientific and Wilmad Lab Glass, respectively. pH was adjusted using sodium hydroxide or hydrogen chloride and monitored with an AB15 pH meter (Fisher Scientific) or a UB10 pH meter (Denver Instrument), unless noted otherwise.

Site-Directed Mutagenesis, Protein Expression, and Purification. Point mutations, protein expression and purification for horse heart cyt *c* variants were performed as previously described.[70] Desired point mutations were introduced in the pBTR plasmid encoding horse heart cytochrome *c* using a QuikChange kit (Agilent) and confirmed by DNA sequencing as well as MALDI of the purified protein samples at the Molecular Biology & Proteomics Core Facility (Dartmouth College). Extinction coefficients of protein variants were determined from hemochrome assays in a100 mM sodium phosphate buffer at pH 7.4 as previously described.[87]

Spectroscopic Measurements. All spectroscopic measurements were obtained at 22 ± 2 ^{o}C, unless noted otherwise. Ferric proteins were freshly prepared with excess potassium ferricyanide and purified by size exclusion (PD-10 desalting column) or ion-exchange (Sepharose HP SP) chromatography prior to spectroscopic measurements. Absorption spectra were recorded using an Agilent 8453 diode-array spectrophotometer. CD spectra were measured on a JASCO-J815 CD spectropolarimeter equipped with a variable

temperature Peltier cell device (JASCO, Inc.). Fluorescence spectra were measured on a Horiba Jobin Yvon Fluorolog-3 spectrofluorometer equipped with an automatic polarizer.

Stock protein samples were diluted to final protein concentrations ranging from 7 to 10 μM with buffers (100 mM sodium phosphate buffer at pH 7.4, 100 mM acetate buffer at pH 4.0, or a HCl + 0.1 M NaCl buffer at pH 2.0). All spectral measurements were performed with the same protein stock, to ensure equal protein concentrations across different spectral measurements. CD spectra were baseline corrected with the spectrum of the buffer. For fluorescence measurements, intrinsic tryptophan (Trp59) was excited at 290 nm and its emission recorded at 300 to 400 nm using entrance and exit slits of 10 nm.

^{1}H NMR spectra of ferric proteins were recorded on a 500 MHz Bruker NMR spectrometer (Bruker Biosciences) at 25 ºC. Freshly oxidized protein at final concentrations ranging from 0.5 to 2.7 mM in either a 50 mM sodium phosphate buffer or a 50 mM acetic acid d_4 buffer in 100% D_2O was prepared. For ^{1}H NMR pH titrations with the ferric G41S, freshly purified and oxidized protein was exchanged into a 50 mM acetic acid d_4 buffer in 100% D_2O at pD 4.5. After the initial measurement, the same protein sample were then exchanged into a 50 mM sodium phosphate buffer in 100% D_2O at pD 7.4. For the pH titration measurements, pD of the sample was adjusted using small amounts of HCl or NaOD with an Accumet micro pH meter (Fisher Scientific).

pH Titrations and Analyses. Solutions containing final protein concentrations ranging from 8 to 10 μM or 200 to 300 μM in a 100 mM sodium phosphate buffer at pH 7.4 were used to monitor the absorption profiles of the Soret and the CT band, respectively. Stock protein solutions were split into two aliquots to be used for either alkaline or acidic pH titrations. Electronic absorption in the Soret region (350 to 500 nm) were monitored in pH

ranges 1.9 to 11.1 for WT, pH 2.0 to 10.7 for K72A, pH 2.0 to 9.3 for Y48H, and pH 1.8 to 10.4 for G41S. Electronic absorption in the CT region (580 to 750 nm) were monitored in pH ranges 1.8 to 10.6 for WT, pH 2.0 to 11.3 for K72A, pH 1.9 to 10.2 for Y48H, and pH 1.8 to 9.9 for G41S.

Changes in the absorption spectra with pH were analyzed using SVD, as described previously.[33] Electronic absorption spectra of the Soret region from pH ranges 2.5 to 11.08 for WT, pH 2.5 to 10.7 for K72A, pH 2.5 to 9.3 for Y48H, and pH 2.5 to 10.4 for G41S, and electronic absorption spectra of the CT region from pH ranges 2.5 to 10.6 for WT, pH 2.5 to 11.3 for K72A, pH 2.5 to 10.2 for Y48H, and pH 2.4 to 9.9 for G41S, were selected for analyses. Absorption profile matrices (**A**) were then deconvoluted into wavelength-dependent vectors (**U**), square root of the eigenvalues (**S**), and pH-dependent vectors (**V**) as previously described.[33, 88, 89] Number of significant components, *i*, was determined from log of $S_{j,j}$ values, $S_{j,j}$ percentages $(\frac{S_{j,j}^2}{\sum_{j=1}^{k} S_{j,j}^2})\times 100\%$, error levels $(\sqrt{\frac{\sum_{j=i}^{k} S_{j,j}^2}{\sum_{j=1}^{k} S_{j,j}^2}})$, autocorrelation of U(λ) and V(pH) matrices, as previously described.[88, 89 33]

Selected pH-dependent vectors (**V**) from both the Soret and CT regions were globally fitted to eq 5.1 using SigmaPlot 10.0:

$$f(x)=\sum \frac{B_i+A_i\times 10^{n(pK_{app,i}-pH)}}{1+10^{n(pK_{app,i}-pH)}}+C \qquad (5.1)$$

where A_i and B_i are the slope and y-intercept of the *i*th transition, pK_{app} is the apparent pK_a for the *i*th transition, *n* is the number or protons involved in the *i*th transition, and C is a constant.

Spectra of the respective components were deconvoluted using eq 5.2:

$$D = AF^{-1} \tag{5.2}$$

where D is the spectra of the component, A is the absorption of the spectra at a given pH, and F is the fractional population change of the major component as a function of pH. The spectrum of the i^{th} component (D_i) can be obtained $D_i = (A\text{-}D_{ref}F_{ref})F_i^{-1}$, where A = U × S × V matrices with significant components obtained from the SVD analysis, F_i is the fractional population of the i^{th} component, D_{ref} is the spectra of the reference protein, and F_{ref} is the changes in the fractional population of the reference proteins.

For WT, K72A, and Y48H, SVD analysis detected three significant components in volved in the pH conditions monitored. In these variants, the spectrum of the Met-ligated species (D2) was obtained by using WT spectra at pH 1.9 (acid-denatured, H_2O-ligated) as D1 and at pH 10.0 (Lys-ligated) as reference spectra.

For the G41S variant, the SVD analysis repeatedly detected four significant components involved in the pH conditions monitored. Force-fitting the vectors obtained from the deconvolution of the titration spectra with three significant components yielded in poor fits of the data.

In the G41S variant, spectrum of the additional component, D2, was obtained by using WT spectra at pH 1.9 (acid denatured H_2O-ligated) for D1, pH 7.4 for D3(Met-

ligated), and pH 10.0 (Lys -ligated) for D4 as references at similar ionic conditions. To check whether our D3 component in G41S was similar to Met-ligated WT cyt *c* at pH 7.4, spectrum of the D3 component was deconvoluted using WT spectra at pH 1.9 as D1, pH 10.0 as D4, and the deconvoluted D2. Similar analyses were performed for the CT region of G41S. To obtain a better view of how the Soret peaks were shifting between the two components, the deconvoluted spectra of the D2 and D3 components were normalized based on the assumption of the extinction coefficient at λ_{max} of the Soret band of the D3 component should equal to that of the WT (ε_{409} = 106 $mM^{-1}cm^{-1}$).

Measurements of Reduction Potentials. Shimadzu UV-1201 scanning spectrophotometer equipped with a spectroelectrochemistry kit (Pine Research Instrumentation) was used to perform electrochemistry titrations for WT and G41S at pH 4.0. Samples containing 75 μM protein with equimolar concentration of mediators (2,3,5,6-tetramethyl phenylenediamine,[90] 1,2,-Naphthoquionine,[91] Gallocyanine,[92, 93] 2-hydroxy-1,4-naphthoquinone,[92, 93] and sodium anthraquinone-2-sulfonate monohydrate[90]) were prepared in a 100 mM acetate buffer at pH 4.0 (μ = 0.1 M), thoroughly degassed with N_2-vaccuum purges. . Measurements were performed with a gel-calomel electrode (GCE) and a Pt honeycomb inside a glovebox. The absorbance values at 550 nm were baseline corrected assuming a linear line between the two isosbestic points. The dependence of these values on external potential, *E*°, was then fitted to eq 5.3:

$$f(x)=\frac{A_m}{10^{(x-E°)/1000\times n/0.059}+1} \quad (5.3)$$

where A_m is the absorbance (or the fraction) of the ferrous protein, $E°$ is the reduction potential of the heme iron, and n is the number of electrons transferred in the reaction. The fitted potentials were then referenced to the standard hydrogen electrode (SHE) using $E°_{SHE} = E°_{GCE} + 213$ mV.

Eq. 5.3 is based on the Nernst equation for the reduction reaction where ferric protein (ferric) is reduced to the ferrous state (ferrous) (eq 5.4):[18]

$$E = E^{\circ} + \frac{RT}{nF} \ln\left(\frac{[\text{ferric}]}{[\text{ferrous}]}\right) \tag{5.4}$$

where E is the applied potential in volts, E° is the reduction potential of the heme iron in volts, R is the gas constant, T is the temperature, n is the number of electrons, F is the Faraday's constant. At 25 °C, RT/F reduces to 0.059.

This equation can be rearranged to eq. 5.5

$$10^{(E-E^{\circ}\times\frac{n}{0.059})} = \frac{[\text{ferric}]}{[\text{ferrous}]} \tag{5.5}$$

And since $[E_T] = [\text{ferric}] + [\text{ferrous}]$, we find that (eq 5.6):

$$\frac{1}{10^{\left(E-E^{\circ}\times\frac{n}{0.059}\right)} + 1} = \chi_{\text{ferrous}} \tag{5.6}$$

where χ_{ferrous} is the fraction of the ferrous species. Since $A = \varepsilon c l$, relationship to A_{550} can also be made, where E_T becomes A_{550} with fully reduced species in cyt *c* where changes in A_{550} band only stem from the formation of the reduced heme iron, yielding eq. 5.3.

Results

In this thesis, K72A, G41S, and Y48H variants of horse heart cyt *c* have been characterized in prior chapters. Spectroscopic characterization, including monitoring the alkaline transition, for ferric WT, G41S and Y48H are explored in Chapter 3. Similar characterization of ferric K72A, along with the measurement of reduction potentials for WT, K72A, G41S, and Y48H, are presented in Chapter 4.

pH Titrations. Spectral changes in the Soret and CT regions at pH conditions ranging from 2.5 up to 11 were separately monitored for ferric WT, K72A, G41S, and Y48H variants of horse heart cyt *c* (Figures 5.1 to 5.4). For WT, K72A, and Y48H variants, SVD analyses identified three significant components involved in the observed pH range. Thus, pH titration for WT, K72A, and Y48H were fit to a two-transition model and pK_a values of the two transitions were obtained (Table 5.1).

In G41S, SVD analyses consistently identified four significant components from the electronic absorption data over the pH range from 2.5 up to 10.4. Since previous SVD analysis of the pH titration profile for G41S monitoring only the alkaline pH range detected the same number of significant components as in the WT protein (Chapter 3), fits of the pK_a parameter for the alkaline transition was used as constraints in fitting the wide pH transition data for G41S. Force-fitting of the significant vectors to fit with three components with fixed pK_a value of the alkaline transition led to poor fits in the acidic pH range. Thus, significant vectors obtained from SVD analysis for G41S was fitted to a three-transition model.

Figure 5.1. pH titration and SVD analyses for WT, monitoring the changes in the Soret and CT regions in at 22 ± 2 °C, for pH ranges from 2.5 to 11.08 for Soret and 2.5 to 10.6 for CT regions (μ = 0.1 M). Shown are the electronic absorption spectra in the (A) Soret region or the (B) CT region from neutral (pH 7.4, black) to acidic (red) or to alkaline (blue) conditions, (C) significant vectors and fits, (D) fractional populations, and (E) the deconvoluted spectrum of the second component obtained by using WT spectra at pH 1.9 and pH 10.0 as inputs, compared to the spectrum of WT at pH 7.4 as a reference for the Met-ligated ferric heme.

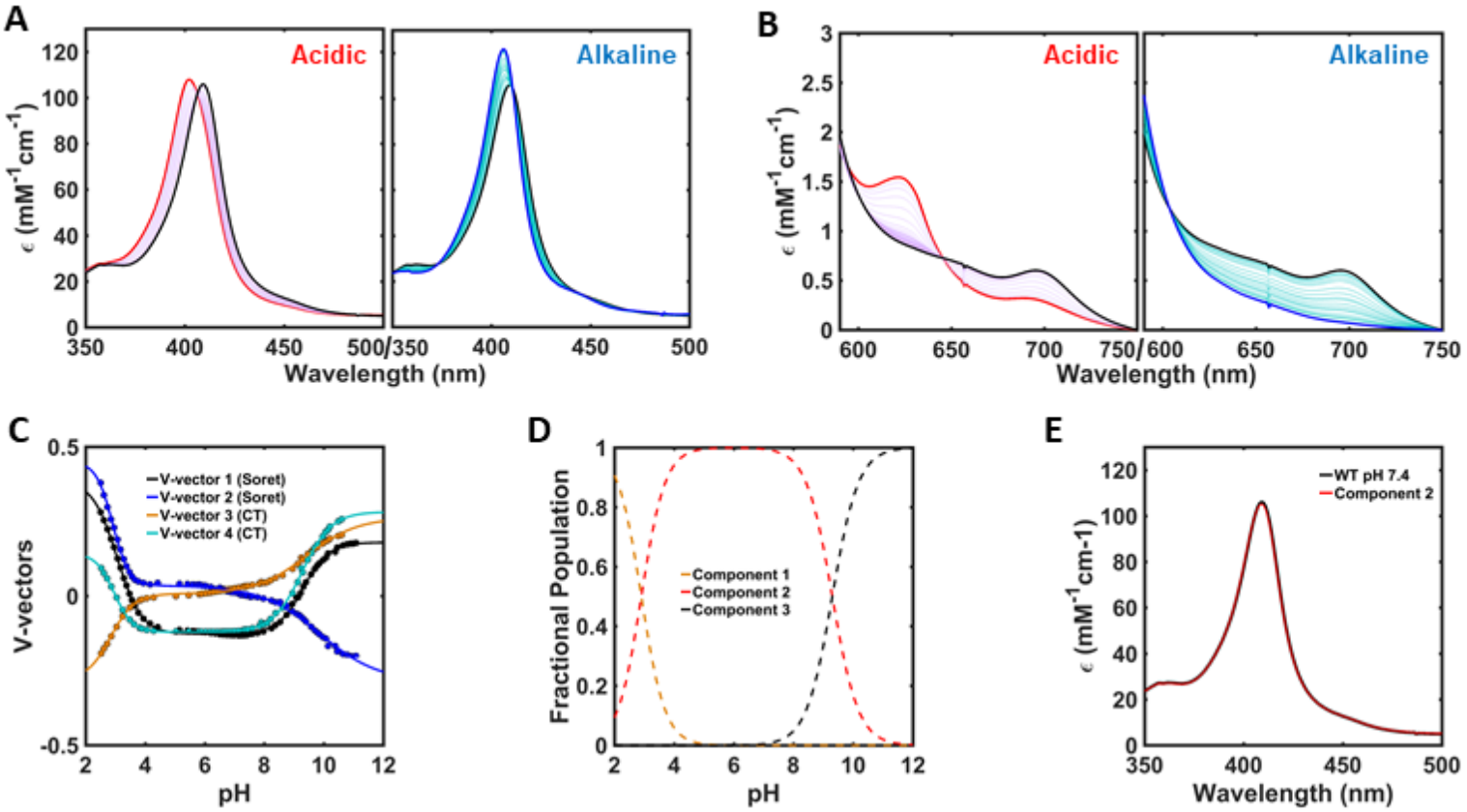
A
Acidic
Alkaline
ϵ (mM-1cm-1)
Wavelength (nm)
B
Acidic
Alkaline
ϵ (mM-1cm-1)
Wavelength (nm)
C
V-vector 1 (Soret)
V-vector 2 (Soret)
V-vector 3 (CT)
V-vector 4 (CT)
V-vectors
pH
D
Component 1
Component 2
Component 3
Fractional Population
pH
E
WT pH 7.4
Component 2
ϵ (mM-1cm-1)
Wavelength (nm)

Figure 5.2. pH titration and SVD analyses for K72A monitoring changes in the Soret and CT regions at 22 ± 2 °C, for pH ranges from 2.5 to 10.7 for Soret and 2.5 to 11.3 for CT regions (μ = 0.1 M). Shown are the electronic absorption spectra in the (A) Soret region or the (B) CT region from neutral (pH 7.4, black) to acidic (red) or to alkaline (blue) conditions, (C) significant vectors and fits, (D) fractional populations, and (E) the deconvoluted spectrum of the second component obtained by using WT spectra at pH 1.9 and pH 10.0 as inputs, compared to the spectrum of WT at pH 7.4 as a reference for the Met-ligated ferric heme.

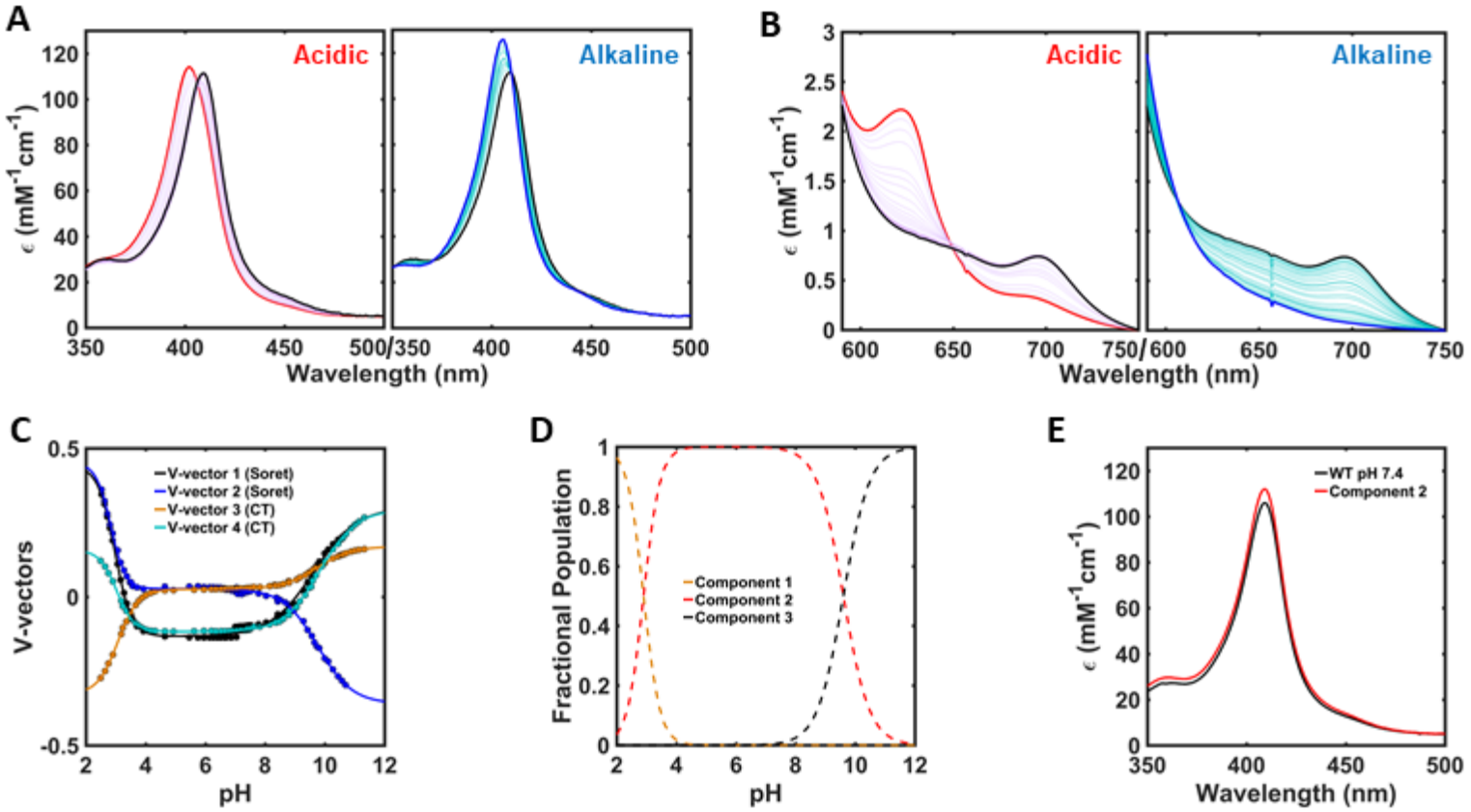
A
Acidic
Alkaline
ϵ (mM-1cm-1)
Wavelength (nm)
B
Acidic
Alkaline
ϵ (mM-1cm-1)
Wavelength (nm)
C
V-vector 1 (Soret)
V-vector 2 (Soret)
V-vector 3 (CT)
V-vector 4 (CT)
V-vectors
pH
D
Component 1
Component 2
Component 3
Fractional Population
pH
E
WT pH 7.4
Component 2
ϵ (mM-1cm-1)
Wavelength (nm)

Figure 5.3. pH titration and SVD analyses for Y48H monitoring changes in the Soret and CT regions at room temperature, for pH ranges from 2.5 to 9.3 for Soret and 2.5 to 10.2 for CT regions (μ = 0.1 M). Shown are the electronic absorption spectra for the (A) Soret region or the (B) CT region from neutral (pH 7.4, black) to acidic (red) or to alkaline (blue) conditions, (C) significant vectors and fits, (D) fractional populations, and (E) the deconvoluted spectrum of the second component obtained by using WT spectra at pH 1.9 and pH 10.0 as inputs, compared to the spectrum of WT at pH 7.4 as a reference for the Met-ligated ferric heme.

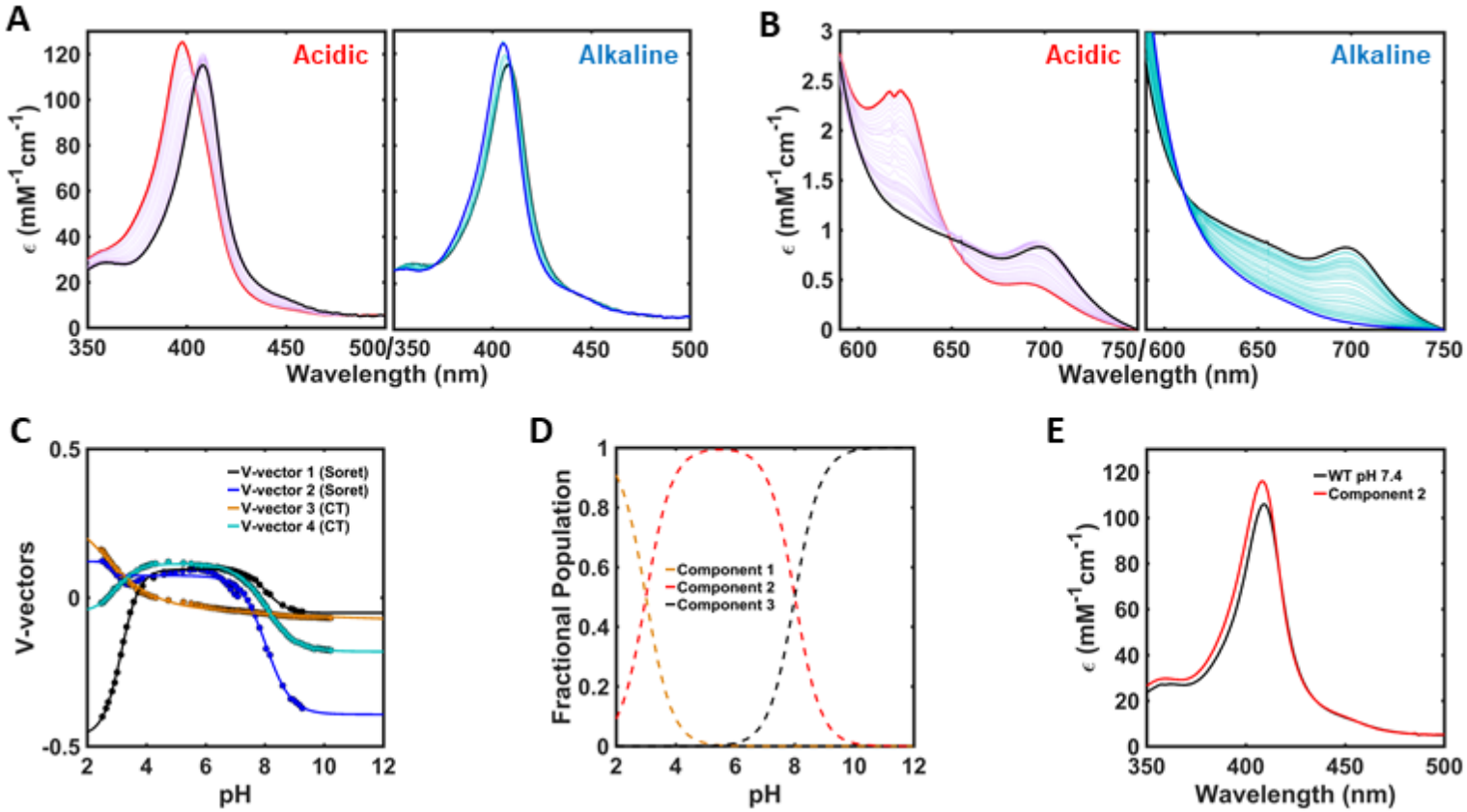
A
Acidic
Alkaline
ϵ (mM-1cm-1)
Wavelength (nm)
B
Acidic
Alkaline
ϵ (mM-1cm-1)
Wavelength (nm)
C
V-vector 1 (Soret)
V-vector 2 (Soret)
V-vector 3 (CT)
V-vector 4 (CT)
V-vectors
pH
D
Component 1
Component 2
Component 3
Fractional Population
pH
E
WT pH 7.4
Component 2
ϵ (mM-1cm-1)
Wavelength (nm)

Figure 5.4 pH titration and SVD analyses for G41S monitoring changes in the Soret and CT regions at 22 ± 2 °C, for pH ranges from 2.5 to 10.4 for Soret and 2.4 to 9.9 for CT regions (μ = 0.1 M). Shown are the electronic absorption spectra for the (A) Soret region or the (B) CT region from neutral (pH 7.4, black) to acidic (red) or to alkaline (blue) conditions, (C) significant vectors and fits, (D) fractional populations, and (E) the deconvoluted spectra of the second component obtained by using WT spectra at pH 1.9, 7.4, and 10.0 as inputs, third component obtained by using WT spectra at pH 1.9, 10, and second component as inputs, compared to the spectrum of the WT at pH 7.4 as a reference of the Met-ligated heme, shown for the Soret (left) and CT (right) regions. The Soret band regions are shown (left, insert) with the spectrum of the third component corrected so that $\varepsilon_{409} = 106\ mM^{-1}cm^{-1}$.

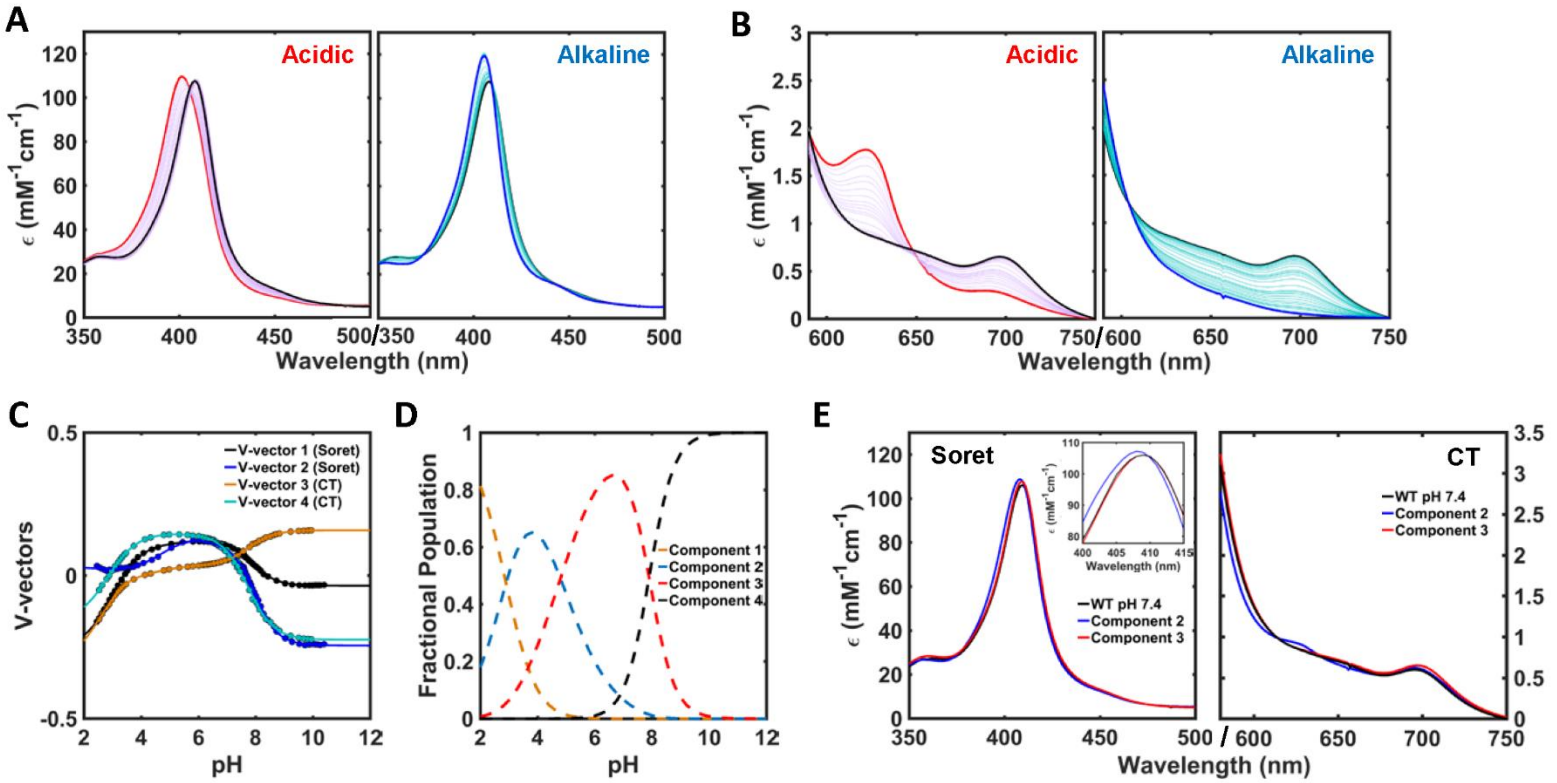
A
Acidic
Alkaline
ϵ (mM-1cm-1)
Wavelength (nm)
B
Acidic
Alkaline
ϵ (mM-1cm-1)
Wavelength (nm)
C
V-vector 1 (Soret)
V-vector 2 (Soret)
V-vector 3 (CT)
V-vector 4 (CT)
V-vectors
pH
D
Component 1
Component 2
Component 3
Component 4
Fractional Population
pH
E
Soret
WT pH 7.4
Component 2
Component 3
ϵ (mM-1cm-1)
Wavelength (nm)
CT
WT pH 7.4
Component 2
Component 3
Wavelength (nm)

For all four variants, fitted pK_a value of one of the transitions obtained from global fitting of the significant vectors, were within error of the alkaline transition parameters obtained in the absence of acidic transition data (compare Table 5.1 to Tables 3.5 and 4.3). Similarities in the fitted pK_a parameters for the alkaline transition suggested that the models used to describe the spectral changes in the wide pH range were appropriate.

For WT, the λ_{max} the Soret band blueshifts to 400 nm from 409 nm with decrease in pH (Figure 5.1A). The absorbance of the 695 nm CT band decrease, along with an increase in the absorbance at - 620 nm, associated with a high-spin H_2O-ligated heme iron species (Figure 5.1B). These spectral changes are consistent with the replacement of heme axial ligand Met by H_2O. From pH titrations in both Soret and CT regions, two significant vectors are observed, suggesting that the protein undergoes two transitions with three species in the range of monitored pH conditions (Figure 5.1C). In the pH ranges observed, fractional population calculations suggest that the Met-ligated species does not fully disappear by pH 2.5 (Figure 5.1D). Global fitting of the significant vectors reveals two pK_a values (Figure 5.1C and Table 5.1). The pK_a value 9.3 ± 0.2 for the alkaline transition is in good agreement with previously published values for the same protein.[34] The pK_a of the acidic transition obtained in this study was slightly higher than reported values in literature by ~ 0.4 pK_a units.[35] Our pK_a value for the acidic transition may be higher, perhaps because the spectra obtained at pH $\leq$ 2.5 were not considered for analysis due to shifts in the baseline possibly from protein denaturation at lower pH conditions. Deconvoluted spectrum of the component obtained with reference spectra for the Lys-ligated and acid-denatured H_2O-ligated species reveals a spectrum in good agreement to the independently measured spectrum of the Met-ligated WT at pH 7.4 (Figure 5.1E).

Table 5.1. Parameters for the pH-Dependent Transitions in Cyt *c* Variants[a]

Variant	pK_{a1}	n_1	pK_{a2}	n_2	pK_{a3}	n_3
WT[b]	2.9 ± 0.06	1.1 ± 0.06	n.a.	n.a.	9.3 ± 0.02	1
K72A	2.9 ± 0.03	1.6 ± 0.09	n.a.	n.a.	9.6 ± 0.02	1
G41S	2.9 ± 0.10	0.84 ± 0.10	5.0 ± 0.1	1.0 ± 0.2	7.9 ± 0.01	1
Y48H	3.0 ± 0.05	1.0 ± 0.05	n.a.	n.a.	8.0 ± 0.02	1

[a]In a 100 mM sodium phosphate buffer at pH 7.4 and 22 ± 2 °C. The total number of protons during the transition (n_3) was fixed to 1 during fittings for all alkaline transitions. The values of the alkaline transition parameters obtained from separate fittings (Tables 3.5 and 4.3) are in good agreement with the values obtained from the global fitting of the entire pH range.

[b]WT reference, pK_{a1} = 2.5 and n = 1.14 from ref. [35].

For K72A, spectral changes in the Soret and CT regions from pH 7.4 to 2.5 are comparable to those observed in WT (Figures 5.2A and B). There are differences in the magnitude of the 620 nm band extinction coefficient at pH 2.5, suggesting that the extent of acid unfolding of K72A may be different from that of WT (Figures 5.1B and 5.2B). Although pK_a of the K72A acidic transition is comparable to that of WT, a different number of protons is involved in the acidic transition of WT and K72A (Table 5.1). Like WT, there are three components involved in the pH range 2.5 up to 11.3 for K72A (Figures 5.2C and D). The deconvoluted spectrum of the second component involved in the pH transition in K72A is comparable to that of the Met-ligated WT species at pH 7.4 (Figure 5.2E).

For Y48H, the spectral features observed at pH 2.5 are different from those observed in WT. With decrease in pH, the λ_{max} of the Soret band blueshifts to 400 nm as observed in WT, but the extinction coefficient of Y48H at this wavelength is much higher than that of WT (Figure 5.3A). The increase in the extinction coefficient of the 620 nm band for Y48H at pH 2.5 is greater than that of observed in WT, and the 695 nm CT band is still observable, but diminished, at this pH (Figure 5.3B). However, the extrapolated pK_a and *n* values are within error of WT, and the number of components involved in the transition does not change (Figures 5.3C and D). These results suggest that although there may be some structural differences in WT and Y48H, the acid transition in Y48H is generally comparable in the two variants (Table 5.1).

For G41S, SVD analysis consistently identified four significant components, and three transitions were required to describe the changes in the spectral series within the pH range 2.5 to 10.4 in the Soret region and pH 2.4 to 9.9 in the CT region. This transition occurs at mildly acidic conditions at pK_a ~5.0 involving a net transfer of a single proton

(Table 5.1). Spectrum of this additional species was deconvoluted using the spectra of WT protein at pH 1.9, 7.4, and 10.0 as references for H_2O-ligated, Met-ligated, and Lys-ligated species. Multiple attempts were made to deconvolute the spectrum of the additional component using fewer reference spectra, spectrum of the unfolded protein in 6 M GuHCl, and bisH_2O-ligated yeast cyt *c* spectra. However, such attempts yielded the deconvoluted spectrum of the Met-ligated species that did not correspond to the Met-ligated spectrum at pH 7.4, and three reference spectra were needed to obtain the spectra of the additional species.

Comparison of the deconvoluted spectrum of the additional component shows that the λ_{max} of the Soret band is at 409 nm, with comparable extinction coefficients to Met-ligated WT at pH 7.4 (Figure 5.4E, left), and the CT band at 695 nm also present (Figure 5.4E, right). However, the additional component a shift and broadening of the Soret band (Figure 5.4E, see inset). Further, the deconvoluted spectrum of the additional species shows an increase in the extinction coefficient near the 620 nm band despite comparable extinction coefficient of the 695 nm CT band to that of WT-like Met-ligated spectrum at pH 7.4 (Figure 5.4E, right).

Heme Coordination and Protein Fold of the Additional Species. To understand the properties of a distinct species in G41S detected from the SVD analysis, spectral data from multiple techniques were compared to those of WT

Electronic Absorption Spectra. For WT, the electronic absorption spectrum at pH 7.4 is similar to the spectrum at pH 4.0. The λ_{max} of the Soret band is at 409 nm, typical of a Met-ligated cyt *c* at both pH conditions (Figure 5.5A, left).

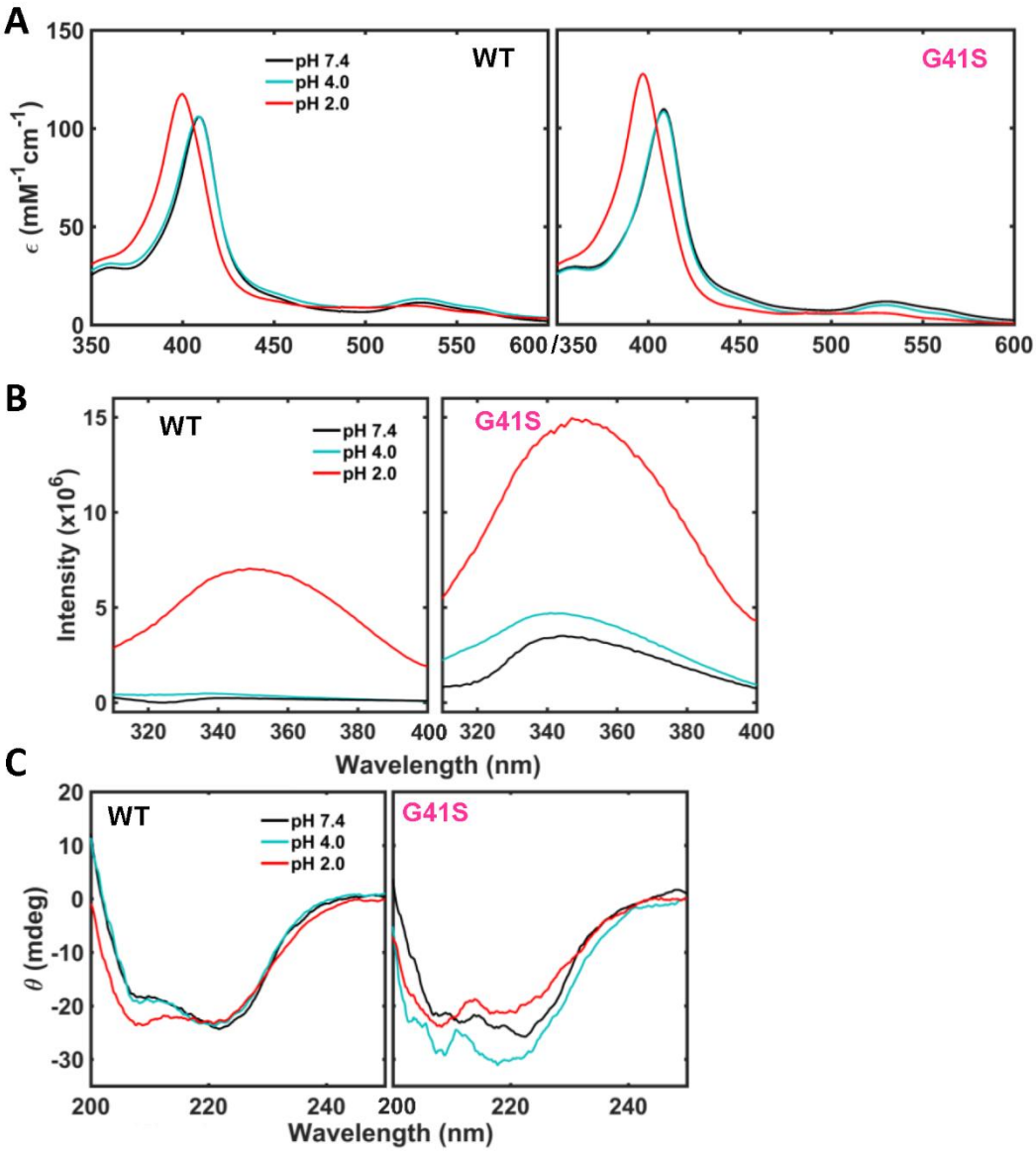

Figure 5.5. (A) Electronic absorption spectra of WT (left) and G41S (right) at pH 7.4 (black), 4.0 (teal), and 2.0 (red) in μ = 0.1 M buffers at room temperature, unless otherwise noted. (B) Fluorescence emission spectra of Trp59 (λ_{ex} = 290 nm) of WT (left) and G41S (right) variants of horse heart cyt *c* at pH 7.4 (black), 4.0 (teal), and 2.0 (red) in μ = 0.1 M buffers at room temperature, normalized to [cyt *c*] = 10 μM. (C) Far-UV CD spectra of WT (left) and G41S (right) variants of horse heart cyt *c* at 20 °C and pH 7.4 (black), 4.0 (teal), and 2.0 (red), normalized to [cyt *c*] = 20 μM and *l* = 1mm.

Decreasing the pH to 2.0 unfolds the protein, and λ_{max} of the Soret band shifts to 400 nm, commonly observed for a H_2O-ligated high-spin heme species in acid-denatured WT cyt *c*.[18, 34]

For G41S, the electronic absorption spectra at pH 7.4 and 4.0 are comparable and λ_{max} of the Soret band is at 408 nm (Figure 5.5A, right). Like in WT, the peak of the Soret absorption band does not change between the two pH conditions. Decreasing the pH 2.0 shifts the λ_{max} to 397 nm, and increase in the extinction coefficient is observed, commonly observed for the H_2O-ligated high-spin heme species.

***Tryptophan Fluorescence*.** Based on the X-ray crystal structure of the native state,[20] single Trp residue in cyt *c*, Trp59, is positioned near the 60's helix and HP7. In the folded state, Trp59 fluorescence is quenched by the heme; when the distance between Trp59 and the heme increases, Trp59 fluorescence is no longer quenched and its emission increases. This dependency of Trp59 emission to proximity of the heme makes it a good spectroscopic probe to determine the distance between Trp59 and the heme.[94-97]

For WT, the Trp59 fluorescence is fully quenched by the heme for both pH 7.4 and 4.0 conditions and Trp59 fluorescence is minimal (Figure 5.5B, left).[97] At pH 2.0, the protein is acid-unfolded, the intensity of the Trp59 fluorescence increases (Figure 5.5B, left).

For G41S, Trp59 fluorescence spectra are different from that of WT at all studied pH conditions. Unlike WT, the Trp59 fluorescence of G41S is less quenched at pH 7.4 (Figure 5.5B, right), suggesting that the packing of the protein in the 60's helix region is perturbed. The fluorescence intensity of the G41S Trp59 increases at pH 4.0; it is higher

than that of WT at pH 4.0 and only slightly lower than that of WT at pH 2.0 (Figure 5.5B). At pH 2.0, the fluorescence intensity of Trp59 in the acid denatured form of G41S is higher than that of WT (Figure 5.5B).

Far-UV CD Spectra. In WT, far-UV CD spectra at pH 7.4 and 4.0 are comparable to each another, with prominent negative signals at 210 and 222 nm, indicative of the α-helical structure (Figure 5.5C, left). At pH 2.0 under same ionic conditions (μ = 0.1 M), only the 210 nm signal increases in magnitude and 222 nm signal remains unchanged (Figure 5.5C, left). In the acid-unfolded state, the protein secondary structure is sensitive to the ionic conditions of the solution.[98] CD spectra of horse heart cyt *c* with a zinc-substituted heme at low ionic (μ = 0.02 M) conditions have shown greatly diminished peak at 222 nm and increased peak near 208 nm,[98] similar to apocyt *c* far-UV CD spectrum[99, 100] or horse cyt *c* spectrum at pH 2 in the absence of additional salt.[40] At higher ionic conditions μ = 0.2 to 1 M and pH 2.0 to 2.5, the MG species is observed and the intensity of the 222 nm peak regains the intensity similar to that of the folded WT protein .[98, 101, 102] The similarity of spectral features of our WT spectrum and reported spectra of the MG state suggest that the acid-denatured species in the WT spectrum at pH 2.0 is closer to the MG state than the fully acid-unfolded state.

Spectral features of the far-UV CD spectrum of G41S at pH 7.4 are comparable to those of WT, with negative peaks at 210 and 222 nm (Figure 5.5C, right). However, differences are apparent at pH 4.0. For G41S, the negative signals at 222nm and at 210 nm increase in magnitude (Figure 5.5C, right), suggesting that the secondary structure of the intermediate species at pH 4.0 is different from the species at pH 7.4. The spectrum of G41S at pH 4.0 is also distinct from the spectrum at pH 2.0 (Figure 5.5B).

Reduction Potential. Reduction potential values provide insights into the identity of the heme ligand and extent of heme encapsulation. Therefore, these parameters can be used to evaluate the extent of structural perturbations. Hysteresis between the results from the reduction and oxidation titrations for both G41S and WT are observed (Figures 5.6C and D). Possibility for this difference is the shift in baseline during the measurements, or if the system was not fully equilibrated prior to measurements during the oxidative electrochemical titration. However, The reduction potential of the WT protein obtained from the reductive electrochemical titration at pH 4.0 is within error of the value reported for the WT protein at near-neutral pH,[103] providing some confidence in the reduction potentials obtained in the reductive directions (Table 5.2).

For G41S, the reduction potential of the heme iron is lower than that of WT at pH 4.0 by approximately 50 mV (Table 5.2). This difference is greater than the < 10 mV reduction potential difference observed from ferricyanide titrations at pH 7.4 (Table 4.5), but less than differences in reduction potentials between Met-ligated hemes and His-, imidazole- or H_2O-ligated hemes.[16, 33, 104]

At pH 4.0, G41S is in a mixture of that contains 10% acid-unfolded species based on the SVD analysis (Figure 5.4D). Far-UV CD spectra suggest that the acid-denatured state of the G41S variant at $\mu = 0.1$ M is more like the MG state (Figure 5.5C). Reduction potential of the MG form is higher than the reduction potential of G41S measured at pH 4.0,[105] suggesting that the decrease observed in the reduction potential is not from the contributions from the acid-unfolded species.

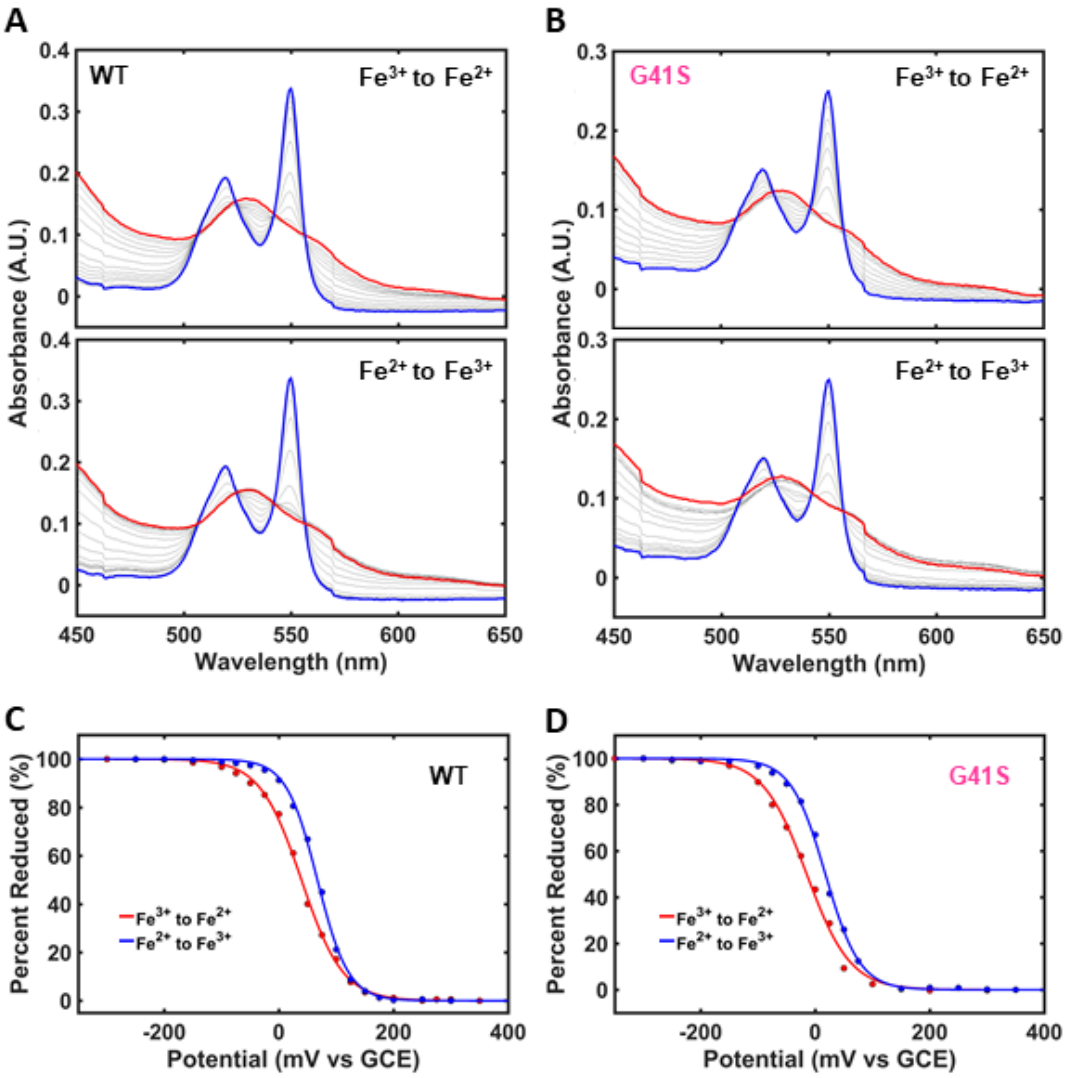

Figure 5.6. Electronic absorption spectra for (A) WT and (B) G41S variants of horse heart cyt *c* are shown at various potentials in reductive (top) and oxidative (bottom) directions in 100 mM sodium acetate buffer at pH 4.0 at μ = 0.1 M. Percent of ferrous protein calculated from the absorbance at 550 nm are plotted against applied external potential (versus GCE), are plotted with the fits for the (C) WT and (D) G41S.

Table 5.2. Reduction Potentials of WT and G41S[a]

Variants	pH	$E°$ (mV vs SHE)
WT	7.4	255[a]
	4.0	252 ± 2 (280 ± 2)[b]
	2.2	233 ± 5[c]
G41S	4.0	198 ± 4 (231 ± 2)

[a]From ref. [103].

[b]From this work, reductive (oxidative) direction.

[c]From ref.[105], versus NHE. Measured at 25 °C in aqueous HCl solution with 0.5 M chloride, for the MG state.

Since the reduction potential of G41S at pH 7.4 is only ~10 mV lower than that of WT from ferricyanide titrations, we can conclude that the reduction potential of the distinct species is lower than the native Met-ligated state and the MG state.

^{1}H NMR at Various pH Conditions. For ferric WT, methyl signals of the Met80-ligated heme porphyrin and proton peaks of the heme-ligated Met80 and His18 do not change from pD conditions 6.5 to 4.5 at room temperature (Figure 5.7),[106] a strong indication that the heme ligation and the heme electronic environment are unaffected in the observed pD range. This is in good agreement with spectroscopic data that suggest no differences in heme ligation or the polypeptide fold in ferric WT at pH 7.4 and 4.5 (Figure 5.5).[33, 51]

For ferric G41S, however, differences in ^{1}H NMR spectra are observed, notably with the 3- methyl signal of the heme porphyrin and the ε- and γ- proton signals of Met80 with a change in pD from 7.4 to 4.2 (Figure 5.8). With a decrease in pD, an additional peak emerges between the 8- and 3- methyl signals, and the intensity of the 3- methyl signal decreases relative to that of the 8-methyl signal. These spectral changes are also accompanied by a decrease in the intensity of the ε-proton signal of Met80, with a corresponding increase in another signal in the downfield -20 ppm region of the spectrum with lower pD. Interestingly, positions of the δ- and ε- protons of the heme-ligated His18 do not change with pD, unlike the signals of Met80 and heme porphyrin methyls. Further, the pH-dependent change observed in ^{1}H NMR is fully reversible. This suggests that the additional species observed between pD conditions 5.9 and 4.5 is not a product of irreversible protein denaturation. Instead, it is likely due to a folding intermediate that forms during the acid-induced unfolding transition in G41S.

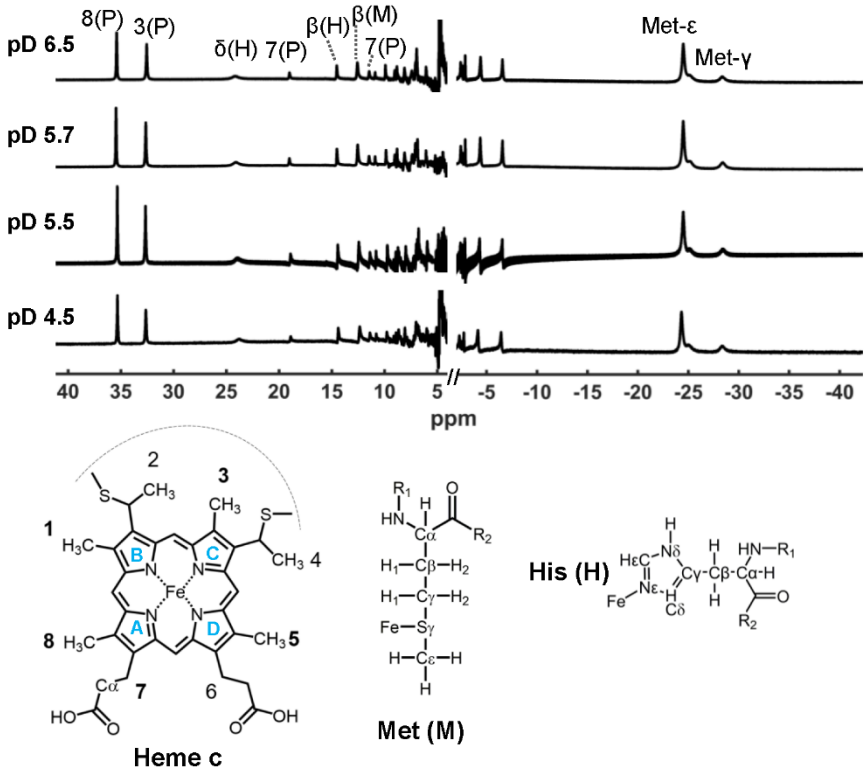

Figure 5.7. (Top) ^{1}H NMR spectra of ferric WT at pD 6.5, 5.7, 5.5, and 4.5 at 25 °C in either a 50 mM sodium phosphate or a 50 mM acetic acid-d_4 buffer in 100 % D_2O. Spectra were obtained independently, and titrations were not performed. (Bottom) Structure of *c*-type heme, Met, and His, with the labeling nomenclature.

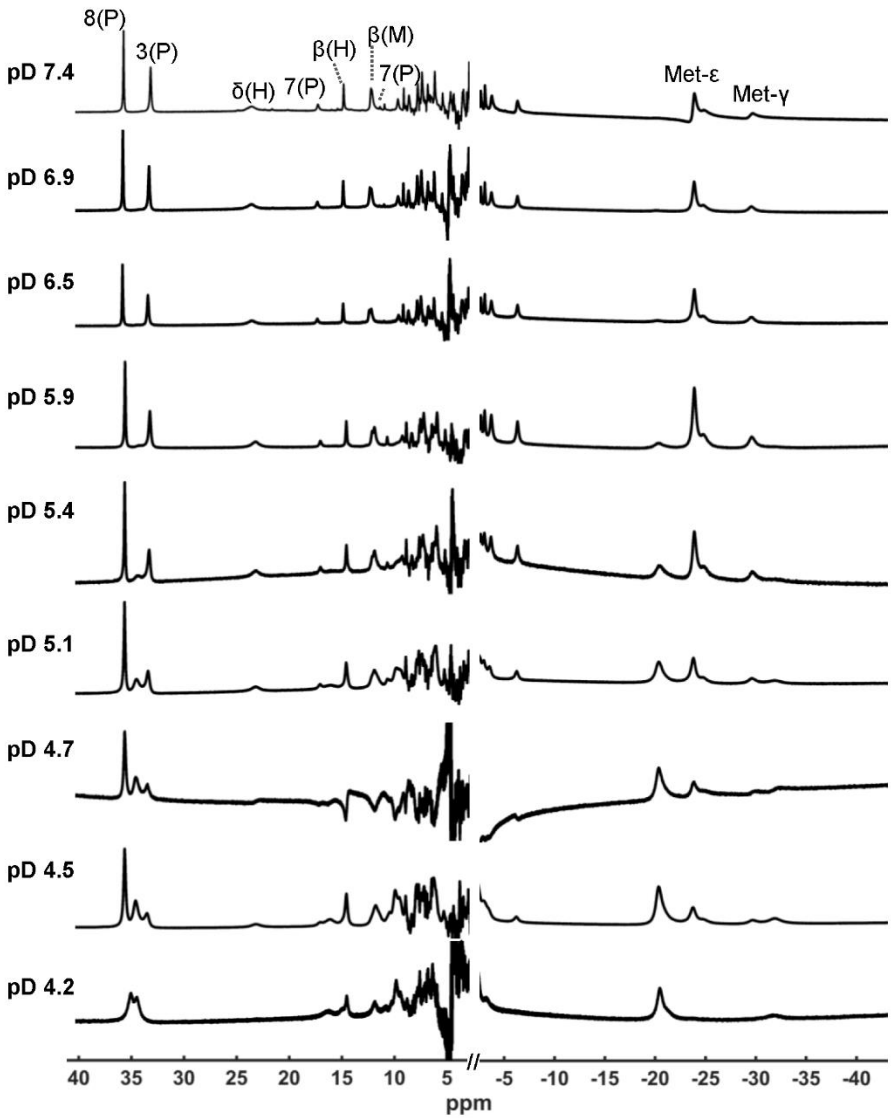

Figure 5.8. ^{1}H NMR spectra of ferric G41S at pD 7.4, 6.9, 6.5, 5.9, 5.4, 5.1 4.7, 4.5, and 4.2 at 25 °C in either a 50 mM sodium phosphate or a 50 mM acetic acid-d_4 buffer in 100% D_2O. pD was adjusted using NaOD or HCl as necessary.

Discussion

Previously, SVD analysis of the pH titration measurements for T78V/K79G variant in yeast cyt *c* detected a similar transition with a pK_a = 5.0 ± 0.1.[32] This species was assigned to be due to an acidic transition, where the axial ligand of the heme switch from Met-ligated to H_2O/His-ligated form. G41S also undergoes a transition at pK_a ~5, but is different from that of T78V/K79G variant in yeast cyt *c*. For T78V/K79G, electronic absorption spectra shows that λ_{max} of the Soret band blueshifts to 401 nm at pH 4.5 from 406 nm at pH 7.4 increases in intensity, and the reduction potential decreases by ~10 mV upon decreasing the pH from 7.4 to 4.5.[32] Although similar pK_a was observed in the pH titration profile of G41S, changes observed with T78V/K79G yeast cyt *c* are not observed in G41S horse heart cyt *c*. Electronic absorption spectra of the protein at both pH 7.4 and 4.0 shows that the λ_{max} of the Soret band at 408 nm is unchanged at both pH 7.4 and 4.0 (Figure 5.5A). Thus, it is unlikely that for G41S, the transition at pK_a ~ 5.1 is that for the formation of H_2O/His-ligated species, as electronic absorption spectra do not detect a shift in the λ_{max}. Thus, it is most likely that the distinct species observed in G41S still contains the Met-ligated heme iron species.

Changes are observed, not in the heme ligation, but in the structural features in G41S. Trp59 fluorescence measurements and CD spectra suggest that there are changes in the protein fold for G41S at pH 4.0 that are different from the fold at both pH 7.4 and 2.0. Since the heme iron ligation likely did not change, the ~50 mV decrease in the reduction potential for G41S at pH 4.0 is probably due to the changes in the structure that exposes the heme to the solvent.

Possible Involvement of Heme Propionates in the Acid Transition. Polypeptide packing changes during acid unfolding. Under extremely acidic conditions, carboxyl groups of the peptide backbone are protonated, and increase in the intramolecular repulsion between the charged groups causes the protein to unfold.[41, 42] Other residues are protonated as well, potentially breaking up any HB contacts.

Protonation of some groups near loop C triggers the unfolding of loop C in the cooperative acid unfolding process. Many mutational studies have suggested a role for loop C in cooperativity of acid unfolding transition.[27, 69, 75] A possible intermediate in the later stages of the folding transition has been observed in WT horse heart cyt *c* at pH 3, where loop C is rearranged into a β-sheet and a readily displaced Met80 is present.[44] HX experiments with horse heart WT cyt *c* suggested that stability of loop C coincides with the formation of the MG state,[12] and His26 or HP groups argued to be the protonating groups due to the contacts made with loop C.[12, 27, 44, 69, 75] The features of the distinct species observed in the G41S variant suggest changes in native packing, possibly due to loop C rearrangements. The pK_a of this transition is at ~ 5.0, suggesting residues Asp, Glu, and His as possible protonating groups. Of these residues, Glu61, His26, and His33 could potentially be responsible for the transition.

However, it is unlikely that either of these candidates is the source of the protonated group in the observed single-proton intermediate transition in G41S. Comparison of the ^{1}H NMR spectra reveals that the signals of the δ- and β-protons of the heme-ligated His18 are unaffected, suggesting that the region near the loop C and 20's loop containing His26 are likely the same as in WT (Figures 5.7 and 5.8). Although the Trp59 fluorescence intensity of the new species increases (Figure 5.5B), Glu61 is solvent-exposed,[20] and is unlikely that

the pK_a would increase with rearrangements in the polypeptide fold. Although loop C is near the 20's loop that contains both His26 and His33, examination of the X-ray crystal structure of horse heart WT cyt *c* shows that His33 does not make side chain interactions with loop C,[20] and pK_a of His26 is lower than 3,[18] making both His residues unlikely candidates to be responsible for the transition with the pK_a at ~5.

Could the HPs be involved in the protonation process? Propionic acids have an intrinsic pK_a of 4.88.[107] The pK_a values of model dipyrrole and monopyrrole monopropionic acid compounds also range from 4.6 to 4.8, depending on the concentration of water in the solvent.[108] pH titrations of ferric and ferrous horse heart cyt *c* assigned one of HPs to have a pK_a < 4.5 and another to have a pK_a > 9.[109] These data show that at least one of the HP pK_a value is close to the experimentally observed pK_a value of ~5 in G41S. Further, HP6 and HP7 are within HB and vdW distances with residues in loop C. Thus, changes to the connectivity to HPs groups could potentially affect its protonation properties.

In the ^{1}H NMR, spectra noticeable changes are observed in the region containing 8- and 3- methyl signals of the Met-ligated heme. DFT calculations of the heme orbitals show that both methyl groups are sensitive to the protonation of HP7, and structural changes in ring A containing HP7 alter the electronic environment of ring C, which contains the 3-methyl group.[29] From our ^{1}H NMR pH titration measurements for G41S, changes in the signals are observed in regions where the 8- and 3-methyl signals are present. It is possible that protonation of HP7 alters the relative intensities of the 8- and 3-methyl signals. However, more detailed studies are required to quantify the changes in the

^{1}H NMR spectra and to see if the new peak forming at 35 ppm is a shifted signal from 8- or 3-methyl.

Interestingly, not all perturbations in loop C led to the formation of the distinct species observed in G41S. pH titrations done with Y48H variant of horse heart cyt *c* do not show the presence of an additional species, despite also having perturbed loops C and D. Comparison of ^{1}H NMR spectra at pD conditions 7.4 and 4.5 shows downfield shifts of 8- and 3-methyl signals at lower pD values (Figure 3.12A) but no new signals were detected. Examination of the X-ray crystal structure of human Y48H offers clues as to why a distinct species observed for the horse heart G41S cyt *c* variant is not observed in the horse heart Y48H cyt *c* variant. The X-ray crystal structure of Y48H variant in human cyt *c* shows that His48 forms a HB with HP6.[110] In horse heart cyt *c*, Y48H mutation could also offer the potential HB contact with HP6, and perhaps, this additional HB prevents one of the HP groups from being protonated at mildly acidic conditions.

Conclusion

In the G41S horse heart cyt *c* variant, a distinct, previously uncharacterized species has been observed at mildly acidic conditions. This species appears at physiological pH conditions and likely has a lower reduction potential, not due to changes in ligation, but possibly due to the structural perturbations near the heme. Interestingly, this species is not observed in the Y48H horse heart cyt *c* variant, which also has a perturbed loop C. This difference between G41S and Y48H horse heart cyt *c* variants may stem from differences in contacts involving HP6, highlighting the possible role of the polypeptide packing near this region. These results suggest that loop C contacts may shield some groups from protonation and prevent the protein from easily accessing nonnative conformations.

Future Works

Additional experiments are required to truly assess whether the changes observed in the ^{1}H NMR are occurring in the HPs or elsewhere in the protein, and whether one or both of 3- and 8-methyls are reflecting the changes in the electronic environment of the heme. Isotope labeling can be used to better track the changes in the heme. Uniform ^{13}C labeling have been used in *c*-type heme proteins,[29, 111] which allows monitoring of the heme carbon signals. However, to better identify where the changes are occurring, targeted heme porphyrin labeling can also be used.[112-114] By using ^{13}C-NMR, the changes in specific heme carbons can be monitored with respect to pH,[112] clarifying the region of the heme that changes are being observed. To understand if these changes in the heme porphyrin ring are related to the local changes in loop C, uniform ^{13}C- and ^{15}N- labeling can be used to obtain the structural information from multidimensional NMR at pH condition where the distinct species is at high population. Recent studies with WT and MG-like L94G horse heart cyt *c* variant shows that this technique is sufficient even for loosely packed MG-like cyt *c*.[115]

To test whether the differences in HP6 connectivity results in favoring of the distinct species, pH-titrations of a double variant G41S/Y48H or G41S/F46Y can be performed to test whether including a possible HB group in the vicinity of the HP6 modifies formation of this species at near physiological conditions.

References

1. Feller, G. Psychrophilic enzymes: from folding to function and biotechnology. *Scientifica* **2013**, 512840 (2013).

2. D'Amico, S., Marx, J.C., Gerday, C. & Feller, G. Activity-stability relationships in extremophilic enzymes. *The Journal of biological chemistry* **278**, 7891-7896 (2003).

3. Feller, G. Life at low temperatures: is disorder the driving force? *Extremophiles* **11**, 211-216 (2007).

4. Feller, G. & Gerday, C. Psychrophilic enzymes: molecular basis of cold adaptation. *Cell Mol Life Sci* **53**, 830-841 (1997).

5. Gerday, C. *et al.* Psychrophilic enzymes: a thermodynamic challenge. *Biochim Biophys Acta* **1342**, 119-131 (1997).

6. Englander, S.W. & Mayne, L. The case for defined protein folding pathways. *P Natl Acad Sci USA* **114**, 8253-8258 (2017).

7. Maity, H., Maity, M., Krishna, M.M.G., Mayne, L. & Englander, S.W. Protein folding: The stepwise assembly of foldon units. *P Natl Acad Sci USA* **102**, 4741-4746 (2005).

8. Alvarez-Paggi, D. *et al.* Multifunctional Cytochrome c: Learning New Tricks from an Old Dog. *Chem Rev* **117**, 13382-13460 (2017).

9. Krishna, M.M.G., Maity, H., Rumbley, J.N., Lin, Y. & Englander, S.W. Order of steps in the cytochrome c folding pathway: Evidence for a sequential stabilization mechanism. *J Mol Biol* **359**, 1410-1419 (2006).

10. Maity, H., Maity, M. & Englander, S.W. How cytochrome c folds, and why: Submolecular foldon units and their stepwise sequential stabilization. *J Mol Biol* **343**, 223-233 (2004).

11. Krishna, M.M.G., Lin, Y., Mayne, L. & Englander, S.W. Intimate view of a kinetic protein folding intermediate: Residue-resolved structure, interactions, stability, folding and unfolding rates, homogeneity. *J Mol Biol* **334**, 501-513 (2003).

12. Krishna, M.M.G., Lin, Y., Rumbley, J.N. & Englander, S.W. Cooperative omega loops in cytochrome c: Role in folding and function. *J Mol Biol* **331**, 29-36 (2003).

13. Kristinsson, R. & Bowler, B.E. Communication of stabilizing energy between substructures of a protein. *Biochemistry* **44**, 2349-2359 (2005).

14. Hoang, L., Maity, H., Krishna, M.M., Lin, Y. & Englander, S.W. Folding units govern the cytochrome c alkaline transition. *J Mol Biol* **331**, 37-43 (2003).

15. Maity, H., Rumbley, J.N. & Englander, S.W. Functional role of a protein foldon - An Omega-Loop foldon controls the alkaline transition in ferricytochrome c. *Proteins* **63**, 349-355 (2006).

16. Battistuzzi, G., Borsari, M., Cowan, J.A., Ranieri, A. & Sola, M. Control of cytochrome c redox potential: Axial ligation and protein environment effects. *J Am Chem Soc* **124**, 5315-5324 (2002).

17. Marques, H.M. Insights into porphyrin chemistry provided by the microperoxidases, the haempeptides derived from cytochrome c. *Dalton T*, 4371-4385 (2007).

18. Moore, G.R. & Pettigrew, G.W. *Cytochromes c : evolutionary, structural, and physicochemical aspects*. (Springer-Verlag, Berlin ; New York; 1990).

19. Rajagopal, Badri S. *et al.* The hydrogen-peroxide-induced radical behaviour in human cytochrome c–phospholipid complexes: implications for the enhanced pro-apoptotic activity of the G41S mutant. *Biochem J* **456**, 441-452 (2013).

20. Bushnell, G.W., Louie, G.V. & Brayer, G.D. High-resolution three-dimensional structure of horse heart cytochrome c. *J Mol Biol* **214**, 585-595 (1990).

21. Berghuis, A.M. & Brayer, G.D. Oxidation State-Dependent Conformational-Changes in Cytochrome-C. *J Mol Biol* **223**, 959-976 (1992).

22. Kalpage, H.A. *et al.* Serine-47 phosphorylation of cytochrome c in the mammalian brain regulates cytochrome c oxidase and caspase-3 activity. *The FASEB Journal* **33**, 13503-13514 (2019).

23. Caffrey, M.S., Daldal, F., Holden, H.M. & Cusanovich, M.A. Importance of a Conserved Hydrogen-Bonding Network in Cytochromes-C to Their Redox Potentials and Stabilities. *Biochemistry* **30**, 4119-4125 (1991).

24. Ciaccio, C. *et al.* The Met80Ala and Tyr67His/Met80Ala mutants of human cytochrome c shed light on the reciprocal role of Met80 and Tyr67 in regulating ligand access into the heme pocket. *Journal of inorganic biochemistry* **169**, 86-96 (2017).

25. Tognaccini, L. *et al.* Structure-function relationships in human cytochrome c: The role of tyrosine 67. *Journal of inorganic biochemistry* **155**, 56-66 (2016).

26. Ying, T. *et al.* Tyrosine-67 in cytochrome c is a possible apoptotic trigger controlled by hydrogen bonds via a conformational transition. *Chemical communications (Cambridge, England)*, 4512-4514 (2009).

27. Baddam, S. & Bowler, B.E. Mutation of asparagine 52 to glycine promotes the alkaline form of iso-1-cytochrome c and causes loss of cooperativity in acid unfolding. *Biochemistry* **45**, 4611-4619 (2006).

28. Karsisiotis, A.I. *et al.* Increased dynamics in the 40-57 Omega-loop of the G41S variant of human cytochrome c promote its pro-apoptotic conformation. *Scientific reports* **6**, 30447 (2016).

29. Liptak, M.D., Fagerlund, R.D., Ledgerwood, E.C., Wilbanks, S.M. & Bren, K.L. The Proapoptotic G41S Mutation to Human Cytochrome c Alters the Heme Electronic Structure and Increases the Electron Self-Exchange Rate. *J Am Chem Soc* **133**, 1153-1155 (2011).

30. Goldes, M.E., Jeakins-Cooley, M.E., McClelland, L.J., Mou, T.C. & Bowler, B.E. Disruption of a hydrogen bond network in human versus spider monkey cytochrome c affects heme crevice stability. *Journal of inorganic biochemistry* **158**, 62-69 (2016).

31. Deacon, O.M., White, R.W., Moore, G.R., Wilson, M.T. & Worrall, J.A.R. Comparison of the structural dynamic and mitochondrial electron-transfer properties of the proapoptotic human cytochrome c variants, G41S, Y48H and A51V. *Journal of inorganic biochemistry* **203**, 110924 (2020).

32. Deng, Y., Weaver, M.L., Hoke, K.R. & Pletneva, E.V. A Heme Propionate Staples the Structure of Cytochrome c for Methionine Ligation to the Heme Iron. *Inorg Chem* **58**, 14085-14106 (2019).

33. Gu, J., Shin, D.W. & Pletneva, E.V. Remote Perturbations in Tertiary Contacts Trigger Ligation of Lysine to the Heme Iron in Cytochrome c. *Biochemistry* **56**, 2950-2966 (2017).

34. Theorell, H. & Akesson, A. Studies on cytochrome c. III. Titration curves. *J Am Chem Soc* **63**, 1818-1820 (1941).

35. Theorell, H. & Akesson, A. Studies on cytochrome c. II. The optical properties of pure cytochrome c and some of its derivatives. *J Am Chem Soc* **63**, 1812-1818 (1941).

36. Amacher, J.F. *et al.* A Compact Structure of Cytochrome c Trapped in a Lysine-Ligated State: Loop Refolding and Functional Implications of a Conformational Switch. *J Am Chem Soc* **137**, 8435-8449 (2015).

37. Assfalg, M. *et al.* Structural model for an alkaline form of ferricytochrome c. *J Am Chem Soc* **125**, 2913-2922 (2003).

38. Nold, S.M., Lei, H.T., Mou, T.C. & Bowler, B.E. Effect of a K72A Mutation on the Structure, Stability, Dynamics, and Peroxidase Activity of Human Cytochrome c. *Biochemistry* **56**, 3358-3368 (2017).

39. Weinkam, P. *et al.* Characterization of alkaline transitions in ferricytochrome c using carbon-deuterium infrared probes. *Biochemistry* **47**, 13470-13480 (2008).

40. Babul, J. & Stellwagen, E. Participation of the protein ligands in the folding of cytochrome c. *Biochemistry* **11**, 1195-1200 (1972).

41. Goto, Y., Calciano, L.J. & Fink, A.L. Acid-Induced Folding of Proteins. *P Natl Acad Sci USA* **87**, 573-577 (1990).

42. Goto, Y., Takahashi, N. & Fink, A.L. Mechanism of Acid-Induced Folding of Proteins. *Biochemistry* **29**, 3480-3488 (1990).

43. Engilberge, S., Rennie, M.L. & Crowley, P.B. Calixarene capture of partially unfolded cytochrome c. *Febs Lett* **593**, 2112-2117 (2019).

44. Balakrishnan, G. *et al.* A conformational switch to beta-sheet structure in cytochrome c leads to heme exposure. Implications for cardiolipin peroxidation and apoptosis. *J Am Chem Soc* **129**, 504-505 (2007).

45. Battistuzzi, G., Borsari, M. & Sola, M. Redox properties of cytochrome c. *Antioxid Redox Sign* **3**, 279-291 (2001).

46. Marques, H.M. Peroxidase activity of the hemeoctapeptide N-acetylmicroperoxidase-8. *Inorg Chem* **44**, 6146-6148 (2005).

47. Baldwin, D.A., Marques, H.M. & Pratt, J.M. Hemes and Hemoproteins .5. Kinetics of the Peroxidatic Activity of Microperoxidase-8 - Model for the Peroxidase Enzymes. *Journal of inorganic biochemistry* **30**, 203-217 (1987).

48. Lei, H. & Bowler, B.E. Naturally Occurring A51V Variant of Human Cytochrome c Destabilizes the Native State and Enhances Peroxidase Activity. *J Phys Chem B* **123**, 8939-8953 (2019).

49. Lei, H., Nold, S.M., Motta, L.J. & Bowler, B.E. Effect of V83G and I81A Substitutions to Human Cytochrome c on Acid Unfolding and Peroxidase Activity below a Neutral pH. *Biochemistry* **58**, 2921-2933 (2019).

50. Lei, H.T. & Bowler, B.E. Humanlike substitutions to Omega-loop D of yeast iso-1-cytochrome c only modestly affect dynamics and peroxidase activity. *Journal of inorganic biochemistry* **183**, 146-156 (2018).

51. Deng, Y.L., Zhong, F.F., Alden, S.L., Hoke, K.R. & Pletneva, E.V. The K79G Mutation Reshapes the Heme Crevice and Alters Redox Properties of Cytochrome c. *Biochemistry* **57**, 5827-5840 (2018).

52. Deacon, O.M., Svistunenko, D.A., Moore, G.R., Wilson, M.T. & Worrall, J.A.R. Naturally Occurring Disease-Related Mutations in the 40-57 Omega-Loop of Human Cytochrome c Control Triggering of the Alkaline Isomerization. *Biochemistry* **57**, 4276-4288 (2018).

53. Balut, C. *et al.* Measurement of cytosolic and mitochondrial pH in living cells during reversible metabolic inhibition. *Kidney International* **73**, 226-232 (2008).

54. Porcelli, A.M. *et al.* pH difference across the outer mitochondrial membrane measured with a green fluorescent protein mutant. *Biochemical and biophysical research communications* **326**, 799-804 (2005).

55. Weinberg, J.M., Davis, J.A., Roeser, N.F. & Venkatachalam, M.A. Role of intracellular pH during cytoprotection of proximal tubule cells by glycine or acidosis. *Journal of the American Society of Nephrology* **5**, 1314 (1994).

56. Gores, G.J., Nieminen, A.L., Wray, B.E., Herman, B. & Lemasters, J.J. Intracellular pH during "chemical hypoxia" in cultured rat hepatocytes. Protection by intracellular acidosis against the onset of cell death. *The Journal of clinical investigation* **83**, 386-396 (1989).

57. Nilsson, C., Kagedal, K., Johansson, U. & Ollinger, K. Analysis of cytosolic and lysosomal pH in apoptotic cells by flow cytometry. *Methods in cell science : an official journal of the Society for In Vitro Biology* **25**, 185-194 (2003).

58. Akhmedov, D. *et al.* Mitochondrial matrix pH controls oxidative phosphorylation and metabolism-secretion coupling in INS-1E clonal β cells. *The FASEB Journal* **24**, 4613-4626 (2010).

59. Iverson, S.L. & Orrenius, S. The cardiolipin-cytochrome c interaction and the mitochondrial regulation of apoptosis. *Arch Biochem Biophys* **423**, 37-46 (2004).

60. Kawai, C. *et al.* pH-Sensitive Binding of Cytochrome c to the Inner Mitochondrial Membrane. Implications for the Participation of the Protein in Cell Respiration and Apoptosis. *Biochemistry* **48**, 8335-8342 (2009).

61. Qian, T., Nieminen, A.L., Herman, B. & Lemasters, J.J. Mitochondrial permeability transition in pH-dependent reperfusion injury to rat hepatocytes. *The American journal of physiology* **273**, C1783-1792 (1997).

62. Dyson, H.J. & Beattie, J.K. Spin state and unfolding equilibria of ferricytochrome c in acidic solutions. *Journal of Biological Chemistry* **257**, 2267-2273 (1982).

63. Indiani, C. *et al.* Effect of pH on axial ligand coordination of cytochrome c" from Methylophilus methylotrophus and horse heart cytochrome c. *Biochemistry* **39**, 8234-8242 (2000).

64. Jeng, M.F., Englander, S.W., Elove, G.A., Wand, A.J. & Roder, H. Structural description of acid-denatured cytochrome c by hydrogen exchange and 2D NMR. *Biochemistry* **29**, 10433-10437 (1990).

65. Oellerich, S., Wackerbarth, H. & Hildebrandt, P. Spectroscopic Characterization of Nonnative Conformational States of Cytochrome c. *The Journal of Physical Chemistry B* **106**, 6566-6580 (2002).

66. Cohen, J.S. & Hayes, M.B. Nuclear magnetic resonance titration curves of histidine ring protons. V. Comparative study of cytochrome c from three species and the assignment of individual proton resonances. *The Journal of biological chemistry* **249**, 5472-5477 (1974).

67. Stellwagen, E. & Babul, J. Stabilization of the globular structure of ferricytochrome c by chloride in acidic solvents. *Biochemistry* **14**, 5135-5140 (1975).

68. Hamada, D. *et al.* Role of heme axial ligands in the conformational stability of the native and molten globule states of horse cytochrome c. *J Mol Biol* **256**, 172-186 (1996).

69. Battistuzzi, G. *et al.* Role of Met80 and Tyr67 in the low-pH conformational equilibria of cytochrome c. *Biochemistry* **51**, 5967-5978 (2012).

70. Hanske, J. *et al.* Conformational properties of cardiolipin-bound cytochrome c. *P Natl Acad Sci USA* **109**, 125-130 (2012).

71. Godbole, S. & Bowler, B.E. Effect of pH on formation of a nativelike intermediate on the unfolding pathway of a Lys 73 --> His variant of yeast iso-1-cytochrome c. *Biochemistry* **38**, 487-495 (1999).

72. Duncan, M.G., Williams, M.D. & Bowler, B.E. Compressing the free energy range of substructure stabilities in iso-1-cytochrome c. *Protein Sci* **18**, 1155-1164 (2009).

73. Krishna, M.M., Hoang, L., Lin, Y. & Englander, S.W. Hydrogen exchange methods to study protein folding. *Methods* **34**, 51-64 (2004).

74. Milne, J.S., Mayne, L., Roder, H., Wand, A.J. & Englander, S.W. Determinants of protein hydrogen exchange studied in equine cytochrome c. *Protein Sci* **7**, 739-745 (1998).

75. Baddam, S. & Bowler, B.E. Thermodynamics and kinetics of formation of the alkaline state of a Lys 79 -> Ala/Lys 73 -> His variant of iso-1-cytochrome C. *Biochemistry* **44**, 14956-14968 (2005).

76. Krishna, M.M.G., Maity, H., Rumbley, J.N. & Englander, S.W. Branching in the sequential folding pathway of cytochrome c. *Protein Sci* **16**, 1946-1956 (2007).

77. Wandschneider, E., Hammack, B.N. & Bowler, B.E. Evaluation of cooperative interactions between substructures of iso-1-cytochrome c using double mutant cycles. *Biochemistry* **42**, 10659-10666 (2003).

78. Redzic, J.S. & Bowler, B.E. Role of hydrogen bond networks and dynamics in positive and negative cooperative stabilization of a protein. *Biochemistry* **44**, 2900-2908 (2005).

79. Sinibaldi, F. *et al.* Rupture of the hydrogen bond linking two Omega-loops induces the molten globule state at neutral pH in cytochrome c. *Biochemistry* **42**, 7604-7610 (2003).

80. Hao, Z.Y. *et al.* Specific ablation of the apoptotic functions of cytochrome c reveals a differential requirement for cytochrome c and apaf-1 in apoptosis. *Cell* **121**, 579-591 (2005).

81. Morison, I.M. *et al.* A mutation of human cytochrome c enhances the intrinsic apoptotic pathway but causes only thrombocytopenia. *Nat Genet* **40**, 387-389 (2008).

82. De Rocco, D. *et al.* Mutations of cytochrome c identified in patients with thrombocytopenia THC4 affect both apoptosis and cellular bioenergetics. *Bba-Mol Basis Dis* **1842**, 269-274 (2014).

83. Englander, S.W., Mayne, L. & Krishna, M.M. Protein folding and misfolding: mechanism and principles. *Quarterly reviews of biophysics* **40**, 287-326 (2007).

84. Hu, W.B., Kan, Z.Y., Mayne, L. & Englander, S.W. Cytochrome c folds through foldon-dependent native-like intermediates in an ordered pathway. *P Natl Acad Sci USA* **113**, 3809-3814 (2016).

85. Xu, Y., Mayne, L. & Englander, S.W. Evidence for an unfolding and refolding pathway in cytochrome c. *Nat Struct Biol* **5**, 774-778 (1998).

86. Jeng, M.F. & Englander, S.W. Stable submolecular folding units in a non-compact form of cytochrome c. *J Mol Biol* **221**, 1045-1061 (1991).

87. Berry, E.A. & Trumpower, B.L. Simultaneous determination of hemes a, b, and c from pyridine hemochrome spectra. *Analytical biochemistry* **161**, 1-15 (1987).

88. Galo, A.L. & Colombo, M.F. Singular Value Decomposition and Ligand Binding Analysis. *J Spectrosc* (2013).

89. Hendler, R.W. & Shrager, R.I. Deconvolutions Based on Singular-Value Decomposition and the Pseudoinverse - a Guide for Beginners. *J Biochem Bioph Meth* **28**, 1-33 (1994).

90. Pintscher, S. *et al.* Tuning of Hemes b Equilibrium Redox Potential Is Not Required for Cross-Membrane Electron Transfer. *The Journal of biological chemistry* **291**, 6872-6881 (2016).

91. Verissimo, A.F., Sousa, F.L., Baptista, A.M., Teixeira, M. & Pereira, M.M. Thermodynamic redox behavior of the heme centers of cbb3 heme-copper oxygen reductase from Bradyrhizobium japonicum. *Biochemistry* **46**, 13245-13253 (2007).

92. Nakajima, H. *et al.* Redox properties and coordination structure of the heme in the co-sensing transcriptional activator CooA. *The Journal of biological chemistry* **276**, 7055-7061 (2001).

93. Zahn, J.A., Arciero, D.M., Hooper, A.B. & Dispirito, A.A. Cytochrome c' of Methylococcus capsulatus Bath. *Eur J Biochem* **240**, 684-691 (1996).

94. Wu, P. & Brand, L. Resonance energy transfer: methods and applications. *Analytical biochemistry* **218**, 1-13 (1994).

95. Lakowicz, J.R. *Principles of Fluorescence Spectroscopy*, Edn. 2nd. (Kluwer Academic/ Plenum, New York; 1999).

96. Chhabra, D. & dos Remedios, C.G. Fluorescence Resonance Energy Transfer, in *eLS* (

97. Sanchez, K.M., Schlamadinger, D.E., Gable, J.E. & Kim, J.E. Förster Resonance Energy Transfer and Conformational Stability of Proteins. An Advanced Biophysical Module for Physical Chemistry Students. *Journal of Chemical Education* **85**, 1253 (2008).

98. Tremain, S.M. & Kostic, N.M. Molten-globule and other conformational forms of zinc cytochrome c. Effect of partial and complete unfolding of the protein on its electron-transfer reactivity. *Inorg Chem* **41**, 3291-3301 (2002).

99. Fisher, W.R., Taniuchi, H. & Anfinsen, C.B. On the role of heme in the formation of the structure of cytochrome c. *The Journal of biological chemistry* **248**, 3188-3195 (1973).

100. Stellwagen, E., Rysavy, R. & Babul, G. The conformation of horse heart apocytochrome c. *The Journal of biological chemistry* **247**, 8074-8077 (1972).

101. Vassilenko, K.S. & Uversky, V.N. Native-like secondary structure of molten globules. *Bba-Protein Struct M* **1594**, 168-177 (2002).

102. Nakamura, S., Seki, Y., Katoh, E. & Kidokoro, S. Thermodynamic and Structural Properties of the Acid Molten Globule State of Horse Cytochrome c. *Biochemistry* **50**, 3116-3126 (2011).

103. Eddowes, M.J. & Hill, H.A.O. Electrochemistry of Horse Heart Cytochrome-C. *J Am Chem Soc* **101**, 4461-4464 (1979).

104. Zhong, F., Alden, S.L., Hughes, R.P. & Pletneva, E.V. Comparing Properties of Common Bioinorganic Ligands with Switchable Variants of Cytochrome c. *Inorg Chem* (2021).

105. Santucci, R. *et al.* Anion size modulates the structure of the A state of cytochrome c. *Biochemistry* **39**, 12632-12638 (2000).

106. Rosell, F.I., Ferrer, J.C. & Mauk, A.G. Proton-linked protein conformational switching: Definition of the alkaline conformational transition of yeast iso-1-ferricytochrome c. *J Am Chem Soc* **120**, 11234-11245 (1998).

107. International Union of Pure and Applied Chemistry. Commission on Equilibrium Data., Serjeant, E.P., Dempsey, B. & International Union of Pure and Applied Chemistry. Commission on Electrochemical Data. *Ionisation constants of organic acids in aqueous solution*. (Pergamon Press, Oxford ; New York; 1979).

108. Holmes, D.L. & Lightner, D.A. Synthesis and acidity constants of 13CO2H-labelled dicarboxylic acids. pKas from 13C-NMR. *Tetrahedron* **52**, 5319-5338 (1996).

109. Hartshorn, R.T. & Moore, G.R. A denaturation-induced proton-uptake study of horse ferricytochrome c. *Biochem J* **258**, 595-598 (1989).

110. Deacon, O.M. *et al.* Heightened Dynamics of the Oxidized Y48H Variant of Human Cytochrome c Increases Its Peroxidatic Activity. *Biochemistry* **56**, 6111-6124 (2017).

111. Turner, D.L. Determination of haem electronic structure in His-Met cytochromes c by 13C-NMR. The effect of the axial ligands. *Eur J Biochem* **227**, 829-837 (1995).

112. Behr, J., Hellwig, P., Mäntele, W. & Michel, H. Redox Dependent Changes at the Heme Propionates in Cytochrome c Oxidase from Paracoccus denitrificans: Direct Evidence from FTIR Difference Spectroscopy in Combination with Heme Propionate 13C Labeling. *Biochemistry* **37**, 7400-7406 (1998).

113. Li, J., Deslouches, B., Cosloy, S.D. & Russell, C.S. A heme-deficient strain of Escherichia coli has a three-base pair deletion in a “hotspot” in hemA. *Biochimica et Biophysica Acta (BBA) - Gene Structure and Expression* **1626**, 102-105 (2003).

114. Bryson, D., Lim, P.L., Lawson, A., Manjunath, S. & Raner, G.M. Isotopic labeling of the heme cofactor in cytochrome P450 and other heme proteins. *Biotechnology letters* **33**, 2019-2026 (2011).

115. Naiyer, A., Islam, A., Hassan, M.I., Ahmad, F. & Sundd, M. Backbone and side chain 1H, 15N and 13C chemical shift assignments of the molten globule state of L94G mutant of horse cytochrome-c. *Biomolecular NMR Assignments* **14**, 37-44 (2020).

Chapter 6

Perturbations in the Intraprotein Hydrogen-Bonding Network Trigger Lysine Ligation to the Heme and Enhance Peroxidase Activity in Cytochrome *c*

This chapter was adapted with permission from *Biochemistry*, **2017**, *56*, 2950-2966.

Spectral data for K73A/K79G/M80K were provided by Dr. Fangfang Zhong

EPR data were obtained in collaboration with Drs. Fangfang Zhong and Jie Gu

Peroxidase activity measurements were performed in collaboration with Dr. Jie Gu

The plasmid for WT horse heart cyt *c* was provided by Dr. Kara L. Bren

Introduction

Composed of relatively weak interactions, HB networks can have a major effect on the structural and functional properties of enzymes. The activity of an enzyme is often tuned based on how HB networks rearrange or pack the protein backbone around the active site.[1] For example, in human transketolase the HB distance between the two active site glutamates is decreased to lower the barrier for substrate turnover,[2] and in caspase-1 the HB network is rearranged to stabilize the substrate binding loop containing catalytic residues in the activated form.[3] Such tuning of weak interactions has been suggested to differentiate enzymes with otherwise similar amino acid sequences in the active site.[4, 5] One example is cyt *c*, a small heme-containing multifunctional protein.[6] Peroxidases contain a heme group, which has intrinsic peroxidase activity.[7] In cyt *c*, the intrinsic peroxidase activity is suppressed by the peptide backbone,[8, 9] and the protein functions as an electron carrier rather than a peroxidase.[6, 10]

Many HBs around the heme in cyt *c* are conserved among different types of species, including the inner HB network that loosely packs the flexible protein segment (residues 70 to 85, loop D) around the heme.[6, 11] In the native state, cyt *c* maintains a compact globular form, with the heme iron ligated by His18 and Met80 (Figure 6.1).[11] The critical inner HB network consists of residues from different regions of the protein, Tyr67 in the 60's helix, Thr78 in loop D, and Asn52 in loop C, linked by a structural water. This HB network stabilizes the native fold of the protein, encapsulating the heme to tune the reduction potential of the heme iron,[12, 13] and allow cyt *c* to participate in the cellular oxidative phosphorylation pathway as an electron carrier.[10]

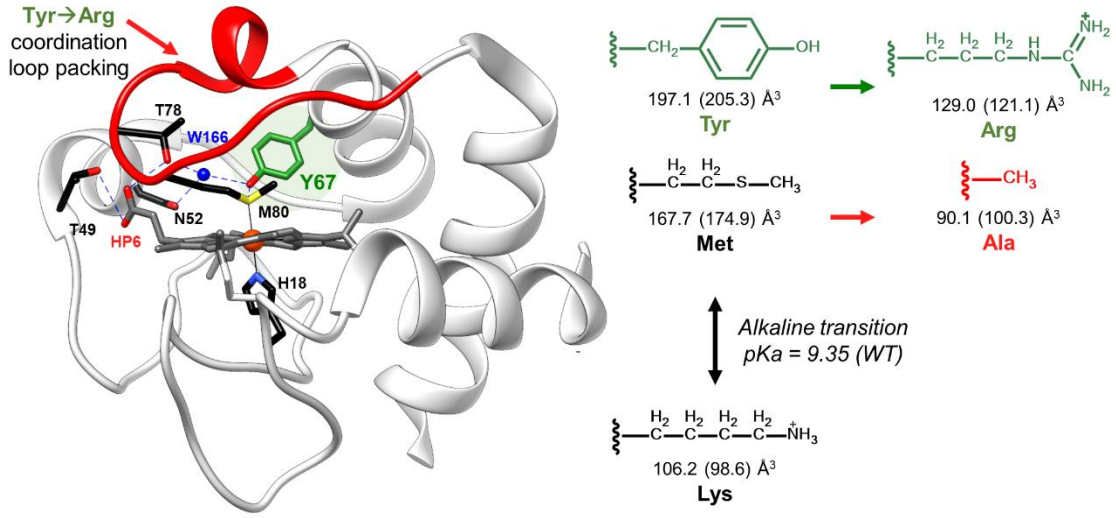

Figure 6.1. Structure of WT horse heart cyt *c* (Protein Data Bank entry 1HRC).[11] Highlighted are the residues participating in the intraprotein HB networks immediately around the coordination sphere of interest. Coordination of the loop D packing was perturbed by mutating Tyr67 (green) to Arg, which also participates in the HB network formed by Met80, Thr78, and Asn52. Major perturbation of this loop can potentially influence the HB contacts of HP6, which is HB to both Thr49 and Thr78. Shown on the right are the corresponding side chains of the amino acids introduced into the variants studied as well as Lys, with the side chain volumes (SC_{vol}) of the amino acids shown when buried and in solution (in parentheses) ($SC_{vol} = V_{aa} - V_{gly}$).[14]

Disruption of the inner HB network is linked to conformational rearrangements that can result in the replacement of Met80 at the ferric heme iron ligand by Lys,[15-17] His,[18, 19] or small molecules.[20] This rearrangement is readily observed at alkaline pH conditions, when either Lys73 or Lys79 replace Met80.[21-24] Mechanistic studies have suggested that the deprotonation of a yet unknown "trigger group" precedes the replacement of Met80.[22, 24] Besides deprotonating the trigger group, perturbation to the native polypeptide fold can also cause conformational rearrangements. Unfolding studies with chemical denaturants show that Met80 is replaced at the heme iron by other ligands, such as Lys or His,[9, 25-27] highlighting the importance of this network in preserving the native Met-ligation.

Conformational switching is crucial for initiating cyt *c*-mediated apoptosis. Binding cyt *c* to CL on the surface of the inner membrane perturbs the tertiary fold of the protein and disrupts the Met80-heme ligation to promote the peroxidase function of the protein.[28, 29] Here, the axial ligand must be occupied by H_2O_2 to initiate peroxidase activity. However, in the CL-induced unfolded state, Lys, His, and hydroxide-ligated heme iron species are observed at physiological conditions.[30, 31] Although Lys-ligation is common at alkaline conditions, several studies have shown that local perturbations in the inner HB network can induce Lys-ligation at a lower pH.[15, 17] For example, the T78C/K79G yeast cyt *c* variant with a modified HB network, forms Lys-ligated species at near-neutral pH.[15] Similar changes in the alkaline transition have been observed in horse heart cyt *c* containing nitrated Tyr74, and this modification has been proposed to present a steric strain on Glu66 and affect the HB network.[17] Yet not all perturbations of the HB network promote conformational rearrangement to form the Lys-ligated species at earlier pH conditions. The Y67F cyt *c* variant, designed to eliminate a key HB in the inner HB network, increases

both the stability and pK_a of the alkaline transition.[17, 32, 33] Thus, it is unclear what types of perturbations in the HB network promote the conformational rearrangement to the Lys-ligated species.

To better relate the role of the inner HB network in inducing rearrangements that favor the Lys-ligated species, we have introduced a Y67R mutation in horse heart cyt *c*. Previously, the Y67R variant has been studied in both human and yeast proteins. In both human and yeast cyt *c*, this mutation has been shown to increase the peroxidase activity of the protein.[34, 35] However, the relationship between the increase in peroxidase activity and a particular structural perturbation has not been clear. In peroxidases, distal Arg has been argued to provide a stabilizing charge on the leaving oxygen atom in H_2O_2 and promote the heterolytic cleavage of the O-O bond, as well as donate a HB to and stabilize the compound I species.[36] Similarly, placement of an Arg residue in the heme cavity of cyt *c* has been suggested to promote H_2O_2 cleavage by mimicking the active site of peroxidases.[35] The catalytic efficiency of peroxidase reaction in Y67R cyt *c* increased by an order of magnitude in human cyt *c*,[35] and between one to three orders of magnitude in yeast cyt *c* depending on the temperature.[37] Yet, activity enhancement in Y67R is much lower compared to peroxidases at similar conditions,[38, 39] leaving much to be clarified. Further, the identity of the heme iron ligand in Y67R has been ambiguous. Previous IR studies with human Y67R cyt *c* have suggested the presence of either a Lys, OH^-, or even His, to occupy the 6th axial position in the ferric state.[35]

Our studies show that the Y67R variant is Lys-ligated at neutral pH and lacks a native tertiary structure. We propose that the inner HB network contributes to conformational rearrangement. We also rationalize the increase in peroxidase activity of

the Lys-ligated species by considering the Lys binding kinetics. We observe that in the absence of a compact native fold, Lys more readily dissociates from the ferric heme at near-neutral pH conditions. This finding suggests that in the CL-bound state, Lys-ligated species may not hinder the peroxidase activity of the protein.

Material and Methods

General. Chemicals were purchased from Millipore Sigma Co. and Fischer Scientific Inc. unless otherwise noted. All solutions were prepared using water purified to 18 MΩ·cm resistivity using a Barnstead E-Pure Ultrapure Water Purification System, and pH adjusted with ± 0.02 accuracy using an AB15 pH meter (Fischer Scientific). Data analyses and visualizations were performed using Matlab R2013a-R2017a (MathWorks), SigmaPlot 10.0 (Systat Software), Origin 8 (OriginLab Corp.), and Chimera v.1.10.2 (UCSF).[40]

Site-Directed Mutagenesis, Protein Expression, and Purification. Wild-type (WT) horse heart cytochrome *c* was purchased from Sigma-Aldrich (C2506). Desired point mutations were introduced in the pBTR plasmid encoding horse heart cytochrome *c* using a QuikChange kit (Agilent),[41] and confirmed by sequencing at the Molecular Biology & Proteomics Core Facility (Dartmouth College) and using FinchTV v.1.4.0 (Geospiza).

Large-scale protein expression was performed as previously described,[29] except with 2L of TB media in a 2.8-L flask to prevent heme degradation and increase protein yield. Protein extraction was performed at 4 °C using French Press to prevent thermal denaturation. Purification was performed using a 10 mM sodium phosphate buffer at pH 7.4 as previously described,[29] except for Y67R mutation-containing proteins, where the purification was performed using a 10 mM HEPES buffer at pH 8.0. Mutations and purity

of the expressed proteins were confirmed by MALDI at the Molecular Biology & Proteomics Core Facility (Dartmouth College).

Sample Preparations. Potassium ferricyanide and sodium dithionite were added in excess to prepare ferric and ferrous proteins, respectively. Excess redox reagents were removed, unless noted otherwise, and protein samples were exchanged into a desired buffer using a size-exclusion (PD-10 desalting column, GE healthcare) or an ion-exchange (Sepharose HP SP, GE-Healthcare) column. Ferrous proteins were prepared in a nitrogen-filled glovebox (COY Laboratory Products), and samples were sealed in a quartz cuvette (Starna Scientific) or a Shigemi NMR tube (Wilmad Lab Glass) inside the glovebox prior to measurements.

Spectroscopic Measurements. All experiments were performed at 22 ± 2 °C unless noted otherwise. Electronic absorption spectra were obtained on an Agilent 8453 diode-array spectrophotometer. Pyridine hemochrome assays were performed in either a 100 mM sodium phosphate buffer at pH 7.4 or in a 100 mM sodium acetate buffer at pH 4.5 to obtain extinction coefficients as previously described.[42]

Low-temperature (10 K) EPR spectra were recorded on a Bruker EMX 300 X-band EPR spectrometer (Bruker Biosciences Corp), using the following experimental parameters: microwave frequency of 9.49 GHz, microwave power of 3.21 mW, modulation frequency of 100 kHz, modulation amplitude of 1.00 G, and time constant of 20.48 ms. All samples were purified by ion-exchange chromatography and dialyzed against the desired buffer for a minimum of two hours. Depending on the global stability of the protein, Y67R variants were freshly prepared and never frozen to minimize denaturation. All buffers were chelated and glassware acid-washed to minimize signals from metal ions in the EPR

spectra. Protein concentrations in the sample were between 200 and 500 μM and contained 20 to 30 % (*v*/*v*) glycerol as a cryoprotectant to help preserve the structural integrity of the protein.[43-45] All EPR data were processed using Bruker WinEPR version 2.22, revision 10.

^{1}H NMR spectra were recorded on a 500 MHz Bruker NMR spectrometer (Bruker Biosciences) at 25 °C. Samples were prepared in a 50 mM sodium phosphate or a 50 mM acetic acid d_4 buffer in either 100% D_2O for ferric samples or containing 10% (*v*/*v*) D_2O for ferrous samples. Proteins were exchanged into appropriate buffers using 10 kDa centrifugal ultrafiltration devices (Millipore). Final protein concentrations were around 500 μM to 1 mM; a small amount of dithionite (1 mM) was added to ferrous samples and additional degassing/N_2 purge cycles performed using anaerobic cuvettes to prevent autooxidation during measurements. 1D ^{1}H NMR spectra of the ferric proteins were recorded using a superWEFT pulse sequence[46] with a recycle delay of 220 ms for low-spin or 110 ms for high-spin heme species. For ferrous proteins, 1D ^{1}H NMR and 2D ^{1}H NOESY spectra were obtained using excitation sculpting with gradients to suppress the water signal.[47] All NMR data were analyzed using Bruker TopSpin version 3.2.

CD spectra and temperature melting curves were obtained on a JASCO-J815 CD spectropolarimeter equipped with a variable-temperature Peltier cell device (JASCO, Inc.) under constant flow of N_2. Far-UV, near-UV, and visible CD spectra of the proteins were obtained ensuring the electronic absorption did not exceed absorbance of 1 at wavelengths of interest. For far-UV spectra, buffers did not contain chloride to minimize unwanted signals.[48] Experimental parameters were as follows: average of 6 scans, 0.1 nm pitch, at 100 nm/min. The lamps were preheated for at least 20 minutes, and chambers were purged with N_2 for 5 minutes prior to each measurement.

Chemical Denaturation. Ultrapure GuHCl was dissolved in the desired buffer and concentration of GuHCl in the stock solution was calculated using refractive index (ΔN) measurements.[49] A series of GuHCl solutions was then prepared and pH of these solutions was adjusted to desired values. Solutions were stored under foil at room temperature and used within 5 days.

Changes in the electronic absorption spectra in the Soret region and changes in the α-helical content were monitored, as a function of GuHCl concentration by UV-vis spectroscopy and CD, respectively. The dependence of ratios of the two wavelengths identified as maxima and minima in the difference absorption spectra or ellipticity versus GuHCl concentration were fitted to eq 6.1:[50]

$$f(x)=\frac{[m_f[\mathrm{GuHCl}]+b_f+(m_u[\mathrm{GuHCl}]+b_u)\exp(\frac{m_D([\mathrm{GuHCl}]-[\mathrm{GuHCl}]_{1/2})}{RT})]}{[1+\exp(\frac{m_D([\mathrm{GuHCl}]-[\mathrm{GuHCl}]_{1/2})}{RT})]} \quad (6.1)$$

where m_f and b_f are the slope and y-intercept of the signal from the folded protein, respectively, and m_u and b_u are the slope and y-intercept of the signal from the unfolded protein, respectively. R is the gas constant, T is the experimental temperature, $[\mathrm{GuHCl}]_{1/2}$ is the midpoint of the unfolding transition, and m_D is the slope of the unfolding transition. The Gibbs free energy of unfolding, ΔG_D, was calculated from the fitted parameters m_D and $[\mathrm{GuHCl}]_{1/2}$ using eq 6.2:[51]

$$\Delta G_D = m_D[\mathrm{GuHCl}]_{1/2} \quad (6.2)$$

Thermal Denaturation. Samples containing protein in concentrations between 15 and 25 μM were used to record CD ellipticity at 222 nm in the temperature range between 20 to 90 °C in 1 °C increments, at a rate of 1 °C /min. CD spectra of the samples at 90 °C were obtained before and after the temperature melt. Thermal denaturation under these conditions for the variants studied was ≥ 83% reversible. The dependence of ellipticity at 222 nm versus temperature was fitted to eq 6.3:[52]

$$f(x)=\frac{m_f T+b_f+(m_u[\mathrm{GuHCl}]+b_u)\exp[\frac{-\Delta H_{D,vH}}{R}(\frac{1}{T}-\frac{1}{T_m})]}{1+\exp[\frac{-\Delta H_{D,vH}}{R}(\frac{1}{T}-\frac{1}{T_m})]} \quad (6.3)$$

where m_f and b_f are the slope and y-intercept of the signal from the folded protein, respectively, and m_u and b_u are the slope and y-intercept of the signal from the unfolded protein, respectively. R is the gas constant, T_m is the midpoint of the unfolding transition, and $\Delta H_{D,vH}$ is the van't Hoff enthalpy of denaturation at T_m.

Spectroelectrochemical Measurements. A Shimadzu UV-1201 scanning spectrophotometer equipped with a spectroelectrochemistry kit (Pine Research Instrumentation) was used to perform electrochemistry titrations. Samples were prepared, and experiments were performed as previously described,[53] with the addition of brief degassing and N_2 purges of samples in anaerobic cuvettes prior to measurements. Electronic absorption at 550 nm were plotted as a function of the external potential and these dependencies were fitted to eq 6.4:[6]

$$f(x)=\frac{A_m}{10^{(x-E°)/1000\times n/0.059}+1} \quad (6.4)$$

where A_m is the absorption of the ferrous protein in the absence of ferric protein, $E°$ is the reduction of the heme iron, and n is the number of electrons transferred in the reaction.

pH Titration and SVD Analysis. For accurate analysis of changes in the Soret and CT bands, two separate spectral series were examined in the 350 to 650 nm range and 590 to 720 nm range, respectively. Protein concentrations of 10 to 15 μM were used for the Soret region and protein concentrations of 75 to 100 μM were used for the CT band region. The pH of the samples was adjusted using 1 M solutions of sodium hydroxide or hydrogen chloride. Electronic absorption spectra were recorded on an Agilent 8453 diode-array spectrophotometer.

SVD analyses of the pH titration profiles of the variants were conducted as previously described.[54, 55] The obtained pH titration profile **A** (λ_m, pH_n) was deconvoluted into wavelength dependence vectors **U** (λ, x-value), square roots of the eigenvalues **S** (*k*, significance), and pH dependence **V** (pH, populations for the corresponding **S** vector) using the MATLAB SVD function ($\mathbf{A}=\mathbf{U}\cdot\mathbf{S}\cdot\mathbf{V}^T$). Number of significant components, *i*, was determined from log of $S_{j,j}$ values, $S_{j,j}$ percentages ($\frac{S_{j,j}^2}{\sum_{j=1}^{k} S_{j,j}^2}$)×100%, error levels ($\sqrt{\frac{\sum_{j=i}^{k} S_{j,j}^2}{\sum_{j=1}^{k} S_{j,j}^2}}$), autocorrelation of U(λ) and V(pH) matrices, as previously described.[54, 55]

Selected pH-dependent vectors, **V**, were globally fitted to eq 6.5 using SigmaPlot 10.0:

$$\mathbf{V} = \sum \frac{B_i + A_i \times 10^{n(pK_{app,i} - pH)}}{1 + 10^{n(pK_{app,i} - pH)}} + C \qquad (6.5)$$

where A_i and B_i are the slope and y-intercept of the *i*th transition, pK_{app} is the apparent pK_a for the *i*th transition, *n* is the number of protons involved in the *i*th transition, and C is a constant. Based on the determination of significant components, a two-state model was used to describe the alkaline transition of the variants, and spectra of the respective components were deconvoluted using eq 6.6:

$$D = AF^{-1} \tag{6.6}$$

where D is the electronic absorption spectrum of a component *i*, A is the electronic absorption spectra of the protein at a given pH, and F is the fractional population change of a component *i* as a function of pH. A spectrum of a certain component (D_{input}) can be used as a constraint to obtain the spectra of the rest of the components using the equation $D_{output} = (A - D_{input}F_{input})F_{rest}^{-1}$, where F_{input} is the change in fractional population of the species having the input spectrum and F_{rest} are the changes in fractional populations for the rest of the species. Although this approach was used for WT, input-independent analysis was used for Y67R/M80A due to the uncertainty of the ligation state of the species involved in the transition.

pH-Jump and Imidazole Binding Kinetics. Rapid-mixing experiments were performed using a BioLogic SFM-300 stopped-flow instrumentation. Ferric proteins samples were prepared in either a 5 mM sodium phosphate buffer (pH 7.4) containing 100 mM sodium chloride for a downward pH jump or in a 5 mM sodium acetate buffer (pH 4.5) containing 100 mM sodium chloride for an upward pH jump. The jump buffers contained 18 mM of buffer (pH 4.5-5.5: sodium acetate; pH 6.0-6.5: bisTris; pH 6.0-6.2: MES; pH 6.5-8.0: sodium phosphate) with 100 mM sodium chloride. The electronic absorption spectra

between 250 and 600 nm were recorded immediately (deadtime of 10 ms) after mixing the jump buffers with the protein solution in a 5:1 ratio. Absorbance changes as a function of time were fitted to monoexponential functions. The final pH was confirmed by using a UB-10 pH meter (Denver Instrument) with the mixtures of the jump buffers and protein buffers in the same ratio as used in the stopped-flow experiments.

pH-jump experiments were analyzed according to scheme 6.1, adapted from previous studies of the cyt *c* alkaline transition:[22, 56]

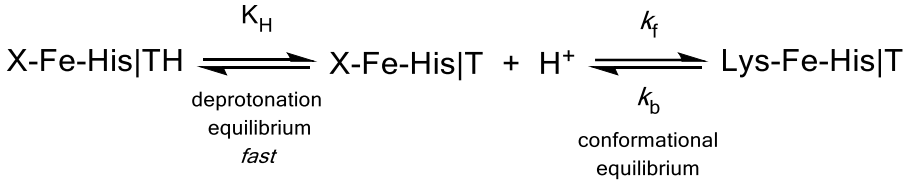

(Scheme 6.1)

In the mechanism, the initial step involves a rapid deprotonation of the "trigger group" (T) of the species with the heme iron ligated by X (Met in WT cyt *c*), with an equilibrium constant K_H. Following conformational change, the alkaline (Lys-ligated heme iron) species is formed; this transition is described as a conformational equilibrium with forward (k_f) and reverse (k_b) rate constants for the formation of the alkaline species. Assuming the deprotonation equilibrium is fast compared to the conformational transitions, eq 6.7 is used to fit the observed rate versus pH data:[56]

$$k_{obs}=k_b+k_f\frac{K_H}{K_H+[H^+]} \tag{6.7}$$

where rate constant k_f and K_H were determined from the fits of the observed rate constants (k_{obs}). For the purposes of fitting the data, the average of the k_{obs} at the initial lower pH

range was averaged to set the rate constant k_b due to the scarcity of the datapoints at pH conditions below 4. pH jump experiments were not conducted at lower pH conditions as signs of denaturation were observed at pH < 4.

To independently measure k_b (k_{off}^{Lys}), imidazole binding kinetic and equilibrium experiments were also conducted.

$$\text{Lys-Fe-His} \underset{k_{on}^{Lys}}{\overset{k_{off}^{Lys}}{\rightleftharpoons}} \text{Fe-His}$$

and

$$\text{Fe-His + Im} \underset{k_{on}^{Lys}}{\overset{k_{off}^{Lys}}{\rightleftharpoons}} \text{Im-Fe-His}$$

(Scheme 6.2)

Equilibrium measurements of imidazole binding to the heme iron were performed by observing changes in the Soret region upon mixing aliquots of protein solutions to solutions containing imidazole at different concentrations.[57] Both the protein and the imidazole solutions were prepared in a 100 mM sodium phosphate buffer at pH 7.4. Final concentrations of imidazole were varied from 0 to 20 mM, with final protein concentration of 9 μM. Samples were equilibrated at room temperature for at least 30 min before absorption spectra were recorded. Changes in the Soret absorption band with imidazole concentrations were fitted to eq 6.8 to obtain the apparent dissociation constant, K_D^{app}.

$$\Delta A_{Soret} = \frac{A_{max}[Im]}{K_D^{app} + [Im]} \tag{6.8}$$

The pH-independent dissociation constant for binding of imidazole to the heme iron was obtained using equation 6.9, with the acid dissociation constant of the imidazolium (K_a) of 10^{-7}.[57, 58]

$$K_D = K_D^{app}\left(1+\frac{[H^+]}{K_a}\right) \tag{6.9}$$

Kinetic binding experiments were conducted using a stopped-flow instrument. Stock protein samples containing 50 μM protein in a 100 mM sodium phosphate buffer at pH 7.4 were mixed with imidazole samples containing 150 mM imidazole in a 100 mM sodium phosphate buffer at pH 7.4. Solutions were mixed to yield different ratios of imidazole to protein, with a final protein concentration of 8 μM. Absorption spectra in the range between 250 and 600 nm were recorded for 60 s after mixing. Changes in absorbance at 413 nm were fitted to a monoexponential function to yield k_{obs}^{Im} at a specific imidazole concentration.

The observed rate constant for imidazole binding is expressed by eq 6.10:[59]

$$k_{obs}^{Im} = \frac{k_{off}^{Lys}k_{on}^{Im}[Im]+k_{on}^{Lys}k_{off}^{Im}}{k_{off}^{Lys}+k_{on}^{Im}[Im]+k_{on}^{Lys}k_{off}^{Im}} \tag{6.10}$$

which reduces to eq 6.12, with the steady-state approximation for the five-coordinate Fe-His species and assumption that $k_{on}^{Lys} >> k_{off}^{Lys}+k_{off}^{Im}$:

$$\frac{1}{\alpha k_{obs}^{Im}} = \frac{1}{k_{off}^{Lys}} + \frac{K_D}{k_{off}^{Im}[Im]} \tag{6.12}$$

and where α is defined as eq 6.13:

$$\alpha = \frac{[\mathrm{Im}]/K_\mathrm{D}}{1 + [\mathrm{Im}]/K_\mathrm{D}} \tag{6.13}$$

At high concentrations of imidazole, $[\mathrm{Im}]/K_\mathrm{D} >> 1$, $\alpha \approx 1$, and eq 6.13 gets simplified to eq 6.14:

$$\frac{1}{k_\mathrm{obs}^\mathrm{Im}} = \frac{1}{k_\mathrm{off}^\mathrm{Lys}} + \frac{K_\mathrm{D}}{k_\mathrm{off}^\mathrm{Im}[\mathrm{Im}]} \tag{6.14}$$

Values of $k_\mathrm{obs}^\mathrm{Im}$ versus imidazole concentration were then fitted to eq 6.14 to obtain rate constants $k_\mathrm{off}^\mathrm{Lys}$ and $k_\mathrm{off}^\mathrm{Im}$.[60]

Peroxidase Assays

Assays performed to obtain pH-dependent peroxidase activity rates with Y67R were performed in a freshly prepared 25 mM sodium acetate buffer at pH 4.5 and 5.5, a 25 mM MES buffer at pH 6.0 and 6.5, and a 25 mM HEPES buffer at pH 7.4. Each assay contained final concentrations of 1.0 mM H_2O_2, 200 μM ABTS, and 1 μM freshly prepared ferric protein. In these conditions, the maximum velocity is reached as determined from WT horse heart cyt *c*. Based on Michaelis-Menten kinetics, at substrate concentrations where V_max is achieved, observed initial rate should be reflective of k_cat, the turn-over number. Activity assays for CL-bound cyt *c* were performed by mixing solutions of the protein and the liposomes (at 750-molar excess of total lipid concentration) in a 1:1 (*v*/*v*) ratio to avoid aggregation; protein and CL-containing vesicle solutions were incubated for at least 30 minutes at room temperature prior to adding other components of the assay. Samples were

not incubated with H_2O_2 due to signs of heme degradation. H_2O_2 was prepared in buffers and its concentration was measured using absorbance at 240 nm (ε_{240} = 43.6 M^{-1} cm^{-1}).[61] ABTS (AMRESCO) was used as a substrate to monitor peroxidase activity. For each assay, formation of ABTS cation radical, $ABTS^{\cdot+}$, was monitored at 735 nm (ε_{735} = 14 $mM^{-1}cm^{-1}$)[62] in 1 s intervals for a total of 120 seconds at room temperature (22 ± 2 °C). Linear phase of the reaction was then fitted to a single polynomial function to obtain the slope of the phase, which corresponded to the initial velocity of the reaction. These rates were corrected by the extinction coefficient of ABTS and protein concentration and averaged over three to six trials to obtain the initial reaction rates of the horse cyt *c* variants.

All other assays were performed at room temperature in a freshly prepared 25 mM HEPES buffer at pH 7.4 containing 0.1 mM DTPA. Prior to the addition of DTPA, the buffer was treated with Chelex-100 (Bio-Rad) resin, which was then filtered out using Rapid-Flow 0.2 μm membrane filter (Nalgene). Addition of DTPA did not affect the observed peroxidase activity. Activities of negative controls that contained protein without either of substrates, H_2O_2 or ABTS, or both H_2O_2 and ABTS but no protein, were below the limit of detection. H_2O_2 was prepared in a HEPES buffer, and its concentration was measured using absorbance at 240 nm. Maximum final concentrations of H_2O_2 ranged from 20 μM to 200 μM, depending on the variant. For the variants, the maximum final concentrations of H_2O_2 for the assays were chosen as the highest concentration of H_2O_2 that did not cause heme degradation as evaluated absorbance of the protein samples in the Soret region. Although spectra of MP8 species shows that the absorbance of the Soret band initially decreases in the presence of H_2O_2,[63] recent studies with horse heart cyt *c* shows that decrease in the Soret band observed at high H_2O_2 concentrations are accompanied by

unfolding of the polypeptide.[64] Final protein concentrations were around 1 to 2 μM, and when the concentrations of H_2O_2 were varied, the highest concentrations of ABTS where substrate inhibition was not observed were chosen to satisfy pseudo-first order conditions. For each variant, highest ABTS concentration to be used for peroxidase assays was determined by performing assays where the concentrations of H_2O_2 were fixed and concentrations of ABTS were varied from 0 to 2 mM (Figure 6.2). Formation of $ABTS^{\cdot+}$ was monitored at 735 nm in 1 s intervals. The slope of the linear portion of the curve was determined using a linear fit in MATLAB and used as a measure of the initial reaction rate (initial velocity, v).

Peroxidases follow a ping-pong mechanism, where sequential reactions with two substrates are required for enzymatic activity.[65, 66] The first substrate H_2O_2 coordinates to the heme iron to form Compound I (Cmpd I), which then consumes the second substrate ABTS to form Compound II (Cmpd II), and then Cmpd II reacts with an another ABTS substrate to yield the resting enzyme (Scheme 6.3).[66]

$$\mathrm{E + H_2O_2} \xrightarrow{k_{1obs}} \mathrm{Cmpd\ I + H_2O}$$

$$\mathrm{Cmpd\ I + ABTS} \xrightarrow{k_{2obs}} \mathrm{Cmpd\ II + ABTS^{\cdot+}}$$

$$\mathrm{Cmpd\ II + ABTS} \xrightarrow{k_3} \mathrm{E + H_2O + ABTS^{\cdot+}}$$

(Scheme 6.3)

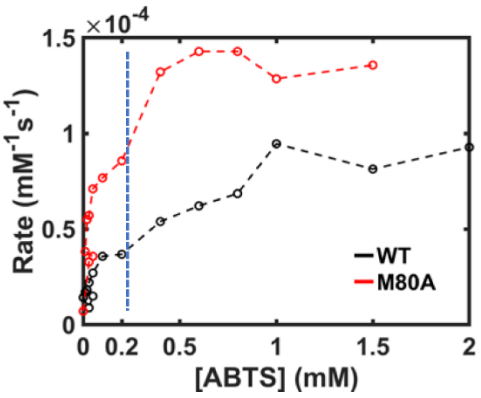

Figure 6.2. A representative Michaelis-Menten plot showing the rate of the intrinsic peroxidase activity versus the concentration of ABTS for WT and M80A horse heart cyt *c*. These measurements were performed in a 25 mM sodium acetate buffer at pH 4.5 containing 0.1 mM DTPA, 1 to 2 µM of cyt *c*, and 1 mM H_2O_2. The start of the inhibition phase is indicated (blue dotted line), which occurs at around 200 µM of ABTS. Similar signs of substrate inhibition were observed in other variants studied (Y67R and Y67R/M80A in particular), already at pH 6.5, suggesting that there is a possible conformational difference between pH 7.4 and 6.5 in these variants. pH dependence is expected, particularly if there are conformational changes at different pH conditions and the heme is more readily exposed to H_2O_2. Since signs of heme bleaching (a progressive decrease in the absorption of the Soret band only in the presence of H_2O_2 and buffer) were observed in structurally perturbed variants, lower concentrations of H_2O_2 were used when comparing the activities of the variants.

The sequential ping-pong mechanism was used to obtain rate constants k_{1obs} and k_3 describing peroxidase activity of cyt *c* variants. [65, 66]

The rates of $ABTS^{\cdot+}$ formation in the ping-pong mechanism can be expressed in terms of Michaelis-Menten parameters according to eq 6.15:[66]

$$\frac{v}{2[\text{protein}]} = \frac{V_{max}[ABTS][H_2O_2]}{K_M^{ABTS}[H_2O_2] + K_M^{H_2O_2}[ABTS] + [H_2O_2][ABTS]} \tag{6.15}$$

where K_M^{ABTS} and $K_M^{H_2O_2}$ are the Michaelis-Menten constant for ABTS and H_2O_2 binding, respectively.

To obtain the rate constants k_{1obs} and k_3, two types of assays were performed. [ABTS] was varied at fixed $[H_2O_2]$ to measure k_3 (eq 2.12) and $[H_2O_2]$ was varied at fixed [ABTS] to measure k_{1obs} (eq 2.13). Formation of $ABTS^{\cdot+}$ over time, was observed in both types of experiments, and initial velocity, *v*, was obtained from the first derivative of the linear phase of this assay.

Under pseudo-first order conditions, the dependence of rates on concentration of a substrate can be fitted to a classic hyperbolic Michaelis-Menten expression (eq 6.16):

$$v = \frac{ax}{b+x} = \frac{V_{max}[substrate]}{K_M + [substrate]} = \frac{k_{cat}[substrate]}{K_M + [substrate]} \tag{6.16}$$

At fixed H_2O_2 conditions, eq 6.15 is rearranged to eq 6.17

$$\frac{v}{2[\text{protein}]} = \frac{k_3[ABTS][H_2O_2]}{[H_2O_2] + {}^{k_3}/_{k_{1obs}}[ABTS]} \tag{6.17}$$

A set of assays were performed at a fixed concentration of H_2O_2 and varied concentrations of ABTS. To obtain k_3 values, assays were repeated at a different fixed concentration of H_2O_2. Data were then fitted to eq 6.17 for each set H_2O_2 conditions. k_3 values were then calculated from the parameters of fits obtained from eq 6.17 under various set H_2O_2 concentrations according to eq 6.18.

$$k_3 = \frac{k_{cat}}{2K_M^{ABTS}} \tag{6.18}$$

Using the general hyperbolic function (eq. 6.16), a and b values from the dependence in eq 6.19 are obtained, where a and b is defined by eqs 6.20 and 6.21.

$$v = \frac{a[H_2O_2]}{b+[H_2O_2]} \tag{6.19}$$

$$a = 2[\text{protein}]k_3[\text{ABTS}] \tag{6.20}$$

$$b = \left(k_3 / k_{1obs}\right)[\text{ABTS}] \tag{6.21}$$

The slope of the plot of a versus b yields k_{1obs} (eq 6.22):

$$\frac{k_{cat}}{K_M^{H_2O_2}} = \frac{a}{b} = \frac{2k_3[\text{ABTS}]}{\left(k_3 / k_{1obs}\right)[\text{ABTS}]} = 2k_{1obs} \tag{6.22}$$

which rearranges to eq 6.23.

$$k_{1\text{obs}} = \frac{k_{\text{cat}}}{2K_{\text{M}}^{\text{H}_2\text{O}_2}}$$

(6.23)

Unlike conventional peroxidases, cyt *c* requires dissociation of the sixth ligand (Met or Lys) to allow for H_2O_2 coordination to the heme iron (Schemes 6.4 and 6.5).

$$\text{Cyt}_{\text{Lys}} \underset{k_{\text{f}}^{Lys}}{\overset{k_{\text{b}}^{Lys}}{\rightleftarrows}} \text{Cyt}_{\text{off}}^{\text{T}} \overset{1/K_{\text{H}}}{\rightleftarrows} \text{Cyt}_{\text{off}}^{\text{TH}} \xrightarrow{k_1[\text{H}_2\text{O}_2]} \text{Cmpd I}$$

(Scheme 6.4)

$$\text{Cyt}_{\text{Met}} \underset{k_{\text{f}}^{Met}}{\overset{k_{\text{b}}^{Met}}{\rightleftarrows}} \text{Cyt}_{\text{off}} \xrightarrow{k_1[\text{H}_2\text{O}_2]} \text{Cmpd I}$$

(Scheme 6.5)

The apparent rate constant for the Cmpd I formation $k_{1\text{obs}}$ in a six-coordinate heme iron in cyt *c* variants depends on the rate constants of binding k_{f}^{X} and dissociation k_{b}^{X} of the endogenous ligand X (in our case, Met and Lys),[67] and k_1, the traditional rate constant for the formation of the Cmpd I species upon H_2O_2 coordination.[66-68]

Treatment of Lys-ligated Species. For Lys-bound species Cyt_{Lys}, the mechanism of the formation of Cmpd I follows scheme 6.4. As in the analysis of the alkaline transition, it is important to consider the equilibrium constant linked to the deprotonation of the trigger group, K_{H}, in the analysis of peroxidase activity as well, as it is linked to a pH-dependent Lys-ligation. The rate of the Cmpd I formation is given by eq 6.24:

$$\frac{d[Cyt_{off}^{TH}]}{dt} = k_{1obs}[H_2O_2][Cyt_{Total}] = k_1[H_2O_2][Cyt_{off}^{TH}]$$

(6.24)

With assumptions of steady-state conditions for Cyt_{off}^{TH} and rapid protonation of Cyt_{off}^{T}, eq 6.25 is obtained:

$$\frac{d[Cyt_{off}^{TH}]}{dt} = -k_1[H_2O_2][Cyt_{off}^{TH}] + \left(\left(k_b^{Lys} \left[Cyt_{Lys} \right] - k_f^{Lys} [Cyt_{off}^{T}] \right) \left(\frac{[H^+]}{K_H} \right) \right) = 0$$

(6.25)

With the total cyt *c* concentration given by eq 6.26,

$$[Cyt_{Total}] = \left[Cyt_{Lys} \right] + [Cyt_{off}^{T}] + [Cyt_{off}^{TH}]$$

(6.26)

K_H is be expressed according to eq 6.27.

$$\frac{1}{K_H} = \frac{[Cyt_{off}^{TH}]}{[Cyt_{off}^{T}][H^+]}$$

(6.27)

With the appropriate substitutions, eq 6.26 is rearranged to eq 6.27:

$$[Cyt_{Total}] = \left(\frac{K_H}{k_b[H^+]} \right) [Cyt_{off}^{TH}] \left(k_1[H_2O_2] + k_f^{Lys} + k_b^{Lys} \left(1 + \left(\frac{[H^+]}{K_H} \right) \right) \right)$$

(6.27)

Since $k_{1obs}[Cyt_{Total}] = k_1[Cyt_{off}^{TH}]$ from eq 6.24, k_{1obs} is then expressed by eq 6.25, which is rearranged to obtain k_1 (eq 6.26):

$$k_{1\text{obs}} = \frac{k_1 k_{\text{b}}^{Lys}\left(\frac{[\text{H}^+]}{K_{\text{H}}}\right)}{k_1[\text{H}_2\text{O}_2] + k_{\text{f}}^{Lys} + k_{\text{b}}^{Lys}\left(1+\frac{[\text{H}^+]}{K_{\text{H}}}\right)}$$

(6.25)

$$k_1 = \frac{k_{1\text{obs}}\left(k_{\text{f}}^{Lys} + k_{\text{b}}^{Lys}\left(1+\frac{[\text{H}^+]}{K_{\text{H}}}\right)\right)}{k_{\text{b}}^{L}\left(\frac{[\text{H}^+]}{\text{K}_{\text{H}}}\right) - k_{1\text{obs}}\,[\text{H}_2\text{O}_2]}$$

(6.26)

Treatment of Met-ligated Species. Since Met ligand does not have to get deprotonated to dissociate from the heme iron,[6] the mechanism simplifies to Scheme 6.5. Assuming steady-state conditions for Cyt_{off}, eq 6.27 is obtained:

$$\frac{\text{d}[\text{Cyt}_{\text{off}}]}{\text{dt}} = -k_1[\text{H}_2\text{O}_2][\text{Cyt}_{\text{off}}] + \left(k_{\text{b}}^{Met}[\text{Cyt}_{\text{Met}}] - k_{\text{f}}^{Met}[\text{Cyt}_{\text{off}}]\right) = 0$$

(6.27)

Total cyt *c* concentration given by eq 6.28:

$$[\text{Cyt}_{\text{Total}}] = [\text{Cyt}_{\text{Met}}] + [\text{Cyt}_{\text{off}}]$$

(6.28)

And with the appropriate substitutions we can rearrange to get eq 6.29:

$$[\text{Cyt}_{\text{Total}}] = \frac{[\text{Cyt}_{\text{off}}]\left(k_1[\text{H}_2\text{O}_2] + k_{\text{f}}^{Met} + k_{\text{b}}^{Met}\right)}{k_{\text{b}}^{Met}}$$

(6.29)

Since $k_{1\text{obs}}[\text{H}_2\text{O}_2][\text{Cyt}_{\text{Total}}] = k_1[\text{H}_2\text{O}_2][\text{Cyt}_{\text{off}}]$, $k_{1\text{obs}}$ is expressed according to eq 6.30:

$$k_{1\text{obs}} = \frac{k_1 k_{\text{b}}^{Met}}{k_1[\text{H}_2\text{O}_2] + k_{\text{f}}^{Met} + k_{\text{b}}^{Met}} \tag{6.30}$$

Rearrangements of eq 6.30 results in eq 6.31 for calculations of k_1:

$$k_1 = \frac{k_{1\text{obs}}\left(k_{\text{f}}^{Met} + k_{\text{b}}^{Met}\right)}{k_{\text{b}}^{Met} - k_{1\text{obs}}[\text{H}_2\text{O}_2]} \tag{6.31}$$

where $k_{1\text{obs}}$ is the observed k_1.

For Lys-ligated species, k_{f}. k_{b}, and K_{H} values obtained from pH jump experiments were used as values for $k_{\text{f}}^{\text{Lys}}$, $k_{\text{b}}^{\text{Lys,}}$ and K_{H}. Since proteins denature at high alkaline conditions, the high-pH range of the dependences is less well defined and the K_{H} values in Table 4 represent only the lower estimate. Thus, we have elected to use upper bounds of K_{H} in our calculations of k_1.

For Met-ligated species, the Met dissociation rate, $k_{\text{b}}^{\text{Met}}$, was assumed to be the rate limited by the opening of the heme pocket for ferric cyt *c* (60 s^{-1}),[60] and Met association rate, $k_{\text{f}}^{\text{Met}}$, was estimated to be the equilibrium constant for Met-heme binding for ferrous cyt *c*, where $k = 8\times10^4$ s^{-1}.[69] It is possible that $k_{\text{f}}^{\text{Met}}$ is overestimated for ferric cyt *c*, as a soft Met is a poor ligand for the hard ferric heme iron. The dissociation constant for AcMet binding to MP8 is lower for ferrous heme iron than in ferric heme iron,[58] and assuming that the rate constant of the opening of the heme crevice is independent of heme iron oxidation, the rate for association needs to be higher for the ferrous heme iron than the ferric iron. Furthermore, time-resolved spectroscopic studies with NO-bound cyt *c* have shown that while a sub-population of Met80 rebinding in ferric cyt *c* is slower than in ferrous cyt *c*, a

major component in both oxidation states have similar Met80 rebinding kinetics, raising the possibility that protein structure (rather than the redox state of the heme iron) may also govern the dynamics of Met80.[70]

For M80A, $k_{1obs} = k_1$, and the sixth coordination site in M80A is occupied by the H_2O ligand as in conventional peroxidases.

Results

Initial Characterization of the Y67R variant. In the ferric horse heart Y67R cyt *c* variant, the Soret band maximum, λ_{max}, is at 406 nm at pH 7.4, blue shifted compared to the λ_{max} of WT at 409 nm (Figure 6.3A, top and Table 6.1). The 695 nm CT band, found in the Met-ligated WT protein, is not observed in Y67R (Figure 6.3A, inset). The ^{1}H NMR spectrum at pH 7.4 confirms the absence of the native Met-ligated species in the ferric Y67R variant. The γ-ethyl and ε-methyl signals observed for the Met-ligated WT in the upfield region are not present in Y67R (Figure 6.3D). The signals near 35 ppm corresponding to the 8- and 3-methyl protons of the heme porphyrin for Met-ligated species are absent, and instead, new sets of signals in the 25 to 5 ppm region are observed. The position of the new signals are consistent with those in the Lys-ligated cyt *c*.[22, 71]

Ferrous Y67R has a comparable electronic absorption spectrum to that of WT at pH 7.4, but a higher extinction coefficient for the Soret band (Figure 6.3A, bottom). However, ^{1}H NMR spectra of the two variants are different. The signals observed in the upfield region for Met80 are shifted downfield in Y67R compared to those in WT (Figure 6.3C), and the spectrum of Y67R is comparable to that of chloramine-T treated cyt *c* that contains chemically oxidized Met80.[72]

Figure 6.3. Spectra of WT (black) and Y67R (orange) horse heart cyt *c* at pH 7.4. (A) Absorption spectra of ferric (top) and ferrous (bottom) proteins. (B) Structures of heme, His and Met showing the labeling nomenclature. (C) ^{1}H-NMR spectra of ferrous proteins and (D) ^{1}H-NMR spectra of ferric proteins. Numbered signals correspond to protons in the heme porphyrin,[73] with the identity of the iron ligand in parenthesis. Other labels correspond to M= Met80 or H= His18, e = Gly29 αH, and f= Pro30 δH. Signals labeled with an asterisk are from protons of Met-SO.[72]

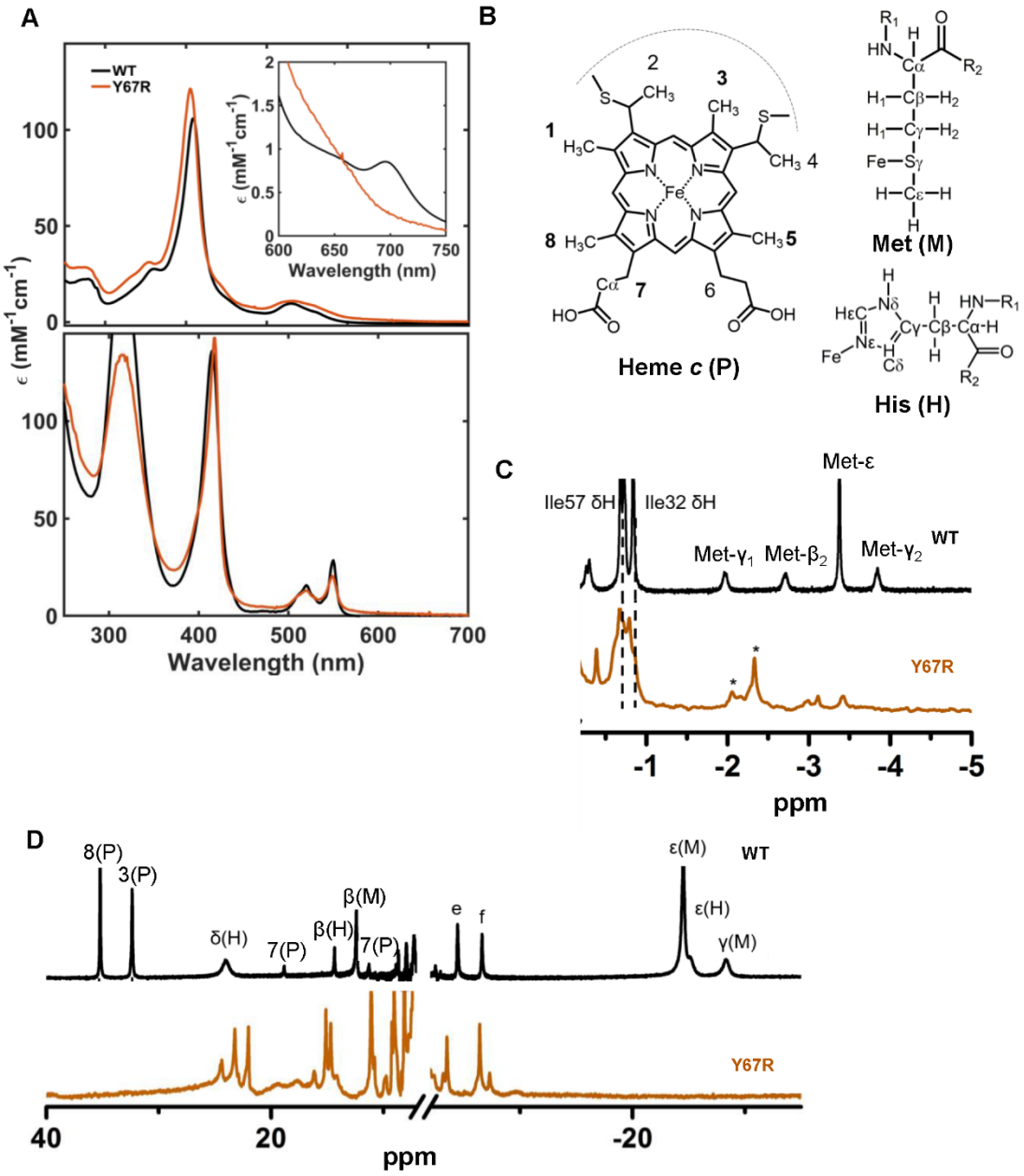
A
WT
Y67R
100
50
0
ϵ (mM-1cm-1)
2
1.5
1
0.5
0
600 650 700 750
Wavelength (nm)
100
50
0
300 400 500 600 700
Wavelength (nm)
B
Heme c (P)
Met (M)
His (H)
C
Ile57 δH
Ile32 δH
Met-ε
Met-γ1
Met-β2
Met-γ2
WT
Y67R
-1 -2 -3 -4 -5
ppm
D
8(P)
3(P)
δ(H)
7(P)
β(H)
β(M)
7(P)
e
f
ε(M)
ε(H)
γ(M)
WT
Y67R
40 20 -20
ppm

Table 6.1. Extinction Coefficients of WT and Y67R Horse Heart Cyt *c*[a]

Variant	pH	Soret peak	ε ($mM^{-1}cm^{-1}$)
WT[b]	7.0	410	106
Y67R	7.4	406	121.3
	4.5	400	130.4

[a]Determined by pyridine hemochrome assays.[42] Proteins were in either a 100 mM sodium phosphate buffer at pH 7.4 or a 100 mM sodium acetate buffer at pH 4.5.

[b]From ref. [74], for horse heart cyt *c*. The spectrum in this reference was taken at 2 nm intervals, but comparison of spectra taken at similar pH conditions and at 1 nm intervals show that the λ_{max} of the Soret is observed at 409 nm.

MALDI measurements show a deviation of the molecular weight from expected values consistent with the addition of a single oxygen atom (Figure 6.4 and Table 6.2). No additional peaks are observed, suggesting that in the Y67R variant, the entire population has its Met80 oxidized. Near-UV CD spectra at pH 7.4 suggest that the native tertiary structure observed in WT is absent in Y67R (Figure 6.5). This structural perturbation most likely stems from having a large, charged residue in the inner cavity of the heme pocket, as oxidation of Met80 does not influence the tertiary packing of the protein.[72] Since the Y67R mutation disrupts the inner HB network and thus the packing of the heme crevice, it is no surprise that Met80 may be more readily exposed to molecular oxygen.

The shift in electronic absorption spectra with change in pH suggests that the Lys-ligated species observed at pH 7.4 is lost at lower pH (Figure 6.6). The band with λ_{max} near 620 nm for the H_2O-bound high-spin species increases in intensity as pH is lowered (pK_a = 5.26) (Figure 6.6D), suggesting that Lys is readily replaced by a water molecule. In Y67R, the loss of the native ligation and changes in the tertiary structure are accompanied by the decrease in thermal and chemical stability compared to those of WT (Tables 6.3 and 6.4).[29, 75] Acid unfolding occurs in Y67R with a pK_a of 3.24 ± 0.02, compared to that of WT with a pK_a of 2.5 reported in literature.[76] Although the acid unfolding transition occurs earlier in Y67R than in WT, detection of a distinct acid unfolding transition suggests that while the polypeptide fold of Y67R is disrupted in the H_2O-ligated state at mildly acidic conditions, it is different from that of the acid-unfolded state.

The reduction potential of Y67R is lower than that of WT at pH 7.4 (Table 6.5).[13] Lowering the pH conditions to 4.5 increases the reduction potential, but the reduction potential of Y67R is still lower than that of Met-ligated WT cyt *c* (Table 6.5).

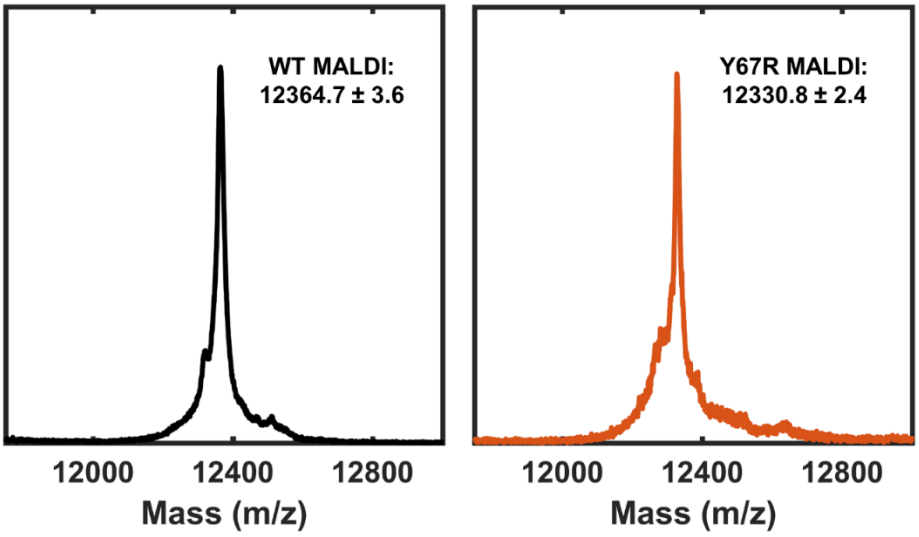

Figure 6.4. MALDI of horse heart cyt *c* WT (acetyl G1) (top, left) and Y67R (top, right).

Table 6.2. MALDI of WT and Y67R Horse Heart Cyt *c*.

Sample	Expected	MALDI	Δexpected	Δexp - Δexp_{WT}[a]
WT(acetyl G1)	12360.1	12364.7 ± 3.6	+ 4.6 ± 3.6	--
Y67R	12310.0	12330.8 ± 2.4	+ 20.8± 2.4	+16.2± 4.3

[a] $\Delta exp - \Delta exp_{WT}$ are used to correct the Δexpected, assuming the deviation from the MALDI and expected value for the WT should be equal.

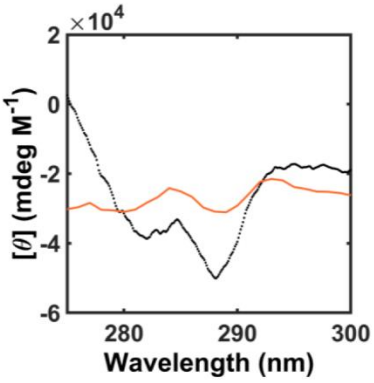

Figure 6.5. Plot showing the near-UV ([cyt *c*] = 200 μM, *l* = 2 mm) CD spectra of WT (black) and Y67R (orange) cyt *c* variants at pH 7.4 in a 100 mM sodium phosphate buffer at pH 7.4.

Figure 6.6. (A) Plot showing the pH titration profile of Y67R from pH 2.68 to 8.4 in a 10 mM HEPES pH 8.0 buffer. Highlighted are the maximum acidic (red) and maximum alkaline (blue) conditions observed, with a selection of traces between the pH ranges observed (grey). (B) Plot showing the change in absorption at 406 nm as a function of pH in the acidic pH region for Y67R (orange circle). Fit of the data in acidic pH region (blue line) are shown, with a pK_a of 3.24 ± 0.02 and n of 2 ± 0.27. (C) pH titration profile for Y67R from pH 2.41 to 8.1 in a 10 mM HEPES buffer at pH 8.0. (D) Plot showing the change in absorption at 625 nm as a function of pH in the alkaline pH region for Y67R (orange circle). Fit of the data in alkaline pH region (blue line) are shown, with a pK_a of 5.26 ± 0.07 and n of 0.8 ± 0.09. pH titration data from mildly acidic to mildly alkaline pH was analyzed using the 620 nm CT band, since changes in the Soret band were minimal.

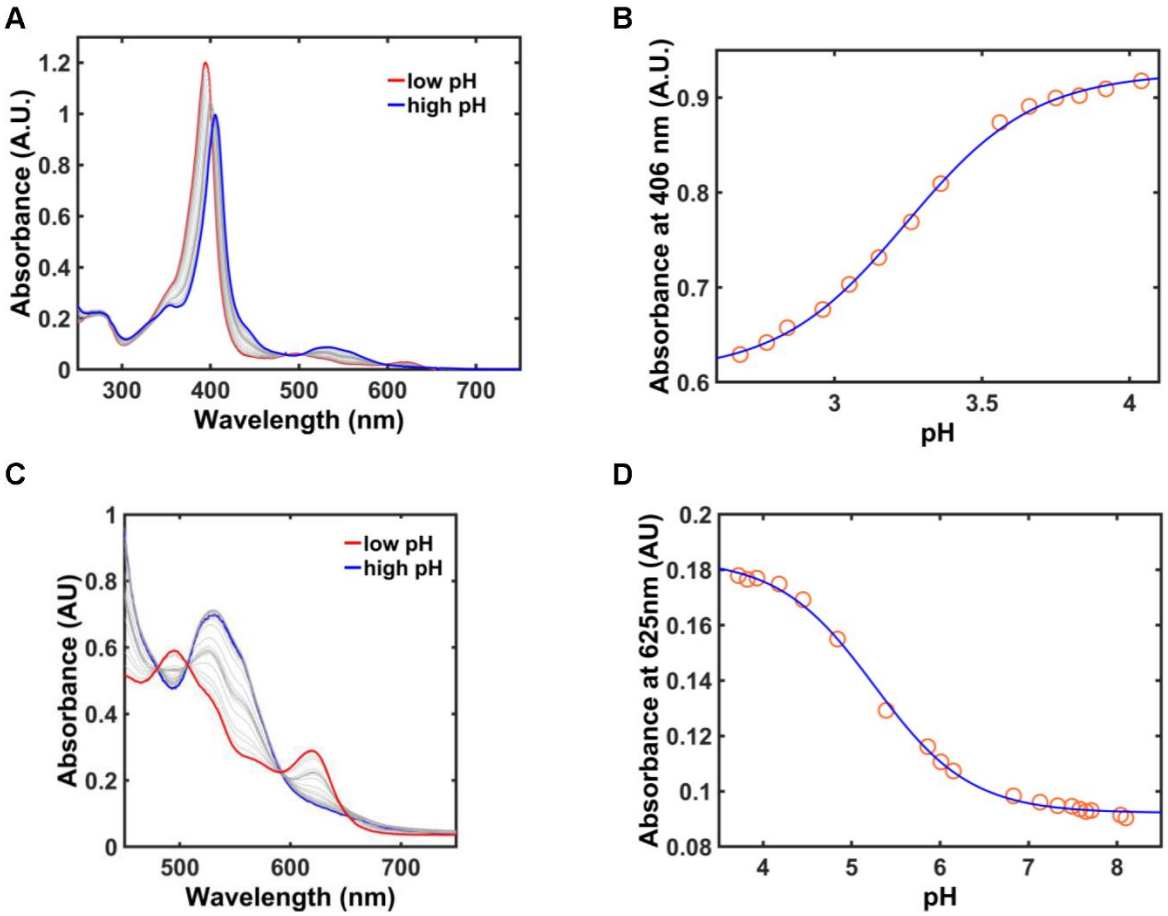
A
Absorbance (A.U.)
Wavelength (nm)
low pH
high pH
B
Absorbance at 406 nm (A.U.)
pH
C
Absorbance (AU)
Wavelength (nm)
low pH
high pH
D
Absorbance at 625nm (AU)
pH

Table 6.3. Thermal Stability Parameters of WT and Y67R Horse Heart Cyt *c*[a]

Variant	pH	T_m (°C)
WT	7.0[b]	84.1[b]
	4.5	71.1 ± 1.0
Y67R	7.4	70.5 ± 6.1
	4.5	57.8 ± 8.3

[a]Measured by monitoring the ellipticity at 222 nm, from 20 to 90 °C measured every 1°C. The values are averaged over three runs. Samples contained 20 μM protein in either a 100 mM sodium phosphate buffer at pH 7.4 or a 100 mM sodium acetate buffer at pH 4.5.

[b]From ref. [77].

Table 6.4. Global Thermodynamic Parameters of GuHCl Unfolding for WT and Y67R Horse Heart Cyt *c*

	Circular Dichroism[a]			UV-vis[b]		
Variant	$[GuHCl]_{1/2}$ (M)	m_D (kJ mol^{-1} M^{-1})	ΔG_D (kJ mol^{-1})	$[GuHCl]_{1/2}$ (M)	m_D (kJ mol^{-1} M^{-1})	ΔG_D (kJ mol^{-1})
			pH 7.4			
WT[c]	2.7 ± 0.1	11.5 ± 2.6	31.1 ± 7.1	2.6 ± 0.1	11.3 ± 2.7	29.3 ± 7.1
Y67R	1.6 ± 0.4	9.2 ± 7.2	14.7 ± 12.1	1.5 ± 1.0	10.0 ± 23.8	15.0 ± 37.1
			pH 4.5			
WT	2.6 ± 0.1	9.8 ± 0.2	25.1 ± 1.1	2.7 ± 0.1	10.0 ± 3.7	27.0 ± 10.0
Y67R	1.6 ± 0.7	10.0 ± 20.6	16 ± 33.7	2.4 ± 0.6	4.4 ± 3.5	10.6 ± 8.8

[a]Monitored is the ellipticity at 222 nm, performed at 22 ± 2 °C.

[b]Monitored is the ratio of wavelengths with maximum change observed in the Soret peak, determined by the difference spectra of the folded and unfolded states, performed at 22 ± 2 °C.

[c]From ref [29], ΔG_D recalculated based on the rounded $[GuHCl]_{1/2}$ and m_D parameters, based on eq 6.2.

Table 6.5. Reduction Potentials of WT and Y67R in Horse Heart Cyt *c*

Variant	pH	Potential (mV, vs SHE)
WT	7.8	255[a]
	4.0	252 ± 2 (280 ± 2)[b]
Y67R	7.4	31 ± 3 (34 ± 4)[c]
	4.5	71 ± 8 (149 ± 3)[c]

[a]From ref [13] at pH 7.8.

[b]From chapter 5.

[c]This work, reductive (oxidative) direction reduction potentials vs SHE, determined from spectroelectrochemistry experiments performed at 22 ± 2 °C. Potentials obtained from fitting the data to eq. 6.4 were converted to SHE from GCE by adding 215 mV to the fitted $E°$ value. Fixing $n = 1$ during data fitting did not alter the fitted $E°$ value.

Signs of hysteresis are observed in oxidation and reduction directions of the electrochemical titrations (Figure 6.7), possibly from what could be irreversibility in the process.

Intrinsic peroxidase activity for Y67R is higher than those for WT within the pH range 7.4 to 4.5 (Table 6.6 and Figure 6.8). In the presence of CL, the peroxidase activity of Y67R is higher than that of WT. However, the peroxidase activity rates of Y67R are not increased in the presence of CL at pH conditions lower than 7.4 (Figure 6.8 and Table 6.6).

Oxidation of Met80 in WT cyt *c* has been reported to alter the pK_a value for the alkaline transition, peroxidase activity, and the electrochemical properties of the protein.[78, 79] Oxidized Met80 alters the functional properties of the protein, making it difficult to isolate whether the changes in function stems from the structural perturbation with the Y67R mutation or from oxMet80.

To reveal the effects of the Y67R mutation independent of the oxidized Met80 on protein structure and function, an additional mutation, M80A, was included. Previous studies have shown that M80A mutation does little to perturb the overall structure of cytochrome *c*.[80, 81] We thus hypothesized that M80A substitution in addition to the Y67R mutation should not dramatically alter the spectral features, enzymatic characteristics, and stability of the protein when compared to the variant with only the Y67R mutation. M80A was also characterized as a control, and Y67R/M80A variant was used as a model to explore the effects of having Arg instead of Tyr in residue position 67.

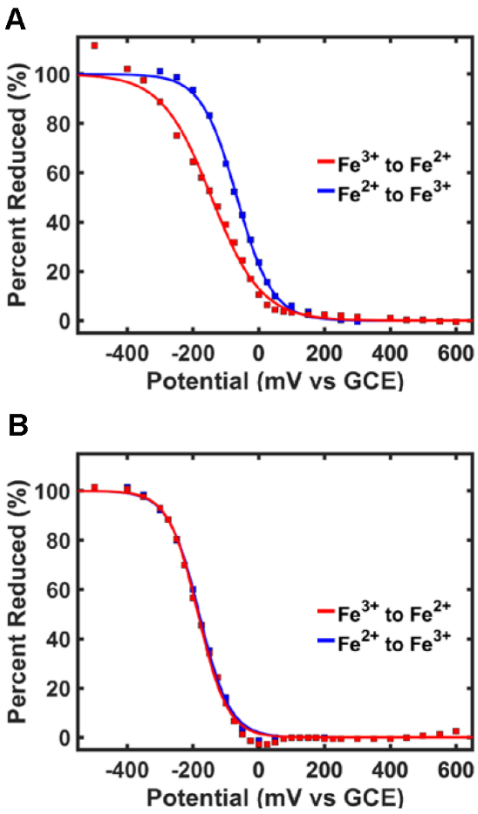

Figure 6.7. Plots showing the percent of the ferrous protein based on the absorbance at 550 nm versus potential (versus GCE) are plotted with the fits for the reductive (blue) and oxidative (red) directions for horse heart cyt *c* Y67R variant at A) pH 4.5 and B) pH 7.4.

Table 6.6. Initial Rates of Peroxidase Activity for WT and Y67R Horse Heart Cyt *c* at

Variant	Rate (mM/s)	
	Intrinsic	CL-bound[a]
	pH 7.4	
WT	$8.5 \pm 0.07 \times 10^{-6}$	$9.1 \pm 0.7 \times 10^{-5}$
Y67R	$1.3 \pm 0.04 \times 10^{-4}$	$2.1 \pm 0.5 \times 10^{-4}$
	pH 6.5	
WT	$1.4 \pm 0.09 \times 10^{-5}$	$1.6 \pm 0.07 \times 10^{-4}$
Y67R	$4.3 \pm 0.3 \times 10^{-4}$	$1.9 \pm 0.05 \times 10^{-4}$
	pH 5.5	
WT	$2.6 \pm 0.3 \times 10^{-5}$	$5.1 \pm 0.2 \times 10^{-5}$
Y67R	$3.5 \pm 0.2 \times 10^{-4}$	$1.3 \pm 0.03 \times 10^{-4}$
	pH 4.5	
WT	$3.0 \pm 0.8 \times 10^{-5}$	$4.7 \pm 0.9 \times 10^{-5}$
Y67R	$2.4 \pm 0.4 \times 10^{-4}$	$5.2 \pm 0.9 \times 10^{-5}$

[a]Cyt *c* bound to CL vesicles, with the ratio of protein to vesicle concentrations being 1:750.

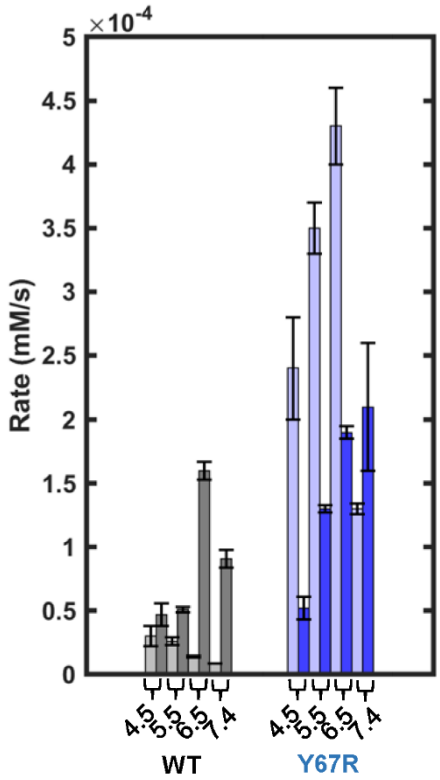

Figure 6.8. Bar graphs of initial rates of intrinsic (lighter bars) and CL-bound (darker bars) peroxidase activity at pH 4.5 to 7.4. Shown are the rates for WT (black) and Y67R (blue).

Characterization of Ligation, Structural Properties, and Stability of Y67R/M80A, M80A, and WT at pH 7.4. The λ_{max} of the Soret band in the electronic adsorption spectrum of ferric Y67R/M80A is blueshifted to 406 nm at pH 7.4 relative to that of WT at 409 nm (Figure 6.9A). Further, the extinction coefficient of Y67R/M80A at λ_{max} is higher than that of WT,[74] but comparable to the increase observed in semi-synthetic M80A horse heart cyt *c* (Table 6.7).[82] Consistent with the lack of Met-ligated heme, the CD spectrum of the Soret region for Y67R/M80A shows the lack of the negative band at 416 nm observed in WT (Figure 6.10).[6] However, the split Q-band features of the hydroxide-ligated M80A are not seen in the electronic absorption spectra of Y67R/M80A,[82-84] suggesting that hydroxide is not the heme ligand in Y67R/M80A despite having similar features of the Soret band (Figure 6.9A). ^{1}H NMR spectra confirm this conclusion, as the spectral features of a hydroxide-ligated heme iron species found at 16, 14.5, and 13.5 ppm seen in M80A are not observed in the ^{1}H NMR spectrum of Y67R/M80A (Figure 6.11A). Instead, the heme methyl signals of Y67R/M80A in the ^{1}H NMR spectra (Figure 6.11A) closely resemble those of Lys-ligated alkaline cyt *c*.[22, 71]

EPR spectra also corroborate our conclusions based on the ^{1}H NMR spectra, as features in the EPR spectrum of Y67R/M80A are comparable to those of Lys-ligated *c*-type cytochromes[22, 85, 86] rather than those of hydroxide-ligated M80A or Met-ligated species (Figure 6.11C). Inspection of the upfield region in the ^{1}H NMR spectra for ferrous Y67R/M80A suggests that Lys is coordinated to the ferrous heme iron (Figures 6.11B and 6.12). Observed signals of the spectra for Y67R/M80A are not as well-defined as in Lys-ligated ferrous K73A/K79G/M80K (M80K*) yeast cyt *c* or M100K *Thiobacillus vergutus* cyt c_{550}.[15, 85]

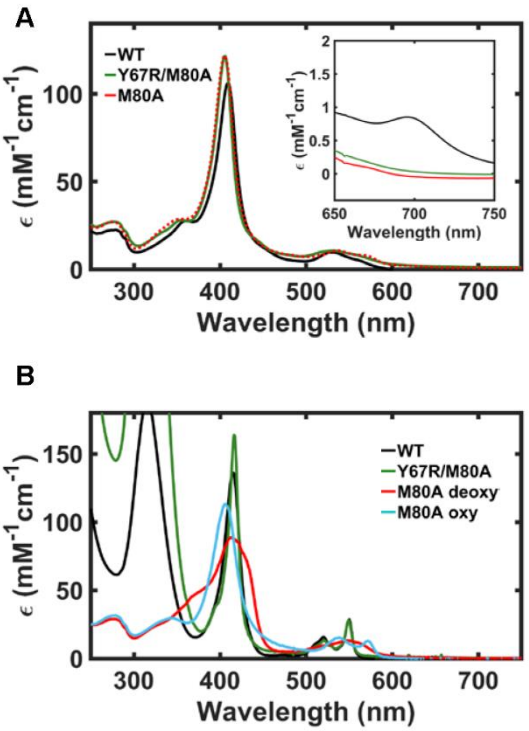

Figure 6.9. Electronic absorption spectra of (A) ferric and (B) ferrous WT (black), Y67R/M80A (green), and M80A (red and teal) at pH 7.4 and 22 ± 2ºC.

Table 6.7. Extinction Coefficients for Horse Heart Cyt *c* Variants.

		Ferric		*Ferrous*	
Variant	pH	λ_{max} (nm)	ε ($mM^{-1}cm^{-1}$)	λ_{max} (nm)	ε ($mM^{-1}cm^{-1}$)
WT	7.0[a]	410	106	415	125
M80A	7.0[b]	405	121.7	--	--
	4.5[b]	400	164.4	--	--
Y67R/M80A	7.4	406	121.6	416	163.7
	4.5	400	168.4	413	172.7

[a] From ref. [74]. [b]From ref. [82]

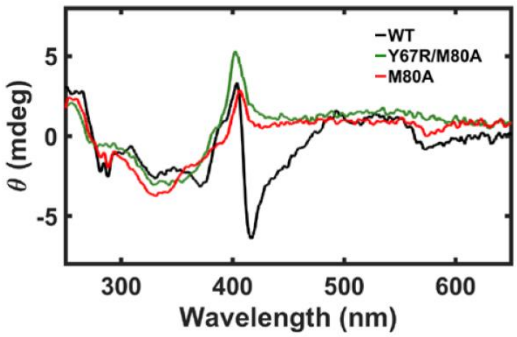

Figure 6.10. CD spectra in the Soret region of WT (black), Y67R/M80A (green), and M80A (red) at pH 7.4 and 22 ± 2 ºC. Protein concentrations were 50 μM and the path length *l* was 2 mm in these experiments.

Figure 6.11. ^{1}H NMR spectra at 25 ºC and EPR spectra at 10 K of WT (black), Y67R/M80A (green), and M80A (red) at pH (or pD) 7.4. ^{1}H NMR spectra of (A) ferric and (B) ferrous proteins, with signals numbered corresponding to protons in the heme porphyrin (see Figure 6.3B for numbering), with the identity of the Lys ligand in parentheses for the alkaline state. Spectra of alkaline WT (gray, pD 10.5) with identification of peaks based on literature,[22] are shown for comparison. (C) EPR spectra.

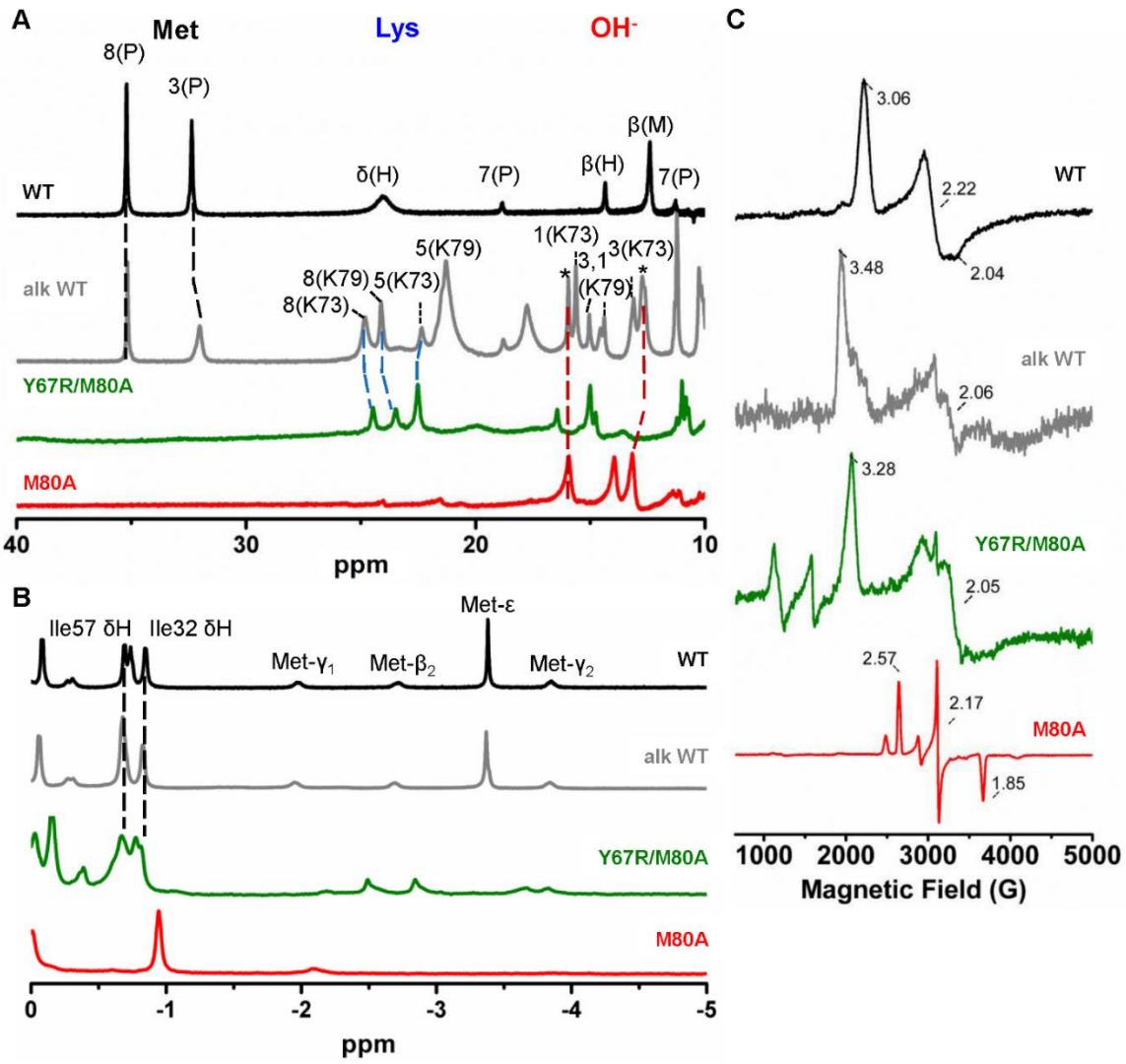
A
Met
Lys
OH-
8(P)
3(P)
β(M)
δ(H)
7(P)
β(H)
7(P)
WT
1(K73)
3,1
3(K73)
5(K79)
8(K79)
5(K73)
(K79)
8(K73)
alk WT
Y67R/M80A
M80A
40
30
20
10
ppm
B
Ile57 δH
Ile32 δH
Met-ε
Met-γ1
Met-β2
Met-γ2
WT
alk WT
Y67R/M80A
M80A
0
-1
-2
-3
-4
-5
ppm
C
3.06
2.22
WT
2.04
3.48
alk WT
2.06
3.28
Y67R/M80A
2.05
2.57
2.17
M80A
1.85
1000
2000
3000
4000
5000
Magnetic Field (G)

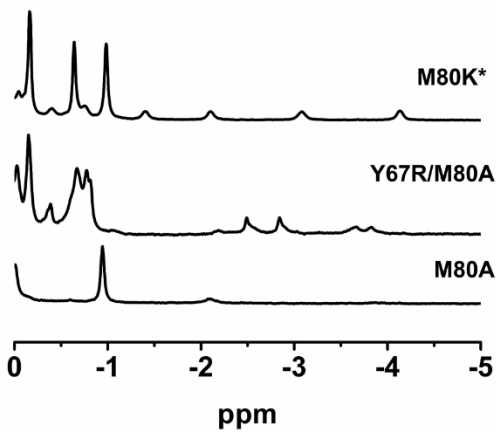

Figure 6.12. Upfield region of the ^{1}H NMR spectra of ferrous Lys-ligated K73A/K79G/M80K (M80K*) yeast *iso*-1-cyt *c*, and ferrous horse heart cyt *c* variants, Y67R/M80A and M80A, at 25 ºC in a 50 mM sodium phosphate buffer at pH 7.4 containing 10% D_2O (*v*/*v*). ^{1}H NMR spectrum of ferrous M80K* was provided by Dr. Fangfang Zhong.

However, similar set of less defined signals have been observed in the -2 to -4 ppm range for Lys-ligated *E. coli*-expressed M80E yeast cyt *c* and carboxymethylated horse heart cyt *c*.[87] Electronic absorption spectra suggest that the broadening of the Soret and Q-band features observed for M80A are not observed for Y67R/M80A (Figure 6.9B).

For WT cyt *c*, the reduction potential decreases dramatically from 225 mV for the native Met-ligated heme iron (255 mV) to -205 mV for the alkaline Lys-ligated heme iron.[13, 88] A decrease in the reduction potential is also observed in the Y67R/M80A variant compared to Met-ligated WT (Table 6.8), and the reduction potential is consistent with a Lys-ligated heme iron.[88] This change is expected, as the reduction potential is proportional to the equilibrium constant of the ferrous and ferric species.[6] Due to this relationship, heme iron ligands will influence the equilibrium constant and thus the reduction potential.[6] Based on HSAB theory, the heme iron ligand will have a preference for either the reduced or oxidized state of the heme iron.[68] Unlike soft Met, a hard base Lys will prefer a hard ferric heme iron instead of the soft ferrous heme iron, and so the reduction potential of Lys ligated heme iron is negative compared to the reduction potential of Met ligated heme iron. Although the decrease in the reduction potential for the Y67R/M80A variant is not as dramatic as that observed with the Lys-ligated heme iron in WT cyt *c* at alkaline pH, the reduction potential of -80 ± 7 mV in Y67R/M80A is comparable in magnitude to Lys-ligated M80K* yeast cyt *c* variant reported in the literature at near-neutral pH conditions (-94 ± 2 mV).[15]

The two titration curves of the electrochemical titration do not fully overlap with each other for Y67R/M80A. This hysteresis of the electrochemical titration curves could stem from irreversibility in the system due to differences in relaxation times depending on

Table 6.8. Reduction Potentials of Horse Heart Cyt *c* Variants.

Variant	pH	Axial ligand	E° (mV vs SHE)
WT	7.8	Met	255[a]
	10.0	Lys	-205[b]
Y67R/M80A	4.5	H_2O	-54 ± 7 (-22 ± 3)
	7.4	Lys	-80 ± 7 (-56 ± 1)
M80A	4.5	H_2O	16 ± 6 (32 ± 3)
	7.4	OH^-	-33 ± 4 (--)
	7.0	--	185[d]

[a]From ref. [13]. [b]From ref. [88]. [c]Reductive (oxidative) direction. [d]From ref. [84].

the oxidation state of the protein,[89] or due to differences in protein interactions with the electrode surface upon changes in the formal charge of the protein.[90]

The discrepancy between the M80A reduction potential values in the literature[84] and this study (Table 6.8) could be due to the differences in experimental pH conditions and methods. The value from a single-point extrapolation obtained from ferricyanide titration will be different from that of a direct electrochemical titration using mediators in the solution. However, the general trend reported both in this study and in the literature for M80A[84] is consistent with the data from the model AcMP8 compound, whose reduction potential decrease with the low-spin hydroxide ligated heme iron compared to the high-spin H_2O-ligated heme iron.[7] Further, reduction potentials obtained from immobilized yeast cyt *c* M80A variants show a significant decrease compared to WT at similar conditions (-201 mV versus 370 mV at pH 7.0).[91] CD spectra of the ferric variants in the far- and near-UV regions were obtained to compare the extent of the secondary and tertiary structural perturbations in the variants upon mutations (Figure 6.13). M80A has a similar secondary or tertiary polypeptide fold to that of WT, providing further evidence that Met80 ligation alone does not affect the protein fold. In contrast, the spectra of Y67R/M80A variant are dramatically altered compared to that of WT. In the far-UV spectrum, the α-helical signals at 222 nm are still present, but an increase in the negative signals between the 200 to 215 nm region are observed, possibly due to the increased random-coil character (Figure 6.13A). In addition, the near-UV spectra of Y67R/M80A show the magnitude CD signals is greatly diminished in comparison to those of M80A and WT, suggesting a lack of native tertiary structure in Y67R/M80A (Figure 6.13B).

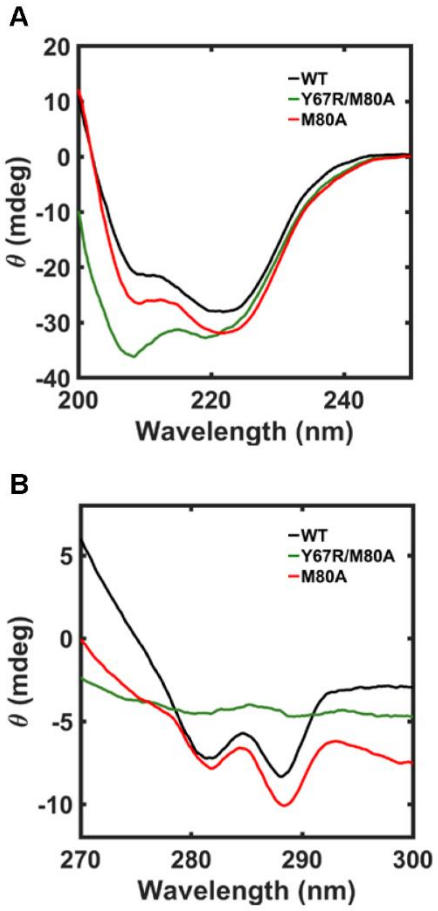

Figure 6.13. (A) Far-UV ([cyt *c*] = 20 μM, and *l* = 1 mm) and (B) near-UV ([cyt *c*] = 200 μM, and *l* = 2 mm) CD spectra of WT (black), Y67R/M80A (green), and M80A (red) in a 100 mM sodium phosphate buffer at pH 7.4 and 22 ± 2 ºC.

Global stability parameters with respect to thermal and chemical denaturation were obtained by monitoring the α-helical signals with CD spectroscopy. Thermal and chemical denaturation parameters for M80A are comparable to those for WT,[6, 29, 77] suggesting that a simple removal of the Met80 does not change the thermodynamic characteristics of the protein (Table 6.9). In contrast, the Y67R/M80A variant shows a marked decrease in stability parameters.

Characterization of Ligation, Structural Properties, and Stability of Y67R/M80A, M80A, and WT at pH 4.5. For WT, the electronic absorption, ^{1}H NMR, and EPR spectra are unchanged at pH 4.5 (Figure 6.14) compared to those at pH 7.4 (Figures 6.9 and 6.11) and are consistent with a Met-ligated heme iron. In comparison, the electronic spectra for both M80A and Y67R/M80A exhibit different spectral characteristics at pH 4.5 than those at pH 7.4 (Compare Figures 6.9A and 6.14A). The λ_{max} of the Soret absorption band for both M80A and Y67R/M80A blueshifts to 400 nm, and extinction coefficients are similar (Figure 6.14A and Table 6.7). This blueshift is accompanied by a formation of the CT band at 620 nm, a characteristic of the high-spin H_2O-coordinated heme iron (Figure 6.14A, inset). The ^{1}H NMR spectrum in the downfield region confirms the presence of the high-spin heme for both Y67R/M80A and M80A in the downfield region near 55 ppm (Figure 6.15). Changes in this high-spin feature observed in ^{1}H NMR with changes in pH for M80A (Figures 6.16A).

For Y67R/M80A, the EPR peaks characteristic of the Lys-bound heme are no longer present at pH 4.5 (Figure 6.14C). Instead, two sets of signals are seen: a characteristic signal of high-spin H_2O-ligated heme iron species at g value near 6, as well as a set of signals near g values of 3 and 1.5 (Figure 6.14C).

Table 6.9. Thermodynamic Parameters for the Unfolding Transitions of Horse Heart Ferricytochrome *c* Variants[a]

		Thermal Denaturation		GuHCl Denaturation		
Variant	pH	T_m (K)	ΔH_D (kJ mol^{-1})	[GuHCl]$_{1/2}$ (M)	m_D (kJ mol^{-1} M^{-1})	ΔG_D(kJ mol^{-1})
WT	7.4	357.1[b]	360 ± 30[b]	2.7 ± 0.1[c]	11.5 ± 2.6[c]	31.1 ± 7.1[c]
	4.5	344 ± 1.0	205 ± 30	2.6 ± 0.1	9.8± 0.2	25.1 ± 0.7
Y67R/M80A	7.4	344 ± 1.5	133 ± 4	1.7 ± 0.1	10.3 ± 0.1	17.5 ± 1.0
	4.5	328 ± 0.4	151 ± 1	1.4 ± 0.04	9.6 ± 1.3	13.4 ± 1.9
M80A	7.4	357 ± 0.7	306 ± 79	2.71 ± 0.02	10.3 ± 0.6	27.9 ± 1.6
	4.5	349 ± 1.1	344 ± 55	2.6 ± 0.1	11.6 ± 0.3	30.2 ± 1.4

[a]Monitored is ellipticity at 222 nm. [b]From differential scanning calorimetry, pH 7.0, ref. [77]. [c]From ref. [29].

Figure 6.14. (A) Electronic absorption spectra at 22 ± 2 ºC, (B) ^{1}H NMR spectra at 25 ºC, and (C) EPR spectra at 10 K of ferric WT (black), Y67R/M80A (green), and M80A (red) in a 100 mM sodium acetate buffer at pH 4.5 for (A) and (C), or in a 50 mM acetic acid d_4 buffer in 100 % D_2O at pD 4.5.

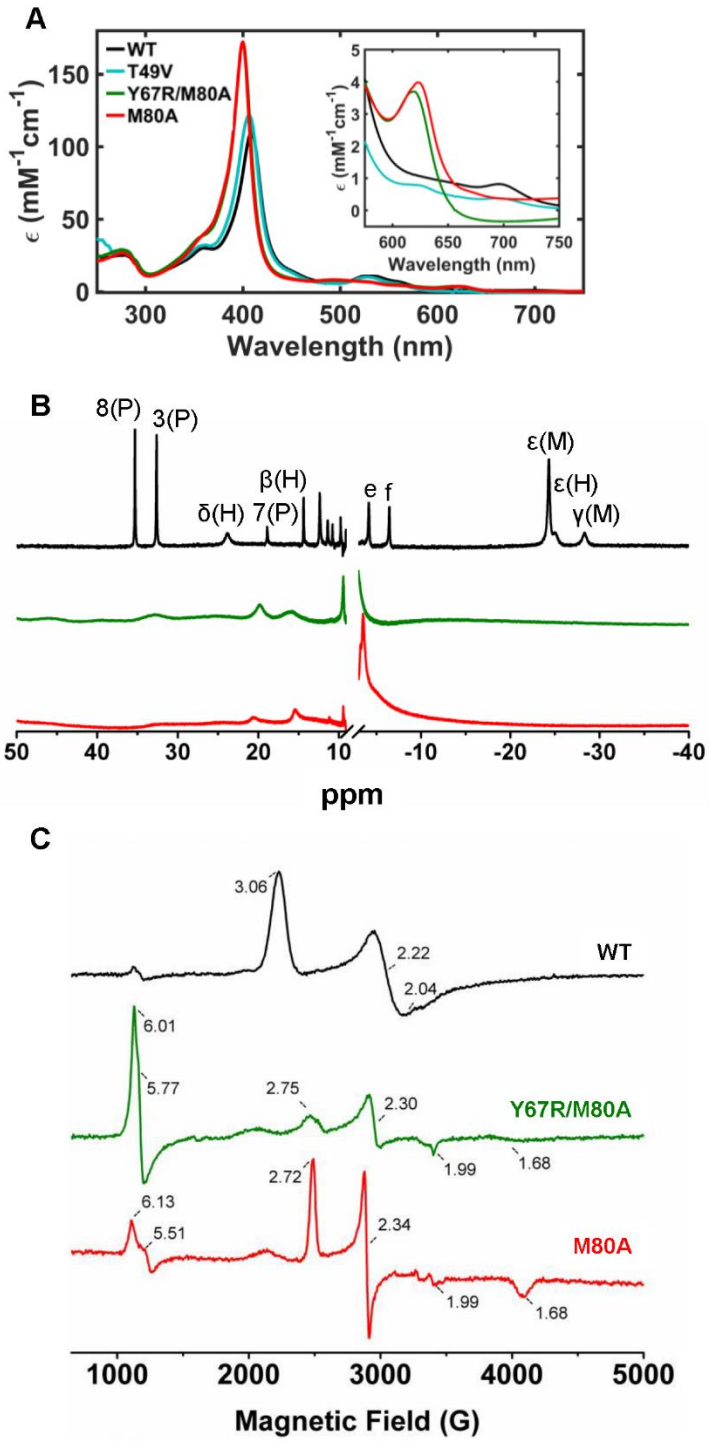
A
WT
T49V
Y67R/M80A
M80A
ϵ (mM-1cm-1)
Wavelength (nm)
B
δ(P)
3(P)
δ(H)
7(P)
β(H)
e
f
ε(M)
ε(H)
γ(M)
ppm
C
3.06
2.22
2.04
WT
6.01
5.77
2.75
2.30
Y67R/M80A
1.99
1.68
2.72
6.13
5.51
2.34
M80A
1.99
1.68
Magnetic Field (G)

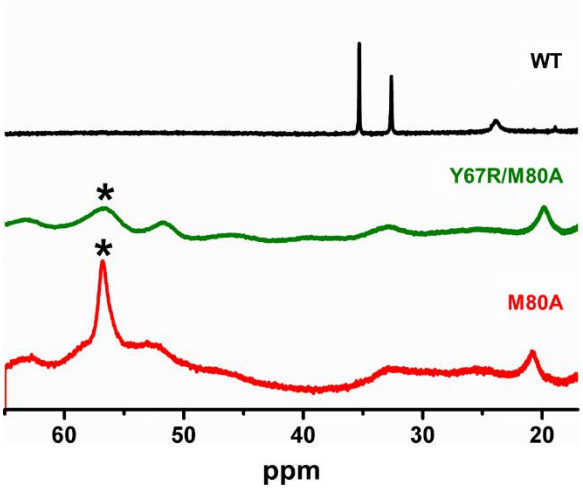

Figure 6.15. ^{1}H NMR spectra of ferric WT, Y67R/M80A, and M80A variants in a 50 mM acetic acid d_4 buffer at pD 4.5 and 25 ºC. The signal associated with the high-spin heme iron species is labeled by *.

Figure 6.16. Spectra of ferric M80A at different pH values: (A) ^{1}H NMR spectra at 25 ºC, with signals of the hydroxide-ligated heme iron marked with asterisks (* and **); (B) normalized intensities of the selected NMR peaks, plotted along the fraction of the hydroxide-ligated form of M80A as a function of pH; (C) EPR spectra at 10 K; (D) UV-visible spectral changes with pH at 22 ± 2 ºC (top) and fit of the absorbance changes (bottom).

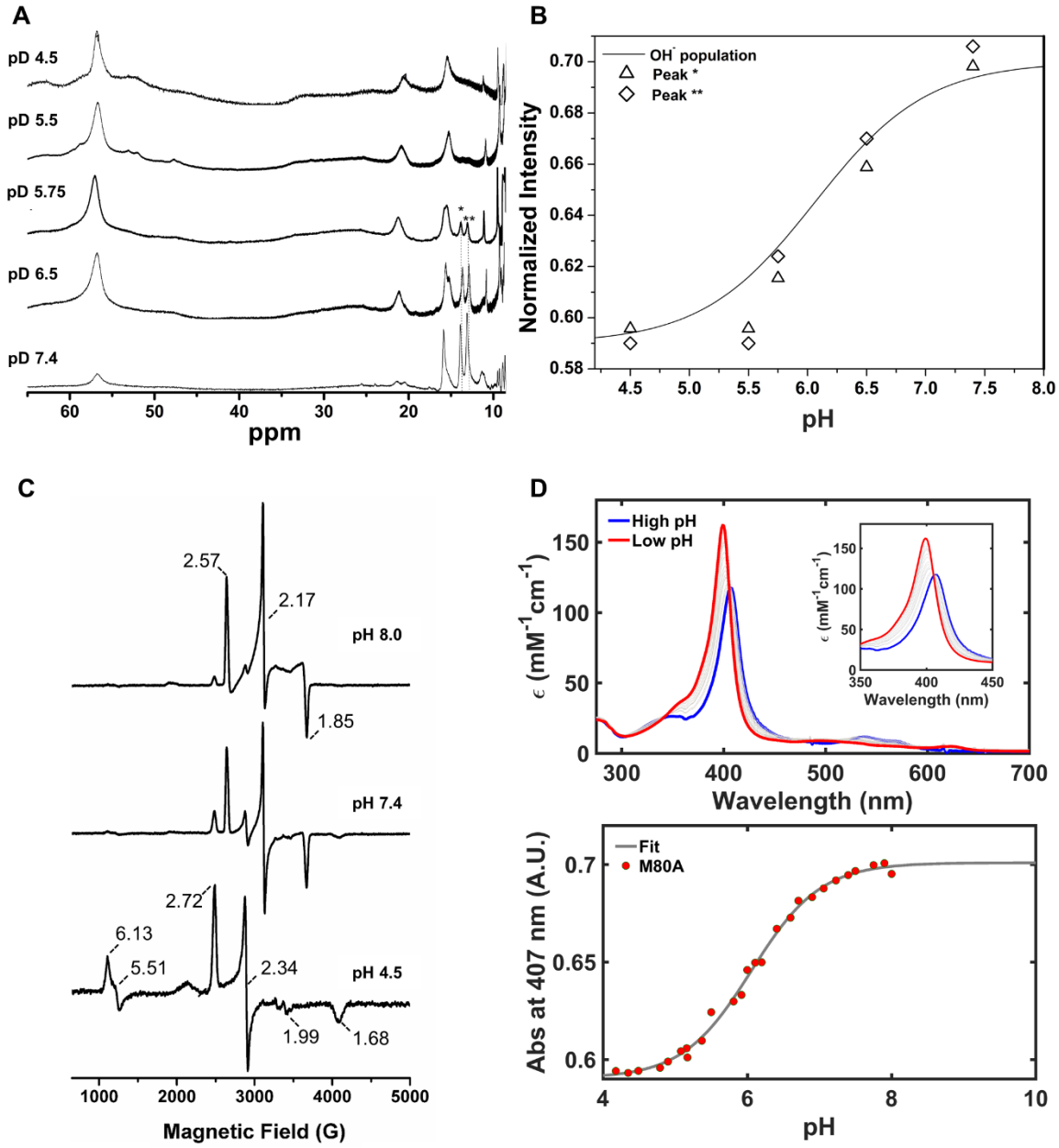
A
pD 4.5
pD 5.5
pD 5.75
pD 6.5
pD 7.4
*
**
60
50
40
30
20
10
ppm
B
OH- population
Peak *
Peak **
Normalized Intensity
0.70
0.68
0.66
0.64
0.62
0.60
0.58
4.5
5.0
5.5
6.0
6.5
7.0
7.5
8.0
pH
C
2.57
2.17
pH 8.0
1.85
pH 7.4
2.72
6.13
5.51
2.34
pH 4.5
1.99
1.68
1000
2000
3000
4000
5000
Magnetic Field (G)
D
High pH
Low pH
ϵ (mM-1cm-1)
150
100
50
0
300
400
500
600
700
Wavelength (nm)
ϵ (mM-1cm-1)
150
100
50
0
350
400
450
Wavelength (nm)
Fit
M80A
Abs at 407 nm (A.U.)
0.7
0.65
0.6
4
6
8
10
pH

Similar sets of signals are observed for M80A (Figure 6.16C). In the yeast analogue of M80A, the EPR spectrum at pH 4.0 has a single high-spin signal at $g \approx 6$, without any minor signals at higher magnetic fields.[86] In M80A yeast cyt *c*, pK_a of the H_2O- to hydroxide-ligated heme iron species ligand switch is at ~5.6, and the high-spin signal reported in literature at pH 4.0 is that of H_2O-ligated heme iron.[86] However, in horse heart M80A cyt *c*, two sets of signals are observed (Figures 6.16C). It is likely that the two sets of signals arise from the H_2O-ligated heme iron species in the high-spin and low-spin states, respectively. Similar sets of signals have been previously reported for AcMP8 species[7] and acid-denatured cyt *c*,[92] and these signals were proposed to stem from the relative positioning of the *d*-orbital levels.[7, 92]

The far-UV spectra for all the variants at pH 4.5 show no significant changes in the compared to the spectra at pH 7.4 (Figure 6.17A). This is true for the near-UV and visible spectra as well (Figures 6.17B and C). Although there does not seem to be an obvious change in spectral properties, chemical and thermal stability for Y67R/M80A decrease at lower pH (Table 6.9). This trend is consistent with results of HX experiments for WT horse heart cyt *c*.[93] However, a greater decrease in stability parameters are observed with Y67R/M80A upon decrease in pH compared to those of WT. This change in stability observed in Y67R/M80A is not due to the absence of Met80, as the stability of M80A at pH 4.5 does not markedly decrease from pH 7.4 to 4.5, and the stability of M80A at pH 4.5 is much higher than that of Y67R/M80A at pH 4.5 (Table 6.9). Stability parameters of Y67R/M80A at pH 4.5 is comparable to those of Y67R at pH 4.5, (Table 6.4), suggesting that the change in stability most likely arises from the structural perturbation caused by the Y67R mutation, and not the M80A mutation, in the Y67R/M80A variant.

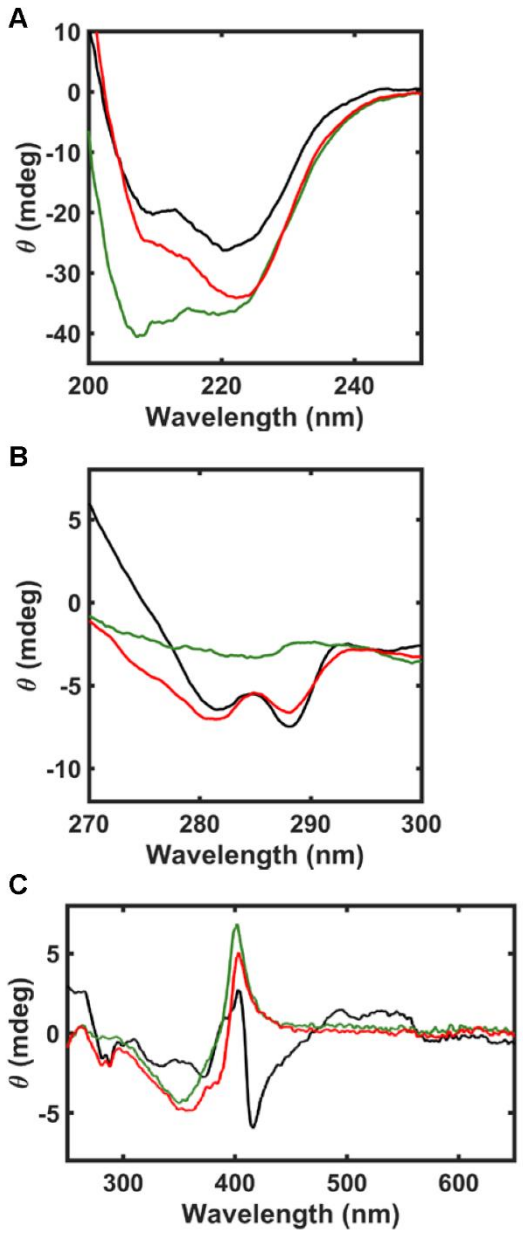

Figure 6.17. CD spectra in the (A) far-UV ([cyt *c*] = 20 μM, and *l* = 1 mm), (B) near-UV ([cyt *c*] = 200 μM, and *l* = 2 mm), and (C) Soret ([cyt *c*] = 50 μM, and *l* = 2 mm) regions of WT (black), Y67R/M80A (green), and M80A (red) in a 100 mM sodium acetate buffer at pH 4.5 and 22 ± 2 ºC.

pH-Dependent Changes in Ligation. Spectral characterization of Y67R/M80A has revealed that Lys is the ferric heme ligand at pH 7.4 (Figure 6.11) and Lys is replaced by a different ligand at pH 4.5 (Figure 6.14). To better understand the mechanism of this pH-dependent change in ligation and discern the species involved in the transition, electronic absorption spectra at a wide range of pH conditions were obtained (Figure 6.18A). SVD analysis was performed to determine the major species involved in the transition, identify their spectra, and determine the pK_a value of the conformational transitions. Two sets of pH titration profiles in the 350 to 500 nm range (Soret band, Figure 6.18) and 590 to 720 nm range (CT band, Figure 6.19) were used to determine the components involved in the transition by matrix analysis, with the selected V_i(pH) vectors (V-vectors) globally fitted to yield the pK_a value of the transition (Table 6.10). Separate analyses of the sets of titration data consistently have shown that the pH transition of Y67R/M80A involved two species—that of the high-spin H_2O species and the low-spin species.

Since the electronic absorption spectra of the Lys- and hydroxide-ligated cyt *c* are similar,[82, 86] we have considered the possibility that in Y67R/M80A, both the hydroxide-ligated and the Lys-ligated heme iron species may be present (Figure 6.9A). This possibility was ruled out by obtaining the spectra at pH 10.5 (Figure 6.20). At pH 10.5, EPR and NMR spectra strongly suggest that it is Lys, and not hydroxide, that is bound to the heme iron for Y67R/M80A (Figure 6.20), as is the case for alkaline WT. EPR spectra lack the distinct peak corresponding to the hydroxide-ligated heme iron observed in M80A (Figure 6.16C), so Y67R/M80A likely do not contain detectable amounts of hydroxide-ligated heme species.

Figure 6.18. (A) Electronic absorption spectra of Y67R/M80A over the pH range from 4.0 to 8.3 at 22 ± 2 ºC. (B) Plots of the **V** vectors from SVD analysis of these spectra. (C) Fractional populations F_i of the two components using a pK_a value of 5.6. (D) Spectra of the two components from SVD analysis are compared to that of the H_2O-ligated M80A at pH 4.5 and 2.0 with 1 M added salt (to mimic MG conditions) (top) and Lys-ligated WT at pH 10.5 (bottom). (Figure made by Dr. Jie Gu)

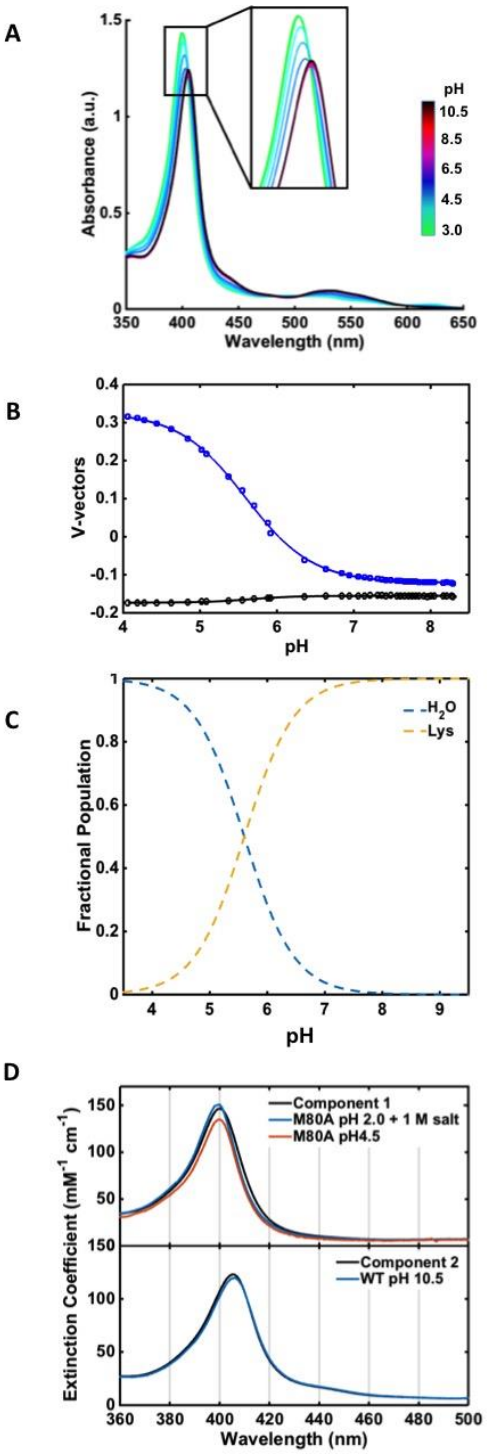
A
Absorbance (a.u.)
Wavelength (nm)
pH
10.5
8.5
6.5
4.5
3.0
B
V-vectors
pH
C
Fractional Population
pH
H_2O
Lys
D
Extinction Coefficient (mM^{-1} cm^{-1})
Wavelength (nm)
Component 1
M80A pH 2.0 + 1 M salt
M80A pH4.5
Component 2
WT pH 10.5

Table 6.10. Parameters for the pH-Dependent Transitions in Horse Heart Ferricytochrome *c*

Variant	Ligand Exchange	Region Monitored	pK_a	*n*
WT[a]	His/H_2O → His/Met		2.5	1.14
	His/Met → His/Lys		9.35	1.0
Y67R/M80A	His/H_2O → His/Lys	Soret	5.6 ± 0.1	1.0 ± 0.1
		CT	5.6 ± 0.1	1.0 ± 0.1
M80A	His/H_2O → His/OH^-	Soret	6.1 ± 0.1[b]	± 0.1

[a]From ref. [21] [b]A similar value has been reported in studies of semisynthetic M80A.[82]

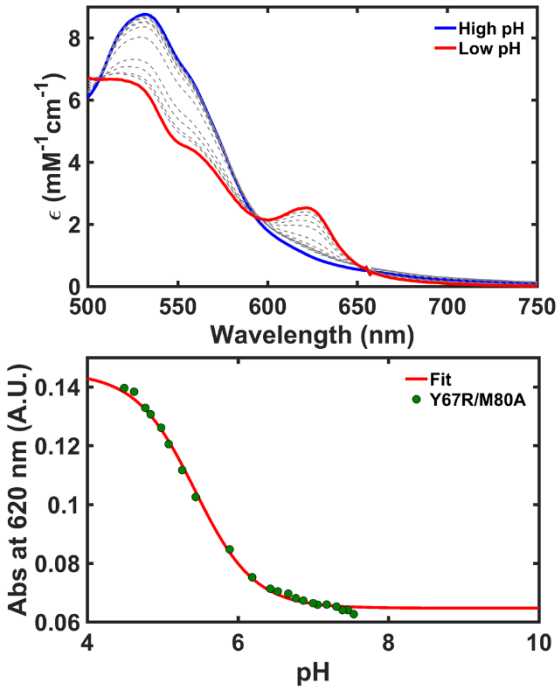

Figure 6.19. (A) pH dependence of the CT region of Y67R/M80A absorption spectra at 22 ± 2 ºC; spectra at high (pH = 8.05, blue), low (pH = 3.94, red) pH, and selected intermediate (gray) pH values are shown. (B) Absorbance values at 620 nm versus pH (green) and corresponding fit. Points below pH 4.5 and above 7.5 were omitted from the analysis of this variant due to large drift in the spectral baselines suggesting protein denaturation at increasingly acidic and basic conditions.

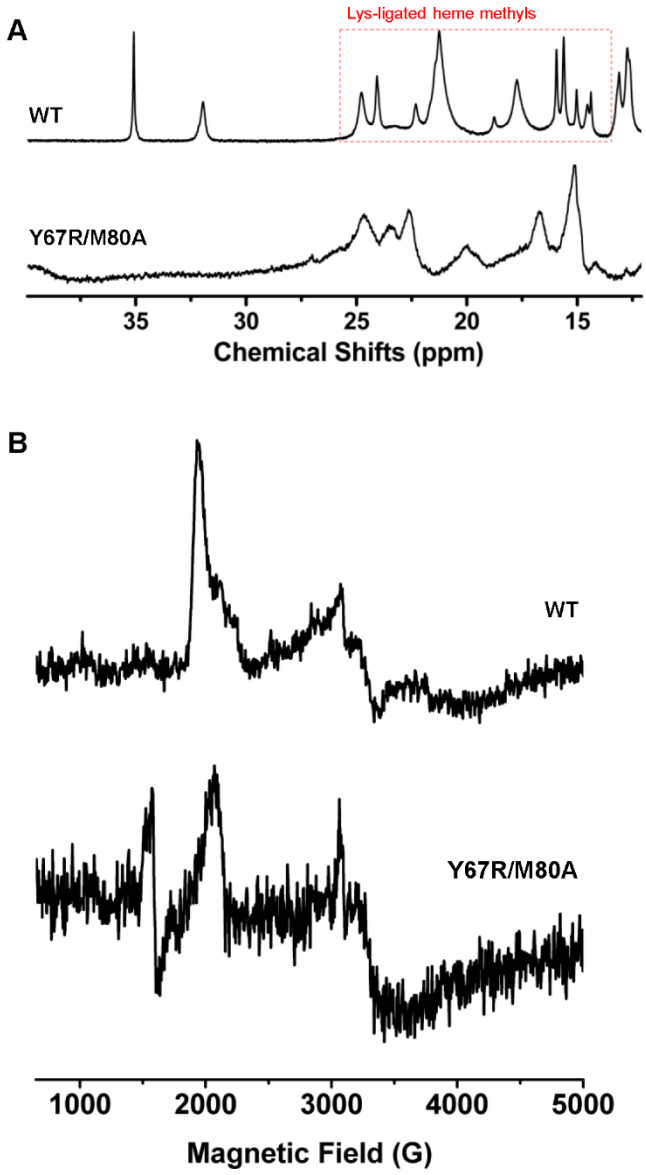

Figure 6.20. (A) ^{1}H NMR spectra in the downfield region for ferric WT and Y67R/M80A horse heart cyt *c* at 25 ºC. Samples were in a 50 mM sodium borate buffer with 100% D_2O at pD 10.5. Heme methyl signals observed in alkaline Lys-ligated cyt *c* are indicated (red dotted box). (B) EPR spectra ferric WT and Y67R/M80A at 10 K. Samples were in a 50 mM sodium borate buffer at pH 10.5with 20 % glycerol (*v*/*v*).

pH titrations using the ^{1}H NMR and EPR measurements also show that the hydroxide-ligated species is not populated during the transition (Figure 6.21). EPR spectra lack the signal associated with the hydroxide-ligated heme iron (g_z = 2.57, Figure 6.16C) in the entire pH range, from 10.5 to 4.5 (Figure 6.21A). In the ^{1}H NMR spectra, the heme methyl resonances between 15 and 25 ppm characteristic of the Lys-ligated heme iron (Figure 6.11A), are the only signals present in the pH range from pD 10.5 to 5.75 (Figure 6.21B). Signals found for the hydroxide-ligated heme iron species observed in M80A (Figure 6.16A) are not present in this pD range in the spectra of Y67R/M80A. At pD 5.75, near the pK_a obtained from the electronic absorption spectra, the ^{1}H NMR spectrum is a combination of the spectra at pD 7.4 and 4.5, further confirming that the bound-ligand transitions between Lys and H_2O and does not involve a hydroxide-ligated heme iron species (Figure 6.21B). Furthermore, if the coordinated species had included hydroxide as an intermediate, the pK_a value for the transition would have been significantly higher.

Values of pK_a for coordinated water in proteins with His/H_2O heme vary widely and are heavily dependent on exposure of the coordination site. The pK_a of 6.1 for M80A is in the lowest values reported (Table 6.10 and Figure 6.16D), but in MP8, where the heme coordination site is fully exposed, the pK_a increases to 9.6.[7] For Y67R/M80A, the tertiary packing at near-neutral pH is greatly perturbed (Figure 6.13B), suggesting that the heme and its H_2O ligand in this variant is more solvent exposed than those in M80A. Thus, had hydroxide been a heme ligand in Y67R/M80A, the pK_a of this species would have been greater than 6.1, and we would have observed the spectroscopic signature of this species in ^{1}H NMR and EPR at the titration midpoint.

Figure 6.21. (A) EPR spectra of M80K* yeast cyt *c* at pH 7.4; Y67R/M80A horse heart cyt *c* at pH 10.5, pH 7.4, pH 6.5, pH 5.5, and pH 4.5; M80A horse heart cyt *c* at pH 4.5. Each sample contained 200 to 300 μM protein in a 50 mM borate buffer at pH 10.5; 50 mM sodium phosphate buffer at pH 7.4 to 6.5; 50 mM MES buffer at pH 5.5; 50 mM sodium acetate buffer at pH 4.5. Except for M80K*, 20% glycerol (*v*/*v*) were added for all samples. Spectra were obtained at 10 K. Signals attributed to Lys-bound (blue) and high-spin H_2O species (red) are indicated (dotted line). EPR spectrum for M80K* was provided by Dr. Fangfang Zhong. (B) pH-dependence of the downfield region of the ^1H NMR spectra of ferric Y67R/M80A at 25 ºC. Buffers used were 50 mM sodium acetate at pD 4.5 and 5.75; 50 mM sodium phosphate at pD 7.4; 50 mM sodium borate at pD 10.5; all buffers were prepared with 100% D_2O.

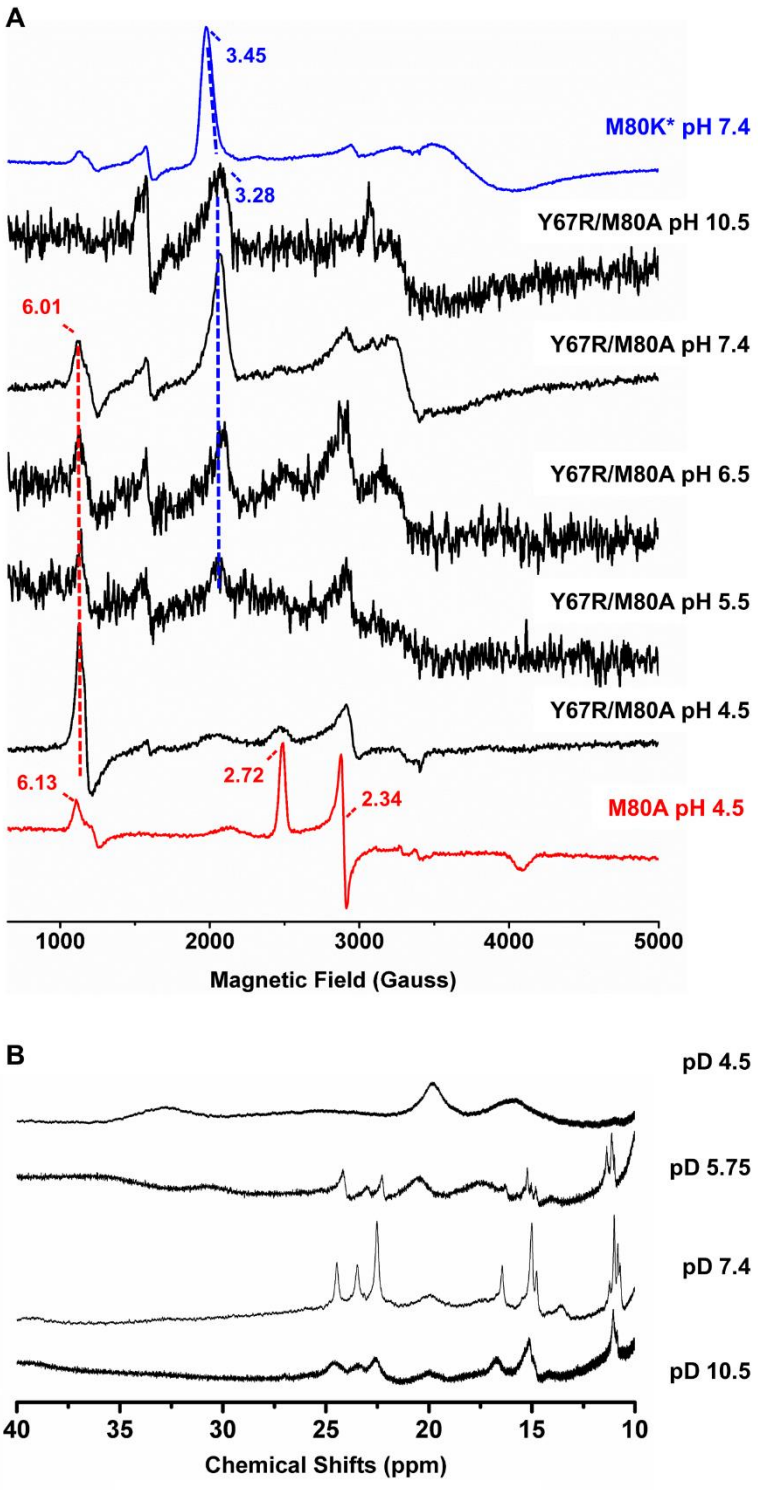
A
3.45
M80K* pH 7.4
3.28
Y67R/M80A pH 10.5
6.01
Y67R/M80A pH 7.4
Y67R/M80A pH 6.5
Y67R/M80A pH 5.5
Y67R/M80A pH 4.5
6.13
2.72
2.34
M80A pH 4.5
1000
2000
3000
4000
5000
Magnetic Field (Gauss)
B
pD 4.5
pD 5.75
pD 7.4
pD 10.5
40
35
30
25
20
15
10
Chemical Shifts (ppm)

Based on the spectra at different pH conditions and pK_a comparisons, we conclude that Lys is replaced by H_2O in the Y67R/M80A variant, and that sizable population of the hydroxide-ligated heme species is not present in the pH range observed.

Spectral baselines change significantly at pH conditions above 7.4 and at mildly acidic conditions, suggesting that the stability of the protein at Y67R/M80A diminishes and the protein aggregates (Figures 6.20 and 6.21). It is possible that there may be spectral contributions from the more solvent-exposed heme species of denatured protein. However, analyses of the EPR and ^{1}H NMR spectra support a pK_a value obtained from the Soret spectra of pK_a = 5.6 (Figure 6.22), even at high protein concentrations where contribution from protein aggregates may be greater. Furthermore, plotting the signals of Lys-ligated species as a function of pH correspond well to the fitted lines of the population of the two-state conformers calculated from the SVD analysis with the pK_a value of 5.6 (Figure 6.18C). Even if there are denatured species, this does not provide a sizable contribution to the spectral signals at the observed pH conditions.

The pH-dependent heme iron ligand switch between Lys and H_2O for Y67R/M80A can be explained by a two-state model, and the components involved can be confirmed by the component spectra obtained from the SVD analysis (Figure 6.18D). The spectrum of one of the components resembles that of H_2O-ligated M80A at pH 4.5 (Figure 6.14A) and is even closer to that of M80A under MG conditions (Figure 6.18D, top). These results agree with the ligand assignment to be H_2O at pH 4.5 and flexible tertiary structure observed for the Y67R/M80A variant under acidic conditions (Figures 6.14 and 6.17B). The spectrum of another component extracted from the analysis is comparable to that of Lys-ligated WT cyt *c* at pH 10.5 (Figure 6.18D, bottom).

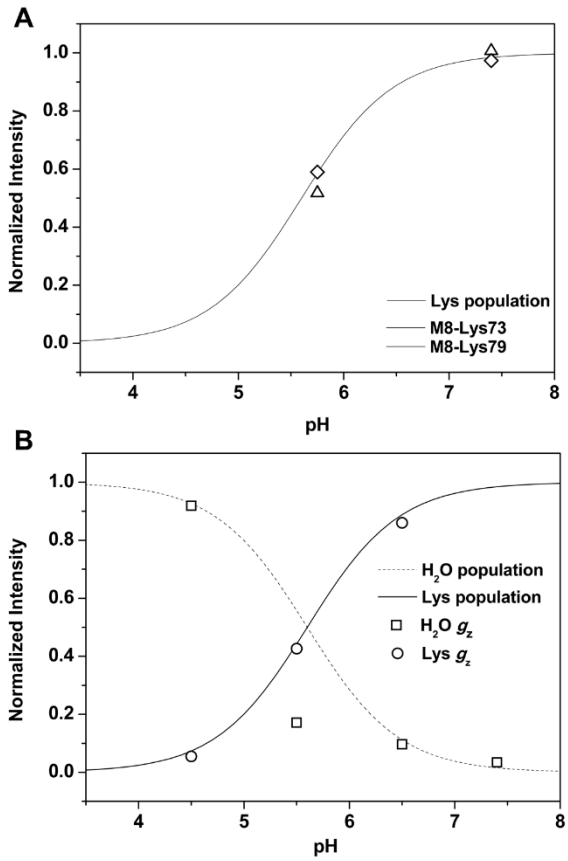

Figure 6.22. pH dependence of the intensities of selected signals (data in Figure 6.21) from (A) ^{1}H NMR and (B) EPR spectra of ferric Y67R/M80A. Solid lines are the populations of the Lys-ligated forms, and dashed lines are the populations of the H_2O-ligated form as a function of pH. (Figure made by Dr. Jie Gu)

pH-Jump Kinetics and Lys Dissociation Rates from Imidazole Binding Experiments. Rate constants associated with transitions from the Lys-ligated conformer for Y67R/M80A were obtained from time-dependent changes in the absorption spectra upon downward and upward pH jumps (Table 6.11). All kinetic data obtained were fit to single-exponential progress curves (Figure 6.23A) and show dependence on pH, with $k_{obs} \approx k_b$ at lower pH values where $[H^+] >> K_H$ (the acid dissociation constant of the protonating "trigger" group), and $k_{obs} = k_f + k_b$ at higher pH values where $[H^+] << K_H$ (Figure 6.24). To get an accurate fit for the K_H value from the data set, k_b has been set as the average of the k_{obs} values at lower pH conditions. From the rate constants k_f and k_b, the conformational equilibrium constant K_C (the ratio of forward and backward rate constants, k_f/k_b) has been obtained to calculate the apparent pK_a value (pK_a = pK_H + pK_C), which is in good agreement with the pK_a values obtained from pH titrations monitoring the Soret or CT transition (compare Tables 6.10 and 6.11).

Both K_C and pK_H in Y67R/M80A contribute to lowering the apparent pK_a (Table 6.11). Furthermore, pK_H of the "trigger" group in Y67R/M80A is 6.9 ± 0.4, much lower than the 11.5 ± 0.1 in WT cyt *c* It is then likely that conformational effects imposed by the Y67R/M80A mutation is in close vicinity of the "trigger" group. The rate constant for the formation of the Lys-ligated conformer, k_f, is similar in Y67R/M80A and WT. The major difference is observed in the rate constant for the back conversion from the Lys-ligated conformer, k_b, which is about an order of magnitude higher than that of WT (Table 6.11). Unlike in WT, the Lys-ligation is readily lost in Y67R/M80A, presumably because of its highly perturbed tertiary structure and diminished global stability (Figure 6.13B and Table 6.9).

Table 6.11. Kinetic Parameters for the Alkaline Transition and Imidazole Binding for Horse Heart Ferricytochrome *c* Variants

Variant	k_f (s^{-1})	k_b (s^{-1})	K_C	pK_H[c]	pK_H + pK_c	K_D^{Im} (M)	k_{obs}^{Im} (s^{-1})
WT	10.5 ± 0.2[a]	0.048	219± 4	11.5 ± 0.1	9.2 ± 0.1	9.5×10^{-2}[b]	60 ± 15
Y67R/M80A	7.7 ± 1.9	0.78 ± 0.38	9.9 ± 5.4	6.9 ± 0.4	5.9 ± 0.5	2.9×10^{-4}	0.79 ± 0.05

[a]From ref. [77]. [b]Calculated from values in ref. [57]. [c]Determined from the fit of the data in Figure 6.24.

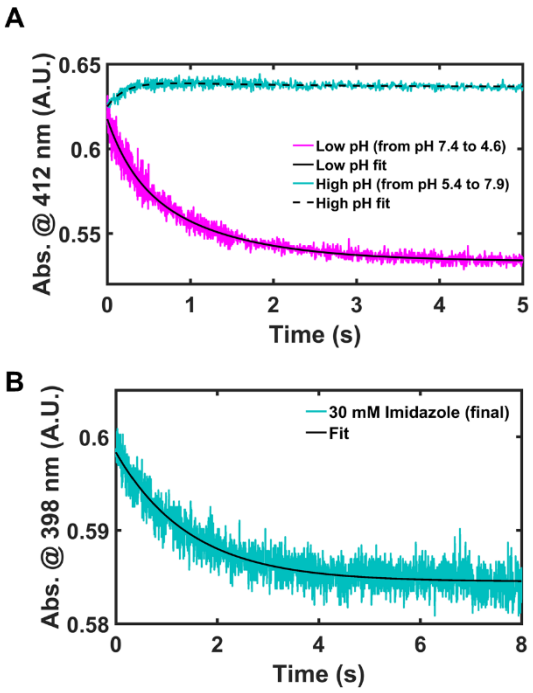

Figure 6.23. Representative kinetic traces from (A) pH jumps from pH 7.4 to 4.6 and from pH 5.4 to 7.9, and (B) measurements of imidazole binding kinetics at pH 7.4. Mixing experiments were performed at 22 ± 2 ºC.

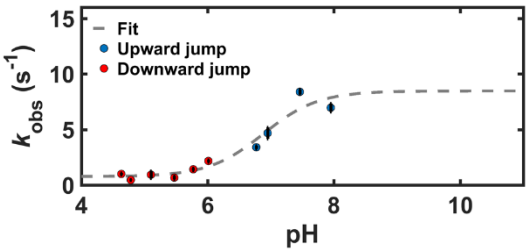

Figure 6.24. Plot of k_{obs} vs pH, with the fit to eq 6.7 (gray, dashed line) for Y67R/M80A. Results from downward (red circles) and upward (blue circles) pH-jump experiments at 22 ± 2 ºC are shown.

Y67R/M80A variant readily binds exogenous imidazole, which readily replaces the endogenous Lys ligand, as seen with the concentration-dependent changes in the absorption spectra (Figure 6.23B). In accordance with eq 6.14, the rate constant k_{obs}^{Im} is independent of the concentration of the exogenous ligand when [Im]>>K_D, as the term $K_D/(k_{off}^{Im}[Im])$ becomes negligible at high ligand concentrations. The rate constant k_{obs}^{Im} obtained from imidazole binding experiments is within error of the k_b values obtained from pH-jump experiments (Table 6.11). Similarities in the two rate constants suggests that the rate constant k_b obtained from pH-jump experiments reports on the dissociation of Lys from the heme iron, and that the Lys dissociation is the rate-limiting step for the back conversion from the Lys-ligated conformer in Y67R/M80A.

The pH-independent K_D^{Im} value was calculated using eq 6.9 to from the pH-dependent the K_D^{app}value obtained from fitting the data from eq 6.8 (Figure 6.25). The K_D^{Im} value is over an order of magnitude lower for Y67R/M80A than that for WT (Table 6.11).[57] Imidazole more readily binds to the heme iron of Y67R/M80A than of WT (Table 6.11), suggesting a more exposed heme pocket in the former variant. K_D^{Im} of Y67R/M80A is in good agreement with the equilibrium constant found for the imidazole binding in AcMP8 (2.5×10^{-4} M at pH 8.0),[58] rather than with that for WT (Table 6.11). In AcMP8, the heme is fully exposed to the solvent unlike in WT cyt *c*. As such, K_D^{Im} for WT is higher than that for AcMP8, suggesting that the complexation of the Imidazole to the heme iron is lower in WT compared to AcMP8 (assuming the Imidazole dissociation is similar for both ferric hemes). Thus, similarities in the K_D^{Im} parameter for Y67R/M80A to AcMP8 rather than the WT implies that the heme in Y67R/M80A is more solvent-exposed than the heme in WT.

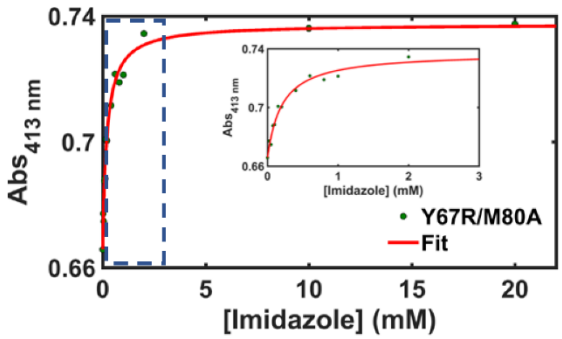

Figure 6.25. A plot showing the changes in absorption at 413 nm with increase in imidazole concentration for the Y67R/M80A horse heart cyt *c* variant (green dot), with the fit of the curve (red line). Zoomed in region at low imidazole concentrations (blue dotted line) are shown in the inset.

Peroxidase Activity. To compare with conventional peroxidases and model compounds,[8, 63, 66, 67, 94-108] assays of intrinsic peroxidase activity at varying concentrations of substrates have been performed (Figure 6.26).[66] Although classical Michaelis-Menten kinetics have been used to describe the peroxidase activity of cyt *c*,[9] we wanted to attempt to separate the relative contributions from protein packing and Lys-ligation at near-neutral pH and determine apparent k_1 (k_{1obs}) and k_3 values.

Variations in k_1 or k_{1obs} in cyt *c*, reflect differences in the electronic structure and accessibility of the heme group. Accessibility of the heme is modulated by its encapsulation within the polypeptide; dissociation of endogenous ligands also plays a major role in altering the k_1 of the protein.[7, 9] The rate constant k_{1obs} for Y67R/M80A increases significantly compared to those in WT and M80A (Figure 6.27A). Catalytic residues near the heme that promote heterolytic cleavage of H_2O_2 also influence k_1. The rate constant for k_{1obs} in Y67R/M80A is, however, lower than that for conventional peroxidases (Table 6.12).

To enable peroxidase function in cyt *c*, the axial ligand must first dissociate to provide an open coordination site for H_2O_2. The rate constant k_{1obs} depends then on the rate constants for Met and Lys binding to the heme iron (Schemes 6.4 and 6.5). The ease of the axial ligand dissociation and will influence the value of k_{1obs}, as an open coordination is a prerequisite for peroxidase activity. Furthermore, heme accessibility is crucial for substrate access. If the vicinity around the heme is tightly regulated and compact, it would be less likely for exogenous ligands to access the heme, even with a readily available open coordination site.

Figure 6.26. Representative progress curve, Michaelis-Menten plots, and fits (for k_{1obs} and k_{3obs}) for peroxidase assays using ABTS. **A**) Representative progress curve for WT (200 μM ABTS, 1 mM H_2O_2, 1.1 μM cyt *c* in a 25 mM HEPES + 0.1 mM DTPA buffer at pH 7.4). **B**) Representative Michaelis-Menten plot for determining k_3, with H_2O_2 in excess, with fit (solid line). Shown is for M80A (0-200 μM ABTS, 437 μM H_2O_2, 1.1 μM cyt *c* in a 25 mM HEPES + 0.1 mM DTPA buffer at pH 7.4). Experimental k_3 was found by using the equation $k_3 = k_{cat}/(2K_M)$. **C**) Representative Michaelis-Menten plot for determining k_1 (left) by obtaining V^{H2O2} and $K_M{}^{H2O2}$ with ABTS in excess. Representative plot to extrapolate experimental k_1 from V^{H2O2} and $K_M{}^{H2O2}$ obtained at various concentrations of ABTS (right). Shown is the Michaelis-Menten plot for Y67R/M80A at pH 7.4 (left, 200 mM ABTS, with H_2O_2 ranging from 0 to 200 mM H_2O_2, 1.1 μM cyt *c* in a 25 mM HEPES + 0.1 mM DTPA buffer at pH 7.4) and the linear extrapolation of k_1 (right, from 50 and 100 mM ABTS, 0 to 200 mM H_2O_2, 1.1 μM cyt *c* in a 25 mM HEPES + 0.1 mM DTPA buffer at pH 7.4).

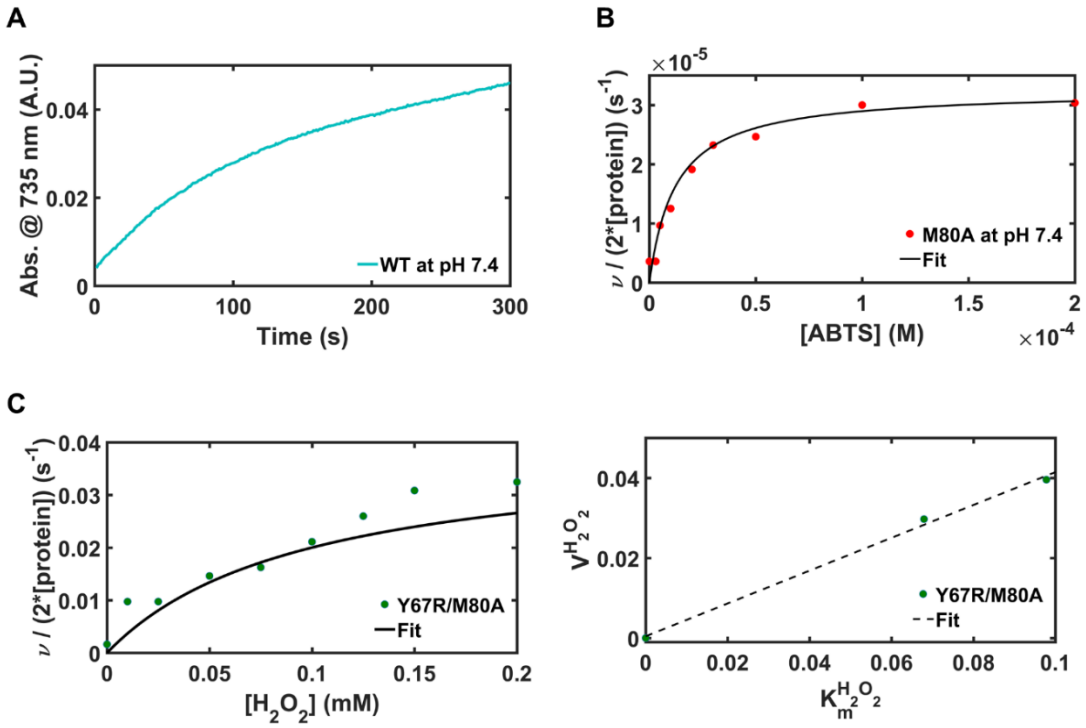
A
Abs. @ 735 nm (A.U.)
0.04
0.02
0
0
100
200
300
Time (s)
WT at pH 7.4
B
×10-5
3
2
1
0
ν / (2*[protein]) (s-1)
M80A at pH 7.4
Fit
0
0.5
1
1.5
2
[ABTS] (M)
×10-4
C
0.04
0.03
0.02
0.01
0
ν / (2*[protein]) (s-1)
Y67R/M80A
Fit
0
0.05
0.1
0.15
0.2
[H2O2] (mM)
0.04
0.02
0
V H2O2
Y67R/M80A
Fit
0
0.02
0.04
0.06
0.08
0.1
K H2O2 m

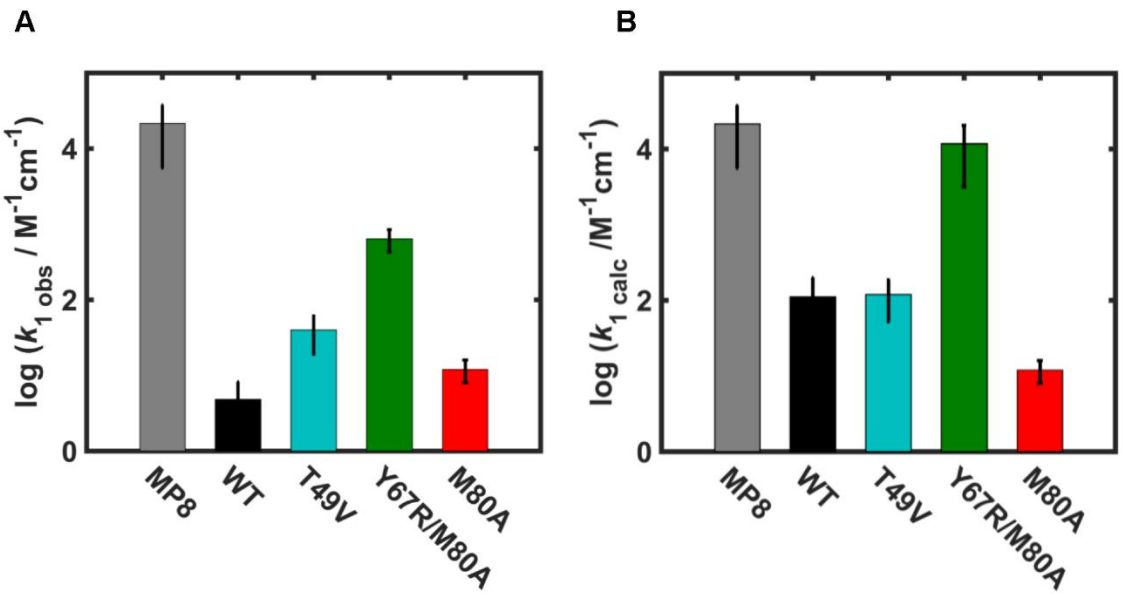

Figure 6.27. Comparison of (A) k_{1obs} (observed k_1) and (B) k_{1calc} (calculated k_1 based upon model) for WT, T49V, Y67R/M80A, and M80A horse heart cyt *c* variants at pH 7.4 to the literature k_1 values of MP8 from refs. [67] and [98]. k_{1obs} for T49V was obtained from ref. [109].

Table 6.12. Rate Constants for the Formation of Compound I (k_{1obs})[a]

	k_{1obs} ($M^{-1}s^{-1}$)	pH
Pseudo-peroxidases		
Cyt *c* (Horse Heart)		
WT	4.8 ± 3.5	7.4
T49V	$(4.0 \pm 2.1) \times 10^1$	7.4
Y67R/M80A	$(6.4 \pm 2.1) \times 10^2$	7.4
M80A	$(1.2 \pm 0.4) \times 10^1$	7.4
WT	7[b,c]	7.0
WT, with CL	1×10^1[b,c]	7.0
Cyt c_{550} (*P. versutus*)		
WT	2.6[d]	5.0
WT unfolded, 6 M GuHCl	3×10^3[d]	5.0
	1.2×10^3[e]	5.0
Mb (Human)	3.2×10^2[f]	6.0
Mb (Sperm Whale)	7.6×10^2[g]	6.0
MP8	4.4×10^3[h]	7.4
	$1.5\text{-}4.7 \times 10^4$[i]	7.5
MP11	2.1×10^3[j]	7.0
	1.7×10^2[j]	10.4
Peroxidases from plants, fungi, bacteria		
Horseradish peroxidase	1.4×10^7[k]	7.4
	9×10^6[l]	5.4
Spanish broom peroxidase	2.5×10^5[m]	6.0
Royal palm tree peroxidase	5.4×10^5[n]	6.0
	3.3×10^5[n]	6.9
Versatile peroxidase	1.3×10^6[o]	3
	3.5×10^6[o]	3.0
Cytochrome c peroxidase (Yeast)	3.9×10^7[p]	6.0
Mammalian peroxidases		
Myeloperoxidase (Bovine)	1.8×10^7[q]	7.1
Lactoperoxidase (Bovine)	1.1×10^7[r]	7.0
Eosinophil peroxidase (Human)	4.3×10^7[s]	7.0

[a] k_{1obs} for cyt *c* variants and k_1 for conventional peroxidases. [b] Calculated from reported k_{cat} and $[H_2O_2]$ using $k_1 = k_{cat}/2[H_2O_2]$ ($M^{-1}s^{-1}$). [c] From ref. [94], contained protein to CL ratio of 1:40. [d] From ref. [8]. [e] From ref. [95]. [f] From ref [96]. [g] From ref. [97]. [h] From ref. [67]. [i] From ref. [98]. [j] From ref. [99]. [k] From ref. [100]. [l] From ref. [101]. [m] From ref. [66]. [n] From ref. [102]. [o] From ref. [103]. [p] From ref. [104]. [q] From ref. [107]. [r] From ref. [108]. [s] From ref. [110].

In peroxidases, oxidizing substrates (like ABTS) access the heme edge (heme δ-meso carbon or 8-methyl group), rather than the activated oxygen in the heme center.[111, 112] Similar assumptions can be made with the cyt *c* variants,[113] as the value of k_3 for MP systems and peroxidases are along the similar orders of magnitude.[63, 66, 103] With these considerations, the peroxidase activity of cyt *c* should be regulated by two main factors: 1) availability of the open coordination site (ligand dissociation if the intrinsic axial ligand is present) and 2) accessibility of the heme (compactness of the active site and the protein scaffold).

To better differentiate heme accessibility due to protein packing and ligation, "ligand-free" values of k_1 were calculated using kinetic parameters for Met- and Lys-binding and dissociation. Like the k_{1obs} rate constant, the calculated k_1 rate constant of the Y67R/M80A variant is higher compared to both WT and M80A (Figure 6.27B and Table 6.12). Interestingly, k_1 value for M80A is the lowest among the variants studied, suggesting that in this variant, the protein may fold more tightly around the heme than it does in WT.

Rates of Compound II reduction provide additional information regarding the differences in the heme environment (Figure 6.28). The k_3 values for WT and M80A are within error of one another, consistent with minimal changes in protein structure with the M80A mutation (Figure 6.28 and Table 6.13). The value of k_3 for Y67R/M80A is higher than those for WT and M80A, and comparable in magnitude to the CL-bound WT (Table 6.13).[94]

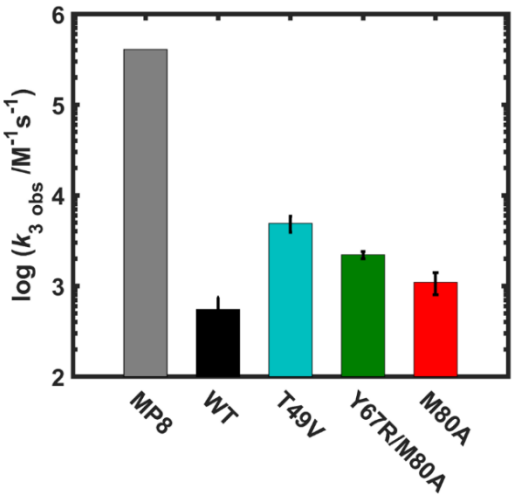

Figure 6.28. Experimental observed rate constants k_{3obs} (k_3) of the variants. Respective MP8 rates are from refs. 7 and [98]. k_3 for T49V was obtained from ref. [109].

Table 6.13. Rate Constants for the Reduction of Compound II by ABTS (k_3)

Variant	k_3 ($M^{-1}s^{-1}$)	pH
Pseudo-peroxidases		
Cyt *c*		
WT	$(5.5 \pm 2.0) \times 10^{2}$[a]	7.4
T49V	$(4.9 \pm 1.0) \times 10^{3}$[a]	7.4
Y67R/M80A	$(2.2 \pm 0.2) \times 10^{3}$[a]	7.4
M80A	$(1.1 \pm 0.3) \times 10^{3}$	7.4
WT	3×10^{2}[a,b]	7.0
WT, with CL	1.6×10^{3}[a,b]	7.0
MP8	4.08×10^{5}[c]	10.7
Conventional Peroxidases		
Spanish broom peroxidase	2.6×10^{5}[d]	6.0
Versatile peroxidase	4.8×10^{6}[e]	3.0

[a]Calculated from k_{cat} and K_m using $k_3 = k_{cat}/2K_m$ ($M^{-1}s^{-1}$). [b]From ref. [94]. [c]From ref. [63]. [d]From ref. [66]. [e]From ref. [103].

Amongst the variants in this study, Y67R/M80A has the highest values of k_1 and k_3. Yet, the activity rate values for Y67R/M80A are still orders of magnitude smaller than those for MP8 or peroxidases (Tables 6.12 and 6.13). This large difference in the magnitude of the activity rate values suggest that Lys-ligation in Y67R/M80A hinders H_2O_2 coordination and that the polypeptide packs limits substrate access to the heme edge.

Discussion

Role of Loop D Packing in Protecting Residue 80. The identity of residue 67 is critical for the proper function of cyt *c*. Studies with different side chain substitutions of Tyr67 have shown that, depending on the substituted residue, changes in stability, pK_a of the alkaline transition, peroxidase activity, and reduction potential are observed.[32, 33, 37, 114] Not all mutations in this position alter the packing and fold of the protein, suggesting that the peptide backbone can tolerate some perturbations. However, there is a limit to what changes the protein peptide can accommodate without altering the global fold. Replacement of Tyr with Arg in position 67 introduces a large, charged residue within the tightly packed hydrophobic heme cavity.[14, 115] This perturbs the native packing of the protein, and CD experiments specifically show that structural signals observed in native cyt *c* are diminished (Figures 6.13 and 6.17). Even so, the heme iron is Lys-ligated rather than hydroxide-ligated (Figure 6.11).

There seems to be a propensity for the protein to preserve protein fold, rather than native Met ligation to the heme iron. Native packing of the polypeptide, particularly along loop D is highly conserved in cyt *c*.[6, 116, 117] In M80A variant of horse heart cyt *c*, CD

experiments show that the native fold is present in this variant, and Lys does not coordinate to the heme iron as it does in Y67R/M80A (Figures 6.11 and 6.13).

In this work, we have observed oxidation of Met80 in Y67R horse heart cyt *c* (Figure 6.4 and Table 6.2). Oxidation of Met80 alone does not perturb the tertiary packing of the protein, but perturbation of tertiary fold may influence the extent of Met80 oxidation. Cyt *c* with chemically oxidized Met80 does not show loss of tertiary structure.[72] Studies of the CL-bound cyt *c* have shown that molecular oxygen can readily oxidize Met80.[78] In T49V horse heart cyt *c*, a variant with smaller perturbations in the tertiary structure compared to Y67R, only a minor population of the Met is oxidized.[75] In comparison, Y67R contains oxidized Met80 for the entire population (Figure 6.4). Perhaps in Y67R, Met80 is more readily exposed to molecular oxygen due to the presence of a bulky, charged residue in position 67 that interferes with forming the compact, native fold. Although it is not clear whether similar oxidative damages have been observed in previous studies of yeast and human Y67R cyt *c* variants,[35, 37] this particular mutation in these systems is likely to be as intrusive as it is in horse heart cyt *c*. Thus, it would not be surprising if Met80 has been susceptible to oxidative damage in both yeast and human Y67R cyt *c* variants.

Alkaline Transition and Trigger Groups. In cyt *c*, stability and flexibility of loop D has been correlated to the properties of alkaline transition.[118] Even minor perturbations in and around loop D can affect the pK_a of this transition, as observed with variants that have been studied over the years (Figure 6.29 and Table 6.14).[6, 22, 32, 86, 118-130] Besides loop D, various mutational studies at or around loop C, closest to the HP6, have revealed that the pK_a of the alkaline transition is sensitive to structural changes in this region.[121, 123, 129]

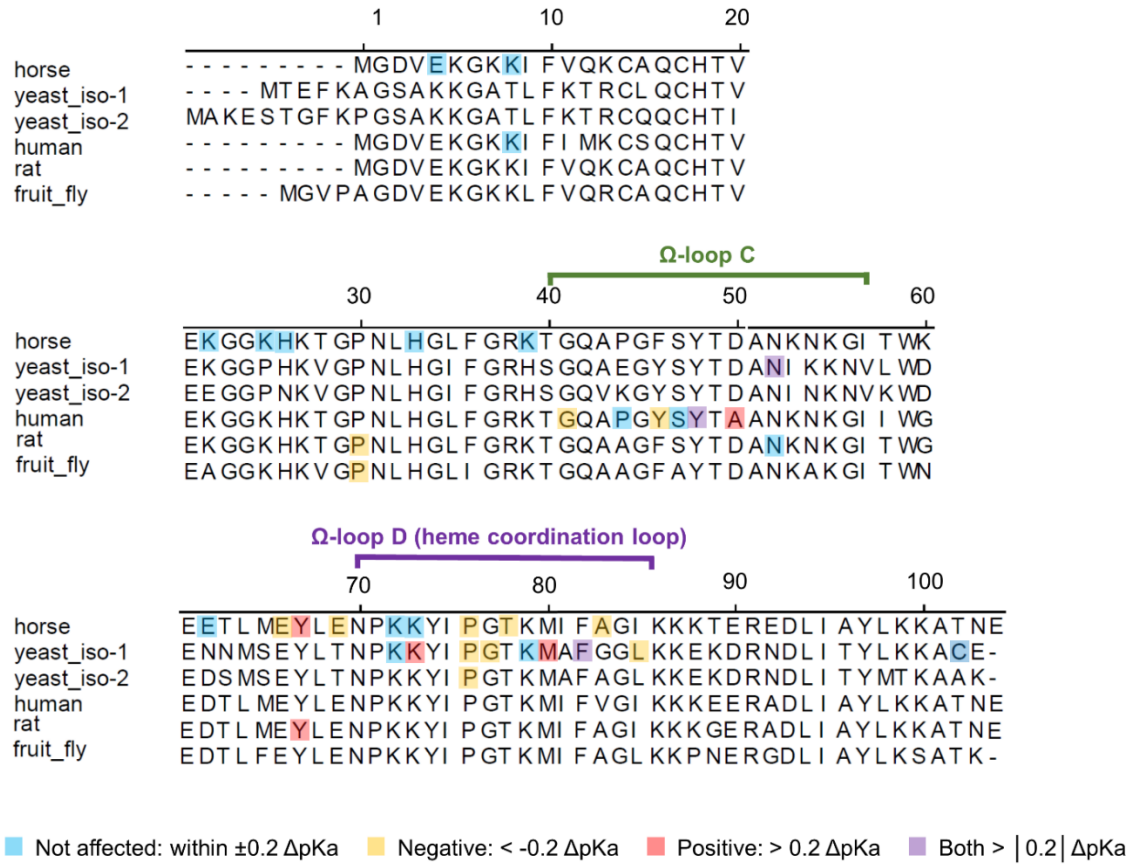

Figure 6.29. Sequence alignment of cyt *c* from various species, for which information about mutational effects on the pK_a value for the alkaline transition is available. Highlighted are mutation sites, color-coded by the magnitude and the direction of the change in the pK_a value. Table 6.14 lists the mutants and their respective pK_a values.

Table 6.14. pK_a Values for the Alkaline Transition in Previously Studied Variants of Ferricytochrome c^a

Species	Variant	pK_a^{alk}	Ref. Protein	ΔpK_a^b	Reference
Horse	WT (1)	9.35	--	--	Ref. [6]
	WT (2)	9.22 ± 0.06	(1)	-0.13 ± 0.06	Ref. [119]
	H26N/H33N (3)	9.16	(1)	-0.19	Ref. [118]
	E4G/H26N/H33N	9.15	(3)	-0.01	
	K8G/H26N/H33N	9.10	(3)	-0.06	
	K22G/H26N/H33N	9.23	(3)	0.07	
	K25G/H26N/H33N	9.27	(3)	0.11	
	H26N/H33N/K39G	9.18	(3)	0.02	
	H26N/H33N/E62G	9.15	(3)	-0.01	
	H26N/H33N/E66G	8.46	(3)	-0.7	
	H26N/H33N/E66A	8.64	(3)	-0.52	
	H26N/H33N/E69G	8.61	(3)	-0.55	
	H26N/H33N/P76G	7.50	(3)	-1.66	
	H26N/H33N/K72G (4)	9.02	(3)	-0.14	
	H26N/H33N/K72G/K73G	9.00	(4)	-0.02	
Horse	Y67F	10.65	(1)	1.3	Ref. [32]
	A83P	8.95	(1)	-0.4	
	T78N/A83P	8.25	(1)	-1.1	
	T78N	8.10	(1)	-1.25	
Yeast *iso*-1	WT[d] (5)	8.5	--	--	Ref. [120]
	C102T (6)	8.5	(5)	0	
	N52I	9.4	(5)	0.9	Ref. [121]
	K72A/C102T (7)	8.5	(6)	0	Ref. [122]
	K73A/C102T	8.82 ± 0.02	(6)	0.32 ± 0.02	Ref. [22]

	K79A/C102T (8)	8.44 ± 0.01	(6)	-0.06 ± 0.01	
	N52G/K79A/C102S	7.46 ± 0.02	(8)	-0.98 ± 0.02	Ref. [123]
	L85A/C102T (9)	7.7 ± 0.1	(6)	-0.8 ± 0.1	Ref. [124]
	K72A/L85A/C102S	7.84 ± 0.06	(9)	0.14 ± 0.12	
	K73H/K79A/C102S	6.70 ± 0.03	(8)	-1.74 ± 0.03	Ref. [125]
	F82G/C102T	8.4	(6)	-0.1	Ref. [120]
	F82S/C102T	7.7	(6)	-0.8	
	F82L/C102T	7.2	(6)	-1.3	
	F82I/C102T	7.2	(6)	-1.3	
	F82W/C102T	9.95 ± 0.08	(6)	1.45 ± 0.08	Ref. [126]
	M80E/C102T	11.55 ± 0.11	(6)	3.05 ± 0.11	Ref. [86]
	M80D/C102T	9.25 ± 0.08	(6)	0.75 ± 0.08	
	P76A/C102T	7.83 ± 0.14	(6)	-0.67 ± 0.14	Ref. [127]
	G77A/C102T (10)	8.00 ± 0.23	(6)	-0.5 ± 0.23	
	P76A/G77A/C102T	6.88 ± 0.15	(10)	-1.12 ± 0.27	
	K72A/C102S (11)	8.8 ± 0.1	--		Ref. [53]
	K79G (12)	8.6 ± 0.1	(11)	0.2 ± 0.1	Ref. [131]
	T49V/K79G	6.7 ± 0.1	(12)	2.1 ± 0.1	Ref. [132]
	T78V/K79G	6.7 ± 0.1	(12)	2.1 ± 0.1	
Yeast *iso*-2	WT[d] (13)	8.45	--	--	Ref. [128]
	P76G[d]	6.7	(13)	-1.75	
Human	WT	9.9	--	--	
	WT	9.5	--	--	
	WT	9.3 ± 0.4	--	--	Ref. [129]
	WT[f] (14)	9.56 ± 0.1	--	--	Ref. [130]
	Y46F	8.9	(14)	-0.66 ± 0.1	Ref. [129]
	K8R(15)	9.63 ± 0.07	(14)	0.07 ± 0.12	
	K8R/P44S(16)	9.51 ± 0.05	(15)	-0.12 ± 0.09	
	K8R/P44S/Y46F(17)	9.15 ± 0.02	(16)	-0.36 ± 0.05	
	K8R/P44S/Y46F/S47T(18)	9.05 ± 0.01	(17)	-0.1± 0.02	
	K8R/P44S/Y46F/S47T/A50E	9.32 ± 0.03	(18)	0.27 ± 0.03	

	Y48F	10.3	(14)	0.74 ± 0.1	
	Y48E	7.0	(14)	-2.56 ± 0.1	Ref. [133]
	Y48I	6.9	(14)	-2.66 ± 0.1	
	G41S	7.8 ± 0.3	(14)	-1.76 ± 0.32	
	G41A	8.1 ± 0.5	(14)	-1.46 ± 0.51	
	G41T	6.7 ± 0.2	(14)	-2.86 ± 0.22	
	T28D	9.9 ± 0.2	(14)	0.34 ± 0.22	Ref. [134]
	T28A	8.9 ± 0.1	(14)	-0.66 ± 0.14	
	S47D	9.2 ± 0.1	(14)	-0.36 ± 0.14	
	S47A	9.1 ± 0.0	(14)	-0.46 ± 0.1	
	I81A	8.98 ± 0.02	(14)	-0.58 ± 0.1	Ref. [135]
	V83G	10.04 ± 0.02	(14)	0.48 ± 0.1	
	G41S	8.5 ± 0.2	(14)	-1.06 ± 0.22	Ref. [136]
	Y48H	8.4 ± 0.1	(14)	-1.16 ± 0.14	
	I81A	9.4 ± 0.2	(14)	-0.16 ± 0.22	
	V83G	10.1 ± 0.1	(14)	0.54 ± 0.14	
	I81A/V83G	9.7 ± 0.1	(14)	0.14 ± 0.14	
	A51V	8.3 ± 0.1	(14)	-1.26 ± 0.14	Ref. [137]
Fruit Fly	WT (19)	9.0	--	--	Refs. [33, 114]
	P30A	8.2	(19)	-0.8	Ref. [138]
Rat	WT	9.5	--	--	Refs. [33, 114]
	WT	9.6	--	--	Ref. [138]
	WT (20)[f]	9.55 ± 0.05	--	--	
	P30A	8.5	(20)	-1.05 ± 0.05	
	P30V	5.9	(20)	-3.65 ± 0.05	
	Y67F	10.7	(20)	-1.15 ± 0.05	Refs. [33, 114]
	N52I	9.5	(20)	-0.05 ± 0.05	Ref. [121]

Footnote for Table 6.14.

[a]The list is not comprehensive, only variants related to reference proteins by a single point mutation are listed.

[b]$\Delta pK_a = pK_a^{alk}$ (variant) – pK_a (reference protein).

[c]Semisynthetic protein prepared by reaction of the synthetic peptide with the cyt *c* fragment after CNBr-treatment.

[d]With Cys at position 102.

[e]Cys102 modified by treatment with methyl methanethiosulfonate.

[f]Average value of multiple values reported for WT (listed above).

Elimination and/or modification of the HB at or near the HP6 is enough to tune the pK_a of the transition, as previously observed with T49V variant in horse heart cyt *c*.[109] Tyr67 has been implicated in a highly conserved inner HB network with Met80 and an internal water that is in contact with Thr78 and Asn52.[6, 11, 116] Even without the direct HB interaction, this network keeps HP6, loops C and D in communication with one another; modifications to this network also alter the pK_a of the alkaline transition (Table 6.14).

Mutations in Y67R/M80A dramatically lower the pK_a of the alkaline transition in cyt *c* (Table 6.10), and Lys coordinates to the heme iron at a near-neutral pH (Figure 6.11). In Y67R/M80A, the observed pK_a decreases because of the favorable equilibrium to the Lys-ligated form and the decrease in pK_H. The transition is not solely determined by the deprotonation of the Lys side chain; the pK_H can be lower than the pK_a of a coordinating Lys ligand(s) that can range from 10.5 to 12 in horse heart cyt *c*.[139, 140] However, the pK_H of Y67R/M80A is consistent with the iron-bound pK_a of the H_2O ligand in M80A, raising the question as to whether hydroxide-ligated heme iron is present in the transition.

Previously, hydroxide-ligated heme iron has been suggested to be a possible intermediate species in the alkaline transition.[126] This species has been observed in the X-ray crystal structure of yeast K72A cyt *c*, where Met80 has been swung out of the heme crevice and hydroxide was bound to the heme, requiring modest structural perturbations near Met80.[141] Replacing Met80 with small ligands require modest structural rearrangements. Comparison of the NMR solution structure of cyanide-bound WT and native WT horse heart cyt c has shown that residues 77 to 85 rearrange and 50's helix shifts to replace Met80 with cyanide.[142] In the absence of Met80, small exogenous ligands can coordinate to the heme iron without structural rearrangements, as observed from structural

comparisons between native WT and cyanide-bound M80A yeast cyt *c*.[142] Although hydroxide species were not detected spectroscopically in Y67R variants, it is possible that hydroxide-ligated heme iron forms transiently. Y67R/M80A does not contain Met80 and lacks a compact native fold. Yet, it is likely that the formation of hydroxide-ligated heme iron species does not drive the alkaline transition in Y67R/M80A; M80A with the similar pK_a is not ligated at near-neutral pH as is with Y67R/M80A (Figure 6.16).

Instead, the presence of a loosely structured loop in Y67R/M80A may facilitate the alkaline transition at near-neutral pH. The value of k_f for Y67R/M80A is not higher than that for WT, but k_b value is greater, implying a readily dissociating Lys ligand and readily rearranged loop D. In the alkaline transition, Lys73 and 79 are the preferred ligands to replace Met80. Structural studies suggest loop D rearrangement is required to coordinate either Lys73 or 79 to the heme iron.[15, 143, 144] Further, ^{1}H NMR studies with urea- and GuHCl-denatured horse heart cyt *c* have shown that partial unfolding of the protein has allowed Lys (either Lys73 or Lys79) to replace the Met80 ligand at neutral pH conditions, well below the intrinsic pK_a of Lys in solution.[26, 27] Even in this case, hydroxide is not a detectable species, strongly suggesting that that flexible tertiary structure and increased dynamics in loop D allow Lys to readily coordinate to the heme iron in Y67R/M80A.

The identity of the trigger group for the alkaline transition has been widely speculated, including Tyr67, W166, or HP groups (particularly HP6), as possible candidates.[145] Mutations at Tyr67 have shed some light on the identity of the trigger group. Had Tyr67 been the trigger group, pK_a of the alkaline transition would have increased when replaced with Arg in Y67R/M80A, or the mechanism eliminated when replaced with a non-protonatable residue. However, this is not the case, as observed by mutational studies with

both Y67F and Y67R/M80A; the pK_a still changes in Y67F,[32] while the pK_a decreases in Y67R/M80A (Table 6.10). Yet, perturbations at residue 67 do alter the alkaline transition, suggesting that Tyr67 may be a part of, or near, the trigger group. Examination of the X-ray crystal structure of Y67F yeast cyt *c* has shown that the inner water molecule (W166) cannot be located in this variant, suggesting changes to the inner HB network.[146] Perhaps, the Y67R/M80A mutation perturbs the alkaline transition and affects the trigger group because it modifies the packing in loop D, altering the environment of the trigger group.

Loop D Packing and Axial Ligation to the Heme Iron Control Peroxidase Activity in Cyt c. Although cyt *c* is not a peroxidase, it has peroxidase activity due to the presence of the heme. Usually, this activity is suppressed with a compact native packing and ligand to limit the accessibility of the heme crevice and to prevent heme axial coordination of H_2O_2.[8, 9] In the steps leading to apoptosis, cyt *c* binds to CL in the mitochondrial membrane. Interaction with CL unfolds the protein, exposing the heme and enhancing its peroxidase activity.[147] Unfolding of cyt *c* yields higher peroxidase activity, highlighting the role of the compact protein fold in suppressing the peroxidase activity.[8, 94, 95] Smaller structural perturbations also increase the activity, as observed with T49V horse heart cyt *c*.[75] True to this trend, the k_1 value increases with a decrease in protein fold in the series with WT, M80A, and Y67R/M80A horse heart cyt *c* variants (Figure 6.27).

The presence of a compact protein fold alone does not fully suppress the peroxidase activity. Since the axial site must be occupied by H_2O_2, the peroxidase activity is also dependent on the rate of the dissociation of the sixth ligand. As observed with partially unfolded cyt c_{550}, peroxidase activity can be suppressed if the axial site is occupied by a ligand with slow rates of dissociation, such as His.[148] On the other hand, the activity is less

suppressed if the axial ligand is readily replaced, as observed in myoglobin.[96, 97] In Met-ligated cyt *c*, the rate of this process is limited by the opening of the heme crevice, which in turn depends on the intrinsic dynamics of loop D. With Met80 ligation, changes in tertiary structure increase peroxidase activity, as observed by the T49V variant.[109] Lys dissociation is a slow process,[149] as expected for a nitrogen base Lys and ferric heme iron.[15, 68] Thus, in the WT protein, the peroxidase activity of the Lys-ligated form is low.[9, 150]

However, this does not mean that Lys-ligated heme iron always results in lower peroxidase activity compared to Met-ligated heme iron. Even in Lys-ligated protein, the heme is in a conformational equilibrium between the 5-coordinate Lys dissociated and 6-coordinate Lys-ligated heme iron species. Species with dissociated Lys ligand would have peroxidase activity, and the total observed activity will depend on the population of the Lys dissociated species. Forming the Lys- ligated heme species is pH dependent, as observed with the Lys-ligated M100K variant in cyt c_{550} or in the M80K* yeast cyt *c* variant.[15, 151] We observe higher peroxidase activity in Lys-ligated Y67R/M80A than in WT at pH 7.4, but the reverse is true at alkaline pH (Figure 6.30). Lys-ligation is pH-dependent, and Lys dissociation precedes H_2O_2 coordination to the heme. As described by eq 6.26, the rate constant k_1 depends on solution pH and K_H. Further, k_1 is also dependent on k_b. In Y67R/M80A, perturbations in loop D allow Lys to dissociate more readily than in WT, contributing to the increase in k_1. Lys ligation is not favored under neutral and acidic conditions, and the ligand is readily replaced by H_2O_2.

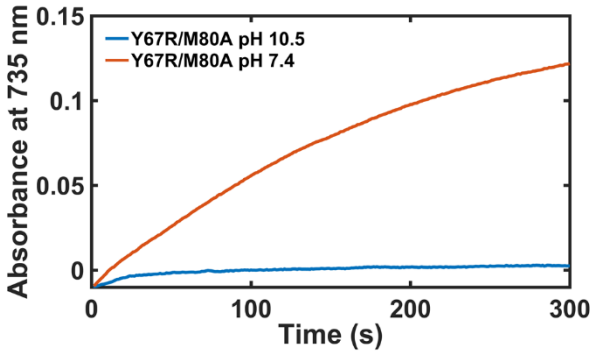

Figure 6.30. Traces of peroxidase assays for Y67R/M80A at pH 10.5 (blue) and 7.4 (orange). Formation of $ABTS^{\cdot+}$ was monitored at 735 nm for 300 seconds, at 1 second interval. Concentrations were 1 μM protein, 200 μM ABTS, with 200 μM.

Lys-ligated species has been observed for the CL-bound cyt *c*.[152] Comparison of the rate constant k_{1obs} for H_2O-ligated M80A and Lys-ligated Y67R/M80A shows that H_2O_2 more readily displaces Lys than hydroxide. Perhaps the CL-denatured species behaves similarly to the perturbed Y67R/M80A variant, and the peroxidase activity increases because the heme is coordinated by a faster dissociating Lys ligand at physiological pH. Comparison of rate constant k_3 between variants suggest an increase in heme exposure with the structural perturbations (Figure 6.28), but overall, the rate constant k_3 is lower than k_{1obs} (Table 6.13).[94] Perhaps CL-induced peroxidase activity increases k_1 to compensate for the less efficient k_3, and Lys-ligation may even serve to protect the heme from forming the His-ligated species that suppress peroxidase activity.[8]

Conclusion

Spectroscopic studies have shown that in the ferric forms of Y67R horse heart cyt *c* variants, the heme is Lys-ligated at neutral pH conditions. The structural perturbation at position 67 has altered the packing of loop D, favoring Lys coordination even in the presence of Met. The loss of native loop D packing not only favors the formation of the Lys-ligated form, but expose Met80 to oxidative damage, showing that native loop D packing may also be important for preserving the native Met80. These findings highlight the existence of a cross-talk between the different regions of cyt *c*, showing how perturbations in one region are communicated throughout the network. Y67R/M80A variant is a better peroxidase than the Met-ligated or hydroxide-ligated heme at neutral pH due to a readily dissociating Lys ligand and unstructured loop D. These findings offer support for the role of the Lys-ligated species in the CL-bound cyt *c* as apoptotic peroxidases.

References

1. del Sol, A., Tsai, C.J., Ma, B. & Nussinov, R. The origin of allosteric functional modulation: multiple pre-existing pathways. *Structure* **17**, 1042-1050 (2009).

2. Dai, S. *et al.* Low-barrier hydrogen bonds in enzyme cooperativity. *Nature* **573**, 609-613 (2019).

3. Datta, D., Scheer, J.M., Romanowski, M.J. & Wells, J.A. An Allosteric Circuit in Caspase-1. *J Mol Biol* **381**, 1157-1167 (2008).

4. D'Amico, S., Marx, J.C., Gerday, C. & Feller, G. Activity-stability relationships in extremophilic enzymes. *The Journal of biological chemistry* **278**, 7891-7896 (2003).

5. Smalas, A.O., Heimstad, E.S., Hordvik, A., Willassen, N.P. & Male, R. Cold adaption of enzymes: structural comparison between salmon and bovine trypsins. *Proteins* **20**, 149-166 (1994).

6. Moore, G.R. & Pettigrew, G.W. *Cytochromes c : evolutionary, structural, and physicochemical aspects*. (Springer-Verlag, Berlin ; New York; 1990).

7. Marques, H.M. Insights into porphyrin chemistry provided by the microperoxidases, the haempeptides derived from cytochrome c. *Dalton T*, 4371-4385 (2007).

8. Diederix, R.E.M., Ubbink, M. & Canters, G.W. Effect of the protein matrix of cytochrome c in suppressing the inherent peroxidase activity of its heme prosthetic group. *Chembiochem* **3**, 110-112 (2002).

9. Diederix, R.E.M., Ubbink, M. & Canters, G.W. Peroxidase activity as a tool for studying the folding of c-type cytochromes. *Biochemistry* **41**, 13067-13077 (2002).

10. Alberts, B., Wilson, J.H. & Hunt, T. *Molecular biology of the cell*, Edn. 5th. (Garland Science, New York; 2008).

11. Bushnell, G.W., Louie, G.V. & Brayer, G.D. High-resolution three-dimensional structure of horse heart cytochrome c. *J Mol Biol* **214**, 585-595 (1990).

12. Battistuzzi, G., Borsari, M. & Sola, M. Redox properties of cytochrome c. *Antioxid Redox Sign* **3**, 279-291 (2001).

13. Eddowes, M.J. & Hill, H.A.O. Electrochemistry of Horse Heart Cytochrome-C. *J Am Chem Soc* **101**, 4461-4464 (1979).

14. Harpaz, Y., Gerstein, M. & Chothia, C. Volume changes on protein folding. *Structure* **2**, 641-649 (1994).

15. Amacher, J.F. *et al.* A Compact Structure of Cytochrome c Trapped in a Lysine-Ligated State: Loop Refolding and Functional Implications of a Conformational Switch. *J Am Chem Soc* **137**, 8435-8449 (2015).

16. Ying, T., Wang, Z.H., Zhong, F., Tan, X. & Huang, Z.X. Distinct mechanisms for the pro-apoptotic conformational transition and alkaline transition in cytochrome c. *Chemical communications (Cambridge, England)* **46**, 3541-3543 (2010).

17. Abriata, L.A. *et al.* Nitration of Solvent-exposed Tyrosine 74 on Cytochrome c Triggers Heme Iron-Methionine 80 Bond Disruption: NUCLEAR MAGNETIC RESONANCE AND OPTICAL SPECTROSCOPY STUDIES *. *Journal of Biological Chemistry* **284**, 17-26 (2009).

18. Pinheiro, T.J., Elöve, G.A., Watts, A. & Roder, H. Structural and kinetic description of cytochrome c unfolding induced by the interaction with lipid vesicles. *Biochemistry* **36**, 13122-13132 (1997).

19. Colon, W., Wakem, L.P., Sherman, F. & Roder, H. Identification of the predominant non-native histidine ligand in unfolded cytochrome c. *Biochemistry* **36**, 12535-12541 (1997).

20. Diaz-Moreno, I., Garcia-Heredia, J.M., Diaz-Quintana, A., Teixeira, M. & De la Rosa, M.A. Nitration of tyrosines 46 and 48 induces the specific degradation of cytochrome c upon change of the heme iron state to high-spin. *Bba-Bioenergetics* **1807**, 1616-1623 (2011).

21. Theorell, H. & Akesson, A. Studies on cytochrome c. III. Titration curves. *J Am Chem Soc* **63**, 1818-1820 (1941).

22. Rosell, F.I., Ferrer, J.C. & Mauk, A.G. Proton-linked protein conformational switching: Definition of the alkaline conformational transition of yeast iso-1-ferricytochrome c. *J Am Chem Soc* **120**, 11234-11245 (1998).

23. Rosell, F.I. in Biochemistry and Molecular Biology, Vol. PhD 218 (University of British Columbia, 1999).

24. Martinez, R.E. & Bowler, B.E. Proton-mediated dynamics of the alkaline conformational transition of yeast iso-1-cytochrome c. *J Am Chem Soc* **126**, 6751-6758 (2004).

25. Hammack, B., Godbole, S. & Bowler, B.E. Cytochrome c folding traps are not due solely to histidine-heme ligation: direct demonstration of a role for N-terminal amino group-heme ligation11Edited by P. E. Wright. *J Mol Biol* **275**, 719-724 (1998).

26. Russell, B.S. & Bren, K.L. Denaturant dependence of equilibrium unfolding intermediates and denatured state structure of horse ferricytochrome c. *J Biol Inorg Chem* **7**, 909-916 (2002).

27. Russell, B.S., Melenkivitz, R. & Bren, K.L. NMR investigation of ferricytochrome c unfolding: detection of an equilibrium unfolding intermediate and residual structure in the denatured state. *Proc Natl Acad Sci U S A* **97**, 8312-8317 (2000).

28. Kagan, V.E. *et al.* Cytochrome c acts as a cardiolipin oxygenase required for release of proapoptotic factors. *Nat Chem Biol* **1**, 223-232 (2005).

29. Hanske, J. *et al.* Conformational properties of cardiolipin-bound cytochrome c. *P Natl Acad Sci USA* **109**, 125-130 (2012).

30. Bradley, J.M., Silkstone, G., Wilson, M.T., Cheesman, M.R. & Butt, J.N. Probing a complex of cytochrome c and cardiolipin by magnetic circular dichroism spectroscopy: implications for the initial events in apoptosis. *J Am Chem Soc* **133**, 19676-19679 (2011).

31. Capdevila, D.A. *et al.* Active Site Structure and Peroxidase Activity of Oxidatively Modified Cytochrome c Species in Complexes with Cardiolipin. *Biochemistry* **54**, 7491-7504 (2015).

32. Wallace, C.J.A. *et al.* Substitutions Engineered by Chemical Synthesis at 3 Conserved Sites in Mitochondrial Cytochrome-C - Thermodynamic and Functional Consequences. *Journal of Biological Chemistry* **264**, 15199-15209 (1989).

33. Luntz, T.L., Schejter, A., Garber, E.A.E. & Margoliash, E. Structural Significance of an Internal Water Molecule Studied by Site-Directed Mutagenesis of Tyrosine-67 in Rat Cytochrome-C. *P Natl Acad Sci USA* **86**, 3524-3528 (1989).

34. Ying, T. *et al.* Tyrosine-67 in cytochrome c is a possible apoptotic trigger controlled by hydrogen bonds via a conformational transition. *Chemical communications (Cambridge, England)*, 4512-4514 (2009).

35. Tognaccini, L. *et al.* Structure-function relationships in human cytochrome c: The role of tyrosine 67. *Journal of inorganic biochemistry* **155**, 56-66 (2016).

36. Poulos, T.L. Heme Enzyme Structure and Function. *Chem Rev* **114**, 3919-3962 (2014).

37. Ying, T.L. *et al.* Tyrosine-67 in cytochrome c is a possible apoptotic trigger controlled by hydrogen bonds via a conformational transition. *Chem Commun*, 4512-4514 (2009).

38. Wang, Z.-H. *et al.* Converting Cytochrome c into a Peroxidase-Like Metalloenzyme by Molecular Design. *Chembiochem* **8**, 607-609 (2007).

39. Savenkova, M.I., Kuo, J.M. & Ortiz de Montellano, P.R. Improvement of peroxygenase activity by relocation of a catalytic histidine within the active site of horseradish peroxidase. *Biochemistry* **37**, 10828-10836 (1998).

40. Pettersen, E.F. *et al.* UCSF Chimera--a visualization system for exploratory research and analysis. *Journal of computational chemistry* **25**, 1605-1612 (2004).

41. Patel, C.N., Lind, M.C. & Pielak, G.J. Characterization of horse cytochrome c expressed in Escherichia coli. *Protein expression and purification* **22**, 220-224 (2001).

42. Berry, E.A. & Trumpower, B.L. Simultaneous determination of hemes a, b, and c from pyridine hemochrome spectra. *Analytical biochemistry* **161**, 1-15 (1987).

43. Vagenende, V., Yap, M.G.S. & Trout, B.L. Mechanisms of Protein Stabilization and Prevention of Protein Aggregation by Glycerol. *Biochemistry* **48**, 11084-11096 (2009).

44. Vinck, E. *et al.* Analyzing heme proteins using EPR techniques: the heme-pocket structure of ferric mouse neuroglobin. *JBIC Journal of Biological Inorganic Chemistry* **11**, 467 (2006).

45. Leigh, J.S. & Reed, G.H. Electron paramagnetic resonance studies in frozen aqueous solutions. Elimination of freezing artifacts. *The Journal of Physical Chemistry* **75**, 1202-1204 (1971).

46. Inubushi, T. & Becker, E.D. Efficient detection of paramagnetically shifted NMR resonances by optimizing the WEFT pulse sequence. *Journal of Magnetic Resonance (1969)* **51**, 128-133 (1983).

47. Hwang, T.L. & Shaka, A.J. Water Suppression That Works. Excitation Sculpting Using Arbitrary Wave-Forms and Pulsed-Field Gradients. *Journal of Magnetic Resonance, Series A* **112**, 275-279 (1995).

48. Kelly, S.M., Jess, T.J. & Price, N.C. How to study proteins by circular dichroism. *Bba-Proteins Proteom* **1751**, 119-139 (2005).

49. Nozaki, Y. [3] The preparation of guanidine hydrochloride, in *Methods in Enzymology*, Vol. 26 43-50 (Academic Press, 1972).

50. Pace, C.N. The stability of globular proteins. *CRC critical reviews in biochemistry* **3**, 1-43 (1975).

51. Pace, C.N. Determination and analysis of urea and guanidine hydrochloride denaturation curves. *Methods in enzymology* **131**, 266-280 (1986).

52. Pielak, G.J. *et al.* Protein thermal denaturation, side-chain models, and evolution: amino acid substitutions at a conserved helix-helix interface. *Biochemistry* **34**, 3268-3276 (1995).

53. Zhong, F.F., Lisi, G.P., Collins, D.P., Dawson, J.H. & Pletneva, E.V. Redox-dependent stability, protonation, and reactivity of cysteine-bound heme proteins. *P Natl Acad Sci USA* **111**, E306-E315 (2014).

54. Galo, A.L. & Colombo, M.F. Singular Value Decomposition and Ligand Binding Analysis. *J Spectrosc* (2013).

55. Hendler, R.W. & Shrager, R.I. Deconvolutions Based on Singular-Value Decomposition and the Pseudoinverse - a Guide for Beginners. *J Biochem Bioph Meth* **28**, 1-33 (1994).

56. Davis, L.A., Schejter, A. & Hess, G.P. Alkaline isomerization of oxidized cytochrome c. Equilibrium and kinetic measurements. *The Journal of biological chemistry* **249**, 2624-2632 (1974).

57. Viola, F. *et al.* Azide, cyanide, fluoride, imidazole and pyridine binding to ferric and ferrous native horse heart cytochrome c and to its carboxymethylated derivative: A comparative study. *Journal of inorganic biochemistry* **62**, 213-222 (1996).

58. Tezcan, F.A., Winkler, J.R. & Gray, H.B. Effects of ligation and folding on reduction potentials of heme proteins. *J Am Chem Soc* **120**, 13383-13388 (1998).

59. Sutin, N., Jaffe, M.R., Fay, D.P. & Cefola, M. Kinetics and mechanism of the formation of the monothenoyltrifluoroacetone complexes of nickel(II), cobalt(II), copper(II), and iron(III). *J Am Chem Soc* **93**, 2878-2886 (1971).

60. Sutin, N. & Yandell, J.K. Mechanisms of the reactions of cytochrome c. Rate and equilibrium constants for ligand binding to horse heart ferricytochrome c. *The Journal of biological chemistry* **247**, 6932-6936 (1972).

61. Arnao, M.B., Acosta, M., del Río, J.a., Varón, R. & García-Cánovas, F. A kinetic study on the suicide inactivation of peroxidase by hydrogen peroxide. *Biochim. Biophys. Acta Bioenerg.* **1041**, 43-47 (1990).

62. Wang, Z., Matsuo, T., Nagao, S. & Hirota, S. Peroxidase activity enhancement of horse cytochrome *c* by dimerization. *Org. Biomol. Chem.* **9**, 4766-4769 (2011).

63. Yeh, H.C., Wang, J.S., Su, Y.O. & Lin, W.Y. Stopped-flow kinetic study of the H2O2 oxidation of substrates catalyzed by microperoxidase-8. *J Biol Inorg Chem* **6**, 770-777 (2001).

64. Tomášková, N. *et al.* Early modification of cytochrome c by hydrogen peroxide triggers its fast degradation. *International journal of biological macromolecules* **174**, 413-423 (2021).

65. Dunford, H.B. *Heme peroxidases*. (John Wiley, New York; 1999).

66. Perez Galende, P. *et al.* Kinetics of Spanish broom peroxidase obeys a Ping-Pong Bi-Bi mechanism with competitive inhibition by substrates. *International journal of biological macromolecules* **81**, 1005-1011 (2015).

67. Marques, H.M. Peroxidase activity of the hemeoctapeptide N-acetylmicroperoxidase-8. *Inorg Chem* **44**, 6146-6148 (2005).

68. Bertini, I., Gray, H.B., Stiefel, E.I. & Valentine, J.S. *Biological inorganic chemistry : structure and reactivity*. (University Science Books, Sausalito, Calif.; 2007).

69. Larsen, R.W. Ligand binding subsequent to CO photolysis of methionine-modified cytochrome c. *Biochim Biophys Acta* **1619**, 15-22 (2003).

70. Kruglik, S.G., Yoo, B.K., Lambry, J.C., Martin, J.L. & Negrerie, M. Structural changes and picosecond to second dynamics of cytochrome c in interaction with nitric oxide in ferrous and ferric redox states. *Physical chemistry chemical physics : PCCP* **19**, 21317-21334 (2017).

71. Ferrer, J.C. *et al.* Identification of Lys79 as an Iron Ligand in One Form of Alkaline Yeast Iso-1-Ferricytochrome-C. *J Am Chem Soc* **115**, 7507-7508 (1993).

72. Myer, Y.P., Kumar, S., Kinnally, K. & Pande, J. Methionine-Oxidized Horse Heart Cytochromes-C .2. Conformation and Heme Configuration. *J Protein Chem* **6**, 321-342 (1987).

73. Feng, Y.Q., Roder, H. & Englander, S.W. Assignment of paramagnetically shifted resonances in the 1H NMR spectrum of horse ferricytochrome c. *Biophysical journal* **57**, 15-22 (1990).

74. Margoliash, E. & Frohwirt, N. Spectrum of horse-heart cytochrome c. *Biochem J* **71**, 570-572 (1959).

75. Gu, J., Shin, D.W. & Pletneva, E.V. Remote Perturbations in Tertiary Contacts Trigger Ligation of Lysine to the Heme Iron in Cytochrome c. *Biochemistry* **56**, 2950-2966 (2017).

76. Theorell, H. & Akesson, A. Studies on cytochrome c. II. The optical properties of pure cytochrome c and some of its derivatives. *J Am Chem Soc* **63**, 1812-1818 (1941).

77. Sedlak, E. Characterization of the polyanion-induced molten globule-like state of cytochrome c. *Biopolymers* **86**, 119-126 (2007).

78. Capdevila, D.A. *et al.* Specific methionine oxidation of cytochrome c in complexes with zwitterionic lipids by hydrogen peroxide: potential implications for apoptosis. *Chem Sci* **6**, 705-713 (2015).

79. Zhong, F. & Pletneva, E.V. Ligation and Reactivity of Methionine-Oxidized Cytochrome c. *Inorg Chem* **57**, 5754-5766 (2018).

80. Bren, K.L., Gray, H.B., Banci, L., Bertini, I. & Turano, P. Paramagnetic H-1-Nmr Spectroscopy of the Cyanide Derivative of Met80ala-Iso-1-Cytochrome-C. *J Am Chem Soc* **117**, 8067-8073 (1995).

81. Godoy, L.C. *et al.* Disruption of the M80-Fe ligation stimulates the translocation of cytochrome c to the cytoplasm and nucleus in nonapoptotic cells. *P Natl Acad Sci USA* **106**, 2653-2658 (2009).

82. Bren, K.L. & Gray, H.B. Structurally Engineered Cytochromes with Novel Ligand-Binding Sites - Oxy and Carbonmonoxy Derivatives of Semisynthetic Horse Heart Ala80 Cytochrome-C. *J Am Chem Soc* **115**, 10382-10383 (1993).

83. Lu, Y., Casimiro, D.R., Bren, K.L., Richards, J.H. & Gray, H.B. Structurally Engineered Cytochromes with Unusual Ligand-Binding Properties - Expression of Saccharomyces-Cerevisiae Met-80-]Ala Iso-1-Cytochrome-C. *P Natl Acad Sci USA* **90**, 11456-11459 (1993).

84. Wallace, C.J. & Clark-Lewis, I. Functional role of heme ligation in cytochrome c. Effects of replacement of methionine 80 with natural and non-natural residues by semisynthesis. *The Journal of biological chemistry* **267**, 3852-3861 (1992).

85. Ubbink, M. *et al.* Characterization of Mutant Met100lys of Cytochrome C-550 from Thiobacillus-Versutus with Lysine-Histidine Heme Ligation. *Biochemistry* **33**, 10051-10059 (1994).

86. Silkstone, G.G., Cooper, C.E., Svistunenko, D. & Wilson, M.T. EPR and optical spectroscopic studies of Met80X mutants of yeast ferricytochrome c. Models for intermediates in the alkaline transition. *J Am Chem Soc* **127**, 92-99 (2005).

87. Silkstone, G., Stanway, G., Brzezinski, P. & Wilson, M.T. Production and characterisation of Met80X mutants of yeast iso-1-cytochrome c: spectral, photochemical and binding studies on the ferrous derivatives. *Biophys Chem* **98**, 65-77 (2002).

88. Barker, P.D. & Mauk, A.G. Ph-Linked Conformational Regulation of a Metalloprotein Oxidation Reduction Equilibrium - Electrochemical Analysis of the Alkaline Form of Cytochrome-C. *J Am Chem Soc* **114**, 3619-3624 (1992).

89. Schlereth, D.D., Schuhmann, W. & Schmidt, H.-L. Spectroelectrochemical characterization of ultra-thin films formed by electropolymerization of phenothiazine derivatives on transparent gold electrodes. *J Electroanal Chem* **381**, 63-70 (1995).

90. Jeuken, L.J.C. & Armstrong, F.A. Electrochemical Origin of Hysteresis in the Electron-Transfer Reactions of Adsorbed Proteins: Contrasting Behavior of the

"Blue" Copper Protein, Azurin, Adsorbed on Pyrolytic Graphite and Modified Gold Electrodes. *The Journal of Physical Chemistry B* **105**, 5271-5282 (2001).

91. Casalini, S., Battistuzzi, G., Borsari, M., Ranieri, A. & Sola, M. Catalytic reduction of dioxygen and nitrite ion at a Met80Ala cytochrome c-functionalized electrode. *J Am Chem Soc* **130**, 15099-15104 (2008).

92. Jordan, T., Eads, J.C. & Spiro, T.G. Secondary and tertiary structure of the A-state of cytochrome c from resonance Raman spectroscopy. *Protein science : a publication of the Protein Society* **4**, 716-728 (1995).

93. Krishna, M.M.G., Maity, H., Rumbley, J.N. & Englander, S.W. Branching in the sequential folding pathway of cytochrome c. *Protein Sci* **16**, 1946-1956 (2007).

94. Patriarca, A. *et al.* Conversion of cytochrome c into a peroxidase: inhibitory mechanisms and implication for neurodegenerative diseases. *Arch Biochem Biophys* **522**, 62-69 (2012).

95. Diederix, R.E.M. *et al.* Kinetic stability of the peroxidase activity of unfolded cytochrome c: Heme degradation and catalyst inactivation by hydrogen peroxide. *Inorg Chem* **42**, 7249-7257 (2003).

96. Witting, P.K., Mauk, A.G. & Lay, P.A. Role of tyrosine-103 in myoglobin peroxidase activity: Kinetic and steady-state studies on the reaction of wild-type and variant recombinant human myoglobins with H2O2. *Biochemistry* **41**, 11495-11503 (2002).

97. Redaelli, C. *et al.* Characterization and peroxidase activity of a myoglobin mutant containing a distal arginine. *Chembiochem* **3**, 226-233 (2002).

98. Baldwin, D.A., Marques, H.M. & Pratt, J.M. Hemes and Hemoproteins .5. Kinetics of the Peroxidatic Activity of Microperoxidase-8 - Model for the Peroxidase Enzymes. *Journal of inorganic biochemistry* **30**, 203-217 (1987).

99. Clore, G.M., Hollaway, M.R., Orengo, C., Peterson, J. & Wilson, M.T. The Kinetics of the Reactions of Low-Spin Ferric Heme Undecapeptide with Hydrogen-Peroxide. *Inorg Chim a-Bioinor* **56**, 143-148 (1981).

100. Baek, H.K. & Vanwart, H.E. Elementary Steps in the Formation of Horseradish-Peroxidase Compound-I - Direct Observation of Compound-0, a New Intermediate with a Hyperporphyrin Spectrum. *Biochemistry* **28**, 5714-5719 (1989).

101. Chance, B. The Kinetics and Stoichiometry of the Transition from the Primary to the Secondary Peroxidase Peroxide Complexes. *Arch Biochem Biophys* **41**, 416-424 (1952).

102. Zamorano, L.S., Cuadrado, N.H., Galende, P.P., Roig, M.G. & Shnyrov, V.L. Steady-state kinetics of *Roystonea regia* palm tree peroxidase. *Journal of Biophysical Chemistry* **3**, 16-28 (2012).

103. Ruiz-Duenas, F.J. *et al.* Protein Radicals in Fungal Versatile Peroxidase CATALYTIC TRYPTOPHAN RADICAL IN BOTH COMPOUND I AND COMPOUND II AND STUDIES ON W164Y, W164H, AND W164S VARIANTS. *Journal of Biological Chemistry* **284**, 7986-7994 (2009).

104. Erman, J.E., Vitello, L.B., Miller, M.A. & Kraut, J. Active-Site Mutations in Cytochrome-C Peroxidase - a Critical Role for Histidine-52 in the Rate of Formation of Compound-I. *J Am Chem Soc* **114**, 6592-6593 (1992).

105. Furtmuller, P.G., Burner, U., Jantschko, W., Regelsberger, G. & Obinger, C. Two-electron reduction and one-electron oxidation of organic hydroperoxides by human myeloperoxidase. *Febs Lett* **484**, 139-143 (2000).

106. Bolscher, B.G.J.M. & Wever, R. A Kinetic-Study of the Reaction between Human Myeloperoxidase, Hydroperoxides and Cyanide - Inhibition by Chloride and Thiocyanate. *Biochim Biophys Acta* **788**, 1-10 (1984).

107. Marquez, L.A., Huang, J.T. & Dunford, H.B. Spectral and Kinetic-Studies on the Formation of Myeloperoxidase Compound-I and Compound-Ii - Roles of Hydrogen-Peroxide and Superoxide. *Biochemistry* **33**, 1447-1454 (1994).

108. Furtmuller, P.G. *et al.* Reaction of lactoperoxidase compound I with halides and thiocyanate. *Biochemistry* **41**, 11895-11900 (2002).

109. Gu, J. in Chemistry, Vol. Doctor of Philosophy (Dartmouth College, Hanover, New Hampshire; 2016).

110. Furtmuller, P.G., Burner, U., Regelsberger, G. & Obinger, C. Spectral and kinetic studies on the formation of eosinophil peroxidase compound I and its reaction with halides and thiocyanate. *Biochemistry* **39**, 15578-15584 (2000).

111. Ator, M.A. & Demontellano, P.R.O. Protein Control of Prosthetic Heme Reactivity - Reaction of Substrates with the Heme Edge of Horseradish-Peroxidase. *Journal of Biological Chemistry* **262**, 1542-1551 (1987).

112. Miller, V.P., Depillis, G.D., Ferrer, J.C., Mauk, A.G. & Demontellano, P.R.O. Monooxygenase Activity of Cytochrome-C Peroxidase. *Journal of Biological Chemistry* **267**, 8936-8942 (1992).

113. Wang, Z.H., Matsuo, T., Nagao, S. & Hirota, S. Peroxidase activity enhancement of horse cytochrome c by dimerization. *Org Biomol Chem* **9**, 4766-4769 (2011).

114. Feinberg, B.A., Petro, L., Hock, G., Qin, W.Y. & Margoliash, E. Using entropies of reaction to predict changes in protein stability: tyrosine-67-phenylalanine

variants of rat cytochrome c and yeast Iso-1 cytochromes c. *J Pharmaceut Biomed* **19**, 115-125 (1999).

115. Bandyopadhyay, D. & Mehler, E.L. Quantitative expression of protein heterogeneity: Response of amino acid side chains to their local environment. *Proteins: Structure, Function, and Bioinformatics* **72**, 646-659 (2008).

116. Zaidi, S., Hassan, M.I., Islam, A. & Ahmad, F. The role of key residues in structure, function, and stability of cytochrome-c. *Cell Mol Life Sci* **71**, 229-255 (2014).

117. Alvarez-Paggi, D. *et al.* Multifunctional Cytochrome c: Learning New Tricks from an Old Dog. *Chem Rev* **117**, 13382-13460 (2017).

118. Maity, H., Rumbley, J.N. & Englander, S.W. Functional role of a protein foldon - An Omega-Loop foldon controls the alkaline transition in ferricytochrome c. *Proteins* **63**, 349-355 (2006).

119. Saigo, S. Kinetic and equilibrium studies of alkaline isomerization of vertebrate cytochromes c. *Biochim Biophys Acta* **669**, 13-20 (1981).

120. Pearce, L.L., Gartner, A.L., Smith, M. & Mauk, A.G. Mutation-Induced Perturbation of the Cytochrome-C Alkaline Transition. *Biochemistry* **28**, 3152-3156 (1989).

121. Schejter, A. *et al.* Effects of Mutating Asn-52 to Isoleucine on the Heme-Linked Properties of Cytochrome-C. *Biochem J* **302**, 95-101 (1994).

122. Pollock, W.B.R., Rosell, F.I., Twitchett, M.B., Dumont, M.E. & Mauk, A.G. Bacterial expression of a mitochondrial cytochrome c. Trimethylation of Lys72 in yeast iso-1-cytochrome c and the alkaline conformational transition. *Biochemistry* **37**, 6124-6131 (1998).

123. Baddam, S. & Bowler, B.E. Mutation of asparagine 52 to glycine promotes the alkaline form of iso-1-cytochrome c and causes loss of cooperativity in acid unfolding. *Biochemistry* **45**, 4611-4619 (2006).

124. McClelland, L.J. & Bowler, B.E. Lower Protein Stability Does Not Necessarily Increase Local Dynamics. *Biochemistry* **55**, 2681-2693 (2016).

125. Baddam, S. & Bowler, B.E. Thermodynamics and kinetics of formation of the alkaline state of a Lys 79 -> Ala/Lys 73 -> His variant of iso-1-cytochrome C. *Biochemistry* **44**, 14956-14968 (2005).

126. Rosell, F.I. *et al.* Characterization of an alkaline transition intermediate stabilized in the Phe82Trp variant of yeast iso-1-cytochrome c. *Biochemistry* **39**, 9047-9054 (2000).

127. Black, K.M. & Wallace, C.J.A. Probing the role of the conserved beta-II turn Pro-76/Gly-77 of mitochondrial cytochrome c. *Biochem Cell Biol* **85**, 366-374 (2007).

128. Nall, B.T., Zuniga, E.H., White, T.B., Wood, L.C. & Ramdas, L. Replacement of a Conserved Proline and the Alkaline Conformational Change in Iso-2-Cytochrome-C. *Biochemistry* **28**, 9834-9839 (1989).

129. Goldes, M.E., Jeakins-Cooley, M.E., McClelland, L.J., Mou, T.C. & Bowler, B.E. Disruption of a hydrogen bond network in human versus spider monkey cytochrome c affects heme crevice stability. *Journal of inorganic biochemistry* **158**, 62-69 (2016).

130. Garcia-Heredia, J.M. *et al.* Nitration of tyrosine 74 prevents human cytochrome c to play a key role in apoptosis signaling by blocking caspase-9 activation. *Bba-Bioenergetics* **1797**, 981-993 (2010).

131. Deng, Y.L., Zhong, F.F., Alden, S.L., Hoke, K.R. & Pletneva, E.V. The K79G Mutation Reshapes the Heme Crevice and Alters Redox Properties of Cytochrome c. *Biochemistry* **57**, 5827-5840 (2018).

132. Deng, Y., Weaver, M.L., Hoke, K.R. & Pletneva, E.V. A Heme Propionate Staples the Structure of Cytochrome c for Methionine Ligation to the Heme Iron. *Inorg Chem* **58**, 14085-14106 (2019).

133. Garcia-Heredia, J.M. *et al.* Tyrosine phosphorylation turns alkaline transition into a biologically relevant process and makes human cytochrome c behave as an anti-apoptotic switch. *J Biol Inorg Chem* **16**, 1155-1168 (2011).

134. Guerra-Castellano, A., Diaz-Moreno, I., Velazquez-Campoy, A., De la Rosa, M.A. & Diaz-Quintana, A. Structural and functional characterization of phosphomimetic mutants of cytochrome c at threonine 28 and serine 47. *Biochim Biophys Acta* **1857**, 387-395 (2016).

135. Lei, H., Nold, S.M., Motta, L.J. & Bowler, B.E. Effect of V83G and I81A Substitutions to Human Cytochrome c on Acid Unfolding and Peroxidase Activity below a Neutral pH. *Biochemistry* **58**, 2921-2933 (2019).

136. Deacon, O.M., Svistunenko, D.A., Moore, G.R., Wilson, M.T. & Worrall, J.A.R. Naturally Occurring Disease-Related Mutations in the 40-57 Omega-Loop of Human Cytochrome c Control Triggering of the Alkaline Isomerization. *Biochemistry* **57**, 4276-4288 (2018).

137. Deacon, O.M., White, R.W., Moore, G.R., Wilson, M.T. & Worrall, J.A.R. Comparison of the structural dynamic and mitochondrial electron-transfer properties of the proapoptotic human cytochrome c variants, G41S, Y48H and A51V. *Journal of inorganic biochemistry* **203**, 110924 (2020).

138. Koshy, T.I., Luntz, T.L., Schejter, A. & Margoliash, E. Changing the Invariant Proline-30 of Rat and Drosophila-Melanogaster Cytochromes-C to Alanine or Valine Destabilizes the Heme Crevice More Than the Overall Conformation. *P Natl Acad Sci USA* **87**, 8697-8701 (1990).

139. Grimsley, G.R., Scholtz, J.M. & Pace, C.N. A summary of the measured pK values of the ionizable groups in folded proteins. *Protein Sci* **18**, 247-251 (2009).

140. Weinkam, P. *et al.* Characterization of alkaline transitions in ferricytochrome c using carbon-deuterium infrared probes. *Biochemistry* **47**, 13470-13480 (2008).

141. McClelland, L.J., Mou, T.C., Jeakins-Cooley, M.E., Sprang, S.R. & Bowler, B.E. Structure of a mitochondrial cytochrome c conformer competent for peroxidase activity. *P Natl Acad Sci USA* **111**, 6648-6653 (2014).

142. Yao, Y. *et al.* Solution structure of cyanoferricytochrome c: ligand-controlled conformational flexibility and electronic structure of the heme moiety. *J Biol Inorg Chem* **7**, 539-547 (2002).

143. Ness, S.R., Lo, T.P. & Mauk, A.G. Structural models for the alkaline conformers of yeast iso-1-ferricytochrome c. *Israel J Chem* **40**, 21-25 (2000).

144. Assfalg, M. *et al.* Structural model for an alkaline form of ferricytochrome c. *J Am Chem Soc* **125**, 2913-2922 (2003).

145. Cherney, M.M. & Bowler, B.E. Protein dynamics and function: Making new strides with an old warhorse, the alkaline conformational transition of cytochrome c. *Coordin Chem Rev* **255**, 664-677 (2011).

146. Berghuis, A.M., Guillemette, J.G., Smith, M. & Brayer, G.D. Mutation of tyrosine-67 to phenylalanine in cytochrome c significantly alters the local heme environment. *J Mol Biol* **235**, 1326-1341 (1994).

147. Muenzner, J. & Pletneva, E.V. Structural transformations of cytochrome c upon interaction with cardiolipin. *Chem Phys Lipids* **179**, 57-63 (2014).

148. Worrall, J.A. *et al.* The effects of ligand exchange and mobility on the peroxidase activity of a bacterial cytochrome c upon unfolding. *Chembiochem* **6**, 747-758 (2005).

149. Zhong, F., Alden, S.L., Hughes, R.P. & Pletneva, E.V. Comparing Properties of Common Bioinorganic Ligands with Switchable Variants of Cytochrome c. *Inorg Chem* (2021).

150. Diederix, R.E.M., Ubbink, M. & Canters, G.W. The peroxidase activity of cytochrome c-550 from Paracoccus versutus. *Eur J Biochem* **268**, 4207-4216 (2001).

151. Worrall, J.A.R., van Roon, A.-M.M., Ubbink, M. & Canters, G.W. The effect of replacing the axial methionine ligand with a lysine residue in cytochromec-550 from Paracoccus versutus assessed by X-ray crystallography and unfolding. *The FEBS Journal* **272**, 2441-2455 (2005).

152. Sinibaldi, F. *et al.* Role of lysines in cytochrome c-cardiolipin interaction. *Biochemistry* **52**, 4578-4588 (2013).

Chapter 7

BisHis-Ligation to the Heme Iron Species Suppresses Peroxidase Activity in Cardiolipin-bound Y67H Horse Heart Cytochrome *c*

pH titrations with unfolded Y67H and H26N/H33N horse heart cyt *c* were performed together with Morgan Pak.

Introduction

Heme proteins are ubiquitous and vary in function. Hemes have innate ET and peroxidase properties because of the iron center, which are highly influenced by their polypeptide sequences and fold as these properties define the heme axial ligation and second-sphere interactions.[1, 2] Differences in the first- and second-sphere interactions allow some of the heme proteins (such as CcO, cyt c_3, and cyt c_7) to participate in biological ET pathways,[3, 4] while others (such as nitrophorins or cytochrome *c* peroxidase (CcP)) behave as small-molecule carriers or peroxidases, respectively.[5-7] Perturbations in the polypeptide chain can alter the reactivity of the heme group, and allow the heme protein to be multifunctional. For example, replacement of the active site His residues in the heme-containing nitrite reductases causes topological changes near the *c*-heme, affecting nitrite reduction but not oxygen reduction.[8] *R. sphaeroides* heme proteins (SHP), thought to be the terminal electron acceptor in the ET pathway for the reduction of peroxide or hydroxylamine, have been shown to bind small molecules, such as molecular oxygen and nitric oxide upon loss of the heme axial Asn ligand.[9 10] Thus, relating how the polypeptide tunes the heme ligation and environment is critical for understanding functional switching in heme proteins.

Mitochondrial cyt *c* is a good model to study the structure-mediated switch in function. Cyt *c* shuttles electrons between cyt bc_1 and CcO in the oxidative phosphorylation pathway, but functions as an apoptotic peroxidase in the presence of CL.[11, 12] The heme iron in cyt *c* is axially coordinated by His18 and Met80 in the native state of the protein.[3] Heme coordination and polypeptide fold are conserved among many species,[13] and ET properties are similar between WT proteins.[14-24] Compact packing of the native protein

suppresses the intrinsic peroxidase activity of the heme.[25-27] Binding to CL allows cyt *c* to lose its native fold and Met80 ligation, exposing the heme for peroxidase activity.[28, 29]

The nature of the CL-bound species and the origin of the enhanced apoptotic peroxidase activity are still the subject of debate. Upon binding to CL, cyt *c* loses its α-helical secondary structure,[30] which is consistent with unfolding of the polypeptide chain. Fluorescence labeling studies suggest that in the early stages of CL-binding, rearrangement in loop C is observed within the first minute of the interaction;[31] UV RR experiments showed that rearrangement of loop C into a β-sheet disrupts the Met80-Fe bond in cyt *c*.[32] Denaturation experiments show that extensive unfolding of the protein enhances peroxidase activity.[33, 34] However, CL-bound cyt *c* at high CL concentrations exists in an equilibrium between the compact and the extended forms.[29, 35] Although peroxidase activity requires an open axial ligand to allow H_2O_2 coordination to the heme,[36] MCD and resonance Raman (RR) studies have revealed the presence of bisHis and Lys-His heme species in the CL-bound state.[37-39] These heme species have been shown to suppress peroxidase activity in studies with M100K cyt c_{550} variant and unfolded *c*-type cytochromes.[34] Further, Tyr radicals have also been implicated in the enhancement of peroxidase activity,[40] complicating the picture as to the origin of the increased apoptotic peroxidase activity in the CL bound state.

There has been a long interest in Tyr67 due to the proximity to the heme and its role in the highly conserved HB network involving Met80.[13] This Tyr67-Met80 contact in the native cyt *c* is argued to provide the bulk of the entatic contribution from the protein backbone to maintain the weak Fe-S(Met) bond intact.[27, 41, 42] Tyr67 is argued to be a favored radical acceptor in the CL-bound cyt *c* complex,[12, 40] and oxidation of Tyr67

enhances intrinsic peroxidase activity.[43] Multiple mutational studies involving Tyr67 have been performed with cyt *c* proteins from different species. Elimination of Tyr67-Met80 bond in the Y67F variant decreases the reduction potential and increases the thermal stability of both ferric and ferrous species, compared to those of WT. [17, 44, 45 46-48] Decrease of peroxidase activity has also been observed in the presence of CL for Y67F,[40] and Tyr67 has been suggested to be necessary for CL-bound apoptotic peroxidase activity.[49] Yet, Y67F yeast cyt *c* has been shown to be less prone to heme degradation and less sensitive to increase in H_2O_2 concentration than WT,[50] suggesting that both structural properties and stability of the protein may be relevant for peroxidase activity.

Polypeptide mutations in cyt *c* are linked to disease,[51-54] and mutational studies help provide insight into how structural perturbations in the first- and second-sphere interaction alter cyt *c* function. The relationship between structure and stability in switching from an electron carrier to peroxidase function has been further probed with the Y67H variant,[55-58] but how Y67H mutation affects the first- and second-sphere interactions is yet to be clarified. This variant has widely been studied in the human, horse heart, and yeast cyt *c* ,[55-58] initially designed to mimic peroxidases by introducing a distal His in the heme cavity.[55] In yeast cyt *c*, Y67H mutation decreased the thermal stability of the protein.[56] An increase in intrinsic peroxidase activity has been observed in yeast Y67H, [55, 56] and hypothesized to be caused by the presence of a His near the heme. A His residue in the vicinity of the heme behaves as an acid-base catalyst for the activation of H_2O_2 in peroxidases[59] and multifunctional proteins such as myoglobin.[60] Yet, the peroxidase activity rates in Y67H variants are still lower than those of true peroxidases, and not markedly higher than the rates obtained from oxidation of guaiacol by AcMP8, a heme

model compound that only contains amino acid residues 14 to 21.[36, 61] The Y67H variant was also studied in human and horse heart cyt *c*, but in contrast to yeast Y67H cyt *c*, changes in k_{cat} and K_M peroxidase activity parameters were small or within error compared to those of WT.[57, 58, 62] The activity has not been enhanced in the presence of CL for horse heart Y67H cyt *c*, but enhancements in catalytic efficiency were observed in CL-bound horse heart WT cyt *c*.[58] In the absence of Met80, His67 has been suggested to coordinate to the heme iron in both human and yeast cyt *c*,[63, 64] but it is unclear if this coordination also takes place in Met80-containing Y67H variants.

The increase in intrinsic peroxidase activity in Y67H has been argued to stem from placement of a distal His near the heme.[65] However, this explanation does not fully address the variation observed in peroxidase activities among different species. There are hints of changes in stability and structure near the heme with the mutation.[56, 64] CV measurements at pH 7.0 show that Y67H horse heart cyt *c* has a higher reduction potential than that of WT by nearly 150 mV.[58] However, this value is high compared to those in other variants that are Met-ligated.[3] These structural and functional changes should be considered in rationalizing peroxidase activity. It is ambiguous whether the increase in Y67H peroxidase activity is due to the heme pocket mimicking a peroxidase or if there are other structural explanations that have not been explored. Limited spectroscopic data with the Y67H variant makes it a challenge to link different aspects of structural properties to changes in peroxidase activity. Further, peroxidase activities of Y67H variants so far have been measured at neutral pH, higher than the biological pH cyt *c* is exposed to—in the mitochondrial intermembrane space (pH 6.88) and in the cytosol (pH 5.8) in apoptotic cells.[66, 67]

To better understand the peroxidase activity in cyt *c*, we chose to take a more comprehensive look at the Y67H variant of horse heart cyt *c*. Stability, fold, and ligation of the heme iron were characterized at different pH conditions. Structural properties were related to peroxidase function, and changes in ET properties upon the mutation were also clarified. These studies provide insights into the nature of the CL-bound cyt *c* species and postulate the origin of the enhanced apoptotic peroxidase activity in cyt *c*.

Materials and Methods

General. All solutions and buffers were prepared using water from Barnstead E-Pure Ultrapure Water Purification System, purified to a resistivity of 18 MΩ·cm. Reagents and columns were purchased from Sigma-Aldrich and GE Healthcare, respectively, unless noted otherwise. Gas-tight Hamilton syringes were used for all titrations and quantitative dilutions. Buffers were chelated using a Chelex resin and glassware was washed with HCl prior to use to eliminate metal ion impurities. pH of the solutions was monitored using either an AB15 pH meter (Fisher Scientific) or an UB10 pH meter (Denver Instrument), and pH was adjusted with either NaOH or HCl.

Site-Directed Mutagenesis, Protein Expression, and Purification. Point mutations, protein expression and purification for horse heart cyt *c* variants were performed as previously described.[29]

Spectroscopic Measurements. All spectroscopic measurements were obtained at room temperature (22 ± 2 ºC) unless noted otherwise. Ferric proteins were prepared with excess potassium ferricyanide and purified by size exclusion (PD-10 desalting column) or ion-exchange (Sepharose HP SP) chromatography prior to spectroscopic measurements.

Absorption spectra were recorded using an Agilent 8453 diode-array spectrophotometer. CD spectra were measured on a JASCO-J815 CD spectropolarimeter. Quartz cuvettes and tubes were purchased from Starna Scientific and Wilmad Lab Glass, respectively. Pyridine hemochrome assays were conducted to determine the extinction coefficients of Y67H horse cyt *c* variant as previously described,[68] in a 100 mM sodium phosphate buffer at pH 7.4 or in a 100 mM sodium acetate buffer at pH 4.5.

Solutions containing 5 to 10 μM of freshly prepared ferric protein in a 1 mm pathlength quartz cuvette were used to obtain the CD spectra in the far-UV region (200 to 250 nm), with an average of 5 scans. CD spectra were baseline-corrected with the spectrum of the buffer or by assuming that the ellipticity at 250 nm is 0. All spectra were normalized to 20 μM of protein with a pathlength l = 1 mm. Solutions containing 40 to 50 μM protein in a 4 mm pathlength quartz cuvette were used to obtain the CD spectra of Y67H in the UV-visible region (250 to 650 nm), with the average of 3 scans and baselined with the spectra of the appropriate buffer. Spectra were then normalized to 50 μM of protein with l = 2 mm to compare to the WT spectra obtained at different pathlength. Prior and during CD spectral measurements, the chamber was thoroughly degassed with N_2, cuvettes were sealed, and spectra were measured at room temperature (22 ± 2 °C).

Low-temperature EPR spectra were obtained at 10 K on a Bruker EMX 300 X-band spectrometer (Bruker Biosciences). Spectra were acquired using the following parameters: microwave frequency of 9.49 GHz, microwave power of 3.21 mW, modulation frequency of 100 kHz, modulation amplitude of 3.21 mW, modulation amplitude of 1.00 G, and time constant of 20.48 ms. Protein stocks were freshly oxidized and purified. Samples of the

protein were prepared in either a 10 mM HEPES buffer at pH 8.0, a 50 mM sodium phosphate buffer at pH 7.4, or a 50 mM sodium acetate buffer at pH 4.5.

^{1}H NMR spectra of ferric and ferrous cyt *c* were recorded on a 500 MHz Bruker NMR spectrometer (Bruker Biosciences) at 25 ºC. ^{1}H NMR measurements of ferric cyt *c* variants, freshly oxidized protein varying from 0.5 to 2.7 mM in either a 50 mM sodium phosphate buffer at pD 7.4 or a 50 mM acetic acid d_4 (or sodium acetate) buffer at pD 4.5 in 100% D_2O were prepared. For ^{1}H NMR measurements of ferrous cyt *c* variants, proteins were freshly reduced with dithionite and purified by a size-exclusion column inside a N_2-filled anaerobic glovebox. Samples containing 1 to 2 mM protein in a thoroughly degassed 50 mM sodium phosphate buffer at pH 7.4 or a 50 mM sodium acetate buffer at pH 4.5 with 10% D_2O (*v*/*v*) were prepared. Measurements and analyses were performed as previously described.[69]

GuHCl Titration Measurements. Ultrapure guanidine hydrochloride (GuHCl, Alfa Aesar) was dissolved in either a 100 mM sodium phosphate buffer at pH 7.4 or a 100 mM sodium acetate buffer at pH 4.5. Concentration of GuHCl stock was determined by measurements of the refractive index of the solution. Stock solution was then used to prepare solutions with GuHCl concentrations ranging from 0 to 6 M GuHCl, and pH was readjusted as necessary. These solutions were used within 5 days. Protein samples were aliquoted using a Hamilton syringe and final protein concentrations ranged from 3 to 10 μM for global stability measurements. Prior to measurements, the prepared protein solutions were allowed to equilibrate for at least 30 minutes. CD ellipticity at 222 nm was recorded using a 1-mm pathlength quartz cuvette for global stability measurements, averaged over 5 scans for global stability measurements. Electronic absorption in the Soret

region (350 to 450 nm) was monitored using a 1-cm pathlength quartz cuvette. Ratio of wavelengths with maximum change observed in the Soret band was determined by the difference spectra of the protein in solution with either 0 M or 6 M GuHCl. To obtain the stability parameters in respect to GuHCl denaturation, both the ellipticity data from CD measurements and ratio obtained from the electronic absorption measurements were fitted to eq 7.1:[70, 71]

$$f([\text{GuHCl}]) = \frac{[m_f[\text{GuHCl}]+b_f+(m_u[\text{GuHCl}]+b_u)\exp(\frac{m_D([\text{GuHCl}]-[\text{GuHCl}]_{1/2})}{RT})]}{[1+\exp(\frac{m_D([\text{GuHCl}]-[\text{GuHCl}]_{1/2})}{RT})]} \quad (7.1)$$

where m_f and b_f, m_u and b_u are the slope and *y*-intercept of the signal (or percentage) of the folded and unfolded regions, respectively; R is the gas constant and T is the experimental temperature. With the midpoint of the transition, $[\text{GuHCl}]_{1/2}$, and slope of the transition, m_D, Gibbs free energy of unfolding (ΔG_D) was calculated using eq 7.2:[70, 71]

$$\Delta G_D = m_D[\text{GuHCl}]_{1/2} \quad (7.2)$$

pH Titrations. Solution containing 170 μM ferric proteins in a 10 mM HEPES buffer at pH 8.0 was used to monitor changes in the CT absorption band (580 to 750 nm) in the pH range from 2.8 to 8.5 at room temperature. The spectra were individually baseline-corrected, setting the average absorption value from 800 to 850 nm as zero. The transition in the acidic range (from pH 3.0 to 7.0) was fitted to eq 7.3:[72]

$$\varepsilon_{695}=\frac{\varepsilon_A+\varepsilon_N(10^{n(pK_a-pH)})}{1+(10^{n(pK_a-pH)})} \quad (7.3)$$

where ε_{695} is the extinction coefficient at 695 nm, ε_A is the extinction coefficient at the acidic pH, ε_N is the extinction coefficient at the neutral pH, *n* is the number of protons associated in the transition, and pK_a is the apparent pK_a of the transition. Although the absorption spectra of the CT band decreased in intensity near pH 8, the transition at alkaline pH was not fitted because the full transition was not obtained from the pH titrations.

pH titrations in the unfolded state were performed together with Morgan Pak. Solution containing 8 μM protein and 6 M GuHCl in a 100 mM sodium phosphate buffer at pH 7.4 was prepared and equilibrated for at least 30 minutes prior to measurements. Prior to the addition of protein, pH of the 100 mM sodium phosphate buffer containing 6 M GuHCl was readjusted as necessary. The electronic absorption spectra of the solution at pH values from 2.9 to 7.4 were recorded. Difference spectra between the spectra at pH 2.9 and 7.4 were calculated, and ratio of wavelengths with the maximum change observed in the Soret peak was for each spectrum obtained from pH ranges 2.9 to 7.4. The titration data was fit to eq 7.3.

Reduction Potential Measurements. Spectroelectrochemical measurements were performed as previously described (Chapter 5). Samples containing 75 to 100 μM protein with equimolar concentration of mediators (p-Benzoquinone,[73] 2,3,5,6-tetramethyl phenylenediamine,[74] phenazine methosulfate,[74] gallocyanine,[75, 76] and 2-hydroxy-1,4-naphthoquinone,[75, 76]) were prepared in either a 100 mM sodium phosphate buffer at pH 7.4 or a 100 mM sodium acetate buffer at pH 4.5. Fraction of reduced species was calculated based on the electronic absorption at 550 nm, and these values were plotted as a function of the external potential, *E*. These dependencies were then fitted to eq 7.4:[15]

$$f(E)=\frac{A_m}{10^{(x-E^\circ)/1000\times n/0.059}+1} \quad (7.4)$$

where A_m is the absorbance (or the fraction) of the ferrous protein, $E°$ is the reduction potential of the heme iron, and n is the number of electrons transferred in the reaction.

The electronic absorption spectra were recorded at voltage intervals of 25 or 50 mV. The fitted potentials were referenced to the standard hydrogen electrode (SHE), using $E°_{SHE} = E°_{GCE} + 215$ mV.

Time-Dependent Saturation Transfer NMR. Protein stock samples of ferric and ferrous cyt *c* were prepared inside an anaerobic glovebox in a thoroughly degassed 50 mM sodium acetate buffer at pH 4.5 with 10% D_2O (*v*/*v*). Solutions containing total of 1.9 to 2 mM protein, with a 9 to 1 ratio of ferrous to ferric cyt *c*, were prepared anaerobically, and sealed using a Shigemi NMR tube.

^{1}H NMR spectra ferrous species were obtained at 25 °C by selectively saturating the Met80 methyl resonance of the ferric species in 10 ms increments, with a time delay ranging from 0.01 to 0.2 s in 0.01 s increments, 0.2 to 1 s in 0.2 s increments, and 1 to 4 s in 0.5 s increments prior to applying a 90° pulse magnetization and recording the spectra (on-spectra). Spectra of the ferrous protein (off-spectra) were subtracted from the obtained spectra (on-spectra) prior to each saturation transfer measurements. Signs of auto-oxidation were observed during the measurements in the Y67H variant, as the intensity of the Met80 methyl signals decreased in the off-spectra. Thus, ratios of the on- and off-spectra were used for fittings. Total intensity of the methyl protons (or ratios) in the ferrous Met80 species in respect to time was fitted to eq 7.5:[77, 78]

$$M(t)=\frac{M_0}{1+k_{\mathrm{obs}}T_1}(1+k_{obs}T_1e^{-(k_{\mathrm{obs}}+1/T_1)t})$$

(7.5)

where $M(t)$ is the intensity of the observed resonance (or ratio), M_0 is the intensity of the resonance (or ratio) at t = 0, k_{obs} is the first-order rate constant assuming complete saturation of the ferric species, T_1 (magnetization lifetime) of cyt *c*, and *t* is the delay time prior to applying the 90° pulse magnetization after saturation.

During the total time delay prior to the signal detection, the saturated ferric species is not only recovering with a specific lifetime (T_1), but also is in constant self-exchange with the ferrous species at a rate of interconversion between the two species defined by the rate constant k_{ESE}. In the spectra, the intensity of the signals for the methyl protons of the ferrous species decreases with an increase in the delay time due to self-exchange between ferric and ferrous protein in solution. Therefore, the k_{obs} value obtained from eq 7.5 is the *observed* rate constant k_{ESE} and dividing the k_{obs} value by the concentration of the ferric species in the sample yields the k_{ESE} value.

In biological systems where the donor (D) and acceptor (A) are in separate protein complexes, the ET mechanism is bimolecular, and the rate constant k_{DA}, is a combination of rate constants in eq 7.6:[79, 80]

$$k_{\mathrm{DA}}=(k_{\mathrm{DD}}k_{\mathrm{AA}}\mathrm{K}_{\mathrm{DA}})^{1/2}$$

(7.6)

where k_{DD} and k_{AA} are the rate constants of self-exchange reactions for D or A, respectively, K_{DA} is the equilibrium constant.

When a protein acts both as a D and an A, k_{DA} is the ESE rate constant, k_{ESE}. In cases where the reduction potentials of D and A is different, K_{DA} is expressed by eq 7.7:[81]

$$K_{DA}=\exp\left(\frac{nF\Delta E^{\circ}}{RT}\right) \quad (7.7)$$

Preparation of Liposome Vesicles. All lipids were obtained from Avanti Polar Lipids, Inc., and vesicles were prepared using the extruder apparatus equipped with an enclosed warmer (Eastern Scientific LLC) and membranes (Eastern Scientific LLC) with pore radius of 0.1 μm. Lipids TOCL and DOPC were mixed in a 1 to 1 molar ratio in a 25 mM HEPES buffer at pH 7.4, as previously described.[31] Vesicle solutions were used within the day. Vesicle sizes and distributions were determined using dynamic light scattering (DLS) instrument (Wyatt Technologies), as previously described.[29, 31]

Peroxidase Activity Assays. Assays were performed in a freshly prepared 25 mM sodium acetate buffer at pH 4.5 and 5.5, a 25 mM MES buffer at pH 6.0 and 6.5, and a 25 mM HEPES buffer at pH 7.4. All substrates were kept on ice and in the dark prior use, and all protein solutions and buffer were kept at room temperature. Protein samples were kept in the dark to avoid heme bleaching. A colorimetric substrate, ABTS (AMRESCO), was used to monitor the peroxidase activity. Formation of the $ABTS^{+\cdot}$ product was monitored at 735 nm (ε_{735} = 14 $mM^{-1}cm^{-1}$).[82] Each assay contained final concentrations of 1.0 mM H_2O_2, 200 μM ABTS, and 1 μM freshly prepared ferric protein. Under these conditions, the maximum velocity is reached and k_{cat} does not change with increasing concentrations of [ABTS] as determined from preliminary assays with WT horse heart cyt *c*, and concentration of H_2O_2 did not cause heme degradation as evaluated by the rapid disappearance of the Soret band, as previously described in Chapter 6. Based on the

Michaelis-Menten formalism, at substrate concentrations where V_{max} is achieved, the observed initial rate should be reflective of k_{cat}, the turn-over number. Activity assays for CL-bound cyt *c* were performed by mixing solutions of the protein and the liposomes (at 750-molar excess of total lipid) in a 1 to 1 (*v*/*v*) ratio to avoid aggregation; solutions of the protein and CL-containing lipid vesicles were incubated for at least 30 minutes at room temperature prior to adding other components of the assay. Samples were not incubated with H_2O_2 to avoid heme degradation. For each assay run, the absorbance signal at 735 nm was recorded every second for a total of 120 seconds at room temperature (22 ± 2 °C). Linear phase of the reaction was then fitted to obtain the slope that corresponds to the initial velocity of the reaction. These rates were divided by the extinction coefficient of ABTS and protein concentration and averaged over three to six trials to obtain the initial reaction rates.

Results

Heme Coordination and Fold. To assess whether the heme iron coordination is affected by placing a His residue at position 67, electronic absorption spectra were obtained at pH 4.5 and 7.4. The heme iron ligands were identified by CD, EPR and ^{1}H NMR spectroscopy. Mutational effects on the overall secondary structure of the polypeptide were also probed using CD spectroscopy.

Electronic Absorption Spectra. At pH 7.4, the electronic absorption spectrum of ferric horse heart Y67H cyt *c* differs from that of WT. The λ_{max} of the Soret band is blue shifted to 408 nm (ε = 117.4 $mM^{-1}\cdot cm^{-1}$) and has a higher extinction coefficient than the WT protein (ε = 106 $mM^{-1}cm^{-1}$) (Figure 7.1A).

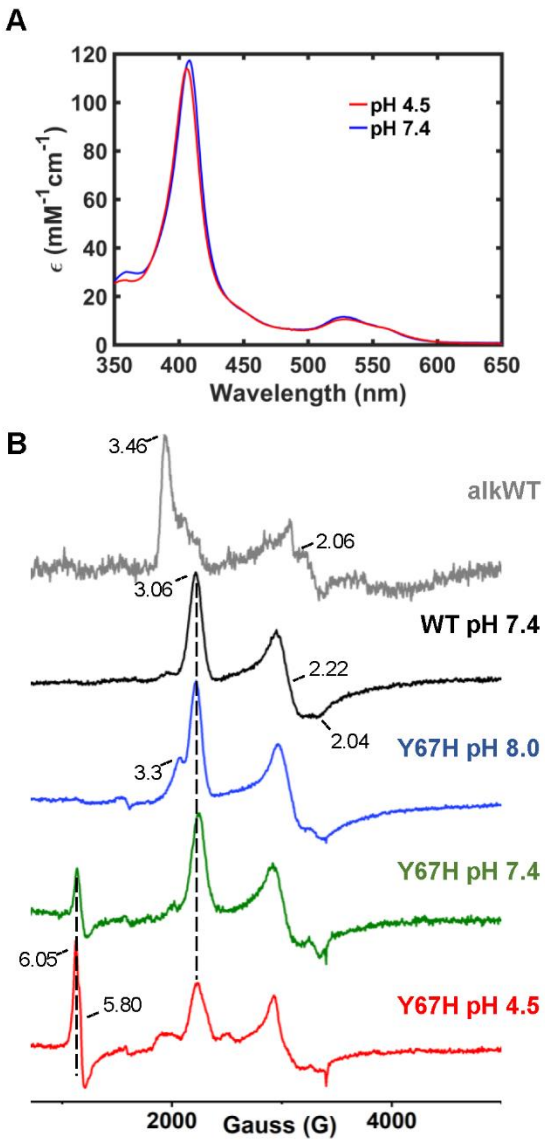

Figure 7.1. (A) Electronic absorption spectra of horse heart Y67H cyt *c* variant at pH 4.5 (red) and pH 7.4 (blue), measured at 22 ± 2 °C. (B) Low-temperature EPR spectra of the horse heart cyt *c* variants. Shown are the spectra for WT at pH 10.5 (alkWT, gray) and at pH 7.4(black), and for Y67H at pH 4.5 (red), at pH 7.4 (green), and at pH 8.0 (blue).

This difference between the two variants persists at pH 4.5, as the peak of the Soret band further blueshifts to 406 nm (ε = 114.1 $mM^{-1}{\cdot}cm^{-1}$) (Figure 7.1A). The 695 nm CT band observed in the Met-ligated WT cyt *c* is also detected at both pH 7.4 and 4.5 (Figure 7.2A). The loss of the CT band occurs at mildly acidic conditions for Y67H (pK_a of 4.63 ± 0.02) (Figure 7.2B). In contrast a similar loss of the CT band is observed at lower pH for WT cyt *c* (pK_a = 3.45 ± 0.02).[83, 84] Although the spectra at high pH conditions were not recorded, it is likely that the replacement of the Met80 ligand also occurs at lower pH in Y67H than in WT.[83] There are no differences in the electronic absorption spectra for the variants upon reduction of the heme iron at pH 7.4 (Figure 7.3). Similar features are observed with the ferrous Y67H variant at pH 4.5 as was at pH 7.4, and the λ_{max} of the band is at 415 nm. However, in the electronic absorption spectra for ferrous Y67H at pH 4.5, λ_{max} is at 413 nm, with lower extinction coefficient at pH 4.5 than at pH 7.4 (Figure 7.3). Furthermore, the extinction coefficient of the resolved α-band at 550 nm observed ferrous Met-ligated cyt *c* is decreased (Figure 7.3). Thus, it is likely that the ferrous Y67H sample at pH 4.5 prepared for measuring the electronic absorption spectrum contains partially oxidized species.

EPR spectra. Low-temperature EPR spectra at pH 4.5, 7.4, and 8.0 for Y67H show spectral features of the Met-ligated ferric heme iron species as observed in the WT protein at pH 7.4 (Figure 7.1B). However, the Met-ligated ferric heme iron species are not the only species present under these pH conditions.

At pH 7.4, the Y67H cyt *c* variant also shows the features of the high-spin species, typical of the H_2O-ligated heme iron (compare Figure 7.1B to Figures 6.14C and 6.16C).

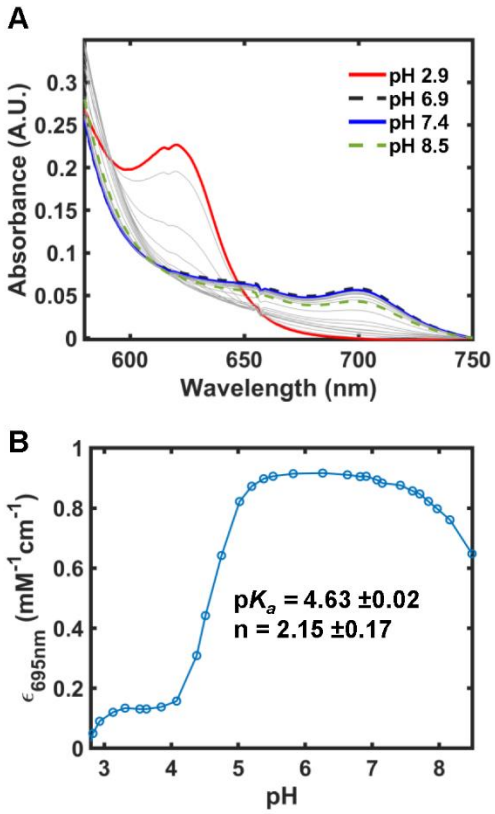

Figure 7.2. (A) Changes in the electronic absorption spectra in the pH range from 2.8 to 8.5 for the horse heart Y67H cyt *c* variant. Spectra at pH 2.9 (red, solid), 6.9 (black, dotted), 7.4 (blue, solid), and 8.5 (green, dotted) are highlighted. Several of spectra from other pH conditions are also shown (grey). (B) Changes in the extinction coefficient of the 695 nm CT band (ε_{695nm}) in the pH range from 2.8 to 8.5, with line connecting the dots to guide the eye. the transition at mildly acidic conditions, from pH 3.5 to 6.5, was fit separately from transitions at acidic (pH < 3.5) and mildly alkaline (pH > 6.5), as the alkaline and acidic transitions were not fully monitored.

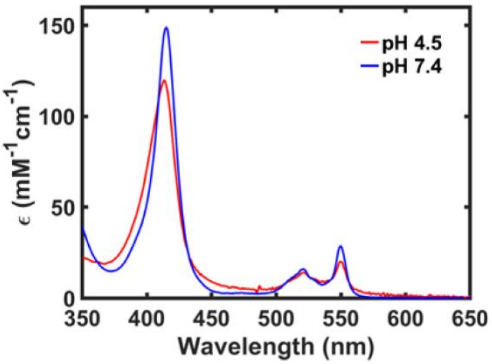

Figure 7.3. Electronic absorption spectra of ferrous Y67H horse heart cyt *c* at pH 4.5 (red) and at pH 7.4 (blue). In the pH 4.5 spectra, λ_{max} of the Soret band is shifted and the signal of the α-band is lower, suggesting that theprotein is partially oxidized. At pH 7.4, ε_{415} = 148..9 $mM^{-1}cm^{-1}$ as determined from pyridine hemochrome assays.

At pH 4.5, this feature is more prominent, and the features of the Met-ligated heme iron are decreased, suggesting that the heme iron becomes H_2O-ligated. Low-spin features of the hydroxide-bound heme are not observed at pH 8.0 (Figure 7.1B), suggesting that another ligand coordinates to the heme iron under these conditions. However, a shoulder peak is observed at g_z = 3.3 for Y67H at pH 8.0 (Figure 7.1B). Similar signals were observed in Lys-ligated Y67R/M80A (Figure 6.11C) at near-neutral pH (g_z ~ 3.3) and in Lys-ligated WT cyt *c* at alkaline conditions (g_z ~ 3.5 to 3.3),[15, 85] suggesting that satellite signals observed for Y67H at pH 8.0 may be from a small population of Lys-ligated heme iron species.

^{1}H NMR Spectra. ^{1}H NMR spectra of both ferric and ferrous Y67H cyt *c* suggest that the heme iron in the protein is Met-ligated at pH 4.5 (Figure 7.4). The methyl signals of the Met80-bound heme porphyrin (Figure 7.4B) and the heme-bound Met80 ligand (Figure 7.4C) for the ferric Y67H protein are shifted compared to those for ferric WT. However, similar shifts in the methyl signals compared to those in WT were also observed in ferric yeast Y67H cyt *c*.[86] . The ^{1}H NMR spectra of ferrous Y67H and WT variants are very similar (Figure 7.4D).

CD Spectra. CD spectral features in the visible region are sensitive to the buckling of the heme plane and to changes in heme ligation,[15, 87, 88] and are a good indicator of conformational changes in the heme crevice.[63] In the CD spectra, a large Cotton effect can be observed in the Soret region, thought to be due to the interactions of allowed π—π^* of the heme porphyrin.[89, 90] This feature is commonly observed in heme proteins,[15] including cyt *c*.[87] Changes in this CD feature have been suggested to reflect the reorganization of the polypeptide chain around the heme and the residue interactions with heme orbitals.[89, 91]

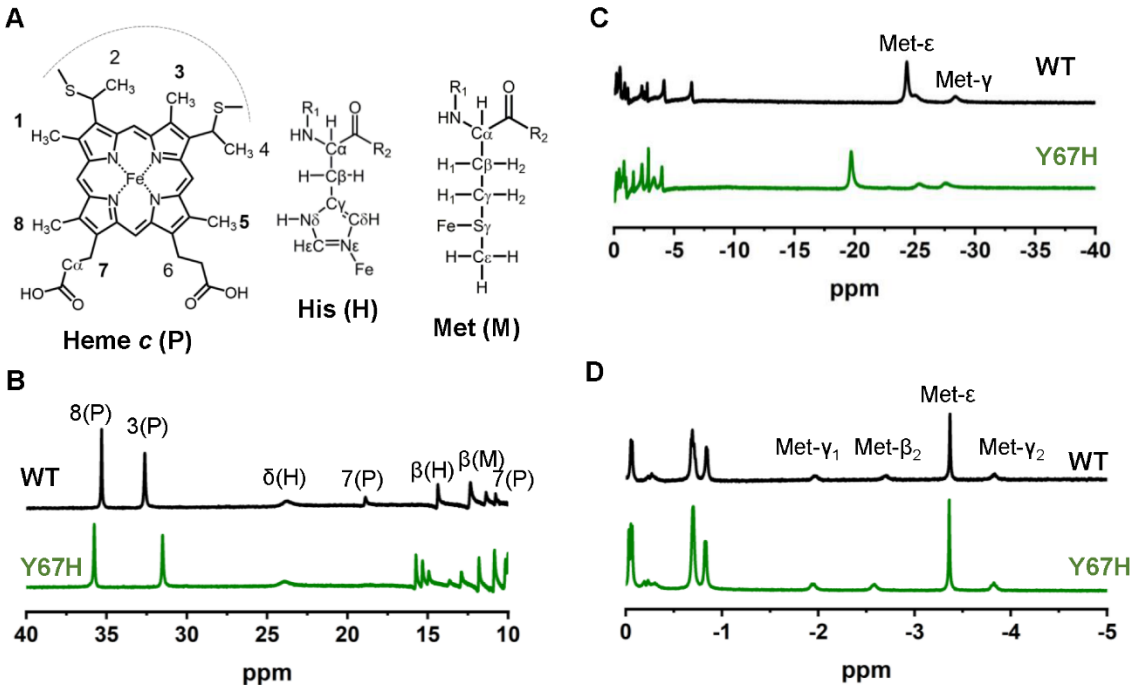

Figure 7.4. (A) Identification notations of the heme and Met protons for labeling signals in the ^{1}H NMR of the (B) downfield and (C) upfield regions of ferric WT (black) and Y67H (green) cyt *c* variants, and the (D) upfield regions of the ferrous WT (black) and Y67H (green) cyt *c* variants, at 25 °C in a 50 mM sodium acetate buffer with 10% D_2O (*v*/*v*) at pH 4.5 or in a 50 mM acetic acid d_4 buffer with 100 % D_2O (*v*/*v*) at pD 4.5.

As reported previously,[15, 87] CD spectra of WT horse heart cyt *c* in the Soret region show the Cotton effect at both pH 7.4 and 4.5 (Figure 7.5). For Y67H, the spectrum at pH 7.4 is comparable to that of WT (Figure 7.5B), suggesting that the polypeptide interactions with the heme are largely unaffected by the mutation. At pH 4.5, however, the intensity of the negative band at 416 nm for the Y67H variant is smaller compared to that of WT (Figure 7.5A), suggesting changes in the polypeptide around the heme.

Far-UV CD spectra of WT cyt *c* are similar at both pH 7.4 and 4.5 (Figure 7.6), with negative peaks at 222 and 210 nm characteristic of the α-helical secondary structure. In the Y67H cyt *c* variant, the far-UV CD spectra are different under two pH conditions (Figure 7.6). At pH 7.4, negative peaks at 222 and 210 nm observed in WT are also observed in Y67H (Figure 7.6B). At pH 4.5, Y67H also shows comparable 222 nm features observed in WT (Figure 7.6A). However, the 210 nm signal at pH 4.5 is more negative in Y67H than in WT, suggestive of an increase in random-coil character in Y67H at lower pH (Figure 7.6A).

Electronic absorption and EPR spectra of the Y67H variant suggest that Met80 is the predominant ligand to the heme iron at pH 7.4 but is replaced by H_2O at pH 4.5. This switch in heme iron ligation is accompanied by changes in the polypeptide packing, and changes in the spectral features sensitive to polypeptide structure are observed in the CD spectra for Y67H. In the absence of ligand change as in WT, CD spectra are comparable at both pH conditions.

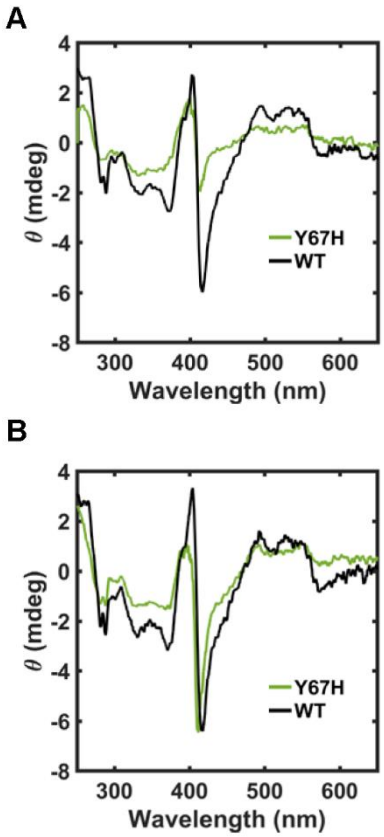

Figure 7.5. CD spectra showing the Soret region for ferric WT (black) and Y67H (green) variants of horse heart cyt *c* at (A) pH 4.5 or (B) pH 7.4 conditions. Spectra of Y67H were measured at 20 ºC and l = 4 mm, and normalized to [cyt *c*] = 50 μM and l = 2 mm to compare to the spectra of WT.

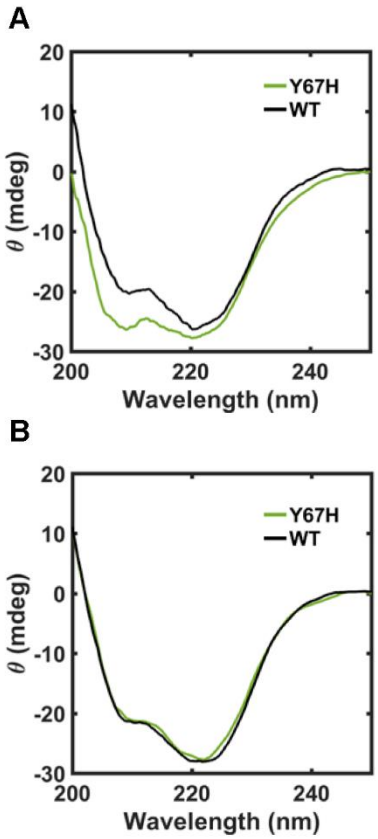

Figure 7.6. Far-UV CD spectra of ferric WT (black) and Y67H (green) variants of horse heart cyt *c* at (A) pH 4.5 or (B) pH 7.4 conditions. Spectra were measured at 20 ºC and *l* = 1 mm and normalized to [cyt *c*] = 20 μM.

Global Stability.

Chemical Denaturation with GuHCl. At pH 7.4, the global stability with respect to GuHCl denaturation, ΔG_D, of Y67H is lower than that of WT (Figure 7.7A and Table 7.1). The lower $[GuHCl]_{1/2}$ parameter for Y67H suggests that the protein is less tightly packed than WT, and lower denaturant concentrations are sufficient to break the intermolecular contacts in the native state (Table 7.1). The m_D parameter of Y67H is within error to that of WT (Table 7.1). However, error bars observed in m_D parameter of Y67H suggests that this parameter may also be lower than that of WT. The m_D parameter is proportional to the change in the solvent exposure in transition from the folded and the unfolded state.[92] The m_D parameter of a variant could be lower than m_D of WT if the native state of the variant is more solvent exposed than that of WT, or if the unfolded state of the variant is less solvent exposed than that of WT.

GuHCl titrations monitoring the electronic absorption spectra of the Soret band in Y67H have shown that the polypeptide unfolding around the heme deviates from the two-state unfolding model at pH 7.4, unlike in GuHCl titrations monitoring the α-helical signals of the protein (Figures 7.7B and C). Such discrepancy in the unfolding transition has not been reported for WT horse heart cyt *c*.[29] This difference between the variants suggests that there are changes in the heme crevice upon the mutation in the protein. The presence of intermediate species during unfolding could affect the m_D parameter from the analysis of data with the two-state unfolding model.

Since His67 is spatially close to Met80 in the native protein and the Met80-containing loop D is one of the first to unfold during unfolding, we wanted to see whether His67 coordinates to the heme iron.

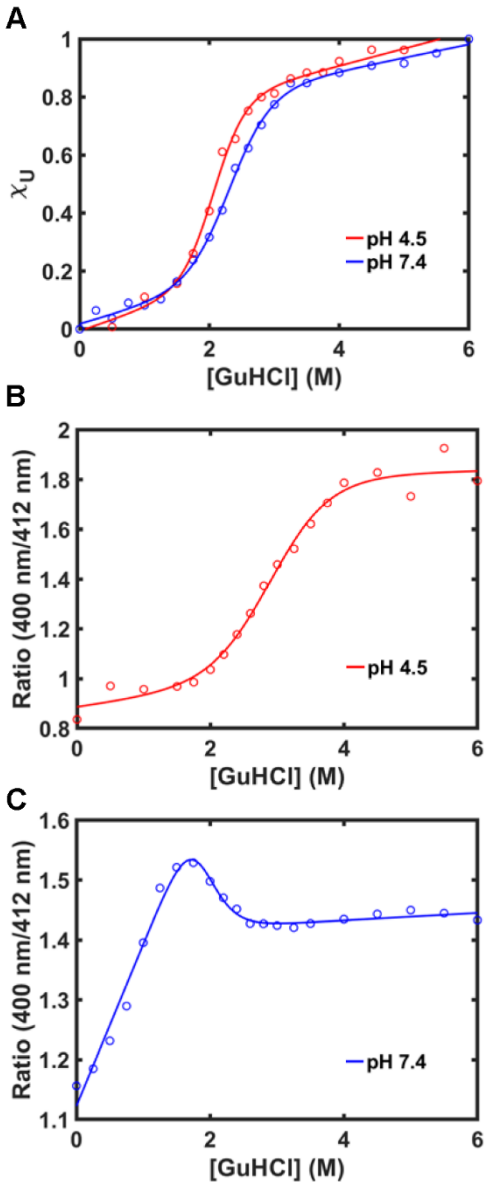

Figure 7.7. GuHCl denaturation data for ferric Y67H at pH 4.5 (red) and 7.4 (blue) at 22 ± 2 °C (A) monitored by observing changes in the ellipticity at 222 nm, showing the fraction of the unfolded species with changes in GuHCl concentration, and monitored by observing changes in the electronic absorption of the Soret band at (B) pH 4.5 and (C) pH 7.4. The choice of wavelengths for the ratio was determined by subtracting the electronic absorption spectrum of the cyt *c* variant at 0 from the spectrum of the protein at 6 M GuHCl conditions.

Table 7.1. Global Thermodynamic Parameters for GuHCl Unfolding of Horse Heart Cyt *c* Variants

	Circular Dichroism[a]			Electronic Absorption[b]		
Variant	$[GuHCl]_{1/2}$ (M)	m_D (kJ mol^{-1} M^{-1})	ΔG_D (kJ mol^{-1})	$[GuHCl]_{1/2}$ (M)	m_D (kJ mol^{-1} M^{-1})	ΔG_D (kJ mol^{-1})
			Horse Heart			
			pH 7.4			
WT[c]	2.7 ± 0.1	11.5 ± 2.6	31.1 ± 7.1	2.6 ± 0.1	11.3 ± 2.7	29.3 ± 7.1
M80A[d]	2.7 ± 0.02	10.3 ± 0.6	27.9 ± 1.6	2.6 ± 0.2	10.0 ± 7.6	26.0 ± 19.9
Y67H[e]	2.3 ± 0.1	7.6 ± 1.3	17.5 ± 5.0	--	--	--
			pH 4.5			
WT[d]	2.6 ± 0.1	9.8 ± 0.2	25.1 ± 1.1	2.7 ± 0.1	10.0 ± 3.7	27.0 ± 10.0
M80A[d]	2.6 ± 0.1	11.6 ± 0.3	30.2 ± 1.4	2.1 ± 0.1	10.0 ± 2.6	21.0 ± 5.5
Y67H	2.1 ± 0.2	6.9 ± 1.2	14.5 ± 2.9	2.9 ± 0.3	5.5 ± 2.5	15.9 ± 7.4
			Iso-1 yeast			
WT[f]	3.01	6.90	20.8	--	--	--
M80A[g]	2.42	2.15	5.20	--	--	--
M80A/Y67A[g]	2.88	2.10	6.05	--	--	--

Table 7.1 Footnotes

[a]Monitored is the ellipticity at 222 nm, performed at 22 ± 2 °C.

[b]Monitored is the ratio of wavelengths with maximum change observed in the Soret band of the electronic absorption spectra, determined by the difference spectra of the folded and unfolded states. Titrations were performed at 22 ± 2 °C.

[c]From ref. [29]. ΔG_D was recalculated based on rounded $[GuHCl]_{1/2}$ and m_D parameters.

[d]CD data from ref. [69]. ΔG_D was recalculated based on $[GuHCl]_{1/2}$ and m_D parameters.

[e]Plot of the ratio of wavelengths from the electronic absorption spectra as a function of GuHCl concentration does not fit to a two-transition state model and were not fitted at pH 7.4.

[f]From ref. [93]. Urea unfolding at 25 °C, $[GuHCl]_{1/2}$ calculated from reported ΔG_D and m_D parameters.

[g]From ref. [94]. Urea unfolding at 25 °C, $[GuHCl]_{1/2}$ calculated from reported ΔG_D and m_D parameters.

His-coordination to the heme is readily observed in unfolded WT cyt *c*. In horse heart WT cyt *c*, there are two additional His residues besides His18: His26 and His33.[15] In the unfolded state, these His residues coordinate to the heme when deprotonated at neutral pH conditions .[95] The presence of this His-misligated species can be observed in the electronic absorption spectra, as the Soret absorption band redshifts upon the transition from H_2O-ligated high-spin to His-ligated low-spin heme iron species.[96] Although additional mutations to the native His26 and His33 residues were not made in this work, differences in the pK_a values for high-spin to low-spin transition in the unfolded state in WT and Y67H could offer some clues as to whether His67 coordinates to the heme iron in the unfolded state. Previous mutational studies have shown that elimination of less preferred heme ligand, His26, in the H26Q variant of horse heart cyt *c* did not affect the pK_a, of this transition.[96] On the contrary, elimination of the preferred heme ligand, His33, in the H33N variant changed the observed pK_a of the transition in the unfolded state.[96] Elimination of His residues increase the pK_a of transition in the H26N/H33N variant in horse heart cyt *c* (Table 7.2 and Figure 7.8), and similar trends are observed in yeast cyt *c*.[97, 98] These literature results suggest that the pK_a of the transition from the high-spin to the low-spin heme iron would decrease in the Y67H variant compared to H26N/H33N variant, and pK_a different from that of WT if His67 competes with His33 in forming the misligated state.

The Y67H variant shows a transition from the high-spin to the low-spin heme iron species as pH increases (Figure 7.9A). This transition occurs under mildly acidic conditions (Figure 7.9B), but the introduction of His67 decreases the pK_a of the composite transition from all the His residues compared to that in WT (Table 7.2).

Table 7.2. pK_a Values of Ferric Cyt *c* Variants in GuHCl-Containing Solutions

Variant	pK_a	*n*
	Horse Heart	
WT[a]	5.71 ± 0.05	1.38 ± 0.09
H26Q[a]	5.60 ± 0.05	1.50 ± 0.06
H33N[a]	6.11 ± 0.05	1.10 ± 0.08
H26N/H33N[b]	6.71 ± 0.04	0.85 ± 0.07
Y67H[b]	5.40 ± 0.03	0.92 ± 0.05
	Iso-1 yeast	
TM[c]	5.94 ± 0.08	0.9 ± 0.1
TM+H26[c]	5.31 ± 0.06	0.9 ± 0.1
TM+H54[c]	4.99 ± 0.01	0.7 ± 0.1
AcTM[d]	7.38 ± 0.05	1.03 ± 0.17
AcTM+H26[d]	5.31 ± 0.06	1.00 ± 0.07
AcTM+H33[d]	5.26 ± 0.04	1.11 ± 0.08
AcTM+H54[d]	4.81 ± 0.06	0.94 ± 0.07
AcTM+H89[d]	5.97 ± 0.06	0.81 ± 0.01
AcTM+H100[d]	6.34 ± 0.02	0.77 ± 0.13
A81H[e]	6.1 ± 0.9	0.85 ± 0.06

[a]From ref. [96], in a 50 mM sodium phosphate buffer containing 4.5 M GuHCl at pH 8.0.

[b]This work, in a 100 mM sodium phosphate buffer containing 6 M GuHCl at pH 7.4, at 22 ± 2 °C. For H26N/H33N variant, fixing $n = 1$ yielded pK_a of 6.74 ± 0.04.

[c]From ref. [97], containing 3 M GuHCl. The protein was expressed in yeast; TM contains H26N, H33N, and H39Q mutations. His residue was then introduced at a desired site.

[d]From ref. [98], containing 3 M GuHCl; base protein is AcTM with no surface His with *N*-terminal acetylation (H26N, H33N, H39Q, K(-2)L, T(-5)S). A His residue was then introduced at a desired site. The protein was expressed in yeast.

[e]From ref. [99], containing 0.6 M GuHCl and 0.1 M NaCl, at 22 ± 1 °C. pK_a = 6.8 ± 0.4 at 0 M GuHCl and 0.1 M NaCl. The protein was expressed in yeast.

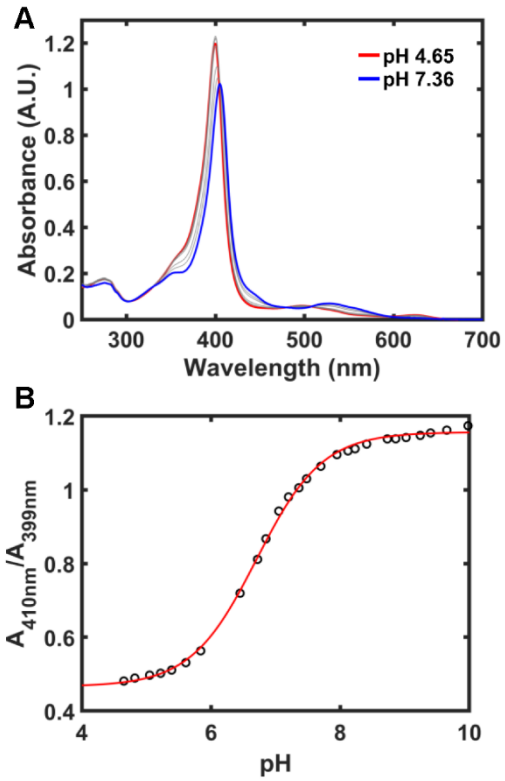

Figure 7.8. (A) Electronic absorption spectra of the H26N/H33N variant of horse heart cyt *c* with 6 M GuHCl in the pH range from 4.65 to 10.23. Highlighted are the spectra at pH 4.65 (red) and pH 7.36 (blue). The spectra at pH 10.23 and 7.36 are comparable. A selection of spectra between pH 4.65 and 7.36 are also shown (grey). (B) The ratio of the absorbances at 410 and 399 nm, at 22 ± 2 °C as a function of pH (black circles), with the fit of the dependence to eq 7.3 (red line).

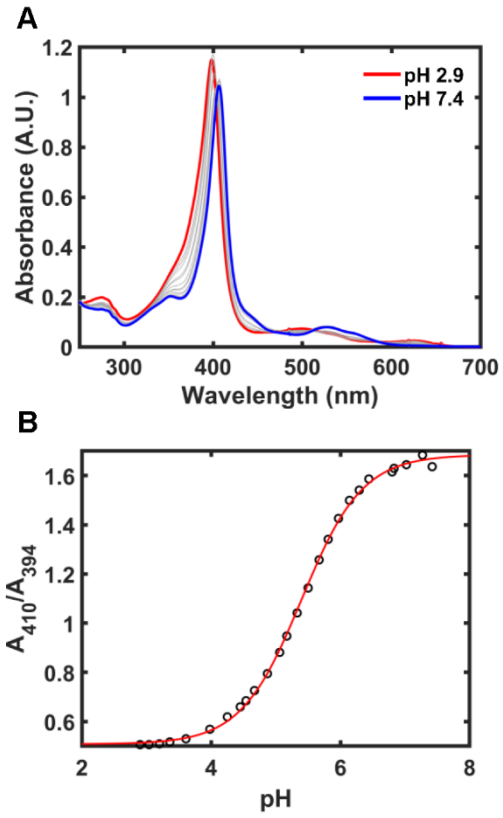

Figure 7.9. A) Electronic absorption spectra of the Y67H variant of horse heart cyt *c* with 6 M GuHCl in the pH range from 2.9 to 7.4. Highlighted are the spectra at pH 2.9 (red) and pH 7.4 (blue). A selection of spectra between pH 2.9 and 7.4 are shown (grey) (B) The ratio of the absorbances at 410 and 394 nm, at 22 ± 2 °C as a function of pH (black circles), with the fit of the dependence to eq 7.3 (red line).

The decrease in the pK_a observed in Y67H relative to the pK_a value in WT is nearly similar to the decrease in the pK_a value observed with the H33N variant when compared to the pK_a value in WT.[96] Had His67 not coordinated to the heme iron in the unfolded state, we should have observed a similar pK_a value to that in WT.

At pH 4.5, global unfolding studies by CD spectroscopy of the Y67H cyt *c* variant have revealed that the ΔG_D, $[GuHCl]_{1/2}$, and m_D parameters are lower than those of WT (Table 7.1). In contrast to pH 7.4 data, unfolding transitions monitoring the heme crevice and secondary structure changes have revealed comparable stability parameters (Figure 7.7B). However, large error bars for ΔG_D and $[GuHCl]_{1/2}$ parameters make it difficult to conclude if there might be differences in these values for Y67H and WT (Table 7.1). Further, large error bars for the Y67H variant make it difficult to quantify how much stability may have decreased with pH.

Electrochemical Properties. Reduction potentials and self-exchange rate constants were measured to correlate how structural changes induced by the Y67H mutation affect the ET properties of the protein.

Reduction Potentials from Reductive (and Oxidative) Titrations. At pH 7.4, Y67H has a lower reduction potential compared to that of WT (Table 7.3). Since the protein also has a population of the H_2O-ligated species at this pH based on EPR, this species may contribute to the difference in the reduction potentials. Spectroelectrochemical measurements have revealed a hysteresis between results of titrations in the reductive and oxidative directions (Figures 7.10 and 7.11B). The reduction potential of Y67H is lower at pH 4.5 than at pH 7.4 (Table 7.3). At pH 4.5, ferric Y67H is a mixture of 65% H_2O-ligated and 35% Met-ligated heme iron species (Figure 7.2B).

Table 7.3. Reduction Potentials of Cyt *c* Variants from Reductive (and Oxidative) Directions of Spectroelectrochemistry Titrations

Variant	pH	Potential (mV, vs SHE)
	Horse Heart	
WT	7.8	255[a]
	7.0	263 ± 2[b]
	4.0	252 ± 2 (280 ± 2)[c]
Y67H	7.4	231 ± 3 (248 ± 3)[d]
	4.5	107 ± 3 (288 ± 3)[d]
Y67F	7.0	246 ± 4[b]
M80A	7.4	-33.4 ± 4.3 (--)[e]
	4.5	16.4 ± 4.9 (32.2 ± 2.4)[e]
	Rat	
WT	7.0	261 ± 2[f], *259*[g]
Y67F	7.0	236 ± 2[f]
	Iso-1 yeast	
WT	7.0	280 ± 2[f], 272 ± 2[h]
	6.0	210 ± 2[i], 290[j]
Y67F	7.0	220 ± 1[f]
	6.0	234[j], 236[k]
M80A	7.2	-170 ± 2[l]
	7.0	-201 ± 2[m]
M80A/Y67A	7.2	-196 ± 2[k]
	7.0	-219 ± 2[n]
M80A/Y67H	7.0	-207 ± 2[n]

Table 7.3 Footnotes

[a]From ref. [16] at pH 7.8.

[b]From ref. [44], versus NHE, measured using CV at pH 7.0.

[c]From chapter 6.

[d]This work, reduction potentials vs SHE, determined from reductive (and oxidative) spectroelectrochemistry titration experiments performed at 22 ± 2 °C. Potentials from fittings were converted to SHE by adding 215 mV to the fitted $E°$ value. Fixing $n = 1$ did not alter the fitted $E°$ value.

[e]From ref. [69].

[f]From ref. [17], vs SHE from square-wave voltammetry, in a 50 mM Tris buffer with 100 mM NaCl at pH 7.0. Expressed in yeast, contains TmK72.

[g]From ref. [47].

[h]From ref. [18], versus SHE at pH 7.0 and μ = 0.327 M at 25 °C.

[i]From ref. [100], versus SHE. In a 10 mM phosphate buffer with 5 mM sodium perchlorate at pH 6.0, measured at 21 ± 0.1 °C using CV with immobilized cyt *c* on polycrystalline gold electrode. Expressed in *E. coli* and possesses a C102T background mutation.

[j]From ref. [101], versus SHE at 25 °C and pH 6.0, μ = 0.1 M. Contains C102T mutation and expressed in yeast.

[k]From ref. [45], at pH 6.0 with μ = 0.1 M and 25 °C. Contains C102T mutation and expressed in yeast.

Table 7.3 Footnotes, continued

[l]From ref. [94], versus SHE, measured using CV at 21 ± 1 °C in a 10 mM phosphate buffer with 100 mM sodium perchlorate at pH 7.2.

[m]From ref. [102], versus SHE, measured using CV with immobilized cyt *c* on polycrystalline gold electrode, at 25 °C in a 10 mM phosphate buffer with 0.1M sodium chloride at pH 7.0. Proteins contain C102T background mutation.

[n]From ref. [103], versus SHE. Measured using CV in a 5 mM phosphate buffer with 5 mM sodium perchlorate at pH 7.0.

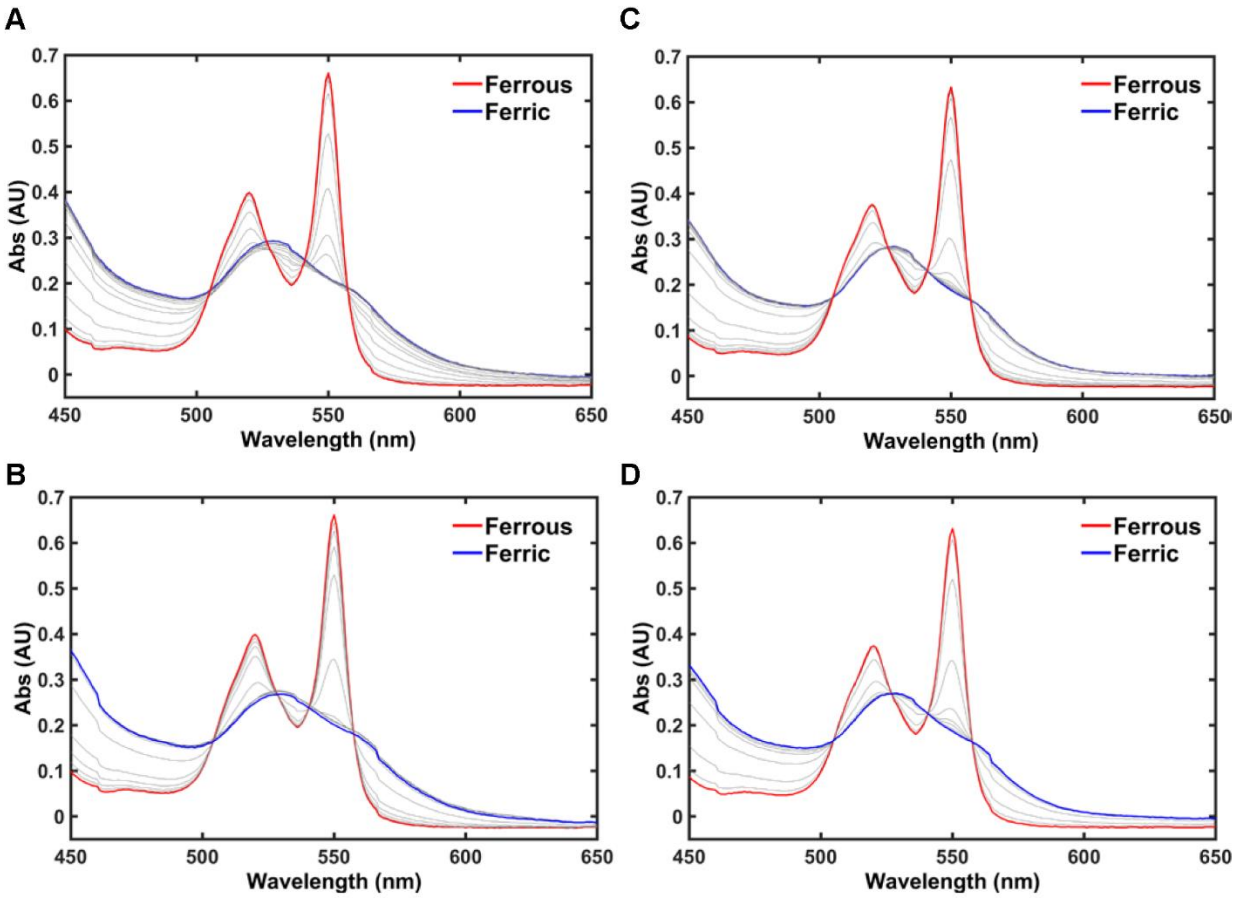

Figure 7.10. Electronic absorption spectra for Y67H at pH 4.5 from titrations in A) reductive and B) oxidative directions in a 100 mM sodium acetate buffer at pH 4.5, and at pH 7.4 from titrations in C) reductive and D) oxidative directions in a 100 mM sodium phosphate buffer at pH 7.4. Spectral measurements were taken at applied potentials in the range (versus GCE) from 500 mV to -400 mV for the reductive titration at pH 4.5, and -300 to 400 mV for the oxidative titration at pH 4.5. Likewise, spectral measurements were taken at applied potentials in the range (versus GCE) from 500 mV to -400 mV for the reductive titration at pH 4.5, and -300 to 500 mV for the oxidative titration at pH 7.4. Spectra at the beginning or the end of the titration measurements corresponding to the ferrous species (red) or the ferric species (blue) are highlighted. Selection of spectra during the titration are also shown (grey).

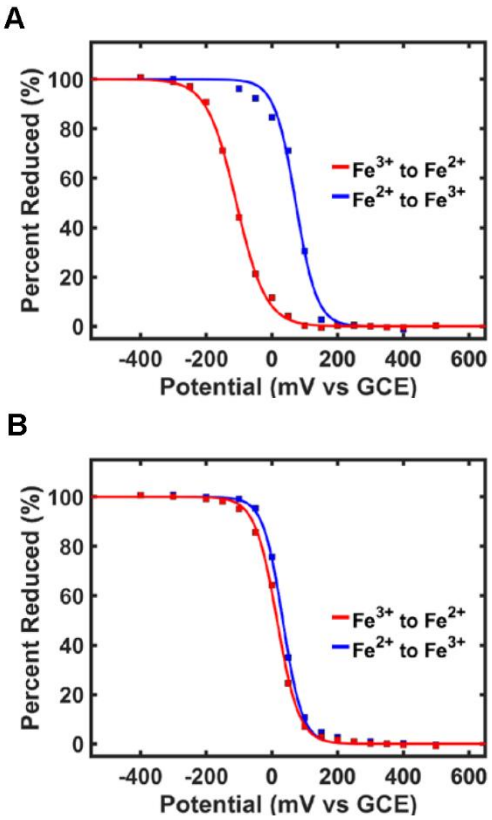

Figure 7.11. Plots showing percent of reduced species as a function of the applied potential (versus GCE), with fits to eq 7.4, for the reductive (blue) and oxidative (red) directions of titrations for the Y67H variant of horse heart cyt *c* at (A) pH 4.5 and (B) pH 7.4.

If we assume that the reduction potentials of M80A and WT represent the H_2O-ligated and Met-ligated heme species (Table 7.3), respectively, and that the observed reduction potential is a sum of the fractional contributions of the species ($E°_{obs} = (f_{M80A} \times E°_{M80A}) + (f_{WT} \times E°_{WT})$), then the Y67H reduction potential is estimated to be 109 ±3 mV, which is in good agreement with the observed potential of 107 ± 3 mV. Further, CD spectra suggest an increase in random-coil character in its secondary structure (Figure 7.6A). This increase likely favors the solvent exposure of the heme, resulting in decrease of the reduction potential.[15, 104, 105] The potential of Y67H from oxidative titrations is comparable to that of WT at pH 4.0 (Table 7.3), suggesting that the heme iron is Met-ligated in the ferrous state. Had the ferrous species consist of similar populations of the H_2O-ligated and Met-ligated heme species as in the ferric state, the potential would have been 119 ± 2 mV, again assuming that the reduction potentials of M80A and WT in the oxidative titrations represent the H_2O-ligated and Met-ligated heme iron (Table 7.3). Since the estimated value is much lower than the observed value of 288 ±3 mV (Table 7.3), the heme iron ligation is likely to be different in the ferrous state and the ferric state.

Electron Self-Exchange Rate Constant (k_{ESE}) at pH 4.5. Since the reduction potential of Y67H at pH 4.5 was lower than that of WT and changes in secondary structure for Y67H were observed, we wanted to probe whether the kinetics of ET are also affected. Time-dependent saturation transfer NMR was used to obtain the k_{ESE} value for both Y67H and WT at pH 4.5 (Figure 7.12). The k_{ESE} values of the WT protein at pH 4.5 is comparable to the previously published values for the human and horse heart WT cyt *c* at pH 7.0.[77, 106] Similarities in k_{ESE} values for pH 7.0 and 4.5 in WT are expected, as structural properties of WT are similar at pH 7.4 and 4.5.

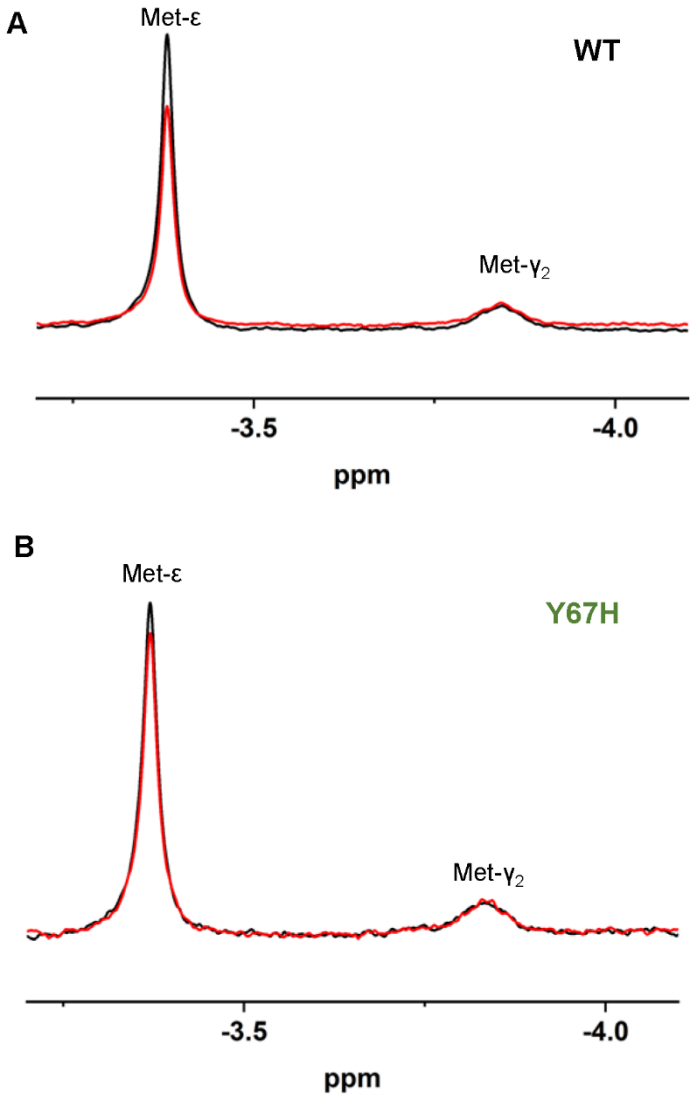

Figure 7.12. Representative ^{1}H NMR data from time-dependent saturation experiments for A) WT and B) Y67H at pH 4.5. The intensity of the Met-ε signals were monitored (numbering based on Figure 3A) before (off-spectra, black) and after (on-spectra, red) the saturation pulse with a specified delay time (*t*). Shown spectra are at *t* = 1.2 s for WT and *t* = 0.14 s for Y67H.

Interestingly, the k_{ESE} value for Y67H is within error of that for WT at pH 4.5 (Figure 7.13), despite the observed changes in the structure at this pH. In cyt *c*, the heme edge is implicated in many of the protein-protein interactions with the biological ET partners.[107-109] Changes in the secondary structure upon the Y67H mutation at pH 4.5 as suggested by CD measurements (Figure 7.6A), may increase the exposure of the heme edge and alter k_{ESE}.

Peroxidase Activity. At substrate conditions where V_{max} is achieved, the initial rate is reflective the catalytic turnover rate. In the pH range from 4.5 to 7.4, the intrinsic peroxidase activity of WT cyt *c* is low but increases slightly at acidic pH conditions (Figure 7.14 and Table 7.4). This trend is reversed in the presence of CL, with the peroxidase activity peaking at around pH 6.5. For Y67H, peroxidase activity is higher than that of WT, even at pH conditions 6.5 and 7.4, when the heme is mostly Met-ligated, and the protein has a α-helical content comparable to that of WT (Figure 7.14). At lower pH, when the population of the H_2O-ligated heme iron species is greater, the intrinsic peroxidase activity of Y67H is enhanced, and are comparable to that of H_2O-ligated M80A variant (Table 7.4). Trends in the CL-bound species are similar to those of WT where CL bound activity is higher at pH 6.5 and 7.4 than in pH 4.5 or 5.5 (Figure 7.14). However, unlike in WT, enhancements in CL-bound peroxidase activity are not observed compared to intrinsic peroxidase activity with Y67H at pH 6.5 and 7.4 (Table 7.4).

Discussion

Folded State of Y67H. CD spectra suggest that in the Met-ligated state, Y67H has a polypeptide packing and heme environment comparable to those of WT.

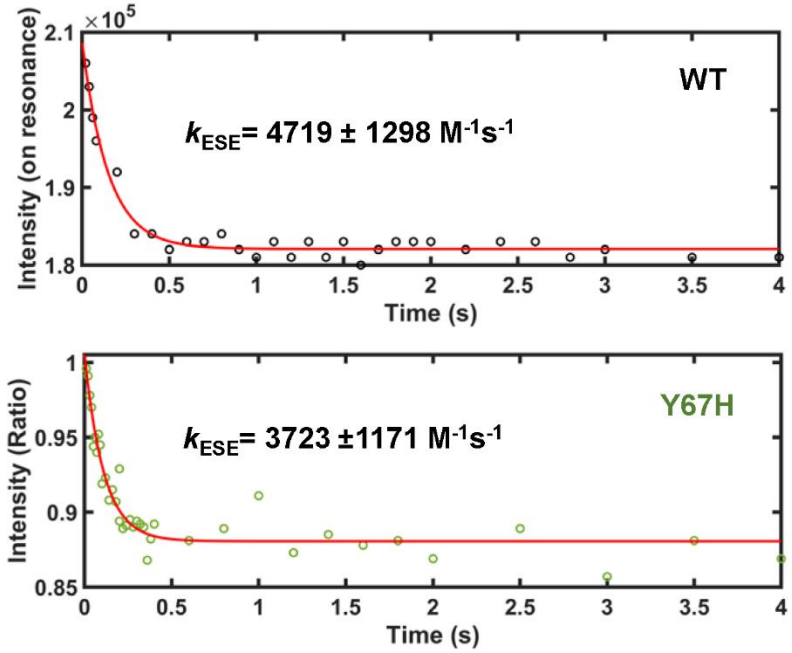

Figure 7.13. Intensity of the signal for methyl protons of Met80 for the ferrous species (either as the detected intensity or the ratio of the signal intensities with or without the saturation pulse) as a function of time, for WT (top, black circles) and Y67H (bottom, green circles) in a 50 mM sodium acetate buffer at pH 4.5 with 10% D_2O (*v*/*v*).

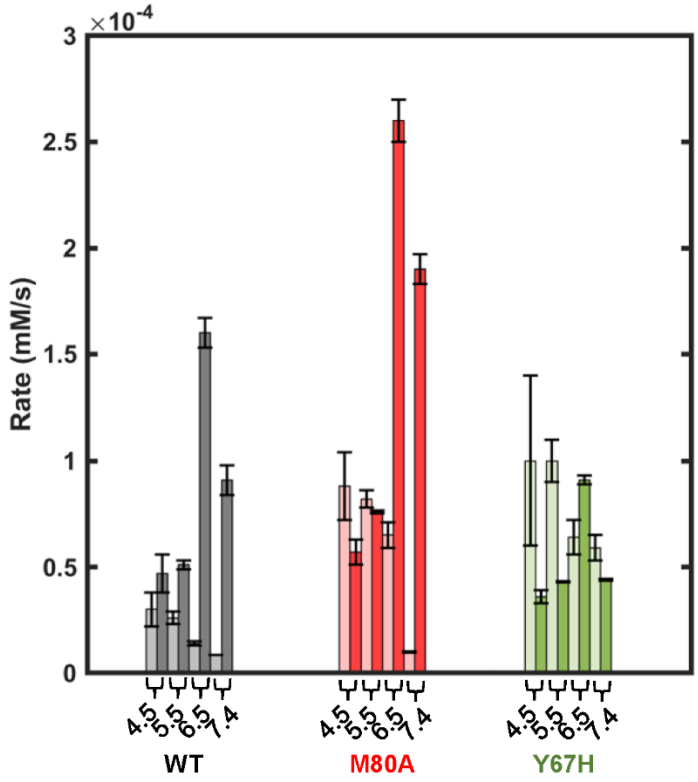

Figure 7.14. Initial rates of peroxidase activity with (darker bars) and without (lighter bars) CL at pH 4.5 to 7.4 for WT (black), M80A (red), and Y67H (green) variants of horse heart cyt *c*.

Table 7.4. Rates of Peroxidase Activity for Variants of Horse Heart Cyt *c* at Various pH Values

Variant	Rate (mM/s)	
	Intrinsic	CL-bound[a]
	pH 7.4	
WT	$8.5 \pm 0.07 \times 10^{-6}$	$9.1 \pm 0.7 \times 10^{-5}$
M80A	$1.0 \pm 0.03 \times 10^{-5}$	$1.9 \pm 0.07 \times 10^{-4}$
Y67H	$5.9 \pm 0.6 \times 10^{-5}$	$4.4 \pm 0.05 \times 10^{-5}$
	pH 6.5	
WT	$1.4 \pm 0.09 \times 10^{-5}$	$1.6 \pm 0.07 \times 10^{-4}$
M80A	$6.5 \pm 0.6 \times 10^{-5}$	$2.6 \pm 0.1 \times 10^{-4}$
Y67H	$6.4 \pm 0.8 \times 10^{-5}$	$9.1 \pm 0.2 \times 10^{-5}$
	pH 5.5	
WT	$2.6 \pm 0.3 \times 10^{-5}$	$5.1 \pm 0.2 \times 10^{-5}$
M80A	$8.2 \pm 0.4 \times 10^{-5}$	$7.6 \pm 0.07 \times 10^{-5}$
Y67H	$1.0 \pm 0.1 \times 10^{-4}$	$4.3 \pm 0.04 \times 10^{-5}$
	pH 4.5	
WT	$3.0 \pm 0.8 \times 10^{-5}$	$4.7 \pm 0.9 \times 10^{-5}$
M80A	$8.8 \pm 1.6 \times 10^{-5}$	$5.7 \pm 0.6 \times 10^{-5}$
Y67H	$1.0 \pm 0.4 \times 10^{-4}$	$3.6 \pm 0.3 \times 10^{-5}$

[a]Ratio of the protein to lipid vesicle concentrations was 1:750.

Despite the similar ligation and structural properties to that of WT at pH 7.4, EPR spectra suggest that a minor population in Y67H has Met80 replaced by H_2O at pH 7.4. The reduction potential is lower than that of WT, likely because of a small population of H_2O-ligated heme iron species. M80A variant has a fold and stability similar to that of WT, but the H_2O-ligated heme iron species at pH 4.5 has a lower reduction potential compared to that of WT by over 200 mV.[69, 110, 111] Thus, the presence of the H_2O-ligated species in Y67H is expected to decrease the reduction potential at pH 7.4. Our measured potential (Table 7.3) is ~180 mV lower than the previously reported value of 410 mV.[58] One possible explanation for this discrepancy can be due to differences in experimental methods used to measure the reduction potentials of the protein.

Because residue at position 67 is far away from the HP groups or the heme edge, and it is unlikely that the mutation itself markedly decreases the solvent exposure of the heme and increase the reduction potential by nearly 150 mV from the value of WT. Even for the Y67F variant that has a tight heme pocket and a higher global stability, the reduction potential is still lower than that of WT.[16, 17, 44, 46, 47] In globular proteins, a polar His residue may be more solvent exposed than hydrophobic residues such as Phe.[112] Further, reduction potential measurements of immobilized M80A and M80A/Y67H yeast cyt *c* have revealed similar *E*° values for the two variants at pH 7, due to the compensatory behavior of the enthalpic and entropic terms for the heme iron reduction.[103] An increase in the reduction potential was previously observed for yeast Y48K, whose reduction potential increased by 117 mV compared to that of WT, despite having a greatly perturbed secondary structure, rapid auto-oxidation, and presence of the high-spin heme iron species.[113] Immobilization of yeast cyt *c* on the gold electrode raised the reduction potential by 100 mV compared to

protein in solution, and this increase in reduction potential was argued to be due to the electrostatic repulsion among densely packed positively charged protein on the electrode surface.[114] There may have been interactions of the protein with the electrode that affected previously reported CV measurements with Y67H that increased the measured reduction potential, providing a possible explanation for the differences between the two measurements.

Presence of a H_2O-ligated species at pH 7.4 for Y67H variant in horse heart cyt *c* suggests that Y67H mutation enhances local fluctuations in loop D, but in the folded state, bisHis ligation is not observed at pH 7.4. RR measurements with Y67H/M80A and Y67H variants of human cyt *c* have shown the presence of bisHis-ligated heme iron species in the absence of Met80, with a corresponding decrease in α-helical content.[63] The His67 residue has been suggested to coordinate to the heme in Y67H/M80A as coordinating other innate His residues require more extensive perturbations in the tertiary structure.[63] In yeast cyt *c*, a similar bisHis ligated species was observed in the Y67H/M80V variant,[64] but not in the Y67H/M80D or Y67H/M80A variants.[64, 115] Differences in Y67H/M80X human and yeast cyt *c* variants suggest that His67 coordination to the heme may depend on the dynamics and packing of loop D, and not necessarily the identity of the residue 80. In yeast cyt *c* K72 is trimethylated to provide steric hinderance and influences loop D reorganization—something that is not observed in human or horse cyt *c*.[116-119] Examination of X-ray crystal structures of WT cyt *c* shows that Tyr67-Met80 bond places the 60's helix away from the heme. It is likely that the replacement of Tyr67 with His allows the protein to stabilize fluctuations that bring 60's helix close to the axial site of the heme under certain conditions. Whether His67 coordinates to the heme or not depends on how readily Met80 is displaced

and if loop D can rearrange to allow a bisHis ligated heme species to form in the folded state. Thus, even if Y67H does not show a bisHis species in the folded state, it is likely that the protein still experiences similar structural fluctuations that bring 60's helix closer to the heme as suggested in the Y67H/M80X variants.

The far-UV CD spectrum of Y67H is different from that of WT at pH 4.5, suggesting changes in the secondary structure. While the lack of Met80 coordination does not alter global stability, the m_D parameter of Y67H is lower than that of WT or M80A at both pH 7.4 and 4.5. Since the m_D value is proportional to the change in solvent -exposed surface area upon unfolding,[92] lower m_D value may result from either the native state being less compact or the denatured state being more compact. Both scenarios could affect the m_D parameter in Y67H. At both pH conditions, Y67H contains heme species where the Met80 ligand is replaced by H_2O. Analysis of the X-ray crystal structure of Met80-ligand dissociated yeast K72A or TmK72 cyt *c* shows that the heme is solvent-exposed when loop D rearranges to accommodate Met80 ligand dissociation from the heme iron.[116] At pH 7.4, formation of more compact intermediate species with His67 acting as a heme ligand during the unfolding of the polypeptide could also contribute to altering the m_D parameter.

The ferrous Y67H species is Met-ligated at both pH 4.5 and 7.4 (Table 7.3 and Figures 7.3 and 7.4D). Spectral features in the electronic absorption spectra suggest that oxy- or deoxy- species observed in ferrous M80A (see Figure 6.9),[111, 120] are not observed in ferrous Y67H (Figures 7.3 and 7.10). At both pH 7.4 and 4.5, the ferric heme iron in Y67H is either Met- or H_2O-ligated, and upon reduction, population containing the H_2O-ligated species is Met-ligated. There is a higher population of the H_2O-ligated species at pH 4.5 than at pH 7.4.

Comparison of k_{ESE} values suggests that these changes do not affect kinetics at pH 4.5. According to semi-classical theory, ET rate constant k_{ET} depends on the driving force of the reaction (ΔG, dependent on the difference in reduction potential between the D and A), the electronic coupling of the electron donor and the acceptor (H_{DA}), and reorganization energy (λ).[80, 121] In k_{ESE}, ΔG = 0, and the k_{ET} is dependent on parameters λ and H_{DA}. Both λ and H_{DA} parameters are influenced by the polypeptide; H_{DA} is dependent on covalent bonds, hydrogen bonds, and through-space contacts,[122] while λ reflect changes in structure and solvation that affects the first- and second-sphere contacts.[121]

Previous studies of the Y67F variant suggest that elimination of the Tyr67-Met80 bond increases the dynamics of the loops C, D, and the 20's loop, minimizing λ and increasing H_{DA}.[44, 123-125] A decrease in λ with the increased protein flexibility has been argued to occur due to decrease in second-sphere λ of the protein matrix and solvent.[44] Perhaps, loop dynamics are also increased in Y67H upon elimination of the inner HB bond, and increase the k_{ESE} value in the Met-ligated state for Y67H at pH 7.4. ESE rates for Y67H are much faster at pH 7.4 than at 4.5 and were not possible to measure with NMR experiments (compare to Figure 7.15). For Y67H at pH 4.5, however, higher populations of proteins undergo conformational rearrangements associated with redox-linked ligand switch. Conformational rearrangements could alter solvent accessibility to the heme and increased random coil character in the polypeptide may hinder proteins from forming optimal bimolecular contacts for ET. These structural changes affect the reorganization energy and electronic coupling to increase the barrier to ET, and k_{ESE} would not be increased.

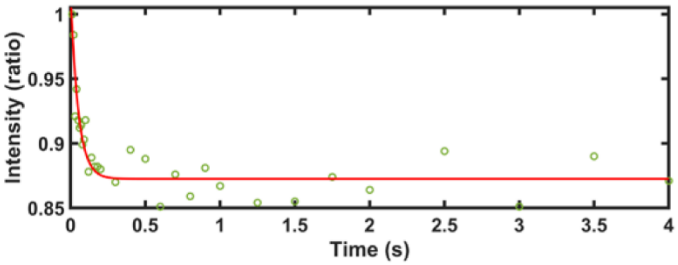

Figure 7.15. Intensity of the signal for methyl protons of Met80 for ferrous species (as ratio of the signal intensities with or without the saturation pulse) as a function of time for Y67H (green circles) in a 50 mM sodium phosphate buffer at pH 7.4 with 10% D_2O (*v*/*v*), containing 1 mM of ferric protein. A fit of the data is shown to guide the eye (red line). A rapid decrease in signal intensity has prevented a reliable fit of the data at pH 7.4.

Electrochemical measurements with immobilized yeast M80A cyt *c* have shown that the loss of Met-ligation decreases k_{ET} to the electrode compared to that for WT.[103] Additional replacement of Tyr67 to His or Ala further decreases k_{ET} compared to that for M80A, argued to be caused by alterations in the protein conformation near residue position 67.[103] The M80A/Y67X variants had comparable reduction potentials,[103] and eq 7.6 suggests that the decrease in k_{ET} from protein to the electrode most likely stems from decrease in k_{ESE} in these variants. MD simulations correlated the decrease in flexibility of loops C and D (measured by RMSF and HB persistence) to increases in the activation energy.[44] In Y67H, the ligand exchange between Met in ferrous heme iron and H_2O in ferric heme iron most likely requires changes in the dynamics of loop D, as well as solvent rearrangement. Even if the electronic coupling were to increase due to increased exposure of the heme, the extensive conformational rearrangement of the polypeptide may increase reorganizational energy, resulting in a comparable k_{ESE} rate constants for Y67H and WT at pH 4.5.

Implications in Intrinsic Peroxidase Activity. Previous studies measuring the peroxidase activity of the Y67H mutation containing variants in yeast, human, and horse heart cyt *c* have been conflicting, as higher, lower, or comparable activities have been observed compared to the activity for WT. [56, 61, 65] [57, 63] Further, observed changes in heme ligation and solvation of the heme pocket with the Y67H mutation have not been explained in the context of peroxidase activity.

Some intrinsic peroxidase activities were performed under high concentrations of H_2O_2 and at times were pre-incubated with H_2O_2.[55, 56] Signs of oxidative damage were observed in horse heart cyt *c* within minutes even at the ratio of 1 to 100 of the protein to

H_2O_2.[126] Further, chemical modifications of polypeptide residues with H_2O_2 have shown to increase peroxidase activity in horse heart cyt *c*.[43, 127] These H_2O_2-induced effects can complicate interpretation of changes to intrinsic peroxidase activity. Decreased stability and heme pocket disruptions in Y67H may increase accessibility of residues such as Met80.[43, 128] We have hypothesized that comparing intrinsic peroxidase activities at lower H_2O_2 concentrations and measuring initial rates in the absence of pre-incubation may help to avoid contributions from chemical modifications from H_2O_2. Further, although guaiacol has been widely used as a colorimetric substrate to monitor the peroxidase activity,[34, 65] there are benefits of using ABTS. MP8 reaction with ABTS is well known, and the initial steps to form the compound I species have been well studied.[129, 130]

Peroxidase activity in six-coordinate heme protein requires dissociation of an axial ligand to allow H_2O_2 to coordinate to the heme. Spectroscopic data suggest that in Y67H, some population of the protein contain hemes where the Met80 ligand is replaced by H_2O at near-neutral pH (Figures 7.1 and 7.2). Studies with K72A, TmK72, and K79H variants in yeast cyt *c* have shown that increases in peroxidase activity is observed with increases in loop D dynamics that promotes Met80 dissociation from the heme iron.[116, 131] As observed previously,[65] peroxidase activity of the Met-ligated Y67H is higher than that of the hydroxide-ligated M80A or Met-ligated WT at pH 7.4 (Figure 7.14), suggesting that Met80 dissociates more readily in Y67H than in WT.

If the intrinsic peroxidase activity increased because of a distal His, similar rate enhancement observed at pH 7.4 should be present at pH 6.5. At pH 6.5, His67 is expected to be deprotonated, as distal His in cytochrome *c* peroxidase (CcP) was calculated with a pK_a ranging from 5.1 to 5.4.[132]. If His67 acted similarly to distal His in classical

peroxidases, the intrinsic peroxidase activity for Y67H would have been enhanced at pH 6.5 compared to those for WT or M80A, and more so than at pH 7.4. Yet, intrinsic peroxidase activity of Y67H is comparable to that of M80A at pH 6.5 (Figure 7.14 and Table 7.4). Further, activities of Y67H at pH 7.4 and 4.5 are comparable to one another (Figure 7.14 and Table 7.4). Thus, the increase in intrinsic peroxidase activity of the Y67H variant cannot be fully explained by the role of a distal His as an acid-base catalyst.

The increase in the solvent accessibility of the heme pocket increases access by the ROS to the heme iron, enhancing peroxidase activity. Cyt *c* unfolds sequentially, and loops C and D unfold prior to the 60's helix that contains residue 67.[133, 134] The partially unfolded species is observed in Y67H at pH 7.4 and low GuHCl concentrations may be related to the partially unfolded forms in early unfolding steps involving changes in loop D. Studies with varying concentrations of urea suggest that partial unfolding of loops C and D that exposes the heme to the solvent enhances peroxidase activity.[135] In the absence of Tyr67, additional connections to keep loop D folded disappear. MD simulations on the Y67F variant suggest that perturbation of the Tyr67-Met80 HB interaction increases the dynamics of loops C and D.[44] It is likely that similar behavior is observed in Y67H, explaining the increase in intrinsic peroxidase activity in the Met-ligated Y67H at pH 7.4 and 6.5. The activity at pH 5.5 and 4.5 are enhanced for Y67H compared to that for WT, as the heme iron is H_2O-ligated under these conditions in Y67H.

Unfolded State of Y67H. In Y67H, there are compact structures in the unfolded state that do not exist in WT. In unfolded cyt *c,* the loss of the Met80 ligand allows the heme iron to be misligated by His residues and *N*-terminal amino group in the polypeptide chain, forming kinetic traps in the cyt *c* folding pathway.[95, 136-138] Misligation depends on the pK_a

of the coordinating His residue and is detected by the presence of low-spin heme species with spectral features consistent of bis-His adducts.[139] Upon protonation of the His sidechain, the heme becomes H_2O-ligated and can be detected as a high-spin heme species, with a transition that has an observed pK_a that includes both the protonation of the coordinating His residue and the conformational rearrangement equilibrium for His-coordination. Multiple His residues can compete for the axial site of the heme,[140] and the properties of the polypeptide chain between the stretch of residues containing the coordinating His and the heme can also alter the preference of one His over the other in forming the misligated species.[98]

His67 alters the observed pK_a of the high-spin to low-spin heme transition in the presence of the misligating sites present in WT, suggesting that His67 does coordinate to the heme iron in the unfolded state. Further, residue 67 is expected to form contacts with the heme in the unfolded state. Previous studies introducing His at positions 33, 54, and 72 in the polypeptide chain have revealed that these regions of the polypeptide chain have strong tendency to bind to the heme, and are implicated in driving the hydrophobic collapse during cyt *c* folding.[97, 98, 141] Transient compact species has been detected to form near residues 39, 50, and 66 from labeling studies with yeast cyt *c*; this compact species is thought to be driven by hydrophobic interactions.[142] Although residue 67 has not been examined in these studies, residues at and near the 60's helix are known to form frequent contacts with the heme, [97, 98, 141, 142]. and reflects the behavior of the protein region that includes residue 67.

In Y67H, it is likely that His67 coordination to the heme upon partial unfolding of loop D stabilizes the intermediate species. The stability of the 60's helix is higher than

those of loops C and D, and at low GuHCl conditions, loop D is expected to unfold prior to the 60's helix because this latter region is stabilized by the most stable *N*- and *C*-terminal helices.[143-145] Thus, unfolding of loop D and loss of the Met80 ligation to the heme may provide an open site for His67 to coordinate to the heme without extensive unfolding of the polypeptide chain. Further, loops C and D are not obligated to unfold concomitantly.[144] Then, His67 coordination may occur even with partial unfolding of the polypeptide chain in loop D, unlike His26 or 33 which require extensive unfolding.[95, 146] Previous studies of the Y67H/M80A variant of human cyt *c* suggest that His67 can coordinate to the heme with minor structural perturbations.[63] Far-UV CD spectrum of this variant has shown a decrease in α-helical character compared to WT, and even in the folded state, His67 is suggested to ligate to the heme iron.[63] Comparison of K73H/L85A and K73H variants of yeast cyt *c* show that local destabilization of loop D leads to the formation of the His-ligated species, linking formation of the His73-ligated species to local stability near the heme.[147] In WT, bisHis-ligated intermediates are not readily observed species at low concentrations of GuHCl,[29] as the native protein does not have His residues in the 60's helix. In the unfolded state, Y67H is in a mixture of the His-ligated species and the H_2O-ligated species, and their relative population depends on pH. Since residue 67 is near the heme, His67 in Y67H could coordinate to the heme iron upon loop D unfolding at pH 7.4.

Because Y67H has a propensity to unfold and His67 coordinates to the heme, the Y67H variant could help to understand the reactivity of the CL-bound cyt *c* ensemble and the role of the bisHis-ligated species. Residue 67 is positioned near the proposed contact sites with CL,[31] but is also in close proximity to the heme. Since Y67H forms the bisHis

ligated heme species upon partial unfolding, one could expect that His67/His18 form is also readily present in the CL-bound ensemble.

Implications of Non-native Intermediates for Peroxidase Activity of CL-bound Cyt c. Binding of cyt *c* to the membrane surface containing CL depends on both the ionic strength and pH conditions of the solution.[148] Multiple modes of CL and cyt *c* binding have been observed,[28] but cyt *c* is believed to be dominated by peripheral (electrostatic) contacts at high CL concentrations where large-scale unfolding occurs.[31, 35, 149, 150] Residue 67 is located at one of the proposed lipid anchorage regions relevant at low CL concentrations, and perturbations in this region decrease binding of the protein to the CL-containing lipid vesicles.[151, 152] It is possible that perturbation in one of the CL-interacting sites may make binding of cyt *c* to CL-containing membranes less favored at low CL concentrations because residue-specific interactions that form favorable contacts are no longer present. However, residue 67 is not near the surface regions argued to interact with CL at higher CL concentrations, suggesting that CL-interaction may not be perturbed by the Y67H mutation depending on the CL concentration.[150]

The role of the heme ligation in influencing the peroxidase activity in the CL-bound cyt *c* is still not fully defined. Different species, including 5-coordinate or 6-coordinate H_2O/OH^-, His, and Lys-ligated heme have been observed.[37-39, 149] The 5-coordinate species has been directly implicated in peroxidase activity because of the readily available open coordination site for H_2O_2.[39, 153, 154] Studies with MP8 suggest that replacement of H_2O and hydroxide heme ligands depends on the nucleophilic participation of H_2O_2 in the transition state, and peroxidase activity is relevant for both the hydroxide- or H_2O-ligated heme iron species.[2, 130] Between the His- and Lys-ligated hemes, the former has been argued to be

dominant and responsible for the increase in peroxidase activity in the CL-bound species.[39] However, this argument is in conflict with peroxidase activity studies with *c*-type cytochromes. Lys-ligation suppresses peroxidase activity in folded *c*-type cytochromes.[155, 156] Peroxidase activity studies with unfolded cyt c_{550}, c_{551}, *c*, and MP8 suggest that bisHis-coordination inhibits the activity of iron centers.[33, 34]

In the CL-bound state at pH 7.4 and 6.5, the activity of Y67H is lower than that of WT or M80A. Further, the peroxidase activity of Y67H in the presence of CL under these pH conditions does not increase compared to the intrinsic peroxidase activity (Figure 7.14). The peroxidase activity of the CL-bound Y67H can be rationalized by evoking the equilibrium between the non-native compact and extended species.[29] The Y67H mutation is not on the surface of the protein in the native fold, and it should not interfere with the massive unfolding of the protein on the CL surface. Furthermore, global stability of Y67H is lower than that of WT (Table 7.1), and Y67H should readily unfold on the CL-containing membrane surface since CL acts similarly as a denaturant. At pH 7.4, the CL-bound Y67H is likely to have more bisHis-ligated heme species than in either WT or M80A due to the presence of His67. The bisHis heme species has very low peroxidase activity,[34] and helps explain the lack of enhancement in peroxidase activity upon the mutation at pH 7.0.[58] However, the peroxidase activity is still present under these conditions for both WT and Y67H because the extended species without the bisHis heme ligation, is part of the ensemble. Fluorescence measurements show the increased distance between the 60's helix and the heme in the CL-bound cyt *c* ensemble,[31] despite propensity for the residues in 60's helix to interact with the heme.[142] Thus, some of the extended structures in Y67H may not

contain His67-ligated heme species. Differences in CL-bound activity observed with the Y67H mutation likely arises from the nonnative compact species.

At pH 4.5 and 5.5, where the population of bisHis-ligated species is low (Figure 7.9), peroxidase activities of the CL-bound cyt *c* are comparable for WT and Y67H, and not that different from that of M80A activity (Figure 7.14 and Table 7.4). Without the bisHis-ligated heme species, the activity is no longer suppressed and becomes comparable to that of WT (Figure 7.14 and Table 7.4). This trend in activity with pH suggests that at high CL concentrations, the increase in the peroxidase activity reflects the action of extended species.

Comments on Discrepancies Observed in Various CL-Liposome Studies. The driving force for forming protein interactions with the lipid surface can be described by peripheral contacts, dominated by hydrophobic, electrostatic, and hydrogen bonding interactions, which in turn depend on the anionic lipid content, character of the protein surface, and electrolyte content.[157-161] These interactions are not static and can even trigger conformational rearrangements in proteins such as in multi-protein complex II of P13K, or in local folding events as observed in unstructured regions of Atg16 or antibacterial/Alzheimer peptides.[158, 162, 163] Thus, these interactions are not homogeneous. Likewise, it is important to consider the heterogeneity of the CL-bound ensemble in understanding protein function. The consideration of the heterogeneity of the CL-bound ensemble helps to explain discrepancies of mutational effects in different studies of peroxidase activity of cyt *c*. For example, imidazole-binding studies show that His-ligation to the heme suppresses peroxidase activity.[34] Yet, peroxidase activity is still present, and even enhanced, in unfolded cyt *c* in solution,[34] bound to CL-containing membranes, or

adhered on a gold surface with anionic self-assembled monolayer,[164] despite the presence of bisHis-ligated heme species . Had the conformational ensemble been homogeneous and consisted of only bisHis-ligated heme species, these differences in activities should not be observed. If we consider the heterogeneity in the unfolded ensemble,[142] variations depending on the degree of protein unfolding result in differences in peroxidase activity.

Lipid content can affect conformational rearrangements and interactions of the lipid-bound proteins,[35, 165] and one then should be careful in comparing enzymatic activity at different lipid conditions. CL-bound cyt *c* is sensitive to changes in the CL content and lipid to protein ratios (see Figures A1.8, A1.9, and A2.3 for examples). NMR studies at lower protein-to-CL ratio (1:4) suggest homogeneous native-like conformations, in contrast to studies at higher ratios (1:15), where more dynamic behavior of the polypeptide is observed.[166, 167] Kinetic studies show that initial interactions are influenced by the available surface area of the lipid membrane surface at high CL concentrations.[31, 35] CL concentration also affects the conformational distribution of the lipid-bound ensemble, as native-like forms have been observed at low CL concentrations while an increase in the population of 5-coordinate species observed with the higher CL content.[153]

These differences may offer alternate explanations for the discrepancies of results from mutational studies of the CL-bound cyt *c*. For example, the decrease in peroxidase activity for the Y67F variant in horse heart cyt *c* has been attributed to the lack of Tyr67 that provides a distal radical required in peroxidase activity.[40] Radicals have been observed to enhance peroxidase activity, and it is with no doubt that such a mechanism could be one of possible mechanisms that explain the peroxidase activity of cyt *c*. However, if radical formation on Tyr residues had been the sole reason for the enhanced peroxidase activity,

the activity for CL-bound Y67H should have been lower than that of the CL-bound WT or M80A at near neutral pH. Peroxidase activity has been observed with MP8 models, but their activity peaks at mildly alkaline conditions as formation of the Compound I species depends on deprotonation of H_2O_2.[2] Differences in peroxidase activity are observed with variations in CL or lipid-to-protein concentrations (Figure 3.21). Some peroxidase assays, have been performed at low CL concentrations or protein to lipid ratio (1:20),[40] where specific lipid-protein interactions are suggested to be dominant over peripheral contacts.[149] Changes in protein stability may also affect the CL-bound peroxidase activity. Peroxidase activity of unfolded cyt *c* on gold surface with anionic self-assembled monolayer is different for variants with surface mutations of Lys-to-Ala, affecting the surface charge of the protein.[164] This activity dependence on surface charge of the protein suggests that difference in activity may arise from how the protein adheres and unfolds on a charged surface.[164] Thus, in conditions where peripheral contacts dominate the cyt *c* binding to CL, differences in how the protein unfolds on the surface may influence peroxidase activity. The Y67F variant has a higher global stability than WT (Table 7.5),[46, 47] and may require higher CL concentrations to fully unfold the protein. The population of the extended species or 5-coordinate species are dependent on the concentration of CL (and thus anionic charge of the surface),[35, 153] and one can imagine that for more stable cyt *c* variants, more anionic charge is required to unfold the protein to a similar extent as in WT.

Table 7.5. Thermal Denaturation Parameters for Previously Studied Y67 Variants of Cyt *c*

Variant	T_m (°C)
Iso-1 yeast	
WT[a]	>85
Y67R[a]	30
Y67H[a]	50
Horse Heart	
WT	64[b]
Y67F	107[b]
Rat	
WT	60[c]
Y67F	90[c]

[a]From ref. [56]. From CD measurements monitoring ellipticity at 222 nm in a 100 mM phosphate buffer at pH 7.0.

[b]From ref. [46], from monitoring the CT band at 695 nm as a function of temperature with protein obtained from semi-synthesis. Samples contain 170 µm protein for WT and 250 µm for Y67F, in a 10 mM sodium cacodylate buffer with 10 mM NaCl at pH 7.

[c]From ref. [47], expressed in yeast.

Conclusion

At near-neutral pH conditions, the heme iron in Y67H is Met-ligated as it is in WT. A minor population of H_2O-ligated species is detected by EPR. Polypeptide fold, global stability, and reduction potential of Y67H are comparable to WT at pH 7.4. At pH 4.5, Met-ligation to the heme iron is lost in ferric Y67H, and the H_2O-ligated heme iron species is formed. This switch in ligation not only affects the stability and the fold of the protein, but also alters the reduction potential. The k_{ESE} rate constant is comparable to that of WT, likely due to structural rearrangement associated with redox-linked ligand switch that will affect both H_{DA} and λ parameters important for ET. Y67H also has a propensity to unfold and form the partially unfolded His-ligated heme species, including those with His67 coordinating to the heme iron. Because the misligated bisHis heme species forms when Y67H is partially unfolded, it serves as a good model to resolve the contradictions surrounding the role of bisHis-ligated heme species in peroxidase activity of the CL-bound cyt *c*. Changes in peroxidase activity with pH show that decrease in bisHis-ligated heme species increases peroxidase activity, illustrating that the increase in CL-bound peroxidase activity does not stem from the bisHis species. Discrepancies of previous studies likely stem from differences in the used CL content, which strongly affects the type of protein interaction with the CL-containing membranes. This difference affects the extent of the rearrangements, and heavily influences the acquired peroxidase activity of the protein.

References

1. Battistuzzi, G., Borsari, M., Cowan, J.A., Ranieri, A. & Sola, M. Control of cytochrome c redox potential: Axial ligation and protein environment effects. *J Am Chem Soc* **124**, 5315-5324 (2002).

2. Marques, H.M. Peroxidase activity of the hemeoctapeptide N-acetylmicroperoxidase-8. *Inorg Chem* **44**, 6146-6148 (2005).

3. Liu, J. *et al.* Metalloproteins containing cytochrome, iron-sulfur, or copper redox centers. *Chem Rev* **114**, 4366-4469 (2014).

4. Pokkuluri, P.R. *et al.* Structure of a novel dodecaheme cytochrome c from Geobacter sulfurreducens reveals an extended 12 nm protein with interacting hemes. *Journal of structural biology* **174**, 223-233 (2011).

5. Andersen, J.F., Weichsel, A., Balfour, C.A., Champagne, D.E. & Montfort, W.R. The crystal structure of nitrophorin 4 at 1.5 å resolution: transport of nitric oxide by a lipocalin-based heme protein. *Structure* **6**, 1315-1327 (1998).

6. Weichsel, A., Andersen, J.F., Champagne, D.E., Walker, F.A. & Montfort, W.R. Crystal structures of a nitric oxide transport protein from a blood- sucking insect. *Nat Struct Biol* **5**, 304-309 (1998).

7. Nóbrega, C.S., Raposo, M., Van Driessche, G., Devreese, B. & Pauleta, S.R. Biochemical characterization of the bacterial peroxidase from the human pathogen Neisseria gonorrhoeae. *Journal of inorganic biochemistry* **171**, 108-119 (2017).

8. Cutruzzolà, F. *et al.* The nitrite reductase from Pseudomonas aeruginosa: Essential role of two active-site histidines in the catalytic and structural properties. *Proceedings of the National Academy of Sciences* **98**, 2232-2237 (2001).

9. Meyer, T.E. & Cusanovich, M.A. Soluble cytochrome composition of the purple phototrophic bacterium, Rhodopseudomonas sphaeroides ATCC 17023. *Biochimica et Biophysica Acta (BBA) - Bioenergetics* **807**, 308-319 (1985).

10. Leys, D. *et al.* Crystal Structures of an Oxygen-binding Cytochrome cfrom Rhodobacter sphaeroides *. *Journal of Biological Chemistry* **275**, 16050-16056 (2000).

11. Alvarez-Paggi, D. *et al.* Multifunctional Cytochrome c: Learning New Tricks from an Old Dog. *Chem Rev* **117**, 13382-13460 (2017).

12. Kagan, V.E. *et al.* Cytochrome c acts as a cardiolipin oxygenase required for release of proapoptotic factors. *Nat Chem Biol* **1**, 223-232 (2005).

13. Zaidi, S., Hassan, M.I., Islam, A. & Ahmad, F. The role of key residues in structure, function, and stability of cytochrome-c. *Cell Mol Life Sci* **71**, 229-255 (2014).

14. Rajagopal, Badri S. *et al.* The hydrogen-peroxide-induced radical behaviour in human cytochrome c–phospholipid complexes: implications for the enhanced pro-apoptotic activity of the G41S mutant. *Biochem J* **456**, 441-452 (2013).

15. Moore, G.R. & Pettigrew, G.W. *Cytochromes c : evolutionary, structural, and physicochemical aspects*. (Springer-Verlag, Berlin ; New York; 1990).

16. Eddowes, M.J. & Hill, H.A.O. Electrochemistry of Horse Heart Cytochrome-C. *J Am Chem Soc* **101**, 4461-4464 (1979).

17. Feinberg, B.A., Petro, L., Hock, G., Qin, W.Y. & Margoliash, E. Using entropies of reaction to predict changes in protein stability: tyrosine-67-phenylalanine variants of rat cytochrome c and yeast Iso-1 cytochromes c. *J Pharmaceut Biomed* **19**, 115-125 (1999).

18. Cutler, R.L., Pielak, G.J., Mauk, A.G. & Smith, M. Replacement of cysteine-107 of Saccharomyces cerevisiae iso-1-cytochrome c with threonine: improved stability of the mutant protein. *Protein Eng* **1**, 95-99 (1987).

19. Battistuzzi, G. *et al.* Redox chemistry and acid-base equilibria of mitochondrial plant cytochromes c. *Biochemistry* **38**, 5553-5562 (1999).

20. Josephs, T.M. *et al.* Conformational change and human cytochrome c function: mutation of residue 41 modulates caspase activation and destabilizes Met-80 coordination. *J Biol Inorg Chem* **18**, 289-297 (2013).

21. Battistuzzi, G., Borsari, M., Sola, M. & Francia, F. Redox thermodynamics of the native and alkaline forms of eukaryotic and bacterial class I cytochromes c. *Biochemistry* **36**, 16247-16258 (1997).

22. Bushnell, G.W., Louie, G.V. & Brayer, G.D. High-resolution three-dimensional structure of horse heart cytochrome c. *J Mol Biol* **214**, 585-595 (1990).

23. Kalpage, H.A. *et al.* Serine-47 phosphorylation of cytochrome c in the mammalian brain regulates cytochrome c oxidase and caspase-3 activity. *The FASEB Journal* **33**, 13503-13514 (2019).

24. Berghuis, A.M. & Brayer, G.D. Oxidation State-Dependent Conformational-Changes in Cytochrome-C. *J Mol Biol* **223**, 959-976 (1992).

25. Tezcan, F.A., Winkler, J.R. & Gray, H.B. Effects of ligation and folding on reduction potentials of heme proteins. *J Am Chem Soc* **120**, 13383-13388 (1998).

26. Sutin, N. & Yandell, J.K. Mechanisms of the reactions of cytochrome c. Rate and equilibrium constants for ligand binding to horse heart ferricytochrome c. *The Journal of biological chemistry* **247**, 6932-6936 (1972).

27. Kroll, T. *et al.* Resonant Inelastic X-ray Scattering on Ferrous and Ferric Bis-imidazole Porphyrin and Cytochrome c: Nature and Role of the Axial Methionine–Fe Bond. *J Am Chem Soc* **136**, 18087-18099 (2014).

28. Muenzner, J. & Pletneva, E.V. Structural transformations of cytochrome c upon interaction with cardiolipin. *Chem Phys Lipids* **179**, 57-63 (2014).

29. Hanske, J. *et al.* Conformational properties of cardiolipin-bound cytochrome c. *P Natl Acad Sci USA* **109**, 125-130 (2012).

30. Sinibaldi, F. *et al.* The key role played by charge in the interaction of cytochrome c with cardiolipin. *J Biol Inorg Chem* (2016).

31. Muenzner, J., Toffey, J.R., Hong, Y.N. & Pletneva, E.V. Becoming a Peroxidase: Cardiolipin-Induced Unfolding of Cytochrome c. *J Phys Chem B* **117**, 12878-12886 (2013).

32. Balakrishnan, G. *et al.* A conformational switch to beta-sheet structure in cytochrome c leads to heme exposure. Implications for cardiolipin peroxidation and apoptosis. *J Am Chem Soc* **129**, 504-505 (2007).

33. Diederix, R.E.M., Ubbink, M. & Canters, G.W. Effect of the protein matrix of cytochrome c in suppressing the inherent peroxidase activity of its heme prosthetic group. *Chembiochem* **3**, 110-112 (2002).

34. Diederix, R.E.M., Ubbink, M. & Canters, G.W. Peroxidase activity as a tool for studying the folding of c-type cytochromes. *Biochemistry* **41**, 13067-13077 (2002).

35. Hong, Y.N., Muenzner, J., Grimm, S.K. & Pletneva, E.V. Origin of the Conformational Heterogeneity of Cardiolipin-Bound Cytochrome c. *J Am Chem Soc* **134**, 18713-18723 (2012).

36. Baldwin, D.A., Marques, H.M. & Pratt, J.M. Hemes and Hemoproteins .5. Kinetics of the Peroxidatic Activity of Microperoxidase-8 - Model for the Peroxidase Enzymes. *Journal of inorganic biochemistry* **30**, 203-217 (1987).

37. Bradley, J.M., Silkstone, G., Wilson, M.T., Cheesman, M.R. & Butt, J.N. Probing a complex of cytochrome c and cardiolipin by magnetic circular dichroism spectroscopy: implications for the initial events in apoptosis. *J Am Chem Soc* **133**, 19676-19679 (2011).

38. Sinibaldi, F. *et al.* Role of lysines in cytochrome c-cardiolipin interaction. *Biochemistry* **52**, 4578-4588 (2013).

39. Capdevila, D.A. *et al.* Active Site Structure and Peroxidase Activity of Oxidatively Modified Cytochrome c Species in Complexes with Cardiolipin. *Biochemistry* **54**, 7491-7504 (2015).

40. Kapralov, A.A. *et al.* Topography of tyrosine residues and their involvement in peroxidation of polyunsaturated cardiolipin in cytochrome c/cardiolipin peroxidase complexes. *Bba-Biomembranes* **1808**, 2147-2155 (2011).

41. Mara, M.W. *et al.* Metalloprotein entatic control of ligand-metal bonds quantified by ultrafast x-ray spectroscopy. *Science* **356**, 1276-1280 (2017).

42. Bren, K.L. & Raven, E.L. Locked and loaded for apoptosis. *Science* **356**, 1236-1236 (2017).

43. Yin, V., Shaw, G.S. & Konermann, L. Cytochrome c as a Peroxidase: Activation of the Precatalytic Native State by H2O2-Induced Covalent Modifications. *J Am Chem Soc* **139**, 15701-15709 (2017).

44. Oviedo-Rouco, S. *et al.* Electron transfer and conformational transitions of cytochrome c are modulated by the same dynamical features. *Arch Biochem Biophys* **680**, 108243 (2020).

45. Rafferty, S.P. *et al.* Mechanistic and structural contributions of critical surface and internal residues to cytochrome c electron transfer reactivity. *Biochemistry* **35**, 10784-10792 (1996).

46. Wallace, C.J.A. *et al.* Substitutions Engineered by Chemical Synthesis at 3 Conserved Sites in Mitochondrial Cytochrome-C - Thermodynamic and Functional Consequences. *Journal of Biological Chemistry* **264**, 15199-15209 (1989).

47. Luntz, T.L., Schejter, A., Garber, E.A.E. & Margoliash, E. Structural Significance of an Internal Water Molecule Studied by Site-Directed Mutagenesis of Tyrosine-67 in Rat Cytochrome-C. *P Natl Acad Sci USA* **86**, 3524-3528 (1989).

48. Lett, C.M., Berghuis, A.M., Frey, H.E., Lepock, J.R. & Guillemette, J.G. The role of a conserved water molecule in the redox-dependent thermal stability of iso-1-cytochrome c. *The Journal of biological chemistry* **271**, 29088-29093 (1996).

49. Maguire, J.J. *et al.* Known unknowns of cardiolipin signaling: The best is yet to come. *Bba-Mol Cell Biol L* **1862**, 8-24 (2017).

50. Villegas, J.A., Mauk, A.G. & Vazquez-Duhalt, R. A cytochrome c variant resistant to heme degradation by hydrogen peroxide. *Chem Biol* **7**, 237-244 (2000).

51. Morison, I.M. *et al.* A mutation of human cytochrome c enhances the intrinsic apoptotic pathway but causes only thrombocytopenia. *Nat Genet* **40**, 387-389 (2008).

52. De Rocco, D. *et al.* Mutations of cytochrome c identified in patients with thrombocytopenia THC4 affect both apoptosis and cellular bioenergetics. *Bba-Mol Basis Dis* **1842**, 269-274 (2014).

53. Johnson, B. *et al.* Whole exome sequencing identifies genetic variants in inherited thrombocytopenia with secondary qualitative function defects. *Haematologica* **101**, 1170-1179 (2016).

54. Uchiyama, Y. *et al.* A novel CYCS mutation in the alpha-helix of the CYCS C-terminal domain causes non-syndromic thrombocytopenia. *Clin Genet* **94**, 548-553 (2018).

55. Wang, Z.-H. *et al.* Converting Cytochrome c into a Peroxidase-Like Metalloenzyme by Molecular Design. *Chembiochem* **8**, 607-609 (2007).

56. Ying, T. *et al.* Tyrosine-67 in cytochrome c is a possible apoptotic trigger controlled by hydrogen bonds via a conformational transition. *Chemical communications (Cambridge, England)*, 4512-4514 (2009).

57. Tognaccini, L. *et al.* Structure-function relationships in human cytochrome c: The role of tyrosine 67. *Journal of inorganic biochemistry* **155**, 56-66 (2016).

58. Patriarca, A. *et al.* Conversion of cytochrome c into a peroxidase: inhibitory mechanisms and implication for neurodegenerative diseases. *Arch Biochem Biophys* **522**, 62-69 (2012).

59. Franzen, S. *et al.* Proximal cavity, distal histidine, and substrate hydrogen-bonding mutations modulate the activity of Amphitrite ornata dehaloperoxidase. *Biochemistry* **45**, 9085-9094 (2006).

60. Khan, K.K., Mondal, M.S., Padhy, L. & Mitra, S. The role of distal histidine in peroxidase activity of myoglobin. *Eur J Biochem* **257**, 547-555 (1998).

61. Poulos, T.L. Heme Enzyme Structure and Function. *Chem Rev* **114**, 3919-3962 (2014).

62. Koshland Jr, D.E. The application and usefulness of the ratio kcat/KM. *Bioorganic Chemistry* **30**, 211-213 (2002).

63. Ciaccio, C. *et al.* The Met80Ala and Tyr67His/Met80Ala mutants of human cytochrome c shed light on the reciprocal role of Met80 and Tyr67 in regulating ligand access into the heme pocket. *Journal of inorganic biochemistry* **169**, 86-96 (2017).

64. Ying, T., Wang, Z.H., Zhong, F., Tan, X. & Huang, Z.X. Distinct mechanisms for the pro-apoptotic conformational transition and alkaline transition in cytochrome c. *Chemical communications (Cambridge, England)* **46**, 3541-3543 (2010).

65. Wang, Z.H. *et al.* Converting cytochrome c into a peroxidase-like metalloenzyme by molecular design. *Chembiochem* **8**, 607-609 (2007).

66. Porcelli, A.M. *et al.* pH difference across the outer mitochondrial membrane measured with a green fluorescent protein mutant. *Biochemical and biophysical research communications* **326**, 799-804 (2005).

67. Nilsson, C., Kagedal, K., Johansson, U. & Ollinger, K. Analysis of cytosolic and lysosomal pH in apoptotic cells by flow cytometry. *Methods in cell science : an official journal of the Society for In Vitro Biology* **25**, 185-194 (2003).

68. Berry, E.A. & Trumpower, B.L. Simultaneous determination of hemes a, b, and c from pyridine hemochrome spectra. *Analytical biochemistry* **161**, 1-15 (1987).

69. Gu, J., Shin, D.W. & Pletneva, E.V. Remote Perturbations in Tertiary Contacts Trigger Ligation of Lysine to the Heme Iron in Cytochrome c. *Biochemistry* **56**, 2950-2966 (2017).

70. Pace, C.N. Measuring and increasing protein stability. *Trends in biotechnology* **8**, 93-98 (1990).

71. Pace, C.N. Determination and analysis of urea and guanidine hydrochloride denaturation curves. *Methods in enzymology* **131**, 266-280 (1986).

72. Zhong, F.F., Lisi, G.P., Collins, D.P., Dawson, J.H. & Pletneva, E.V. Redox-dependent stability, protonation, and reactivity of cysteine-bound heme proteins. *P Natl Acad Sci USA* **111**, E306-E315 (2014).

73. Verissimo, A.F., Sousa, F.L., Baptista, A.M., Teixeira, M. & Pereira, M.M. Thermodynamic redox behavior of the heme centers of cbb3 heme-copper oxygen reductase from Bradyrhizobium japonicum. *Biochemistry* **46**, 13245-13253 (2007).

74. Pintscher, S. *et al.* Tuning of Hemes b Equilibrium Redox Potential Is Not Required for Cross-Membrane Electron Transfer. *The Journal of biological chemistry* **291**, 6872-6881 (2016).

75. Nakajima, H. *et al.* Redox properties and coordination structure of the heme in the co-sensing transcriptional activator CooA. *The Journal of biological chemistry* **276**, 7055-7061 (2001).

76. Zahn, J.A., Arciero, D.M., Hooper, A.B. & Dispirito, A.A. Cytochrome c' of Methylococcus capsulatus Bath. *Eur J Biochem* **240**, 684-691 (1996).

77. Liptak, M.D., Fagerlund, R.D., Ledgerwood, E.C., Wilbanks, S.M. & Bren, K.L. The Proapoptotic G41S Mutation to Human Cytochrome c Alters the Heme Electronic Structure and Increases the Electron Self-Exchange Rate. *J Am Chem Soc* **133**, 1153-1155 (2011).

78. Katki, H., Weiss, G.H., Kiefer, J.E., Taitelbaum, H. & Spencer, R.G.S. Optimization of Magnetization Transfer Experiments to Measure First-Order Rate Constants and Spin-Lattice Relaxation Times. *NMR in Biomedicine* **9**, 135-139 (1996).

79. Wherland, S. & Gray, H.B. Metalloprotein Electron-Transfer Reactions - Analysis of Reactivity of Horse Heart Cytochrome-C with Inorganic Complexes. *P Natl Acad Sci USA* **73**, 2950-2954 (1976).

80. Marcus, R.A. On Theory of Electron-Transfer Reactions .6. Unified Treatment for Homogeneous and Electrode Reactions. *J Chem Phys* **43**, 679-& (1965).

81. Deng, Y.L., Zhong, F.F., Alden, S.L., Hoke, K.R. & Pletneva, E.V. The K79G Mutation Reshapes the Heme Crevice and Alters Redox Properties of Cytochrome c. *Biochemistry* **57**, 5827-5840 (2018).

82. Re, R. *et al.* Antioxidant activity applying an improved ABTS radical cation decolorization assay. *Free radical biology & medicine* **26**, 1231-1237 (1999).

83. Theorell, H. & Akesson, A. Studies on cytochrome c. II. The optical properties of pure cytochrome c and some of its derivatives. *J Am Chem Soc* **63**, 1812-1818 (1941).

84. Godbole, S. & Bowler, B.E. Effect of pH on formation of a nativelike intermediate on the unfolding pathway of a Lys 73 --> His variant of yeast iso-1-cytochrome c. *Biochemistry* **38**, 487-495 (1999).

85. Rosell, F.I., Ferrer, J.C. & Mauk, A.G. Proton-linked protein conformational switching: Definition of the alkaline conformational transition of yeast iso-1-ferricytochrome c. *J Am Chem Soc* **120**, 11234-11245 (1998).

86. Lan, W.X. *et al.* Structural Basis for Cytochrome c Y67H Mutant to Function as a Peroxidase. *Plos One* **9** (2014).

87. Myer, Y.P. & Harbury, H.A. Optical rotatory dispersion of cytochrome c. *P Natl Acad Sci USA* **54**, 1391-1398 (1965).

88. Yong, F.C. & King, T.E. Optical Rotatory Dispersion of Some c' and cc' Cytochromes. *Journal of Biological Chemistry* **245**, 2457-2464 (1970).

89. Nagai, M., Nagai, Y., Imai, K. & Neya, S. Circular dichroism of hemoglobin and myoglobin. *Chirality* **26**, 438-442 (2014).

90. Hsu, M.C. & Woody, R.W. The origin of the heme Cotton effects in myoglobin and hemoglobin. *J Am Chem Soc* **93**, 3515-3525 (1971).

91. Pielak, G.J., Oikawa, K., Mauk, A.G., Smith, M. & Kay, C.M. Elimination of the negative soret Cotton effect of cytochrome c by replacement of the invariant phenylalanine using site-directed mutagenesis. *J Am Chem Soc* **108**, 2724-2727 (1986).

92. Bowler, B.E. Thermodynamics of protein denatured states. *Mol Biosyst* **3**, 88-99 (2007).

93. Godbole, S., Dong, A., Garbin, K. & Bowler, B.E. A lysine 73-->histidine variant of yeast iso-1-cytochrome c: evidence for a native-like intermediate in the unfolding pathway and implications for m value effects. *Biochemistry* **36**, 119-126 (1997).

94. Paradisi, A. *et al.* Met80 and Tyr67 affect the chemical unfolding of yeast cytochrome c: comparing the solution vs. immobilized state. *RSC Chemical Biology* **1**, 421-435 (2020).

95. Elove, G.A., Bhuyan, A.K. & Roder, H. Kinetic mechanism of cytochrome c folding: involvement of the heme and its ligands. *Biochemistry* **33**, 6925-6935 (1994).

96. Colon, W., Wakem, L.P., Sherman, F. & Roder, H. Identification of the predominant non-native histidine ligand in unfolded cytochrome c. *Biochemistry* **36**, 12535-12541 (1997).

97. Godbole, S. & Bowler, B.E. A histidine variant of yeast iso-1-cytochrome c that strongly affects the energetics of the denatured state. *J Mol Biol* **268**, 816-821 (1997).

98. Hammack, B.N., Smith, C.R. & Bowler, B.E. Denatured state thermodynamics: residual structure, chain stiffness and scaling factors. *J Mol Biol* **311**, 1091-1104 (2001).

99. Bandi, S. & Bowler, B.E. Effect of an Ala81His Mutation on the Met80 Loop Dynamics of Iso-1-cytochrome c. *Biochemistry* **54**, 1729-1742 (2015).

100. Battistuzzi, G. *et al.* Effects of mutational (Lys to Ala) surface charge changes on the redox properties of electrode-immobilized cytochrome c. *J Phys Chem B* **111**, 10281-10287 (2007).

101. Berghuis, A.M., Guillemette, J.G., Smith, M. & Brayer, G.D. Mutation of tyrosine-67 to phenylalanine in cytochrome c significantly alters the local heme environment. *J Mol Biol* **235**, 1326-1341 (1994).

102. Casalini, S., Battistuzzi, G., Borsari, M., Ranieri, A. & Sola, M. Catalytic reduction of dioxygen and nitrite ion at a Met80Ala cytochrome c-functionalized electrode. *J Am Chem Soc* **130**, 15099-15104 (2008).

103. Casalini, S. *et al.* Electron Transfer Properties and Hydrogen Peroxide Electrocatalysis of Cytochrome c Variants at Positions 67 and 80. *The Journal of Physical Chemistry B* **114**, 1698-1706 (2010).

104. Battistuzzi, G., Borsari, M. & Sola, M. Redox properties of cytochrome c. *Antioxid Redox Sign* **3**, 279-291 (2001).

105. Battistuzzi, G., Borsari, M. & Sola, M. Medium and temperature effects on the redox chemistry of cytochrome c. *Eur J Inorg Chem*, 2989-3004 (2001).

106. Dixon, D.W., Hong, X. & Woehler, S.E. Electrostatic and Steric Control of Electron Self-Exchange in Cytochromes C, C551, and B5. *Biophysical journal* **56**, 339-351 (1989).

107. Solmaz, S.R.N. & Hunte, C. Structure of complex III with bound cytochrome c in reduced state and definition of a minimal core interface for electron transfer. *Journal of Biological Chemistry* **283**, 17542-17549 (2008).

108. Sakamoto, K. *et al.* NMR basis for interprotein electron transfer gating between cytochrome c and cytochrome c oxidase. *Proc Natl Acad Sci U S A* **108**, 12271-12276 (2011).

109. Shimada, S. *et al.* Complex structure of cytochrome c-cytochrome c oxidase reveals a novel protein-protein interaction mode. *Embo J* **36**, 291-300 (2017).

110. Wallace, C.J. & Clark-Lewis, I. Functional role of heme ligation in cytochrome c. Effects of replacement of methionine 80 with natural and non-natural residues by semisynthesis. *The Journal of biological chemistry* **267**, 3852-3861 (1992).

111. Bren, K.L. & Gray, H.B. Structurally Engineered Cytochromes with Novel Ligand-Binding Sites - Oxy and Carbonmonoxy Derivatives of Semisynthetic Horse Heart Ala80 Cytochrome-C. *J Am Chem Soc* **115**, 10382-10383 (1993).

112. Rose, G., Geselowitz, A., Lesser, G., Lee, R. & Zehfus, M. Hydrophobicity of amino acid residues in globular proteins. *Science* **229**, 834-838 (1985).

113. Lett, C.M. & Guillemette, J.G. Increasing the redox potential of isoform 1 of yeast cytochrome c through the modification of select haem interactions. *Biochem J* **362**, 281-287 (2002).

114. Bortolotti, C.A. *et al.* The redox chemistry of the covalently immobilized native and low-pH forms of yeast iso-1-cytochrome c. *J Am Chem Soc* **128**, 5444-5451 (2006).

115. Battistuzzi, G. *et al.* Role of Met80 and Tyr67 in the low-pH conformational equilibria of cytochrome c. *Biochemistry* **51**, 5967-5978 (2012).

116. McClelland, L.J., Mou, T.C., Jeakins-Cooley, M.E., Sprang, S.R. & Bowler, B.E. Structure of a mitochondrial cytochrome c conformer competent for peroxidase activity. *P Natl Acad Sci USA* **111**, 6648-6653 (2014).

117. McClelland, L.J. *et al.* The response of Omega-loop D dynamics to truncation of trimethyllysine 72 of yeast iso-1-cytochrome c depends on the nature of loop deformation. *J Biol Inorg Chem* **20**, 805-819 (2015).

118. Pollock, W.B.R., Rosell, F.I., Twitchett, M.B., Dumont, M.E. & Mauk, A.G. Bacterial expression of a mitochondrial cytochrome c. Trimethylation of Lys72 in yeast iso-1-cytochrome c and the alkaline conformational transition. *Biochemistry* **37**, 6124-6131 (1998).

119. Nold, S.M., Lei, H.T., Mou, T.C. & Bowler, B.E. Effect of a K72A Mutation on the Structure, Stability, Dynamics, and Peroxidase Activity of Human Cytochrome c. *Biochemistry* **56**, 3358-3368 (2017).

120. Lu, Y., Casimiro, D.R., Bren, K.L., Richards, J.H. & Gray, H.B. Structurally Engineered Cytochromes with Unusual Ligand-Binding Properties - Expression of Saccharomyces-Cerevisiae Met-80-]Ala Iso-1-Cytochrome-C. *P Natl Acad Sci USA* **90**, 11456-11459 (1993).

121. Bertini, I., Gray, H.B., Stiefel, E.I. & Valentine, J.S. *Biological inorganic chemistry : structure and reactivity*. (University Science Books, Sausalito, Calif.; 2007).

122. Beratan, D.N., Betts, J.N. & Onuchic, J.N. Protein electron transfer rates set by the bridging secondary and tertiary structure. *Science* **252**, 1285-1288 (1991).

123. Gu, J. *et al.* Control of cytochrome c redox reactivity through off-pathway modifications in the protein hydrogen-bonding network. *Chemical communications (Cambridge, England)* **50**, 5355-5357 (2014).

124. Alvarez-Paggi, D. *et al.* Electrostatically Driven Second-Sphere Ligand Switch between High and Low Reorganization Energy Forms of Native Cytochrome c. *J Am Chem Soc* **135**, 4389-4397 (2013).

125. Alvarez-Paggi, D., Zitare, U. & Murgida, D.H. The role of protein dynamics and thermal fluctuations in regulating cytochrome c/cytochrome c oxidase electron transfer. *Biochim Biophys Acta* **1837**, 1196-1207 (2014).

126. Valderrama, B. & Vazquez-Duhalt, R. Electron-balance during the oxidative self-inactivation of cytochrome c. *Journal of Molecular Catalysis B: Enzymatic* **35**, 41-44 (2005).

127. Tomášková, N. *et al.* Early modification of cytochrome c by hydrogen peroxide triggers its fast degradation. *International journal of biological macromolecules* **174**, 413-423 (2021).

128. Zhong, F. & Pletneva, E.V. Ligation and Reactivity of Methionine-Oxidized Cytochrome c. *Inorg Chem* **57**, 5754-5766 (2018).

129. Adams, P.A. The Peroxidasic Activity of the Heme Octapeptide Microperoxidase-8 (Mp-8) - the Kinetic Mechanism of the Catalytic Reduction of H2o2 by Mp-8 Using 2,2'-Azinobis-(3-Ethylbenzothiazoline-6-Sulfonate) (Abts) as Reducing Substrate. *J Chem Soc Perk T 2,* 1407-1414 (1990).

130. Marques, H.M. Insights into porphyrin chemistry provided by the microperoxidases, the haempeptides derived from cytochrome c. *Dalton T*, 4371-4385 (2007).

131. Cherney, M.M., Junior, C.C. & Bowler, B.E. Mutation of Trimethyllysine 72 to Alanine Enhances His79-Heme-Mediated Dynamics of Iso-1-cytochrome c. *Biochemistry* **52**, 837-846 (2013).

132. Chreifi, G. *et al.* Crystal structure of the pristine peroxidase ferryl center and its relevance to proton-coupled electron transfer. *Proc Natl Acad Sci U S A* **113**, 1226-1231 (2016).

133. Hu, W.B., Kan, Z.Y., Mayne, L. & Englander, S.W. Cytochrome c folds through foldon-dependent native-like intermediates in an ordered pathway. *P Natl Acad Sci USA* **113**, 3809-3814 (2016).

134. Maity, H., Maity, M. & Englander, S.W. How cytochrome c folds, and why: Submolecular foldon units and their stepwise sequential stabilization. *J Mol Biol* **343**, 223-233 (2004).

135. Tomášková, N., Varhač, R., Lysáková, V., Musatov, A. & Sedlák, E. Peroxidase activity of cytochrome c in its compact state depends on dynamics of the heme region. *Biochimica et Biophysica Acta (BBA) - Proteins and Proteomics* **1866**, 1073-1083 (2018).

136. Pierce, M.M. & Nall, B.T. Coupled kinetic traps in cytochrome c folding: His-Heme misligation and proline isomerization11Edited by C. R. Matthews. *J Mol Biol* **298**, 955-969 (2000).

137. Pierce, M.M. & Nall, B.T. Fast folding of cytochrome c. *Protein science : a publication of the Protein Society* **6**, 618-627 (1997).

138. Hammack, B., Godbole, S. & Bowler, B.E. Cytochrome c folding traps are not due solely to histidine-heme ligation: direct demonstration of a role for N-terminal amino group-heme ligation11Edited by P. E. Wright. *J Mol Biol* **275**, 719-724 (1998).

139. Babul, J. & Stellwagen, E. The existence of heme-protein coordinate-covalent bonds in denaturing solvents. *Biopolymers* **10**, 2359-2361 (1971).

140. Muthukrishnan, K. & Nall, B.T. Effective concentrations of amino acid side chains in an unfolded protein. *Biochemistry* **30**, 4706-4710 (1991).

141. Godbole, S., Hammack, B. & Bowler, B.E. Measuring denatured state energetics: deviations from random coil behavior and implications for the folding of iso-1-cytochrome c. *J Mol Biol* **296**, 217-228 (2000).

142. Pletneva, E.V., Gray, H.B. & Winkler, J.R. Many faces of the unfolded state: Conformational heterogeneity in denatured yeast cytochrome c. *J Mol Biol* **345**, 855-867 (2005).

143. Mayne, L. & Englander, S.W. Two-state vs. multistate protein unfolding studied by optical melting and hydrogen exchange. *Protein Sci* **9**, 1873-1877 (2000).

144. Krishna, M.M.G., Maity, H., Rumbley, J.N., Lin, Y. & Englander, S.W. Order of steps in the cytochrome c folding pathway: Evidence for a sequential stabilization mechanism. *J Mol Biol* **359**, 1410-1419 (2006).

145. Maity, H., Maity, M., Krishna, M.M.G., Mayne, L. & Englander, S.W. Protein folding: The stepwise assembly of foldon units. *P Natl Acad Sci USA* **102**, 4741-4746 (2005).

146. Bai, Y.W., Sosnick, T.R., Mayne, L. & Englander, S.W. Protein-Folding Intermediates - Native-State Hydrogen-Exchange. *Science* **269**, 192-197 (1995).

147. McClelland, L.J. & Bowler, B.E. Lower Protein Stability Does Not Necessarily Increase Local Dynamics. *Biochemistry* **55**, 2681-2693 (2016).

148. Kawai, C. *et al.* pH-Sensitive Binding of Cytochrome c to the Inner Mitochondrial Membrane. Implications for the Participation of the Protein in Cell Respiration and Apoptosis. *Biochemistry* **48**, 8335-8342 (2009).

149. Oellerich, S., Lecomte, S., Paternostre, M., Heimburg, T. & Hildebrandt, P. Peripheral and Integral Binding of Cytochrome c to Phospholipids Vesicles. *The Journal of Physical Chemistry B* **108**, 3871-3878 (2004).

150. Pandiscia, L.A. & Schweitzer-Stenner, R. Coexistence of Native-like and Non-Native Partially Unfolded Ferricytochrome c on the Surface of Cardiolipin-Containing Liposomes. *The Journal of Physical Chemistry B* **119**, 1334-1349 (2015).

151. Rajagopal, B.S., Silkstone, G.G., Nicholls, P., Wilson, M.T. & Worrall, J.A.R. An investigation into a cardiolipin acyl chain insertion site in cytochrome c. *Bba-Bioenergetics* **1817**, 780-791 (2012).

152. Kalanxhi, E. & Wallace, C.J.A. Cytochrome c impaled: Investigation of the extended lipid anchorage of a soluble protein to mitochondrial membrane models. *Biochem J* **407**, 179-187 (2007).

153. Pandiscia, L.A. & Schweitzer-Stenner, R. Coexistence of Native-Like and Non-Native Cytochrome c on Anionic Liposomes with Different Cardiolipin Content. *The Journal of Physical Chemistry B* **119**, 12846-12859 (2015).

154. Deacon, O.M. *et al.* Heightened Dynamics of the Oxidized Y48H Variant of Human Cytochrome c Increases Its Peroxidatic Activity. *Biochemistry* **56**, 6111-6124 (2017).

155. Worrall, J.A.R., van Roon, A.-M.M., Ubbink, M. & Canters, G.W. The effect of replacing the axial methionine ligand with a lysine residue in cytochromec-550 from Paracoccus versutus assessed by X-ray crystallography and unfolding. *The FEBS Journal* **272**, 2441-2455 (2005).

156. Diederix, R.E.M., Ubbink, M. & Canters, G.W. The peroxidase activity of cytochrome c-550 from Paracoccus versutus. *Eur J Biochem* **268**, 4207-4216 (2001).

157. Ladokhin, A.S. & White, S.H. Protein Chemistry at Membrane Interfaces: Non-additivity of Electrostatic and Hydrophobic Interactions. *J Mol Biol* **309**, 543-552 (2001).

158. Seelig, J. Thermodynamics of lipid–peptide interactions. *Biochimica et Biophysica Acta (BBA) - Biomembranes* **1666**, 40-50 (2004).

159. Poolman, B., Spitzer, J.J. & Wood, J.M. Bacterial osmosensing: roles of membrane structure and electrostatics in lipid–protein and protein–protein interactions. *Biochimica et Biophysica Acta (BBA) - Biomembranes* **1666**, 88-104 (2004).

160. Spitzer, J.J. & Poolman, B. Electrochemical structure of the crowded cytoplasm. *Trends Biochem Sci* **30**, 536-541 (2005).

161. McLaughlin, S. & Aderem, A. The myristoyl-electrostatic switch: a modulator of reversible protein-membrane interactions. *Trends in Biochemical Sciences* **20**, 272-276 (1995).

162. Rostislavleva, K. *et al.* Structure and flexibility of the endosomal Vps34 complex reveals the basis of its function on membranes. *Science* **350**, aac7365 (2015).

163. Popelka, H. *et al.* Membrane Binding and Homodimerization of Atg16 Via Two Distinct Protein Regions is Essential for Autophagy in Yeast. *J Mol Biol* **433**, 166809 (2021).

164. Ranieri, A. *et al.* A bis-histidine-ligated unfolded cytochrome c immobilized on anionic SAM shows pseudo-peroxidase activity. *Electrochemistry Communications* **14**, 29-31 (2012).

165. Seddon, A.M., Curnow, P. & Booth, P.J. Membrane proteins, lipids and detergents: not just a soap opera. *Biochimica et Biophysica Acta (BBA) - Biomembranes* **1666**, 105-117 (2004).

166. Mandal, A. *et al.* Structural Changes and Proapoptotic Peroxidase Activity of Cardiolipin-Bound Mitochondrial Cytochrome c. *Biophysical journal* **109**, 1873-1884 (2015).

167. Spooner, P.J.R. & Watts, A. Cytochrome c interactions with cardiolipin in bilayers: a multinuclear magic-angle spinning NMR study. *Biochemistry* **31**, 10129-10138 (1992).

Chapter 8

Calorimetric Characterization of Proton-Coupled Electron Transfer Thermodynamics in *R. rubrum* Cytochrome c_2

Preparation of the *R. rubrum* cyt c_2 WT plasmid was prepared by Dr. Fangfang Zhong.

Preparation of the *R. rubrum* cyt c_2 plasmid containing a H42F mutation was prepared by Jessica Carpenter.

The compound $Co(terpy)_2(CF_3SO_3)_2$ was synthesized by Dr. Alexandre Pletnev.

Introduction

Many metalloproteins have mechanisms to deliver protons and electrons in PCET mechanisms with high specificity and control,[1-4] using simple amino acids to form proton and electron channels to catalyze and control complex chemical reactions in the metal centers.[5] The development of experimental methods has increased our knowledge of how these mechanisms play out in metalloproteins, and theoretical descriptions of ET,[6, 7] PT,[8] and PCET[9, 10] mechanisms has provided a basis to provide many of the explanations for these processes in biological systems. However, there is a gap in understanding how these transfer mechanisms are controlled in metalloproteins. Although much is known about the biological ET, understanding of biological PT is lacking in comparison.

This gap in knowledge for PT compared to ET arises in part due to the differences between electrons and protons, and different complexities involved in studying these different pathways. Many ET mechanisms in proteins utilize metal cofactors that have distinct spectroscopic and/or chemical properties compared to other components of the protein.[11, 12] Unique properties of the metal have been utilized to study biomolecular ET mechanisms, such as by attaching electron donors to the polypeptide to induce ET,[13] or replacing the metal.[14] Besides metal centers, residues in the polypeptide chain are involved in ET pathways. The residues can provide structural support to increase coupling between the metal centers as observed in azurin dimers,[15] provide redox active Tyr or Trp residues that allow electron (hole) hopping through long distances, [1, 5, 13, 16] or provide through-bond pathways through the polypeptide backbone as observed in studies with yeast cyt *c*.[17] In combination with mutational studies, mechanisms of biological ET has been extensively studied and well-characterized in many protein systems.[18]

Like ET, biological PT mechanisms can also involve the metal cofactor and the polypeptide chain. PT occurs within HB distances, and involves multiple titratable groups, such as amino acid residues or the porphyrin molecule, that can donate or accept protons in multiple HB relays to transfer protons over long distances.[5] Although there are powerful spectroscopic methods to track protons in biological systems such as ^{1}H NMR,[12] identifying and assigning ionizing groups can be complicated.[19] In proteins, many amino acids have titratable groups with pK_a values in the physiological range.[3] Further, depending on the solvent accessibility of the residue and properties of the nearby residues, pK_a of an amino acid residue can shift dramatically. For example, a wide range of pK_a values for surface His residues and heme propionate groups between similar *c*-type cytochromes are observed.[20] Local conformational rearrangements and slight structural changes within the protein can also affect the pK_a of the titratable groups, and complicate the efforts in differentiating the groups participating in the PT pathway. These challenges are amplified in large metalloproteins, where many more titrating groups are present and spectroscopic signatures of these groups are more likely to overlap.[19]

Since we are interested in understanding the thermodynamics of PT, we have decided to characterize a PCET mechanism of a small protein, *R. rubrum* cyt c_2. Like the well-studied counterpart cyt *c* in the *c*-type family, cyt c_2 also has a covalently bound heme, with Met91 and His18 as axial heme ligands. Unlike cyt *c*, cyt c_2 has a pH-dependent reduction potential in the native Met-ligated state, with pK_a values at neutral pH and at mildly acidic pH conditions.[21, 22] Previously, many studies have been performed to identify the ionizing group responsible for the pH-dependent reduction potential, mainly by attempting to assign the pK_a of protons in the heme porphyrin and ionizable amino acids

using ^{1}H and ^{15}N NMR spectroscopy.[23-25] Analysis of these NMR measurements have suggested His42, or a combination of His42 and a nearby HP7 within a HB distance (Figure 8.1) to be a potential candidate to be the source of the pH-dependent reduction potential.[20, 22-27 20, 23] In a similar *c*-type cytochrome, cyt c_{551}, examination of ^{1}H NMR spectra and reduction potential measurements have suggested that HP7 is the sole ionizing group in PCET, despite having a nearby histidine residue similar to cyt c_2.[28] A recent study with a model porphyrin compound has shown that proton transfer can occur through the heme propionate,[29] making HP7 a potential candidate in PCET mechanism.

Identifying ionizing groups solely based on pK_a assignments can be misleading and experimental limitations have complicated many attempts to characterize the ionizing group in the PCET mechanism of cyt c_2. Signs of conformational rearrangement in cyt c_2 have been observed,[26, 27] and line broadening complicated many of the NMR studies,[23] Thus, additional characterization will help clarify the PCET mechanism in cyt c_2. Thermodynamic characterization, independent of spectroscopic data, can provide additional information to better understand the PCET mechanism in cyt c_2. PT involving breaking and forming HBs should be thermodynamically observable, and such thermodynamic characterizations to obtain ionization constants for amino acid residues in protein have been previously performed by NMR and van't Hoff analysis in myoglobin.[30] Although thermodynamic characterizations using ^{1}H NMR are possible, we opted to use isothermal titration calorimetry (ITC) to measure the thermodynamics of PCET reactions in cyt c_2 to avoid complications in interpreting the pH-dependent changes in spectra that were previously observed. [23, 26, 27] Calorimetric measurements can distinguish the molecular groups that participate in PT due to their different ionization enthalpies.[31]

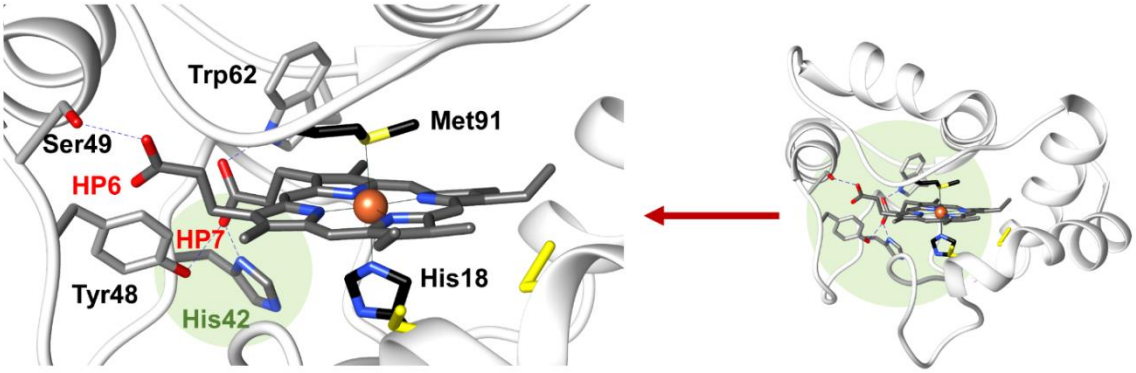

Figure 8.1. Structure of *R. rubrum* cyt c_2 (PDB ID 3C2C), with the inner HB network shown (left). His42 is HB to HP7 and is proposed to participate in the PCET mechanism in cytc_2. Of the residues forming HB contacts with the HP groups, His42 is the only residue with a pK_a that will fall within the pH range PCET reactions are observed in WT cyt c_2. H42F variant is designed to break the HB between the residue 42 and HP7, which should theoretically eliminate a proton donor in the PCET mechanism without perturbing the heme pocket.

Although ITC is commonly used to characterize binding reactions, [32, 33] it can also be used to characterize other reactions in metalloproteins. Besides binding studies, ITC has also been utilized in characterizing ET mechanisms in cyt *c* and inorganic complexes,[34] making it a useful tool to characterize thermodynamic properties in non-binding reactions. A theoretical model has been previously developed for characterizing PT using ITC,[35] and ET-coupled ligand switch mechanisms in yeast cyt *c* that thermodynamically mimics PCET systems has been recently characterized using ITC.[19]

This chapter provides a calorimetric characterization of the PCET mechanism in *R. rubrum* cytc_2. Previous spectroscopic studies have suggested that His42 is the ionizable group in the cyt c_2 PCET mechanism. To test this hypothesis, WT and H42F variant of *R. rubrum* cyt c_2 are compared to see whether absence of His42 shows differences in the thermodynamics of PCET. Calorimetric measurements at pH conditions ranging from 7.8 up to 6.6 suggest that elimination of His42 greatly alters the pH-dependent thermodynamic profile for PCET. Perturbation of the PCET thermodynamic profile in H42F variant confirms that His42 is an essential participant in the PCET mechanism. Participation of HP7 as an ionizable group is not ruled out, as its participation in the PCET mechanism could not be confirmed. Previous electrochemical measurements have shown that the reduction potential of H42F varies with pH. Reduction potentials of the variants obtained from calorimetric measurements are presented, and possible explanations to observed variations in H42F are also presented.

Materials and Methods

General. All solutions and buffers were prepared using water from Barnstead E-Pure Ultrapure Water Purification System, purified to a resistivity of 18 MΩ cm, pH adjusted

with ± 0.02 accuracy using an AB15 pH meter (Fischer Scientific). Data analyses and visualizations were performed using Matlab R2017a-R2019a (MathWorks), MicroCal PEAQ-ITC Analysis Software (Malvern), Excel (Microsoft) and Chimera v.1.10.2 (UCSF). Reagents were purchased from Sigma-Aldrich unless noted otherwise. The compound $Co(terpy)_2(CF_3SO_3)_2$ was synthesized by Dr. Alexandre Pletnev.

Site-Directed Mutagenesis, Protein Expression, and Purification A pET22b(+) plasmid system containing the WT sequence for *R. rubrum* cyt c_2 with carbenicillin and ampicillin resistance was provided by Dr. Fangfang Zhong. Cyt c_2 plasmid containing the H42F mutation was provided by Jessica Carpenter. Protein expression and purification were performed as previously described.[36]

Protein stocks were concentrated and exchanged into a 100 mM sodium phosphate buffer at pH 7.4 and stored at 4 °C. Since signs of protein aggregation were observed, protein stocks were freshly repurified by ion-exchange chromatography and centrifuged at 13,000 rpm for 1 min using a tabletop centrifuge prior to use. Differences in the UV-vis were not observed between the protein samples from the concentrated stocks, and repurification using an ion-exchange column did not yield any differences in the absorption spectra.

ITC. All buffers contained 10 mM buffer, with the final ionic concentrations adjusted with NaCl to μ = 0.1 M, with pH ranges from 5.6 to 7.8 in 0.2 pH increments. Temperature coefficients were considered, and pH was adjusted for use at 25 °C. Buffers used were as follows: MOPS (pH 7.8 to 6.8), Tris (pH 7.8 to 7.0), citrate (pH 7.2 to 6.0), bisTris (pH 7.2 to 6.0), phosphate (pH 7.8 to 6.2), MES (pH 6.6 to 5.6), acetate (pH 5.6), piperazine (pH 6.2 to 5.6), ACES (pH 6.6 to 6.0) and TES (pH 7.8 to 6.8). For each pH condition,

experiments were repeated with at least three different buffers, unless otherwise noted. All solutions were freshly prepared and degassed prior to use.

All sample preparations were performed in a N_2-filled glovebox (COY Laboratory Products). Ferric proteins were prepared with excess ferricyanide ($K_3Fe(CN)_6$) and ferrous proteins prepared with excess dithionite, and buffer-exchanged into a desired buffer by size exclusion columns (PD-10 desalting column, GE Healthcare) to remove the oxidant or the reductant. Columns were pretreated with either ferricyanide or dithionite and washed with a desired buffer prior to loading the columns with the stock protein solution. Concentrations of the protein samples were obtained from the absorption of the Soret band ($\varepsilon_{412,\,ox}$ = 118.4 $mM^{-1}cm^{-1}$ for WT and $\varepsilon_{415,\,red}$ = 131.5 $mM^{-1}cm^{-1}$ for WT and H42F).[36] All protein stock solutions used in the electrochemical titrations contained 70 to 180 μM of protein.

$Co(terpy)_2(CF_3SO_3)_2$ ($E°$ = 270 mV in a pH 6.5 phosphate buffer at μ = 0.1 M)[37] and $K_3Fe(CN)_6$ ($E°$ = 420 mV, in a pH 7.2 Tris buffer at μ = 0.1 M)[38] were used either as an oxidant or a reductant, respectively. Stock solutions containing these compounds were prepared in appropriate buffers, and concentrations measured spectroscopically ($[Co(terpy)_2]^{2+}$, ε_{505} = 1.4 $mM^{-1}cm^{-1}$, assuming $\varepsilon_{510} = \varepsilon_{505}$; $[Fe(CN)_6]^{3-}$, ε_{420} = 1 $mM^{-1}cm^{-1}$).[34, 39] All stock solutions containing $[Co(terpy)_2]^{2+}$ or $[Fe(CN)_6]^{3-}$ ranged from 1 to 3 mM.

Stock solutions of electrochemical compounds were titrated into protein solutions (Figure 8.2) using a MicroCal PEAQ-ITC instrumentation (Malvern). Each run consisted of 30 to 35 injections with 180 seconds/injection and stirring speed of 750 rpm, at 25.0 ± 0.2 °C.

Figure 8.2. (A) A schematic of the ITC instrumentation is shown (left). Sample cell contains protein, and a set amount of titrant (oxidant or reductant in this study) is injected into the sample cell. Depending on whether the reaction is exothermic or endothermic, the instrument regulates the temperature to make sure the temperature of the sample is consistent with the temperature read-out in the reference cell. Readout of the reaction details the amount of energy required to cool (exothermic reaction) or heat (endothermic reaction) the sample cell throughout the course of the reaction (right). (B) Parameters obtained from a typical ITC measurement are shown, where the reaction is assumed to be a binding reaction. Thermograms are baseline adjusted and peaks integrated, and concentration normalized to present a binding isotherm. Slope of the titration curve provides the observed equilibrium constant, K_{ITC}, total difference in the heat provides the observed heat of the reaction, ΔH_{ITC}, and the mid-point of the titration curve provides the total stoichiometry of the reaction, N, based on the syringe-to-cell molar ratio.[40]

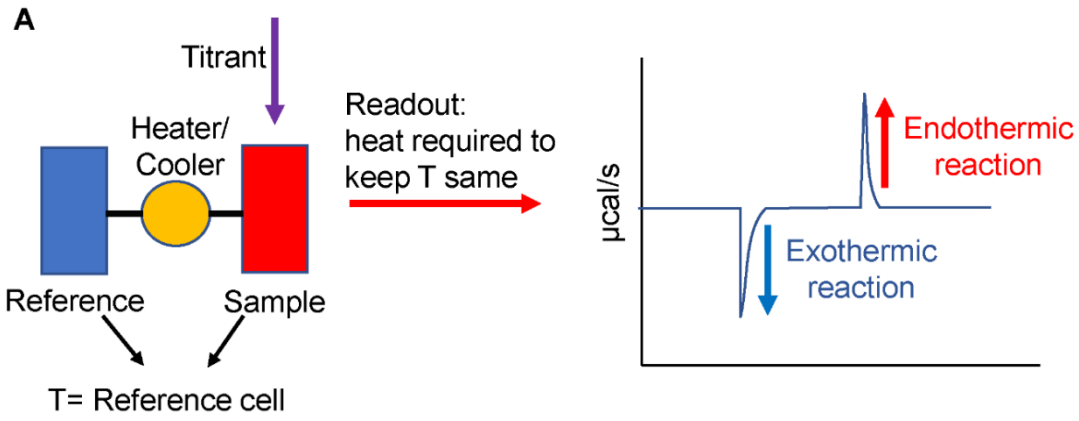
A
Titrant
Heater/
Cooler
Reference
Sample
T= Reference cell
Readout:
heat required to
keep T same
µcal/s
Endothermic
reaction
Exothermic
reaction

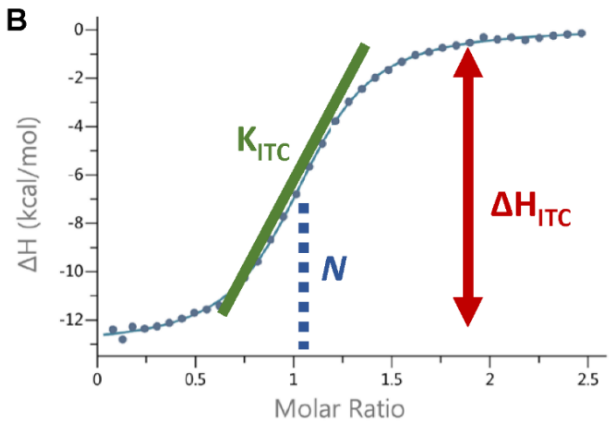
B
ΔH (kcal/mol)
0
-2
-4
-6
-8
-10
-12
0
0.5
1
1.5
2
2.5
Molar Ratio
K_ITC
N
ΔH_ITC

Initial 10 injections contained injection volumes ranged from 0.5 to 0.8 µl/injection for the initial 10 injections, subsequent injection volumes increased to total of 1µl/injection for up to 20 injections, and last 5 injections contained injection volumes of 2 µl/injection. Injections were timed to ensure that the peaks observed in the raw data returned to equilibrium prior to additional injections.

During each injection, the ITC instrument adjusted the amount of power applied to the sample cell to maintain the same temperature (isothermal) between the reference cell and the sample cell. In the case of an exothermic reaction, the instrument reduced the amount of power applied to the sample cell, and a downward peak was observed in the raw data; the reverse was observed for an endothermic reaction (Figure 8.2).[40] Before each experiment, the difference in power between the reference and sample cell (DP) value at equilibration step was ensured to be between 5 and 6 µcal/s.

All ITC experiments were conducted within the accepted *c*-window ($1 \times 10^4 < K < 1 \times 10^7$).[32] Most titrations were repeated 2-4 times under each buffer and pH conditions. For some conditions, repeat measurements were not made and error bars were not obtained. All measurements were conducted under constant purge of N_2 inside a custom-made plexiglass glovebox. Data analyses were performed using the Microcal PEAQ-ITC Analysis software (Malvern), and fits of the generated integrated isotherms obtained using a one-site binding model.[40] Titrations with $[Fe(CN)_6]^{3-}$ and WT cyt c_2 at lower pH conditions did not yield thermograms within the desired *c*-window ($1 \times 10^4 < K < 1 \times 10^7$),[32, 40] requiring a different compound to be used for the electrochemical titrations with WT cyt c_2 (Figure 8.3).

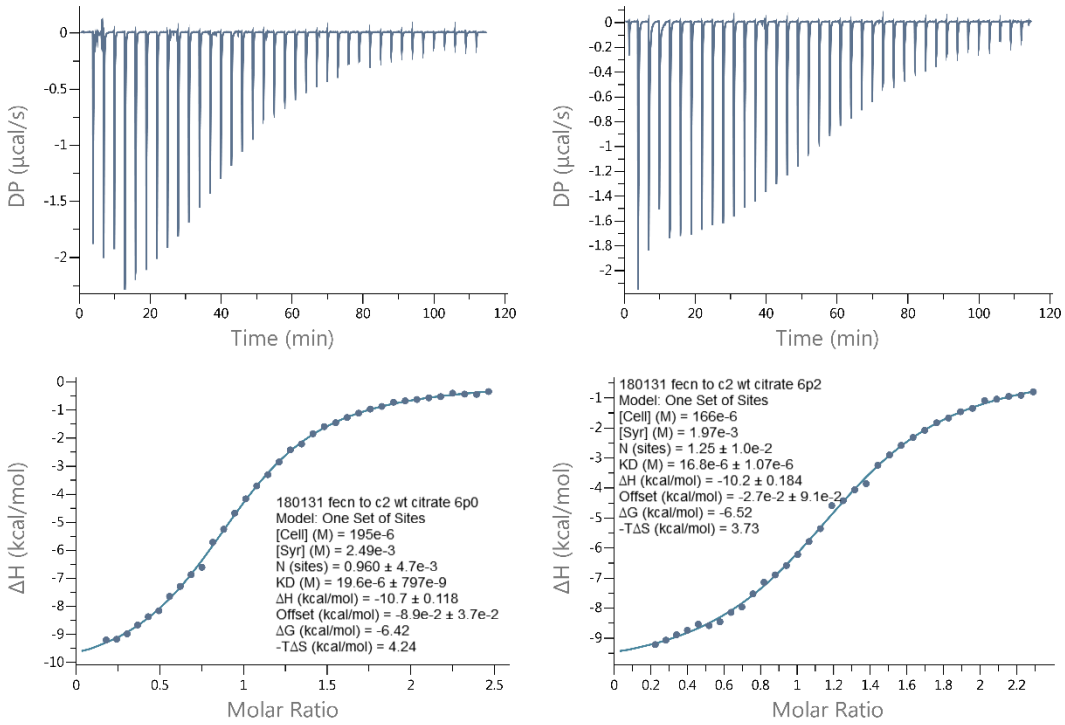

Figure 8.3. Representative thermograms for the oxidation of ferrous WT cyt c_2 with $[Fe(CN)_6]^{3-}$ in a 10 mM citrate phosphate buffer (μ = 0.1 M) at pH 6.0 (left) or at pH 6.2 (right) and 25.0 ± 0.2 °C.

Previous CV measurements showed that the reduction potential of *R. rubrum* cyt c_2 varies by nearly 60 mV with pH (311 ± 2 mV to 370 ± 2 mV from pH 8.0 to 5.0).[36] Since the driving force of the ET reactions are dependent on the difference in the reduction potentials of the electron donor and the acceptor, increased reduction potential of WT cyt c_2 at lower pH ranges would also affect the driving force of the ET reaction. Therefore, $[Fe(CN)_6]^{3-}$ was used as an oxidant at pH 7.8 to 6.8 (Figure 8.4A), while $[Co(terpy)_2]^{2+}$ was used as a reductant at pH 6.6 to 5.6 (Figure 8.4B). Reaction of reduced WT cyt c_2 in the presence of $[Co(terpy)_2]^{2+}$ yielded no heats (Figure 8.5), suggesting that no other significant side reactions occur between $[Co(terpy)_2]^{2+}$ and the reduced protein that contribute to the total observed enthalpy (ΔH_{ITC}). In H42F, $Fe(CN)_6^{3-}$ was an appropriate oxidant for the full pH range considered (Figure 8.4C). Since half reaction enthalpies can be obtained by ITC,[34] calorimetric titrations of $[Co(terpy)_2]^{2+}$ with $[Fe(CN)_6]^{3-}$ were performed to calculate the enthalpy of the half reaction (ΔH_{HR}) for $Co^{3+/2+}$ in the $[Co(terpy)_2]^{2+}$ complex. Calorimetric titrations with the inorganic compounds were performed in a 10 mM phosphate buffer at pH 7.4 and 6.6 with μ = 0.1 M at 25 °C. At pH 7.4, 5.2 mM of $[Fe(CN)_6]^{3-}$ were titrated into 315 μM of$[Co(terpy)_2]^{2+}$, and at pH 6.6, and 4.97 mM of $[Fe(CN)_6]^{3-}$ were titrated into 307 μM of $[Co(terpy)_2]^{2+}$ at pH 7.4.

Results and Analyses

Under certain conditions where PCET occurs, ET of the metal center and PT reactions are coupled and proceed simultaneously.[4] This is the case in cyt c_2, where heme oxidation/reduction reactions of cyt c_2 in ferrous (cyt c_2^{2+}) and ferric (cyt c_2^{3+}) states are coupled with a transfer of a single proton between two protonating groups, A_1 and A_2 (Scheme 8.1).

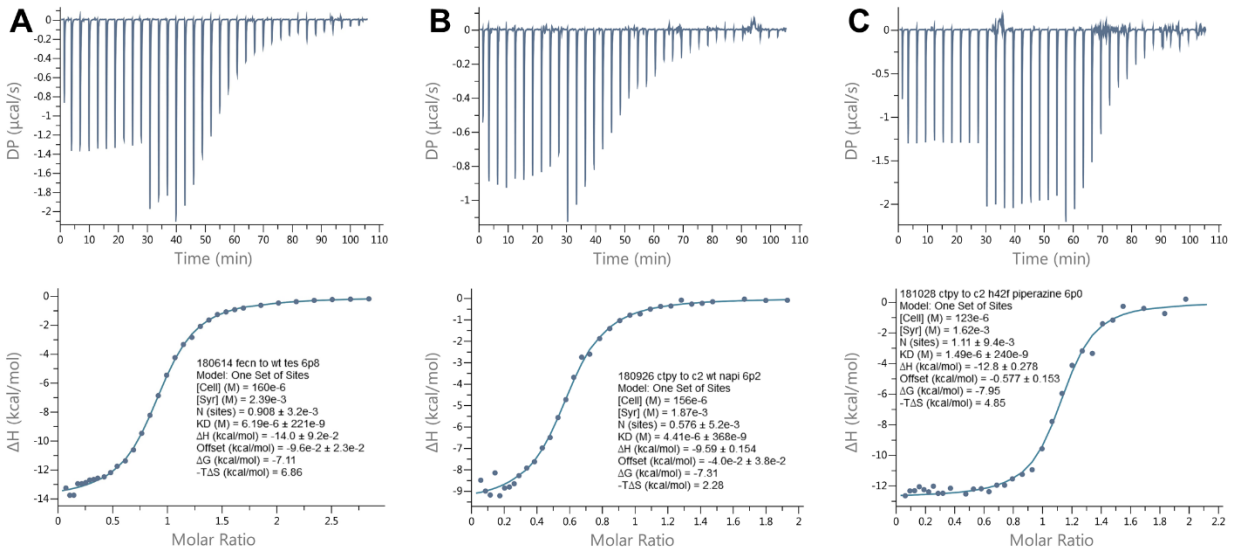

Figure 8.4. Representative thermograms for WT cytc_2 (A) oxidative or (B) reductive titrations, and H42F cytc_2 (C) oxidative titration, with raw (top) and baseline corrected (bottom) thermograms for each reaction.

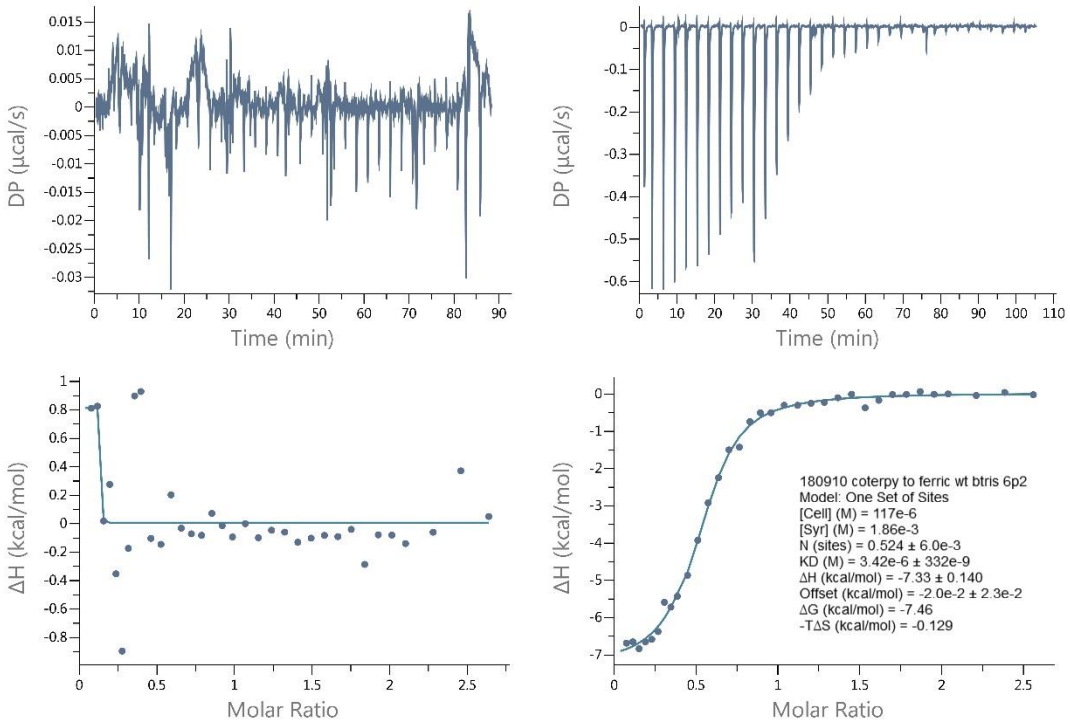

Figure 8.5. Representative thermograms for the titration of ferrous WT cyt c_2 with $[Co(terpy)_2]^{2+}$ (left), compared to the titration of ferric WT cyt c_2 with $[Co(terpy)_2]^{2+}$ (right) in a 10 mM bisTris buffer (μ = 0.1 M) at pH 6.2 and 25.0 ± 0.2 °C.

$$\begin{array}{c} \text{Cyt } c_2^{2+} \\ (A_1H^+ + A_2) \end{array} \rightleftharpoons \begin{array}{c} \text{Cyt } c_2^{3+} \\ (A_1 + A_2H^+) \end{array}$$

(Scheme 8.1)

During PCET, deprotonation of A_1 in the ferrous state is accompanied by the protonation of A_2 in the ferric state.

Fractional Population of the Protonated Species. Based on scheme 8.1, the protein is in different protonation states based on the pK_a of the protonating groups A_1 and A_2. Henderson-Hasselbach equation can be rearranged to describe the fractional population of a species (A) at a given pK_a and pH (eq 8.1):

$$10^{pKa\text{-}pH} = \frac{n_{HA}}{n_A} = \frac{n_{HA}}{1\text{-}n_{HA}}$$

(8.1)

where n_{HA} is the fractional population of the protonated species and n_A is the fractional population of the deprotonated species, and the total fractional population of the species can be expressed as $n_{HA}+n_A = 1$. Rearranging eq 8.1 gives us the fractional population of the protonated species at a given pH for a single species (eq 8.2).

$$n_{HA} = \frac{10^{pKa\text{-}pH}}{(1+10^{pKa\text{-}pH})}$$

(8.2)

Fractional population of protonated species A_1 with pK_{a1} can then be described as (eq 8.3):

$$n_1 = \frac{10^{pKa1\text{-}pH}}{(1+10^{pKa1\text{-}pH})}$$

(8.3)

and the fractional population of protonated species A_2 with pK_{a2} as (eq 8.4):

$$n_2 = \frac{10^{pKa2-pH}}{(1+10^{pKa2-pH})}$$

(8.4)

The net fractional protons as a difference of proton uptake and release from two protonating can be described for a specific pH condition (eq 8.5):

$$\Delta n = n_1 - n_2$$

(8.5)

Calorimetric Characterization of the PCET Mechanism in Cyt *c*$_2$.

Raw thermograms of the titrations show sharp, well-defined peaks, although some noise in the baseline is observed (Figure 8.4). Integration of the raw thermograms gives the following parameters: K_{ITC} (observed equilibrium dissociation constant), N (reaction stoichiometry), and ΔH_{ITC} (enthalpy of the total reaction) (Figure 8.2).[32]

***Calculation of protonation enthalpy in PCET mechanism of cyt c*$_2$.**

ITC measurements report on the total heat of all reactions in the cell (ΔH_{ITC}). This requires consideration of thermodynamic contributions from buffer deprotonation/protonation reactions during PT and from ET reactions of the oxidant (Oxd) or the reductant (Red) in the reaction, in addition to the thermodynamic contributions from the changes within the protein (Scheme 8.2).

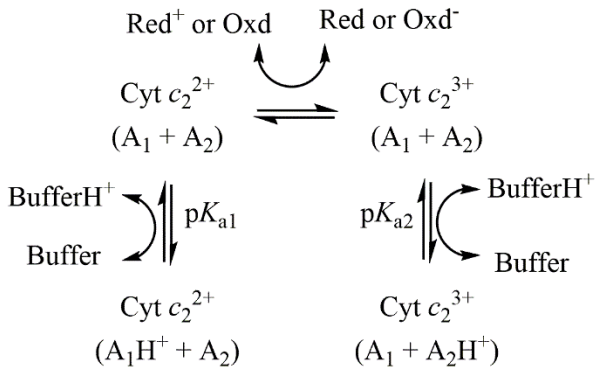

(Scheme 8.2)

In addition to the thermodynamic contributions associated with the half reaction of reduction for the heme ($\Delta H_{HR\ heme}^{3+/2+}$) and ionization enthalpy of protonating groups A_1 (ΔH_1) and A_2 (ΔH_2), there are thermodynamic contributions from ionization of the buffer (ΔH_{ion}) and half reaction enthalpies of reduction associated with the compounds $[Co(terpy)_2]^{2+}$ ($\Delta H_{HR}^{Ctpy3+/2+}$) and $[Fe(CN)_6]^{3-}$ ($\Delta H_{HR}^{FeCN3+/2+}$).

The overall chemical equilibrium describing the oxidation reaction of cyt c_2 can be described as follows (eq 8.6):

$$\text{Oxd} + \text{cyt } c_2^{2+} + (A_1H)_{n1} + (n_2)A_2 + (n_1)\text{Buffer} + (n_2)\text{HBuffer} \rightleftharpoons$$
$$\text{Oxd}^- + \text{cyt } c_2^{3+} + (n_1)A_1 + (n_1)\text{Hbuffer} + (A_2H)_{n2} + (n_2)\text{Buffer} \quad (8.6)$$

Since ITC measures the total heat of the reaction, the total heat of the oxidation reaction ($\Delta H_{ITC,ox}$) is equivalent to the sum of the following reaction components, according to Hess's law (Scheme 8.3):

	Description of Reaction	Reaction	ΔH
1)	Ionization of reduced protein	$A_1H \rightleftharpoons A_1 + H^+$	$+n_1\Delta H_1$
2)	Deionization of buffer	$H^+ + \text{buffer} \rightleftharpoons \text{Hbuffer}$	$-n_1\Delta H_{ion}$
3)	Oxidation of heme in cyt c_2	$\text{heme}^{2+} \rightleftharpoons \text{heme}^{3+}$	$-\Delta H_{HR\ heme}^{3+/2+}$
4)	Reduction of Fe^{3+} in $[Fe(CN)_6]^{3-}$	$Fe^{3+} \rightleftharpoons Fe^{2+}$	$+\Delta H_{HR}^{FeCN3+/2+}$
5)	Deionization of oxidized protein	$A_2 + H^+ \rightleftharpoons A_2H$	$-n_2\Delta H_2$
6)	Ionization of buffer	$\text{Hbuffer} \rightleftharpoons H^+ + \text{buffer}$	$+n_2\Delta H_{ion}$

(Scheme 8.3)

We can then obtain the expression for $\Delta H_{ITC,ox}$ as the sum of ΔH associated with each of the components in the reaction (eq 8.7).

$$\Delta H_{ITC,ox} = (-n_1+n_2)\Delta H_{ion} + (-\Delta H_{HR\ heme}^{3+/2+} + \Delta H_{HR}^{FeCN3+/2+} + n_1\Delta H_1 - n_2\Delta H_2) \quad (8.7)$$

Likewise, the reduction reaction of cyt c_2 can be described as follows (eq 8.8):

$$\text{Red}^+ + \text{Cyt } c_2^{3+} + (n_1)A_1 + (n_1)\text{Hbuffer} + (n_2)A_2H + (n_2)\text{buffer} \rightleftharpoons$$
$$\text{Red} + \text{cyt } c_2^{2+} + (n_1)A_1H + (n_1)\text{buffer} + (n_2)A_2 + (n_2)\text{HBuffer} \quad (8.8)$$

and again, the total heat of the reduction reaction measured in the ITC ($\Delta H_{ITC,re}$) is equivalent to the sum of the following components in the reaction (Scheme 8.4).

	Description of Reaction	Reaction	Change in ΔH
1)	Deionization of reduced protein	$A_1 + H^+ \rightleftharpoons A_1H$	$(-n_1\Delta H_1)$
2)	Ionization of buffer	$\text{Hbuffer} \rightleftharpoons H^+ + \text{buffer}$	$(+n_1\Delta H_{ion})$
3)	Reduction of heme in cyt c_2	$\text{heme}^{3+} \rightleftharpoons \text{heme}^{2+}$	$+\Delta H_{HR}^{heme3+/2+}$
4)	Oxidation of Co^{2+} in $[Co(terpy)_2]^{2+}$	$Co^{2+} \rightleftharpoons Co^{3+}$	$-\Delta H_{HR}^{Ctpy3+/2+}$
5)	Ionization of oxidized protein	$A_2H \rightleftharpoons A_2 + H^+$	$(+n_2\Delta H_2)$
6)	Deionization of buffer	$H^+ + \text{buffer} \rightleftharpoons \text{Hbuffer}$	$(-n_2\Delta H_{ion})$

(Scheme 8.4)

and according to the Hess's Law, rearranging the equation gives the total observed heat (ΔH_{ITC}) (eq 8.9).

$$\Delta H_{ITC,re} = (n_1\text{-}n_2)\Delta H_{ion} + (\Delta H_{HR\ heme}{}^{3+/2+} - \Delta H_{HR}{}^{Ctpy3+/2+} - n_1\Delta H_1 + n_2\Delta H_2) \quad (8.9)$$

Comparison of eqs 8.7 and 8.9 show the relationship between $\Delta H_{ITC,ox}$ and $\Delta H_{ITC,re}$.(eq 8.10).

$$\Delta H_{ITC,\ re} = -\Delta H_{ITC,ox} \quad (8.10)$$

A close inspection of eq 8.7 and 8.9 shows that these equations have the form of a linear expression (y = mx + b), where the slope is the buffer-independent net transfer of protons (Δn), and the intercept is the buffer-independent combined enthalpies of the reaction (ΔH_{inter}). To obtain these parameters, ΔH_{ITC} at various ΔH_{ion} is required. Total heats from electrochemical titrations for WT (Tables 8.1 and 8.2) and H42F (Tables 8.3 and 8.4) cyt c_2 have been measured for various buffers at different pH conditions. Plotting ΔH_{ITC} measured in terms of ΔH_{ion} yields a linear plot (Figures 8.6 to 8.9), where the slope and the intercept at a given pH condition can be obtained. Since the total number of calorimetric measurements for each buffer differed within the same pH conditions, linear fit of the data was performed with entire data set instead of average ΔH_{ITC} for each buffer. Fits of the data obtained from the average values were within error to that of the fits obtained from the entire data set. The slope is the net proton movement of the reaction at a given pH, Δn, and the intercept is the combined enthalpy from the oxidation changes of the protein and the metal compound, and the ionization of the groups involved in the PT (Tables 8.5 and 8.6).

Table 8.1. ΔH_{ITC} for the Oxidation of Ferrous WT cyt c_2[a]

pH	Buffer	ΔH_{ion} (kcal/mol)	ΔH_{ITC} (kcal/mol)
7.8	Tris	11.34	-14.2
	MOPS	5.04	-12.7 ± 0.1
	Phosphate	0.86	-11.7
7.6	Tris	11.34	-14.3
	TES	7.68	-13.1
	MOPS	5.04	-12.6 ± 0.1
	Phosphate	0.86	-11.5 ± 0.1
7.4	Tris	11.34	-14.3
	TES	7.68	-13.4
	MOPS	5.04	-12.7 ± 0.1
	Phosphate	0.86	-11.5 ± 0.1
7.2	Tris	11.34	-14.5
	TES	7.68	-13.9
	BisTris	6.76	-13.3
	MOPS	5.04	-12.7 ± 0.2
	Phosphate	0.86	-11.5 ± 0.1
	Citrate	-0.81	-11.5
7.0	TES	7.68	-13.6
	BisTris	6.76	-13.2 ± 0.8
	MOPS	5.04	-12.8 ± 0.2
	Phosphate	0.86	-11.1 ± 0.1
	Citrate	-0.81	-10.8 ± 0.4
6.8	TES	7.68	-14.0
	BisTris	6.76	-13.3 ± 0.3
	MOPS	5.04	-12.7 ± 0.1
	Phosphate	0.86	-10.8 ± 0.1[b]
	Citrate	-0.81	-10.0 ± 0.2

Table 8.1. Footnotes

[a]Samples were in a 10 mM buffer with μ = 100 mM (ionic strength adjusted with NaCl). Calorimetric measurements monitoring titrations of stock $[Fe(CN)_6]^{3-}$ solution into ferrous WT cyt c_2 were performed at 25.0 ± 0.2 °C. Error bars are standard deviation of the values obtained from multiple measurements, ranging from two to four depending on the buffer. In cases where only single measurements were made, error bars were not included. ΔH_{ion} values are from literature.[31]

[b]Error bar calculated from error propagation using error of individual fits obtained from the ITC software, for multiple runs. This method was utilized when the fitted values were identical to one another and yielded artificial error of zero when compared between values.

Table 8.2. ΔH_{ITC} for the Reduction of Ferric WT cyt c_2[a]

pH	Buffer	ΔH_{ion} (kcal/mol)	ΔH_{ITC} (kcal/mol)
6.6	ACES	7.27	-5.7 ± 0.3
	BisTris	6.76	-7.2 ± 0.1
	Phosphate	0.86	-10.2
	Citrate	-0.81	-11.9 ± 0.6
6.4	ACES	7.27	-7.2 ± 0.2
	BisTris	6.76	-6.4 ± 0.1
	Phosphate	0.86	-10.0 ± 0.4
	Citrate	-0.81	-10.4 ± 0.6
6.2	Piperazine	7.43	-7.3 ± 0.1
	ACES	7.27	-7.7 ± 0.6
	BisTris	6.76	-7.3 ± 0.1
	Phosphate	0.86	-9.6
	Citrate	-0.81	-9.9 ± 0.5
6.0	Piperazine	7.43	-8.0 ± 0.3
	ACES	7.27	-7.8 ± 0.3
	BisTris	6.76	-7.6 ± 0.2
	MES	3.52	-8.8
	Citrate	-0.81	-10.4 ± 0.5
5.8	Piperazine	7.43	-7.9 ± 0.2
	MES	3.52	-8.5
	Citrate	-0.81	-10.5 ± 0.7
5.6	Piperazine	7.43	-8.2 ± 0.1
	Citrate	-0.81	-9.6

[a]Samples were in a 10 mM buffer with μ = 100 mM (ionic strength adjusted with NaCl). Calorimetric measurements monitoring titrations of stock $[Co(terpy)_2]^{2+}$ solution into ferric WT cyt c_2 were performed at 25.0 ± 0.2 °C. Error bars are standard deviation of the values obtained from multiple measurements, ranging from two to four depending on the buffer. In cases where only single measurements were obtained, error bars were not included. ΔH_{ion} values are from literature.[31]

Table 8.3. ΔH_{ITC} for the Oxidation of Ferric H42F cyt c_2 from pH 7.8 to 6.8[a]

pH	Buffer	ΔH_{ion} (kcal/mol)	ΔH_{ITC} (kcal/mol)
7.8	Tris	11.34	-14.1 ± 0.04
	TES	7.68	-12.3
	MOPS	5.07	-12.8
	Phosphate	0.86	-12.5
7.6	Tris	11.34	-14.1 ± 0.05
	TES	7.68	-13.4
	Phosphate	0.86	-12.7 ± 0.05
7.4	Tris	11.34	-13.5
	TES	7.68	-13.1
	BisTris	6.76	-13.5
	Phosphate	0.86	-12.9 ± 0.05
7.2	Tris	11.34	-14.3
	TES	7.68	-13.5
	Phosphate	0.86	-12.9 ± 0.05
	Citrate	-0.81	-12.9
7.0	TES	7.68	-14.1
	BisTris	6.76	-13.5 ± 0.07
	MOPS	5.04	-13.7 ± 0.2
	Phosphate	0.86	-13.2
	Citrate	-0.81	-12.7
6.8	TES	7.68	-13.7
	BisTris	6.76	-13.5
	MOPS	5.04	-13.5 ± 0.1
	Phosphate	0.86	-12.7 ± 0.1
	Citrate	-0.81	-12.2 ± 0.1

[a]Samples were in a 10 mM buffer with μ = 100 mM (ionic strength adjusted with NaCl). Calorimetric measurements monitoring titrations of stock $[Fe(CN)_6]^{3-}$ solution into ferrous H42F cyt c_2 were performed at 25.0 ± 0.2 °C. Error bars are standard deviation of the values obtained from multiple measurements, ranging from two to four depending on the buffer. In cases where only single measurements were obtained, error bars were not included. ΔH_{ion} values are from literature.[31]

Table 8.4. ΔH_{ITC} for the Oxidation of Ferric H42F cyt c_2 from pH 6.6 to 5.6[a]

pH	Buffer	ΔH_{ion} (kcal/mol)	ΔH_{ITC} (kcal/mol)
6.6	ACES	7.27	-12.4 ± 0.8
	BisTris	6.76	-13.6 ± 0.6
	Phosphate	0.86	-11.5
	Citrate	-0.81	-11.8 ± 0.6
6.4	ACES	7.27	-12.1 ± 0.5
	BisTris	6.76	-14.5 ± 0.6
	Citrate	-0.81	-12.1 ± 0.5
6.2	Piperazine	7.43	-13.3 ± 0.1
	ACES	7.27	-11.5 ± 2.3
	BisTris	6.76	-12.6 ± 0.5
	Phosphate	0.86	-12.1
	Citrate	-0.81	-11.6 ± 0.7
6.0	Piperazine	7.43	-14.0 ± 0.8
	ACES	7.27	-13.2
	BisTris	6.76	-13.8 ± 0.4
	Citrate	-0.81	-12.3 ± 0.5
5.8	Piperazine	7.43	-14.5 ± 0.3
	Citrate	-0.81	-12.4 ± 0.8

[a]Samples were in a 10 mM buffer with μ = 100 mM (ionic strength adjusted with NaCl). Calorimetric measurements monitoring titrations of stock $[Fe(CN)_6]^{3-}$ solution into ferrous H42F cyt c_2 were performed at 25.0 ± 0.2 °C. Error bars are standard deviation of the values obtained from multiple measurements, ranging from two to four depending on the buffer. In cases where only single measurements were obtained, error bars were not included. ΔH_{ion} values are from literature.[31]

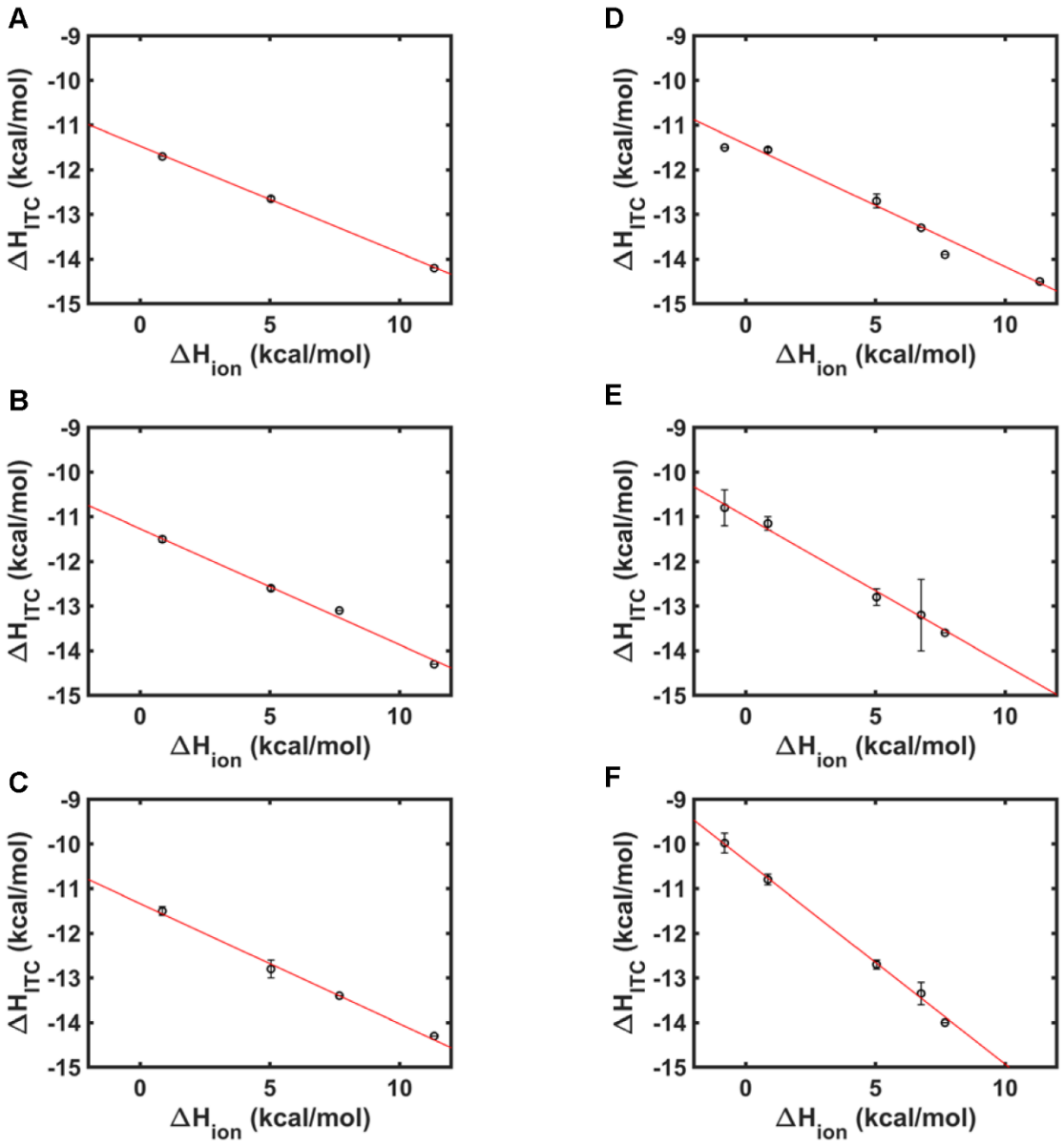

Figure 8.6. Plots showing the dependence of ΔH_{ITC} on ΔH_{ion} for the oxidation reaction of ferrous WT cyt c_2 by $[Fe(CN)_6]^{3-}$ at (A) pH 7.8, (B) pH 7.6, (C) pH 7.4, (D) pH 7.2, (E) pH 7.0, and (F) pH 6.8 at 25.0 ± 0.2 °C. Measured average enthalpies of a specific buffer for WT cyt c_2 are shown (black circles), with error between measurements when available. Linear fit of the data is shown (red line).

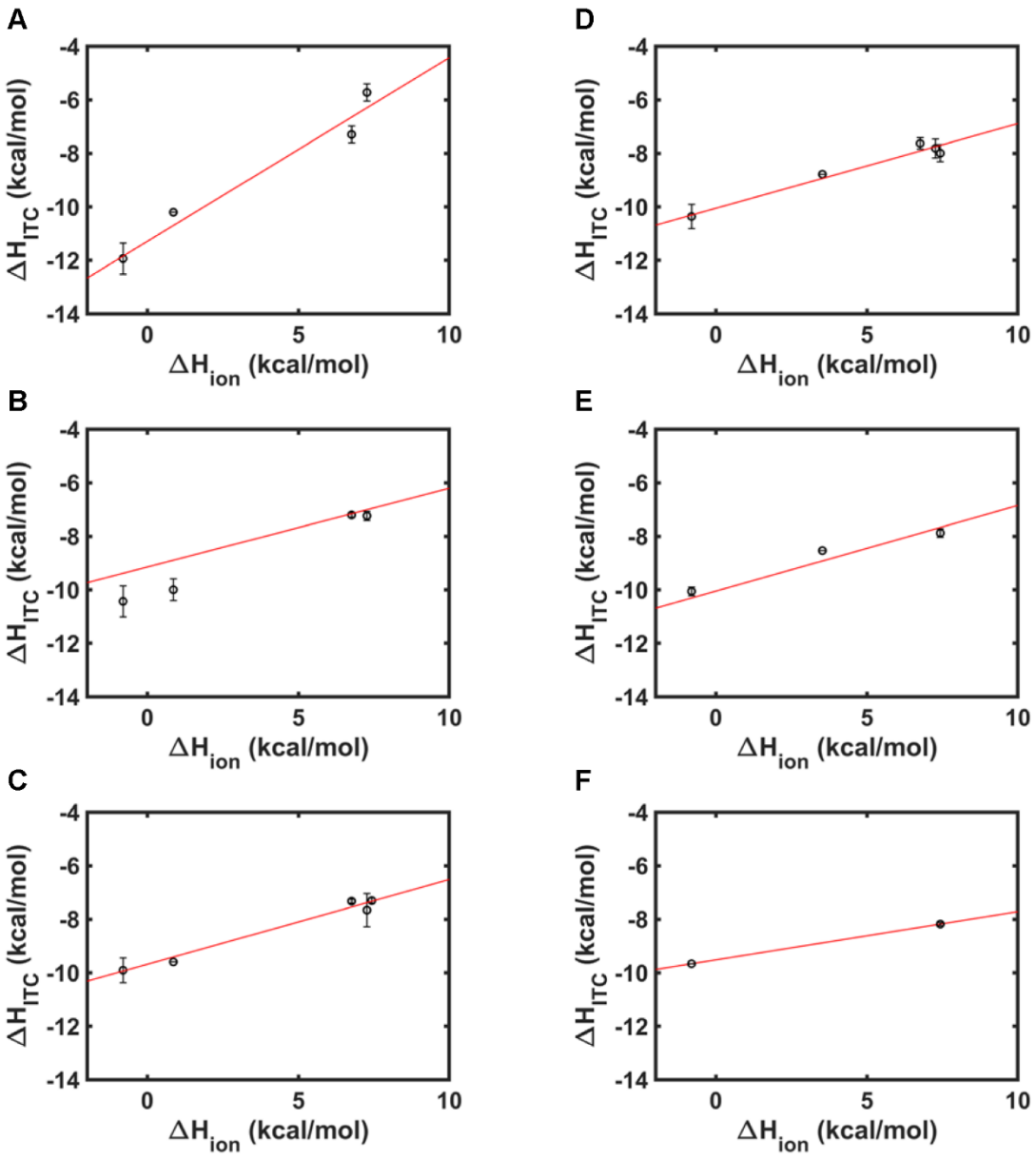

Figure 8.7. Plots showing the dependence of ΔH_{ITC} on ΔH_{ion} for the oxidation reaction of ferric WT cyt c_2 by $[Co(terpy)_2]^{2+}$at (A) pH 6.6, (B) pH 6.4, (C) pH 6.2, (D) pH 6.0, (E) pH 5.8, and (F) pH 5.6 at 25.0 ± 0.2 °C. Measured average enthalpies of a specific buffer for WT cyt c_2 are shown (black circles), with error between measurements when available. Linear fit of the data is shown (red line).

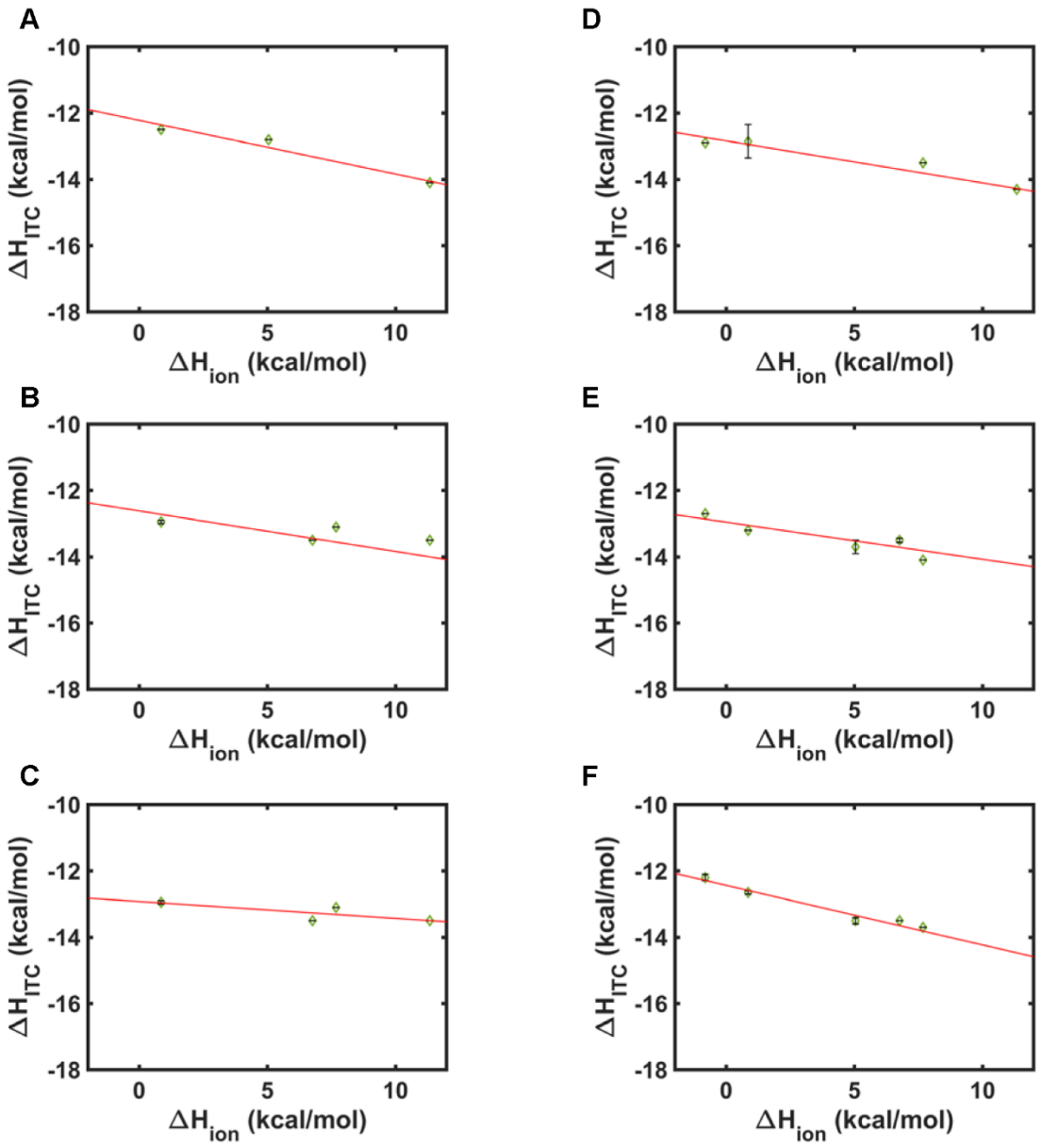

Figure 8.8. Plots showing the dependence of ΔH_{ITC} on ΔH_{ion} for the oxidation reaction of ferrous H42F cyt c_2 by $[Fe(CN)_6]^{3-}$ at (A) pH 7.8, (B) pH 7.6, (C) pH 7.4, (D) pH 7.2, (E) pH 7.0, and (F) pH 6.8 at 25.0 ± 0.2 °C. Measured average enthalpies of a specific buffer for H42F cyt c_2 are shown (green circles), with error between measurements when available. Linear fit of the data is shown (red line).

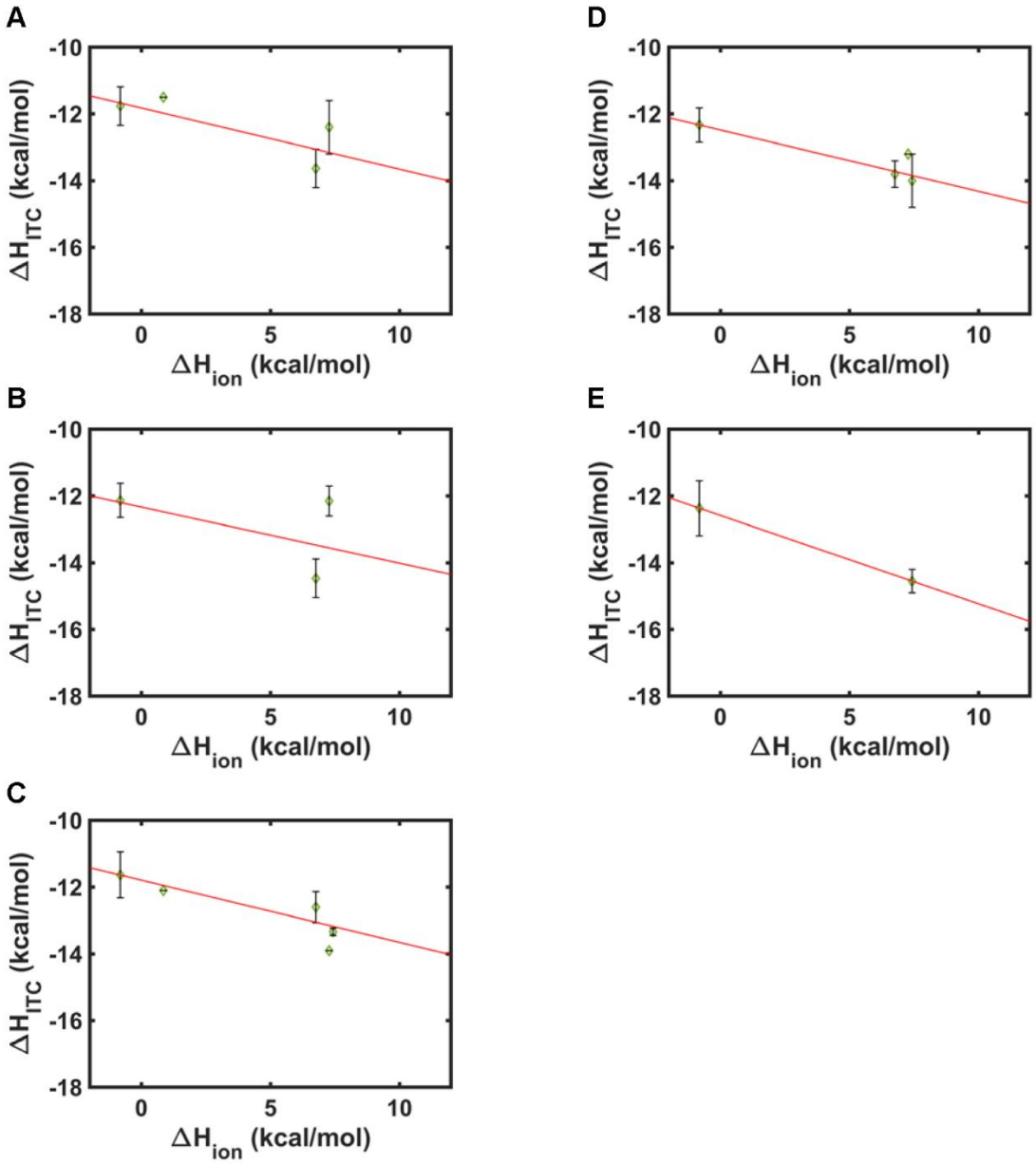

Figure 8.9. Plots showing the dependence of ΔH_{ITC} on ΔH_{ion} for the oxidation reaction of ferrous H42F cyt c_2 by $[Fe(CN)_6]^{3-}$ at (A) pH 6.6, (B) pH 6.4, (C) pH 6.2, (D) pH 6.0, and (E) pH 5.8 at 25.0 ± 0.2 °C. Measured average enthalpies of a specific buffer for H42F cyt c_2 are shown (green circles), with error between measurements when available. Linear fit of the data is shown (red line).

Table 8.5. Net PT and Ionization Enthalpies for the Reduction of WT cyt c_2[a]

pH	Δn	ΔH_{inter} (kcal/mol)
7.8	0.24 ± 0.03	11.47 ± 0.23
7.6	0.26 ± 0.03	11.27 ± 0.16
7.4	0.27 ± 0.06	11.33 ± 0.37
7.2	0.27 ± 0.05	11.43 ± 0.3
7.0	0.33 ± 0.15	10.99 ± 0.80
6.8	0.45 ± 0.05	10.37 ± 0.24
6.6	0.69 ± 0.15	-11.29 ± 0.8
6.4	0.42 ± 0.09	-10.18 ± 0.44
6.2	0.32 ± 0.08	-9.68 ± 0.47
6.0	0.32 ± 0.08	-10.05 ± 0.49
5.8	0.27 ± 0.06	-9.79 ± 0.32
5.6	0.18 ± 0.15	-9.51 ± 0.90

[a]From oxidation reactions between ferrous cyt c_2 and $[Fe(CN)_6]^{3-}$ at pH 7.8 to 6.8, and from reduction reactions between ferric cyt c_2 and $[Co(terpy)_2]^{2+}$ at pH 6.6 to 5.6. Values of Δn and ΔH_{inter} were obtained from linear fits of the ΔH_{ITC} versus ΔH_{ion} plots, and error bars are from the linear fit. Signs were adjusted accordingly for all values obtained from oxidation reactions as reduction reactions based on the relationship at eq 8.12.

Table 8.6. Net PT and Ionization Enthalpies for the Reduction of H42F cyt c_2[a]

pH	Δn	ΔH_{inter} (kcal/mol)
7.8	0.16 ± 0.1	12.22 ± 0.81
7.6	0.12 ± 0.03	12.62 ± 0.28
7.4	0.05 ± 0.07	12.92 ± 0.45
7.2	0.13 ± 0.07	12.84 ± 0.41
7.0	0.11 ± 0.08	12.95 ± 0.45
6.8	0.18 ± 0.04	12.44 ± 0.19
6.6	0.18 ± 0.20	11.82 ± 1.05
6.4	0.17 ± 0.29	12.33 ± 1.6
6.2	0.19 ± 0.12	11.79 ± 0.71
6.0	0.18 ± 0.16	12.48 ± 0.95
5.8	0.27 ± 0.33	12.58 ± 1.55

[a]From oxidation reactions between ferrous cyt c_2 and $[Fe(CN)_6]^{3-}$ at pH 7.8 to 5.8. Values of Δn and ΔH_{inter} were obtained from linear fits of the ΔH_{ITC} versus ΔH_{ion} plots. Signs were adjusted accordingly for all values obtained from oxidation reactions as reduction reactions based on the relationship at eq 8.12. In some cases, error bars were not present due to the scarcity of points in the ΔH_{ITC} versus ΔH_{ion} plots.

Net proton uptake.

Net proton (Δn) versus pH yields a buffer-independent proton plot for both WT and H42F (Figure 8.10). In WT cyt c_2, a dependence on Δn is observed with pH (Figure 8.10A). Fitting the WT data to eq 8.7 yields pK_{a1} = 7.1 ± 0.2 and pK_{a2} = 6.2 ± 0.2.

In contrast, the H42F buffer-independent proton influx plot did not fit well to eq 8.7 (Figure 8.10B). Although large error bars may be due to the scarcity of the points at certain pH conditions, the net flux of protons is hard to define even in cases where multiple data sets were obtained (Figures 8.8E, F and 8.9A to D).

Enthalpies for Protonation in Cyt c_2. The intercept of the linear fit obtained from plotting ΔH_{ITC} measured in terms of ΔH_{ion} is the combined enthalpy from the oxidation changes of the protein and the metal compound, and the ionization of the groups involved in the PT (Tables 8.5 and 8.6). Thus, we get the expressions for the intercepts for the oxidation ($\Delta H_{inter,ox}$; eq 8.11) and reduction reactions ($\Delta H_{inter,re}$; eq 8.12).

$$\Delta H_{inter,ox}=\Delta H_{HR}^{FeCN3+/2+}-\Delta H_{HR}^{heme3+/2+}+ n_1\Delta H_1- n_2\Delta H_2 \tag{8.11}$$

$$\Delta H_{inter,re}=-\Delta H_{HR}^{Ctpy3+/2+}+\Delta H_{HR}^{heme3+/2+}- n_1\Delta H_1+ n_2\Delta H_2 \tag{8.12}$$

Correcting the ΔH_{HR} associated with the reductant/oxidant and the heme and defining n_1 and n_2 (eqs 8.3 and 8.4) shows the enthalpies of the ionization of the groups A_1 and A_2 for the oxidation reaction (eq 8.13) and the reduction reaction (eq 8.14).

$$\Delta H_{inter,ox}-\Delta H_{HR}^{FeCN3+/2+}+\Delta H_{HR}^{heme3+/2+}= \left(\frac{10^{(pKa1-pH)}}{(1+10^{pKa1-pH})}\right)\Delta H_1- \left(\frac{10^{(pKa2-pH)}}{(1+10^{pKa2-pH})}\right)\Delta H_2 \tag{8.13}$$

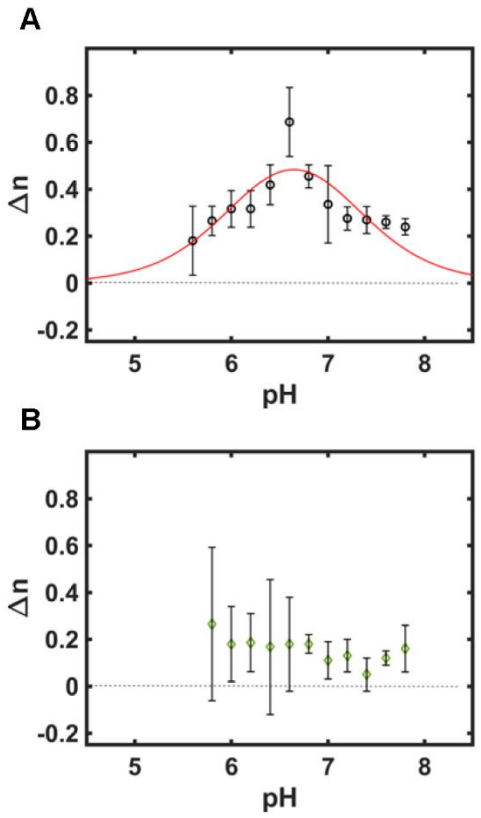

Figure 8.10. Plot showing the change in Δn with pH for (A) WT cyt c_2 (black circle) with fit to eq 8.5 and for (B) H42F cyt c_2 (green diamond), at 25.0 ± 0.2 °C. Dotted line at Δn = 0 is shown to guide the eye.

$$\Delta H_{inter,re}+\Delta H_{HR}^{Ctpy3+/2+}-\Delta H_{HR}^{heme3+/2+}=-\left(\frac{10^{(pKa1-pH)}}{(1+10^{pKa1-pH})}\right)\Delta H_1+\left(\frac{10^{(pKa2-pH)}}{(1+10^{pKa2-pH})}\right)\Delta H_2 \quad (8.14)$$

where we define the net enthalpy from the ionization of the A_1 and A_2 in the protein as ΔH_P (eq 8.15):

$$\Delta H_P=-\left(\frac{10^{(pKa1-pH)}}{(1+10^{pKa1-pH})}\right)\Delta H_1+\left(\frac{10^{(pKa2-pH)}}{(1+10^{pKa2-pH})}\right)\Delta H_2 \quad (8.15)$$

Calculation of half reaction enthalpy ΔH_{HR} for $[Co(terpy)_2]^{2+}$. Half reaction enthalpy of reduction for $[Co(terpy)_2]^{2+}$ ($\Delta H_{HR}^{Ctpy3+/2+}$) have been obtained from isothermal titrations with $[Fe(CN)_6]^{3-}$, where Co^{2+} in the $[Co(terpy)_2]^{2+}$ complex was oxidized to Co^{3+} with Fe^{3+} in the $[Fe(CN)_6]^{3-}$ complex as a titrant at pH 7.4 and 6.6 (Figure 8.11). These titrations have yielded ΔH_{ITC} values of -13.9 ± 0.5 and -13.5 ± 0.5 kcal/mol at pH 7.4 and 6.6, respectively (Table 8.7). At both pH conditions, the thermogram traces of the oxidation reactions were comparable, with slight deviations in the baseline at low molar titrant conditions. The reaction occurred at a stoichiometry of 1.03 ± 0.07 between the oxidation reaction of $[Co(terpy)_2]^{2+}$ with $[Fe(CN)_6]^{3-}$ at pH 7.4. Deviation from 1 to 1 stoichiometry has been observed at pH 6.6 (0.73 ± 0.02), but comparable ΔH_{ITC} values at two pH conditions have suggested that the reactions are similar at both pH conditions. Possible secondary reactions at low molar titrant concentrations may have contributed to a poor fit in stoichiometry at pH 6.6. Both complexes are assumed to not interact with the buffer, and no deprotonation/protonation events are assumed to occur.

In the calorimetric cell, the following reactions contributing to the enthalpy can be described as follows (Scheme 8.5):

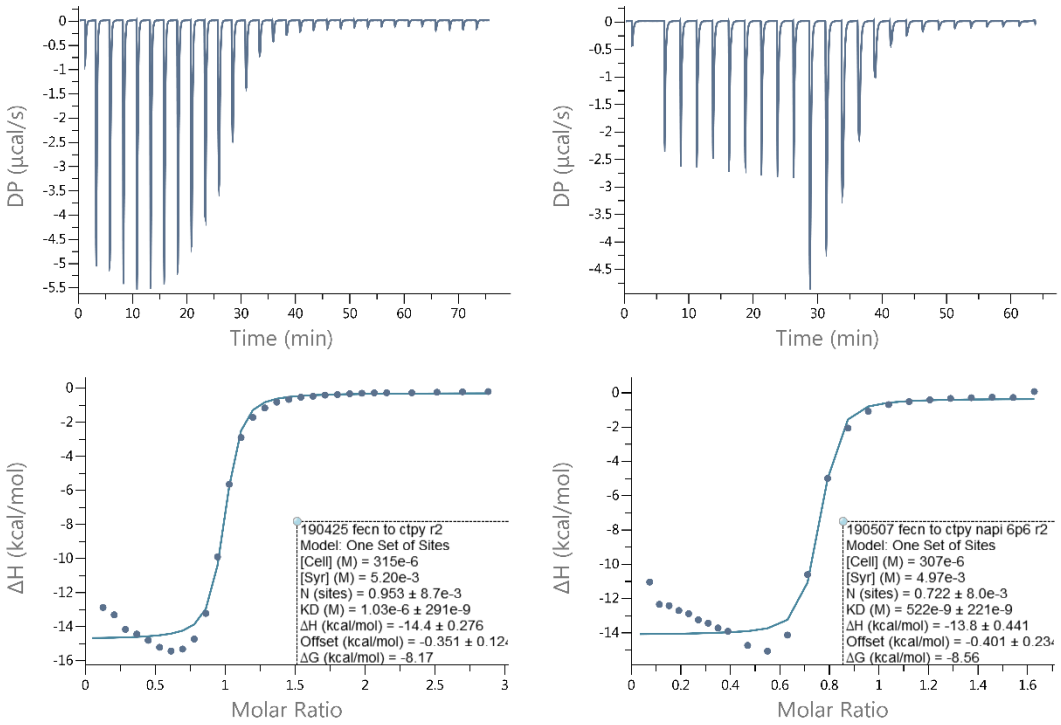

Figure 8.11. Representative thermograms for the oxidation of $[Co(terpy)_2]^{2+}$ with $[Fe(CN)_6]^{3-}$ in a 10 mM sodium phosphate buffer (μ = 0.1 M) at pH 7.4 (left) or at pH 6.6 (right) and 25.0 ± 0.2 °C. Deviation in the baseline at low molar ratios were observed between multiple runs for both pH conditions.

Table 8.7. Parameters Obtained from Calorimetric Titrations of $Fe(CN)_6^{3-}$ and $Co(terpy)_2^{2+}$ [a]

pH	ΔH_{ITC} (kcal/mol)	ΔH_{HR} (kcal/mol)[b]	K_{ITC} ($\times 10^{-7}$)	K_{eq}	N	$E°_{calc}$ (mV)[c]
7.4	-13.9 ±0.5	-6.1 ± 0.5	9.68 ± 0.63	337 ± 46	1.03 ± 0.08	271 ± 3
6.6	-13.5 ±0.5	-6.5 ± 0.2	6.24 ± 0.81	371 ± 52	0.73 ± 0.02	268 ± 4

[a]Monitoring the oxidation reaction of $Co(terpy)_2^{2+}$ using $Fe(CN)_6^{3-}$ as a oxidizing titrant, performed in a 10 mM phosphate buffer (μ = 0.1 M) at 25.0 ± 0.2 °C.

[b]Calculated from assuming the half reaction enthalpy for $Fe(CN)_6^{3-}$ is -20.0 kcal/mol.

[c]Calculated reduction potential of $Co(terpy)_2^{3+}$ is based on assuming that the reduction potential of Fe^{3+} in $Fe(CN)_6^{3-}$ is 420 mV. The calculated value has an average of 269 ± 4 mV, within error of the reported value of 270 mV in similar ionic conditions at pH 6.5.[37]

	Description of Reaction	Reaction	Change in ΔH
1)	Reduction of Fe^{3+} in $[Fe(CN)_6]^{3-}$	$Fe^{3+} \rightleftharpoons Fe^{2+}$	$(\Delta H_{HR}^{FeCN3+/2+})$
2)	Oxidation of Co^{2+} in $[Co(terpy)_2]^{2+}$	$Co^{2+} \rightleftharpoons Co^{3+}$	$(-\Delta H_{HR}^{Ctpy3+/2+})$

(Scheme 8.5)

Total observed enthalpy in the calorimetric cell (ΔH_{ITC}) can then be described as eq 8.16:

$$\Delta H_{ITC} = (-\Delta H_{HR}^{Ctpy3+/2+}) + \Delta H_{HR}^{FeCN3+/2+} \quad (8.16)$$

From the averaged ΔH_{ITC} values measured at pH 7.4 and 6.6 and the $\Delta H_{HR}^{FeCN3+/2+}$ (-20.0 kcal/mol) value reported in literature,[34] $\Delta H_{HR}^{Ctpy3+/2+}$ was calculated for each pH conditions. Since the calculated half reaction enthalpies (ΔH_{HR}) for the reduction of $[Co(terpy)_2]^{2+}$by $[Fe(CN)_6]^{3-}$at pH 7.4 and 6.6 were within error of each other (Table 8.7), the average value of -6.3 ± 0.5 was used as $\Delta H_{HR}^{Ctpy3+/2+}$.

Using the half reaction enthalpies reported in the literature[34] for the *c*-type heme (-8.8 ±0.3 kcal mol^{-1}) ,$[Fe(CN)_6]^{3-}$ (-20 kcal mol^{-1}), and $[Co(terpy)_2]^{2+}$ (-6.3 ± 0.5) we can obtain the pH-dependent ΔH_p values for each pH for both WT and H42F (Table 8.8). Plot of the pH-dependent ΔH_P versus pH for WT and H42F shows that in WT cyt c_2, the ΔH_P transitions from ~ -7.5 kcal/mol at low pH conditions to 0 kcal/mol at high pH conditions (Figure 8.12). In contrast, ΔH_P does not change in H42F, and is near 0 for all pH conditions monitored (Figure 8.12). Although change in ΔH_P can be fitted to eq 8.17 to obtain ΔH_1 and ΔH_2, lack of resolution in the transition region makes it difficult to obtain ΔH_1 and ΔH_2 independently. However, a close inspection of eq 8.17 shows that at pH conditions where pH << p$K_{a1,2}$, $\Delta H_P = -\Delta H_1 + \Delta H_2$, and at conditions where pH >> p$K_{a1,2}$, $\Delta H_P = 0$.

Table 8.8. ΔH_P of Cytochrome c_2 Variants[a]

	ΔH_P (kcal/mol)	
pH	*WT*	*H42F*
7.8	0.27 ± 0.38	1.02 ± 0.86
7.6	0.07 ± 0.34	1.42 ± 0.41
7.4	0.13 ± 0.48	1.72 ± 0.54
7.2	0.26 ± 0.42	1.64 ± 0.51
7.0	-0.21 ± 0.85	1.75 ± 0.54
6.8	-0.83 ± 0.38	1.24 ± 0.35
6.6	-8.79 ± 0.99	0.62 ± 1.09
6.4	-7.68 ± 0.73	1.13 ± 1.63
6.2	-7.18 ± 0.75	0.59 ± 0.77
6.0	-7.55 ± 0.76	1.28 ± 1.0
5.8	-7.29 ± 0.67	1.38 ± 1.58
5.6	-7.01 ± 1.07	--

[a]Signs were adjusted accordingly for all values obtained from oxidation reactions as reduction reactions based on the relationship at eq 8.12.

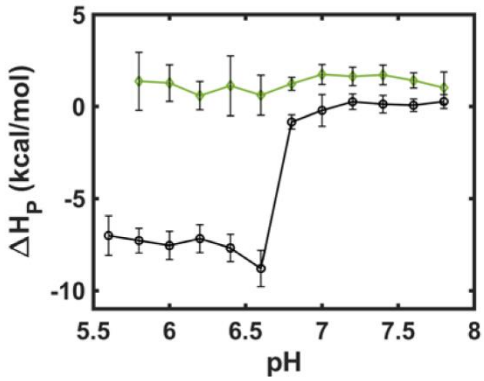

Figure 8.12. Plot showing the net change in ionization enthalpy in the protonating groups in the protein ΔH_P versus pH for WT (black circles) and H42F (green diamond) cyt c_2 at 25.0 ± 0.2 °C. Solid lines connecting the points are shown to guide the eye.

Equilibria Constants (K) Involved in the Reaction

ITC measures heat associated with the reaction, and the fitted equilibrium constant K_{ITC} is equivalent to the observed dissociation constant, as the fitting program assumes the reaction in the cell can be described as scheme 8.6:[32, 34]

$$P + D \rightleftharpoons P^*$$

(Scheme 8.6)

where P consumes D to form P*, defining K_{ITC} as eq 8.17.

$$K_{ITC} = \frac{[P][D]}{[P^*]} \tag{8.17}$$

In our calorimetric measurements of the PCET reactions, we are assuming that binding reactions do not occur. Since reactants are not consumed in the cell, our reaction can be described as scheme 8.7:[34]

$$P + D \rightleftharpoons P^* + D^*$$

(Scheme 8.7)

where P reacts with D, and forms P* and D*, and net consumption of D is not observed. Then, our true equilibrium constant K_{eq} for the PCET reaction can be described as eq 8.18:

$$K_{eq} = \frac{[P^*][D^*]}{[P][D]} \tag{8.18}$$

We also define stoichiometry, *N*, as fraction of the total concentration of D to P, and since reactants are not consumed in PCET reactions (eq 8.19),

$$N = \frac{[D]_{tot}}{[P]_{tot}} = \frac{[D]}{[P]} = \frac{[D^*]}{[P^*]}$$

(8.19)

where in our reactions, the limiting reagent is the total concentration of cyt c_2 in the reaction. Substituting eqs 8.17 and 8.19 to 8.18, we get the relationship between K_{eq} in terms of K_{ITC} obtained from ITC measurements (eq 8.20).[19, 34]

$$K_{eq} = \frac{N[\text{cyt } c_2]_{tot}}{K_{ITC}}$$

(8.20)

In our PCET reaction, equilibria associated with the PCET reaction in cyt c_2 is from the net ET between cyt c_2 (P) and an external electron donor/acceptor (D) (K_{ET}) going from states 1 to 2, and proton dissociation equilibria of groups in protein (P) associated with states 1 and 2, which we can also define as proton binding constants (K_{P1} and K_{P2}, respectively) (scheme 8.8).

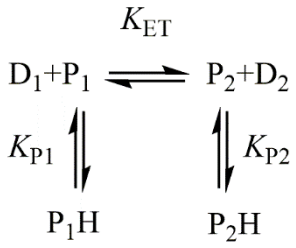

(Scheme 8.8)

Eq 8.18 defines K_{eq} based on the oxidation state of the protein, and $[P]_{tot} = [P_1H] + [P_1] + [P_2H] + [P_2]$. For the oxidation reaction, eq 8.18 is equivalent to eq 8.21:

$$K_{eq} = \frac{([P_2H] + [P_2])[D_2]}{([P_1H] + [P_1])[D_1]}$$

(8.21)

Since both the protein and the electron donor/acceptor complexes are assumed to not bind with the buffer, buffer contributions are not included in calculations of K_{eq}. Microscopic equilibrium constants in the reaction are defined as eqs 8.22 to 8.24:

$$K_{ET} = \frac{[P_2][D_2]}{[P_1][D_1]} \tag{8.22}$$

$$K_{P1} = \frac{[P_1H]}{[P_1][H]} \tag{8.23}$$

$$K_{P2} = \frac{[P_2H]}{[P_2][H]} \tag{8.24}$$

And relate K_{eq} at any activity with the relationship pH = -log(α_{H^+}), substituting eqs 8.22 to 8.24 into eq 8.21 then yields eq 8.25 for the oxidation reaction (if P_1 is ferric species and P_2 the ferrous species according to scheme 8.2).

$$K_{eq} = \frac{K_{ET}(1 + K_{P2}\alpha_H^+)}{(1 + K_{P1}\alpha_H^+)} \tag{8.25}$$

where α_{H^+} is equivalent to 10^{-pH}, while K_{P1} and K_{P2} is equivalent to 10^{pKa1} and 10^{pKa2}, respectively. Eq 8.25 is comparable to the previously derived expression for the protonation-dependent ligand binding reaction.[35] From K_{eq}, protonation-independent reduction potential for the protein ($E°_{corr}$) can be obtained using the relationship between K_{ET} and reduction potentials (eq 8.26):

$$nF\Delta E_m = RT\ln K_{ET} \tag{8.26}$$

where $\Delta E_m = E(D)-E(A)$, the difference in the reduction potentials between the electron donor (D) and the acceptor (A) in the reaction scheme.

Such treatment yields $E°_{corr}$ for WT (Table 8.9), and the calculated reduction potential values are comparable across different buffers at similar pH conditions (Tables 8.10 and 8.11). However, a notable difference in reduction potential is observed when the external electron donor/acceptor is changed around pH 6.6 (Figure 8.13).

There are noticeable deviations in the observed stoichiometry from the expected stoichiometry of these electrochemical titrations at lower pH conditions. Expected stoichiometry of the ET reactions in cyt c_2 is 1 with these complexes, as $[Co(terpy)_2]^{2+}$ and $[Fe(CN)_6]^{3-}$ are commonly used in ET kinetic experiments with *c*-type cytochromes (cyt *c*) and ET rate constants with these complexes are of first order.[41, 42] A possible explanation for the deviation from expected stoichiometry can arise from the lack of definition in regions leading up to the transition region in titrations with $[Co(terpy)_2]^{2+}$, along with decreasing K_{eq} due to increasing reduction potential of cyt c_2 with decrease in pH. The thermograms of electrochemical titrations WT cyt c_2 at lower pH ranges (5.6 to 6.6) with $[Co(terpy)_2]^{2+}$ had less definition near the transition region compared to the thermograms of the titrations at higher pH with $[Fe(CN)_6]^{3-}$, even with similar buffer and ionic conditions (Figure 8.14). This would affect the accuracy of K_{ITC}, calculated K_{eq}, and the estimated $E°$ of WT cyt c_2 in the electrochemical titrations at lower pH ranges with $[Co(terpy)_2]^{2+}$.

In the absence of protonation, K_{eq} is dominated by the ET reaction such that $K_{eq} = K_{ET}$ and $nF\Delta E_m = RT\ln K_{eq}$. Calculation of $E°$ of $[Co(terpy)_2]^{3+/2+}$ from the titration of $[Fe(CN)_6]^{3-}$ into $[Co(terpy)_2]^{2+}$ assuming the reduction potential of $[Fe(CN)_6]^{3-}$ to be 420 mV yields $E°$ of 271 ± 3 mV at pH 7.4 and 268 ± 4 mV at pH 6.6 (Table 8.7), a value within error of the reported value of 273 mV for the reduction potential of $[Co(terpy)_2]^{3+/2+}$ at pH 6.5.[37]

Table 8.9. Equilibria Constants in the PCET Reaction for WT Cyt c_2[a]

pH	N	K_{eq}	K_{ET}	$E°_{corr}$ (mV)	$E°_{obs}$ (mV)
7.8	1.02 ± 0.09	66 ± 5	77 ± 6	308 ± 2	313 ± 2
7.6	1.07 ± 0.05	49 ± 5	63 ± 6	314 ± 3	320 ± 3
7.4	1.02 ± 0.06	47 ± 4	66 ± 6	313 ± 3	321 ± 3
7.2	1.00 ± 0.05	38 ± 3	62 ± 4	314 ± 2	327 ± 2
7.0	1.04 ± 0.1	31 ± 5	60 ± 10	315 ± 4	333 ± 4
6.8	1.00 ± 0.06	22 ± 3	53 ± 8	318 ± 4	341 ± 4
6.6	0.95 ± 0.23	0.10 ± 0.01	0.31 ± 0.03	300 ± 2	328 ± 2
6.4	0.93 ± 0.21	0.08 ± 0.01	0.30 ± 0.03	302 ± 3	336 ± 3
6.2	0.78 ± 0.14	0.06 ± 0.01	0.26 ± 0.04	305 ± 4	344 ± 4
6.0	0.82 ± 0.09	0.05 ± 0.01	0.24 ± 0.03	307 ± 3	349 ± 3
5.8	0.82 ± 0.07	0.04 ± 0.01	0.25 ± 0.04	307 ± 5	352 ± 6
5.6	0.83 ± 0.05	0.03 ± 0.01	0.20 ± 0.03	312 ± 4	360 ± 6

[a]Values were averaged for all values regardless of the buffer conditions, as the equilibrium constant is assumed to be independent of the buffer used for the electrochemical titrations.

Table 8.10. Equilibria Constants for the Oxidation of Ferrous WT cyt c_2 from pH 7.8 to 6.8[a]

pH	Buffer	N	K_{eq}	K_{ET}	$E°_{prot}$ (mV)	$E°_{obs}$ (mV)
7.8	Tris	1.24	71	83.0	307	311
	MOPS	0.96 ± 0.02	62.4 ± 0.79	73.0 ± 0.9	310 ± 0.3	314 ± 0.3
	Phosphate	1.02	61.1	71.5	310	314
7.6	Tris	1.02	48	60.8	315	321
	TES	1.05	57	72.1	310	316
	MOPS	1.04 ± 0.02	51.6 ± 2.7	65.4 ± 3.3	313 ± 1	319 ± 1
	Phosphate	1.11 ± 0.07	45.9 ± 6.1	58.2 ± 7.7	316 ± 3	322 ± 3
7.4	Tris	0.99	51.4	72.6	310	319
	TES	1.04	50.9	71.9	310	319
	MOPS	1.07 ± 0.1	48.8 ± 1.13	68.9 ± 1.59	311 ± 1	320 ± 1
	Phosphate	0.98 ±0.001	40 ± 1.99	56.5 ± 2.8	316 ± 1	325 ± 1
7.2	Tris	0.971	39.5	64.5	313	326
	TES	0.953	39.6	64.6	313	326
	BisTris	1.04	33.9	55.3	317	330
	MOPS	1.03 ± 0.07	39.3 ± 2.53	64.2 ±4.12	313 ± 2	326 ± 2
	Phosphate	0.985 ± 0.04	38.8 ± 1.02	63.2 ± 1.7	314 ± 1	326 ± 1
	Citrate	1.02	33.4	54.4	317	330
7.0	TES	1.03	37.2	72.4	314	331
	BisTris	1.03 ± 0.11	27.2 ± 5.0	53.0 ± 9.74	319 ± 5	336 ± 5
	MOPS	0.975 ± 0.04	33.3 ±3.97	65.0 ± 7.7	313 ± 3	330 ± 3
	Phosphate	1.03 ± 0.05	31.2 ± 0.5	60.9 ± 0.92	314 ± 0.4	332 ± 0.3
	Citrate	0.975 ± 0.05	25.7 ± 2.4	50.1 ± 4.7	320 ± 2	337 ± 2
6.8	TES	0.908	23.5	56.2	317	339
	BisTris	0.99 ± 0.08	17.3 ± 0.91	41.4 ± 2.2	324 ± 1	347 ± 1
	MOPS	0.974 ± 0.04	26 ± 0.1	62.2 ± 0.2	314 ± 0.1	336 ± 0.1
	Phosphate	1 ± 0.02	25.5 ± 0.4	61.1 ± 0.9	314 ± 0.4	337 ± 0.4
	Citrate	1.1	20.1 ± 0.45	48.1 ± 1.07	321 ± 1	336 ± 1

[a]Error bars are the standard deviation of values obtained from each measurement.

Table 8.11. Equilibria Constants for the Reduction of Ferric WT cyt c_2 from pH 6.6 to 5.6[a]

pH	Buffer	N	K_{eq} ($\times 10^{-2}$)	K_{ET}	$E°_{prot}$ (mV)	$E°_{obs}$ (mV)
6.6	ACES	0.95 ± 0.05	9.6 ± 0.3	0.29 ± 0.01	302 ± 1	330 ± 1
	BisTris	0.78 ± 0.01	10.2 ± 0.4	0.30 ± 0.01	301 ± 1	329 ± 1
	Phosphate	1.4 ± 0.2	9.5 ± 0.3	0.28 ± 0.01	302 ± 1	330 ± 1
	Citrate	0.69 ± 0.04	12.2 ± 0.9	0.36 ± 0.03	296 ± 2	324 ± 2
6.4	ACES	0.77 ± 0.07	6.72 ± 0.1	0.25 ± 0.01	306 ± 1	339 ± 1
	BisTris	0.83 ± 0.02	8.3 ± 0.5	0.31 ± 0.02	301 ± 2	334 ± 2
	Phosphate	1.1 ± 0.4	7.13 ± 0.2	0.26 ± 0.01	304 ± 1	338 ± 1
	Citrate	0.88 ± 0.13	8.9 ± 0.1	0.33 ± 0.01	298 ± 0.4	332 ± 0.4
6.2	Piperazine	0.79 ± 0.15	4.88 ± 0.6	0.22 ± 0.03	309 ± 3	348 ± 3
	ACES	0.81 ± 0.15	4.96 ± 0.6	0.22 ± 0.03	309 ± 3	347 ± 3
	BisTris	0.70 ± 0.09	6.55 ± 0.5	0.29 ± 0.02	302 ± 2	340 ± 2
	Phosphate	0.576	4.91	0.22	309	347
	Citrate	0.92 ± 0.02	6.59 ± 0.3	0.29 ± 0.01	301 ± 3	347 ± 3
6.0	Piperazine	0.79 ± 0.06	4.2 ± 0.4	0.22 ± 0.02	309 ± 2	351 ± 2
	ACES	0.87 ± 0.16	4.3 ± 0.1	0.23 ± 0.01	308 ± 1	351 ± 1
	BisTris	0.79 ± 0.03	5.1 ± 0.3	0.27 ± 0.01	304 ± 1	347 ± 1
	MES	0.778	3.64	0.19	312	355
	Citrate	0.85 ± 0.06	5.09 ± 0.3	0.27 ± 0.01	304 ± 1	347 ± 1
5.8	Piperazine	0.84 ± 0.05	3.48 ± 0.1	0.21 ± 0.01	310 ± 1	356 ± 1
	MES	0.913	3.03	0.18	314	360
	Citrate	0.78 ± 0.1	4.9 ± 0.4	0.29 ± 0.02	302 ± 2	348 ± 2
5.6	Piperazine	0.84 ± 0.01	2.7 ± 0.2	0.18 ± 0.01	315 ± 2	363 ± 2
	Citrate	0.72	4.0	0.26	305	353

[a] K_{eq} values were corrected to be equivalent to K_{eq} obtained from oxidation reactions using the relationship $1/K_{eq\ re} = K_{eq\ ox}$. Error bars are the standard deviation of values obtained from each measurement.

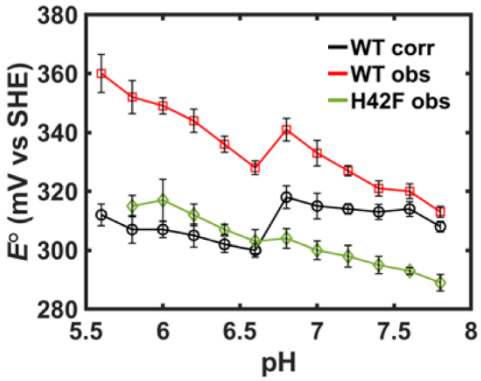

Figure 8.13. Plot showing the calculated reduction potentials ($E°$) from K_{eq} for WT and H42F. Shown are the corrected reduction potential ($E°_{corr}$) from K_{ET} for WT (black), observed reduction potential ($E°_{obs}$) from K_{eq} for WT (red), and the observed reduction potential ($E°_{obs}$) from K_{eq} for H42F (green) versus pH. Reduction potentials were calculated from ΔE_m (eq 8.26).

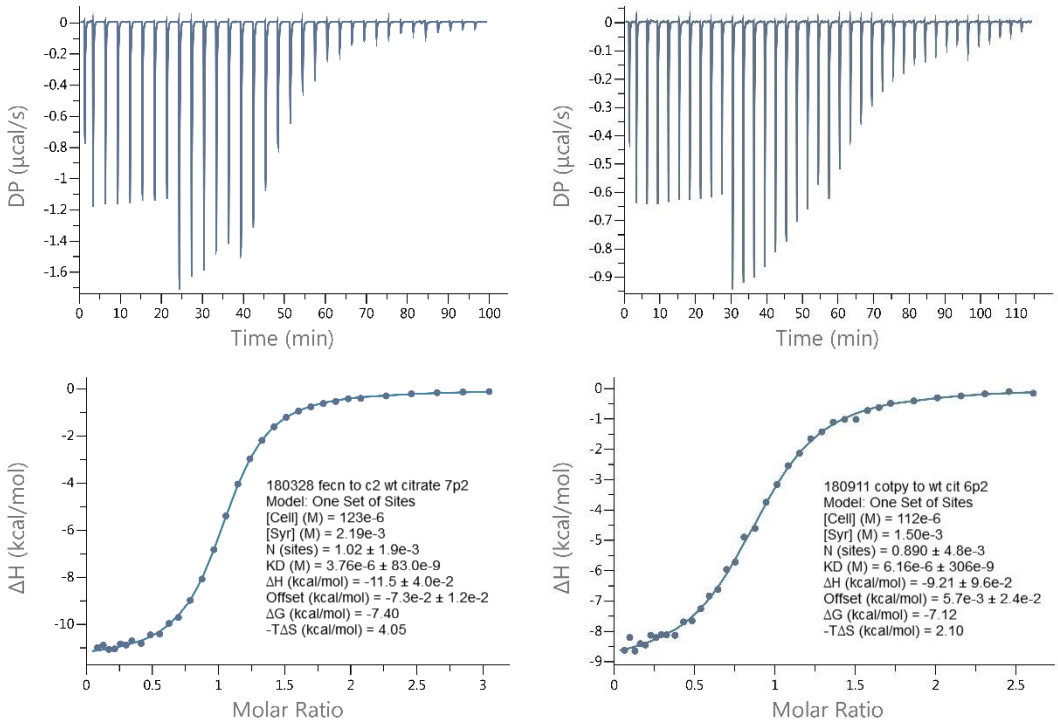

Figure 8.14. Representative thermograms for the (left) oxidation of ferrous WT cyt c_2 with $[Fe(CN)_6]^{3-}$ at pH 7.2 or (right) reduction of ferric WT cyt c_2 with $[Co(terpy)_2]^{2+}$ at pH 7.2 in a 10 mM citrate buffer (μ = 0.1 M) and 25.0 ± 0.2 °C.

This is likely to be the case in H42F, as Δn vs pH plots suggest that the net PT in H42F variant is near 0, unlike in WT. On average, the reduction potentials of H42F do show a slight increase in the reduction potential with decrease in pH (Table 8.12), regardless of the buffers used (Tables 8.13 and 8.14). The range of reduction potentials for H42F observed in these pH ranges are comparable to previously reported values.[36] Assuming $K_{eq} = K_{ET}$ in WT cyt c_2 yielded the observed $E°$ ($E°_{obs}$) (Table 8.9) in the similar electrochemical potential range of 311 to 375 mV observed in electrochemical measurements between pH 8.0 and 5.0.[36]

Discussion

In WT cyt c_2, PT mechanism is coupled to ET mechanism at mildly alkaline to acidic pH conditions.[21, 36] The buffer-independent proton flux plot shows that there is a net uptake of protons in the pH ranges 7.8 to 5.6 (Figure 8.10A), and fits to two pK_a values, 6.2 ± 0.2 and 7.1 ± 0.2. The pK_a values obtained from calorimetric measurements are within error of the reported pK_a values obtained for WT cyt c_2 from pH-dependent CV measurements (pK_a values of 6.02 ± 0.12 and 7.07 ± 0.13),[36] as well as ferricyanide titrations that monitored changes in the 550 nm absorption band (pK_a values of 6.2 and 7.0).[21] In the absence of His42, however, this net proton movement is (Δn) no longer readily observed. Error bars are large, more so for the lower pH conditions than in higher pH conditions, suggesting that the net proton movement in H42F is either greatly diminished or is no longer coupled to ET in H42F. This increase in error is independent of the number of available data set in the experiments, as number of data set in the lower pH conditions is greater than in the higher pH conditions.[36]

Table 8.12. Equilibria Constants in the PCET Reaction for H42F Cyt c_2[a]

pH	N	K_{eq}	$E°_{obs}$ (mV)
7.8	1.02 ± 0.03	168 ± 18	289 ± 3
7.6	1.02 ± 0.05	140 ± 6	293 ± 1
7.4	1.07 ± 0.03	132 ± 15	295 ± 3
7.2	1.05 ± 0.03	120 ± 15	298 ± 4
7.0	1.00 ± 0.05	108 ± 13	300 ± 3
6.8	1.05 ± 0.13	93 ± 11	304 ± 3
6.6	1.26 ± 0.15	99 ± 14	303 ± 4
6.4	1.13 ± 0.10	80 ± 6	307 ± 2
6.2	1.13 ± 0.08	69 ± 10	312 ± 4
6.0	1.17 ± 0.14	58 ± 14	317 ± 7
5.8	1.04 ± 0.13	60 ± 9	315 ± 4

[a]Values were averaged for all values regardless of the buffer conditions, as the equilibrium constant is assumed to be independent of the buffer used for the titration reactions.

Table 8.13. Equilibria Constants for the Oxidation of Ferrous H42F cyt c_2 from pH 7.8 to 6.8[a]

pH	Buffer	N	K_{eq}	$E°_{prot}$ (mV)
7.8	Tris	1.04 ± 0.04	165 ± 15	289 ± 2
	TES	0.92	176	287
	MOPS	1.01	191	285
	Phosphate	1.01	149	292
7.6	Tris	0.99 ± 0.01	136 ± 2	294 ±0.3
	TES	0.98	147	292
	Phosphate	1.08 ± 0.02	140 ± 7	293 ± 1
7.4	Tris	1.13	153	291
	TES	1.09	148	292
	BisTris	1.06	115	298
	Phosphate	1.03 ± 0.01	121 ± 4	297 ± 1
7.2	Tris	1.02	135	294
	TES	1.01	135	294
	Phosphate	1.05 ± 0.01	122 ± 2	297 ± 0.4
	Citrate	1.09	83	307
7.0	TES	1	131	295
	BisTris	1.08 ± 0.04	105 ± 13	301 ± 3
	Phosphate	0.91	105	301
	Citrate	0.97	95	303
6.8	TES	0.96	107	300
	BisTris	0.94	91	304
	MOPS	0.97 ± 0.05	100 ± 2	302 ± 1
	Phosphate	0.96 ± 0.05	100 ± 10	302 ± 3
	Citrate	1.32 ± 0.27	73 ± 12	310 ± 4

[a]Error bars are the standard deviation of values obtained from each measurement. For measurements that were not repeated, errors are not shown.

Table 8.14. Equilibria Constants for the Oxidation of Ferrous H42F cyt c_2 from pH 6.6 to 5.6[a]

pH	Buffer	N	K_{eq}	$E°_{prot}$ (mV)
6.6	ACES	1.43 ± 0.29	119 ± 8	297 ± 2
	BisTris	1.16 ± 0.05	86 ± 14	306 ± 4
	Citrate	1.28 ± 0.13	96 ± 17	303 ± 5
6.4	ACES	1.27 ±0.11	90 ± 1	305 ± 0.3
	BisTris	1.15 ± 0.07	77 ± 3	309 ± 1
	Citrate	1.01 ± 0.29	78 ± 5	308 ± 2
6.2	Piperazine	1.11 ± 0.07	85 ± 5	306 ± 2
	ACES	1.13	66	312
	BisTris	1.13 ± 0.04	61 ± 4	314 ± 1
	Phosphate	1.03	61	315
	Citrate	1.2 ± 0.13	63 ± 9	314 ± 3
6.0	Piperazine	1.22 ± 0.09	74 ± 12	310 ± 4
	ACES	1.06	60	315
	BisTris	1.35 ± 0.23	33 ± 0.6	330 ± 1
	Citrate	1.03 ± 0.03	57 ± 9	317 ± 4
5.8	Piperazine	1.21 ± 0.07	71 ± 5	311 ± 2
	Citrate	0.94 ± 0.07	53 ± 3	318 ± 2

[a]Error bars are the standard deviation of values obtained from each measurement. For measurements that were not repeated, errors are not shown.

It is possible that the ET mechanism in H42F may still be proton-coupled and pH-dependent changes in Δn is buried in the large error bars (Figure 8.10B). However, the pH dependence of the bimolecular rate constants have not shown pH dependence,[36] suggesting that the PCET mechanism is greatly perturbed in the absence of His42.

The pK_a and identity of the protonating groups responsible for the pK_a observed in pH-dependent changes in reduction potentials have been highly speculated. Analysis of earlier ^{1}H NMR experiments with *Pseudomonas* cyt c_{551} have suggested that HP7 ionizes at neutral pH conditions in the presence of non-ligating His that is within hydrogen-bonding distance of HP7.[28] In contrast, previous examinations of ^{15}N NMR and ^{1}H NMR measurements with W *R. rubrum* cyt c_2 have suggested that His42 in *R. rubrum* cyt c_2 ionizes with a near-neutral pK_a of 6.8 in the ferrous state.[23, 24] This was supported by the observations made with the NOE difference spectroscopy that irradiated a methyl group of pH-invariant Leu32, where it was revealed that a typical histidine proton that had a pK_a of 7, supporting the hypothesis that His42, the only non-ligated His in *R. rubrum* cyt c_2, has a higher pK_a than that of HP7.[23, 24] Similar observations were made in other NMR experiments, which suggested that the pK_a pf H42F reduces to 6.2 in the ferric state.[25] Yet, recent analysis of ^{1}H NMR pH titration measurements with ferric WT cyt c_2 have shown that the protons in the methylene group of HP7 titrates with a pK_a of 6.8 ± 0.11,[36] complicating the identification of the participating ionizable groups in PCET. Similarly, other resonances in the NMR spectra have been previously observed to shift with the similar pK_a.[27] This discrepancy has been previously argued to stem from local conformational rearrangements in the protein, as shifts in hyperfine and pseudocontact shifts reflect change in the electronic structure of the heme.[27]

Inspection of ΔH_P from calorimetric measurements offers clues to the identity of the ionizable groups when coupled to ET. Comparison of net enthalpy of ionization in the protein, ΔH_P, in WT and H42F cyt c_2 further suggests that in H42F, PT is no longer coupled to ET (Figure 8.12). In WT cyt c_2, ΔH_P is the sum of the ionization enthalpies of the deprotonating groups in the protein at a given pH and is dependent on the fractional population dictated by the pK_a of each group. At low pH conditions where all species are protonated, ΔH_P simply reflects the total ionization enthalpy for deprotonation of two ionizable groups, which is near -7.5 kcal/mol (Figure 8.12 and Table 8.8). Free histidine has an ionization constant of 7.1 kcal mol^{-1}.[31] Previous analysis of temperature-dependent NMR measurements with myoglobin have shown that histidine ionization constants in a protein environment can range from 3.8 to 8.8 kcal mol^{-1},[30] in which HB contacts can decrease this value by about 2 kcal mol^{-1}. Previously reported calorimetric characterization of aspartic protease shows that solvent-exposed His ionization enthalpy is 7.0 ± 0.2 kcal mol^{-1}.[43] Although the ionization enthalpy of HP groups were not measured, carboxylate groups in aspartates have been shown to have ionization enthalpies of -2.1 ± 0.8 kcal mol^{-1} in proteins,[43] while ionization enthalpy of acetate is -0.1 kcal mol^{-1}.[31] Based on eq 8.15 and scheme 8.2, and assuming that the ionization enthalpy for HP7 has an ionization enthalpy between -2.1 to -0.1, ΔH_P can only be -7.5 kcal mol^{-1} at low pH conditions if the His ionization enthalpy is between 5.4 to 7.4 is the group to be deprotonated in the reduction of cyt c_2.

From our ITC measurements, the transition is most likely present somewhere between pH 6.5 and 7 in WT cyt c_2. Yet, lack of points in this transition makes it difficult to obtain the pK_a value(s) involved in the protein ionization, as the transition is steep. With

the elimination of His42 in H42F cyt c_2 variant, magnitude of ΔH_P is near zero. Large error bars in the lower pH region make it difficult to determine if there is ionization enthalpy contribution from the HP7 in the absence of His42 (Figure 8.12). Ionization enthalpy of carboxylate groups are relatively small in magnitude compared to that of His,[43] and it is likely that the ionization enthalpy of carboxylate groups in the heme propionate can shift depending on the solvent exposure as was observed with His. In combination with observations of Δn with pH (Figure 8.10) and a lack of a pH dependent k_{ESE} in H42F,[36] it is most likely that His42 participates in the PCET mechanism in cyt c_2, and elimination of His42 perturbs the PCET mechanism.

Since ITC measures the total heat of the reaction, there is a possibility that other enthalpic contributions can be present that are not considered in our analysis. Global stability measurements of WT cyt c_2 have shown greater stability at pH 5.0 than at pH 7.4, despite comparable EPR and electronic absorption spectra between pH 5.0 and 8.0 that have suggested that the global fold of the protein is similar at these two pH conditions.[36] Differences in global stability at pH 7.4 and 5.0 suggest possible differences in local dynamics and stability in cyt c_2 as was observed in cyt *c* due to pH-dependent tertiary contacts in the polypeptide fold.[44] Introduction of a hydrophobic Phe near the heme cavity may also affect the local dynamics and stability of the loop. Yet, comparison of ^{1}H NMR spectra of ferric and ferrous WT cyt *c* ranging from pH 8.5 to 4.5 have shown that the peak positions of the heme porphyrin and heme-bound Met91 are unchanged,[36] suggesting that the protein does not experience major structural perturbations at either of the oxidation states. Thus, it is most likely that even if there are additional enthalpic contributions

associated with changes in conformational dynamics, it is small and likely not the dominant factor in the PCET mechanism in WT cyt c_2.

pH-dependent Reduction Potentials. Reduction potential of WT cyt c_2 increases from 311 ± 2 mV at pH 8.0 to 370 ± 2 mV at pH 5.0,[36] similar to the reduction potential range observed from ferricyanide titrations.[21] The observed reduction potentials $E°_{obs}$ for WT cyt c_2 that includes the protonation equilibria yield reduction potentials within the range observed from previous experiments (Table 8.9). Taking the protonation equilibria into account, the corrected reduction potential of the heme ($E°_{corr}$) decreases (Table 8.9), close to $E°_{obs}$ from H42F (Table 8.12). WT cyt c_2 has a slightly higher reduction potential from pH 7.8 to 6.8 than H42F. However, this difference in reduction potential may be due to introducing mutations that directly perturb HB contacts near the HP groups. Comparisons of previous electrochemical titration measurements with ferricyanide and WT cyt c_2 from various species have suggested that natural sequences variations near the heme environment tuned the reduction potential by up to 30 mV.[21] Although the H42F mutation does not affect heme ligation,[36] placement of a hydrophobic Phe near the heme may also affect polypeptide packing and dynamics, which also tune the reduction potential of the protein.[45] These minor conformational rearrangement could potentially shift the reduction potential of cyt c_2. In cyt *c*, shifts in the reduction potential have been observed with perturbations that affect the HB contacts between the polypeptide and the heme.[45-47]

In WT cyt c_2, there is a step-wise increase in $E°_{corr}$ by about ~10 mV between pH 7.8 to 6.8 and 6.6 to 5.6 in WT cyt c_2 (Table 8.9 and Figure 8.13). This is most likely from the changes in the external inorganic compound, and possible changes in the reduction

potentials of the inorganic compounds with pH that may be different between $[Fe(CN)_6]^{3-}$ and $[Co(terpy)_2]^{2+}$. Even in the widely used oxidant, $[Fe(CN)_6]^{3-}$, the reduction potential of this compound has been shown to vary by almost 30 mV in biological buffers, depending on the ionic conditions, buffer concentrations, buffer type, and pH conditions.[38, 48-50] In particular, the reduction potential of $[Fe(CN)_6]^{3-}$ decreases with pH, which should also decrease $E°_{corr}$. Although ionic conditions were kept constant and buffer concentrations low in our experiments, pH conditions were varied by nearly two pH units from pH 7.6 to 5.6 in WT cyt c_2. Previously, the reduction potential of $[Fe(CN)_6]^{3-}$ has been shown to vary ~10 mV between pH 8 and 4.75.[50] Yet, we have assumed that the reduction potential of $[Fe(CN)_6]^{3-}$ does not vary at all pH conditions considered, using the reported reduction potential for $[Fe(CN)_6]^{3-}$ at similar ionic conditions at pH 7.2,[38] well-within reported reduction potential for biological buffers at higher buffer and ionic conditions.[48, 50] This may also explain the ~10 mV shift in the reduction potential observed with decrease in pH with H42F (Table 8.12 and Figure 8.13), despite the perturbed net PT (Figure 8.10).

Furthermore, there may be local variations in structure when the protein interacts with these inorganic complexes at different pH conditions, which may also affect K_{eq}. that were not considered in the calculation of $E°_{corr}$. We decided to use $[Fe(CN)_6]^{3-}$ and $[Co(terpy)_2]^{2+}$ complexes as these compounds were used in ET measurements with cytochrome *c*, a similar ET protein as cyt c_2.[37, 38, 42, 51] Although preferred sites of contacts for Fe- and Co-complexes are suggested to be similar in cyt *c*,[37, 51] the interactions of common inorganic complexes are thought to occur from the interactions near the exposed heme edge.[42] In WT cyt c_2, PCET is thought to involve HP7 and His42, residues near the exposed heme edge. Signs of conformational rearrangement has been observed in *R.*

palustris and *R. rubrum* cyt c_2 in the pH ranges observed in our ITC experiments, as observed from shifts in the heme porphyrin peaks in NMR, UV-vis, and changes in ET kinetics.[22, 27] Perhaps, these local differences also influence $E°_{corr}$.

Additionally, changes in surface charge of the protein may also contribute to the ~10 mV shift over the course of the observed pH range in the $E°_{corr}$ for both WT and H42F cyt c_2 variants. Previous studies have shown that ionic strength of the media alters the reduction potential in *c*-type cytochromes such as cyt c_{552}[52] and cyt *c*.[53] Furthermore, trifluoroacetylation of surface Lys residues in *P. aeruginosa* cyt c_{552} have shown that the reduction potential of the heme iron decreased by approximately 5 mV per surface charge.[54] Thus, the general shift in the $E°_{corr}$ over the acidic to near-neutral pH ranges may also stem from changes in surface charge of our variants.

Conclusion

Spectroscopic characterizations and kinetic ET measurements have suggested the participation of His42 in the cytc_2 PCET mechanism. By using ITC to obtain the total enthalpy involved in the electrochemical reactions, a buffer-independent enthalpy of the ionizable groups participating in the PCET has been characterized. The difference in the enthalpy between the WT and H42F strongly suggests that in WT cyt c_2, His42 does indeed participate in the PT mechanism in PCET. Although the sensitivity of the method does not clearly define the pK_a values of the ionizable groups based on the changes of ΔH_P in respect to pH, ΔH_P calculations in WT cyt c_2 are consistent with having a histidine as an ionizable group in the PCET mechanism. Possibility of a carboxylate group in the HP participating in tandem with histidine as a PT unit is inconclusive with this data set.

When contributions from PT are considered, the reduction potential of the heme in WT cyt c_2 independent of protonation equilibria is comparable to that of the reduction potential of H42F. This shows that in the absence of PT, the heme has similar reduction potentials. Slight variation in the reduction potential is observed in the two variants in the observed pH ranges. This could potentially be due changes in the reduction potential of the inorganic complexes, conformational rearrangement of the protein, or changes in the surface charge with pH.

References

1. Reece, S.Y., Hodgkiss, J.M., Stubbe, J. & Nocera, D.G. Proton-coupled electron transfer: the mechanistic underpinning for radical transport and catalysis in biology. *Philos T R Soc B* **361**, 1351-1364 (2006).

2. Hammes-Schiffer, S. Proton-Coupled Electron Transfer: Moving Together and Charging Forward. *J Am Chem Soc* **137**, 8860-8871 (2015).

3. Alberts, B., Wilson, J.H. & Hunt, T. *Molecular biology of the cell*, Edn. 5th. (Garland Science, New York; 2008).

4. Huynh, M.H.V. & Meyer, T.J. Proton-Coupled Electron Transfer. *Chem Rev* **107**, 5004-5064 (2007).

5. Dempsey, J.L., Winkler, J.R. & Gray, H.B. Proton-coupled electron flow in protein redox machines. *Chem Rev* **110**, 7024-7039 (2010).

6. Marcus, R.A. On Theory of Electron-Transfer Reactions .6. Unified Treatment for Homogeneous and Electrode Reactions. *J Chem Phys* **43**, 679-& (1965).

7. Marcus, R.A. & Sutin, N. Electron transfers in chemistry and biology. *Biochimica et Biophysica Acta (BBA) - Reviews on Bioenergetics* **811**, 265-322 (1985).

8. Borgis, D. & Hynes, J.T. Dynamical theory of proton tunneling transfer rates in solution: general formulation. *Chemical Physics* **170**, 315-346 (1993).

9. Cukier, R.I. & Nocera, D.G. PROTON-COUPLED ELECTRON TRANSFER. *Annual Review of Physical Chemistry* **49**, 337-369 (1998).

10. Hammes-Schiffer, S. & Soudackov, A.V. Proton-Coupled Electron Transfer in Solution, Proteins, and Electrochemistry. *The Journal of Physical Chemistry B* **112**, 14108-14123 (2008).

11. Bertini, I., Gray, H.B., Stiefel, E.I. & Valentine, J.S. *Biological inorganic chemistry : structure and reactivity*. (University Science Books, Sausalito, Calif.; 2007).

12. Que, L. *Physical methods in bioinorganic chemistry : spectroscopy and magnetism*. (University Science Books, Sausalito, Calif.; 2000).

13. Gray, H.B. & Winkler, J.R. Long-range electron transfer. *Proc Natl Acad Sci U S A* **102**, 3534-3539 (2005).

14. Winkler, J.R., Malmstrom, B.G. & Gray, H.B. Rapid Electron Injection into Multisite Metalloproteins - Intramolecular Electron-Transfer in Cytochrome-Oxidase. *Biophys Chem* **54**, 199-209 (1995).

15. Mikkelsen, K.V., Skov, L.K., Nar, H. & Farver, O. Electron self-exchange in azurin: calculation of the superexchange electron tunneling rate. *P Natl Acad Sci USA* **90**, 5443-5445 (1993).

16. Gray, H.B. & Winkler, J.R. Hole hopping through tyrosine/tryptophan chains protects proteins from oxidative damage. *Proc Natl Acad Sci U S A* **112**, 10920-10925 (2015).

17. Gu, J. *et al.* Control of cytochrome c redox reactivity through off-pathway modifications in the protein hydrogen-bonding network. *Chemical communications (Cambridge, England)* **50**, 5355-5357 (2014).

18. Liu, J. *et al.* Metalloproteins containing cytochrome, iron-sulfur, or copper redox centers. *Chem Rev* **114**, 4366-4469 (2014).

19. Zhong, F.F. & Pletneva, E.V. Mechanistic Studies of Proton-Coupled Electron Transfer in a Calorimetry Cell. *J Am Chem Soc* **141**, 9773-9777 (2019).

20. Moore, G.R. & Pettigrew, G.W. *Cytochromes c : evolutionary, structural, and physicochemical aspects*. (Springer-Verlag, Berlin ; New York; 1990).

21. Pettigrew, G.W., Bartsch, R.G., Meyer, T.E. & Kamen, M.D. Redox potentials of the photosynthetic bacterial cytochromes c2 and the structural bases for variability. *Biochim Biophys Acta* **503**, 509-523 (1978).

22. Battistuzzi, G., Borsari, M., Dallari, D., Ferretti, S. & Sola, M. Cyclic Voltammetry and 1H-NMR of Rhodopseudomonas palustris Cytochrome c2. *Eur J Biochem* **233**, 335-339 (1995).

23. Yu, L.P. & Smith, G.M. Assignments of nitrogen-15 and proton NMR resonances and a neutral pH ionization in Rhodospirillum rubrum cytochrome c2. *Biochemistry* **29**, 2914-2919 (1990).

24. Yu, L.P. & Smith, G.M. Nitrogen-15 and proton NMR studies of Rhodospirillum rubrum cytochrome c2. *Biochemistry* **27**, 1949-1956 (1988).

25. Yu, L.P. & Smith, G.M. Characterization of pH-dependent conformational heterogeneity in Rhodospirillum rubrum cytochrome c2 using 15N and 1H NMR. *Biochemistry* **29**, 2920-2925 (1990).

26. Battistuzzi, G., Borsari, M., Ferretti, S., Sola, M. & Soliani, E. Cyclic Voltammetry and 1H-NMR of Rhodopseudomonas Palustris Cytochrome c2 pH-Dependent Conformational States. *Eur J Biochem* **232**, 206-213 (1995).

27. Smith, G.M. & Yu, L.P. High-resolution 1H- and 15N-NMR studies of Rhodospirillum rubrum cytochrome c2. *Biochimica et Biophysica Acta (BBA) - Bioenergetics* **1058**, 75-78 (1991).

28. Leitch, F.A., Moore, G.R. & Pettigrew, G.W. Structural basis for the variation of pH-dependent redox potentials of Pseudomonas cytochromes c-551. *Biochemistry* **23**, 1831-1838 (1984).

29. Warren, J.J. & Mayer, J.M. Proton-Coupled Electron Transfer Reactions at a Heme-Propionate in an Iron-Protoporphyrin-IX Model Compound. *J Am Chem Soc* **133**, 8544-8551 (2011).

30. Bhattacharya, S. & Lecomte, J.T. Temperature dependence of histidine ionization constants in myoglobin. *Biophysical journal* **73**, 3241-3256 (1997).

31. Goldberg, R.N., Kishore, N. & Lennen, R.M. Thermodynamic quantities for the ionization reactions of buffers. *J Phys Chem Ref Data* **31**, 231-370 (2002).

32. Grossoehme, N.E., Spuches, A.M. & Wilcox, D.E. Application of isothermal titration calorimetry in bioinorganic chemistry. *J Biol Inorg Chem* **15**, 1183-1191 (2010).

33. North, M.L. & Wilcox, D.E. Shift from Entropic Cu2+ Binding to Enthalpic Cu+ Binding Determines the Reduction Thermodynamics of Blue Copper Proteins. *J Am Chem Soc* **141**, 14329-14339 (2019).

34. Sorlie, M., Chan, J.M., Wang, H., Seefeldt, L.C. & Parker, V.D. Elucidating thermodynamic parameters for electron transfer proteins using isothermal titration calorimetry: application to the nitrogenase Fe protein. *J Biol Inorg Chem* **8**, 560-566 (2003).

35. Baker, B.M. & Murphy, K.P. Evaluation of linked protonation effects in protein binding reactions using isothermal titration calorimetry. *Biophysical journal* **71**, 2049-2055 (1996).

36. Carpenter, J.M. in Chemistry, Vol. Bachelor of Science (Dartmouth College, Hanover, NH; 2018).

37. Cummins, D. & Gray, H.B. Electron-transfer protein reactivities. Kinetic studies of the oxidation of horse heart cytochrome c, Chromatium vinosum high potential iron-sulfur protein, Pseudomonas aeruginosa azurin, bean plastocyanin, and Rhus vernicifera stellacyanin by pentaammminepyridineruthenium(III). *J Am Chem Soc* **99**, 5158-5167 (1977).

38. Butler, J., Davies, D.M. & Sykes, A.G. Kinetic data for redox reactions of cytochrome c with Fe(CN)5X complexes and the question of association prior to electron transfer. *Journal of inorganic biochemistry* **15**, 41-53 (1981).

39. Farina, R. & Wilkins, G. Electron-Transfer Rate Studies of a Number of Cobalt(2)-Colbalt(3) Systems. *Inorg Chem* **7**, 514-& (1968).

40. Croteau, M.L., Vol. 10144800 245 (Dartmouth College, Ann Arbor; 2016).

41. Meier, M. & van Eldik, R. Volume profile analysis for intermolecular electron transfer between cytochrome c and Co(terpy)22+/3+. *Inorganica Chimica Acta* **225**, 95-101 (1994).

42. Wherland, S. & Gray, H.B. Metalloprotein Electron-Transfer Reactions - Analysis of Reactivity of Horse Heart Cytochrome-C with Inorganic Complexes. *P Natl Acad Sci USA* **73**, 2950-2954 (1976).

43. Xie, D. *et al.* Dissection of the pH Dependence of Inhibitor Binding Energetics for an Aspartic Protease: Direct Measurement of the Protonation States of the Catalytic Aspartic Acid Residues. *Biochemistry* **36**, 16166-16172 (1997).

44. Krishna, M.M.G., Lin, Y., Rumbley, J.N. & Englander, S.W. Cooperative omega loops in cytochrome c: Role in folding and function. *J Mol Biol* **331**, 29-36 (2003).

45. Oviedo-Rouco, S. *et al.* Electron transfer and conformational transitions of cytochrome c are modulated by the same dynamical features. *Arch Biochem Biophys* **680**, 108243 (2020).

46. Deng, Y.L., Zhong, F.F., Alden, S.L., Hoke, K.R. & Pletneva, E.V. The K79G Mutation Reshapes the Heme Crevice and Alters Redox Properties of Cytochrome c. *Biochemistry* **57**, 5827-5840 (2018).

47. Guerra-Castellano, A., Diaz-Moreno, I., Velazquez-Campoy, A., De la Rosa, M.A. & Diaz-Quintana, A. Structural and functional characterization of phosphomimetic

mutants of cytochrome c at threonine 28 and serine 47. *Biochim Biophys Acta* **1857**, 387-395 (2016).

48. Kolthoff, I.M. & Tomsicek, W.J. The oxidation potential of the system potassium ferrocyanide-potassium ferricyanide at various ionic strengths. *J Phys Chem-Us* **39**, 945-954 (1935).

49. Liu, Y., Seefeldt, L.C. & Parker, V.D. Entropies of Redox Reactions between Proteins and Mediators: The Temperature Dependence of Reversible Electrode Potentials in Aqueous Buffers. *Analytical biochemistry* **250**, 196-202 (1997).

50. O'Reilly, J.E. Oxidation-reduction potential of the ferro-ferricyanide system in buffer solutions. *Biochimica et Biophysica Acta (BBA) - Bioenergetics* **292**, 509-515 (1973).

51. Butler, J. *et al.* Preferred Sites for Electron-Transfer between Cytochrome-C and Iron and Cobalt Complexes. *Journal of Biological Chemistry* **258**, 6400-6404 (1983).

52. Goldkorn, T. & Schejter, A. The redox potential of cytochrome c-552 from Euglena gracilis: A thermodynamic study. *Arch Biochem Biophys* **177**, 39-45 (1976).

53. Margalit, R. & SCHEJTER, A. Cytochrome c: A Thermodynamic Study of the Relationships among Oxidation State, Ion-Binding and Structural Parameters. *Eur J Biochem* **32**, 492-499 (1973).

54. Costa, C. & Moore, G.R. The effect of surface charge on the reduction potential and heme propionate ionization of a monoheme cytochrome: spectroscopic and potentiometric studies of trifluoroacetylated cytochrome c551 from Pseudomonas aeruginosa. *Inorganica Chimica Acta* **275-276**, 256-262 (1998).

Chapter 9
Concluding Remarks

This thesis aims to provide further insight into how perturbations in polypeptide peripheral contacts tune protein structure, stability, and function using *c*-type cytochromes. Understanding this structure-function relationship is essential because sequence variations are common in organisms and these variations can introduce unique perturbations to the intramolecular contacts.

In cyt *c*, peripheral contacts involving the heme and loops C and D have been suggested to play a role in tuning the local and dynamic properties of the protein.[1-3] Yet, cyt *c* has similar global fold and stability across many species,[4-6] and understanding of how these differences in contacts influence function has been lacking. Clarifying the function-structure relationship is essential, as cyt *c* structural perturbations introduced in the form of sequence variations are correlated to cause disease and abnormal embryonic development.[7-10]

G41S, Y48H, and K72A mutations that introduced perturbations in loops C and D do not affect the global fold and stability of the protein at near-neutral pH. These structural perturbations, however, have different effects in local properties and function. A variant with the loop D perturbation has been comparable to the WT protein in all aspects. In variants with loop C perturbations, local stability and dynamics of loop D are affected. The heme is more readily accessible, and the functions of the protein are affected: intrinsic peroxidase activity increased, ET properties altered, and the protein is readily rearranged to yield a Lys-ligated conformer at a lower pK_a. These loop C perturbations are different from one another, in G41S. an additional species not observed in other variants, are detected in the acidic unfolding transition. Kinetics of the alkaline transition trends differently in horse variants compared to that of human variants. Structural models show

that perturbations in loop C alter the interloop contact between loops C and D in horse heart cyt *c*, which is different from human cyt *c* variants where more native contacts observed in the WT protein are preserved. Differences in peripheral contacts involving HP6 and residue 46 in loop C have previously been suggested to result in variations in the alkaline transition parameters,[1] and the identity of residue 46 is different between human and horse heart cyt *c*. These results highlight that peripheral contacts near HP6 assist in keeping loop C packed closely to loop D, and tune properties of loop D to influence protein function.

Peripheral contacts that are formed with the heme are important in controlling the polypeptide fold and heme ligation. Some perturbations alter the native tertiary packing of the polypeptide and trigger conformational rearrangements. Local rearrangement of loop D allows a Lys residue to readily replace Met80 even at near-neutral pH conditions. Proper heme ligation and fold are essential, as the identity of the heme ligand alters the reduction potential and peroxidase activity of the protein. This is also true in the cardiolipin-bound state, as the formation of bisHis-ligated species suppresses activity at physiological conditions.

These structure-function relationships observed in cyt *c* are also observed in *R. rubrum* cyt c_2, a protein with a pH-dependent reduction potential. Previous spectroscopic attempts to characterize this protein have been complicated by challenges associated with distinguishing the various ionizable groups, as possible conformational rearrangements and spectral overlap can also alter spectral features.[11] In this protein, His42 is within a HB distance to HP7, and is an essential component in ET. Replacement of His42 with a non-ionizable residue to perturb this contact does not perturb the global fold and heme ligation.[12] However, perturbation of this contact to the heme eliminates the net proton

transfer in the ET mechanism. Furthermore, enthalpic contributions from the polypeptide is no longer observed in the ET mechanism, and proton transfer does not contribute to the observed reduction potential.

This thesis highlights the disconnect between global and local properties of the protein—similarities in global features do not necessarily equate to similarities in local properties. Throughout this thesis, I showed how changes in peripheral contacts modulate local properties and protein function in *c*-type cytochromes, without altering its global properties. I also provided additional insights into how sequence variations are tolerated in nature and how proteins from various species can be similar and different at the same time. These findings and connections are significant, as it serves as a caveat in assuming conservation of global structure equates to conservation in function. Homology modeling and multiple sequence alignments are common approaches to predict and analyze protein structure, function, interactions, and its related mechanisms.[13-15] However, such approaches may ignore the local differences between similar proteins, which may be important to consider in many medical studies, where non-human animal models are commonly used to indirectly assess effects on humans.

There are still some aspects of the structure-function relationship that have not been discussed in detail. In the appendices, preliminary explorations of structure-function relationship in the unfolded states are presented, along with future recommendations.

References

1. Saigo, S. Kinetic and equilibrium studies of alkaline isomerization of vertebrate cytochromes c. *Biochim Biophys Acta* **669**, 13-20 (1981).

2. Hoang, L., Maity, H., Krishna, M.M., Lin, Y. & Englander, S.W. Folding units govern the cytochrome c alkaline transition. *J Mol Biol* **331**, 37-43 (2003).

3. Krishna, M.M.G., Lin, Y., Rumbley, J.N. & Englander, S.W. Cooperative omega loops in cytochrome c: Role in folding and function. *J Mol Biol* **331**, 29-36 (2003).

4. Alvarez-Paggi, D. *et al.* Multifunctional Cytochrome c: Learning New Tricks from an Old Dog. *Chem Rev* **117**, 13382-13460 (2017).

5. Knapp, J.A. & Pace, C.N. Guanidine-Hydrochloride and Acid Denaturation of Horse, Cow, and Candida-Krusei Cytochromes-C. *Biochemistry* **13**, 1289-1294 (1974).

6. Hanske, J. *et al.* Conformational properties of cardiolipin-bound cytochrome c. *P Natl Acad Sci USA* **109**, 125-130 (2012).

7. Hao, Z.Y. *et al.* Specific ablation of the apoptotic functions of cytochrome c reveals a differential requirement for cytochrome c and apaf-1 in apoptosis. *Cell* **121**, 579-591 (2005).

8. De Rocco, D. *et al.* Mutations of cytochrome c identified in patients with thrombocytopenia THC4 affect both apoptosis and cellular bioenergetics. *Bba-Mol Basis Dis* **1842**, 269-274 (2014).

9. Morison, I.M. *et al.* A mutation of human cytochrome c enhances the intrinsic apoptotic pathway but causes only thrombocytopenia. *Nat Genet* **40**, 387-389 (2008).

10. Johnson, B. *et al.* Whole exome sequencing identifies genetic variants in inherited thrombocytopenia with secondary qualitative function defects. *Haematologica* **101**, 1170-1179 (2016).

11. Zhong, F.F. & Pletneva, E.V. Mechanistic Studies of Proton-Coupled Electron Transfer in a Calorimetry Cell. *J Am Chem Soc* **141**, 9773-9777 (2019).

12. Carpenter, J.M. in Chemistry, Vol. Bachelor of Science (Dartmouth College, Hanover, NH; 2018).

13. Wilson, C.A., Kreychman, J. & Gerstein, M. Assessing annotation transfer for genomics: quantifying the relations between protein sequence, structure and function through traditional and probabilistic scores11Edited by F. E. Cohen. *J Mol Biol* **297**, 233-249 (2000).

14. Kelley, L.A., Mezulis, S., Yates, C.M., Wass, M.N. & Sternberg, M.J.E. The Phyre2 web portal for protein modeling, prediction and analysis. *Nature Protocols* **10**, 845-858 (2015).

15. Waterhouse, A. *et al.* SWISS-MODEL: homology modelling of protein structures and complexes. *Nucleic Acids Res* **46**, W296-W303 (2018).

Appendix I

Effects of Structural Perturbations in Cardiolipin-Induced Binding and Unfolding of Cytochrome *c*

Introduction

Interaction of cyt *c* with CL)-containing lipid membrane surface triggers a sequence of events that perturb the native polypeptide fold and heme axial ligation, ultimately increasing the peroxidase activity of the protein.[1] Cyt *c*-CL interaction results in diverse conformations, and is reminiscent of chemically unfolded cyt *c*. As in chemically unfolded cyt *c*, heme iron ligation is varied, and 5-coordinate or 6-coordinate H_2O/OH^-, His, and Lys-ligated heme species have been previously observed in CL-bound cyt *c*.[2-5] Conformational heterogeneity of the polypeptide observed in chemically unfolded cyt *c*,[6-8] and in the presence of high concentrations of CL, where two distinct conformations are observed on the lipid surface: a compact (C), native-like state and an extended (E), extensively unfolded state.[9]

There are many similarities between the perturbed polypeptide structure of cyt *c* in the presence of CL and other chemical denaturants (such as urea and GuHCl) in that it triggers local and/or global unfolding of the polypeptide. However, it is yet unclear whether local interactions in the polypeptide affect the conformational ensemble in the CL-bound state. Unfolding sequences of cyt *c* have been extensively studied by HX experiments, and many local polypeptide interactions have been suggested to play a role in triggering many conformational rearrangements observed in cyt *c*.[10-12] Roles of local interactions, stability, and dynamics in the CL-bound ensemble are yet unclear. While key inter-residue interactions, such as the His26-Pro44 HB, have been suggested to play a role in triggering structural rearrangements in the early steps of CL-binding interaction,[1, 13] large conformational rearrangements are electrostatically driven in CL-bound cyt *c*.[2, 14] Alterations in the available surface area and charge affect conformational equilibrium, and

population shifts between the E and C states have been suggested as a pathway to control the apoptotic peroxidase activity.[14] Electrostatic interactions dominate the conformational equilibrium between E and C states,[14] but it is possible that this equilibrium may be sensitive to perturbations in the polypeptide close to the heme. Inclusion of additional His residues, such as in Y67H variant (Chapter 7), seems to favor the formation of bisHis-ligated species which may affect the population distribution of C and E species. Furthermore, thermal unfolding at low pH conditions and Dns-labeled studies have suggested that CL binding leads to structural rearrangement in residues 37-61.[9, 13] Various heme ligations, including Lys-ligated heme iron species have been observed,[4, 5] highlighting the importance of loop D rearrangement in the CL-bound conformational equilibrium. These findings strongly suggest that CL-induced perturbations and the overall CL-bound ensemble may be sensitive to differences in local dynamics of loops C and D that can also alter the relative stabilities of the stabilized misligated states.

To test this hypothesis, variants with loops C mutations G41S or Y48H, and a variant with loop D mutation K72A, were compared to that of WT horse heart cyt *c* protein. G41S and Y48H mutations are implicated in abnormal apoptotic behavior,[15, 16] and have been shown to perturb dynamics of loop D (Chapter 3), In contrast, K72A mutation in loop D is similar to that of WT (Chapter 4). Despite many differences between these variants, the binding affinities of these cyt *c* variants to CL-containing vesicles (Figures 3.20 and 4.17) and CL-bound peroxidase activities (Tables 3.7 and 4.8, Figures 3.21 and 4.18) are comparable to that of WT. Yet, many of the local properties are different, making these variants good models to see whether local differences in stability and dynamics do not influence the CL-bound ensemble.

To track the changes in the conformational ensemble with the mutations in loops C and D, Glu92Cys mutation at the α-helix of the *C*-terminus has been introduced. Presence of a surface cysteine allows thiol reactive dyes, such as dansyl (Dns) fluorophore, 1,5-IAEDANS, to covalently attach to the protein (Figure A1.1).[17] Attached to cyt *c*, the fluorescence of the Dns fluorophore (donor) is quenched by the iron heme (acceptor) and the observed fluorescence intensity of the dye is diminished compared to the dye in the absence of the heme. The amount of quenching experienced by the fluorophore depends on its distance to the heme, making it a good spectroscopic ruler to track changes in distance between selected sites in the polypeptide and the heme.[18] While steady-state fluorescence measurements show the total fluorescence intensity of the sample, individual quenching events are tracked and distinguished by time-correlated single photon counting (TCSPC) to obtain information regarding the distribution of the donor to acceptor distances of cyt *c*.[6, 18]

In this Appendix, preliminary results are summarized. Initial measurements have shown inconsistencies in the data depending on the spectroscopic measurements, requiring a closer look at how the vesicle solutions have been prepared. Depending on the method of vesicle preparation, differences in spectroscopic data have been observed. Suggestions and possible future recommendations are provided.

Materials and Methods

General. All aqueous solutions were prepared using water from Barnstead E-Pure Ultrapure Water Purification System, purified to a resistivity of 18 MΩ·cm. Reagents and columns were purchased from Millipore Sigma and GE Healthcare, unless noted otherwise.

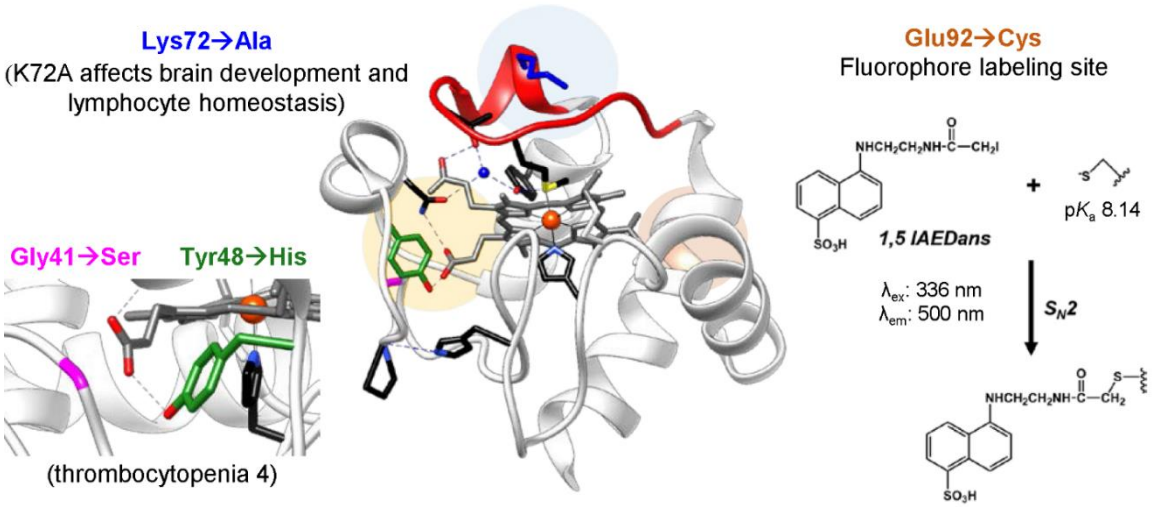

Figure A1.1. Structure of WT horse heart cyt *c* (PDB 1HRC) highlighted with the residues mutated in this study. Mutation of Lys72 to Ala (blue) in mice has been shown to affect brain development and lymphocyte homeostasis.[19] Naturally occurring mutations of Gly41 (pink) and Tyr48 (green) to Ser and His, respectively, have been shown to result in mild thrombocytopenia in humans.[15, 16] Region of the protein that contains the axial ligands to the heme, loop D (residues 70 to 85) is highlighted (red). Cys92 in the *C*-terminal helix have been mutated to Cys (orange) and introduce a labeling site for a dansyl (Dns) fluorophore (1,5 IAEDans).

All labeling reactions, purification and experiments with labeled proteins were performed in the dark. Gas-tight Hamilton syringes were used for quantitative dilutions. pH was adjusted using sodium hydroxide or hydrochloric acid and monitored with an AB15 pH meter (Fisher Scientific) or a UB10 pH meter (Denver Instrument). All buffers were freshly prepared and filtered with a 0.22 μm filter prior to use.

Site-Directed Mutagenesis, Protein Expression, and Purification. Point mutations, protein expression and purification for horse heart cyt *c* variants were performed as previously described.[9] Some variants included the E92C point mutation to introduce a surface cysteine required to label the protein with a fluorescent dye. Desired substitutions were introduced in the pBTR plasmid encoding horse heart cyt *c* using a QuikChange kit (Agilent) and confirmed by DNA sequencing as well as MALDI of the purified protein samples at the Molecular Biology & Proteomics Core Facility (Dartmouth College). Extinction coefficients of protein variants that do not contain the E92C mutation were determined using hemochrome assays[20] in a 25 mM HEPES or a 100 mM sodium phosphate buffer at pH 7.4, in a 25 mM MES buffer with 1 mM DTPA at pH 6.0, or in a 25 mM acetate buffer with 1 mM DTPA at pH 7.4.

Preparation of Fluorophore-Labeled Variants. Freshly harvested proteins containing E92C mutations were first treated with excess dithiothreitol (DTT) to break the intermolecular disulfide bonds between the surface Cys residues. Proteins were then exchanged into a 100 mM sodium phosphate buffer at pH 7.4 using a 50 mL desalting column. After buffer exchange, the protein solution was then diluted to 10 mL, containing 50 to 60 μM protein. A 1 mL solution containing 5 to 7-fold excess of a thiol-reactive dansyl (Dns) fluorescent dye 1,5-IAEDANS (Invitrogen) and 3 to 5% DMSO (*v*/*v*) was

prepared. The Dns-containing solution was slowly added to the protein solution at a rate of drop/3 to 5 seconds under rapid stirring, and the solution allowed to stir at 4 °C for 2 to 3 hours to avoid over-labeling and protein denaturation The reaction was quenched by adding excess DTT, and the protein dialyzed in 10 mM sodium phosphate buffer at pH 7.4 prior to purification on a HiTrap SP HP ion-exchange column to separate the labeled protein from unlabeled protein and excess dye. MALDI measurements confirmed successful labeling reactions. All labeled proteins were stored at 4 °C and used within 5 days.

Preparation of Lipid Vesicles. All lipids were obtained from Avanti Polar Lipids, Inc. Vesicle solutions were filtered using a buffer-treated and dried syringe filter with 0.45 μm pores to remove titanium dust that may have been introduced during sonication and extrusion prior to use. Inclusion of the final filtering step did not alter the vesicle size and distributions. Vesicle sizes and distributions were determined using dynamic light scattering (DLS) instrument (Wyatt Technologies) and were used within the day. Vesicles prepared from previously described methodology yielded vesicles sufficient for peroxidase activity assays.[21, 22] However, further optimization of the vesicle preparation was needed since scatter from the vesicles was observed in fluorescence measurements.

Lipids TOCL and DOPC were mixed in a 1 to 1 molar ratio in a glass vial, with a total lipid concentration of 2.2 to 1.1 mM. The total concentration was decreased to 1.1 mM to ensure better incorporation of the lipids in forming the liposomes, and smaller stock volumes (1 to 1.5 mL) were prepared. The chloroform-suspended lipid mixtures were dried under constant N_2 flow and placed under vacuum for 30 minutes. Desiccated lipid mixtures were then resuspended in a freshly prepared 25 mM HEPES buffer at pH 7.4. Buffers were treated with a Chelex resin (Sigma) to remove excess metal ions in solution prior to use.

Although addition of DTPA to the buffer solution did not alter the vesicle formation (as observed by DLS) and was included in many peroxidase activity assays, DTPA was excluded in the preparation of vesicles used in fluorescence measurements. Resuspended vesicles were fragmented to form small unilamellar vesicles using various techniques.

Sonication Bath. The resuspended lipid stock was incubated in a at 37 °C at 220 rpm for 30 minutes and placed inside an ultrasonic bath sonicator (Branson) for 1 to 1.5 hrs, at 15 min cycles to avoid over sonification. At the end of sonication, the opaque solution cleared slightly and turned translucent white. Vesicles were sonicated at either high or low sonication powers and resulting vesicles compared to determine the effect of sonication power on vesicle-induced scatter. The vesicles were then extruded at 50 °C as using the extruder apparatus equipped with an enclosed warmer (Eastern Scientific LLC) and membranes (Eastern Scientific LLC) with a pore radius of 0.1 μm as previously described.[22] Average radii of the homogeneous vesicles were between 50 to 60 nm, as observed by DLS.

Sonication Tip. The resuspended lipid stock was incubated in a at 37 °C at 220 rpm for 30 minutes and sonicated (30 s on/ 30 s off for 30 min) using an Ultrasonics microtip (Branson) connected to a Fisher Scientific Dismembrator Model 500. The lipid stock was placed inside an ice/water bath to prevent excessive heating from sonification. This method yielded homogeneous vesicles with average radii near 60 nm, larger than previously reported radii of 35 to 43 nm.[9]

Freeze-Thaw. The resuspended lipid stock was incubated in a shaker incubator at 220 rpm under 37 °C for 30 minutes. To increase the incorporation and mixing of the two different lipids in the formation of vesicles, the resuspended lipid stock was then placed at -80 °C

for 10 minutes and thawed under hot tap water (temperatures ranging between 63 to 73 °C), for a total of three cycles. The vesicle solution was then sonicated using the ultrasonics microtip (30 s on/ 30 s off for 15 min) in a water bath, resulting in vesicles with average radii ranging from 60 to 70 nm. In the absence of sonication, extrusion of vesicles after the freeze-thaw cycles resulted in presence of larger radii vesicles, which may have stemmed from rupturing the filters used during manual vesicle extrusion.

Spectroscopic Measurements. Ferric proteins were freshly prepared with excess potassium ferricyanide and purified by size exclusion (PD-10 desalting column) or ion-exchange (Sepharose HP SP) chromatography prior to spectroscopic measurements. Stock protein samples were diluted to 3 to 4ml with desired buffers containing final protein concentrations ranging between 2 to 3 µM using a 100 µl Hamilton syringe for Dns-labeled protein. For non-labeled protein, stock protein solution was diluted to 8 to 9 µM of protein. Stock protein solution contained between 50 to 100 µM, and solutions were not concentrated further to avoid aggregation during sample dilution. Samples used for measuring the fluorescence signals in the folded native state were diluted in a 100 mM sodium phosphate buffer at pH 7.4. Samples used for measuring the fluorescence signals in the denatured state were diluted in a solution containing 6 M GuHCl solution, prepared from dissolving ultrapure GuHCl (Alfa Aesar) in a 100 mM sodium phosphate buffer at pH 7.4 or a 100 mM sodium acetate buffer at pH 4.5. pH of GuHCl solutions were readjusted and solution filtered prior to use. For samples measuring the fluorescence signals in the lipid bound state, stock solutions containing protein or vesicles were slowly mixed dropwise in a 1 to 1 ratio, under high stir, containing the desired concentration of

protein and 250× molar excess of lipids to avoid aggregation. Samples were allowed to equilibrate for at least 30 minutes prior to measurements.

All spectroscopic measurements were obtained at room temperature (22 ± 2 ºC). Different spectral measurements were performed with the same sample, but a fresh aliquot was used for each spectral measurement to prevent signal differences from dye degradation.

Absorption spectra were recorded using an Agilent 8453 diode-array spectrophotometer. Fluorescence spectra were measured on a Horiba Jobin Yvon Fluorolog-3 spectrofluorometer equipped with an automatic polarizer, using a 4 mm pathlength cuvette in the direction of the exit slit. For Dns-labeled protein, Dns dye was excited at 375 nm, and emission recorded from 400 to 600 nm, with the entrance slit bandpass at 3 nm and exit slit bandpass at 5 nm, unless otherwise noted, with a yellow filter was placed in the exit slit to reduce scatter. Samples containing coumarin were excited at 387 nm, and emission recorded from 400 to 600 nm also with the entrance slit bandpass at 3 nm and exit slit bandpass at 5 nm, and a yellow filter was placed in the exit slit to reduce scatter. Spectra were baseline corrected by subtracting the corresponding spectrum of the solution without the protein. To determine the range of protein concentration that shows a linear increase in the fluorescence intensity, spectra of a Dns labeled protein at 6 M GuHCl solution at pH 4.5 with 1 to 20 µM protein were measured. Time-resolved fluorescence energy transfer (TR-FRET) lifetimes were measured by time-correlated single photon counting (TCSPC) at 10,000 counts using a NanoLED-375L diode laser as the excitation source (λ_{ex} = 336 nm, <70 ps pulse width) and Dns emission (λ_{em} = 500 nm) detected with a TBX-04 detector. The diluted solution of LUDOX AS-40 colloidal silica (Sigma Aldrich)

prepared in filtered H_2O was used to measure instrument response function (IRF) as previously described.[9, 21] Coumarin was used as controls, and its emission recorded at 470 nm. Except for TCSPC measurements with the ludox solutions, yellow filter was placed in the detection slit to reduce light scatter in the measurements of the samples. Data analysis of TR-FRET was performed in MATLAB (MathWorks) as previously described.[6, 9]

Results and Discussion

Previous studies with horse heart cyt *c* have reported that labeling the protein with the Dns fluorophore at position 92 have not shown any detectable changes to protein secondary fold and global stability at pH 7.4 when compared to that of non-labeled WT.[9, 23] Fluorescence of Dns fluorophore can be quenched by the heme, resulting in a lowered observed fluorescence intensity of the Dns fluorophore in the folded protein.[9] As such, structural perturbations in the protein that alters the distance between the Dns fluorophore and the heme increase the fluorescence of the Dns fluorophore. Since Dns was placed at position 92, the fluorescence measurements report on the changes in the distance between the *C*-terminal helix and the heme.[21]

Measurement of the steady-state fluorescence of Dns92 cyt *c* shows that the Dns fluorescence intensity in the unfolded protein increases substantially, compared to that of the folded protein at pH 7.4 (Figure A1.2). Analysis of TR-FRET lifetime measurements shows that at denaturing conditions, there is a distinct population that has a greater distance between the donor (Dns fluorophore) and the acceptor (heme) (Figure A1.2). In the CL-bound state at pH 7.4, Dns fluorescence intensity is higher than that of the folded protein, but still lower than that of the unfolded protein.

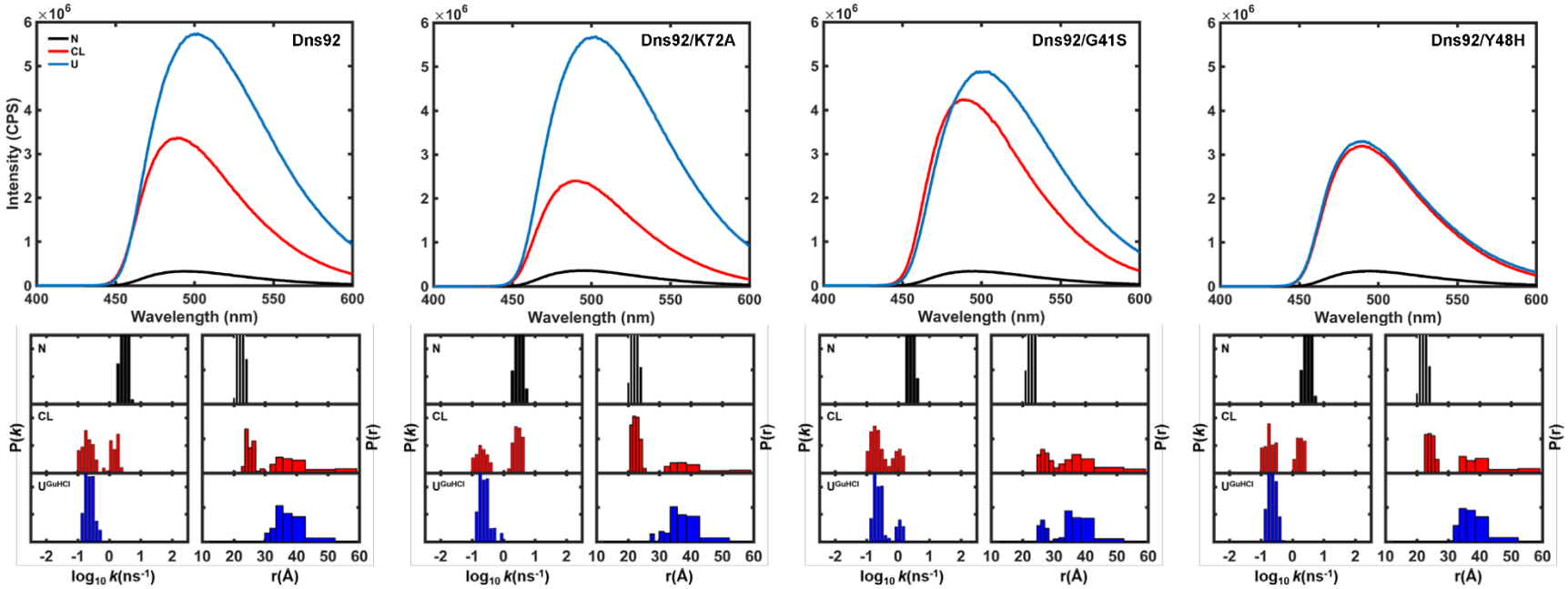

Figure A1.2. (Top) Steady-state fluorescence spectra and (bottom) bar plots comparing the distribution of rate constants (P(*k*), left) and donor-to-acceptor distances (P(r), right) of Dns92-labeled WT (Dns92), K72A (Dns92/K72A), G41S (Dns92/G41S), and Y48H (Dns92/Y48H) variants (3 μM total) in a 25 mM HEPES + 1mM DTPA at pH 7.4 and 25 °C shown for native (black), CL-vesicle bound (50 mol% CL, 750 μM total lipid, red), and unfolded (5 M GuHCl, blue). Steady-state spectra were collected with λ_{ex} = 375 nm and 5nm slit width, using a yellow filter. TCSPC spectra were collected with λ_{ex} = 375 nm and λ_{em} = 500 nm for 10,000 counts.

TR-FRET lifetime measurements show that in the CL-bound state, the protein exists in a heterogeneous ensemble, with native-like compact and unfolded extended species as detected from the *C*-terminal helix (Figure A1.2). These changes observed with Dns92 have been consistent with those reported in literature.[9, 21, 23]

Like that of Dns92, Dns92/K72A, Dns92/G41S, and Dns92/Y48H variants all show comparable steady-state fluorescence spectra, and analysis of TR-FRET measurements suggested similar conformational ensemble in the folded, native state at pH 7.4 (Figures A1.2, top and A1.3A). These fluorescence data are consistent with secondary CD-spectra measurements that have suggested that surface mutations K72A, G41S, or Y48H do not perturb the secondary fold of the protein at pH 7.4 (Figures 3.13 and 4.7). Discrepancies, however, have been observed with the variants in the presence of CL and GuHCl.

In Dns92/K72A, the steady-state fluorescence spectra of the CL-bound species are much lower than that of Dns92, and analysis of TR-FRET lifetime measurements suggests a higher population of native-like species in the presence of high lipid to protein ratio (Figure A1.2). The global stability of K72A is slightly higher than that of WT (Table 4.2). It is then possible that even in the presence of 250-fold excess of lipids, Dns92/K72A contains fewer unfolded-species compared to that of Dns92. Peroxidase activity of measurements of K72A in the presence of CL-containing liposomes shows that the enzymatic activity of K72A is comparable to that of WT at similar lipid to protein ratio conditions (Figure 4.18 and Table 4.8). This suggests that the overall structural perturbation near the heme is comparable between WT and K72A in the presence of CL, although differences may exist in the region near the *C*-terminal helix.

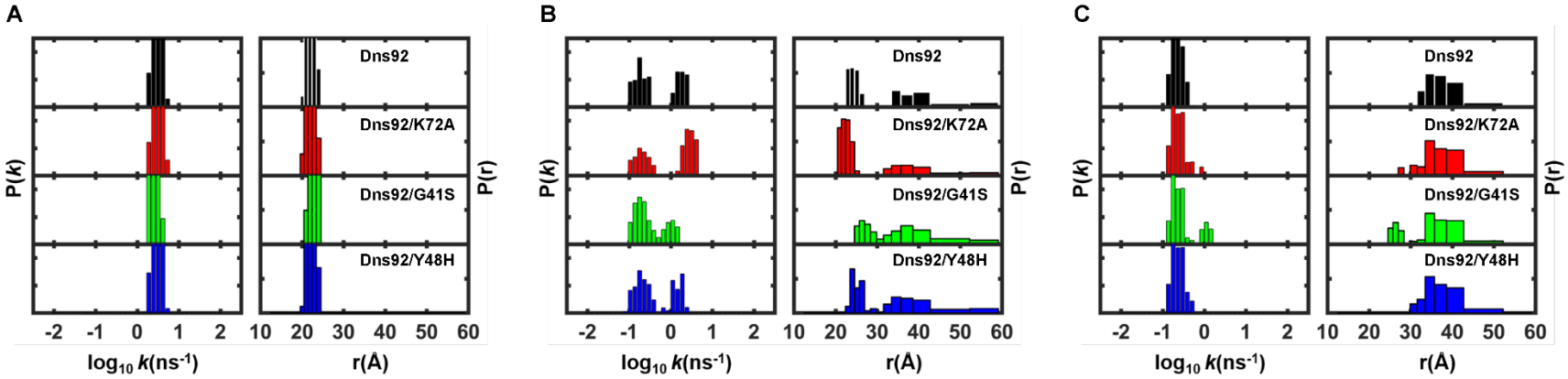

Figure A1.3. Bar plots comparing the distribution of rate constants (P(k), left) and donor-to-acceptor distances (P(r), right) for Dns92 variants (3 μM total) in (A) the folded native state in a 25 mM HEPES + 1mM DTPA buffer at pH 7.4, (B) the CL- bound state in a 25 mM HEPES + 1mM DTPA buffer at pH 7.4 with 750 μM lipid composed of 50 mol% CL and 50% PC, and (C) in the unfolded state with 5 M GuHCl in a 100 mM sodium phosphate buffer at pH 7.4. TCSPC spectra were collected with λ_{ex}=375 nm and λ_{em}=500 nm for 10,000 counts at 25 ° C.

In the presence of 5 M GuHCl, the fluorescence intensity and TR-FRET measurements suggest that the unfolded Dns92/K72A is comparable to Dns92 (Figures A1.2 and A1.3), although slight decrease in the fluorescence intensity is observed (Figure A1.2).

Stability measurements have suggested that the protein will be unfolded by 5 M GuHCl, even with the variants that contain the K72A, G41S, or Y48H mutations (Tables 3.4 and 4.2). Comparisons of TR-FRET data have suggested in the unfolded state, the variants have a high degree of polypeptide unfolding near position 92 as observed with Dns92 (Figure A1.3C). However, in unfolded Dns92/G41S, hints of a minor population with a more compact unfolded species are observed in unfolded Dns92/G41S than in unfolded Dns92 (Figure A1.3C). At pH 7.4, unfolded polypeptide allows His26 or 33 to coordinate to the heme to form the bisHis ligated species,[7] and even the amino group in the *N*-terminal helix have also been shown to coordinate to the heme.[24] Perhaps loop C perturbation at G41S readily allows misligated species to form. Such species are not observed in Dns92/Y48H, a variant that introduces an additional His residue in loop C which could potentially coordinate to the heme in the unfolded state. Further, there are differences between Dns92/Y48H and other variants required a more detailed look at the method of sample preparation and spectra acquisition. TR-FRET measurements suggest that in the unfolded state, the population distribution between Dns92 and Dns92/Y48H are comparable to one another (Figure A1.3C). However, the steady-state fluorescence spectra show a substantial decrease in Dns fluorescence intensity in the unfolded state (Figure A1.2).

Furthermore, reproducibility of the steady-state fluorescence and TR-FRET measurements was of concern, especially with the spectra obtained from the CL-bound species. To avoid over-labeling which could unwillingly increase the number of Dns fluorophore in the protein, the labeling reactions were quenched at earlier time points and contained unlabeled protein fractions prior to chromatography purification. MALDI-TOF measurements consistently have suggested a single Dns label in the variants despite various changes in Dns labeling reactions, making it unlikely the over-labeling to be the cause of inconsistencies in the measured spectra. Variations in concentrations from human error could contribute to the minor differences in the steady-state fluorescence spectra, as Hamilton syringe accuracy is limited to ± 1% of 80% total volume. Yet, large variations in the CL-bound spectra in respect to the protein in denaturing conditions have been repeatedly observed. This persisted despite using dilute protein stock solutions and lower syringe volumes (100 µl syringe versus 250 µl syringe) that decreased the standard deviation of the final protein concentrations to within 0.2 µM across samples. It is unlikely that this concentration deviation is causes the observed variations in fluorescence intensity of the CL-bound samples. Spectra were normalized across variants, and the protein concentrations of the samples are within the range where fluorescence intensity should increase linearly (Figure A1.4). For Dns-labeled proteins, the linear relationship between Dns fluorescence and concentration exists up to 10 µM (Figure A1.4), confirming that normalizing the fluorescence spectra at 2 to to 3 µM of protein concentration assuming a linear relationship is a reasonable assumption.

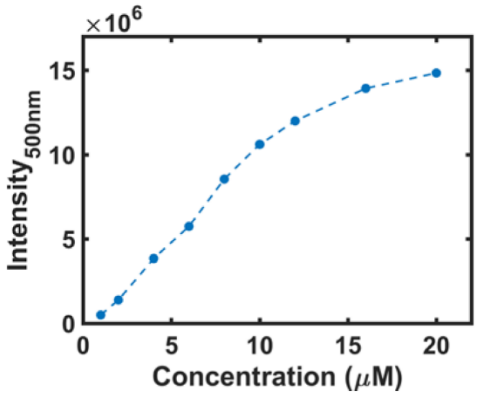

Figure A1.4. Plot showing the change in steady-state fluorescence intensity of Dns in respect to protein concentration for Dns92-labeled proteins. Used were the Dns92/K72A horse cyt *c* variant in a 100 mM sodium acetate buffer at pH 4.5 containing 6M GuHCl.

Although Dns92/K72A was used to observe the changes in fluorescence intensity in respect to concentration, unfolded Dns92/K72A at pH 4.5 should not contain any bisHis-ligated heme species[7] and Dns92 fluorescence should be at its maximum, making it a sufficient upper-limit model for other Dns92 variants.

Effect of Different Vesicle Preparation Methods in Spectral Features.

Various methods of vesicle preparation have been prepared to see whether a particular method of vesicle preparation contribute to increasing the scatter and artificially increase the fluorescence intensity of the Dns labeled protein. Even in previously reported spectra,[9, 21, 23] variations in the ratios of the fluorescence intensity between the CL-bound protein and the native protein are observed depending on the method of vesicle preparation and protein-to-vesicle ratios (Table A1.1). Thus, various stages of sample preparation have been checked to improve the reproducibility and reliability of the data, and to see whether these differences play a part in altering the spectra.

To test this hypothesis, coumarin has been used as a fluorescent probe instead of Dns-labeled protein. Depending on the method of sonication and sonication power, the steady-state fluorescence intensity has been observed (Figure A1.5A). Such variations are not observed in TR-FRET measurement traces (Figure A1.5B). Similar trends in the fluorescence intensity are observed in the Dns92 horse cyt *c*. Depending on the method of sonication used for preparing the liposomes, differences in fluorescence intensity have been observed in respect to the fluorescence intensities of the protein in the unfolded state (Figure A1.6A). Furthermore, the amount of vesicle scatter may change depending on the type of sonication instrument and sonication power used during vesicle preparation.

Table A1.1. Steady-State Fluorescence Spectra of Dns92 Horse Heart Cyt *c* From Literature.[a]

Sample	Peak (nm)	Ratio (CL:N)
Native[b]	480-490	--
CL-bound[b]	490-500	6
Native[c]	475-480	
CL-bound[c]	490-495	9
Native[d]	480	
CL-bound[d]	490	7

[a]Ratios are obtained from comparing the fluorescence intensities of the set peak height of the cardiolipin-bound protein (CL-bound) to the protein in solution (native).

[b]From ref. [9], with 5 μM protein measured in a 25 mM HEPES buffer at pH 7.4, CL-bound samples contained 660 μM total lipid (50 % TOCL and 50% DOPC). Vesicles were sonicated using a microtip sonicator and were filtered using a 0.22 μm filter, with the stock lipid concentration of 3.3 mM.

[c]From ref. [23], with 3 μM protein measured in a 25 mM HEPES buffer at pH 7.4. CL-bound samples contained 750 μM total lipid (50 % TOCL and 50% DOPC). Vesicles were prepared without sonication prior to extrusion, with the stock lipid concentration of 2.2 mM.

[d]From ref. [21], with 3 μM protein measured in a 25 mM HEPES buffer at pH 7.4. CL-bound samples contained 750 μM total lipid (50 % TOCL and 50% DOPC). Vesicles were sonicated using a bath sonicator prior to extrusion, with the stock lipid concentration of 2.2 mM.

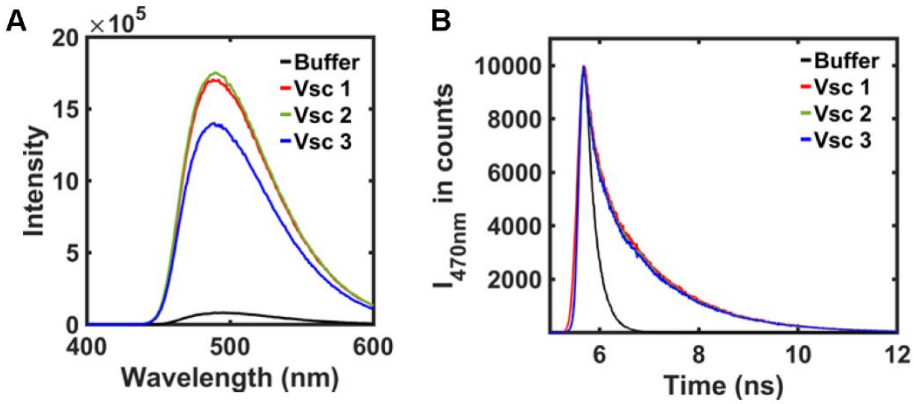

Figure A1.5. (A) Steady-state fluorescence spectra and (B) TCSPC trace for coumarin in a 100 mM sodium phosphate buffer at pH 7.4 (buffer, black), or in a 25 mM HEPES buffer at pH 7.4 with 750 µM total lipid composed of 50 % CL and 50 % PC. Vesicles were prepared using different sonication methods: bath sonicator at low sonication power (vsc 1, red), bath sonicator at high sonication power (vsc 2, green), and microtip sonicator in the presence of an ice bath (vsc 3, blue).

The sonication bath has been replaced between the course of the troubleshooting process, and the fluorescence intensities are different depending on the sonication baths, even at similar high-power settings (compare Figures A1.2 and A1.6A). Spectral differences depending on how the vesicles are prepared are also observed in other spectral measurements. The intensities of the Soret band in the electronic absorption spectra of CL-bound Dns92 cyt *c* varies depending on how the vesicle is prepared, suggesting that differences in the vesicles may also result in local differences in the protein (Figure A1.6B). TR-FRET measurements suggest that there are slight variations in the compact state in the CL-bound protein, although variations from vesicle quality may still be present as observed with controls with coumarin (Figure A1.6D).

Since CL lipids and DOPC have very different phase transition temperatures,[25] and liposome formations are affected by temperature depending on the type of lipid,[26] we have wanted to see if temperature differences are affecting the distribution of TOCL and DOPC lipids, and ultimately affecting how the protein binds and unfolds on the vesicle surface. Thus, lipid suspensions have been exposed to multiple ice and heat shock cycles that are used to help entrapment of water-soluble compounds, as suggested by the lipid manufacturer (Avanti). Total stock lipid concentration has also been varied, and stock concentrations compared between 2.2 mM and 1.1 mM to see whether stock concentrations affect the liposome formation of the two lipids. Although these methods yield vesicle with radii without the adjustments in stock concentrations and heat/shock cycles, differences in the steady-state fluorescence spectra have been observed.

Figure A1.6. (A) Steady-state fluorescence Dns emission spectra normalized to 2 µM, (B) electronic absorption spectra, (C) TCSPC traces and (D) bar plots comparing the distribution of rate constants (P(*k*), left) and donor-to-acceptor distances (P(r), right), of Dns92 horse cyt *c* at 22 ± 2 °C. Various spectra of Dns92 horse heart cyt *c* were obtained for the native state in a 100 mM sodium phosphate buffer at pH 7.4 (black), for the unfolded state in a 6 M GuHCl solution prepared either in a 100 mM sodium acetate buffer at pH 4.5 (red) or in a 100 mM sodium phosphate buffer at pH 7.4 (blue), or in the lipid-bound state in a solution containing total lipid concentration 250 times the protein concentration in a 25 mM HEPES buffer at pH 7.4, prepared either with a bath sonicator (labeled as vsc 1, green) or a microtip sonicator (labeled as vsc 2, purple). For TCSPC measurements, coumarin was also used as controls for vesicle containing solutions, with vesicles prepared with a bath sonicator (yellow) or a microtip sonicator (teal).

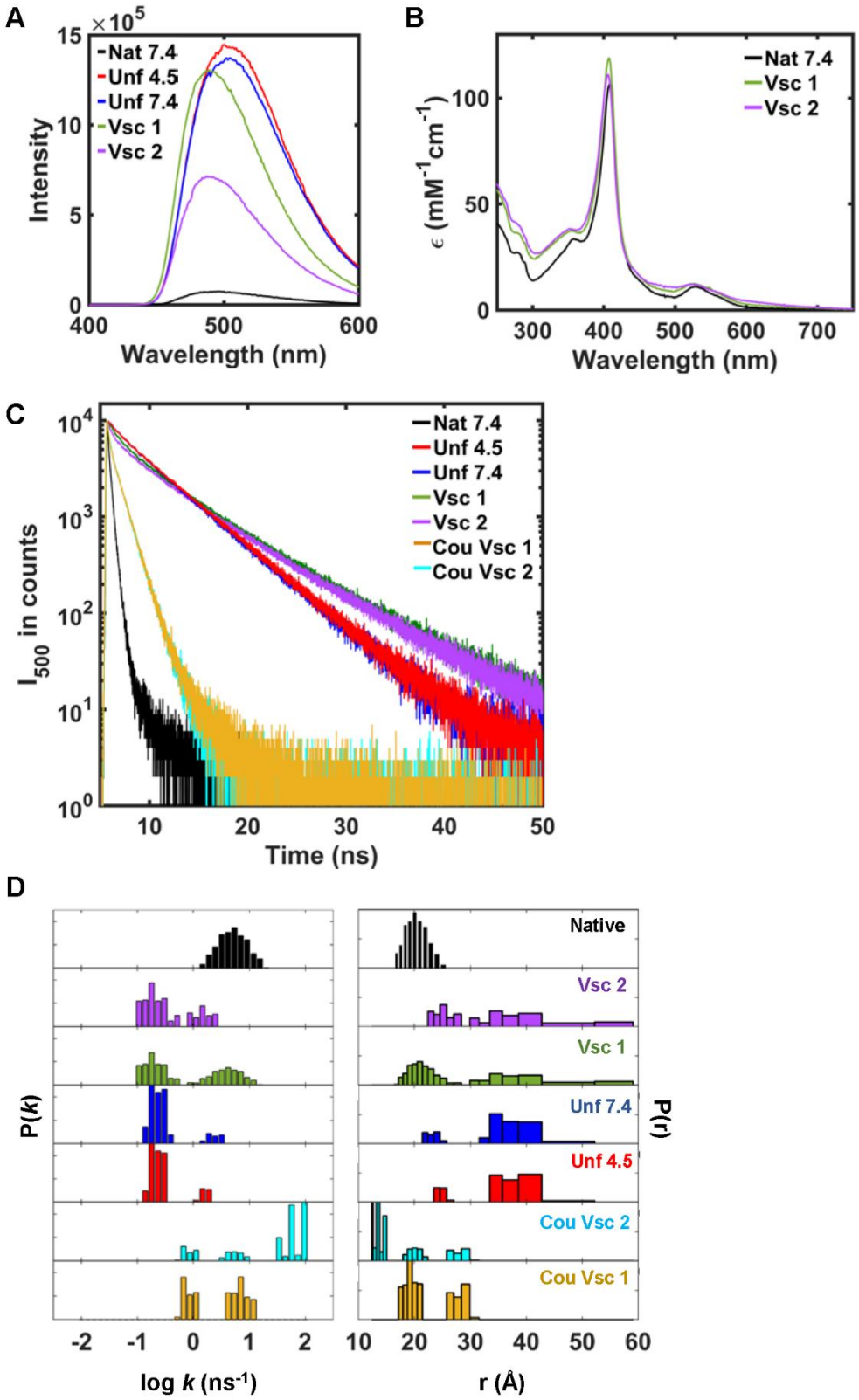
A
×10^5
Intensity
Wavelength (nm)
Nat 7.4
Unf 4.5
Unf 7.4
Vsc 1
Vsc 2
B
ε (mM^-1cm^-1)
Wavelength (nm)
Nat 7.4
Vsc 1
Vsc 2
C
I500 in counts
Time (ns)
Nat 7.4
Unf 4.5
Unf 7.4
Vsc 1
Vsc 2
Cou Vsc 1
Cou Vsc 2
D
P(k)
log k (ns^-1)
P(r)
r (Å)
Native
Vsc 2
Vsc 1
Unf 7.4
Unf 4.5
Cou Vsc 2
Cou Vsc 1

Addition of ice/heat cycles seem to decrease the increase in fluorescence intensity the CL-bound spectra when the vesicles are prepared with extrusion (compare Figure A1.7 vsc 2 to Figure A1.6A, vsc 1). At 1.1 mM stock concentration with heat/ice shock cycles, the fluorescence intensity increase compared to that of 2.2 mM stock concentration with the same microtip sonication method with the fluorescence spectra of the unfolded protein (Figures A1.6A, vsc 2 and A1.7, vsc 1). The fluorescence intensity of the protein samples with these vesicles are much higher than that of the unfolded protein at both pH 4.5 and 7.4, raising the possibility that altering the stock concentration may also contribute to increasing the scatter of the vesicles. Adjustment of slit widths do not affect the spectra and similar trends are observed between the samples (compare Figure A1.7A and A1.7B).

While CL-bound samples have been prepared with 250× molar excess of total lipid to total protein concentration, higher fluorescence intensity has been observed with the sample prepared from 1.1 mM lipid stock containing total 500 μM lipid, compared to that of 750 μM lipid also prepared from the same lipid stock after normalization (Figure A1.7, vsc 1 versus vsc 3). This variation may be due to errors associated with deviations in concentration, and possible differences in mixing more dilute samples of stock solutions. Previous TR-FRET lifetime measurements have shown that liposome crowding affects the conformational ensemble of the CL-bound cyt *c*, decreasing the population of the extensively unfolded species in the presence of higher amounts of protein.[14] Although the samples have been prepared by mixing the protein and lipid solutions at a 1:1 ratio to avoid aggregation, perhaps lowering the total protein and vesicle concentrations also affect how the protein is distributed on the vesicle surface.

Figure A1.7. Steady-state fluorescence measurements of Dns92 horse heart cyt *c*, measured with (A) entrance slit bandpass at 2 nm and exit slit bandpass at 2 nm, or with (B) entrance slit bandpass at 3 nm and exit slit bandpass at 5 nm. Different combinations of slit widths were used to test whether it affected the detected intensity of the fluorophore. Dns fluorophore was excited at 336 nm and its emission recorded from 400 to 600 nm, with a yellow filter in the detection slit to reduce scatter. All solutions, unless otherwise indicated, contained a final protein concentration of 3 μM. Spectra of the protein in the native state were prepared in a 100 mM sodium phosphate buffer at pH 7.4 (black), protein in the unfolded state were prepared in solutions containing 6 M GuHCl in either a 100 mM sodium acetate buffer at pH 4.5 (red) or in a 100 mM sodium phosphate buffer at pH 7.4 (blue). Stock vesicle solutions containing 1.1 mM total lipid was prepared with a microtip sonicator, and stock containing 2.2 mM total lipid prepared with a bath sonicator at high power. Only the 2.2 mM total lipid stock solution was extruded through membranes with a 0.1 μm pore radius. Prior to sonication, lipid solutions were freeze-thawed ice/heat cycles after initial buffer suspension. Vesicle sample prepared from 1.1 mM lipid stock (vsc 1, purple) and sample prepared from 2.2 mM lipid stock (vsc 2, teal) contained 3 μM protein and 750 μM total lipid. To test whether reducing the total protein and lipid concentration decreased the fluorescence intensity of the sample, a sample containing 2 μM protein and 500 μM total lipid were prepared using the 1.1 mM lipid stock and its spectra normalized to 3 μM assuming the fluorescence intensity increases linearly in the 2 to 3 μM range (vsc 3, green).

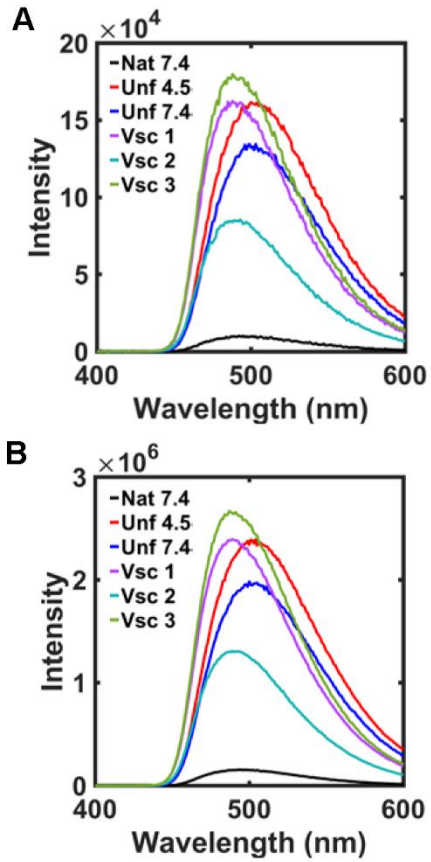
A
×10^4
20
15
10
5
0
Intensity
Nat 7.4
Unf 4.5
Unf 7.4
Vsc 1
Vsc 2
Vsc 3
400
500
600
Wavelength (nm)
B
×10^6
3
2
1
0
Intensity
Nat 7.4
Unf 4.5
Unf 7.4
Vsc 1
Vsc 2
Vsc 3
400
500
600
Wavelength (nm)

These comparisons strongly suggest that the method of vesicle preparation greatly alters the observed fluorescence intensity of the fluorophore and the local protein environments, and when taking measurements across variants, vesicle preparations and lipid concentrations should be consistent to detect differences that arise from polypeptide mutations.

Differences in Protein-to-CL Interactions Across Variants.

Depending on the surface mutations, proteins have local differences at a specific lipid to protein ratios, contributing to the variations observed in the fluorescence intensities of the CL-bound samples. The intensities of the Soret band in the electronic absorption spectra of CL-bound Dns92 cyt *c* vary depending on the relative lipid concentration well above the concentration the protein is fully bound to the CL-containing vesicles (Figure A1.8A). Electronic absorption spectra of the CL-bound cyt *c* are also different at pH 4.5 than at pH 7.4 (Figure A1.9A). For both pH conditions, spectra of proteins with lower lipid-to-protein ratios are different than those with higher lipid-to-protein ratios. While these variations in spectra are less pronounced in WT spectral differences with different lipid-to-protein ratios are more pronounced for variants such as K72A and G41S (Figure A1.8B and C), and more so at lower pH conditions (Figure A1.9B and C). In the absence of CL-containing liposomes, the extinction coefficients of the Soret band from the electronic absorption spectra of K72A and G41S can vary with pH but are not as dramatic (Figures A1.10 and A1.11). Although similar electronic absorption measurements have not been acquired with the Y48H variant, pH-dependent ^{1}H NMR spectra have shown that there also may be a local pH-dependent structural changes in Y48H between pH 7.4 and 4.5 (Figure 3.12A).

Figure A1.8. Electronic absorption spectra of (A) WT, (B) K72A, and (C) G41S horse heart cyt *c* variants with varying concentrations of lipid to protein ratio at 22 ± 2 °C. The samples were prepared in 25 mM HEPES buffer at pH 7.4 and contained 5 μM protein. CL-containing vesicles were composed of 50 % CL and 50 % PC. To avoid aggregation, protein solution and CL-containing solutions were mixed at a 1 to 1 ratio. Samples were incubated for at least 30 min and kept in the dark prior to measurements to avoid heme bleaching. Higher concentrations of liposome ratios were required to obtain WT-like CL-bound spectra for the variants, suggesting some cyt *c* variants may have different properties at low CL/liposome concentrations.

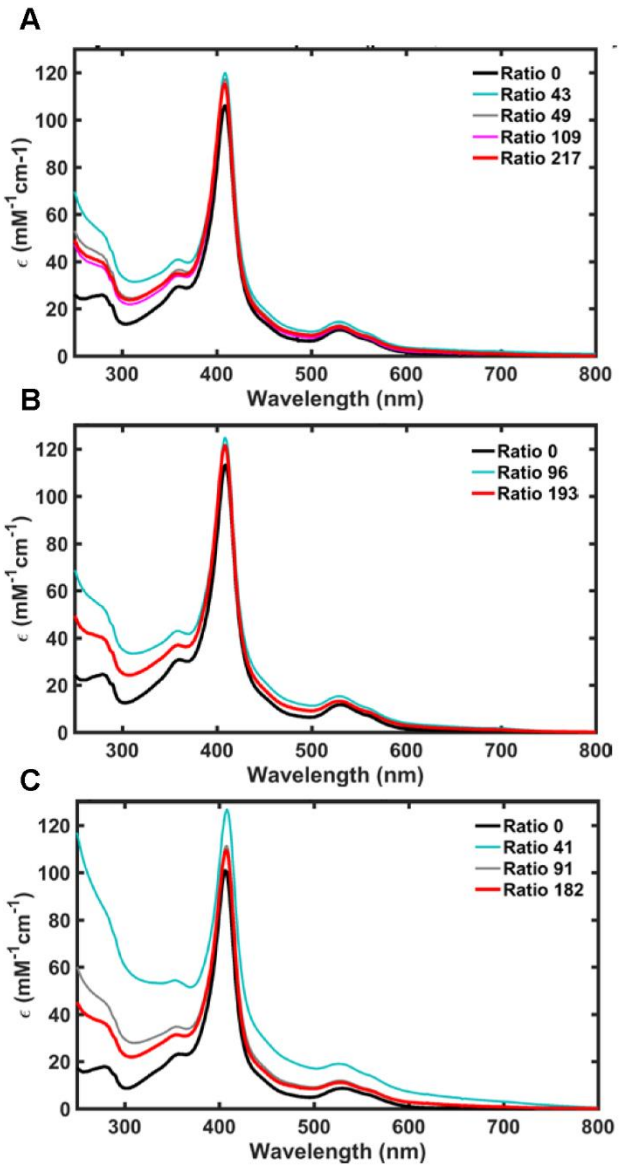
A
Ratio 0
Ratio 43
Ratio 49
Ratio 109
Ratio 217
ϵ (mM-1cm-1)
Wavelength (nm)
B
Ratio 0
Ratio 96
Ratio 193
ϵ (mM-1cm-1)
Wavelength (nm)
C
Ratio 0
Ratio 41
Ratio 91
Ratio 182
ϵ (mM-1cm-1)
Wavelength (nm)

Figure A1.9. Electronic absorption spectra of (A) WT, (B) K72A, and (C) G41S horse heart cyt *c* variants with varying concentrations of lipid to protein ratio at 22 ± 2 °C. The samples were prepared in 25 mM acetate buffer at pH 4.5 and contained 5 μM protein. CL-containing vesicles were composed of 50 % CL and 50 % PC. To avoid aggregation, protein solution and CL-containing solutions were mixed at a 1:1 ratio. Samples were incubated for at least 30 min and kept in the dark prior to measurements to avoid heme bleaching. Higher concentrations of liposome ratios were required to obtain WT-like CL-bound spectra for the variants, suggesting some cyt *c* variants may have different properties at low CL/liposome concentrations.

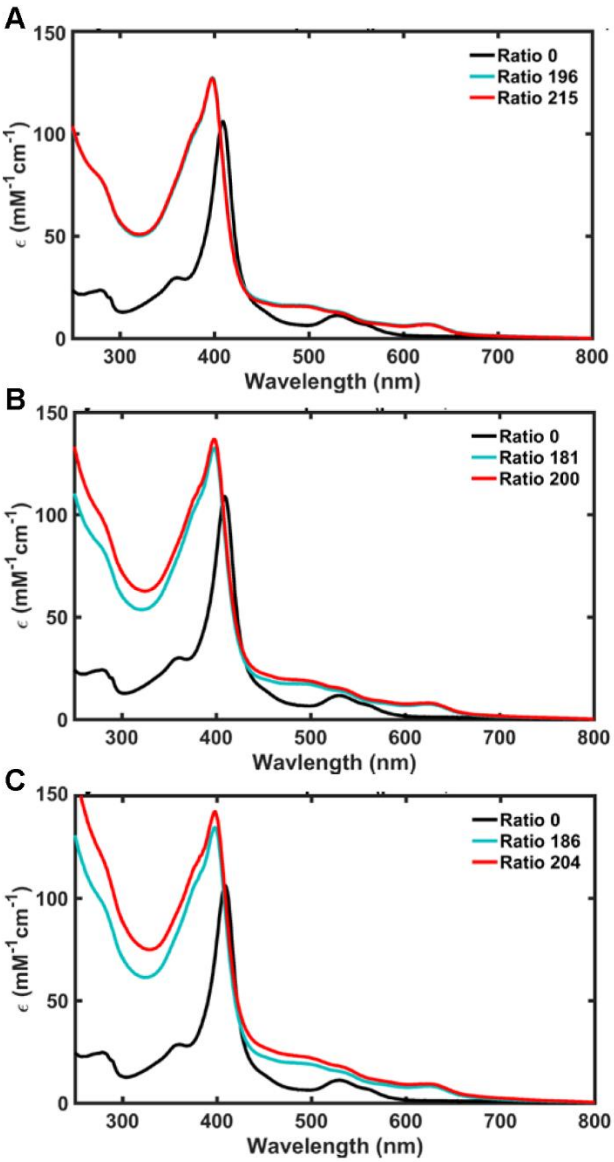
A
Ratio 0
Ratio 196
Ratio 215
ϵ (mM-1cm-1)
Wavelength (nm)
B
Ratio 0
Ratio 181
Ratio 200
ϵ (mM-1cm-1)
Wavlength (nm)
C
Ratio 0
Ratio 186
Ratio 204
ϵ (mM-1cm-1)
Wavelength (nm)

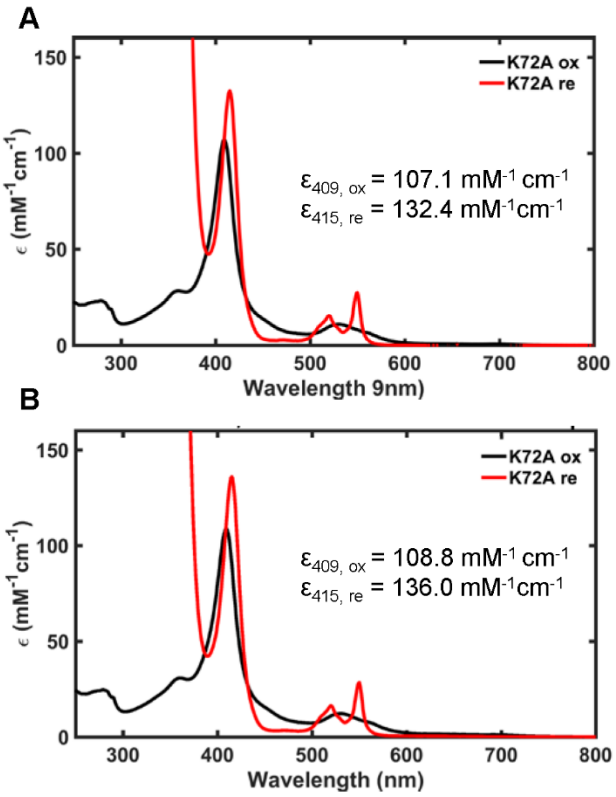

Figure A1.10. Electronic absorption spectra for the ferric (black) and ferrous (red) K72A horse cyt *c* prepared (A) in a 25 mM MES buffer with 1 mM DTPA at pH 6.0, and (B) in a 25 mM acetate buffer with 1 mM DTPA at pH 4.5. Extinction coefficients of the peak of the Soret band are also shown for ferric (ox) and ferrous (re) species.

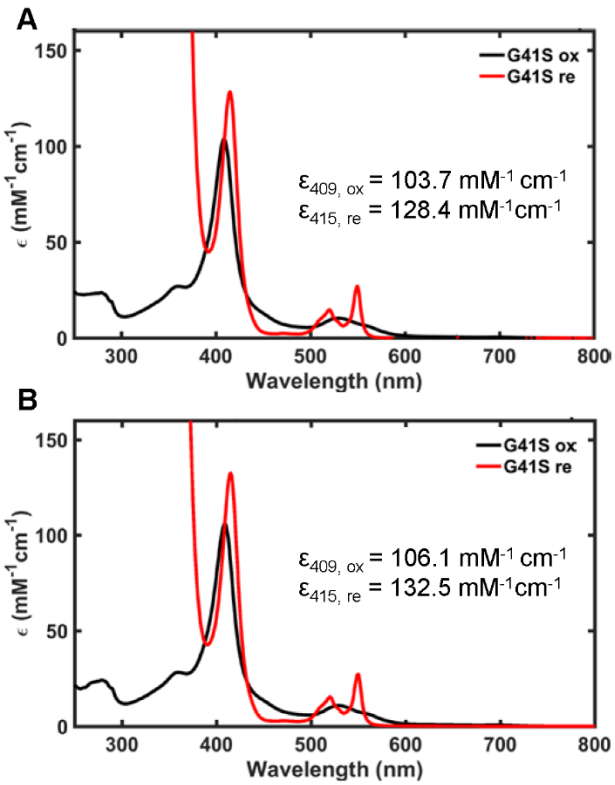

Figure A1.11. Electronic absorption spectra for the ferric (black) and ferrous (red) G41S horse cyt *c* prepared (A) in a 25 mM MES buffer with 1 mM DTPA at pH 6.0, and (B) in a 25 mM acetate buffer with 1 mM DTPA at pH 4.5. Extinction coefficients of the peak of the Soret band are also shown for ferric (ox) and ferrous (re) species.

Unfolded cyt *c* proteins have access to a diverse set of conformations,[6] and local structural perturbations can influence how the protein accesses the diverse conformational ensemble in the unfolded state.[7] Although these structural variations may not be distinguished by the fluorophore when it is placed at residue position 92, it is possible that conformational variations do exist in the CL-bound state, resulting in the differences in the CL-bound electronic absorption spectra.

***Possible Shifts in pH Conditions*.**

Although the pH of GuHCl solutions have been adjusted prior to use, there may have been a shift in the pH conditions during the duration between the sample preparation and measurement. Differences in the steady-state fluorescence spectra of the unfolded species at pH 7.4 and 4.5 are not consistent across various measurements (Figures A1.2, A1.6D, and A1.7) which may suggest a possible shift in pH conditions. This suggests that the differences observed between steady-state fluorescence and TR-FRET measurements may also arise from pH shift in the stock solutions even if they are prepared within the day of use. To test this idea, pH of the samples should be measured after spectroscopic measurements.

Summary and Future Directions

In this Appendix, we have explored how different methods of vesicle preparation affect the intensity of the Dns-labeled protein steady-state fluorescence spectra. Depending on whether the vesicle solution is initially fragmented using a sonication bath or an ultrasonic tip, the method of sonication has altered the fluorescence intensity of the CL-bound cyt *c*. This likely stems from the differences in sonication power applied to the

sample, which can ultimately vary the size distribution of the CL-containing vesicles. Sonication method may not be exact, particularly when the stock lipid solution varies between different experiments. However, the most consistent vesicle stocks are obtained when the stock solutions are prepared in smaller volumes at 2.2 mM total lipid, prepared in sonication baths at high power, and extruded. Furthermore, introduction of heat/ice shock cycles prior to sonification has greatly reduced the amount of scatter observed in the samples. Decreasing the total lipid concentration do not produce reproducible data, and it is likely that there may be differences in lipid incorporation depending on the total lipid concentration. In future experiments, a detailed comparison of the spectra with varied protein-to-lipid ratios may also provide clues to why the differences in observed spectra across variants are observed.

In the initial measurements, vesicle scatter and inconsistencies in the quality of the vesicle stocks may contribute to the differences observed across variants. However, it is most likely that differences in the polypeptide sequence do alter the CL-bound state. The electronic absorption spectra suggests that local changes near the heme is dependent on the relative lipid concentration, and the changes are not uniform across variants. Analysis of initial TR-FRET measurements and steady-state fluorescence spectra raise this possibility, although the differences (if present) are most likely not as readily detectable when the fluorophore is placed in residue position 92. Labeling the fluorophore at residue positions 66 or 39 may provide additional insights, particularly with the surface residue mutations at 41 and 48 that likely affect the local stability of loop C. This would further provide additional insights as to whether local loop C stabilities also affect the conformational heterogeneity in the CL-induced unfolded state.

References

1. Muenzner, J. & Pletneva, E.V. Structural transformations of cytochrome c upon interaction with cardiolipin. *Chem Phys Lipids* **179**, 57-63 (2014).

2. Oellerich, S., Lecomte, S., Paternostre, M., Heimburg, T. & Hildebrandt, P. Peripheral and Integral Binding of Cytochrome c to Phospholipids Vesicles. *The Journal of Physical Chemistry B* **108**, 3871-3878 (2004).

3. Capdevila, D.A. *et al.* Active Site Structure and Peroxidase Activity of Oxidatively Modified Cytochrome c Species in Complexes with Cardiolipin. *Biochemistry* **54**, 7491-7504 (2015).

4. Sinibaldi, F. *et al.* Role of lysines in cytochrome c-cardiolipin interaction. *Biochemistry* **52**, 4578-4588 (2013).

5. Bradley, J.M., Silkstone, G., Wilson, M.T., Cheesman, M.R. & Butt, J.N. Probing a complex of cytochrome c and cardiolipin by magnetic circular dichroism spectroscopy: implications for the initial events in apoptosis. *J Am Chem Soc* **133**, 19676-19679 (2011).

6. Pletneva, E.V., Gray, H.B. & Winkler, J.R. Many faces of the unfolded state: Conformational heterogeneity in denatured yeast cytochrome c. *J Mol Biol* **345**, 855-867 (2005).

7. Colon, W., Wakem, L.P., Sherman, F. & Roder, H. Identification of the predominant non-native histidine ligand in unfolded cytochrome c. *Biochemistry* **36**, 12535-12541 (1997).

8. Diederix, R.E.M., Ubbink, M. & Canters, G.W. Peroxidase activity as a tool for studying the folding of c-type cytochromes. *Biochemistry* **41**, 13067-13077 (2002).

9. Hanske, J. *et al.* Conformational properties of cardiolipin-bound cytochrome c. *P Natl Acad Sci USA* **109**, 125-130 (2012).

10. Krishna, M.M.G., Maity, H., Rumbley, J.N. & Englander, S.W. Branching in the sequential folding pathway of cytochrome c. *Protein Sci* **16**, 1946-1956 (2007).

11. Krishna, M.M.G., Maity, H., Rumbley, J.N., Lin, Y. & Englander, S.W. Order of steps in the cytochrome c folding pathway: Evidence for a sequential stabilization mechanism. *J Mol Biol* **359**, 1410-1419 (2006).

12. Krishna, M.M.G., Lin, Y., Rumbley, J.N. & Englander, S.W. Cooperative omega loops in cytochrome c: Role in folding and function. *J Mol Biol* **331**, 29-36 (2003).

13. Balakrishnan, G. *et al.* A conformational switch to beta-sheet structure in cytochrome c leads to heme exposure. Implications for cardiolipin peroxidation and apoptosis. *J Am Chem Soc* **129**, 504-505 (2007).

14. Hong, Y.N., Muenzner, J., Grimm, S.K. & Pletneva, E.V. Origin of the Conformational Heterogeneity of Cardiolipin-Bound Cytochrome c. *J Am Chem Soc* **134**, 18713-18723 (2012).

15. Karsisiotis, A.I. *et al.* Increased dynamics in the 40-57 Omega-loop of the G41S variant of human cytochrome c promote its pro-apoptotic conformation. *Scientific reports* **6**, 30447 (2016).

16. De Rocco, D. *et al.* Mutations of cytochrome c identified in patients with thrombocytopenia THC4 affect both apoptosis and cellular bioenergetics. *Bba-Mol Basis Dis* **1842**, 269-274 (2014).

17. Brinkley, M. A brief survey of methods for preparing protein conjugates with dyes, haptens and crosslinking reagents. *Bioconjugate Chemistry* **3**, 2-13 (1992).

18. Lakowicz, J.R. *Principles of Fluorescence Spectroscopy*, Edn. 2nd. (Kluwer Academic/ Plenum, New York; 1999).

19. Hao, Z.Y. *et al.* Specific ablation of the apoptotic functions of cytochrome c reveals a differential requirement for cytochrome c and apaf-1 in apoptosis. *Cell* **121**, 579-591 (2005).

20. Patel, C.N., Lind, M.C. & Pielak, G.J. Characterization of horse cytochrome c expressed in Escherichia coli. *Protein expression and purification* **22**, 220-224 (2001).

21. Muenzner, J., Toffey, J.R., Hong, Y.N. & Pletneva, E.V. Becoming a Peroxidase: Cardiolipin-Induced Unfolding of Cytochrome c. *J Phys Chem B* **117**, 12878-12886 (2013).

22. Vincelli, A.J. *et al.* Recombinant Expression, Biophysical Characterization, and Cardiolipin-Induced Changes of Two Caenorhabditis elegans Cytochrome c Proteins. *Biochemistry* **52**, 653-666 (2013).

23. Snider, E.J., Muenzner, J., Toffey, J.R., Hong, Y.N. & Pletneva, E.V. Multifaceted Effects of ATP on Cardiolipin-Bound Cytochrome c. *Biochemistry* **52**, 993-995 (2013).

24. Hammack, B., Godbole, S. & Bowler, B.E. Cytochrome c folding traps are not due solely to histidine-heme ligation: direct demonstration of a role for N-terminal amino group-heme ligation11Edited by P. E. Wright. *J Mol Biol* **275**, 719-724 (1998).

25. Jost, P.C. & Griffith, O.H. *Lipid-protein interactions*. (Wiley, New York; 1982).

26. Marsh, D. Thermodynamics of phospholipid self-assembly. *Biophysical journal* **102**, 1079-1087 (2012).

Appendix II

Characterization of the Heterogeneous Conformational Ensemble in Cytochrome *c*

Introduction

Cyt *c* has a diverse conformational landscape in the unfolded state, where the unfolded polypeptide chain deviates from random-coil behavior and is driven by tertiary hydrophobic interactions.[1] Some of these diverse conformations are readily stabilized when the axial ligand of the heme is misligated with endogenous His residues to form the bisHis-ligated species that differ in stability and local dynamics.[2-4]. These bisHis-ligated species are readily observed in the presence of denaturants, such as GuHCl,[4] SDS,[5] and CL.[6]

Understanding the properties of these misligated states is essential, particularly in studying variants that introduce His mutations in the polypeptide chain. Presence of these misligated states may alter the conformational ensemble of the protein in the unfolded state. To test whether His-containing variants stabilize a different set of misligated states compared to those in WT, preliminary studies with Y48H and Y67H variants are presented in this Appendix. Fluorescence intensities of Trp59, an internal fluorophore buried inside the heme cavity in the native Met-ligated, folded state, have been measured and compared to the spectra of the protein in the unfolded states at pH 7.4 and 4.5 for the Y48H and Y67H variants of horse heart cyt *c*. Preliminary characterization of H26N is presented, with recommendations of future studies that can be performed.

Materials and Methods

General. All aqueous solutions were prepared using water from Barnstead E-Pure Ultrapure Water Purification System, purified to a resistivity of 18 MΩ·cm. Reagents and columns were purchased from Millipore Sigma and GE Healthcare, unless noted otherwise.

Gas-tight Hamilton syringes were used for quantitative dilutions. pH was adjusted using sodium hydroxide or hydrochloric acid and monitored with an AB15 pH meter (Fisher Scientific) or a UB10 pH meter (Denver Instrument). All buffers were freshly prepared and filtered prior to use.

Site-Directed Mutagenesis, Protein Expression, and Purification. Point mutations, protein expression and purification for horse heart cyt *c* variants were performed as previously described.[7] Desired substitutions were introduced in the pBTR plasmid encoding horse heart cyt *c* using a QuikChange kit (Agilent) and confirmed by DNA sequencing as well as MALDI of the purified protein samples at the Molecular Biology & Proteomics Core Facility (Dartmouth College). Extinction coefficients of H26N were determined using hemochrome assays[8] in a 100 mM sodium phosphate buffer at pH 7.4, in a 25 mM MES buffer with 1 mM DTPA at pH 6.0, or in a 25 mM acetate buffer with 1 mM DTPA at pH 4.5.

Spectroscopic Measurements. All spectroscopic measurements were obtained at room temperature (22 ± 2 ºC). Electronic absorption spectra were recorded using an Agilent 8453 diode-array spectrophotometer. Fluorescence spectra were measured on a Horiba Jobin Yvon Fluorolog-3 spectrofluorometer equipped with an automatic polarizer, using a quartz cuvette with a 4 mm pathlength in the direction of the exit slit and 10 mm pathlength in the direction of the entrance slit. Ferric proteins were freshly prepared with excess potassium ferricyanide and purified by size exclusion (PD-10 desalting column) or ion-exchange (Sepharose HP SP) chromatography prior to spectroscopic measurements. GuHCl solutions were prepared from dissolving ultrapure GuHCl (Alfa Aesar) in a 100 mM sodium phosphate buffer at pH 7.4 or a 100 mM sodium acetate buffer at pH 4.5, with pH

readjusted and filtered prior to use. Stock GuHCl solutions were used within a week of preparation.

Steady-State Fluorescence of Trp59. Samples were prepared from freshly oxidized stock protein solutions and diluted to protein concentrations within 8 and 9 μM using a 100 μl Hamilton syringe. Samples used for measuring the fluorescence signals in the folded native state were diluted in a 100 mM sodium phosphate buffer at pH 7.4. Samples used for measuring the fluorescence signals in the denatured state were diluted in a solution containing 6 M GuHCl. Samples were allowed to equilibrate in the dark for at least 30 minutes prior to measurements.

Intrinsic tryptophan (Trp59) was excited at 290 nm and its emission was recorded at 300 to 400 nm with entrance slit bandpass at 5 nm and exist slit bandpass at 3 nm. Spectrum of the solution containing the corresponding buffers were subtracted from the spectra of the samples containing protein. Spectra were normalized to 9 μM after measuring the electronic absorption spectra of the protein samples in 100 mM sodium phosphate buffer at pH 7.4. Concentrations were calculated using the extinction coefficient from the electronic absorption of the Soret band at λ_{max} (ε_{409} = 106 $mM^{-1}\cdot cm^{-1}$ for WT,[9] ε_{408} = 117.4 $mM^{-1}\cdot cm^{-1}$ for Y67H, and ε_{407} = 117.1 $mM^{-1}\cdot cm^{-1}$ for Y48H).

Preparation of CL-Containing Liposome Vesicles. All lipids were obtained from Avanti Polar Lipids, Inc., and vesicles were prepared using the extruder apparatus equipped with an enclosed warmer (Eastern Scientific LLC) and membranes (Eastern Scientific LLC) with pore radius of 0.1 μm. TOCL and DOPC were mixed in a 1 to 1 molar ratio for a total of 2.2 mM, and vesicles were prepared by extrusion as previously described.[10] Prior to extrusion, resuspended vesicle solutions were fragmented using a sonication bath in a short

3 to 5 minute cycles for a total of 25 minutes, until the solution cleared slightly. Lipids were in a freshly prepared 25 mM HEPES buffer at pH 7.4 containing 0.1 mM DTPA. Buffers were treated with a Chelex resin (Sigma) to remove excess metal ions in solution prior to use. Lipid vesicle solutions were used within the day and filtered through a 0.45 μm syringe filter to remove any titanium dust that may have been introduced during extrusion. Vesicle sizes and distributions were determined using dynamic light scattering (DLS) instrument (Wyatt Technologies).

CL-Binding Assays. Solutions containing total lipid concentrations ranging from 40 to 500 μM were mixed with 10 μM ferric protein in a 1:1 (*v*/*v*) ratio. Samples were incubated at room temperature and under foil for at least 30 minutes and was centrifuged for 1 to 1.5 hours using a Beckman Airfuge tabletop ultracentrifuge with a Beckman A-11 motor at 120 000 × *g*. Immediately after centrifugation, electronic absorption spectra of the supernatant were measured and the absorption at the λ_{max} of the Soret band was used to determine the amount of protein left in solution.

Results and Discussion

In the folded, Met-ligated (native) state, the polypeptide chain of WT cyt *c* is tightly packed around the heme,[11] and Trp59, a residue with fluorescent properties in the 60's helix, in kept in close proximity to the heme. The heme moiety can quench the fluorescence of Trp59,[12, 13] and in the native, folded state where Trp59 is close to the heme, the observed emission of Trp59 is minimal (Figure A2.1A). Unfolding of the polypeptide increases the distance between Trp59 and the heme, and fluorescence intensity of Trp59 is observed at a greater intensity (Figure A2.1A). Similar changes are observed with both Y67H and Y48H (Figures A2.1B and C).

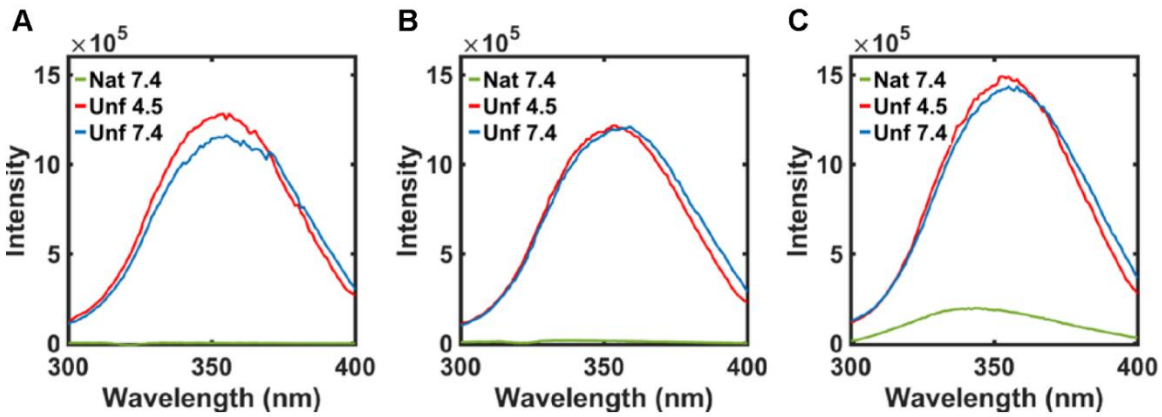

Figure A2.1. Steady-state fluorescence spectra measuring the Trp59 emission (λ_{ex} = 290 nm) for (A) WT, (B) Y67H, and (C) Y48H variants of horse heart cyt *c* at 22 ± 2 °C. Spectra were measured with entrance slit bandpass at 5 nm and exit slit bandpass at 3 nm. Protein samples for the native state were in a 100 mM sodium phosphate buffer at pH 7.4 (green), for the unfolded state were in either a 100 mM sodium acetate buffer at pH 4.5 (red) or a 100 mM sodium phosphate buffer at pH 7.4 (blue) containing 6 M GuHCl. Spectra were normalized to 9 µM protein assuming a linear relationship between fluorescence intensity and concentration at these experimental conditions. Actual samples contained 8.5 µM for WT, 8.3 µM for Y67H, and 8.9 µM for Y48H.

Despite similar trends when comparing between folded and unfolded states, differences are observed across variants.

Fluorescence Intensity in the Folded State.

In the native state at pH 7.4, the fluorescence intensity of Y48H is much higher than that of Y67H or WT (Figure A2.1). This difference in Trp59 fluorescence suggests that the distance between the Trp59 and the heme is increased in Y48H than in Y67H and WT at this pH, and Y48H mutation affects the polypeptide packing of the 60's helix to the heme differently than in other variants at pH 7.4. In contrast, the fluorescence intensity of folded Y67H at pH 7.4 is comparable to that of WT (Figure A2.1A and B).

Fluorescence Intensity in the Unfolded State.

Differences between the Y48H and Y67H variants are more pronounced in the unfolded state. In WT, fluorescence intensity of the unfolded state at pH 7.4 is slightly lower than at pH 4.5 (Figure A2.1A). In comparison, such differences are not observed in Y67H and Y48H variants at similar denaturing conditions (Figures A2.1B and C), as the Trp59 fluorescence intensities are similar at both pH 7.4 and 4.5. Furthermore, fluorescence intensity of Trp59 is much higher for Y48H than for Y67H or WT (compare Figures A2.1C to A2.1A and B). It is puzzling that the fluorescence intensity of Y67H at pH 7.4 is not lower than that of WT, as His67/His18 ligated heme species is expected to form. Additional studies are required to probe if there are differences in the conformational ensemble of the unfolded state between WT and Y67H, and if the distance between Trp59 and the heme is not sensitive to the formation of the 49-residue loop that forms upon ligation of His67 to the heme iron. However, higher fluorescence intensity of Trp59 in Y48H suggests that

generally, Trp59 is farther away from the heme than in WT or Y67H at pH 7.4 and 4.5. This difference in the spectra raises the possibility that the conformation of the protein in the unfolded state is different between Y48H and Y67H or WT.

Conformers with bisHis-ligated hemes in the unfolded protein have different characteristics depending on which endogenous His residue coordinates to the heme. Although both His26 and His33 are located in the loosely structured 20's loop, His33 is the preferred heme ligand over His26.[4] Previous mutational studies have shown that, the pK_a of His-ligand dissociation from the heme iron and stabilities of the residual structures depended on the location of the His residue in the polypeptide, suggesting that certain parts of the protein have a higher affinity for the heme and deviates from random coil behavior.[2, 14] Thus, it is likely that Y67H and Y48H also have different stabilized misligated conformers compared to that of WT.

Differences in local tertiary hydrophobic interactions could also play a role in the unfolded state. TR-FRET measurements with fluorophore-labeled yeast cyt *c* detected an ensemble with compact or extended polypeptide packing in the unfolded state.[1] These compact structures are formed even in the absence of His misligation, and its formation has been argued to be driven by tertiary hydrophobic interactions.[1] In the native state, tertiary interactions near the heme are varied depending on the species. Perhaps, differences in tertiary contacts also play a role in the unfolded state for our variants where Tyr is replaced with His, two residues with different hydrophobicity.[15]

Preliminary studies with His26Asn.

To test whether His residues at positions 67 and 48 compete with His residues in 26 and 33, studies with variants containing only His67 or His48 are required. Previously, variants containing H26N and H33N have been studied in yeast cyt *c*,[2] while variants containing H26Q or H33N have been studied in horse cyt *c*.[4] His26 forms a hydrogen bond with Pro44 and is argued to play an important role in structure and stability,[16, 17] and we wanted to see whether there are differences when His26 with either Asn or Gln by first studying the H26N variant in horse heart cyt *c*. In H26N horse heart cyt *c*, the electronic absorption spectra at pH 7.4 to 4.5 are very much like that of WT, with the peak of the Soret band at 409 nm (Figure A2.2). However, slight variations are observed in the extinction coefficients in both the ferric and ferrous species, suggesting differences in the heme environment. Further studies are required to confirm if having H26Q or H26N in horse heart cyt *c* alters the dynamic features of the loop, and whether the choice of H26 mutation influences the formation of bisHis-ligated heme species with His67 or His48.

Differences in the CL-bound State

Previously, possible variations in the CL-bound state have been observed in apoptotic peroxidase studies with Y67H (Chapter 7). Comparing the apoptotic peroxidase activity of Y67H variant with that of H26N/H33N/Y67H variant would be helpful in clarifying whether the suppressed apoptotic peroxidase activity is due to the His67-ligated heme species. Binding of H26N to CL-containing liposome vesicles is similar to that of WT (Figure A2.3). Electronic absorption spectra of CL-bound H26N horse heart cyt *c* are also comparable to that of WT in high CL ratio conditions (at ratios > 110) at pH 7.4 and 4.5 (compare Figures A2.4 to A1.8A and A1.9A).

Figure A2.2. Electronic absorption spectra for the ferric (black) and ferrous (red) H26N variant of horse heart cyt *c* (A) in a 100 mM sodium phosphate buffer at pH 7.4, (B) in a 25 mM MES buffer with 1 mM DTPA at pH 6.0, and (C) in a 25 mM acetate buffer with 1 mM DTPA at pH 4.5. Extinction coefficients at the λ_{max} of the Soret band are also shown for ferric (ox) and ferrous (re) species.

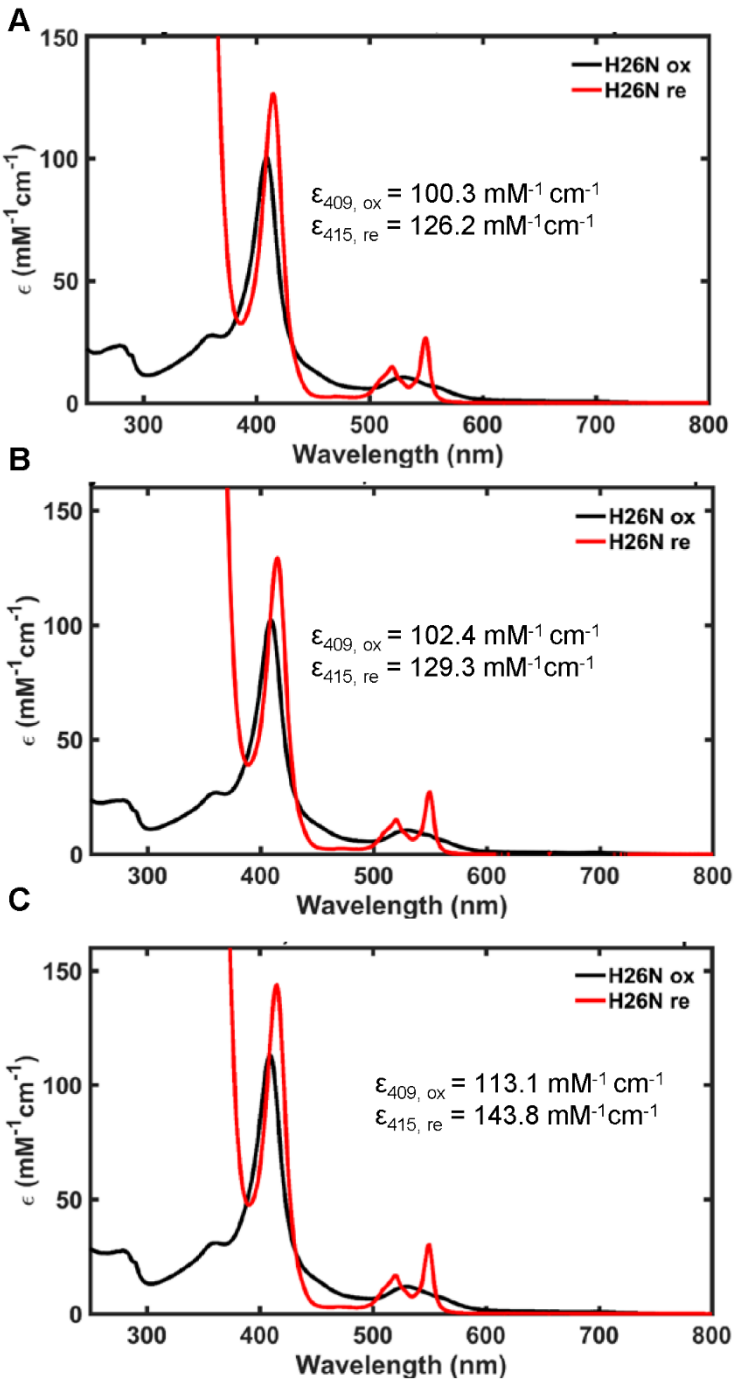
A
H26N ox
H26N re
$\varepsilon_{409,\ ox}$ = 100.3 $mM^{-1}\ cm^{-1}$
$\varepsilon_{415,\ re}$ = 126.2 $mM^{-1}cm^{-1}$
$\epsilon\ (mM^{-1}cm^{-1})$
Wavelength (nm)
B
H26N ox
H26N re
$\varepsilon_{409,\ ox}$ = 102.4 $mM^{-1}\ cm^{-1}$
$\varepsilon_{415,\ re}$ = 129.3 $mM^{-1}cm^{-1}$
$\epsilon\ (mM^{-1}cm^{-1})$
Wavelength (nm)
C
H26N ox
H26N re
$\varepsilon_{409,\ ox}$ = 113.1 $mM^{-1}\ cm^{-1}$
$\varepsilon_{415,\ re}$ = 143.8 $mM^{-1}cm^{-1}$
$\epsilon\ (mM^{-1}cm^{-1})$
Wavelength (nm)

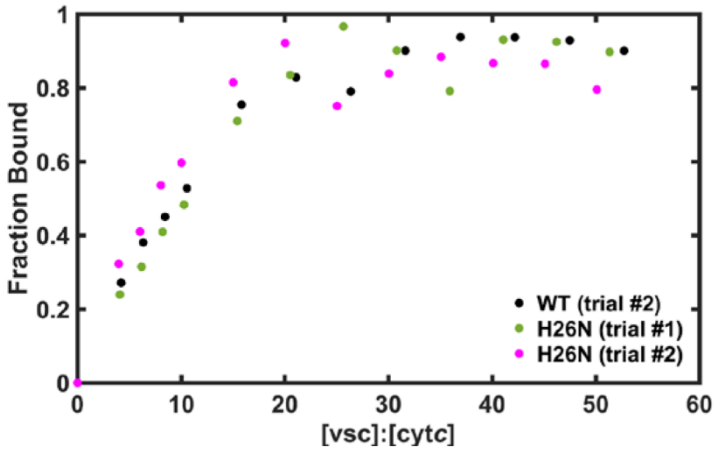

Figure A2.3. A lipid binding assay plot of horse heart cyt *c* variants ([cyt *c*] = 5 μM) with 50 % CL, 50 % PC vesicles, in a 25 mM HEPES +0.1 mM DTPA buffer at pH 7.4 and 22 ± 2 ºC. Shown are the fraction of bound protein in respect to ratio of vesicle to protein concentration for ferric WT (black dots) and H26N (green and pink dots) variants.

Figure A2.4. Electronic absorption spectra of H26N variant of horse heart cyt *c* with varying concentrations of lipid to protein ratio at (A) pH 7.4 and (B) pH 4.5, measured at 22 ± 2 °C. The samples were prepared either in a 25 mM HEPES buffer at pH 7.4 or in a 25 mM acetate buffer at pH 4.5 and contained 5 μM protein. CL-containing vesicles were composed of 50 % CL and 50 % PC. To avoid aggregation, protein solution and CL-containing solutions were mixed at a 1 to 1 ratio. Samples were incubated for at least 30 min and kept in the dark prior to measurements to avoid heme bleaching. Higher concentrations of lipid to protein ratios were required to obtain CL-bound spectra similar to that of WT for the variants, suggesting some cyt *c* variants may have different properties at low CL/total lipid concentrations. Order of mixing (whether adding the protein solution into the vesicle solution of vice versa) did not alter the spectral features of the protein.

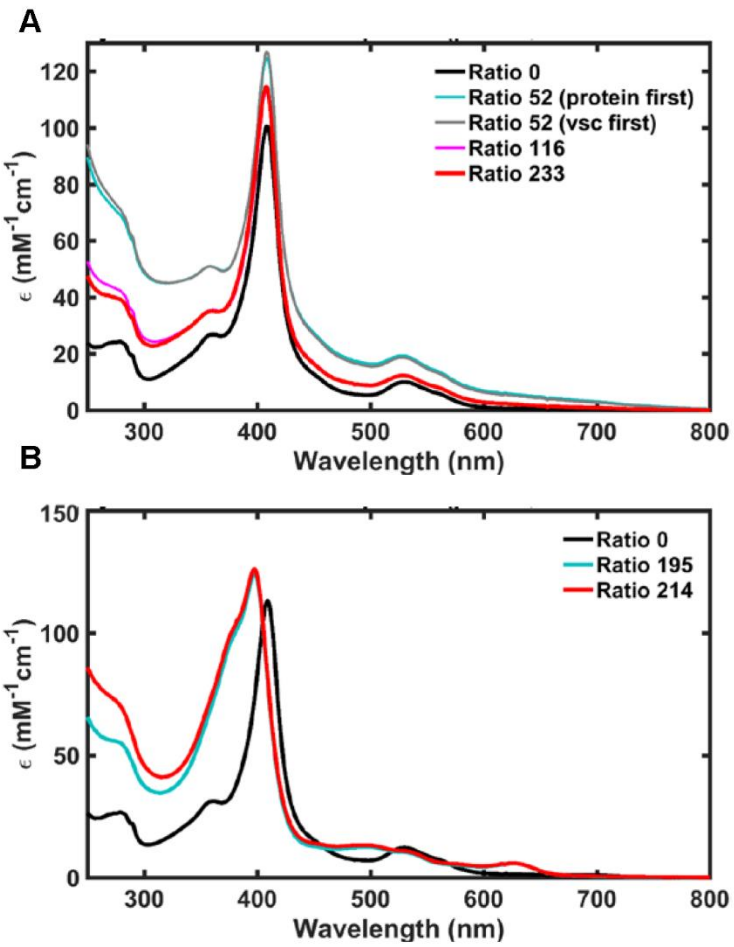
A
Ratio 0
Ratio 52 (protein first)
Ratio 52 (vsc first)
Ratio 116
Ratio 233
ϵ (mM-1cm-1)
Wavelength (nm)
B
Ratio 0
Ratio 195
Ratio 214
ϵ (mM-1cm-1)
Wavelength (nm)

Although differences are observed at lower CL ratios (at ratios < 110) at pH 7.4, differences are not observed between WT and H26N at CL-to-protein ratio content used for CL-bound peroxidase activities (compare Figure A2.4A to A1.8A). These spectral comparisons suggest that H26N is a good background mutation to clarify whether bisHis-species dominates the CL-bound peroxidase activity of Y67H variant at higher pH conditions.

Summary and Future Directions

Steady-state Trp59 fluorescence measurements show that fluorescence intensities for Y48H are higher than that of Y67H or WT in both the folded and the unfolded state (Figure A2.1), suggestive of varying distances between Trp59 and the heme at identical conditions. Perhaps polypeptide packing in the native state and the unfolded conformation(s) are different depending on where the additional His residue is introduced in the polypeptide. To assess differences in the accessed unfolded states with the variants, further studies will be required with H26N/H33N containing variants. The *N*-terminal amino group has also been shown to coordinate to the heme in the unfolded state in yeast cyt *c*.[18] In horse heart cyt *c*, it is likely that similar treatment would not be necessary. Comparison of pK_a values for His26/33 dissociation in 100% and 70% *N*-acetylated horse heart cyt *c* WT proteins is similar, and has been argued that the *N*-terminal group is not a major contributor to the formation of the misligated species.[4]

To assess whether different misligated species forms in the unfolded state for the variants compared to that of WT, pH titrations can be performed with H26N/H33N/Y67H and H26N/H33N/Y48H variants. WT, H26N, H33N, and H26N/H33N variants can be used as control.

Previous pH titrations with unfolded Y67H have suggested that Y67H is also a substantial contributor in forming the bisHis-ligated species. Similar pH titration experiments will provide clues as to whether the His residue, or a water/OH^- couple, coordinates to the heme. If the nonnative His residues coordinate to the heme, which can be observed by a shift in the pK_a of His-ligand dissociation compared to that of H26N/H33N, the local kinetic properties in forming these bisHis-ligated states can be obtained. The kinetics of His-ligation association (k_f) and dissociation (k_b) can be obtained by performing pH jumps and monitoring the Soret band using stopped-flow kinetics. This would allow one to characterize the biophysical properties of the conformations in the unfolded state that are not readily stabilized in WT cyt *c*.

Since the fluorescence intensities are different for Y48H in the folded state and for both Y48H and Y67H in the unfolded state, TR-FRET lifetime measurements can be obtained for the variants. A Dns fluorophore can be covalently attached to residue positions 39 and 50, which has been previously selected to monitor the conformational heterogeneity of the unfolded state in both GuHCl and CL-containing vesicles.[1, 7] Although position 66 has also been previously labeled with Dns fluorophore,[7] this position is adjacent to Y67H and may artificially impede the formation of bisHis-ligated species by His67. If His67 or His48 forms misligated species, the conformational ensemble of the unfolded state should be different compared to the H26N/H33N variant. Dns-labeled H26N/H33N/Y67H and H26N/H33N/Y48H variants can be compared to Y67H and Y48H variants to see whether the His residues in His67 or His48 can compete with either of the naturally occurring His residues. This would be of particular interest to His48, as this mutation likely perturbs the tertiary packing of the 20's loop that contains both His26 and His33, and is implicated in

disease.[19] Such measurements would also help clarify the differences in Dns92 fluorescence observed in Appendix I.

Studies outlined in Chapter 7 with Y67H have suggested that the bisHis-species formed in the CL-bound state and suppresses the CL-bound peroxidase activity of the protein at higher pH conditions. The role of bisHis species can further be tested by performing similar pH-dependent peroxidase activity assays comparing H26N/H33N and H26N/H33N/Y67H to that of WT and Y67H. Had placement of Y67H formed more bisHis-ligated species, lower peroxidase activity should be observed for H26N/H33N/Y67H variant than in H26N/H33N at pH conditions above the measured pK_a of His-ligand dissociation in the unfolded state state. Similar comparisons can be made with Y48H-containing variants, which would provide further insight into how the loop C perturbation near the 20's loop affect dynamics and peroxidase activity, and test whether similar species appear in the CL-bound state. Since Y48H mutation is naturally found in humans, such experiments would also help elucidate how the mutation affects the apoptotic peroxidase activity.

References

1. Pletneva, E.V., Gray, H.B. & Winkler, J.R. Many faces of the unfolded state: Conformational heterogeneity in denatured yeast cytochrome c. *J Mol Biol* **345**, 855-867 (2005).

2. Godbole, S. & Bowler, B.E. A histidine variant of yeast iso-1-cytochrome c that strongly affects the energetics of the denatured state. *J Mol Biol* **268**, 816-821 (1997).

3. Godbole, S., Hammack, B. & Bowler, B.E. Measuring denatured state energetics: deviations from random coil behavior and implications for the folding of iso-1-cytochrome c. *J Mol Biol* **296**, 217-228 (2000).

4. Colon, W., Wakem, L.P., Sherman, F. & Roder, H. Identification of the predominant non-native histidine ligand in unfolded cytochrome c. *Biochemistry* **36**, 12535-12541 (1997).

5. Oellerich, S., Wackerbarth, H. & Hildebrandt, P. Spectroscopic Characterization of Nonnative Conformational States of Cytochrome c. *The Journal of Physical Chemistry B* **106**, 6566-6580 (2002).

6. Oellerich, S., Lecomte, S., Paternostre, M., Heimburg, T. & Hildebrandt, P. Peripheral and Integral Binding of Cytochrome c to Phospholipids Vesicles. *The Journal of Physical Chemistry B* **108**, 3871-3878 (2004).

7. Hanske, J. *et al.* Conformational properties of cardiolipin-bound cytochrome c. *P Natl Acad Sci USA* **109**, 125-130 (2012).

8. Patel, C.N., Lind, M.C. & Pielak, G.J. Characterization of horse cytochrome c expressed in Escherichia coli. *Protein expression and purification* **22**, 220-224 (2001).

9. Margoliash, E. & Frohwirt, N. Spectrum of horse-heart cytochrome c. *Biochem J* **71**, 570-572 (1959).

10. Muenzner, J., Toffey, J.R., Hong, Y.N. & Pletneva, E.V. Becoming a Peroxidase: Cardiolipin-Induced Unfolding of Cytochrome c. *J Phys Chem B* **117**, 12878-12886 (2013).

11. Bushnell, G.W., Louie, G.V. & Brayer, G.D. High-resolution three-dimensional structure of horse heart cytochrome c. *J Mol Biol* **214**, 585-595 (1990).

12. Lakowicz, J.R. *Principles of Fluorescence Spectroscopy*, Edn. 2nd. (Kluwer Academic/ Plenum, New York; 1999).

13. Moore, G.R. & Pettigrew, G.W. *Cytochromes c : evolutionary, structural, and physicochemical aspects*. (Springer-Verlag, Berlin ; New York; 1990).

14. Hammack, B.N., Smith, C.R. & Bowler, B.E. Denatured state thermodynamics: residual structure, chain stiffness and scaling factors. *J Mol Biol* **311**, 1091-1104 (2001).

15. Rose, G., Geselowitz, A., Lesser, G., Lee, R. & Zehfus, M. Hydrophobicity of amino acid residues in globular proteins. *Science* **229**, 834-838 (1985).

16. Balakrishnan, G. *et al.* A conformational switch to beta-sheet structure in cytochrome c leads to heme exposure. Implications for cardiolipin peroxidation and apoptosis. *J Am Chem Soc* **129**, 504-505 (2007).

17. Qin, W., Sanishvili, R., Plotkin, B., Schejter, A. & Margoliash, E. The role of histidines 26 and 33 in the structural stabilization of cytochrome c. *Biochim Biophys Acta* **1252**, 87-94 (1995).

18. Hammack, B., Godbole, S. & Bowler, B.E. Cytochrome c folding traps are not due solely to histidine-heme ligation: direct demonstration of a role for N-terminal amino group-heme ligation11Edited by P. E. Wright. *J Mol Biol* **275**, 719-724 (1998).

19. De Rocco, D. *et al.* Mutations of cytochrome c identified in patients with thrombocytopenia THC4 affect both apoptosis and cellular bioenergetics. *Bba-Mol Basis Dis* **1842**, 269-274 (2014).